
**METALS
AND SUPERCONDUCTORS**

Structure and Physical Properties of Titanium Diselenide Intercalated with Nickel

V. G. Pleschev¹, N. V. Toporova¹, A. N. Titov², and N. V. Baranov^{1,2}

¹ Ural State University, pr. Lenina 51, Yekaterinburg, 620083 Russia

e-mail: valery.pleschov@usu.ru, nadya.toporova@usu.ru

² Institute of Metal Physics, Ural Division, Russian Academy of Sciences, ul. S. Kovalevskoi 18, Yekaterinburg, 620219 Russia

Received November 5, 2003

Abstract—The structure, electrical resistivity, thermopower, and magnetic susceptibility of titanium diselenide intercalated with nickel (Ni_xTiSe_2) are studied systematically in the nickel concentration range $x = 0\text{--}0.5$. In accordance with a model proposed earlier, strong hybridization of the $\text{Ni}3d/\text{Ti}3d$ states is observed, giving rise to suppression of the magnetic moment because of delocalization of the nickel d electrons. It is shown that the strain caused by the $\text{Ni}3d/\text{Ti}3d$ hybridization does not change the local coordination of a titanium atom. © 2004 MAIK “Nauka/Interperiodica”.

1. INTRODUCTION

It was shown in [1, 2] that intercalation of titanium diselenide with transition and noble metals brings about the formation of an impurity band of hybridized $M3d/\text{Ti}3d$ states (M is an intercalated metal). This situation differs radically from the well-studied case of intercalation with alkali metals, where the electrons introduced with an intercalant remain free (metal with a variable Fermi level) [3, 4]. It has been established that this difference is due to the difference in the ionization potential of intercalated impurities. Hybridization of the valence states of an impurity with the $3d$ states of titanium occurs in all cases; however, if the ionization potential of an impurity is lower than a critical value, the hybridized states are significantly higher than the Fermi level and have no effect on the properties of the material [5]. If the ionization potential of an impurity exceeds the critical value, the crystal lattice undergoes compression along the normal to the plane of basal TiSe_2 layers [5], the density of free charge carriers decreases or vanishes [1], the magnetic moment of the impurity is suppressed [6], etc. These experimental observations can be explained in terms of $\text{Ti}\text{--}M\text{--}\text{Ti}$ covalent centers, which act as free-electron traps and cause deformation of the host lattice [5]. It has been found that the degree of localization of conduction electrons on these centers and the degree of lattice deformation are proportional to each other and determined by the position of the impurity band with respect to the Fermi level [1].

The Ni_xTiSe_2 system was first synthesized in the 1970s [7]. The concentration dependences of the unit cell parameters presented in [7] show that the compression strain along the normal to the TiSe_2 layer plane is the highest among all transition-metal compounds studied to date. Therefore, one might expect that this mate-

rial will exhibit all properties characteristic of intercalation compounds with an impurity band lying below the Fermi level. However, the electrical and magnetic properties of Ni_xTiSe_2 and its fine structural features (the Ni atom position, the effect of intercalation on the positions of host atoms, etc.) remain poorly studied. In this work, we performed a detailed study of the atomic structure, resistivity, thermopower, and magnetic susceptibility of Ni_xTiSe_2 .

2. EXPERIMENTAL

Ni_xTiSe_2 samples ($0 < x < 0.5$) were obtained from the following elements using the conventional method of synthesis in an ampoule: titanium (purified by iodide distillation) of 99.99% purity (Aldrich 30.581-2), OSCh-19-5-grade selenium of 99.999% purity, and electrolytic nickel of 99.95% purity. First, titanium diselenide was sintered at 900°C over one week. Then, the material obtained was ground and, after mixing with the corresponding amount of powdered nickel, was pressed and again annealed at 800°C over one week. The sintering temperature was taken lower than the temperature of synthesis of the host compound in order to prevent the substitution of nickel for titanium. Since the material obtained after this annealing was inhomogeneous, it was again ground, pressed, and subjected to annealing. After this procedure, the material generally became sufficiently homogeneous. In [7], it was shown that several different superstructures can form in the material; however, the thermal history of the samples was not detailed. In order to prevent the influence of the ordering of nickel on the physical properties of the material, the samples were quenched from the temperature of the last homogenizing annealing (800°C).

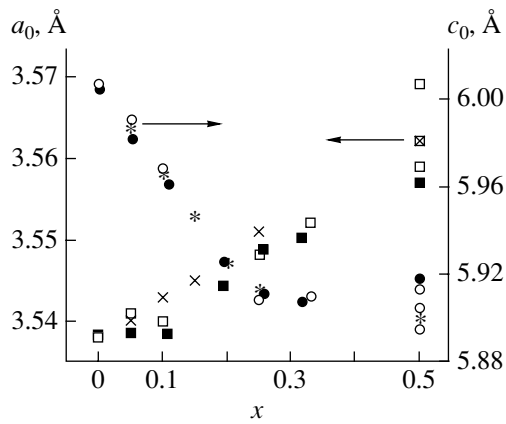


Fig. 1. Concentration dependences of the unit cell parameters a_0 and c_0 of Ni_xTiSe_2 . Filled symbols are data from this work, and open symbols, crosses, and asterisks are data from [7], where the results obtained at two different laboratories are summarized. (The differences between the results are due to the different preparation conditions of the samples.)

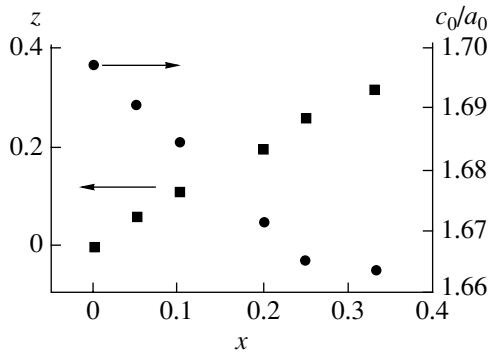


Fig. 2. Dependences of the ratio c_0/a_0 and the coordinate z of the Se atom along the c axis on the nickel concentration.

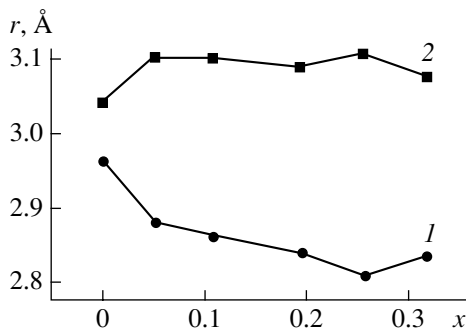


Fig. 3. Dependences of (1) the van der Waals gap width and (2) the Se-Ti-Se layer width on the nickel content in Ni_xTiSe_2 .

X-ray diffraction studies were performed on powder samples using a DRON-4-13 diffractometer (plane graphite monochromator, $\text{CoK}\alpha$ radiation, step 0.01° ,

angle range 14° – 80°). The structural characteristics of Ni_xTiSe_2 were calculated using the method of full-profile refinement of x-ray diffraction patterns (the GSAS software package [8]). The lattice parameters calculated by us agree with the available literature data [7], which indicates the high quality of the material studied by us. The magnetic susceptibility was measured with a SQUID magnetometer (Quantum Design, USA). The resistivity was measured on pressed samples using the conventional four-probe method.

3. RESULTS AND DISCUSSION

The results of full-profile refinement show that the material has the same structure (CdI_2) and belongs to the same space group ($P\bar{3}m1$) as the original host lattice up to the intercalant content $x = 0.33$ without nickel ordering. The coordinates of the unit cell basis are Ti (0, 0, 0), Se ($1/3$, $2/3$, z), and Ni (0, 0, $1/2$). The best fit to the experimental data is obtained in the case where the intercalated Ni atoms are assumed to be in the octahedral positions in the van der Waals gap.

As seen from Fig. 1, nickel intercalation decreases the lattice parameter along the normal to the basal plane (c_0) up to the intercalant concentration $x = 0.25$. This behavior is typical of titanium chalcogenides intercalated with transition metals [1] and is commonly explained by the formation of covalent Ti-Ni-Ti bridges, which pull the host lattice layers closer together. These centers also act as free-carrier traps and can be considered covalent polarons [9]. ARPES studies of the analogous $\text{Ni}_{1/3}\text{TiSe}_2$ system have shown that the formation of such centers is accompanied by the appearance of a dispersionless band approximately 1 eV below the Fermi level [10]. According to [11], an impurity polaron band has similar properties. Since this band is oriented along the M - Γ direction in the Brillouin zone, it was concluded in [10] that this band is formed by the $\text{Ni}3d_{zz}/\text{Ti}3d_{zz}$ hybridized states.

As shown in [5], the amount of strain caused by the formation of the centers mentioned above is determined (for a given host lattice) by the ionization potential of the intercalant. The dimension of the deformed Ti-Ni-Ti cluster along the normal to the basal plane as calculated from the $c_0(x)$ dependence is characterized by the lattice parameter $c_0 = 5.631$ Å, which is close to the value $c_0 = 5.611$ Å calculated in [5] from the ionization potential of the Ni^{2+} ion. This discrepancy can be due to the screening effect not being fully taken into account.

The significant changes in the lattice parameters of TiSe_2 caused by nickel intercalation (a decrease in c_0 and a simultaneous increase in a_0) lead to a change in the ratio c_0/a_0 , which characterizes the distortion of the chalcogen octahedron surrounding a titanium atom [12] (Fig. 2). From the concentration dependences of the Se-Ti-Se layer thickness r_L and the van der Waals gap width r_G shown in Fig. 3, it follows, however, that the

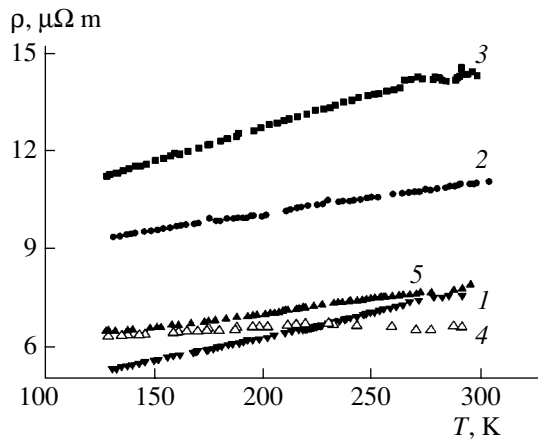


Fig. 4. Temperature dependences of the resistivity of Ni_xTiSe_2 for different values of x : (1) 0.1, (2) 0.2, (3) 0.25, (4) 0.33, and (5) 0.5.

lattice deformation along the normal to the basal plane is due solely to a decrease in the width of the van der Waals gap. If the deformation is of polaron nature, this behavior is quite natural and also indicates that the geometric characteristics of the local surrounding of a Ti atom remain unchanged. The latter fact is very important, because the shape of the chalcogen octahedron determines the mutual arrangement of the $\text{Ti}3d$ bands [13]. If the octahedron is regular in shape, the $\text{Ti}3d_{zz}$, $\text{Ti}3d_{yy}$, and $\text{Ti}3d_{xx-yy}$ orbitals forming the conduction band bottom are degenerate in energy. Extension of the octahedron along the c axis causes the $\text{Ti}3d_{zz}$ orbital to be lower in energy than the orbitals lying in the (x, y) plane, and compression of the octahedron along the c axis has the opposite effect. The decrease in c_0 and increase in a_0 suggest that the chalcogen octahedron is compressed along the c axis and that the $\text{Ti}3d_{zz}/\text{Ni}3d_{zz}$ hybridization becomes weaker, thereby causing polarons to disappear gradually. On the other hand, the constancy of the coordination of Se atoms to titanium indicates that the interaction between the Ti and Ni sublattices does not change in character over the entire concentration range studied. Therefore, an increase in the nickel content causes the polaron concentration to increase but does not change the polaron characteristics.

The conductivity of Ni_xTiSe_2 is close in magnitude to that observed in the original TiSe_2 but is different from that of other materials in which polarons form. The temperature dependence of resistivity is metallic in character for all compositions studied (Fig. 4); i.e., the mobility of charge carriers is fairly high. This result contradicts the conclusion (drawn from the x-ray data) that the conduction band is associated with polarons. For such strong deformation of the lattice, a much higher degree of localization of charge carriers could be expected. It is likely that the conduction band is formed not only by the d_{zz} orbital but also by other Ni orbitals

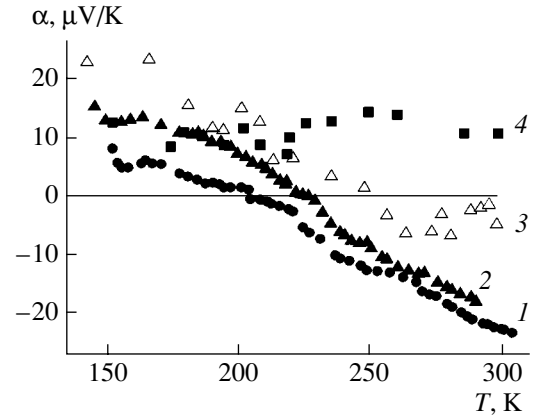


Fig. 5. Temperature dependences of the thermopower of Ni_xTiSe_2 for different values of x : (1) 0.2, (2) 0.25, (3) 0.33, and (4) 0.5.

hybridized with Ti and Se orbitals. In this case, the electrons are less localized and have a higher mobility.

As seen from Fig. 4, the resistivity is maximal for $\text{Ni}_{0.25}\text{TiSe}_2$. It should be noted that, in contrast to other intercalation compounds $M_x\text{TiSe}_2$ ($M = \text{Fe}, \text{Co}, \text{Cr}, \text{Mn}, \text{Ag}$), the conductivity does not increase with the intercalant content in the case of intercalation with nickel. Therefore, the effect of nickel on the conductivity reduces to a change in the mobility of carriers rather than in their density. As shown in [5], the composition with $x = 0.25$ corresponds to the percolation threshold over titanium atoms coordinated to the impurity (site percolation problem for a triangular lattice with nearest neighbor interaction). This result correlates with the discontinuity in slope observed in the concentration dependence of c_0 at nickel content $x = 0.25$ (Fig. 1). It is likely that at $x < 0.25$ the conductivity is associated with the sublattice of sites whose nearest environment does not contain nickel atoms, whereas at $x > 0.25$ it is associated with the sublattice of titanium atoms coordinated to nickel. The point $x = 0.25$ corresponds to the minimum connectivity of both sublattices.

For samples with different intercalant content, the thermopower changes sign as a function of temperature (Fig. 5), which indicates a changeover from p -type to n -type conductivity with heating. The temperature at which this changeover occurs increases monotonically with the nickel content. Therefore, an increase in the intercalant content causes a monotonic change in the ratio between the electron and hole densities, whereas the anomaly observed in the concentration dependence of conductivity is associated with their mobilities. The increase in the contribution from holes to charge transport with increasing intercalant concentration can be due to the increasing localization of electrons in the $\text{Ti}3d_{zz}/\text{Ni}3d$ hybridized band.

The magnetic susceptibility χ of Ni_xTiSe_2 (Fig. 6) is significantly lower than that of analogous compounds

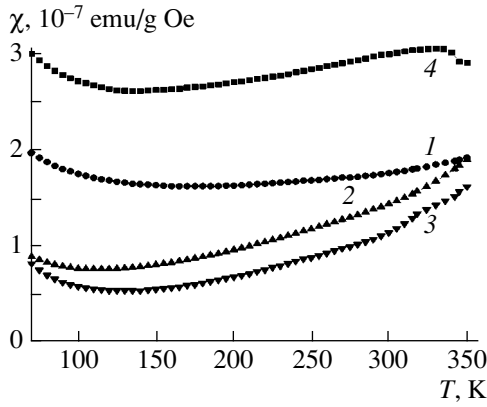


Fig. 6. Temperature dependences of the magnetic susceptibility of Ni_xTiSe_2 for different values of x : (1) 0.1, (2) 0.25, (3) 0.33, and (4) 0.5.

with Cr, Mn, Fe, and Co [14], and its temperature dependence is very weak and cannot be described by the commonly used expression

$$\chi = \chi_0 + \frac{C}{T - \Theta}, \quad (1)$$

where the first term (χ_0) is the temperature-independent diamagnetic contribution from the ionic cores and the Pauli paramagnetic contribution from the conduction electrons and the second term is the Curie–Weiss contribution from localized magnetic moments. Above 80 K, the magnetic susceptibility is observed to increase with heating. Since the Curie–Weiss contribution does not exhibit such behavior, the main contribution can be due only to the conduction electrons. The temperature dependence of this contribution to the magnetic susceptibility is described by [15]

$$\chi_P = \mu_B^2 g(E_F) \left[1 - \left\{ \left(\frac{g'}{g} \right)^2 - \left(\frac{g''}{g} \right) \right\}_{E=E_F} T^2 \right], \quad (2)$$

Table 1. Parameters for calculating the magnetic susceptibility from Eqs. (1) and (2)

Parameter	x			
	0.1	0.25	0.33	0.5
$\chi_0 \times 10^{-7}$, emu/g Oe	1.134	0.285	-0.2015	1.935
$C \times 10^{-6}$, emu K/g Oe	5.852	3.789	6.759	7.184
$P \times 10^{-12}$, emu/g Oe K ²	0.487	1.168	1.281	0.978
$\chi_P \times 10^{-7}$, emu/g Oe	6.134	5.285	4.799	6.935
μ_{eff}, μ_B	0.31	0.17	0.19	0.16

Note: $P = \mu_B^2 g(E_F) \left[\left\{ \left(\frac{g'}{g} \right)^2 - \left(\frac{g''}{g} \right) \right\}_{E=E_F} \right]$, $\chi_P = \chi_0 + \chi_D$,

$$\chi_D = -5 \times 10^{-7} \text{ emu/g Oe.}$$

where g , g' , and g'' are the density of states at the Fermi level and its first and second derivatives with respect to energy, respectively. However, numerical calculation showed that Eq. (2) likewise cannot describe the temperature dependence of χ . We succeeded in describing this dependence with the sum of Eqs. (1) and (2). The corresponding parameters are listed in Table 1. It is interesting that the effective Ni magnetic moments are small, which agrees with the available data for $x = 0.1$ and 0.2 [16]. Such suppression of the magnetic moment was also observed in the Co_xTiSe_2 and Cr_xTiSe_2 systems [6]. Among all analogous intercalated materials, Ni_xTiSe_2 undergoes the maximum compression along the c axis and, accordingly, shows the maximum difference between the experimentally observed magnetic moment and the magnetic moment of the free ion. Another specific feature is the large negative quadratic contribution, which comes either from the strong temperature dependence of the Fermi level position or from the strong energy dependence of the density of states at the Fermi level. This feature is observed over a wide concentration range; therefore, it is unlikely that the significant change in the electron density produced by the intercalant does not cause the Fermi level to leave the region of the strong energy dependence of the density of states. It follows that the quadratic contribution to the temperature dependence of χ is due to the strong temperature dependence of the Fermi level. Such a strong dependence is likely if the charge carriers are polarons. Indeed, a change in temperature causes a change in the carrier polarization in this case, thereby varying the density of states at the Fermi level and the position of the Fermi level [11].

It should be noted that $\text{Ni}_{0.5}\text{TiSe}_2$ differs in terms of its properties from other Ni_xTiSe_2 compounds. In contrast to compositions with $x < 0.5$, this compound belongs to the monoclinic crystal system and is characterized by the $I2/m$ space group, $Z = 4$, and the divergence factor $R_w = 6\%$ (Table 2), which is the result of the $\sqrt{3}a_0 \times a_0 \times 2c_0$ ordering of nickel in van der Waals gaps. The nickel content $x = 0.5$ corresponds to the percolation threshold in the impurity sublattice. This circumstance, as well as the pure topological ordering of the impurity in the van der Waals gaps, can be the reason for the monoclinic distortions. The change in the symmetry of the unit cell causes an increase in the magnetic susceptibility and conductivity, but the conductivity remains p -type in the entire temperature range covered. This conclusion is supported by the fact that the thermopower does not change sign as the nickel content reaches $x = 0.5$ and that the magnetic susceptibility is virtually independent of temperature.

Thus, the coincidence of the percolation threshold in the sublattice of titanium atoms coordinated to nickel with the position of the anomaly in the concentration dependences of the resistivity and lattice parameters and the coincidence of the nickel ordering point with the percolation threshold in the impurity atom sublattice

Table 2. Structural parameters of the Ni_{0.5}TiSe₂ compound

	Ni _{0.5} TiSe ₂ (CuK α)		x	y	z	$U, \text{\AA}^2$
$a_0, \text{\AA}$	6.161 (1)	Ni ($2/m$)	0	0	0	0.12 (1)
$b_0, \text{\AA}$	3.567 (1)	Ti (m)	0.0092 (2)	0	0.2504 (4)	0.05 (2)
$c_0, \text{\AA}$	11.836 (2)	Se1 (m)	0.1643 (6)	1/2	-0.1218 (2)	0.07 (5)
β, deg	90.293 (3)	Se2 (m)	0.3322 (6)	0	0.1184 (1)	0.02 (3)

Note: Thermal parameters U are calculated in the isotropic approximation.

tice suggest that the charge carriers are localized. This conclusion correlates well with the observed suppression of the nickel magnetic moment. However, the carrier localization appears to be significantly different in character from that observed in titanium diselenide intercalated with other transition metals. This difference is likely due to the fact that the hybridized states in which the conduction electrons are localized involve many Ni3d orbitals.

ACKNOWLEDGMENTS

This study was supported by the Russian Foundation for Basic Research (project nos. 01-03-32620, 01-03-96502) and the federal program "Universities of Russia" (project no. UR.01.01.005).

REFERENCES

1. A. Titov, S. Titova, M. Neumann, V. Pleschev, Yu. Yarmoshenko, L. Krasavin, A. Dolgoshein, and A. Kuranov, *Mol. Cryst. Liq. Cryst.* **311**, 161 (1998).
2. A. A. Titov and A. V. Dolgoshein, *Fiz. Tverd. Tela (St. Petersburg)* **40** (7), 1187 (1998) [*Phys. Solid State* **40**, 1081 (1998)].
3. P. C. Klipstein, C. M. Pereira, and R. H. Friend, *Philos. Mag. B* **56** (5), 531 (1987).
4. P. C. Klipstein and R. H. Friend, *J. Phys. C: Solid State Phys.* **20** (26), 4169 (1987).
5. A. A. Titov, A. V. Dolgoshein, I. K. Bdikin, and S. G. Titova, *Fiz. Tverd. Tela (St. Petersburg)* **42** (9), 1567 (2000) [*Phys. Solid State* **42**, 1610 (2000)].
6. A. M. Titov, A. V. Kuranov, V. G. Pleschev, Yu. M. Yarmoshenko, M. V. Yablonskikh, A. V. Postnikov, S. Plogmann, M. Neumann, A. V. Ezhov, and E. Z. Kurmaev, *Phys. Rev. B* **63**, 035 106 (2001).
7. Y. Arnaud, M. Chevreton, A. Ahouanjiou, M. Danot, and J. Rouxel, *J. Solid State Chem.* **18**, 9 (1976).
8. A. C. Larson and R. B. von Dreele, *LANSCE.MS-H805* (Los Alamos National Laboratory, Los Alamos, 1986), NM 87545.
9. N. F. Mott and E. A. Davis, *Electron Processes in Non-Crystalline Materials*, 2nd ed. (Clarendon, Oxford, 1979; Mir, Moscow, 1982).
10. T. Matsushita, S. Suga, and A. Kimura, *Phys. Rev. B* **60** (3), 1678 (1999).
11. A. S. Alexandrov and N. Mott, *Polarons and Bipolarons* (World Sci., Singapore, 1995).
12. T. Hibma, *Structural Aspects of Monovalent Cation Intercalates of Layered Dichalcogenides* (Academic, London, 1982), p. 285.
13. W. V. Liang, in *Proceedings of the NATO Advanced Study Institute Physics and Chemistry of Electrons and Ions in Condensed Matter, Cambridge, UK* (Reidel, Dordrecht, 1984), p. 459.
14. A. V. Kuranov, V. G. Pleschev, A. N. Titov, N. V. Baranov, and L. S. Krasavin, *Fiz. Tverd. Tela (St. Petersburg)* **42** (11), 2029 (2000) [*Phys. Solid State* **42**, 2089 (2000)].
15. S. V. Vonsovskii, *Magnetism* (Nauka, Moscow, 1971; Wiley, New York, 1974).
16. Y. Tazuke and T. Takeyama, *J. Phys. Soc. Jpn.* **66** (3), 827 (1997).

Translated by Yu. Epifanov

METALS
AND SUPERCONDUCTORS

Phonon Spectra of $L1_2$ Ni₃Al and $B2$ NiAl: Ab Initio Calculations

É. I. Isaev*, A. I. Likhtenshtein**, Yu. Kh. Vekilov*, and E. A. Smirnova*

* Moscow State Institute of Steel and Alloys (Technological University), Leninskiĭ pr. 4, Moscow, 119049 Russia

** Nijmegen Science Research Institute of Matter, University of Nijmegen, Nijmegen, 6525 ED Netherlands

Received September 5, 2003; in final form, November 21, 2003

Abstract—Phonon spectra and phonon density of states of intermetallic compounds Ni₃Al and NiAl are studied using the *ab initio* linear-response method. The calculated phonon dispersion curves agree well with the inelastic neutron scattering data available for the crystals under study. © 2004 MAIK “Nauka/Interperiodica”.

1. INTRODUCTION

Nickel alloys have numerous applications in engineering. For example, they are utilized as Invar (Fe–Ni) alloys [1], shape-memory (Ti–Ni) alloys [2], and structural (Ni–Al) alloys [3]. Ni–Al alloys are also widely used in the aircraft industry. Therefore, a lot of studies have been performed on the mechanical [4] and thermodynamic [5] properties of Ni–Al alloys, including *ab initio* studies of the influence of intrinsic point defects on the thermodynamic properties of $B2$ NiAl [6].

However, the lattice dynamics of Ni₃Al and NiAl has not been sufficiently studied. Among the publications on this subject, we may mention the experimental studies carried out by Stassis *et al.* [7] and Mostoller *et al.* [8], where the force constants calculated within the Born–von Karman model involving three and four nearest neighbors were used to interpret experimental inelastic neutron scattering data. The phonon density of states and vibrational entropy of ordered and disordered Ni₃Al alloys have been studied experimentally by Fultz *et al.* [9] and theoretically by Althoff *et al.* [10]. Also, the phonon spectra of Ni_xAl_{1–x} alloys were studied in [11–14] to explore the influence of alloy composition on vibrational spectrum anomalies and their relation to the martensitic transformations occurring in $B2$ Ni–Al alloys. Zhao and Harmon [15] studied (in the framework of the Varma–Weber model [16]) the Kohn anomaly in the $B2$ NiAl phonon spectrum in the Σ direction and attributed this anomaly to both strong electron–phonon interactions and Fermi surface nesting. The same conclusion concerning the importance of the Fermi surface nesting and acoustic phonon mode softening in martensitic transformations of $B2$ NiAl alloys was drawn in a recent paper [17] from calculations of the generalized susceptibility based on the energy spectrum obtained by the *ab initio* LMTO method.

Theoretical studies (including *ab initio* calculations) of the phonon spectra of these compounds are lacking.

In the present work, we perform *ab initio* calculations of the phonon spectra of Ni₃Al and NiAl alloys using the linear response method and ultrasoft pseudopotentials. The calculated phonon spectra and phonon density of states are in good agreement with the inelastic neutron scattering data.

2. CALCULATION TECHNIQUE

The phonon spectra are calculated using the linear response method [18–20]. Let us briefly describe the main points of the theory (details of the method and its application can be found in [21]). It was shown in [22, 23] that, in the harmonic approximation, the force constants of a crystal are determined by the static linear response of the electron subsystem. Calculations of the force constants are based on the Hellmann–Feynman theorem, which states that the derivative of the total energy of the ground state of a system with respect to an external variable is determined by the well-known expression

$$\frac{\partial E}{\partial \lambda} = \int n(r) \frac{\partial V_\lambda(r)}{\partial \lambda} dr, \quad (1)$$

where $V_\lambda(r)$ is an external potential that acts on the electron subsystem and is a continuous function of the parameter λ and $n(r)$ is the electron density.

Expanding the right-hand side of Eq. (1) to second order, we get

$$\begin{aligned} \frac{\partial E}{\partial \lambda_i} = \int & \left[n_0(r) \frac{\partial V_\lambda}{\partial \lambda_i} + \sum_j \lambda_j \frac{\partial n_\lambda(r)}{\partial \lambda_i} \frac{\partial V_\lambda(r)}{\partial \lambda_i} \right. \\ & \left. + n_0(r) \sum_j \lambda_j \frac{\partial^2 V_\lambda(r)}{\partial \lambda_i \partial \lambda_j} \right] dr + O(\lambda^2), \end{aligned} \quad (2)$$

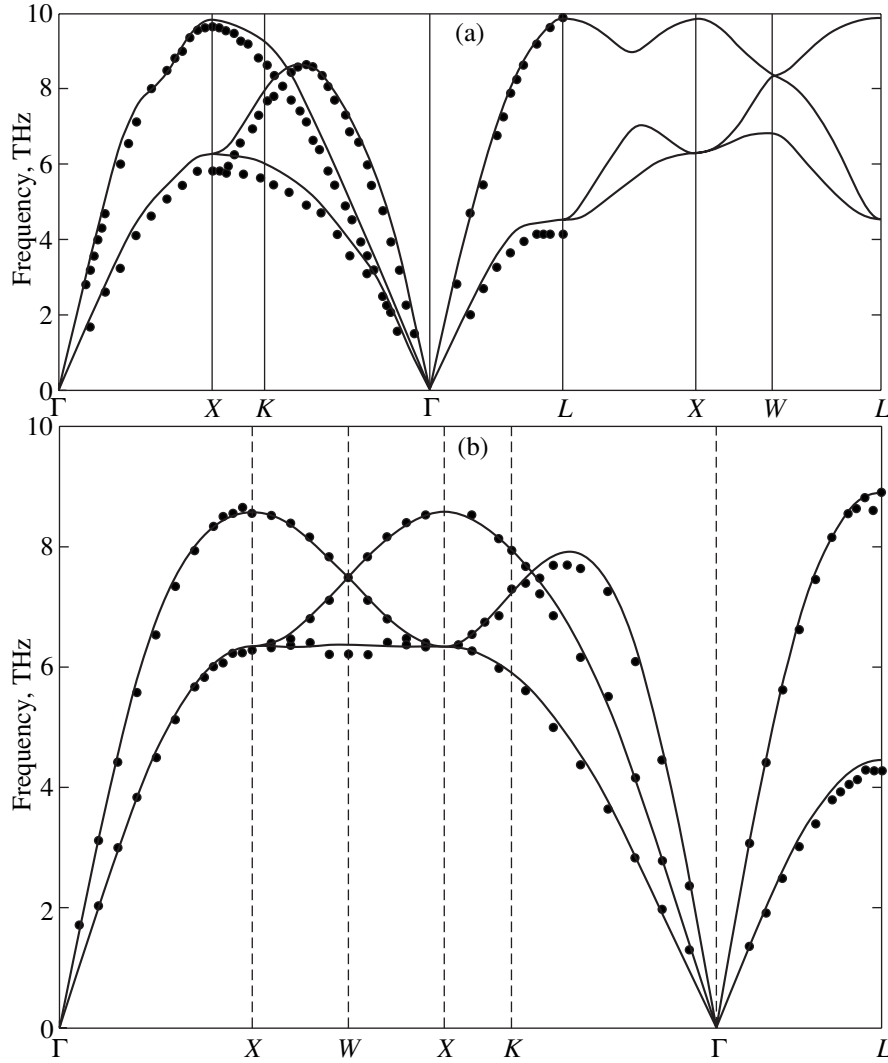


Fig. 1. Calculated phonon spectra of (a) Al and (b) Ni along symmetry directions in the Brillouin zone. Dots are experimental data from [31, 32].

where all derivatives are taken at $\lambda = 0$. Integrating Eq. (2) and taking the second derivative with respect to variables λ_i and λ_j , we can find that the matrix of force constants $C_{\alpha i, \beta j}(R - R')$ consists of two parts, electronic and ionic. Here, α and β are polarization directions; i and j specify the positions of atoms in the elementary cell, and R and R' are the positions of elementary cells in space. Assuming $\lambda = u_{\alpha i}(R)$, we get

$$C_{\alpha i, \beta j}(R - R') = C_{\alpha i, \beta j}^i(R - R') + C_{\alpha i, \beta j}^e(R - R'), \quad (3)$$

where C^i are determined by the second derivative of the Ewald sum. The electronic contribution to the matrix of force constants is determined by the linear response of the charge density and of the ionic potential to atomic displacements and also by the second derivative of the electron-ion interaction energy with respect to the displacements of two ion sites:

$$C_{\alpha i, \beta j}^e(R - R') = \int \left[\frac{\partial n(r)}{\partial u_{\alpha i}(R)} \frac{\partial V_i(r)}{\partial u_{\beta j}(R')} + n_0(r) \frac{\partial^2 V_i(r)}{\partial u_{\alpha i}(R) \partial u_{\beta j}(R')} \right] dr. \quad (4)$$

The external potential $V_i(r)$ in Eq. (4) is defined as the sum of bare ionic pseudopotentials acting on electrons:

$$V_i(r) = \sum_{R, i} v_i(r - R - \tau_i), \quad (5)$$

where the sum is over all atomic positions τ_i in the elementary cell.

For pseudopotentials, we used the ultrasoft pseudopotentials introduced by Vanderbilt [24], which were derived in the Bessel function basis [25].

Comparison of the theoretical and experimental phonon spectra Al and Ni at the $X(100)$, $L\left(\frac{1}{2}, \frac{1}{2}, \frac{1}{2}\right)$, $\frac{1}{2}X(100)$, and $\frac{1}{2}\Sigma\left(\frac{1}{2}, \frac{1}{2}, 0\right)$ points (L and T denote longitudinal and transverse vibration modes, respectively; frequencies are measured in terahertz)

	Al				Ni		
	theory	[34]	[35]	[36]	experiment	theory	experiment [32]
$L(100)$	9.95	9.72	9.51	9.53	9.67**, 9.69***	8.57	8.55
$T(100)$	6.33	5.77	5.83	5.83	5.81**, 5.78***	6.34	6.24
$L\left(\frac{1}{2}, \frac{1}{2}, \frac{1}{2}\right)$	9.98	9.88	9.84		9.9**, 9.69***	8.88	8.88
$T\left(\frac{1}{2}, \frac{1}{2}, \frac{1}{2}\right)$	4.55	4.36	4.33		4.19**, ***	4.42	4.24
$L\left(\frac{1}{2}, 0, 0\right)$	7.57	7.25			7.08**	6.7	6.54
$T\left(\frac{1}{2}, 0, 0\right)$	4.49	4.55			4.14**	4.6	4.49
$L\left(\frac{1}{4}, \frac{1}{4}, 0\right)$						7.87	7.63
$T2\left(\frac{1}{4}, \frac{1}{4}, 0\right)$						6.32	6.15
$T1\left(\frac{1}{4}, \frac{1}{4}, 0\right)$						4.54	4.36

* Our results.

** Data from [31].

*** Data from [37].

Exchange-correlation effects were taken into account using the generalized gradient approximation with correction suggested by Perdew *et al.* [26]. Plane waves with a maximum energy of 30 Ry were used as the basis functions for electrons. When calculating the matrix elements of the Hamiltonian of the system, we took into account the Fourier components of the charge density $n(G)$ with energy up to 400 Ry. When integrating over the Brillouin zone, we used k points generated by the Monkhorst–Pack method [27] and summation over energy bands was performed using Gauss–Hermite functions of the first order [28] with a width of 0.025 Ry. A set of $20 \times 20 \times 20$ k points was used to integrate over the Brillouin zone for Al and Ni, and a set of $16 \times 16 \times 16$ k points was used for Ni_3Al and NiAl . To calculate the matrix of force constants and take the inverse Fourier transform, we used a set of $8 \times 8 \times 8$ q points for Al and a set of $4 \times 4 \times 4$ q points for all other crystals studied. Experimental values of the unit cell parameters were used for all calculations. Spin-polarization calculations were also carried out for Ni and Ni_3Al .

All calculations were performed using the PWSCF software package [29], except for the phonon density of

states, which was computed using the tetrahedron method [30].¹

3. RESULTS AND DISCUSSION

To begin with, we calculated the phonon spectra of pure elements, Ni ($a = 3.52 \text{ \AA}$) and Al ($a = 4.05 \text{ \AA}$), and compared them with the experimental data on inelastic neutron scattering for these crystals. Dispersion curves computed for Al and Ni are presented in Figs. 1a and 1b, respectively. As can be seen from Fig. 1, the theoretical spectra are in good agreement with the experimental data [31–33]. The table lists the phonon spectra for Al and Ni calculated at several high-symmetry points using various methods (in [34], the frozen-phonon method was used). Experimental values at the same points are also presented in the table for comparison. Note that the linear response method [19, 20, 36] gives very close results despite the fact that different versions of it were used (Quong and Klein [36] expressed first-order corrections to the charge density in terms of the static response function using pseudopotentials, while Savrasov [20] used a linear MT orbital

¹ We developed a special computer program to integrate over the Brillouin zone by the tetrahedron method.

basis to calculate the charge density linear response). The phonon spectra of Al and Ni have no pronounced features, which is shown by the absence of anomalies in the structural and physical properties of these metals. The calculated phonon densities of states of Al and Ni (Figs. 2a, 2b, respectively) reproduce all existing features of the spectra. Since both metals have fcc lattices, these features are similar for them (in contrast to [35], where some differences in the shape of the density of states take place for metals with fcc structure (Al, Cu, Pb)). These features are also verified from experimental data for Ni [32] and by calculations of the density of states based on the force constants, which were calculated in the Born–von Karman approximation [31, 32].

Next, we calculated the phonon spectra of Ni₃Al and NiAl using the experimental values of the lattice parameters (3.56 Å for Ni₃Al, 2.887 Å for NiAl). For Ni₃Al (Fig. 3a), there is good agreement with the experimental spectra along the ΓX and ΓM directions [$X = \left(00\frac{1}{2}\right)$, $M = \left(\frac{11}{22}0\right)$ both for acoustic and optical branches]. The situation is more complicated for the ΓR direction, $R = \left(\frac{111}{222}\right)$; the theoretically calculated and

experimental spectra coincide over the entire ΓR segment for the transverse acoustic modes and approximately to the middle of this segment for the longitudinal acoustic modes. For the low optical branches, the agreement between the theoretical and experimental data becomes progressively poorer as the R point is approached (the agreement is good for the upper branches). This discordance may be due to anharmonicity, which is not taken into account in the harmonic approximation. There are also other reasons for this discrepancy.

(1) Numerical instability. We found that, at this point of the Brillouin zone, the calculated spectrum is sensitive to the prescribed calculation accuracy. An increase in the convergence parameter up to 10^{-12} Ry in computing the matrix of force constants improves the agreement between the spectra at this point (Fig. 3b).

(2) The quality of the pseudopotential used for nickel (because this part of the vibrational spectra is determined by it). However, this reason is unlikely, as the spectrum of the pure nickel was reproduced very well.

For NiAl, the agreement between the *ab initio* calculations and the experimental spectra [8] is good along all directions for which there are inelastic neutron scattering data (Fig. 4). Unlike Ni₃Al, the phonon spectrum of NiAl contains several features. Softening of the longitudinal acoustic branch is observed at $\frac{1}{3}\Gamma R$ and $\frac{1}{2}\Gamma M$. Furthermore, there is softening of the transverse

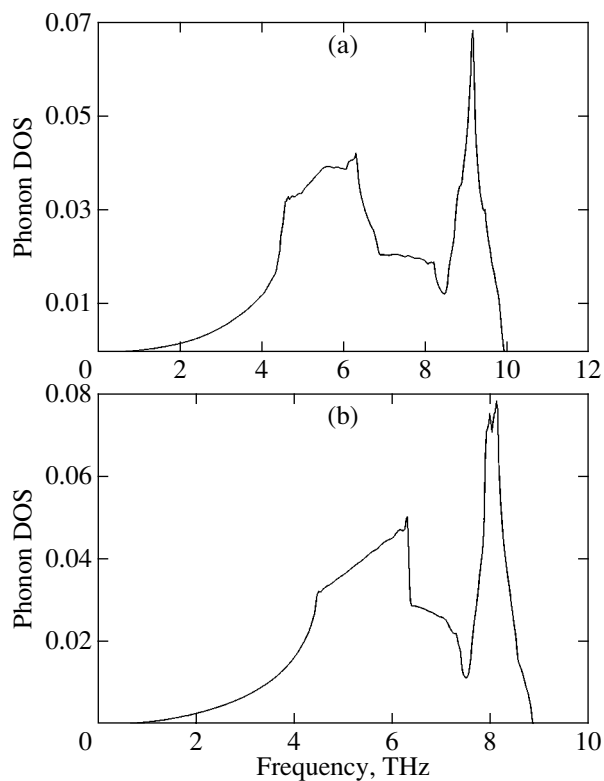


Fig. 2. Calculated phonon density of states of (a) Al and (b) Ni. The density-of-states curves are seen to be almost identical in shape.

acoustic mode $TA1$ along the $[110]$ direction [11, 13]. We also note that the TA mode significantly deviates from linearity along the $[111]$ direction (starting from $\frac{1}{3}\Gamma R$) and becomes concave downward. It is remarkable that no softening of the phonon spectrum was found in [8], where the force constants were fitted using the Born–von Karman method for three and four nearest neighbors. Also, for both intermetallic compounds, the optical branches of the phonon spectrum are separated due to the difference in mass ($M_{Ni}/M_{Al} \approx 2$); analysis of the eigenvalues shows that the upper optical branches are related to the lighter, aluminum atoms.

The calculated phonon densities of states for Ni₃Al and NiAl are shown in Figs. 5a and 5b, respectively. Comparison with the results of previous studies [7–9] shows good agreement. In particular, the density-of-states peak structure is reproduced very well for both intermetallic compounds. The energy gap between the acoustic and optical branches of NiAl (in fact, between the phonon branches of Ni and Al atoms) equals ≈ 1.55 THz and is in good agreement with the value of 1.84 THz obtained by Mostoller *et al.* [8]. The analogous gap in the density of states of Ni₃Al is significantly smaller (0.38 THz) and is almost half the value obtained in [7, 9] (about 0.7 THz). In [10], this gap was

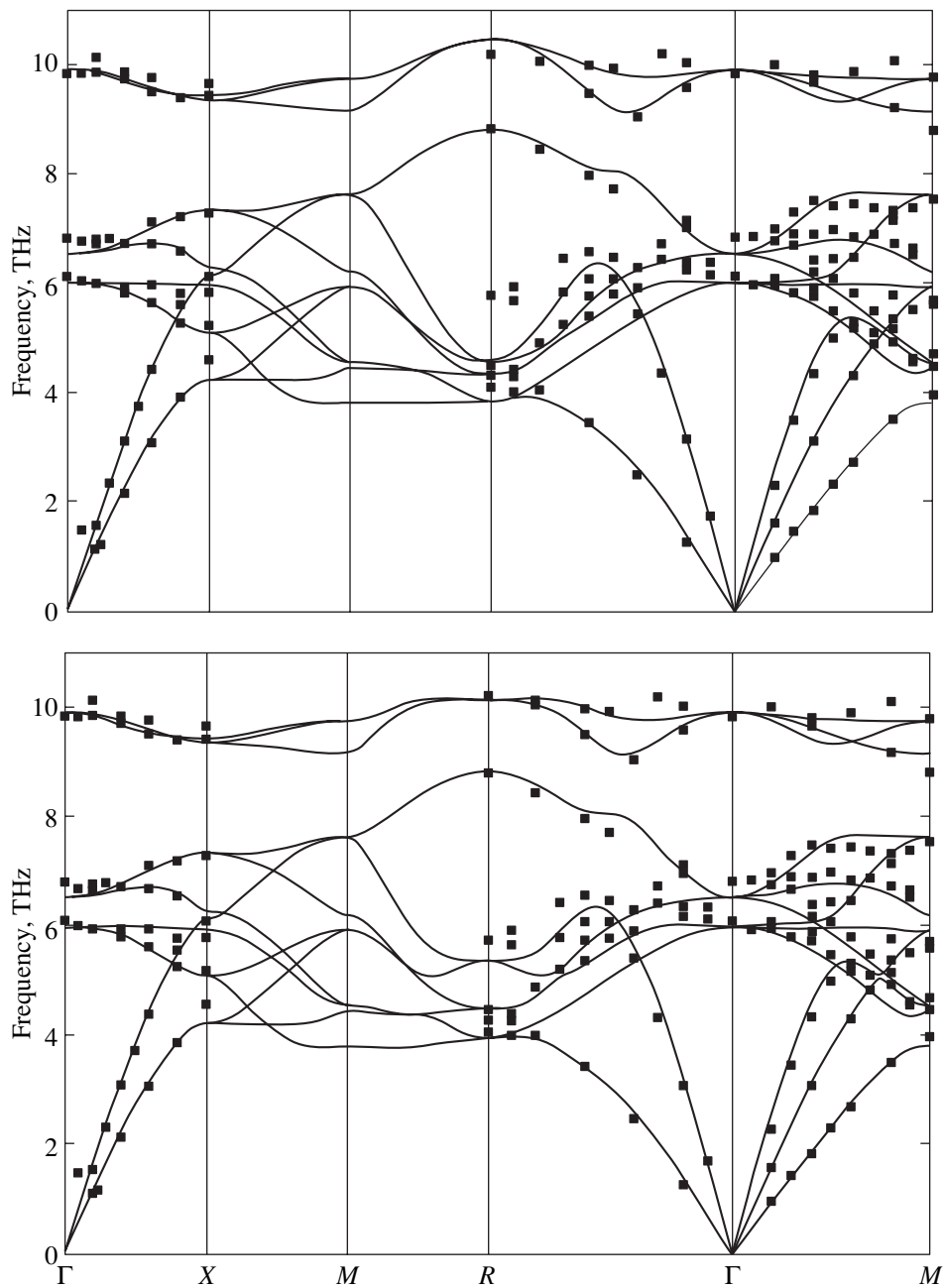


Fig. 3. Phonon spectrum of the intermetallic compound Ni_3Al . Dots are experimental data from [7].

found to be 1 THz. The discrepancy between the data from [7, 9] and [10] is probably due to the fact that different methods were used to obtain the phonon dispersion curves (the Born–von Karman model with the force constants fitted to the experimental spectrum was used in [7, 9], and the embedded-atom method, in [10]) and to integrate over the Brillouin zone. It should be noted that the phonon spectrum gap for Ni_3Al cited by Stassis *et al.* [7] was calculated using the force constants rather than measured experimentally. In [7], the difference between the calculated and measured lower

optical spectrum at the R point around 8 THz was about 0.5 THz, which explains the discrepancy between the data on the density-of-states gap obtained in [7, 9] and in this study. As can be seen from Fig. 3a, there is excellent agreement between the spectra calculated by us and the experimental spectra around 8 THz at the R point.

The largest difference in the frequency distribution function for NiAl (Fig. 5b), in contrast to [8], is found around 8 THz, where there is no pronounced peak; furthermore, another, almost flat section arises near 4 THz.

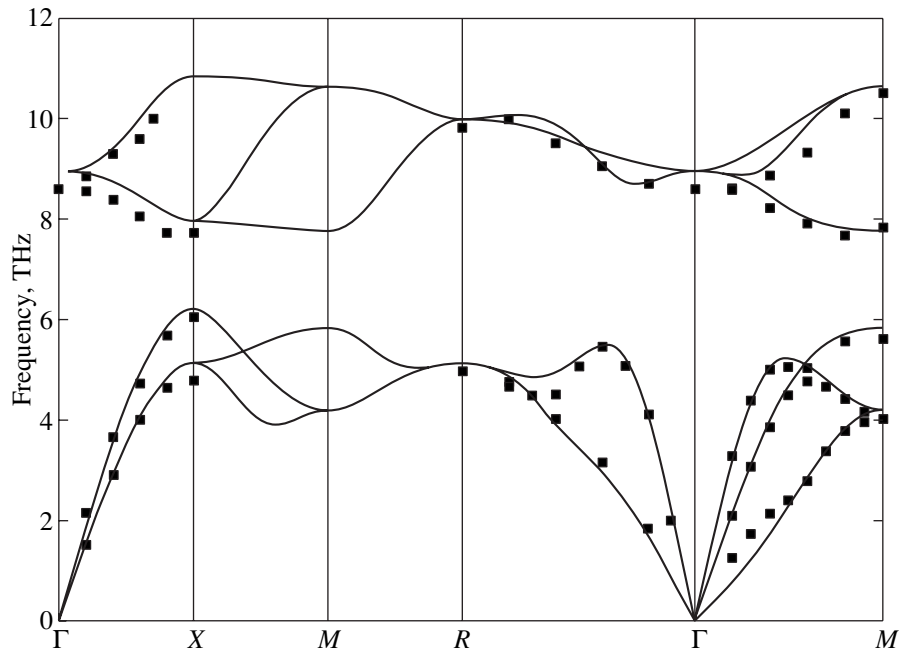


Fig. 4. Phonon spectrum of the intermetallic compound NiAl. Dots are experimental data from [8].

This discrepancy is related to the fact that in [8] the beginning of the optical part of the spectrum in the ΓM direction is less dispersive than follows from our calcu-

lations. The almost flat region is probably due to the zone symmetry near the M point.

4. CONCLUSIONS

In summary, the phonon spectra of $L1_2$ Ni₃Al and $B2$ NiAl calculated in the present work reproduce well all features of the phonon spectra of these intermetallic compounds. Softening of the TA_1 mode along the ΓM direction has been found in NiAl. The appreciable difference between the theoretical and experimental dispersion curves found near the R point of the Brillouin zone in Ni₃Al is probably due to anharmonic effects, which are not accounted for in the harmonic approximation.

ACKNOWLEDGMENTS

This work was supported by the Russian Foundation for Basic Research (project no. 03-02-17061) and the Royal Swedish Academy of Sciences.

REFERENCES

1. M. van Schilfgaard, I. A. Abrikosov, and B. Johansson, *Nature* **400**, 46 (1999).
2. *Shape-Memory Materials and Phenomena—Fundamental Aspects and Applications*, Ed. by C. T. Liu, H. Kunsmann, K. Otsuka, and M. Wuttig (MRS, Pittsburg, 1992), Mater. Res. Soc. Symp. Proc., No. 246.
3. *Intermetallic Compounds*, Ed. by J. H. Westbrook (Wiley, New York, 1967); *High Temperature Ordered Intermetallic Alloys II*, Ed. by N. S. Stoloff, C. C. Koch,

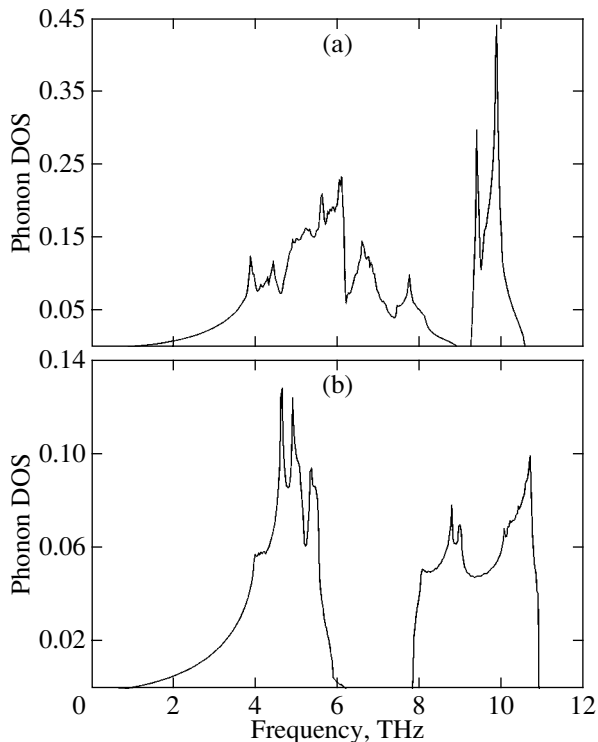


Fig. 5. Calculated phonon density of states of (a) Ni₃Al and (b) NiAl.

- C. T. Liu, and O. Izumi (MRS, Pittsburg 1987), *Mater. Res. Soc. Symp. Proc.*, No. 81.
4. *Ordered Intermetallic-Physical Metallurgy and Mechanical Behaviour*, Ed. by C. T. Liu, R. W. Chan, and S. Sautthoff (Kluwer Academic, Dordrecht, 1992).
 5. I. A. Abrikosov, Yu. H. Vekilov, A. V. Ruban, and D. Ya. Kats, *Solid State Commun.* **80**, 177 (1991); I. A. Abrikosov, A. V. Ruban, D. Ya. Kats, and Yu. H. Vekilov, *J. Phys.: Condens. Matter* **5** (9), 1271 (1993).
 6. P. A. Korzhavnyi, A. V. Ruban, A. Y. Lozovoi, Yu. Kh. Vekilov, I. A. Abrikosov, and B. Johansson, *Phys. Rev. B* **61** (9), 6003 (2000).
 7. C. Stassis, F. X. Kayser, C.-K. Loong, and D. Arch, *Phys. Rev. B* **24** (6), 3048 (1981).
 8. M. Mostoller, R. M. Nicklow, D. W. Zehner, S.-C. Lui, J. M. Mundenar, and E. W. Plummer, *Phys. Rev. B* **40** (5), 2856 (1989).
 9. B. Fultz, L. Anthony, L. J. Nagel, R. M. Nicklow, and S. Spooner, *Phys. Rev. B* **52** (5), 3315 (1995).
 10. J. D. Althoff, D. Morgan, D. de Fontaine, M. Asta, S. M. Foiles, and D. D. Johnson, *Phys. Rev. B* **56** (10), 5705 (1997).
 11. S. M. Shapiro, B. X. Yang, G. Shirane, Y. Noda, and L. E. Tanner, *Phys. Rev. Lett.* **62** (11), 1298 (1989).
 12. S. M. Shapiro, B. X. Yang, G. Shirane, Y. Noda, L. E. Tanner, and D. Schryvers, *Phys. Rev. B* **44** (17), 9301 (1991).
 13. Y. Noda, S. M. Shapiro, G. Shirane, Y. Yamada, and L. E. Tanner, *Phys. Rev. B* **42** (16), 10397 (1990).
 14. S. M. Shapiro, J. Z. Larese, Y. Noda, S. C. Moss, and L. E. Tanner, *Phys. Rev. Lett.* **57** (25), 3199 (1986).
 15. G. L. Zhao and B. Harmon, *Phys. Rev. B* **45** (6), 2818 (1992).
 16. C. M. Varma and W. Weber, *Phys. Rev. Lett.* **39** (17), 1094 (1977); *Phys. Rev. B* **19** (12), 6142 (1979).
 17. I. I. Naumov and O. I. Velikohatniy, *J. Phys.: Condens. Matter* **9** (47), 10339 (1997).
 18. N. E. Zein, *Fiz. Tverd. Tela (Leningrad)* **26** (10), 3028 (1984) [*Sov. Phys. Solid State* **26**, 1825 (1984)].
 19. P. Giannozzi, S. de Gironcoli, P. Pavone, and S. Baroni, *Phys. Rev. B* **43** (19), 7231 (1991).
 20. S. Y. Savrasov, *Phys. Rev. Lett.* **69** (19), 2819 (1992).
 21. S. Baroni, S. de Gironcoli, A. Dal Corso, and P. Giannozzi, *Rev. Mod. Phys.* **73** (2), 515 (2001).
 22. P. D. De Cicco and F. A. Johnson, *Proc. R. Soc. London, Ser. A* **310** (1), 111 (1969).
 23. R. Pick, M. H. Cohen, and R. M. Martin, *Phys. Rev. B* **1** (2), 910 (1970).
 24. D. Vanderbilt, *Phys. Rev. B* **41** (11), 7892 (1990).
 25. A. M. Rappe, K. M. Rabe, E. Kaxiras, and J. D. Joannopoulos, *Phys. Rev. B* **41** (2), 1227 (1990).
 26. J. P. Perdew, K. Burke, and M. Ernzerhof, *Phys. Rev. Lett.* **77** (18), 3865 (1996).
 27. H. J. Monkhorst and J. D. Pack, *Phys. Rev. B* **13** (12), 5188 (1976).
 28. M. Methfessel and A. T. Paxton, *Phys. Rev. B* **40** (6), 3616 (1989).
 29. S. Baroni, A. Dal Corso, S. de Gironcoli, and P. Giannozzi, <http://www.pwscf.org>.
 30. G. Lehmann and M. Taut, *Phys. Status Solidi B* **54** (2), 469 (1972).
 31. G. Gilat and R. M. Nicklow, *Phys. Rev.* **143** (2), 487 (1966).
 32. R. J. Birgeneau, J. Cordes, G. Dolling, and A. D. B. Woods, *Phys. Rev. A* **136** (5), 1359 (1964).
 33. R. Bauer, A. Schmid, P. Pavone, and D. Strauch, *Phys. Rev. B* **57** (18), 11276 (1998).
 34. Pui K. Lam and Marvin Cohen, *Phys. Rev. B* **25** (10), 6139 (1982).
 35. S. Y. Savrasov, *Phys. Rev. B* **54** (23), 16470 (1996).
 36. A. A. Quong and B. M. Klein, *Phys. Rev. B* **46** (17), 10734 (1992).
 37. R. Stedman and G. Nilsson, *Phys. Rev.* **145** (2), 492 (1966).

Translated by G. Tsydynzhapov

**METALS
AND SUPERCONDUCTORS**

Induced Motion of a Fast Josephson Vortex

A. S. Malishevskii and S. A. Uryupin

Lebedev Physical Institute, Russian Academy of Sciences, Leninskii pr. 53, Moscow, 119991 Russia

e-mail: malish@sci.lebedev.ru

Received October 8, 2003; in final form, November 17, 2003

Abstract—A relation is established between the transport current flowing through the entire $S_1IS_2WS_3$ layered structure and the velocity of a fast vortex. The fast vortex exists when the Swihart velocity in the waveguide is significantly higher than that in the Josephson junction. It is demonstrated that the main contribution to the Lorentz force that induces the vortex motion is due to the current flowing through the waveguide and skin layers of the adjacent superconductors. © 2004 MAIK “Nauka/Interperiodica”.

In this paper, we study the forced motion of a single Josephson vortex in an $S_1IS_2WS_3$ layered structure (S_1 , S_2 , S_3 are superconductors; I , W are nonsuperconducting layers). All layers are assumed to be parallel to the yz plane and to be infinite in their plane. The outermost superconducting layers S_1 and S_3 are semi-infinite and extend to $x = -\infty$ and $+\infty$, respectively. The layer I is proposed to be thin enough for Cooper pairs to tunnel. On the contrary, the layer W is assumed to be relatively thick, so that Cooper pairs tunneling through it can be neglected. Hence, the structure under study can be considered a Josephson junction coupled to a planar waveguide with superconducting walls.

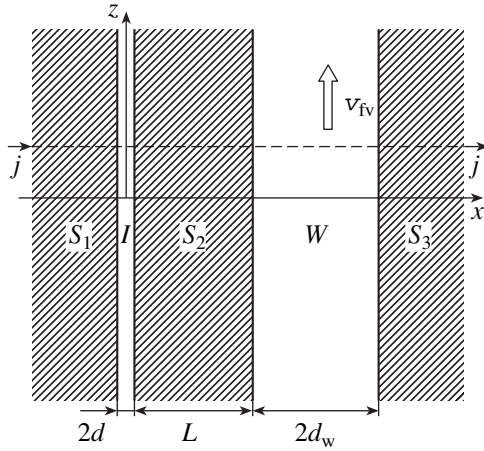
Induced motion of a vortex in a Josephson junction magnetically coupled to a waveguide can be realized in different ways. One way is to pass a transport current through the Josephson junction only. This condition can be satisfied in practice if the Josephson junction is planar [1] and the terminals of a dc current source are connected to the superconducting electrodes S_1 and S_2 . This method was considered theoretically in [2, 3]. It was demonstrated in [3] that the relation between the vortex velocity and a current is determined by the ratio between the Swihart velocities in the Josephson junction V_s and in the waveguide V_{sw} . According to [3], if $V_{sw} < V_s$, then, in the presence of the waveguide, vortices cannot move at speeds close to the Swihart velocity in the waveguide V_{sw} . If $V_{sw} > V_s$, induced motion of vortices in the $S_1IS_2WS_3$ structure is possible not only at $v < V_s$ but also at velocities close to V_{sw} . In the case of $V_{sw} \gg V_s$, the possible induced motion of fast vortices was predicted at a speed close to V_{sw} .

Induced vortex motion can also occur if a transport current flows through the entire structure, i.e., through both the Josephson junction and the waveguide. In this case, a current source should be connected to the outermost superconducting electrodes S_1 and S_3 . This method is generally used in experimental studies of

vortices in structures with coupled Josephson junctions (see, e.g., review [4] and papers [5–9]).

In this paper, we study induced motion of a fast vortex in the case of a transport current flowing through both the Josephson junction and the waveguide, because this case is easy to realize experimentally and is widely used in practice. Our main goal is to uncover new patterns of the induced fast vortex motion and to point out the best conditions for its observation.

In the following, the relation between a transport current and the velocity of a single vortex is established assuming relatively low dissipation both in the Josephson junction and in the waveguide. For the case of $V_{sw} \gg V_s$, where a fast vortex is possible, a simple analytical relation between the current in the structure and the fast vortex velocity is obtained. It is found that a significantly lower current is necessary for the induced motion of a fast vortex when the current is passed through both the Josephson junction and the waveguide as compared to the case where the current is passed through the Josephson junction only. The decrease in the current is determined by the product of the small coupling constant between the Josephson junction and the waveguide by the square of the small ratio of the Swihart velocities in the Josephson junction and waveguide. It is shown that the reduction in the current necessary for inducing vortex motion is due to the large additional contribution from the current that flows in the waveguide and the adjacent skin depth of the superconducting electrodes to the Lorentz force acting on the vortex. Due to this contribution, induced motion of a vortex also occurs when the current is passed through only the waveguide and adjacent superconducting electrodes. Therefore, in addition to the existing methods for exciting vortices, the vortex motion can also be induced with no current passing through the Josephson junction.



$S_1IS_2WS_3$ layered structure. $2d$, $2d_w$, and L are the thicknesses of the Josephson junction, the waveguide, and the superconducting electrode S_2 , respectively; j is the current density flowing through the entire structure; and v_{fv} is the fast vortex velocity.

Let us consider the case where a transport current of density j flows through both the Josephson junction and the waveguide (see figure). Assuming that the electromagnetic fields are independent of the coordinate y , we can describe the layered structure under study by the set of equations (cf. [5–11])

$$\omega_j^2 \sin \varphi(z, t) + \frac{\partial^2 \varphi(z, t)}{\partial t^2} + \omega_j^2 \frac{j}{j_c} + \beta \frac{\partial \varphi(z, t)}{\partial t} = V_s^2 \frac{\partial^2 \varphi(z, t)}{\partial z^2} + SV_s^2 \frac{\partial^2 \varphi_w(z, t)}{\partial z^2}, \tag{1}$$

$$\frac{\partial^2 \varphi_w(z, t)}{\partial t^2} + \frac{16\pi^2 cd_w j}{\phi_0 \epsilon_w} + \beta_w \frac{\partial \varphi_w(z, t)}{\partial t} = V_{sw}^2 \frac{\partial^2 \varphi_w(z, t)}{\partial z^2} + S_w V_{sw}^2 \frac{\partial^2 \varphi(z, t)}{\partial z^2}. \tag{2}$$

Here, $\varphi(z, t)$ and $\varphi_w(z, t)$ are the differences in the order parameter phases of the superconducting electrodes at the interfaces of the Josephson junction and the waveguide, respectively. In Eqs. (1) and (2), we use the following notation: j_c is the critical Josephson current density; ϕ_0 is the magnetic flux quantum; ω_j is the Josephson frequency; $2d_w$ and ϵ_w are the width and dielectric constant of the nonsuperconducting layer W , respectively; V_s and V_{sw} are the Swihart velocities in the Josephson junction and the waveguide, respectively, calculated with allowance for the coupling between them [3]; S and S_w are the coupling constants of the Josephson junction and the waveguide; and β and β_w are constants characterizing dissipation in the Josephson junction and the waveguide due to the single-parti-

cle current passing through the layers I and W , respectively. Equations (1) and (2) are written in the so-called local limit, where the characteristic scales of field variation along the z axis are large as compared to the London penetration depths of the superconducting layers S_1 , S_2 , and S_3 [12, 13].

As follows from Eqs. (1) and (2), the steady vortex motion at a fixed velocity v is described by the equations

$$\omega_j^2 \sin \psi(\zeta) - (V_s^2 - v^2) \psi''(\zeta) + \omega_j^2 \frac{j}{j_c} - \beta v \psi'(\zeta) = SV_s^2 \psi_w''(\zeta), \tag{3}$$

$$-(V_{sw}^2 - v^2) \psi_w''(\zeta) + \frac{16\pi^2 cd_w j}{\phi_0 \epsilon_w} - \beta_w v \psi_w'(\zeta) = S_w V_{sw}^2 \psi''(\zeta), \tag{4}$$

where $\psi(\zeta) \equiv \varphi(z, t)$, $\psi_w(\zeta) \equiv \varphi_w(z, t)$, and $\zeta \equiv z - vt$.

If the current and dissipation are small, Eq. (4) can be approximated as

$$\psi_w''(\zeta) \approx -S_w \frac{V_{sw}^2}{V_{sw}^2 - v^2} \left[\psi''(\zeta) - \beta_w \frac{v}{V_{sw}^2 - v^2} \psi'(\zeta) \right] + \frac{16\pi^2 cd_w j}{\phi_0 \epsilon_w} \frac{j}{V_{sw}^2 - v^2}.$$

Substituting this expression into Eq. (3), we obtain the following equation for $\psi(\zeta)$:

$$\sin \psi(\zeta) - k_j^{-2}(v) \psi''(\zeta) = - \left(1 - S_w \frac{V_{sw}^2}{V_{sw}^2 - v^2} \right) \frac{j}{j_c} + \frac{v \beta(v)}{\omega_j^2} \psi'(\zeta), \tag{5}$$

where

$$k_j(v) \equiv w_j \sqrt{\frac{V_{sw}^2 - v^2}{(v_1^2 - v^2)(v_2^2 - v^2)}},$$

$$v_m^2 \equiv \frac{V_s^2 + V_{sw}^2}{2}$$

$$+ (-1)^m \sqrt{\frac{(V_s^2 - V_{sw}^2)^2}{4} + SS_w V_s^2 V_{sw}^2},$$

$$m = 1, 2,$$

$$\beta(v) \equiv \beta + SS_w \frac{V_s^2 V_{sw}^2}{(V_{sw}^2 - v^2)^2} \beta_w.$$

From Eq. (5), we can find the relation between the vortex velocity and the current density. For this pur-

pose, we take advantage of the results from [14], where the motion of a single Josephson vortex (2π kink) in an isolated Josephson junction with Swihart velocity v_s was studied using the equation

$$\sin \psi(\zeta) - k_{JJ}^{-2}(v) \psi''(\zeta) = -\frac{j}{j_c} + \frac{v\beta}{\omega_j^2} \psi'(\zeta), \quad (6)$$

where $k_{JJ}(v) \equiv \omega_j / \sqrt{v_s^2 - v^2}$. It was shown in [14] that, in the case of low losses, the induced motion of the vortex is characterized by the following $j(v)$ dependence:

$$\frac{j(v)}{j_c} = \frac{4v k_{JJ}(v) \beta}{\pi \omega_j^2}.$$

Since Eqs. (5) and (6) are similar in form, it follows that the relation between the velocity of a 2π kink moving in the $S_1IS_2WS_3$ layered structure and the transport current density has the form

$$\frac{j(v)}{j_c} = \frac{4}{\pi} \left(1 - S_w \frac{V_{sw}^2}{V_{sw}^2 - v^2} \right)^{-1} \frac{v k_j(v) \beta(v)}{\omega_j^2}. \quad (7)$$

This expression differs from the relation

$$\frac{j(v)}{j_c} = \frac{4v k_j(v) \beta(v)}{\pi \omega_j^2}, \quad (8)$$

obtained in [3] for the case of a transport current flowing through the Josephson junction only, by the velocity-dependent factor $[1 - S_w V_{sw}^2 / (V_{sw}^2 - v^2)]^{-1}$. Expression (7) is valid in the limit of a relatively low current and low dissipation, where Eq. (4) can be solved approximately and the right-hand side of Eq. (5) is small.

In the following, we assume that the coupling constants of the Josephson junction and the waveguide are small. Then, for a fast Josephson vortex whose speed lies in the range [3]

$$V_{sw} < v < v_2 \approx \left(1 + \frac{1}{2} S S_w \frac{V_s^2}{V_{sw}^2} \right) V_{sw},$$

we can approximate Eq. (7) as

$$\begin{aligned} \frac{j(v)}{j_c} \approx & \frac{8}{\pi} \frac{1}{\omega_j S_w V_{sw}} \left[\beta + \frac{1}{4} S S_w \frac{V_s^2}{(v - V_{sw})^2} \beta_w \right] \\ & \times (v - V_{sw}) \sqrt{\frac{v - V_{sw}}{v_2 - v}}. \end{aligned} \quad (9)$$

In the case of relatively low losses in the Josephson junction

$$\beta \ll \frac{V_{sw}^2}{S S_w V_s^2} \beta_w, \quad (10)$$

Eq. (9) gives

$$\frac{j(v)}{j_c} \approx \frac{2\beta_w}{\pi \omega_j V_{sw}} \frac{S V_s^2}{\sqrt{(v - V_{sw})(v_2 - v)}}. \quad (11)$$

At

$$v = v_{\min} = \frac{V_{sw} + v_2}{2} \approx \left(1 + \frac{1}{4} S S_w \frac{V_s^2}{V_{sw}^2} \right) V_{sw} \quad (12)$$

transport current (11) reaches a minimum,

$$\frac{j_{\min}}{j_c} \approx \frac{8}{\pi} \frac{1}{S S_w} \frac{\beta_w}{\omega_j}. \quad (13)$$

This lowest value of the current at which the induced motion of a fast vortex takes place is $(8/3\sqrt{3}S)(V_{sw}/V_s)^2 \gg 1$ times smaller than the minimum transport current

$$\frac{j_{\min}}{j_c} \approx \frac{64}{3\sqrt{3}\pi S S_w} \frac{V_{sw}^2}{V_s^2} \frac{\beta_w}{\omega_j} \ll 1 \quad (14)$$

for the case of a current flowing only through the Josephson junction [3]. Note that Eq. (13), obtained under the assumption of low dissipation, as well as Eq. (14), is valid provided $\beta_w/\omega_j \ll S S_w V_s^2/V_{sw}^2$.

Let us make numerical estimates of the minimum current for the following parameters of the layered structure: $S = S_w = 0.4$, $V_{sw} = 3V_s$, and $\beta_w/\omega_j = 10^{-3}$. For this case, the minimum value of the transport current that must be passed through the Josephson junction to excite a fast vortex is found from Eq. (14) to be about $\approx 0.2j_c$. In the case where the current is passed through the entire structure, Eq. (13) gives $j_{\min} \approx 6 \times 10^{-3}j_c$. Therefore, in the latter case, the minimum current is about 35 times smaller.

Thus, the induced motion of a fast vortex is possible at a much lower current density in the case where the transport current is passed through both the Josephson junction and the waveguide as compared to the case where the transport current is passed through the Josephson junction only.

To understand the reason behind this effect, let us analyze the forces with which the transport current acts on a vortex in both cases. If the current flows through the entire structure, the total Lorentz force F_L (per unit length along the y axis) affecting a vortex is the sum of the contributions from the interactions between the current and the magnetic field of the vortex in the Josephson junction, the waveguide, and the skin layers of all

superconductors. The force F_L is proportional to the current density and equals

$$F_L = \frac{\phi_0}{c} \left(1 - S_w \frac{V_{sw}^2}{V_{sw}^2 - v^2} \right) j(v).$$

If the current flows only through the Josephson junction and the two adjacent superconducting electrodes S_1 and S_2 , the contributions to the Lorentz force arise from the interaction between the current and the field in the Josephson junction and in the skin layers of superconductors S_1 and S_2 . The sum of these contributions is

$$F_{LJJ} = \frac{\phi_0 j(v)}{c}.$$

For a fast vortex, we have the approximation

$$F_L \approx \frac{\phi_0}{c} \frac{S_w V_{sw}}{2(v - V_{sw})} j(v) = \frac{S_w V_{sw}}{2(v - V_{sw})} F_{LJJ}.$$

At $v = v_{\min}$, it follows that $F_L \approx (2V_{sw}^2/SV_s^2)F_{LJJ}$. Hence, when the current flows through the entire structure, the Lorentz force F_L is greater than in the case where the current passes only through the Josephson junction. The noticeable increase in F_L is due to the interaction between the current and the field in the waveguide and in the skin layers of the superconducting electrodes S_2 and S_3 . It is in these parts of the layered structure that the magnetic field of the fast vortex is concentrated.

Uniform motion of a vortex takes place when the Lorentz force is balanced by the friction force F_{diss} due to dissipation in the Josephson junction and the waveguide. Since F_{diss} is independent of the way in which the transport current is passed through the structure in the low-dissipation limit and since $F_L \gg F_{LJJ}$ for a fast vortex, the minimum current required to sustain the motion of a fast vortex is lower when the transport current flows through the entire layered structure.

Let us briefly consider the case where the transport current is passed through the waveguide only. In this case, the vortex motion is described by the set of equations (3) and (4), with the transport current j kept only in Eq. (4). Solving them, as before, under the assumption of low dissipation, we find the following relation between the current and the vortex velocity:

$$\frac{j(v)}{j_c} = \frac{4v^2 - V_{sw}^2}{\pi S_w V_{sw}^2} \frac{v k_j(v) \beta(v)}{\omega_j^2}. \quad (15)$$

For a fast vortex moving at a speed (12) close to the Swihart velocity of the waveguide V_{sw} , expression (15) approximately coincides with Eq. (11) if the losses in the Josephson junction are low and satisfy condition (10).

Therefore, the minimum current density required to sustain the induced fast vortex motion is approximately the same in the cases of the current being passed through the entire structure and through the waveguide only.

This result can be easily understood in terms of the above analysis of the forces acting on a fast vortex. Since the magnetic field of the fast vortex is concentrated mainly in the waveguide and the skin layers of the adjacent superconductors, the main contribution to the Lorentz force comes from the current flowing through these regions. The current flowing through the other regions of the $S_1 S_2 W S_3$ structure (where the magnetic field of the vortex is small) makes a small contribution to F_L and, therefore, has only a marginal effect on the character of the function $j(v)$.

To summarize, a much lower current is required to sustain the induced motion of a fast vortex when the current is passed simultaneously through the Josephson junction and the waveguide (or through the waveguide only) than in the case where the current is passed through the Josephson junction only. This new phenomenon is due to the relative increase in the Lorentz force exerted on the vortex by the current when the current is passed through the region where the magnetic field of the fast vortex is mainly concentrated. Based on this result, the following general prediction from the theory of induced vortex motion can be formulated, which also applies to more complicated structures: in order to sustain vortex motion, the current must be passed through those regions of the structure where the magnetic field of the vortex is mainly concentrated.

ACKNOWLEDGMENTS

The authors are grateful to V.P. Silin for his encouragement and helpful suggestions.

This work was supported by the President of the Russian Federation (project nos. NSh-1385.2003.2, MK-1809.2003.02) and the Ministry of Industry, Science, and Technology of the Russian Federation (contract no. 40.012.1.1.1357).

REFERENCES

1. K. K. Likharev, *Introduction to the Dynamics of Josephson Junctions* (Nauka, Moscow, 1985), p. 27.
2. V. V. Kurin and A. V. Yulin, *Phys. Rev. B* **55** (17), 11 659 (1997).
3. A. S. Malishevskii, V. P. Silin, and S. A. Uryupin, *Phys. Lett. A* **306** (2–3), 153 (2002).
4. A. V. Ustinov, *Physica D (Amsterdam)* **123** (1–4), 315 (1998).
5. M. B. Mineev, G. S. Mkrtchyan, and V. V. Schmidt, *J. Low Temp. Phys.* **45**, 497 (1981).

6. S. Sakai, P. Bodin, and N. F. Pedersen, *J. Appl. Phys.* **73** (5), 2411 (1993).
7. A. V. Ustinov, H. Kohlstedt, M. Cirillo, N. F. Pedersen, G. Hallmanns, and C. Heiden, *Phys. Rev. B* **48** (14), 10614 (1993).
8. S. Sakai, A. V. Ustinov, H. Kohlstedt, A. Petraglia, and N. F. Pedersen, *Phys. Rev. B* **50** (17), 12905 (1994).
9. E. Goldobin, A. Wallraff, N. Thyssen, and A. V. Ustinov, *Phys. Rev. B* **57** (1), 130 (1998).
10. A. F. Volkov, *Pis'ma Zh. Éksp. Teor. Fiz.* **45** (6), 299 (1987) [*JETP Lett.* **45**, 376 (1987)].
11. N. Grönbech-Jensen, M. R. Samuelsen, P. S. Lomdahl, and J. A. Blackburn, *Phys. Rev. B* **42** (7), 3976 (1990).
12. Yu. M. Aliev, K. N. Ovchinnikov, V. P. Silin, and S. A. Uryupin, *Zh. Éksp. Teor. Fiz.* **107** (3), 972 (1995) [*JETP* **80**, 551 (1995)].
13. V. P. Silin and S. A. Uryupin, *Zh. Éksp. Teor. Fiz.* **108** (6), 2163 (1995) [*JETP* **81**, 1179 (1995)].
14. D. W. McLaughlin and A. C. Scott, *Phys. Rev. A* **18** (4), 1652 (1978).

Translated by G. Tsydynzhapov

SEMICONDUCTORS AND DIELECTRICS

Effect of Pressure on the Elastic Properties of Silicon Carbide

S. Yu. Davydov

Ioffe Physicotechnical Institute, Russian Academy of Sciences, Politekhnicheskaya ul. 26, St. Petersburg, 194021 Russia
e-mail: sergei.davydov@mail.ioffe.ru

Received November 13, 2003

Abstract—The pressure dependences of the second-order elastic constants C_{ij} and the velocity of sound in 3C-SiC and 2H-SiC crystals are calculated in the framework of the Keating model. The third-order elastic constants C_{ijk} for 3C-SiC are determined from the dependences of the second-order elastic constants C_{ij} on the pressure p . © 2004 MAIK “Nauka/Interperiodica”.

1. INTRODUCTION

Elastic properties of different polytypes of silicon carbide SiC are of great research interest due to the widespread practical use of SiC-based materials. In the absence of external hydrostatic pressure ($p = 0$), the second-order elastic moduli C_{ij} and velocities of sound $v_i(\mathbf{q}) = \sqrt{C_i(\mathbf{q})/\rho}$ (where $C_i(\mathbf{q})$ is a specific combination of elastic moduli C_{ij} , which corresponds to propagation of an acoustic wave with polarization n_i in the direction \mathbf{q} , and ρ is the density of the crystal) can be calculated in the harmonic approximation. In the case when $p \neq 0$, the anharmonicity of the system should be taken into account [1, 2], which provides a means for revising the interatomic potential.

Prikhodko *et al.* [3] carried out density-functional theory calculations of the elastic moduli C_{ij} , derivatives dC_{ij}/dp , and velocities of sound $v_i(\mathbf{q})$ for the cubic modification of silicon carbide. The purpose of the present work was to analyze the results of these calculations within the Keating model of force constants [4], which was used to advantage in describing the elastic properties of $A_N B_{8-N}$ crystals in [5].

2. 3C-SiC: PRESSURE DEPENDENCE OF THE SECOND-ORDER ELASTIC CONSTANTS

According to the Keating model, tetrahedral crystals can be characterized by two force constants, namely, the constant α , which describes the central interaction of the nearest neighbors, i.e., the response to a variation in the bond length, and the constant β , which corresponds to the noncentral interaction of the next-to-nearest neighbors, i.e., the response of the tetrahedron to a variation in the angle between $|sp^3\rangle$ orbitals. The second-order elastic constants have the form

$$C_{11} = \frac{\alpha + 3\beta}{4a_0}, \quad C_{12} = \frac{\alpha - \beta}{4a_0}, \quad C_{44} = \frac{\alpha\beta}{a_0(\alpha + \beta)}. \quad (1)$$

Here, $4a_0$ is the lattice constant of the unstrained crystal and the second-order elastic constants obey the identity

$$R \equiv \frac{C_{44}(C_{11} + C_{12})}{C_S(C_{11} + 3C_{12})} = 1, \quad (2)$$

where $C_S = (1/2)(C_{11} - C_{12})$ is the shear modulus. It should be noted that relationships (1) and (2) are derived for purely covalent crystals of Group IV elements (homopolar bond). Silicon carbide belongs to crystals with a heteropolar bond and, strictly speaking, can be adequately described in terms of the model proposed by Martin [6], who extended the Keating model to ionic-covalent crystals. In this case, the theory treats the effective ion charges and the Coulomb contributions to the elastic constants. Moreover, instead of one noncentral constant β , there appear two constants (β_1, β_2), which describe the response to a variation in the tetrahedral angles between the $|sp^3\rangle$ orbitals centered at the silicon and carbon atoms. However, it can be shown that the ionicity of the silicon-carbon bond is relatively small; hence, the Coulomb contributions can be ignored without a loss of accuracy. Indeed, in the framework of the Harrison method of bonding orbitals [7], the covalence of the silicon-carbon bond is determined to be $\alpha_c = 0.97$ (see, for example, [8]), which corresponds to the ionicity $f_i = 1 - \alpha_c^3 \approx 0.09$ according to Phillips [9]. Then, setting $\beta = (1/2)(\beta_1 + \beta_2)$, we come to the Keating model.

After substituting the elastic moduli $C_{11} = 385$, $C_{12} = 135$, and $C_{44} = 257$ GPa (determined in [3]) into expression (2), we obtain $R \approx 1.35$. This value already casts some doubt on the reliability of the experimental data, because, for diamond and silicon crystals, relationship (2) is accurate to within 1% [4]. It is worth noting that the experimental elastic constants $C_{11} = 410.5$, $C_{12} = 164$, and $C_{44} = 194$ GPa for C-SiC crystals, which are presented in the monograph by Nikanorov and Kardashev [5], satisfy relationship (2) to very high accuracy. A comparison of the results of calculations per-

formed in [3] and the aforementioned experimental values shows that the discrepancy in the elastic moduli increases in the sequence $C_{11} \rightarrow C_{12} \rightarrow C_{44}$: the ratios C_{ij} (taken from [3])/ C_{ij} (taken from [5]) are equal to 0.94, 0.82, and 1.32 respectively. However, it should be noted that, unlike the calculated and experimental values of the elastic modulus C_{44} , the values of the second shear modulus $C_S = (1/2)(C_{11} - C_{12})$ determined only by the constant β almost coincide: $C_S = 125$ [3] and 123 GPa [5]. The bulk moduli $B = (1/3)(C_{11} + 2C_{12})$ are also in reasonable agreement: $B = 218$ [3] and 246 GPa [5]. In our calculations, we started from the experimental data presented in [5], which gave the force constants $\alpha = 98$ N/m and $\beta = 27$ N/m. The Kleinman parameter in terms of the Keating model is determined as $\zeta = (\alpha - \beta)/(\alpha + \beta) \approx 0.57$, which exceeds the value $\zeta = 0.41$ obtained in [5]. Let us now assume (as was done in our earlier calculations of the elastic properties of Group V semimetals [10]) that, under pressure, the force constants vary as follows: $\alpha \rightarrow \tilde{\alpha} = \alpha + ap$ and $\beta \rightarrow \tilde{\beta} = \beta + bp$, where the constants a and b have dimensions of length. Under the above assumption, the elastic constants can be represented in the form

$$\begin{aligned} \tilde{C}_{11} &= C_{11} + \frac{a+3b}{4a_0}p, & \tilde{C}_{12} &= C_{12} + \frac{a-b}{4a_0}p, \\ \tilde{C}_{44} &= \frac{\alpha\beta + (\alpha b + a\beta)p + abp^2}{(\alpha + \beta) + (a+b)p}. \end{aligned} \quad (3)$$

Hereinafter, all quantities that are dependent on pressure are marked by the tilde sign. In order to determine the constants a and b , we used the following derivatives $d\tilde{C}_{ij}/dp$ obtained in [3]: $d\tilde{C}_{11}/dp = 3.49$ and $d\tilde{C}_{12}/dp = 4.06$.¹ As a result, we obtained the constants $a = 17.08$ Å and $b = -0.62$ Å. Note that the constant b was determined from the derivative $d\tilde{C}_S/dp$.

The calculated dependences of the elastic constants \tilde{C}_{ij} on the pressure p for the 3C-SiC crystal are presented in Fig. 1. A comparison with the corresponding dependences obtained in [3] shows that only the curves $\tilde{C}_{44}(p)$ differ significantly. According to [3], an increase in the pressure is accompanied by an insignificant monotonic increase in the shear modulus \tilde{C}_{44} . In our case, as the pressure increases, the shear modulus \tilde{C}_{44} first increases from $\tilde{C}_{44}(0) = 194$ GPa, passes through a maximum value of 198 GPa at a pressure $p_m = 21.5$ GPa, and then smoothly decreases to 178 GPa

¹ Unfortunately, we are not aware of any experimental pressure dependences of the second-order elastic constants of silicon carbide.

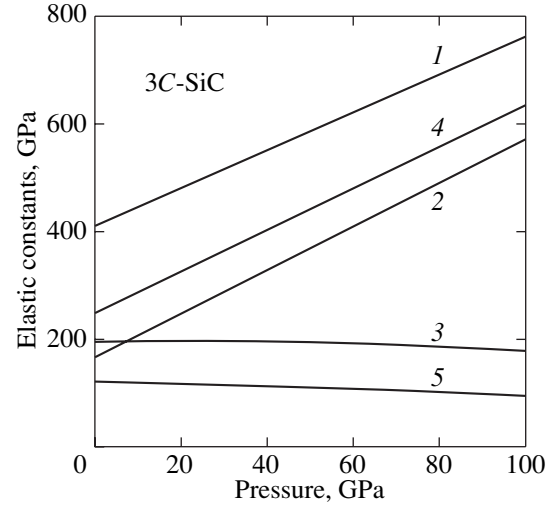


Fig. 1. Pressure dependences of the elastic constants of the 3C-SiC crystal: (1) \tilde{C}_{11} , (2) \tilde{C}_{12} , (3) \tilde{C}_{44} , (4) \tilde{B} , and (5) \tilde{C}_S .

at $p = 100$ GPa. The value of p_m can be found from the condition $d\tilde{C}_{44}/dp = 0$, which leads to the equation

$$p^2 + 2\frac{\alpha + \beta}{a + b}p + \frac{a\beta^2 + b\alpha^2}{ab(a + b)} = 0. \quad (4)$$

3. 3C-SiC: PRESSURE DEPENDENCE OF THE VELOCITY OF SOUND

In order to calculate the velocity of sound $v_i(\mathbf{q}) = \sqrt{C_i(\mathbf{q})/\rho}$, it is necessary to derive the appropriate combinations of elastic constants \tilde{C}_{ij} required to determine the quantities $C_i(\mathbf{q})$. These combinations have the following form (see, for example, [3]):

$$\begin{aligned} C_{[111]}([111]) &= \frac{1}{3}(C_{11} + 2C_{12} + 4C_{44}), \\ C_{[110]}([110]) &= \frac{1}{2}(C_{11} + C_{12} + 2C_{44}), \\ C_{[100]}([100]) &= C_{11}, \\ C_{[010]}([100]) &= C_{[001]}([100]) = C_{[001]}([110]) = C_{44}, \\ C_{[1\bar{1}0]}([111]) &= C_{[11\bar{2}]}([111]) = \frac{1}{3}(C_{11} - C_{12} + C_{44}), \\ C_{[1\bar{1}0]}([110]) &= \frac{1}{2}(C_{11} - C_{12}). \end{aligned} \quad (5)$$

Here, the first three combinations correspond to longitudinal acoustic waves (LA) and the last three combinations, to transverse acoustic waves (TA). Moreover, we should take into account that the density $\tilde{\rho}$ of the crys-

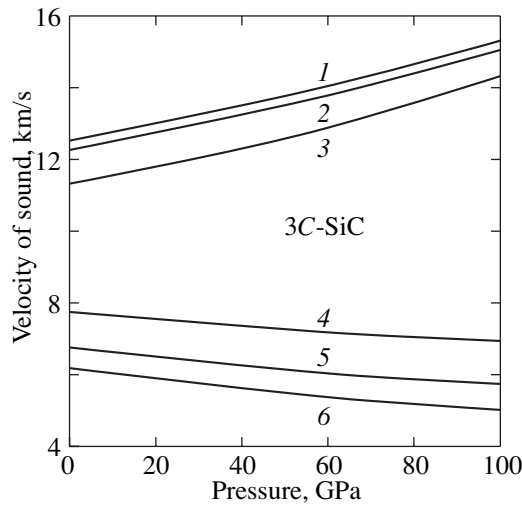


Fig. 2. Pressure dependences of the velocity of sound in the 3C-SiC crystal: (1) $v_{LA}([111])$, (2) $v_{LA}([110])$, (3) $v_{LA}([100])$, (4) $v_{TA}([100]) = v_{TA}([110])$, (5) $v_{TA}([111])$, and (6) $v_{TA}([110])$.

tal also depends on pressure. The pressure \tilde{p} can be written in the form

$$\tilde{p} = \rho \left[1 + (p/B) + \frac{1}{2}(1 - d\tilde{B}/dp)(p/B)^2 \right], \quad (6)$$

where $\rho = 3.21 \text{ g/cm}^3$ [11]. According to the data obtained in [3], we have the derivative $d\tilde{B}/dp = 3.87$, which agrees well with the experimental value of 3.57 [12].

The calculated pressure dependences of the velocity of sound in the 3C-SiC crystal are shown in Fig. 2. It can be seen that the velocity of propagation of longitudinal modes increases with increasing pressure, whereas the velocity of propagation of transversal modes decreases. The only qualitative difference between our results and the data obtained in [3] is associated with the pressure dependence of the velocity $v_{[001]}([110]) = v_{[010]}([100]) = v_{[001]}([100])$. As the pressure p increases, the velocity smoothly decreases in our

Table 1. Derivatives $(dv_i(\mathbf{q})/dp)_{p \rightarrow 0}$ (in km/s GPa)

No.	Acoustic mode	$\mathbf{q} = [100]$	$\mathbf{q} = [110]$	$\mathbf{q} = [111]$
1	<i>L</i>	0.024	0.026	0.027
2	<i>T</i>	-0.007	-0.019	-0.015
3	<i>T</i>	-0.007	-0.009	-0.015
4	<i>L</i>	0.025	0.036	0.040
5	<i>T</i>	0.007	-0.021	-0.009
6	<i>T</i>	0.007	0.007	-0.009

Note: Rows 1–3 present the results obtained in this work, and rows 4–6 present data taken from [3].

case, whereas the function $v_{TA}(p)$ has a maximum at $p \approx 50 \text{ GPa}$ in [3]. The derivatives $(dv_i(\mathbf{q})/dp)_{p \rightarrow 0}$ obtained in this work and in [3] are listed in Table 1. The main discrepancy (i.e., the opposite signs of the slopes) is observed for the modes determined by the shear modulus \tilde{C}_{44} [see the fourth combination in formulas (5)].

Now, we can calculate the Grüneisen parameters $\gamma_i(\mathbf{q})$ defined by the relationship

$$\gamma_i(\mathbf{q}) = \frac{1}{v_i(\mathbf{q})} \frac{dv_i(\mathbf{q})}{dp} B. \quad (7)$$

The results of the calculation are presented in Table 2. Again, the main discrepancy is observed for the modes $v_{[001]}([110]) = v_{[010]}([100]) = v_{[001]}([100])$.

4. 2H-SiC: PRESSURE DEPENDENCE OF THE SECOND-ORDER ELASTIC CONSTANTS

As was shown by Martin [13], the second-order elastic constants for a wurtzite structure can be determined from the elastic constants \tilde{C}_{ij} known for a sphalerite structure. Earlier [14, 15], we extended the approach developed by Martin to polytypes with an arbitrary ratio of the sphalerite and wurtzite structures. Consequently, expressions for the elastic constants C_{ij} of silicon carbide 2H-SiC with a hexagonal structure can be derived using formulas (1), as was done in our previous work [16]. After substituting the force constants α and β , which were determined above, we obtained the following second-order elastic constants at a pressure $p = 0$ (in GPa): $C_{11} = 476$, $C_{33} = 507$, $C_{44} = 142$, $C_{12} = 147$, $C_{13} = 116$, and $C_{66} = (1/2)(C_{11} - C_{12}) = 164.5$. Note that the elastic constants found here exceed those obtained in our earlier work [17] in the framework of the Keating–Harrison model and correlate better with the experimental data taken from handbook [11] (in GPa): $C_{11} = 500$, $C_{33} = 564$, $C_{44} = 168$, $C_{12} = 92$, and $C_{66} = 204$ (data on the elastic modulus C_{13} are not available in [11]).

Figure 3 shows the pressure dependences of the elastic constants \tilde{C}_{ij} for the 2H-SiC crystal. As is clearly seen from Fig. 3, the elastic moduli as functions of pressure can be separated into three groups, each including close values of both \tilde{C}_{ij} and $d\tilde{C}_{ij}/dp$: (i) \tilde{C}_{11} and \tilde{C}_{33} , (ii) \tilde{C}_{12} and \tilde{C}_{13} , and (iii) \tilde{C}_{44} and \tilde{C}_{66} . As the pressure increases, the elastic moduli of the first two groups increase, whereas the elastic moduli of the third group decrease. Unfortunately, we are not aware of any experimental data on the elastic moduli of 2H-SiC crystals.

It is of interest to note that, at an arbitrary ratio of the wurtzite and sphalerite phases (trigonal crystal system, class 32 [18]), some combinations of elastic constants C_{ij}^* (the asterisk refers to the trigonal structure) are invariant [14]:

$$\begin{aligned} C_{11}^* + C_{12}^* &= \frac{2}{3}(C_{11} + 2C_{12} + C_{44}), \\ C_{13}^* &= \frac{1}{3}(C_{11} + 2C_{12} - 2C_{44}), \\ C_{33}^* &= \frac{1}{3}(C_{11} + 2C_{12} + 4C_{44}). \end{aligned} \quad (8)$$

In these expressions, the right-hand sides involve the elastic constants for a cubic crystal. Hence, it follows in particular that the velocity of a longitudinal acoustic wave $v_{LA}([111])$, which is determined by the elastic constant C_{33}^* , is also invariant with respect to the structure of a mixed wurtzite–sphalerite crystal.

With knowledge of the dependences of the elastic constants \tilde{C}_{ij} on the pressure p , it is possible to determine the corresponding pressure dependences of the velocity of sound. In [3], the dependence $v_h(p)$ was calculated for a transverse acoustic wave propagating in the direction $(\mathbf{x} + \mathbf{y})/\sqrt{2}$, where \mathbf{x} coincides with the direction of the hexagonal c axis and \mathbf{y} lies in the basal plane perpendicular to the c axis.² It was assumed that $v_h(p) = \sqrt{C_{66}^h/\rho} = \sqrt{\bar{C}_{66}/\rho}$ and $\bar{C}_{66} = (1/6)(C_{11}^c - C_{12}^c + 4C_{44}^c)$, where the upper indices denote the hexagonal (h) or cubic (c) modification. However, Martin [13] proved that $C_{66}^h = \bar{C}_{66} - \Delta^2/\bar{C}_{44}$, where $\bar{C}_{44} = (1/3)(C_{11}^c - C_{12}^c + C_{44}^c)$ and $\Delta = (C_{11}^c - C_{12}^c - 2C_{44}^c)/3\sqrt{2}$ (see corrections in [14, 15]). Figure 4 depicts the dependence $v_h(p)$, which we calculated in the framework of the theory proposed by Martin [13]. As follows from our calculations, $\delta v_h \approx 1$ km/s). This value differs from the data obtained in [3], according to which the change in the velocity δv_h in the pressure range from 0 to 100 GPa is equal to 0.35 km/s.

5. 3C-SiC: THIRD-ORDER ELASTIC CONSTANTS

A force-field model for calculating the third-order elastic constants \tilde{C}_{ijk} of cubic crystals was proposed by

² This direction of propagation of the acoustic wave is interesting above all in that the orthorhombic shear strain leads to a transition from the wurtzite structure to the NaCl structure [3].

Table 2. Grüneisen parameters $\gamma_i(\mathbf{q})$

No.	Acoustic mode	$\mathbf{q} = [100]$	$\mathbf{q} = [110]$	$\mathbf{q} = [111]$
1	L	0.52	0.52	0.53
2	T	-0.22	-0.76	-0.55
3	T	-0.22	-0.22	-0.55
4	L	0.49	0.63	0.66
5	T	0.17	-0.74	-0.28
6	T	0.17	0.17	-0.28

Note: Rows 1–3 present the results obtained in this work, and rows 4–6 present data taken from [3].

Keating [19]. In the framework of this model, we have

$$\begin{aligned} C_{111} &= \gamma - \delta + 9\varepsilon, \\ C_{112} &= \gamma - \delta + \varepsilon, \\ C_{123} &= \gamma + 3\delta - 3\varepsilon, \\ C_{144} &= \gamma(1 - \zeta)^2 + \delta(1 + \zeta)^2 \\ &\quad + \varepsilon(1 + \zeta)(3\zeta - 1) + C_{12}\zeta^2, \\ C_{166} &= \gamma(1 - \zeta)^2 - \delta(1 + \zeta)^2 \\ &\quad + \varepsilon(1 + \zeta)(3 - \zeta) + C_{12}\zeta^2, \\ C_{456} &= \gamma(1 - \zeta)^3. \end{aligned} \quad (9)$$

Here, γ is the anharmonic force constant describing the central interaction of the nearest neighbors, δ and ε are the anharmonic force constants accounting for the non-central interaction of the next-to-nearest neighbors, and ζ is the Kleinman parameter.³ In order to determine these force constants, we use the results obtained by Birch [20], who derived the following relationships between the elastic constants C_{ij} and C_{ijk} and the derivatives $d\tilde{C}_{ij}/dp$:

$$\begin{aligned} \frac{d\tilde{C}_{11}}{dp} &= -1 - \frac{C_{11} + C_{111} + 2C_{112}}{3B}, \\ \frac{d\tilde{C}_{12}}{dp} &= 1 - \frac{C_{12} + C_{123} + 2C_{112}}{3B}, \\ \frac{d\tilde{C}_{14}}{dp} &= -1 - \frac{C_{44} + C_{144} + 2C_{166}}{3B}. \end{aligned} \quad (10)$$

It should be emphasized that these relationships are valid only in the approximation that is linear with respect to pressure. Relationships (10) make it possible to determine the anharmonic force constants γ , δ , and ε ,

³ As in the case of second-order elastic constants, we disregard the Coulomb contributions and assume that $\delta = (1/2)(\delta_1 + \delta_2)$ and $\varepsilon = (1/2)(\varepsilon_1 + \varepsilon_2)$, where subscripts 1 and 2 refer to silicon and carbon atoms, respectively.

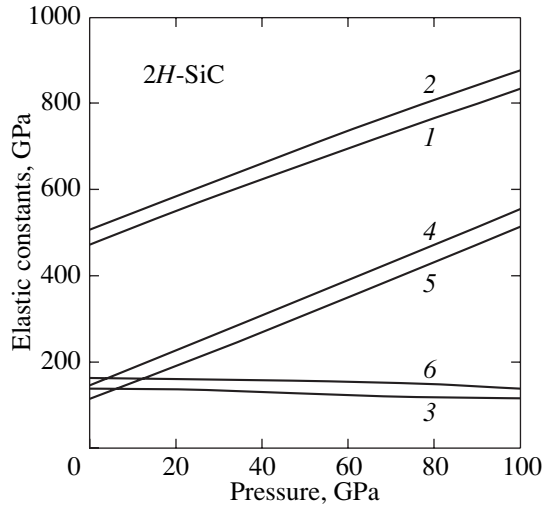


Fig. 3. Pressure dependences of the elastic constants of the 2H-SiC crystal: (1) \tilde{C}_{11} , (2) \tilde{C}_{33} , (3) \tilde{C}_{44} , (4) \tilde{C}_{12} , (5) \tilde{C}_{13} , and (6) \tilde{C}_{66} .

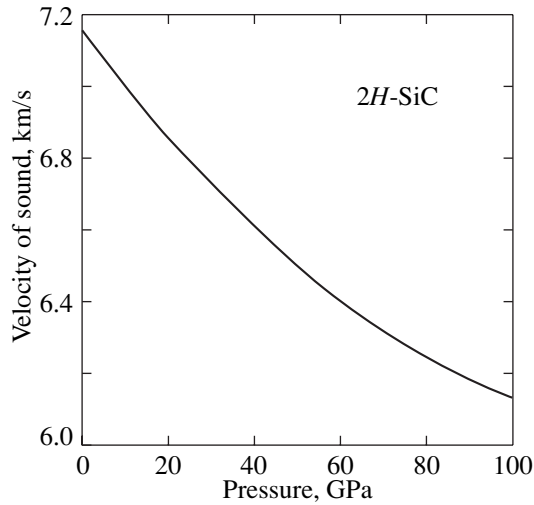


Fig. 4. Pressure dependence of the velocity of sound v_h in the 2H-SiC crystal.

provided the values of $d\tilde{C}_{ij}/dp$ are known. Since the value of the derivative $d\tilde{C}_{44}/dp$ is in doubt, we simplify the problem and assume that $\varepsilon = -\delta$. This equality is completely satisfied for silicon [19]; however, in the case of other semiconductor crystals also, the anharmonic force constants δ and ε are of the same order of magnitude and opposite in sign (see, for example, [21, 22] and references therein). Moreover, the force constant γ is approximately one order of magnitude greater than the force constants δ and $|\varepsilon|$; therefore, the above simplification does not introduce large error into the calculation.

Then, making allowance for the first two relationships (9) and using the data taken from [3], we determine the anharmonic force constants $\gamma = -862$ GPa and $\delta = 82$ GPa.

Finally, we obtain the following third-order elastic constants (in GPa): $C_{111} = -1680$, $C_{112} = -1026$, $C_{123} = -371$, $C_{144} = 3$, $C_{166} = -621$, and $C_{456} = -69.5$. Although we are unaware of any experimental values of the third-order elastic constants of silicon carbide, a comparison of the results of our calculations and the elastic constants C_{ijk} for Si, Ge, InSb, and GaAs crystals [19, 21] shows that our values are quite reasonable. Indeed, for all these crystals, only the elastic constant C_{144} is positive and, moreover, is one to two orders of magnitude smaller than the elastic constant $|C_{111}|$. It is worth nothing that the aforementioned elastic constants obey the following inequalities: $|C_{111}| > |C_{112}| > |C_{166}| > |C_{123}|$ and $|C_{456}| > C_{144}$. In our calculations, we obtained the same relationships.

Let us calculate the derivative $d\tilde{C}_{44}/dp$. For this purpose, we use the last formula (9) and the anharmonic force constants determined above. As a result, we obtain $d\tilde{C}_{44}/dp = -1.08$. According to the calculation data presented in Section 2, the derivative $d\tilde{C}_{44}/dp$ averaged over the pressure range from 0 to 100 GPa is approximately equal to -0.18 , which coincides, at least in sign, with the above result. However, in [3], this quantity was determined to be $d\tilde{C}_{44}/dp = 1.58$, which, in our opinion, leads to a false inference regarding a nonmonotonic pressure dependence of the velocity of propagation of transverse acoustic waves $v_{TA}(p)$ (see Section 3).

In our calculations, we determined the force constants γ and δ with the use of formulas (10) for the derivatives $d\tilde{C}_{11}/dp$ and $d\tilde{C}_{12}/dp$ taken from [3]. However, representing these derivatives in the form $(a + 3b)/4a_0$ and $(a - b)/4a_0$, respectively, we can check the values of constants a and b determined above. As a result, we found that $a = 17.14$ Å and $b = -0.59$ Å, which is in excellent agreement with the values $a = 17.08$ Å and $b = -0.62$ Å determined in Section 2. The good agreement between the force constants obtained by different methods is a consequence of the weak nonlinearity of the dependence $\tilde{C}_{44}(p)$.

Now, we calculate the Grüneisen integrated parameter $\bar{\gamma}$, which is defined by the following formula [22]:

$$\bar{\gamma} = \frac{5\alpha - \beta + 4a_0(3\gamma - \delta + \varepsilon)}{6(\alpha + \beta)}. \quad (11)$$

In this case, we once again assume that $\varepsilon = -\delta$. Then, we obtain $\bar{\gamma} = 0.98$, which almost coincides with the Grüneisen parameter γ_{LA} calculated by Karch *et al.* [23] for longitudinal acoustic waves.

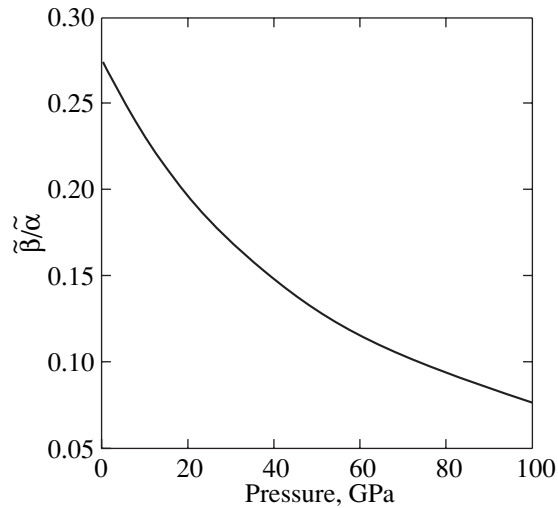


Fig. 5. Pressure dependence of the ratio of the force constants of the noncentral and central interactions $\tilde{\beta}/\tilde{\alpha}$.

In conclusion, we note that the investigation of the effect of pressure on tetrahedral crystals is of interest primarily due to the occurrence of a phase transition from the sphalerite or wurtzite structure to the rock-salt structure under high pressure (see, for example, [24–26] and references therein). In the framework of the Keating–Martin model, the ratio of the force constants β/α decreases with an increase in the ionicity f_i of the bond, i.e., upon transition from purely covalent semiconductor crystals of Group IV elements to tetrahedral compounds A_1B_3 , which, on the scale of ionicities f_i , are adjacent to crystals with a NaCl structure [5, 6, 9, 21, 24]. Figure 5 presents the ratio $\tilde{\beta}/\tilde{\alpha}$ as a function of the pressure p . It follows from this figure that, compared to the central forces, the effect of the noncentral forces decreases with increasing pressure, which is characteristic of ionic crystals.

Thus, we demonstrated that the simple Keating model can compete advantageously with first principles calculations and offers a more adequate description of a number of elastic characteristics of tetrahedral crystals.

ACKNOWLEDGMENTS

This work was supported by the Russian Foundation for Basic Research (project no. 03-02-16054), the International Association of Assistance for the promotion of cooperation with scientists from the New Independent States of the Former Soviet Union (project no. INTAS 01-0603), and the “Science for Peace” NATO program (grant no. SfP 978011).

REFERENCES

1. G. Leibfried, *Gittertheorie der Mechanischen und Thermischen Eigenschaft der Kristalle: Handbuch der Physik* (Springer, Berlin, 1955; GIFML, Moscow, 1963).
2. H. Bottger, *Principles of the Theory of Lattice Dynamics* (Physik, Weinheim, 1983; Mir, Moscow, 1986).
3. M. Prikhodko, M. S. Miao, and W. R. L. Lambrecht, *Phys. Rev. B* **66**, 125201 (2002).
4. P. N. Keating, *Phys. Rev.* **145** (2), 637 (1966).
5. S. P. Nikanorov and B. K. Kardashev, *Elasticity and Dislocation Inelasticity of Crystals* (Nauka, Moscow, 1985).
6. R. M. Martin, *Phys. Rev. B* **1** (11), 4005 (1970).
7. W. A. Harrison, *Electronic Structure and the Properties of Solids: The Physics of the Chemical Bond* (Freeman, San Francisco, 1980; Mir, Moscow, 1983), Vol. 1.
8. S. Yu. Davydov and S. K. Tikhonov, *Fiz. Tekh. Poluprovodn. (St. Petersburg)* **32** (9), 1057 (1998) [*Semiconductors* **32**, 947 (1998)].
9. J. C. Phillips, *Rev. Mod. Phys.* **42** (3), 317 (1970).
10. V. M. Grabov, S. Yu. Davydov, Yu. P. Mironov, and A. M. Dzhumigo, *Fiz. Tverd. Tela (Leningrad)* **27** (7), 2017 (1985) [*Sov. Phys. Solid State* **27**, 1210 (1985)].
11. *Physical Quantities: A Handbook*, Ed. by I. S. Grigor'ev and E. Z. Meilikhov (Énergoatomizdat, Moscow, 1991).
12. I. V. Aleksandrov, A. F. Goncharenko, S. M. Stishov, and E. V. Yakovenko, *Pis'ma Zh. Éksp. Teor. Fiz.* **50** (3), 116 (1989) [*JETP Lett.* **50**, 127 (1989)].
13. R. M. Martin, *Phys. Rev. B* **6** (12), 4546 (1972).
14. A. I. Gubanov and S. Yu. Davydov, *Fiz. Tverd. Tela (Leningrad)* **17** (5), 1463 (1975) [*Sov. Phys. Solid State* **17**, 945 (1975)].
15. S. Yu. Davydov and S. K. Tikhonov, *Fiz. Tverd. Tela (St. Petersburg)* **37** (7), 2221 (1995) [*Phys. Solid State* **37**, 1212 (1995)].
16. S. Yu. Davydov and A. V. Solomonov, *Pis'ma Zh. Tekh. Fiz.* **25** (15), 23 (1999) [*Tech. Phys. Lett.* **25**, 601 (1999)].
17. S. Yu. Davydov and S. K. Tikhonov, *Fiz. Tekh. Poluprovodn. (St. Petersburg)* **30** (7), 1300 (1996) [*Semiconductors* **30**, 683 (1996)].
18. J. F. Nye, *Physical Properties of Crystals: Their Representation by Tensors and Matrices*, 2nd ed. (Clarendon Press, Oxford, 1964; Mir, Moscow, 1967).
19. P. N. Keating, *Phys. Rev.* **149** (2), 674 (1966).
20. P. Birch, *Phys. Rev.* **71** (5), 809 (1947).
21. S. Yu. Davydov, Candidate's Dissertation (Physicotechnical Inst., Leningrad, 1974).
22. M. I. Bell, *Phys. Status Solidi B* **53** (3), 675 (1972).
23. K. Karch, P. Pavone, W. Windl, O. Schutt, and D. Strauch, *Phys. Rev. B* **50** (24), 17054 (1994).
24. J. C. Phillips, *Bonds and Bands in Semiconductors* (Academic, New York, 1960).
25. J. A. Majewski and P. Vogl, *Phys. Rev. B* **35** (18), 9666 (1987).
26. A. J. Skinner and J. P. LaFemia, *Phys. Rev. B* **45** (7), 3557 (1992).

Translated by O. Moskalev

Generation of Shallow Nitrogen–Oxygen Donors as a Method for Studying Nitrogen Diffusion in Silicon

V. V. Voronkov*, A. V. Batunina*, G. I. Voronkova*, and M. G. Mil'vidskii**

* Giredmet State Research Institute for the Rare-Metals Industry, Moscow, 109017 Russia

e-mail: icpm@mail.girmet.ru

** Institute for Chemical Problems of Microelectronics, Bol'shoi Tolmachevskii per. 5, Moscow, 109017 Russia

Received November 25, 2003

Abstract—The nitrogen concentration distribution $C(z)$ obtained after diffusion of nitrogen from the bulk of a sample toward the surface is determined with a high accuracy through subsequent heat treatment at moderate temperatures (for example, at 650°C). This process leads to the formation of shallow thermal donors (nitrogen–oxygen complexes) with a concentration distribution over the depth z of the sample that corresponds to the nitrogen concentration profile $C(z)$ and, therefore, makes it possible to calculate this profile. The proposed method is used to determine the nitrogen concentration profiles $C(z)$ after homogenizing annealing at 950, 1000, and 1050°C. At high oxygen concentrations, the nitrogen transport is promoted by high-rate dissociation of nitrogen dimers. On the other hand, the nitrogen transport is slightly hindered by partial oxidation of nitrogen monomers. The results obtained indicate that the latter effect is not very strong, because the dimeric nitrogen species predominate over the monomeric nitrogen species in the sample and the diffusion profile is determined by the product $D_1K^{1/2}$, where D_1 is the diffusion coefficient of nitrogen monomers and K is the dissociation constant. © 2004 MAIK “Nauka/Interperiodica”.

1. INTRODUCTION

Diffusion of nitrogen impurities in silicon is a technologically important process. Moreover, investigation into the diffusion of nitrogen impurities in silicon provides valuable information on the properties of nitrogen, primarily, on the ratio of dimeric species N_2 (which are predominant at sufficiently low temperatures) to monomeric species N_1 . An analysis of the data available in the literature on the diffusion of nitrogen in silicon crystals was performed in our previous work [1]. It has been established that, in silicon crystals with a low oxygen content, the dimeric (virtually immobile) nitrogen species predominate at doping levels of the order of 10^{15} cm^{-3} and at diffusion temperatures of 1100°C and below [1]. However, the fraction of mobile monomeric nitrogen species is rather large (of the order of 10% at 1000°C). At temperatures close to the melting point, the monomeric nitrogen species become predominant.

The nitrogen transport occurs through the dissociation of immobile interstitial N_2 dimers into mobile interstitial N_1 monomers that diffuse and form new N_2 dimers. For a low-oxygen material, which can be prepared, for example, using the float zone (FZ) technique, the analysis of the nitrogen transport is complicated by the uncertainty in the time required for an N_2 dimer to dissociate into two N_1 atoms [1]: according to different approaches, the dissociation time of N_2 dimers either is very short or can be as long as 5 min (at 1000°C).

This uncertainty is absent in the case when the oxygen content is relatively high (for example, in a material prepared using the Czochralski method), because oxygen produces a very strong catalytic promoting effect on the dissociation of nitrogen dimers [1]. On the other hand, oxygen can hinder nitrogen transport due to the formation of nitrogen–oxygen complexes. The oxidation number of nitrogen dimers is small at temperatures $T > 800^\circ\text{C}$ [1], but the oxidation number of nitrogen monomers can, in principle, be large enough for the nitrogen monomers to have an effect on the nitrogen diffusion. In this respect, investigation into the diffusion of nitrogen in Czochralski silicon can provide new interesting information on the diffusion characteristics of nitrogen species and on the possible interaction of nitrogen with oxygen.

For the purpose of studying the nitrogen diffusion in silicon crystals, we developed and successfully employed a new highly sensitive technique for determining the profile of nitrogen diffusion in a material containing impurities of two types, namely, nitrogen and oxygen impurities. It is known that heat treatment of such a material at moderate temperatures (from 600 to 700°C) brings about the formation of specific shallow thermal donors (nitrogen–oxygen complexes) [2–6]. In our earlier works [5, 6], we analyzed the dependence of the concentration of shallow thermal donors on the total nitrogen concentration and demonstrated that these donors are N_1O_m complexes formed by one N_1 atom and m oxygen atoms (on average, $m = 3$). With knowledge of the depth profile of shallow thermal

donors, which is determined, for example, using the spreading resistance method, it is possible to reconstruct the corresponding diffusion profile of nitrogen.

2. SAMPLE PREPARATION AND EXPERIMENTAL TECHNIQUE

Samples of Czochralski silicon ($12 \times 4 \times 1$ mm in size) were cut from a silicon plate 150 mm in diameter. The crystal was doped with nitrogen from a melt. The nitrogen concentration C increased along the length of the crystal. This concentration was calculated from the known coefficient of nitrogen distribution [7] and was then controlled using secondary ion mass spectrometry [5]. The nitrogen concentration C in the plate used for preparing the samples was approximately equal to $2 \times 10^{15} \text{ cm}^{-3}$. In order to calculate the nitrogen concentration C from the coefficient of the nitrogen distribution more exactly, it should be taken into account that, although the monomeric nitrogen species predominate at the crystallization temperature, the sample also contains dimeric nitrogen species in small amounts [1]. However, this correction only slightly changes the calibration curve relating the nitrogen concentration C and the concentration of shallow thermal donors.

The homogenizing annealing of the samples was carried out at temperatures of 950, 1000, and 1050°C in air. The annealing time (from 5 to 50 min) was chosen so that the size of the surface region in which the nitrogen concentration $C(z)$ considerably decreased as a result of diffusion of nitrogen toward the surface of the sample was convenient for subsequent measurements (several tens of microns). Upon annealing, the samples were quenched on a massive silicon slab.

After homogenizing annealing, shallow thermal donors were generated using standard heat treatment at a temperature of 650°C for 3 h. Under these conditions, the concentration of shallow thermal donors reaches saturation, which corresponds to an equilibrium between nitrogen, oxygen, and the products of their interaction, including N_1O_m complexes (shallow thermal donors). The equilibrium ratio between the concentration N_s of shallow thermal donors and the total concentration C of dissolved nitrogen (predominantly, in the form of unoxidized dimers, oxidized dimers, and shallow thermal donors) can be obtained from the mass action law for the corresponding reactions [5, 6]:

$$N_s^2/(C - N_s) = R. \quad (1)$$

The equilibrium constant R depends on the temperature T and the oxygen concentration C_{ox} (in our samples, the oxygen concentration C_{ox} was maintained constant at approximately $6.7 \times 10^{17} \text{ cm}^{-3}$ with the use of a calibration optical factor of $2.45 \times 10^{17} \text{ cm}^{-2}$). In this case, the equilibrium constant R was close to $2.85 \times 10^{13} \text{ cm}^{-3}$. Relationship (1) holds true over a wide range of nitrogen concentrations C (from 10^{14} to $2 \times 10^{15} \text{ cm}^{-3}$).

In order to convert the measured concentration N_s of shallow thermal donors into the required total nitrogen concentration C , relationship (1) is conveniently rewritten in the form

$$C = N_s(1 + N_s/R). \quad (2)$$

Although relationship (1) and the equilibrium constant R were obtained for samples with a uniform distribution of the nitrogen concentration over the sample depth, they are applicable to any point of the diffusion profile $C(z)$, because the diffusion redistribution of nitrogen between different regions of the sample is insignificant at a relatively low temperature of generation of shallow thermal donors (650°C). Therefore, knowing the measured concentration profile $N_s(z)$ of shallow thermal donors, we can calculate the nitrogen diffusion profile $C(z)$ from expression (2). The concentration $N_s(z)$ is maximum in the bulk of the sample (where the loss of nitrogen due to diffusion is small) and negligible in the immediate vicinity of the surface of the sample (where the nitrogen concentration C drastically decreases as a result of nitrogen diffusion toward the surface).

After homogenizing annealing [which leads to the formation of the concentration profile $C(z)$] and subsequent activation annealing [which results in the formation of the concentration profile $N_s(z)$], the spreading resistance was measured on a cleavage or a surface prepared by grinding. Our samples were lightly doped with boron (acceptor impurity) at a concentration $N_a = 4 \times 10^{14} \text{ cm}^{-3}$, which varied within $\pm 5\%$ from sample to sample. The maximum concentration $N_s(z)$ observed far from the surface did not exceed $2 \times 10^{14} \text{ cm}^{-3}$. Therefore, p -type conductivity was retained throughout the depth of the sample and the measured profile of the spreading resistance was immediately converted into the hole concentration profile $p(z)$. Since the hole concentration profile satisfies the relationship $p(z) = N_a - N_s(z)$, the concentration profile of shallow thermal donors under consideration can be expressed through the hole concentration:

$$N_s(z) = N_a - p(z). \quad (3)$$

The nitrogen diffusion profile was determined as follows: (i) the spreading resistance profile was measured and converted into the hole concentration profile $p(z)$, (ii) the concentration profile of shallow thermal donors was calculated from formula (3), and (iii) the concentration profile $N_s(z)$ was converted into the nitrogen diffusion profile $C(z)$ with the use of relationship (2).

In order to determine the nitrogen diffusion profile reliably, the nitrogen concentration (in the bulk of the sample) should be high enough for generated shallow thermal donors to bring about a noticeable decrease in the hole concentration. To put it differently, the concentration N_s of shallow thermal donors should be compa-

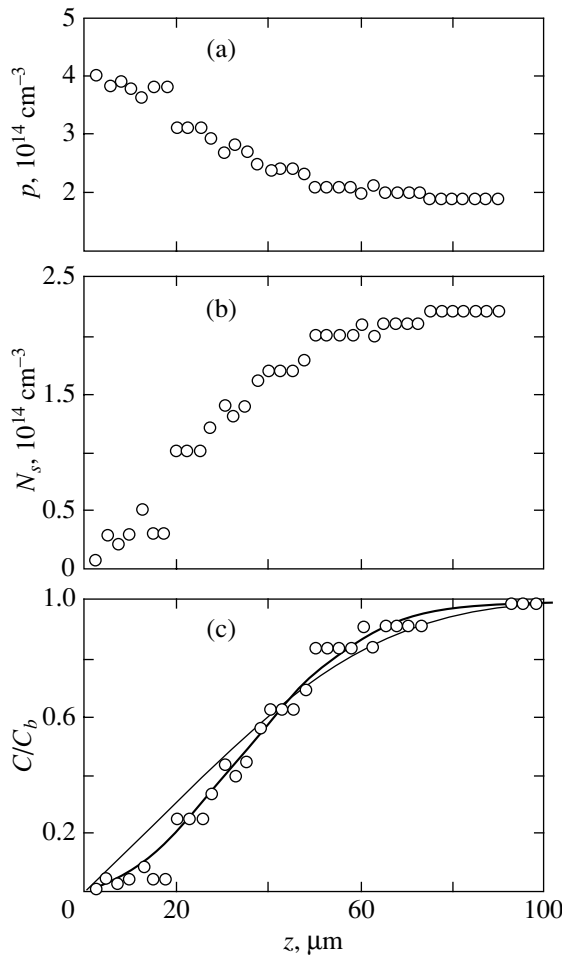


Fig. 1. Distributions of (a) the hole concentration, (b) the concentration of shallow thermal donors, and (c) the calculated total concentration of dissolved nitrogen (normalized to the bulk concentration C_b) over the depth z of the sample upon homogenizing annealing at 1000°C for 15 min.

nable to the boron concentration N_a (or, at least, not be too low as compared to the boron concentration N_a). Therefore, the sensitivity of the proposed method substantially depends on the boron concentration in the material. At a low doping level (for example, at $N_a = 10^{13} \text{ cm}^{-3}$), this method is applicable when the bulk concentration of nitrogen impurities is relatively low (of the order of 10^{13} cm^{-3}). For comparison, the standard method of secondary ion mass spectrometry can be applied only in the case when the nitrogen concentration is appreciably higher than $2 \times 10^{15} \text{ cm}^{-3}$.

3. RESULTS AND DISCUSSION

The predicted hole concentration profile $p(z) = N_a - N_s(z)$ is a monotonically decreasing function of the depth z . Moreover, the hole concentration $p(0)$ in the immediate vicinity of the surface should coincide with the boron concentration N_a , because the nitrogen con-

centration at this point is too low to initiate the generation of shallow thermal donors. In a number of cases, the measured hole concentration profile $p(z)$ corresponds to the predicted profile. However, in other cases, the concentration profile $p(z)$ exhibits an anomalous behavior, which will be discussed below.

It should be noted that the nitrogen diffusion toward the surface in the course of homogenizing annealing can be accompanied by the precipitation of nitrogen. The subsequent generation of shallow thermal donors is controlled only by the nitrogen dissolved in the crystal. In the proposed method, the possible (partial) loss of dissolved nitrogen due to the precipitation manifests itself in a decrease in the bulk concentration of shallow thermal donors. Correspondingly, the bulk nitrogen concentration C calculated from formula (2) should be less than the known total nitrogen concentration ($2 \times 10^{15} \text{ cm}^{-3}$ in our samples). In other words, the method used for determining the nitrogen diffusion profile provides a means for controlling the possible loss of dissolved nitrogen due to the precipitation. It was found that the precipitation of nitrogen becomes noticeable at sufficiently prolonged homogenizing annealings (for example, for 30 min at 1000°C). For shorter times of annealing, the loss of nitrogen through precipitation is insignificant: the calculated bulk concentration C of dissolved nitrogen almost coincides with the initial total nitrogen concentration.

The nitrogen diffusion profile obtained with the use of the above method upon annealing at a temperature of 1000°C for 15 min is depicted in Fig. 1. The hole concentration profile (Fig. 1a) was determined directly from the measured profile of the spreading resistance. The concentration profile of shallow thermal donors (Fig. 1b) was calculated from formula (3). The concentration profile of dissolved nitrogen (Fig. 1c) was reconstructed according to relationship (2). The last profile is represented in a normalized form that is convenient for analyzing the diffusion mechanism: the concentration $C(z)$ is normalized to the bulk nitrogen concentration C_b . The solid lines in Fig. 1c represent the results of the numerical simulation (discussed in the next section).

Another example of reconstructed normalized profiles of nitrogen diffusion upon annealing at 1000°C for 10 min is shown in Fig. 2. It can be seen from Fig. 2 that the nitrogen diffusion profile exhibits a specific feature in the range 20–30 μm corresponding to the surface region. This feature reflects an anomaly in the initial hole concentration profile $p(z)$: the surface concentration of holes is somewhat less than the predicted concentration equal to the boron concentration N_a . The possible reason for the observed anomaly is the diffusion of donor impurities from the surface into the sample bulk. In this case, the surface portion of the profile should be ignored in the theoretical description of nitrogen diffusion.

A similar (but more pronounced) surface anomaly can be seen in the profiles obtained upon annealing at 1000°C for 30 min (Fig. 3). The donor concentration profile calculated from formula (3) involves two portions of different origins (Fig. 3a). It is evident that the surface portion (to a depth of 20 μm) is associated with the diffusion of donor impurities from the surface into the bulk. The remaining portion of the concentration profile can be attributed to shallow thermal donors. Consequently, in the nitrogen diffusion profile (Fig. 3b) formally calculated from expression (2), the portion corresponding to a deeper region reflects the nitrogen diffusion, whereas the surface portion is due to an artefact caused by contamination of the surface. For contaminating donor impurities, the diffusion coefficient is rather small: it is estimated at $3 \times 10^{-10} \text{ cm}^2 \text{ s}^{-1}$ (according to the observed depth of penetration of these impurities). For this reason, only the surface portion of the nitrogen diffusion profile turns out to be distorted. The remaining portion (for a deeper region) can be considered to be the true diffusion profile.

The bulk concentration of shallow thermal donors (at a depth of more than 90 μm) is relatively low (Fig. 3a). As a consequence, the calculated bulk concentration C_b of dissolved nitrogen is decreased and estimated at about 10^{15} cm^{-3} , which amounts to only 50% of the total nitrogen concentration. This implies that, upon annealing at 1000°C for the longest time (30 min), approximately half the initially dissolved nitrogen appears to be lost; i.e., it transformed into precipitates (probably, silicon nitride particles).

4. SIMULATION OF THE PROFILES OF NITROGEN DIFFUSION IN OXYGEN-CONTAINING SILICON

As was noted above, the dissociation of nitrogen dimers N_2 into monomers N_1 (and, correspondingly, the back reaction of dimerization) in a material with a high oxygen content (Czochralski silicon) proceeds at a high rate. The mechanism of fast dissociation involves the preliminary formation of N_2O complexes, followed by their dissociation into N_1O and N_1 (in turn, the N_1O complexes rapidly dissociate into N_1 and O). The high rate of reactions suggests that the concentrations of all reactants (such as unoxidized and oxidized nitrogen dimers and unoxidized and oxidized nitrogen monomers) are characterized by the equilibrium ratio. In particular, the concentration C_2 of N_2 dimers and the concentration C_1 of N_1 monomers are related by the mass action law, that is,

$$C_1^2/C_2 = K, \tag{4}$$

where K is the equilibrium constant for the dissociation of an N_2 dimer into two N_1 monomers. At a diffusion temperature of approximately 1000°C, the equilibrium constant K is estimated at 10^{14} cm^{-3} or less [1]. In addition to N_1 and N_2 species, the oxygen-containing material involves oxidized monomers N_1O_m with different numbers m of oxygen atoms (the total concentration C_1^*) and oxidized dimers N_2O_m with different numbers m of oxygen atoms (the total concentration C_2^*). The contribution of the concentration C_2^* to the total nitrogen concentration is small, whereas the concentration

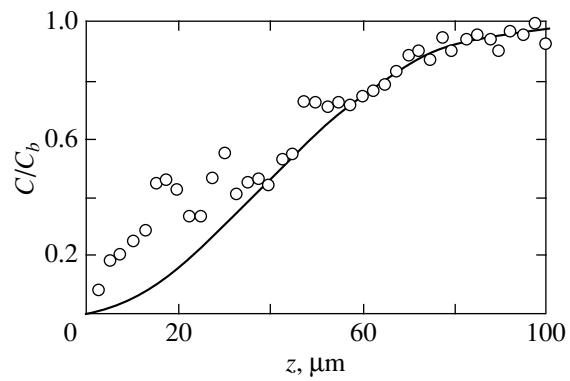


Fig. 2. Calculated normalized profile of the nitrogen concentration upon homogenizing annealing at 1000°C for 10 min.

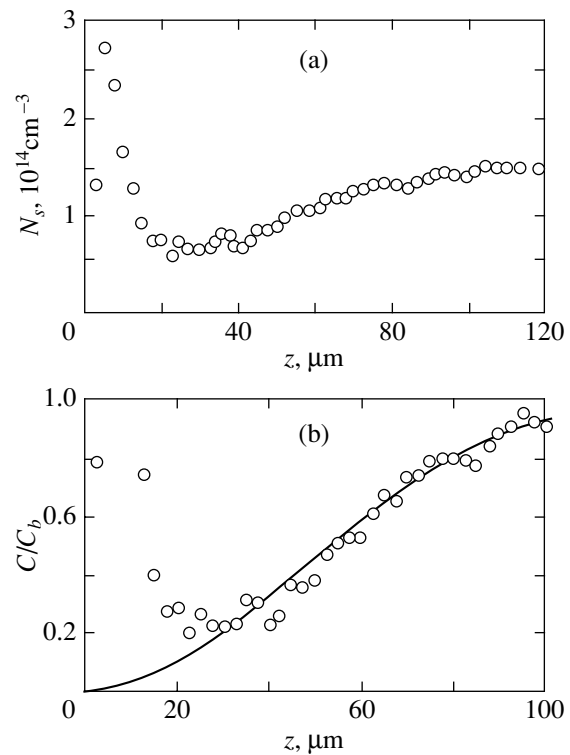


Fig. 3. (a) Profile of the donor concentration and (b) the normalized profile of the nitrogen concentration upon homogenizing annealing at 1000°C for 30 min.

tion to N_1 and N_2 species, the oxygen-containing material involves oxidized monomers N_1O_m with different numbers m of oxygen atoms (the total concentration C_1^*) and oxidized dimers N_2O_m with different numbers m of oxygen atoms (the total concentration C_2^*). The contribution of the concentration C_2^* to the total nitrogen concentration is small, whereas the concentration

C_1^* can, in principle, make a significant contribution to the total nitrogen concentration [1]. Therefore, the total nitrogen concentration C can be determined from the expression

$$C = C_1 + 2C_2 + C_1^* = C_1(1 + G + 2C_1/K). \quad (5)$$

Here, $G = C_1^*/C_1$ is the ratio of the concentrations of oxidized and unoxidized monomers. This quantity is constant and depends on the temperature and the oxygen concentration C_{ox} . In our samples, the oxygen concentration C_{ox} is also constant.

The concentration profile $C(z, t)$ varies with time due to the diffusion of mobile N_1 monomers (with the diffusion coefficient D_1) in accordance with the equation

$$\partial C/\partial t = D_1 \partial^2 C_1/\partial z^2. \quad (6)$$

For a low-oxygen material prepared by the float zone technique (FZ material), when the contribution of oxidized monomers is small, the system of equations (5) and (6) can be reduced to one nonlinear equation,

$$(1 + 4C_1/K) \partial C_1/\partial t = D_1 \partial^2 C_1/\partial z^2. \quad (7)$$

If the contribution of oxidized monomers is large, it is convenient to introduce the total concentration of unoxidized and oxidized nitrogen monomers $C_{1t} = C_1 + C_1^*$. This concentration obeys the same equation (7) but with the parameters K and D_1 replaced by the effective constants, that is,

$$(1 + 4C_{1t}/K_e) \partial C_{1t}/\partial t = D_{1e} \partial^2 C_{1t}/\partial z^2. \quad (8)$$

The effective diffusion coefficient D_{1e} is equal to the product of the diffusion coefficient D_1 into the fraction of mobile monomeric species N_1 in unoxidized and oxidized monomers:

$$D_{1e} = D_1/(1 + G). \quad (9)$$

The effective dissociation constant K_e relates the total concentration C_{1t} of unoxidized and oxidized monomers to the concentration of dimers: $C_{1t}^2/C_2 = K_e$. The effective constant K_e and the parameters K and G are related by the expression

$$K_e = K(1 + G)^2. \quad (10)$$

It should be noted that the effective dissociation constant K_e determines whether the concentration C_2 or the concentration C_{1t} predominantly contributes to the total nitrogen concentration $C = C_{1t} + 2C_2$.

At $K_e \ll C$, the dimeric nitrogen species predominate. The total concentration C is close to $2C_2$, whereas

the monomer concentration C_{1t} is approximately equal to $(K_e C/2)^{1/2}$. In this case, the diffusion equation (8) contains only one product, $D_{1e} K_e^{1/2}$, and two parameters, D_{1e} and K_e . It is important that this product is equal to $D_1 K^{1/2}$; i.e., it does not depend on the oxidation number of nitrogen monomers. The diffusion equation (8) is nonlinear, and its solution substantially differs from the solution of a linear diffusion equation when the diffusion profile is described by an erf function. The nitrogen transport involves dissociation of dominant dimeric nitrogen species, and this process can be described by the dissociative diffusion mechanism.

At $K_e \gg C$, monomeric nitrogen species (for the most part, $N_1 O_m$ complexes) predominate. Consequently, relationship (8) is reduced to the standard linear diffusion equation involving a sole parameter, i.e., the effective diffusion coefficient D_{1e} of monomers. The diffusion profile is described by the erf function.

Note that the criterion for dissociative diffusion $K_e \ll C$ is satisfied for low-oxygen silicon. However, the ratio between the quantities K_e and C for Czochralski silicon is not known in advance; hence, it is necessary to examine both limiting cases. Under the assumption that $K_e \ll C$, we choose the best dissociative diffusion parameter $D_1 K^{1/2}$ in such a way as to ensure the minimum root-mean-square deviation of the theoretical diffusion profile [calculated using relationship (8)] from the experimental profile $C(z)$. For the opposite inequality $K_e \gg C$, the best parameter D_{1e} can be obtained in a similar way. The best theoretical profiles for these two cases are depicted by the solid lines in Fig. 1c. For the dissociative diffusion (thick line), the experimental points are rather well approximated for the parameter $D_1 K^{1/2} = 0.67 \text{ cm}^{1/2} \text{ s}^{-1}$. For the linear diffusion (with a profile similar to the error (erf) function shown by the thin line in Fig. 1c), the results of the theoretical calculations with the effective diffusion coefficient $D_{1e} = 1.4 \times 10^{-8} \text{ cm}^2 \text{ s}^{-1}$ are in worse agreement with the experimental data.

Therefore, we can make the inference that the criterion for dissociative diffusion $K_e \ll C$ is satisfied for the Czochralski silicon samples. According to expression (10), this means that the fraction of unoxidized monomers $C_1/C_{1t} = 1/(1 + G)$ is considerably larger than $(K/C)^{1/2}$, which is approximately equal to 20%. This estimate does not rule out substantial oxidation of the nitrogen monomers (when the ratio $G = C_1^*/C_1$ is of the order of unity) but necessarily excludes very intensive oxidation ($G \gg 1$).

It is of interest to note that, for FZ silicon, the nitrogen diffusion profile measured by secondary ion mass spectrometry after annealing under the same conditions (at 1000°C for 15 min) is adequately described by the standard erf function [8], even though the criterion for dissipative diffusion ($K \ll C$) obviously holds true. This

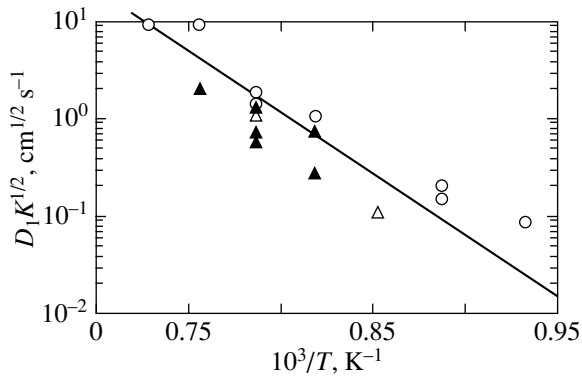


Fig. 4. Dissociative diffusion parameters $D_1 K^{1/2}$ obtained in this work (closed triangles) and calculated in [1] from other data (open symbols).

apparent contradiction can stem from the fact that, in FZ silicon (at a low oxygen concentration), nitrogen dimers dissociate at a low rate with a characteristic time τ comparable to the annealing time. In this case, the nitrogen diffusion profile depends not only on the parameter $D_1 K^{1/2}$ but also on the dissociation time τ and can be similar to the profile described by the erf function [1].

The other measured diffusion profiles are characterized by either a distortion of the surface portion (due to the penetration of contaminating donor impurities) or a considerable precipitation of nitrogen. In the former case, the undistorted profile portion (corresponding to a deeper region) is insufficient for deciding between the aforementioned alternative models. With allowance made for the above inference regarding the dissociative mechanism of nitrogen transport ($K_e \ll C$), the dissociative diffusion parameter $D_1 K^{1/2}$ was determined to be $1.5 \text{ cm}^{1/2} \text{ s}^{-1}$ for the profile obtained upon annealing at 1000°C for 10 min and $0.3 \text{ cm}^{1/2} \text{ s}^{-1}$ for the profile obtained upon annealing at 950°C for 20 min. In the case when the profiles characterized by a noticeable precipitation of nitrogen were processed under the assumption that the normalized profile $C(z)/C_b$ is only slightly distorted as a result of precipitation, we obtained the following dissociative diffusion parameters: $2.25 \text{ cm}^{1/2} \text{ s}^{-1}$ (annealing at 1050°C for 10 min), $0.8 \text{ cm}^{1/2} \text{ s}^{-1}$ (annealing at 1000°C for 30 min), and $0.8 \text{ cm}^{1/2} \text{ s}^{-1}$ (annealing at 950°C for 50 min).

The dissociative diffusion parameters determined in this work are presented in Fig. 4 (closed triangles). The corresponding parameters calculated in [1] for the dissociative diffusion in layers of implanted nitrogen and FZ silicon doped with nitrogen are indicated by open symbols in Fig. 4 (triangles for Czochralski silicon, and circles for FZ silicon). Despite the wide scatter in points, it can be seen that these results are in qualitative agreement. The temperature dependence of the dissociative diffusion parameter (the straight line in Fig. 4) is characterized by an activation energy of approxi-

mately 2.5 eV. This energy is equal to the sum of the migration energy of an N_1 monomer and half the bonding energy of an N_2 dimer. According to [1], the bonding energy of the dimer is equal to 2.2 eV or somewhat higher. Consequently, the migration energy of the monomer is approximately equal to 1.4 eV or somewhat lower.

5. CONCLUSIONS

Thus, the nitrogen diffusion profile for oxygen-containing silicon can be determined by a new highly sensitive method based on the generation of shallow thermal donors with sufficiently prolonged heat treatment at moderate temperatures (at 650°C in the present work). In contrast to the standard method of secondary ion mass spectrometry, the new method is applicable at a relatively low nitrogen concentration, which is dependent on the concentration of acceptor (or donor) impurities in the material. The concentration profile of shallow thermal donors (nitrogen–oxygen complexes) is a function of the total nitrogen concentration. The concentration profile of shallow thermal donors (obtained from the measured spreading resistance) is converted into the nitrogen diffusion profile.

The proposed method was used to demonstrate that the nitrogen transport in Czochralski silicon (as in FZ silicon) occurs through the dissociative mechanism. Dominant (virtually immobile) nitrogen dimers N_2 dissociate into mobile nitrogen monomers N_1 which provide transport of nitrogen impurities. In this case, the diffusion equation is nonlinear and the nitrogen diffusion profile differs substantially from the conventional profile (described by the erf function). This important result implies that the fraction of oxidized (immobile) nitrogen monomers is not very large in Czochralski silicon at diffusion temperatures (approximately 1000°C in this work). Otherwise, oxidized nitrogen monomers rather than nitrogen dimers would predominate in Czochralski silicon and the nitrogen transport would correspond to linear diffusion with an effective diffusion coefficient.

The measured diffusion profiles were processed, and the dissociative diffusion parameters $D_1 K^{1/2}$ were calculated. The results obtained are in agreement with the data available in the literature. All these dissociative diffusion parameters follow a pronounced temperature dependence, even though there is a rather wide scatter in points for different samples. The origin of this scatter remains unclear. Evidently, it is necessary to investigate a considerably larger number of samples in order to obtain more reliable averaged dissociative diffusion parameters.

ACKNOWLEDGMENTS

This work was supported by the Russian Foundation for Basic Research, project no. 02-02-16053A.

REFERENCES

1. V. V. Voronkov and R. Falster, in *Proceedings of the GADEST, 2003*.
2. M. Suezawa, K. Sumino, H. Harada, and T. Abe, *Jpn. J. Appl. Phys., Part 1* **25**, L859 (1986).
3. D. Yang, R. Fan, L. Li, D. Que, and K. Sumino, *Appl. Phys. Lett.* **68**, 487 (1996).
4. A. Hara, M. Aoki, M. Koizuka, and T. Fukuda, *J. Appl. Phys.* **75**, 2929 (1994).
5. V. V. Voronkov, M. Porrini, P. Collareta, M. G. Pretto, R. Scala, R. Falster, G. I. Voronkova, A. V. Batunina, V. N. Golovina, L. V. Arapkina, A. S. Guliaeva, and M. G. Milvidski, *J. Appl. Phys.* **89**, 4289 (2001).
6. V. V. Voronkov, A. V. Batunina, G. I. Voronkova, V. N. Golovina, L. V. Arapkina, N. B. Tyurina, A. S. Gulyaeva, and M. G. Mil'vidskii, *Fiz. Tverd. Tela (St. Petersburg)* **44**, 700 (2002) [*Phys. Solid State* **44**, 727 (2002)].
7. Y. Yatsurugi, N. Akijama, Y. Endo, and T. Nozaki, *J. Electrochem. Soc.* **120**, 975 (1973).
8. T. Itoh and T. Abe, *Appl. Phys. Lett.* **53**, 39 (1988).

Translated by O. Borovik-Romanova

SEMICONDUCTORS
AND DIELECTRICS

Special Points for Calculating Integrals over the Primitive Cell of a Periodic System

R. A. Evarestov* and V. P. Smirnov**

*St. Petersburg State University, ul. Pervogo Maya 100, St. Petersburg, 198504 Russia

**Institute of Fine Mechanics and Optics, St. Petersburg, 197101 Russia

Received December 1, 2003

Abstract—A method is proposed for constructing appropriate sets of special points in the Brillouin zone in which the extended unit cell method is used with a subsequent shift from the center of the reduced Brillouin zone. The proposed method offers several advantages over the commonly used Monkhorst–Pack method. The difference in the construction of sets of special points for the direct and reciprocal lattices is discussed for crystals belonging to a nonsymmorphic space group. The cases of a planar square lattice and an fcc lattice are considered to illustrate general results. © 2004 MAIK “Nauka/Interperiodica”.

1. INTRODUCTION

Calculations of the electronic structure and properties of crystals, as a rule, are currently carried out in terms of the density functional theory (DFT) in a plane-wave basis, using the pseudopotential method to describe the core electrons [1]. In this case, considerable computational effort is required to determine the Fourier transform of the periodic potential in the direct lattice in order to solve the one-electron Kohn–Sham equations in a plane-wave basis. The Fourier coefficients are calculated by interpolating between a finite number of points in a minimum cell of the direct lattice, which, in turn, depends on the number of plane waves involved in the basis used. The optimal choice of interpolation points determines, to a great extent, the efficiency of the entire computation [2]. When the electronic structure of a crystal is calculated self-consistently (both in a plane-wave basis [1] and in a localized atomic-type function basis [3]), the electron density matrix of the crystal is determined approximately by interpolating between its values at a finite number of \mathbf{k} points in the Brillouin zone (BZ) in each iteration cycle of the self-consistent procedure. These points are chosen using the theory of BZ special points (SPs) developed in [4–6]. It was shown in [7] that, for the density matrix of a crystal to remain idempotent, the summation over SPs should be performed by introducing the so-called weighting function, which is equivalent to the imposition of cyclic boundary conditions or consideration of a cyclic cluster [8]. The difficulties that arise when the SP theory is applied to metals are associated with the power-law (rather than exponential) decay of the off-diagonal elements of the density matrix and can be surmounted by using the $\mathbf{k} \cdot \mathbf{p}$ method, which enables one to significantly refine the interpolation based on a finite number of SPs [9]. In this paper, we

develop a unified approach to the construction of a set of SPs for calculating integrals over minimal unit cells of periodic systems (the Wigner–Seitz cell of a direct lattice and the BZ of a reciprocal lattice). This method is based on a scale transformation [going over to an extended unit cell (EUC)] for a direct or a reciprocal lattice; this transformation takes into account the space symmetry of the crystal and makes it possible to choose a set of SPs for which calculations become progressively more accurate as the EUC is increased in size. By extending the approach proposed in [6, 2], we develop a method in which efficient sets of SPs in the BZ are constructed by applying the EUC method and performing a shift from the center of the folded BZ (FBZ); this method offers several advantages over the commonly used Monkhorst–Pack method [5]. (In [6], EUC and FBZ are referred to as LUC (large unit cell) and SBZ (small Brillouin zone), respectively.) The difference in the construction of sets of SPs for the direct and reciprocal lattices is discussed for crystals belonging to a nonsymmorphic space group. The cases of a planar square lattice and an fcc lattice are considered to illustrate general results.

In Section 2, we consider the EUC–FBZ method for constructing a set of SPs in the BZ without and with changing the crystal symmetry (symmetric and nonsymmetric extensions, respectively). The Fourier coefficients of expansion in terms of symmetrized plane waves are calculated for periodic functions defined over a reciprocal lattice. The EUC–FBZ method with a shift from the FBZ center is applied to construct SP sets for planar square and fcc lattices.

In Section 3, the expansion in terms of symmetrized plane waves is considered for periodic functions defined over a direct lattice. Extended unit cells in the reciprocal lattice and reduced Wigner–Seitz cells in the

direct lattice are used. It is shown that, in contrast to symmetrized plane waves in the reciprocal lattice, symmetrized combinations of plane waves in the direct lattice are different for different space groups of the same crystal class and of the same crystal system. This difference is illustrated for double-periodic symmetry groups of the C_{4v} crystal class, more specifically, the symmorphic $P4mm$ and nonsymmorphic $P4bm$ groups. In Section 4, we discuss the application of the results of this work for performing self-consistent calculations of the electronic structure of crystals.

2. EXTENDED UNIT CELL IN THE DIRECT LATTICE AND SPECIAL POINTS IN THE BRILLOUIN ZONE

Let us consider a triply periodic system (bulk crystal) whose direct lattice is characterized by primitive translation vectors \mathbf{a}_i ($i = 1, 2, 3$) possessing the property $(\mathbf{a}_i \cdot \mathbf{b}_j) = 2\pi\delta_{i,j}$ and whose reciprocal lattice is characterized by primitive vectors \mathbf{b}_j ($j = 1, 2, 3$). The transformations of the direct lattice considered in what follows can also be applied to double- and single-periodic systems. The basic translation vectors of an EUC in the direct lattice can be expressed in terms of an integer matrix \hat{L} as

$$\mathbf{a}_j^{(L)} = \sum_i \hat{L}_{ji} \mathbf{a}_i, \quad L \equiv \det \hat{L}. \quad (1)$$

The number of primitive cells in the EUC in the direct lattice is equal to the determinant L of the transformation matrix in Eq. (1). As a primitive cell, we choose the Wigner–Seitz cell. The primitive translation vectors of the direct lattice can be expressed in terms of the basic translation vectors of the EUC as

$$\mathbf{a}_i = \sum_j (\hat{L})_{ij}^{-1} \mathbf{a}_j^{(L)}. \quad (2)$$

It is well known that the space group $F^{(s)}$ of a crystal (where s specifies the space groups belonging to the same crystal class F) contains the group T of translations through vectors $\mathbf{a}_n = \sum_i n_i \mathbf{a}_i$ as an invariant subgroup and that the crystal class F is isomorphic to the factor group $F^{(s)}/T$. Irrespective of whether the space group $F^{(s)}$ of a crystal is symmorphic or nonsymmorphic, the space group of the corresponding reciprocal lattice is symmorphic and belongs to the same crystal class F . The type of reciprocal lattice involved can differ from that of the direct lattice; for example, a direct fcc lattice has as its reciprocal a bcc lattice. Note that the point group F either coincides with the lattice point group F_l or is its subgroup, $F \subseteq F_l$. Under a symmetry operation $f \in F$, translations \mathbf{a}_n of the direct lattice transform into integer combinations of the primitive

vectors. In particular, for the primitive translations, we have

$$f \mathbf{a}_i = \sum_{i'} \hat{f}_{i'i} \mathbf{a}_{i'}. \quad (3)$$

The translation vectors related by point symmetry operations belong to the same star. Let us number the coordination shells in the direct lattice by an index n in increasing order of their radius R_n . A coordination shell can contain a few stars of the direct-lattice vectors related by symmetry operations $f \in F$. In this case, we specify independent stars belonging to the same coordination shell by the index v . Summations over lattice vectors \mathbf{a}_n will be performed as follows: first, we sum over the vectors belonging to the same star v , then over the stars v belonging to the same coordination shell n , and finally over the coordination shells n :

$$\sum_{\mathbf{a}_n} = \sum_n \sum_v \sum_{\mathbf{a}_n \in (nv)}. \quad (4)$$

The translations through direct-lattice vectors $\mathbf{a}_n^{(L)}$ form an infinite translation group $T^{(L)}$:

$$\mathbf{a}_n^{(L)} = \sum_j \tilde{n}_j \mathbf{a}_j^{(L)} \in T^{(L)}, \quad (5)$$

where \tilde{n}_j are integers.

The factor group $\tilde{T}^{(L)} = T/T^{(L)}$ is the finite group of internal direct-lattice translations of the EUC. In this group, the translations \mathbf{a}_n are defined to within a vector $\mathbf{a}_n^{(L)} \in T^{(L)}$; therefore, this group is a group with translation addition modulo $T^{(L)}$.

Transformation (1) of the basic translation vectors is termed symmetric if the point symmetry of the lattice generated by the EUC coincides with the point symmetry of the original lattice (the type of lattice generated can be different, but it must belong to the same crystal system). For a symmetric transformation characterized by a matrix \hat{L} , the matrix $\hat{L} \hat{f} (\hat{L})^{-1}$ must be an integer matrix. Indeed, under symmetry operations of the point group of the crystal, the basic translation vectors $\mathbf{a}_j^{(L)}$ of the EUC are transformed as

$$\begin{aligned} f \mathbf{a}_j^{(L)} &= \sum_j \hat{L}_{ji} f \mathbf{a}_i = \sum_{i'j'} \hat{L}_{ji} \hat{f}_{i'i} (\hat{L}^{-1})_{i'j'} \mathbf{a}_{j'}^{(L)} \\ &= \sum_{j'} (\hat{L} \hat{f} \hat{L}^{-1})_{jj'} \mathbf{a}_{j'}^{(L)}, \end{aligned} \quad (6)$$

where we took into account Eqs. (1)–(3).

If transformation (1) is not symmetric, then the translation group $T^{(L)}$ is characterized by a lower point symmetry $F^{(L)} \subset F$. Translations $\mathbf{a}_n^{(L)}$ can also be broken down into coordination shells and stars with respect to the point group $F^{(L)}$.

As an example, we consider a square lattice characterized by primitive translation vectors $\mathbf{a}_1 = (1, 0)$ and $\mathbf{a}_2 = (0, 1)$ (in units of the lattice parameter a). The corresponding reciprocal lattice is also a square lattice and is characterized by primitive vectors $\mathbf{b}_1 = (1, 0)$ and $\mathbf{b}_2 = (0, 1)$ (in units of $2\pi/a$). Figure 1 shows the basic translation vectors for two symmetric ($\mathbf{a}_1^{(2)}, \mathbf{a}_2^{(2)}$ for $L = 2$ and $\mathbf{a}_1^{(4)}, \mathbf{a}_2^{(4)}$ for $L = 4$) and two nonsymmetric ($\mathbf{a}_1^{(4)}, \mathbf{a}_2^{(4)}$ for $L = 4$ and $\mathbf{a}_1^{(5)}, \mathbf{a}_2^{(5)}$ for $L = 5$) extensions of the primitive cell of the direct lattice. The matrices of the corresponding transformations of the primitive vectors of the original lattice are shown in Tables 1 and 2. For transformation (1) in the direct lattice of the crystal, the corresponding transformation in the reciprocal lattice is characterized by the inverse matrix and has the form

$$\mathbf{b}_j^{(S)} = \sum_i (\hat{L}^{-1})_{ij} \mathbf{b}_i, \quad (\mathbf{a}_j^{(L)}, \mathbf{b}_j^{(S)}) = 2\pi \delta_{jj}. \quad (7)$$

Transformation (7) defines the FBZ, i.e., the Wigner–Seitz cell in the reciprocal lattice corresponding to the EUC in the direct lattice. The volume of the FBZ is L times less than the BZ volume. Any point $\tilde{\mathbf{k}}$ in the FBZ is equivalent to L points in the original BZ,

$$\mathbf{k}_t^{(\tilde{\mathbf{k}})} = \tilde{\mathbf{k}} + \sum_j q_{ij}^{(b)} \mathbf{b}_j^{(S)}, \quad t = 1, 2, \dots, L, \quad (8)$$

because it is joined with these points through translation vectors $\mathbf{b}_j^{(S)}$ of the new reciprocal lattice. The numbers $q_{ij}^{(b)}$ are such that the points $\mathbf{k}_t^{(\tilde{\mathbf{k}})}$ belong to the BZ. Out of the equivalent points that are at the BZ boundary and, therefore, are joined through reciprocal-lattice vectors $\mathbf{b}_m = \sum_{i=1}^3 m_i \mathbf{b}_i$, only one point is taken into account. Figure 2a shows the points in the FBZ for four EUC–FBZ transformations (described in Tables 1, 2).

The transformation corresponding to the transition to an EUC in the direct lattice can be used to construct sets of SPs for calculating the Fourier coefficients of a function $\varphi(\mathbf{k})$ and, in particular, for performing numerical integration of the function over the BZ. The function $\varphi(\mathbf{k})$ is assumed to be periodic in the reciprocal-lattice space with periods \mathbf{b}_j ($j = 1, 2, 3$) and to be invariant under the symmetry operations of the crystal class F of

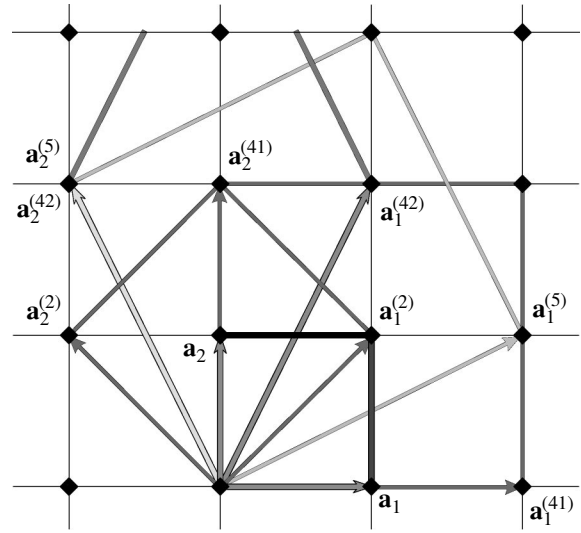


Fig. 1. Primitive translation vectors and translation vectors of two symmetric $\mathbf{a}_1^{(2)}, \mathbf{a}_2^{(2)}$ for $L = 2$; $\mathbf{a}_1^{(4)}, \mathbf{a}_2^{(4)}$ for $L = 4$ and two nonsymmetric ($\mathbf{a}_1^{(4)}, \mathbf{a}_2^{(4)}$ for $L = 4$; $\mathbf{a}_1^{(5)}, \mathbf{a}_2^{(5)}$ for $L = 5$) extensions of the primitive cell of the direct lattice.

the space group $F^{(S)}$ of the crystal. The symmetry of the function $\varphi(\mathbf{k})$ is the same for crystals belonging to any (symmorphic or nonsymmorphic) space group of the crystal class F :

$$\varphi(\mathbf{k} + \mathbf{b}_m) = \varphi(\mathbf{k}) = \varphi(f\mathbf{k}), \quad (9)$$

$$f \in F, \quad \mathbf{b}_m = \sum_{i=1}^3 m_i \mathbf{b}_i.$$

In order to interpolate the function $\varphi(\mathbf{k})$, whose values at a finite set of points are assumed to be known, we use plane waves $\exp(i\mathbf{k} \cdot \mathbf{a}_n)$ that are periodic in the reciprocal-lattice space with periods \mathbf{b}_j ($j = 1, 2, 3$). Since the function $\varphi(\mathbf{k})$ possesses the full symmetry of the crystal, we use symmetrized combinations of plane waves:

$$P_{nv}(\mathbf{k}) = \frac{\sqrt{N_{nv}}}{n_F} \sum_{f \in F} \exp(i f^{-1} \mathbf{k} \cdot \mathbf{a}_n) \quad (10)$$

$$= \frac{\sqrt{N_{nv}}}{n_F} \sum_{f \in F} \exp(i \mathbf{k} \cdot f \mathbf{a}_n),$$

where the subscript n numbers the coordination shells of the vectors $f\mathbf{a}_n$ in increasing order of their radius R_n and v specifies the irreducible stars of vectors belonging to the coordination shell of radius R_n (if there are more than one such stars). Thus, a symmetrized plane wave $P_{nv}(\mathbf{k})$ corresponds to the v th star belonging to the

Table 1. Parameters of SP sets for double-periodic crystals belonging to the C_{4v} crystal class (square lattices)

n	Before shifting					After shifting through $\tilde{\mathbf{k}}$				
	L	M	N	M/N	R_M	L_{eff}	M_{eff}	N_{eff}	$M_{\text{eff}}/N_{\text{eff}}$	$R_{M_{\text{eff}}}$
$\hat{L} = n \begin{pmatrix} 1 & 0 \\ 0 & 1 \end{pmatrix}, \quad L = n^2, \quad \tilde{\mathbf{k}} = \frac{1}{4n}(1, 1)$										
1	1	1	1	1.0	1	4	3	1 (3)	3.0 (1.0)	2
2	4	3	3	1.0	2	16	9	3 (6)	3.0 (1.5)	4
3	9	6	3	2.0	3	36	19	6 (10)	3.2 (1.9)	6
4	16	9	6	1.5	4	64	31	10 (15)	3.1 (2.1)	8
5	25	14	6	2.3	5	100	48	15 (21)	3.2 (2.3)	10
6	36	19	10	1.9	6	144	65	21 (28)	3.1 (2.3)	12
$\hat{L} = n \begin{pmatrix} 1 & 1 \\ -1 & 1 \end{pmatrix}, \quad L = 2n^2, \quad \tilde{\mathbf{k}} = \frac{1}{4n}(1, 1)$										
1	2	2	2	1.0	$\sqrt{2}$	4	3	1 (3)	3.0 (1.0)	2
2	8	5	4	1.2	$2\sqrt{2}$	16	9	3 (6)	3.0 (1.5)	4
3	18	11	6	1.8	$3\sqrt{2}$	36	19	6 (10)	3.2 (1.9)	6
4	32	17	9	1.9	$4\sqrt{2}$	64	31	10 (15)	3.1 (2.1)	8

Note: The values of N_{eff} and $M_{\text{eff}}/N_{\text{eff}}$ that correspond to the SP set with $L = L_{\text{eff}}$ containing the Γ point ($\mathbf{k} = 0$) are given in parentheses.

n th coordination shell of radius R_n in the direct lattice. N_{nv} is the number of rays of the star nv .

The functions $P_{nv}(\mathbf{k})$ form a complete orthonormal set in the space of fully symmetric periodic functions [4]:

$$(P_{nv}(\mathbf{k}), P_{n'v'}(\mathbf{k})) \equiv \frac{1}{V_b} \int_{V_b} P_{nv}^*(\mathbf{k}) P_{n'v'}(\mathbf{k}) d\mathbf{k} = \delta_{nn'} \delta_{vv'} \quad (11)$$

We expand the function $\varphi(\mathbf{k})$ in terms of the symmetrized plane waves $P_{nv}(\mathbf{k})$:

$$\varphi(\mathbf{k}) = \sum_{nv} C_{nv} P_{nv}(\mathbf{k}). \quad (12)$$

Using Eqs. (11), the Fourier coefficients of this expansion can be found to be

$$C_{nv} = \frac{1}{V_b} \int_{V_b} P_{nv}^*(\mathbf{k}) \varphi(\mathbf{k}) d\mathbf{k}. \quad (13)$$

In particular, the zeroth Fourier coefficient

$$C_0 = \frac{1}{V_b} \int_{V_b} \varphi(\mathbf{k}) d\mathbf{k} = \overline{\varphi(\mathbf{k})} \quad (14)$$

is related to the integral of the function $\varphi(\mathbf{k})$ over the BZ.

The translation group $\tilde{T}^{(L)}$ contains a finite number L of elements \mathbf{a}_n . Irreducible representations of the $\tilde{T}^{(L)}$ group are one-dimensional, and their characters are $\chi^{(k_t)}(\mathbf{a}_n) = \exp(-i\mathbf{k}_t \cdot \mathbf{a}_n)$ ($t = 1, 2, \dots, L$), where $\mathbf{k}_t \equiv \mathbf{k}_t^{(\tilde{0})}$ [see Eqs. (8)]. The so-called second orthogonality relation for the characters has the form

$$\sum_{t=1}^L \exp(i\mathbf{k}_t \cdot \mathbf{a}_n) \exp(-i\mathbf{k}_t \cdot \mathbf{a}_n) = L \sum_{\tilde{n}} \delta_{\mathbf{a}_n - \mathbf{a}_n, \mathbf{a}_n^{(L)}}, \quad (15)$$

where \mathbf{a}_n can be considered to be determined to within EUC vectors $\mathbf{a}_n^{(L)}$ [see Eq. (5)]. We multiply Eq. (15) by

Table 2. SP sets for double-periodic crystals belonging to the C_{4v} crystal class (square lattices)

No.	\hat{L}	L	$\tilde{\mathbf{k}}$	M	N	M/N	R_M	w_i	SP
1	$\hat{L}(1, 0)$	1	(0, 0)	1	1	1	1	1	(0, 0)
			(1/4, 1/4)	3	1	3.0	2	1	$(\frac{1}{4}, \frac{1}{4})$
2	$\hat{L}(1, 1)$	2	(0, 0)	2	2	1.0	$\sqrt{2}$	$\frac{1}{2}, \frac{1}{2}$	$(0, 0), (\frac{1}{2}, \frac{1}{2})$
			(1/4, 1/4)	3	1	3.0	2	1	$(\frac{1}{4}, \frac{1}{4})$
3	$\hat{L}(2, 0)$	4	(0, 0)	3	3	1.0	2	$\frac{1}{4}, \frac{1}{2}, \frac{1}{4}$	$(0, 0), (\frac{1}{2}, 0), (\frac{1}{2}, \frac{1}{2})$
			(1/4, 1/4)	3	1	3.0	2	1	$(\frac{1}{4}, \frac{1}{4})$
			(1/4, 0)	5	2	2.5	$2\sqrt{2}$	$\frac{1}{2}, \frac{1}{2}$	$(\frac{1}{4}, 0), (\frac{1}{4}, \frac{1}{2})$
			(1/8, 1/8)	9	3	3.0	4	$\frac{1}{4}, \frac{1}{2}, \frac{1}{4}$	$(\frac{1}{8}, \frac{1}{8}), (\frac{3}{8}, \frac{1}{8}), (\frac{3}{8}, \frac{3}{8})$
4	$\hat{L}(2, 1)$	5	(0, 0)	4	2	2.0	$\sqrt{5}$	$\frac{1}{5}, \frac{4}{5}$	$(0, 0), (\frac{1}{5}, \frac{2}{5})$
			(1/10, 1/5)	7	3	2.3	$\sqrt{10}$	$\frac{1}{5}, \frac{2}{5}, \frac{2}{5}$	$(\frac{1}{2}, 0), (\frac{1}{10}, \frac{1}{5}), (\frac{3}{10}, \frac{2}{5})$
5	$\hat{L}(2, 2)$	8	(0, 0)	5	4	1.2	$2\sqrt{2}$	$\frac{1}{8}, \frac{1}{8}, \frac{1}{4}, \frac{1}{2}$	$(0, 0), (\frac{1}{2}, \frac{1}{2}), (\frac{1}{2}, 0), (\frac{1}{4}, \frac{1}{4})$
			(1/4, 0)	5	2	2.5	$2\sqrt{2}$	$\frac{1}{2}, \frac{1}{2}$	$(\frac{1}{4}, 0), (\frac{1}{4}, \frac{1}{2})$
			(1/8, 1/8)	9	3	3.0	4	$\frac{1}{4}, \frac{1}{2}, \frac{1}{4}$	$(\frac{1}{8}, \frac{1}{8}), (\frac{3}{8}, \frac{1}{8}), (\frac{3}{8}, \frac{3}{8})$
6	$\hat{L}(3, 0)$	9	(0, 0)	6	3	2.0	3	$\frac{1}{9}, \frac{4}{9}, \frac{4}{9}$	$(0, 0), (\frac{1}{3}, 0), (\frac{1}{3}, \frac{1}{3})$
7	$\hat{L}(4, 0)$	16	(0, 0)	9	6	1.5	4	$\frac{1}{16}, \frac{1}{4}, \frac{1}{4}$	$(0, 0), (\frac{1}{4}, 0), (\frac{1}{4}, \frac{1}{4})$
			(1/8, 1/8)	9	3	3.0	4	$\frac{1}{8}, \frac{1}{4}, \frac{1}{16}$	$(\frac{1}{2}, 0), (\frac{1}{2}, \frac{1}{4}), (\frac{1}{4}, \frac{1}{4})$
			(1/8, 1/8)	9	3	3.0	4	$\frac{1}{4}, \frac{1}{2}, \frac{1}{4}$	$(\frac{1}{8}, \frac{1}{8}), (\frac{3}{8}, \frac{1}{8}), (\frac{3}{8}, \frac{3}{8})$

Note: $\hat{L}(n_1, n_2) = \begin{pmatrix} n_1 & n_2 \\ -n_2 & n_1 \end{pmatrix}$, $L(n_1, n_2) = n_1^2 + n_2^2$.

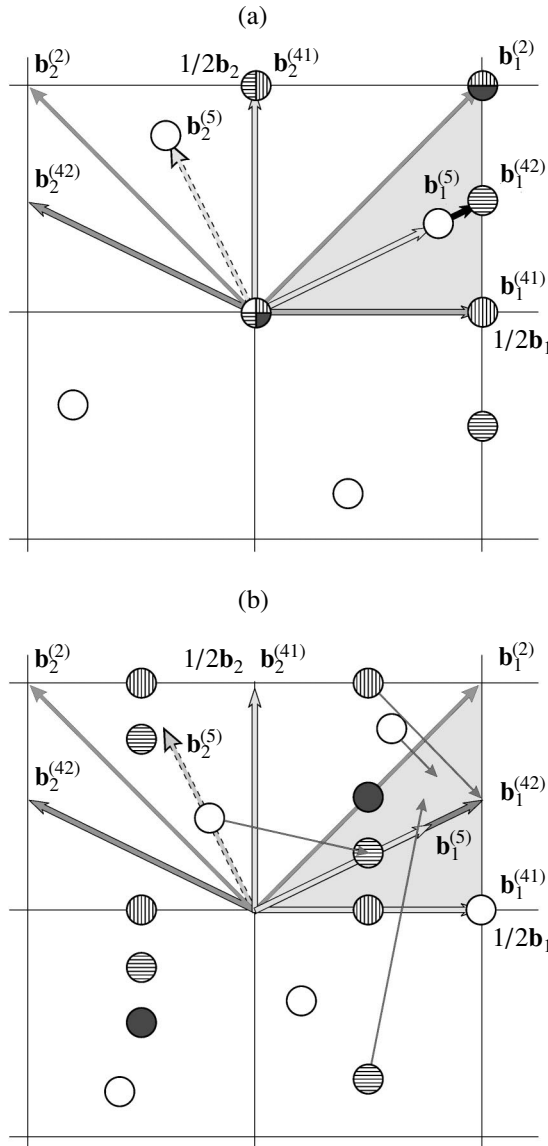


Fig. 2. Special points generated by two symmetric ($\mathbf{a}_1^{(2)}$, $\mathbf{a}_2^{(2)}$ for $L=2$; $\mathbf{a}_1^{(41)}$, $\mathbf{a}_2^{(41)}$ for $L=4$) and two nonsymmetric ($\mathbf{a}_1^{(42)}$, $\mathbf{a}_2^{(42)}$ for $L=4$; $\mathbf{a}_1^{(5)}$, $\mathbf{a}_2^{(5)}$ for $L=5$) extensions of the primitive cell of the direct lattice (a) without shifting ($\tilde{\mathbf{k}} = 0$) and (b) with shifting through $\tilde{\mathbf{k}} \neq 0$.

$\exp(i\tilde{\mathbf{k}} \cdot (\mathbf{a}_n - \mathbf{a}_n'))$ and represent it in the form

$$\begin{aligned} & \sum_{t=1}^L \exp(i\mathbf{k}_t^{(\tilde{\mathbf{k}})} \cdot \mathbf{a}_n) \exp(-i\mathbf{k}_t^{(\tilde{\mathbf{k}})} \cdot \mathbf{a}_n') \\ & = L \sum_{\tilde{\mathbf{n}}} \exp(i\tilde{\mathbf{k}} \cdot (\mathbf{a}_n - \mathbf{a}_n')) \delta_{\mathbf{a}_n - \mathbf{a}_n', \mathbf{a}_{\tilde{\mathbf{n}}}^{(L)}}, \end{aligned} \quad (16)$$

where summation is performed over the shifted set of BZ points given by Eq. (8). Writing Eq. (16) for all vectors $f\mathbf{a}_n$ and $f'\mathbf{a}_n'$ ($f, f' \in F$), i.e., for stars $n\nu$ and $n'\nu'$, and then summing these equations and multiplying the result by $\frac{\sqrt{N_{n\nu}N_{n'\nu'}}}{n_F^2}$, we obtain

$$\begin{aligned} & \sum_{t=1}^L \frac{\sqrt{N_{n\nu}}}{n_F} \sum_{f \in F} \exp(i\mathbf{k}_t^{(\tilde{\mathbf{k}})} \cdot f\mathbf{a}_n) \frac{\sqrt{N_{n'\nu'}}}{n_F} \\ & \times \sum_{f' \in F} \exp(-i\mathbf{k}_t^{(\tilde{\mathbf{k}})} \cdot f'\mathbf{a}_n') = L \frac{\sqrt{N_{n\nu}N_{n'\nu'}}}{n_F^2} \quad (17) \\ & \times \sum_{\tilde{\mathbf{n}}} \sum_{f \in F} \sum_{f' \in F} \exp(i\tilde{\mathbf{k}} \cdot (f\mathbf{a}_n - f'\mathbf{a}_n')) \delta_{f\mathbf{a}_n - f'\mathbf{a}_n', \mathbf{a}_{\tilde{\mathbf{n}}}^{(L)}} \end{aligned}$$

for symmetric and nonsymmetric transformations (1), we thus obtain

$$\begin{aligned} & \sum_{t=1}^L P_{n\nu}(\mathbf{k}_t^{(\tilde{\mathbf{k}})}) P_{n'\nu'}^*(\mathbf{k}_t^{(\tilde{\mathbf{k}})}) \\ & = \begin{cases} L \sum_{\tilde{\mathbf{n}} \tilde{\nu} \nu'', R_{n''} = \min|\mathbf{a}_n - f'\mathbf{a}_n'|}^{\max|\mathbf{a}_n - f'\mathbf{a}_n'|} N_{n''\nu''}^{n\nu, n'\nu'} P_{n''\nu''}(\tilde{\mathbf{k}}) \delta_{n''\tilde{\mathbf{n}}} \delta_{\nu''\tilde{\nu}}, & (18) \\ L \sum_{\tilde{\mathbf{n}} \tilde{\nu} \nu'', R_{n''} = \min|\mathbf{a}_n - f'\mathbf{a}_n'|}^{\max|\mathbf{a}_n - f'\mathbf{a}_n'|} N_{n''\nu''}^{n\nu, n'\nu'} \bar{P}_{n''\nu''}(\tilde{\mathbf{k}}) \delta_{n''\tilde{\mathbf{n}}} \delta_{\nu''\tilde{\nu}}, \end{cases} \end{aligned}$$

respectively, where

$$\bar{P}_{n''\nu''}(\tilde{\mathbf{k}}) = \frac{\sqrt{N_{n''\nu''}}}{n_F} \sum_{f \in F} \sum_{\mathbf{a}_n \in (\tilde{\mathbf{n}}\tilde{\nu})} \exp(i\tilde{\mathbf{k}} \cdot f\mathbf{a}_n) \delta_{f\mathbf{a}_n, \mathbf{a}_{\tilde{\mathbf{n}}}^{(L)}}, \quad (19)$$

$$N_{n''\nu''}^{n\nu, n'\nu'} \equiv \frac{\sqrt{N_{n\nu}N_{n'\nu'}}}{n_F \sqrt{N_{n''\nu''}}},$$

and $\tilde{\mathbf{n}}$ and $\tilde{\nu}$ are indices numbering the coordination shells and stars of vectors $\mathbf{a}_{\tilde{\mathbf{n}}}^{(L)} \in T^{(L)}$. The sum over \mathbf{a}_n in Eq. (19) does not involve all rays of the stars $f\mathbf{a}_n$, only the rays that are vectors $\mathbf{a}_{\tilde{\mathbf{n}}}^{(L)}$ of the coarser lattice.

Since $P_{n\nu}(\mathbf{k})$ and their products are fully symmetric functions, the summation in Eq. (18) over set (8) of points in the BZ can be replaced by summation over representatives of stars j of this set in an irreducible part of the BZ. Let us denote the number of points defined by Eq. (8) in the j th star by $N_j^{(\tilde{\mathbf{k}})}$ and introduce weight-

ing factors $w_j^{(\tilde{\mathbf{k}})} = N_j^{(\tilde{\mathbf{k}})}/L$. With this notation, Eq. (18) can be rewritten as

$$\sum_{j=1}^{N^{(\tilde{\mathbf{k}})}} w_j^{(\tilde{\mathbf{k}})} P_{n\nu}(\mathbf{k}_j^{(\tilde{\mathbf{k}})}) P_{n'\nu'}^*(\mathbf{k}_j^{(\tilde{\mathbf{k}})}) = \begin{cases} \sum_{\substack{\max|\mathbf{a}_n - f'\mathbf{a}_{n'}| \\ \tilde{n}\tilde{\nu} \nu'', R_{n''} = \min|\mathbf{a}_n - f'\mathbf{a}_{n'}|}} N_{n''\nu''}^{n\nu, n'\nu'} P_{n''\nu''}(\tilde{\mathbf{k}}) \delta_{n''\tilde{n}} \delta_{\nu''\tilde{\nu}}, \\ \sum_{\substack{\max|\mathbf{a}_n - f'\mathbf{a}_{n'}| \\ \tilde{n}\tilde{\nu} \nu'', R_{n''} = \min|\mathbf{a}_n - f'\mathbf{a}_{n'}|}} N_{n''\nu''}^{n\nu, n'\nu'} \bar{P}_{n''\nu''}(\tilde{\mathbf{k}}) \delta_{n''\tilde{n}} \delta_{\nu''\tilde{\nu}}, \end{cases} \quad (20)$$

where $N^{(\tilde{\mathbf{k}})}$ is the number of points defined by Eq. (18) in an irreducible part of the BZ.

Let the function $\varphi(\mathbf{k})$ be represented by a truncated Fourier series approximating Eq. (12),

$$\varphi(\mathbf{k}) = \sum_{n=0}^{M-1} \sum_{\nu} C_{n\nu} P_{n\nu}(\mathbf{k}). \quad (21)$$

The number of terms in this sum (M) is referred to as the accuracy of approximation of the function $\varphi(\mathbf{k})$ and of various integrals involving this function.

The left-hand side of Eq. (20) is nonzero only for irreducible stars $f\mathbf{a}_n$ containing vectors $\mathbf{a}_n^{(L)}$ of the coarser lattice; i.e., it is zero, for example, for the stars that belong to the coordination shells with radius R_s lying in the range $0 < R_s < \min|\mathbf{a}_j^{(L)} \neq 0| \equiv R_M$. If $\tilde{\mathbf{k}}$ is chosen so that $P_{n''\nu''}(\tilde{\mathbf{k}}) = 0$ [or $\bar{P}_{n''\nu''}(\tilde{\mathbf{k}}) = 0$, for a nonsymmetric transformation defined by Eq. (1)] for the first coordination shell (or the first several coordination shells) in the coarser lattice, then the accuracy of calculation with a set of SPs can be increased to $M_{\text{eff}} > M$, corresponding to a coordination shell radius $R_{M_{\text{eff}}}$. In this case, the number of SPs in the irreducible part of the BZ can decrease or increase (see below). Thus, the left-hand side of Eq. (20) will be nonzero for stars $f\mathbf{a}_n$ belonging to coordination shells with a radius lying in the range

$$0 < R_s < R_{M_{\text{eff}}} \geq R_M. \quad (22)$$

For the radii to be within range (22), n and n' must be such that $R_s = R_n + R_{n'} < R_{M_{\text{eff}}}$, because $\max|\mathbf{a}_n - f'\mathbf{a}_{n'}| \leq |\mathbf{a}_n| + |\mathbf{a}_{n'}| = R_n + R_{n'}$ ($f' \in F$).

The coefficient $C_{n\nu}$ ($n < M$) of expansion (21) can be calculated from the values of the functions $\varphi(\mathbf{k})$ and

$P_{n\nu}(\mathbf{k}_j^{(\tilde{\mathbf{k}})})$ at points (8) if $R_M + R_n \leq R_{M_{\text{eff}}}$ ($f \in F$). Indeed, we have

$$\sum_j w_j^{(\tilde{\mathbf{k}})} \varphi(\mathbf{k}_j^{(\tilde{\mathbf{k}})}) \cdot P_{n\nu}^*(\mathbf{k}_j^{(\tilde{\mathbf{k}})}) = \sum_{n'=0}^{M-1} \sum_{\nu'} C_{n'\nu'} \sum_j w_j^{(\tilde{\mathbf{k}})} P_{n'\nu'}(\mathbf{k}_j^{(\tilde{\mathbf{k}})}) \cdot P_{n\nu}^*(\mathbf{k}_j^{(\tilde{\mathbf{k}})}) = C_{n\nu}. \quad (23)$$

Using the set of SPs (8), the coefficient $C_{n\nu}$ ($n < M$) is calculated with an accuracy determined by the condition $R_M \leq (R_{M_{\text{eff}}} - R_n)$ and depending on the number n .

In particular, the accuracy of calculation is highest ($M = M_{\text{eff}}$) for the coefficient C_0 ($n = 0, R_n = 0$) given by Eq. (14), i.e., the integral of $\varphi(\mathbf{k})$ over the BZ, and the accuracy is the lowest for the coefficients $C_{M-1, \nu}$, given by integrals (13) with $n = M - 1$. In the latter case, the accuracy M is determined by the inequality $R_{M-1} \leq R_{M_{\text{eff}}}/2$. The quantity $E_{\text{eff}}^{(\tilde{\mathbf{k}})} = M_{\text{eff}}/N^{(\tilde{\mathbf{k}})}$ is called the efficiency of a set of SPs in the BZ.

For a symmetric transformation (preserving the F point symmetry), the sets of SPs (8) with $\tilde{\mathbf{k}} = 0$ consist of integer stars. Shifted sets of SPs (with $\tilde{\mathbf{k}} \neq 0$), as a rule, and sets (8) obtained for nonsymmetric transformations do not possess this property. In any case, relation (23) should be applied to a fully symmetric function $\varphi(\mathbf{k})$, i.e., after symmetrizing it with respect to the point group of the system.

Among nonsymmetric transformations (1), the transformations with $\mathbf{a}_j^{(L)}$ belonging to the same coordination shell of radius R_M in the original lattice are most appropriate for cubic lattices. Such vectors will form the first coordination shell of the new lattice if the sum and difference of any two of them are no less in magnitude than the vectors $\mathbf{a}_j^{(L)}$ themselves. Therefore, the angles $\alpha_{jj'}$ between these vectors must meet the condition $\pi/3 \leq \alpha_{jj'} \leq 2\pi/3$, which can always be satisfied. Thus, one can always construct a sequence of SP sets in which the accuracy of sets increases successively by unity. This sequence also contains SP sets corresponding to symmetrical transformations (1).

Table 2 shows matrices \hat{L} of transformations (1) in the direct lattice and the corresponding SP sets (8) with $\tilde{\mathbf{k}} = 0$. For each of the sets, Table 2 lists the weights $w_j^{(0)}$ of their vectors $\mathbf{k}_j^{(0)}$, the accuracy of the set M for integral (14), and the number of SPs in the set. The accuracy of an SP set can be specified by the radius R_M of the coordination shell of the corresponding translation vectors (in units of the square-lattice constant a). For nonsymmetric extensions of the primitive cell of

the direct lattice, different choices of translation vectors belonging to the same coordination shell can lead to SP sets characterized by different accuracies. Figure 2a shows the FBZ translation vectors corresponding to the transition to the EUCs indicated in Fig. 1.

Using a square lattice as an example, we will show that the efficiency of an SP set constructed by the EUC–FBZ method can be increased by shifting all points in the BZ simultaneously through a vector $\tilde{\mathbf{k}} \neq 0$ (Fig. 2b). It follows from Table 1 that, for the EUC–FBZ transfor-

mation with matrix $\hat{L} = \begin{pmatrix} 1 & 1 \\ -1 & 1 \end{pmatrix}$ and for $\tilde{\mathbf{k}} = (1/4,$

$1/4)$, the SP set has one point in the irreducible part of the BZ (Fig. 2b) instead of two points obtained for $\tilde{\mathbf{k}} = 0$. However, since the star of the vector $\tilde{\mathbf{k}} = (1/4, 1/4)$ consists of four vectors, it turns out that the SP set for $L = 2$ obtained by shifting through the vector $\tilde{\mathbf{k}} = (1/4, 1/4)$ corresponds to the SP set obtained using the matrix

$\hat{L} = \begin{pmatrix} 2 & 0 \\ 0 & 2 \end{pmatrix}$ with $L = 4$ and shifting through the same

vector $\tilde{\mathbf{k}} = (1/4, 1/4)$. Therefore, with appropriate choice of vector $\tilde{\mathbf{k}}$ in the FBZ, fairly efficient SP sets can be constructed even for small extensions of the primitive cell in the direct lattice. Table 2 lists the SP sets with both $\tilde{\mathbf{k}} = 0$ and various shifts $\tilde{\mathbf{k}} \neq 0$ obtained by us for a square lattice with symmetry $F = C_{4v}$. It can be seen from Table 2 that, as regards the efficiency of the SP set obtained, the EUC–FBZ transformation with subsequent shifting is equivalent to the transformation with a larger L_{eff} and, therefore, is characterized by an effectively higher accuracy M_{eff} and a higher value of $E_{\text{eff}} = M_{\text{eff}}/N_{\text{eff}}$.

Table 3 lists the parameters of various SP sets for an fcc lattice (crystal class O_h) obtained using symmetric extensions in the direct lattice with both a diagonal transformation matrix (preserving the fcc Bravais lattice) and off-diagonal matrices corresponding to transitions to simple cubic and bcc lattices. The data from Table 3 complement the results obtained in [2] and indicate the specific EUC–FBZ transformations that lead to the constructed SP sets.

The Monkhorst–Pack method [5] is a specific case of the EUC–FBZ method proposed by us for constructing SP sets in the BZ; this case corresponds to transformation (1) with a diagonal matrix ($\hat{L}_{ji} = n_i \delta_{ji}$; $i, j = 1, 2, 3$) and shifting $\tilde{\mathbf{k}} = \frac{1}{2}(n_1, n_2, n_3)$ for even values of $n_1, n_2,$ and n_3 and without shifting ($\tilde{\mathbf{k}} = 0$) for odd values. It can be seen from Table 3 that, for the fcc Bravais lattice ($n_1 = n_2 = n_3 = n$), the Monkhorst–Pack method

does not give a monotonically increasing accuracy M of SP sets with increasing n . Indeed, for $n = 3, 4, 5, 6,$ and 7 , the Monkhorst–Pack sets of SPs correspond to accuracy $M(M_{\text{eff}}) = 9, 30, 24, 67,$ and 46 , respectively. In the EUC–FBZ method, the accuracy M_{eff} of SP sets increases monotonically with n .

Now, we briefly discuss the relation between the SP sets and the cyclic-cluster model commonly used for calculating defects in crystals [10–12]. In this model, an infinite crystal is replaced by a finite crystal (coinciding with an EUC in the direct lattice) and cyclic boundary conditions are imposed; that is, all translations of the EUC as a whole are assumed to coincide with zero translation. It was shown in [7] that an approximate calculation of the one-electron density matrix of an infinite crystal based on an SP set obtained using the EUC–FBZ method leads to the cyclic-cluster model with a cluster corresponding to the EUC chosen. In this case, the SP sets obtained contain $\tilde{\mathbf{k}} = 0$, because the symmetry group of a cyclic cluster (for symmetric extensions) has an identity representation corresponding to the center of the BZ.

The shifting through vector $\tilde{\mathbf{k}}$ considered above when constructing SP sets corresponds, in fact, to consideration of a larger cyclic cluster, i.e., to an increased accuracy of interpolation over the BZ when calculating the density matrix. Note that, in the cyclic-cluster model, it is expedient to use only symmetric extensions in constructing EUCs, because only in this case is the symmetry of the one-electron density matrix of a crystal preserved. When SP sets are constructed, the infinite-crystal model is considered and nonsymmetric extensions are used only in order to ensure the proper weights in the SP set and appropriate accuracy of the set. As already mentioned above, if an SP set constructed through a nonsymmetric extension is used to calculate the density matrix, summation should be performed over the stars of the vectors in the irreducible part of the BZ that enter the SP set. In the following section, we consider the problem of integrating a fully symmetric function (defined in direct space) over the primitive cell of the direct lattice.

3. EXTENDED UNIT CELL IN THE RECIPROCAL LATTICE AND SPECIAL POINTS IN THE WIGNER–SEITZ CELL

The EUC method for constructing an SP set in the Wigner–Seitz cell is similar to the EUC method for constructing an SP set in the BZ (see Section 2). In this section, we dwell on distinctions between these methods.

Let a function $U(\mathbf{r})$ be fully symmetric with respect to the space group $F^{(s)}$ of a crystal:

$$U(\mathbf{r} + \mathbf{a}_n) = U(\mathbf{r}) = U(f_{\mathbf{t}_j^{(s)}}^{-1} \mathbf{r}), \quad (24)$$

Table 3. Parameters of SP sets for crystals belonging to the O_h crystal class (fcc lattices)

n	Before shifting					After shifting through $\tilde{\mathbf{k}}$				
	L	M	N	M/N	R_M	L_{eff}	M_{eff}	N_{eff}	$M_{\text{eff}}/N_{\text{eff}}$	$R_{M_{\text{eff}}}$
$\hat{L} = n \begin{pmatrix} 1 & 0 & 0 \\ 0 & 1 & 0 \\ 0 & 0 & 1 \end{pmatrix}, \quad L = n^3, \quad \tilde{\mathbf{k}} = \frac{1}{2n}(1, 1, 1)$										
2	8	4	3	1.3	$\sqrt{2}$	32	8	2 (6)	4.0 (1.3)	2
3	27	9	4	2.2	$3\sqrt{2}/2$	108	17	6 (10)	2.8 (1.7)	4.5
4	64	15	8	1.9	$2\sqrt{2}$	256	30	10 (19)	3.0 (1.6)	4
5	125	24	10	2.4	$5\sqrt{2}/2$	500	47	19	2.5	12.5
6	216	34	16	2.1	$3\sqrt{2}$	864	67	28	2.4	18
7	343	46	20	2.3	$7\sqrt{2}/2$	1372	91	44	2.1	24.5
8	512	59	29	2.0	$4\sqrt{2}$	2048	118	60	2.0	32
9	729	75	35	2.1	$9\sqrt{2}/2$	2916	148	85	1.7	40.5
$\hat{L} = n \begin{pmatrix} -1 & 1 & 1 \\ 1 & -1 & 1 \\ 1 & 1 & -1 \end{pmatrix}, \quad L = 4n^3, \quad \tilde{\mathbf{k}} = \frac{1}{4n}(1, 1, 1)$										
1	4	2	2	1.0	1	32	8	2	4.0	2
2	32	8	6	1.3	2	256	30	10	3.0	4
3	108	17	10	1.7	3	864	67	28	2.4	18
4	256	30	19	1.6	4	2048	118	60	2.0	32
$\hat{L} = n \begin{pmatrix} 3 & -1 & -1 \\ -1 & 3 & -1 \\ -1 & -1 & 3 \end{pmatrix}, \quad L = 16n^3, \quad \tilde{\mathbf{k}} = \frac{1}{4n}(1, 1, 1)$										
1	16	6	3	2.0	$\sqrt{3}$	32	8	2	4.0	2
2	128	23	11	2.1	$2\sqrt{3}$	256	30	10	3.0	4
3	432	51	22	2.3	$3\sqrt{3}$	864	67	28	2.4	18
4	1024	89	45	2.0	$4\sqrt{3}$	2048	118	60	2.0	32

Note: The values of N_{eff} and $M_{\text{eff}}/N_{\text{eff}}$ that correspond to the SP set with $L = L_{\text{eff}}$ containing the Γ point ($\mathbf{k} = 0$) are given in parentheses.

where $f_{\mathbf{t}_f^{(s)} \mathbf{n}} \equiv (f | \mathbf{t}_f^{(s)} + \mathbf{a}_n) \in F^{(s)}$ are operations of the symmetry group of the crystal and $\mathbf{t}_f^{(s)}$ are improper translations that accompany orthogonal operations f of the point group F of the crystal (for symmorphic space groups, all improper translations can be considered to be zero translation if the origin of the coordinates is chosen properly). In contrast to fully symmetric func-

tions $\phi(\mathbf{k})$ in reciprocal space, functions $U(\mathbf{r})$ satisfying Eq. (24) have different symmetry for space groups belonging to the same crystal class and the same crystal system because of the difference in the sets of improper translations $\mathbf{t}_f^{(s)}$ that accompany operations $f \in F$.

By analogy with an irreducible part of the BZ in the reciprocal lattice, we can define an irreducible part of

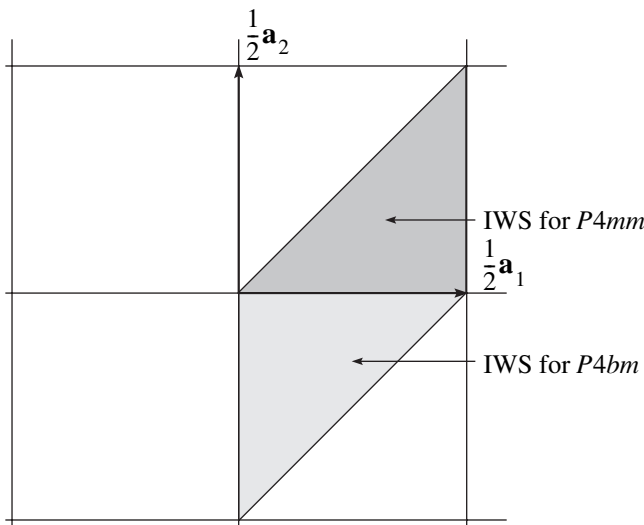


Fig. 3. Irreducible parts of the Wigner–Seitz cell (IWS) for the $P4mm$ and $P4bm$ layer symmetry groups.

the Wigner–Seitz cell (IWS) in the direct lattice as a cell containing one representative of each star $f_{i0}^{(s)} \mathbf{r}$ ($f \in F$). It turns out that IWS cells for different groups of a crystal class and of a crystal system are different (whereas irreducible parts of the BZs of such groups are identical). As an example, we consider two layer groups with a square lattice, $P4mm$ and $P4bm$, belonging to the crystal class C_{4v} . The $P4mm$ group is symmorphic, whereas in the $P4bm$ group all reflections in planes are accompanied by improper translation $(1/2, 1/2)$ through the improper translation vector $\mathbf{t}_\sigma = (\mathbf{a}_1 + \mathbf{a}_2)/2$. Figure 3 shows irreducible parts of the Wigner–Seitz cell for these groups.

In calculations of the electronic structure of crystals performed in a plane-wave basis, this difference should be taken into account when calculating integrals over the Wigner–Seitz cell of the direct lattice (Fourier coefficients). In this case, plane waves $\exp(i\mathbf{b}_m \cdot \mathbf{r})$ symmetrized with respect to space group $F^{(s)}$ [as in Eq. (10)] are used:

$$\begin{aligned} Q_{m\mu}^{(s)}(\mathbf{r}) &= \frac{\sqrt{N_{m\mu}}}{n_F} \sum_{f \in F} \exp(i\mathbf{b}_m \cdot (f|\mathbf{t}_f^{(s)})^{-1} \mathbf{r}) \\ &= \sum_{f \in F} \exp(if\mathbf{b}_m \cdot \mathbf{r}) \cdot \exp(-if\mathbf{b}_m \cdot \mathbf{t}_f^{(s)}). \end{aligned} \quad (25)$$

The symmetrized wave $Q_{m\nu}^{(s)}(\mathbf{r})$ corresponds to the μ th star belonging to the m th coordination shell of radius K_m in the reciprocal lattice. In Eq. (25), $N_{m\mu}$ is the number of rays in the star $m\mu$.

In contrast to the symmetrized combinations of plane waves in reciprocal space in Eq. (10), the symme-

trized plane waves in the direct lattice defined by Eq. (25) are different for different space groups of a crystal class because of the presence of the factor $\exp(-if\mathbf{b}_m \cdot \mathbf{t}_f^{(s)})$. Table 4 lists symmetrized combinations of plane waves $Q_{m\mu}^{(s)}(\mathbf{r})$ for the $P4mm$ and $P4bm$ symmetry groups of crystalline layers belonging to the same crystal class.

When integrals over the Wigner–Seitz cell are calculated approximately, an expansion in terms of $Q_{m\mu}^{(s)}(\mathbf{r})$ is used [as in Eq. (12)],

$$U(\mathbf{r}) = \sum_{m\mu} C_{m\mu}^{(s)} Q_{m\mu}^{(s)}(\mathbf{r}) \quad (26)$$

with subsequent truncation of the series [as in Eq. (21)].

Similarly to set (8), an SP set in the Wigner–Seitz cell has the form

$$\mathbf{r}_t^{(\tilde{\mathbf{r}})} = \tilde{\mathbf{r}} + \sum_j q_{tj} \mathbf{a}_j^{(s)}, \quad t = 1, 2, \dots, L, \quad (27)$$

where vectors $\mathbf{a}_j^{(s)}$ define a folded Wigner–Seitz cell [cf. Eq. (8)]. The numbers q_{tj} are chosen such that the points $\mathbf{r}_t^{(\tilde{\mathbf{r}})}$ lie in the Wigner–Seitz cell; furthermore, out of the equivalent points that are at the boundary of the Wigner–Seitz cell and, therefore, are joined by direct-lattice vectors \mathbf{a}_m , only one point is taken into account.

By analogy with SP sets in the BZ, the accuracy $M^{(L_{\text{eff}})}$ of SP sets with $\tilde{\mathbf{r}} = 0$ in the Wigner–Seitz of the direct lattice is determined by the radius $K_{M_{\text{eff}}} \geq \min_j |\mathbf{b}_j^{(L)}| > 0$. The values of this radius for the first 14 coordination shells of the square lattice are listed in Table 4. As in the theory of SPs in the BZ, integration over the Wigner–Seitz cell can be performed using only points in its irreducible part and the efficiency of an SP set is characterized by the quantity $E_{\text{eff}}^{(\tilde{\mathbf{r}})} = M_{\text{eff}}/N^{(\tilde{\mathbf{r}})}$, which is the ratio of the number of the coordination shell of radius $K_{M_{\text{eff}}}$ in the reciprocal lattice to the number $N^{(\tilde{\mathbf{r}})}$ of SPs in the IWS cell.

We do not consider specific SP sets in the Wigner–Seitz cell, because they can easily be derived from SP sets in the BZ. The coordinates of SPs are measured in units of the primitive vectors of the direct lattice. When choosing an SP set, it should be taken into account that the type of reciprocal lattice involved can differ from the type of the corresponding direct lattice. For example, the data on SP sets listed in Table 3 for the direct fcc lattice can be used to perform integration over the Wigner–Seitz cell of a bcc lattice.

Table 4. Symmetrized plane waves $Q_{m\mu}^{(s)}(\mathbf{r})$ in a square lattice for the $P4mm$ and $P4bm$ symmetry groups of crystalline layers. Vectors \mathbf{K}_s representing the stars of wave vectors and their lengths d_s are given in units of $2\pi/a$, and the coordinates x and y are given in units of a (a is the lattice parameter)

m	\mathbf{K}_s	d_s	$P4mm (C_{4v}^1)$	$P4bm (C_{4v}^2)$
0	(0, 0)	0	1	1
1	(1, 0)	1	$\cos(2\pi x) + \cos(2\pi y)$	0
2	(1, 1)	$\sqrt{2}$	$2\cos(2\pi x)\cos(2\pi y)$	$2\cos(2\pi x)\cos(2\pi y)$
3	(2, 0)	2	$\cos(4\pi x) + \cos(4\pi y)$	$\cos(4\pi x) + \cos(4\pi y)$
4	(2, 1)	$\sqrt{5}$	$\sqrt{2}[\cos(2\pi x)\cos(4\pi y) + \cos(4\pi x)\cos(2\pi y)]$	$\sqrt{2}[\sin(2\pi x)\sin(4\pi y) - \sin(4\pi x)\sin(2\pi y)]$
5	(2, 2)	$2\sqrt{2}$	$2\cos(4\pi x)\cos(4\pi y)$	$2\cos(4\pi x)\cos(4\pi y)$
6	(3, 0)	3	$\cos(6\pi x) + \cos(6\pi y)$	0
7	(3, 1)	$\sqrt{10}$	$\sqrt{2}[\cos(6\pi x)\cos(2\pi y) + \cos(2\pi x)\cos(6\pi y)]$	$\sqrt{2}[\cos(6\pi x)\cos(2\pi y) + \cos(2\pi x)\cos(6\pi y)]$
8	(3, 2)	$\sqrt{13}$	$\sqrt{2}[\cos(4\pi x)\cos(6\pi y) + \cos(6\pi x)\cos(4\pi y)]$	$\sqrt{2}[\sin(4\pi x)\sin(6\pi y) - \sin(6\pi x)\sin(4\pi y)]$
9	(4, 0)	4	$\cos(8\pi x) + \cos(8\pi y)$	$\cos(8\pi x) + \cos(8\pi y)$
10	(4, 1)	$\sqrt{17}$	$\sqrt{2}[\cos(2\pi x)\cos(8\pi y) + \cos(8\pi x)\cos(2\pi y)]$	$\sqrt{2}[\sin(2\pi x)\sin(8\pi y) - \sin(8\pi x)\sin(2\pi y)]$
11	(3, 3)	$3\sqrt{2}$	$2\cos(6\pi x)\cos(6\pi y)$	$2\cos(6\pi x)\cos(6\pi y)$
12	(4, 2)	$\sqrt{20}$	$\sqrt{2}[\cos(8\pi x)\cos(4\pi y) + \cos(4\pi x)\cos(8\pi y)]$	$\sqrt{2}[\cos(8\pi x)\cos(4\pi y) + \cos(4\pi x)\cos(8\pi y)]$
13	(5, 0)	5	$\cos(10\pi x) + \cos(10\pi y)$	0
14	(4, 3)	5	$\sqrt{2}[(6\pi x)\cos(8\pi y) + \cos(8\pi x)\cos(6\pi y)]$	$\sqrt{2}[\sin(6\pi x)\sin(8\pi y) - \sin(8\pi x)\sin(6\pi y)]$

4. CONCLUSIONS

The data obtained in this paper on the optimal SP sets for calculating the Fourier coefficients of periodic functions in the direct and reciprocal lattices are of importance in estimating the accuracy of calculation of the electronic structure of crystals. When a plane-wave basis is used, the accuracy of calculation depends on the number of plane waves in the basis and on the SP set in the Wigner–Seitz cell used to calculate the Fourier coefficients of expansion of the density in terms of symmetrized plane waves $Q_{m\mu}^{(s)}(\mathbf{r})$. The quality of the basis used is characterized by the so-called truncation energy, which is the kinetic energy $K_{\max}^2/2$ corresponding to the plane wave with the maximum reciprocal-lattice vector K_{\max} included in the plane-wave basis. The quality of an SP set is characterized by the accuracy M_{eff} and depends on the radius $R_{M_{\text{eff}}}$. These characteristics of the basis and SP set are often considered to be independent, and the convergence of the results is improved by increasing both the truncation energy (which also depends on the pseudopotentials of the specific atoms of the crystal) and the accuracy of the

SP set in the Wigner–Seitz cell. However, as shown in Section 2, for the basis used (i.e., for a fixed K_{\max}), the SP set should be chosen so that its quality M_{eff} corresponds to the quality of the basis.

When a basis of localized atomic-type functions is used, all relevant integrals of the basis functions can be calculated analytically (without numerical integration over the Wigner–Seitz cell); however, the results of calculations depend on the quality of the basis used. In this case, the accuracy of summation over the BZ should correspond to the size of the cyclic system for which integrals involving basis functions are summed over the direct lattice [7].

ACKNOWLEDGMENTS

The authors are grateful to I.I. Tupitsyn for providing the computer code employed to construct SP sets using the EUC–FBZ method.

REFERENCES

1. M. C. Payne, M. P. Teter, D. C. Allan, T. A. Arias, and J. D. Joannopoulos, Rev. Mod. Phys. **64**, 1045 (1992).

2. J. Moreno and J. M. Soler, Phys. Rev. B **45**, 13891 (1992).
3. C. Pisani, E. Apra, M. Causa, and R. Orlando, Int. J. Quantum Chem. **38**, 395 (1990).
4. D. J. Chadi and M. L. Cohen, Phys. Rev. B **8**, 5747 (1973).
5. H. J. Monkhorst and J. D. Pack, Phys. Rev. B **13**, 5188 (1976).
6. R. A. Evarestov and V. P. Smirnov, Phys. Status Solidi B **119**, 9 (1983).
7. R. A. Evarestov and I. I. Tupitsyn, Fiz. Tverd. Tela (St. Petersburg) **44**, 1582 (2002) [Phys. Solid State **44**, 1656 (2002)].
8. R. A. Evarestov, A. V. Leko, and V. P. Smirnov, Phys. Status Solidi B **128**, 275 (1985).
9. I. J. Robertson and M. C. Payne, J. Phys.: Condens. Matter **2**, 9837 (1990).
10. P. Deak, Phys. Status Solidi B **217**, 9 (2000).
11. T. Bredow, G. Geudtner, and K. Jug, J. Comput. Chem. **22**, 861 (2001).
12. R. A. Evarestov, S. Piskunov, E. A. Kotomin, and G. Borstel, Phys. Rev. B **67**, 064101 (2003).

Translated by Yu. Epifanov

SEMICONDUCTORS
AND DIELECTRICS

Specific Features of Absorption and Luminescence in CsBr : EuOBr Crystals

Yu. V. Zorenko, R. M. Turchak, and I. V. Konstankevich

Franko National University, ul. Lomonosova 8, Lviv, 79044 Ukraine

Received June 9, 2003; in final form, November 3, 2003

Abstract—The specific features of the absorption, photoluminescence, x-ray luminescence, thermally stimulated luminescence, and photostimulated luminescence spectra of CsBr : Eu²⁺ single crystals grown using the Bridgman method are investigated in the temperature range 80–500 K at the highest possible dopant content (0.1–0.4 mol % EuOBr in the batch) required for preparing perfect crystals. It is shown that an increase in the dopant content leads to a broadening of the absorption and photoluminescence excitation bands with maxima at wavelengths of 250 and 350 nm due to the interconfigurational transitions $4f^7(^8S_{7/2}) \rightarrow 4f^65d(e_g, t_{2g})$ in Eu²⁺ ions. The photoluminescence and photostimulated luminescence spectra of CsBr : EuOBr single crystals (0.1–0.4 mol % EuOBr) contain a band at a wavelength of $\lambda_{\max} = 450$ nm and bands at wavelengths of $\lambda_{\max} = 508$ –523 and 436 nm. The last two bands are assigned to Eu²⁺-V_{Cs} isolated dipole centers and Eu²⁺-containing aggregate centers, respectively. It is revealed that the intensity of the luminescence associated with the aggregate centers ($\lambda_{\max} = 508$ –523 nm) is maximum at an EuOBr content of less than or equal to 0.1 mol % and decreases with an increase in the dopant content. The possibility of forming CsEuBr₃-type nanocrystals that are responsible for the green luminescence observed at a wavelength $\lambda_{\max} = 508$ –523 nm in CsBr : Eu crystals is discussed. The intensity of photostimulated luminescence in the CsBr : EuOBr crystals irradiated with x-ray photons is found to increase as the dopant content increases. It is demonstrated that CsBr : EuOBr crystals at a dopant content in the range 0.3–0.4 mol % can be used as x-ray storage phosphors for visualizing x-ray images with high spatial resolution. © 2004 MAIK “Nauka/Interperiodica”.

1. INTRODUCTION

At present, x-ray images are predominantly visualized with the use of BaFBr : Eu materials as storage phosphors [1]. As has been shown in a number of recent works [2–6], alkali halide crystals doped by ruthenium-like or rare-earth ions with $4f$ – $5d$ transitions (in particular, CsBr : Eu²⁺) exhibit better performance characteristics as compared to BaFBr : Eu²⁺ compounds. However, the luminescence properties of CsBr : Eu crystals have been adequately investigated only at low activator contents (0.01–0.1 mol %) [7, 9]. An important feature of the incorporation of Eu²⁺ impurities into the CsBr compound is the formation of Eu²⁺-V_{Cs} dipoles (V_{Cs} is a cation vacancy), which, under specific conditions, can form both associates of dipole centers [9] and nanocrystals or precipitates of other phases [6, 10, 11]. In turn, the formation of these dipoles can bring about substantial changes in the characteristics of storage phosphors [5, 6, 10]. Moreover, it has remained unclear how the optical and luminescence properties of CsBr : Eu crystals are affected by oxygen impurities acting as a compensator (an alternative to the V_{Cs} vacancies) for an excess charge of Eu²⁺ ions in these crystals [10, 12].

The purpose of the present work was to investigate the specific features revealed in the optical spectra of CsBr crystals doped with EuOBr at the highest possible content (0.1–0.4 mol % EuOBr in the batch) required for preparing single-phase materials and to determine

the appropriate conditions for these phosphor crystals to be used to visualize x-ray images.

2. SAMPLE PREPARATION AND EXPERIMENTAL TECHNIQUE

The absorption and luminescence spectra of CsBr : EuOBr crystals upon excitations of different types were investigated as a function of the EuOBr dopant content. The crystals were grown using the Bridgman method from a cesium bromide salt (reagent grade) in evacuated silica tubes at a residual pressure of 1.3 Pa.

The EuOBr compound was synthesized from the crystal hydrate EuBr₃ · 6H₂O upon heat treatment at high temperatures [13]. The EuOBr dopant thus prepared was introduced into the batch at a content varying in the range 0.1–0.4 mol %. At higher dopant contents, the crystals grown contained inclusions of other phases.

The absorption spectra were recorded on a Specord M40 spectrophotometer at a temperature of 300 K. The photoluminescence, x-ray luminescence, thermally stimulated luminescence (TSL), and photostimulated luminescence (PSL) spectra in the temperature range 80–500 K were measured on a photometric setup (SF-4A monochromator) equipped with an FÉU-51 photomultiplier. The photoluminescence was excited with radiation from an LGI-21 nitrogen laser (wave-

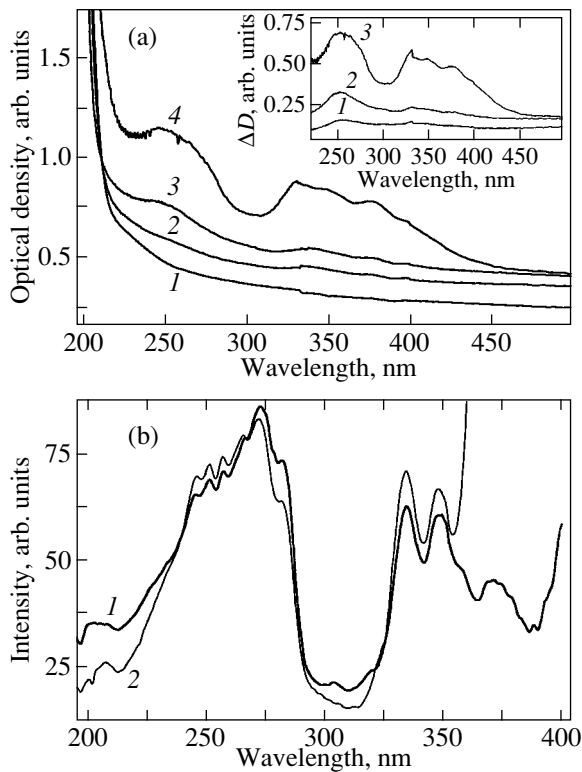


Fig. 1. (a) Absorption spectra of 1-mm-thick CsBr single crystals doped with EuOBr at different contents (N_{EuOBr}): (1) 0, (2) 0.1, (3) 0.2, and (4) 0.4 mol %. $T = 300$ K. The inset shows the difference absorption spectra of CsBr single crystals at EuOBr contents of (1) 0.1, (2) 0.2, and (3) 0.4 mol %. (b) Photoluminescence excitation spectra of CsBr : 0.1 mol % EuOBr single crystals measured at wavelengths of (1) 520 and (2) 440 nm. $T = 80$ K.

length $\lambda = 337.1$ nm; pulse duration, 8 ns). The crystals were irradiated with x-ray photons from a URS instrument (CrK_α radiation, $U_a = 30$ kV, $I = 12$ μA). The photostimulated luminescence of the CsBr : EuOBr crystals irradiated by x-ray photons with a dose of up to 2 R at a temperature of 300 K was measured either under excitation with light at a wavelength in the range 550–750 nm or under radiation from a He–Ne laser ($\lambda = 633$ nm). The emission of the samples was observed through a filter with maximum transmission at a wavelength of 440 nm.

The experiments were carried out using samples stored at room temperature for three months.

3. RESULTS AND DISCUSSION

The absorption spectra of the CsBr : EuOBr crystals measured at a temperature of 300 K (Fig. 1a) exhibit two broad bands with maxima at wavelengths of 250 and 350 nm. As can be seen from Fig. 1a, these bands have a complex vibrational structure. An increase in the dopant content in the crystal leads to an increase in the

intensity of absorption in these bands, their overlapping, and a shift in the long-wavelength edge from 400 to 450 nm. In general, the absorption spectra and the location of the absorption bands of the CsBr : EuOBr crystals are in agreement with those of alkali halide crystals activated by europium in the form of $\text{Eu}^{3+}\text{Hal}_3^-$ [3, 7–9, 12]. The absorption bands observed at wavelengths of 250 and 350 nm are due to the allowed interconfigurational transitions between the $^8S_{7/2}$ ground electron terms of the $4f^7$ shell and the terms of the $4f^65d$ (e_g, t_{2g}) shell, which are split by a crystal field with C_{2v} symmetry. It should be noted that the energies of the electron terms of the $4f^65d$ configuration of Eu^{2+} ions are less than those of the 6P_j electron terms of the $4f^7$ configuration. Consequently, the absorption and emission of the CsBr : EuOBr crystals are not accompanied by $4f^7-4f^7$ transitions and the spectra do not exhibit characteristic line structure. The fine structure of the absorption spectra is predominantly associated with the electrostatic interaction between d and f electrons and the spin–orbit interaction.

Apart from the $\text{Eu}^{2+}-V_{\text{Cs}}$ single dipole centers, which were identified using EPR spectroscopy in [5, 9], the CsBr : Eu^{2+} crystals contain more complex aggregate centers that can be formed as a result of thermal annealing [6, 10]. According to the data obtained by Savel'ev *et al.* [9], aggregation occurs even at room temperature. Therefore, the formation of these centers can be responsible for the shift observed in the long-wavelength absorption edge in the range 400–450 nm for CsBr : EuOBr crystals (at a dopant content ranging from 0.1 to 0.4 mol %) as compared to the location of this edge for the crystals at a lower dopant content (~ 0.01 at. %) [8]. It is characteristic that, upon quenching of the CsBr : EuOBr crystals from 500 to 290 K, the long-wavelength edge of the absorption band at 350 nm is shifted to 400 nm. Apparently, this shift is caused by the dominant contribution of the $\text{Eu}^{2+}-V_{\text{Cs}}$ isolated dipole centers to the absorption of the crystal. However, long-term storage (over the course of three months) of the samples at 295 K leads to an opposite shift in the long-wavelength absorption edge of this band, which is most likely associated with the aggregation processes. It should be noted that these processes are also responsible for the complex dependence of the luminescence spectra of the CsBr : EuOBr crystals on the activator content (Fig. 2).

The luminescence of Eu^{2+} ions in CsBr : Eu crystals is observed upon the allowed interconfigurational transitions between the e_g (t_{2g}) electron terms of the $4f^65d$ shell and the $^8S_{7/2}$ ground electron terms of the $4f^7$ shell [7, 8]. The photoluminescence spectra of the CsBr : EuOBr single crystals (0.1–0.4 mol % EuOBr) measured upon excitation into the long-wavelength absorption band of Eu^{2+} ions with the use of N_2 laser radiation at wave-

length $\lambda = 337.1$ nm (Fig. 2a) contain not only the well-known luminescence band due to the presence of $\text{Eu}^{2+}-V_{\text{Cs}}$ isolated dipole centers [5, 9] in the blue spectral range 435–450 nm but also a luminescence band (not described earlier in the literature) in the green spectral range. The photoluminescence of the $\text{CsBr}:\text{EuOBr}$ crystals depends on the activator content in a complex manner. For an EuOBr content of 0.1 mol %, the luminescence band with a maximum at a wavelength of 508 nm is dominant in the spectrum of the $\text{CsBr}:\text{0.1 mol \% EuOBr}$ single crystal (Fig. 2a, curve 2). An increase in the activator content to 0.2–0.4 mol % leads to an increase in the intensity of the luminescence associated with the $\text{Eu}^{2+}-V_{\text{Cs}}$ isolated dipole centers in the range 400–500 nm and a decrease in the intensity of luminescence in the range 500–600 nm to the point where it disappears completely (Fig. 2a, curves 3, 4). As the EuOBr content increases from 0.1 to 0.2 and 0.4 mol %, the maximum of the green luminescence band shifts to the long-wavelength range from 508 to 523 and 550 nm, respectively. The maxima of the blue luminescence band for $\text{CsBr}:\text{Eu}$ crystals at the aforementioned EuOBr contents are located at wavelengths of 436, 440, and 450 nm, respectively. It is evident that such a non-trivial dependence of the intensity of the luminescence bands on the EuOBr content in the $\text{CsBr}:\text{EuOBr}$ crystals is not a result of their overlapping but is a manifestation of the formation of luminescence centers that are more complex than the $\text{Eu}^{2+}-V_{\text{Cs}}$ isolated dipole centers.

Important information regarding these centers can be obtained from a detailed analysis of the luminescence excitation spectra (Fig. 1b), especially for the bands observed in the green (Fig. 1b, curve 1) and blue (Fig. 1b, curve 2) spectral ranges. It can be seen from Fig. 1b that, for the $\text{CsBr}:\text{EuOBr}$ single crystal (0.1 mol % EuOBr), the luminescence excitation spectrum measured at a wavelength of 520 nm (curve 1) is slightly broadened. This broadening can be judged from a comparison of the positions of the peaks observed in the short-wavelength wing of the excitation band at 250 nm and the positions of the peaks in the long-wavelength wing of the excitation band at 350 nm with those of the corresponding excitation bands in the luminescence excitation spectrum of the $\text{CsBr}:\text{EuOBr}$ single crystal (0.1 mol % EuOBr) measured at 440 nm (curve 2). As follows from the estimated shift (0.21 eV) between the corresponding bands in the ranges 202–208 and 370–375 nm, the crystal field strength responsible for the spectral characteristics of Eu^{2+} ions in centers of green luminescence is 9% greater than the crystal field strength for centers of blue luminescence associated with the $\text{Eu}^{2+}-V_{\text{Cs}}$ isolated dipole centers.

Figure 2b depicts the x-ray luminescence spectra of pure (curve 1) and europium-activated (0.2–0.4 mol % EuOBr) (curves 3, 4) CsBr crystals. For pure CsBr crystals, the luminescence with a maximum in the wavelength range 490–500 nm at room temperature is associated with the α centers [14], whereas the lumi-

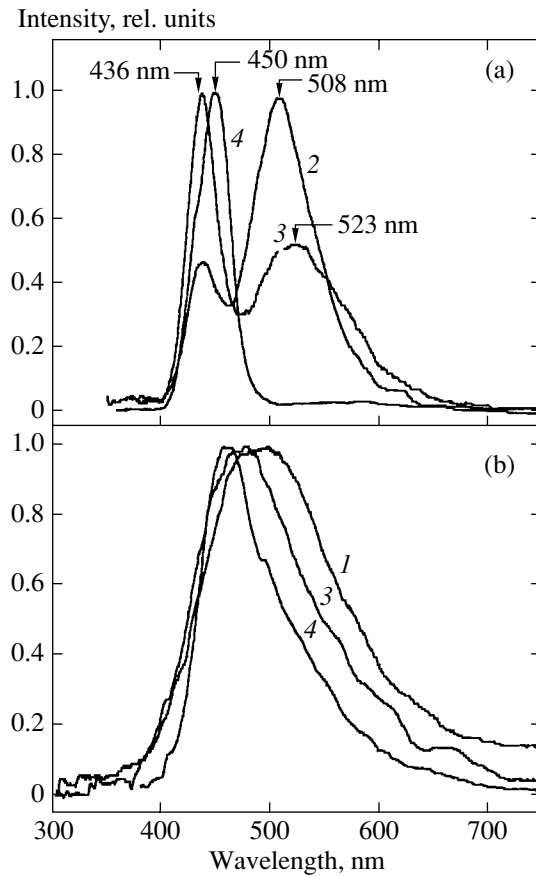


Fig. 2. (a) Photoluminescence spectra upon excitation with nitrogen (N_2) laser radiation ($\lambda = 337.1$ nm) and (b) x-ray luminescence spectra of CsBr single crystals at different EuOBr contents: (1) 0, (2) 0.1, (3) 0.2, and (4) 0.4 mol %. $T = 300$ K. The spectra are normalized to the maximum intensity.

nescence observed at 80 K is assigned to self-trapped π excitons at a wavelength $\lambda_{\text{max}} = 330$ nm [12, 14]. As the activator content increases, the maximum of the x-ray luminescence band shifts toward the blue spectral range. This shift can be explained by the increase in the rate of recombination through Eu^{2+} centers. The mechanism of this process involves intermediate trapping of holes by $\text{Eu}^{2+}-V_{\text{Cs}}$ centers or their associates, followed by recombination with electrons and a transfer of energy to Eu^{2+} ions.

The thermally stimulated luminescence spectra of the $\text{CsBr}:\text{EuOBr}$ single crystals irradiated with x-ray photons at a temperature of 80 K and then heated to 300 K (Fig. 3a, curves 2–4) exhibit peaks at 105, 137, 152, 162, and 186 K. The thermally stimulated luminescence spectra of the $\text{CsBr}:\text{EuOBr}$ single crystals (0.4 mol % EuOBr) irradiated at a temperature of 300 K and heated to 500 K (Fig. 3b) contain peaks at 335 and 420 K. A comparison of the thermally stimulated luminescence spectra of the CsBr single crystals activated with EuOBr (curves 2–4) and the spectra of pure CsBr

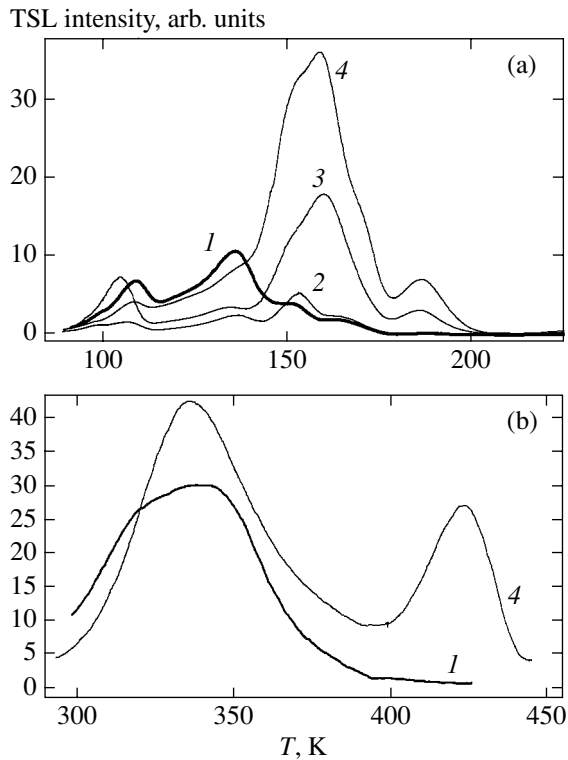


Fig. 3. Thermally stimulated luminescence spectra of (1) pure CsBr and (2–4) CsBr : Eu^{2+} single crystals at different activator contents in the temperature ranges (a) 80–225 and (b) 290–450 K. Activator content: (1) 0, (2) 0.1, (3) 0.2, and (4) 0.4 mol %.

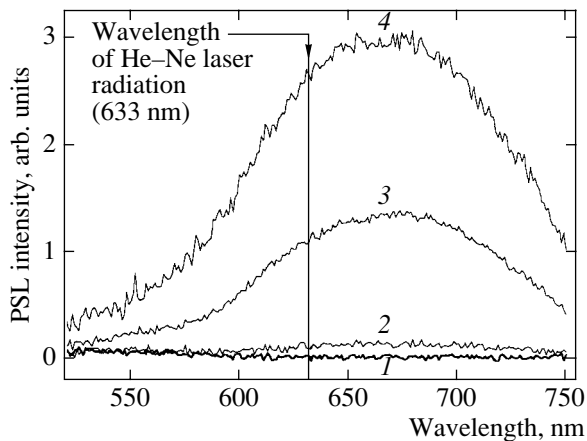


Fig. 4. Photostimulated luminescence excitation spectra of CsBr single crystals at different EuOBr activator contents: (1) 0, (2) 0.1, (3) 0.2, and (4) 0.4 mol %. $T = 300$ K.

single crystals (curve 1) shows that the peaks observed at 152, 162, 186, 335, and 425 K are associated with the introduction of Eu^{2+} impurities into the pure crystal. The spectral composition of the thermally stimulated luminescence of the CsBr : EuOBr single crystals

(0.4 mol % EuOBr) in the range of the most intense peaks revealed at temperatures of 162 and 420 K corresponds to the luminescence band with a maximum in the wavelength range 440–450 nm. On this basis, we can argue that thermal depletion of trapping centers results in excitation of Eu^{2+} centers through the recombination of electrons and holes localized at $\text{Eu}^{2+}-V_{\text{Cs}}$ dipoles or at their associates. Therefore, by analogy with the inferences made in [15], the high-temperature peaks observed at 335 and 420 K in the thermally stimulated luminescence spectra can be attributed to thermal depletion of F centers (V_{Cs} cation vacancies) and F_z centers (F centers stabilized by the nearest neighbor $\text{Eu}^{2+}-V_{\text{Cs}}$ dipoles). It seems likely that the thermally stimulated luminescence peaks in the range 150–190 K can be associated with the formation of F^- centers (i.e., F centers with an additionally localized electron). Note that the generation of these centers in KI : Eu^{2+} crystals at temperatures in the range 123–173 K was observed by Novosad and Streletska [12]. Under the above assumption, the thermally stimulated luminescence peaks observed at 152 and 162 K can be assigned to F_z^- centers with different coordinations of $\text{Eu}^{2+}-V_{\text{Cs}}$ dipoles, whereas the peak at 186 K can be attributed to F^- single centers.

In the case when the crystals subjected to preliminary irradiation with x-ray photons at 300 K are then excited with light in the wavelength range 550–750 nm (Fig. 4), there appears an intense photostimulated luminescence band in the blue spectral range. This band exhibits a maximum in the wavelength range 650–675 nm in the photostimulated luminescence excitation spectrum and corresponds to the absorption of F and F_z centers [3, 6, 12]. The spectral composition of the photostimulated luminescence, as a whole, corresponds to the photoluminescence spectra (Fig. 2) and is governed by the recombination of electrons (photoionized in F -like centers) with holes trapped by $\text{Eu}^{2+}-V_{\text{Cs}}$ dipoles and their associates. An increase in the activator content leads to an increase in the intensity of photostimulated luminescence with a dominant contribution from the luminescence of $\text{Eu}^{2+}-V_{\text{Cs}}$ isolated dipole centers in the wavelength range 440–450 nm.

An analysis of the experimental results obtained revealed that the CsBr : EuOBr single crystals accumulate the energy from x-ray photons. For the same irradiation dose, the higher the dopant content, the greater the light sum accumulated by the crystals. It should be noted that an EuOBr dopant content in the range 0.3–0.4 mol % is optimum for preparing high-quality crystals used as storage phosphors for visualizing x-ray images with high spatial resolution. The luminescence band of the CsBr : EuOBr single crystal (0.4 mol % EuOBr) with a maximum at a wavelength of 450 nm virtually coincides with the luminescence band of CsBr crystals doped with EuBr_3 [6] and lies well away from

the photostimulated luminescence excitation band. This condition is necessary for practical application of the CsBr : EuOBr single crystal (0.4 mol % EuOBr) as a storage phosphor, in particular, for screens with a high spatial resolution. For optical reading of information recorded with these crystals, it is expedient to use radiation from a He–Ne laser at wavelength $\lambda = 633$ nm. However, in this case, the He–Ne laser radiation and photostimulated luminescence excitation spectrum need to be matched more closely (Fig. 4).

Another way to improve the properties of phosphors based on CsBr : Eu²⁺ crystals with the aim of increasing the photostimulated luminescence intensity is to produce photosensitive centers in the form of Eu²⁺-containing nanocrystals or precipitates of other phases that are characterized by a greater carrier-capture cross section than that for Eu²⁺–V_{Cs} isolated dipole centers [6, 7]. Analysis of the possible types of such structures in CsBr crystals presents considerable difficulties, because the phase diagram of the Cs–Br–Eu system is not yet known. Nonetheless, some conclusions can be drawn on the basis of the luminescence characteristics of CsBr crystals doped with EuOBr at different concentrations. In particular, we can state that, apart from the Eu²⁺–V_{Cs} isolated dipole centers, which are characterized by the photoluminescence and photostimulated luminescence bands at a wavelength of 450 nm (Fig. 2a, curve 4), the CsBr : EuOBr single crystals (0.1–0.4 mol % EuOBr) contain several types of centers responsible for the photoluminescence and photostimulated luminescence bands observed at wavelengths of 508–523 and 436 nm (Fig. 2a, curve 2).

The spectral composition of the photoluminescence and photostimulated luminescence bands of aggregate centers in CsBr crystals and the photoluminescence excitation spectra suggest that the centers of green and blue luminescence are associated with the Eu²⁺ ions located at lattice sites with different symmetries. This is confirmed by the fact that the crystal field strength for centers of green luminescence exceeds the crystal field strength for centers of blue luminescence by 9% and that the photoluminescence and photostimulated luminescence spectra for the former centers are substantially shifted (by 70 nm) toward the long-wavelength range as compared to those for centers of blue luminescence, which are characteristic of Eu²⁺ ions in the crystal field with C_{2v} symmetry. It is worth noting that, among the large variety of materials characterized by Eu²⁺ luminescence [16], only crystals with a perovskite-type structure (in particular, EuAlO₃ crystals) exhibit luminescence in the green spectral range (510–520 nm).

In [18, 19], it was found that annealing of CsCl–PbCl₂ and CsBr–CdBr₂ solid solutions containing 0.5–1.0 mol % Pb²⁺ (or Cd²⁺) at temperatures $T = 160$ – 200°C leads to the formation of CsPbCl₃ and CsCdBr₃ nanocrystals with a perovskite-type structure and sizes

equal to 250–300 lattice constants of these materials. Nikl *et al.* [18] proposed a mechanism of formation of such nanocrystals. By analogy with this mechanism, we can assume that similar nanocrystals of the CsEuBr₃ type are formed in EuOBr-doped CsBr single crystals with a CsCl structure at a dopant content of 0.1–0.2 mol %. This assumption is supported by the results obtained in [6, 7], according to which the considerable changes in the intensity of photostimulated luminescence in CsBr : EuBr₃ (0.01–5.00 mol % EuBr₃) powders annealed in the temperature range 160–220°C are associated with the formation of CsEuBr₃ and Cs₄EuBr₆ nanocrystals. In [6, 7], the above inference regarding the formation of these nanocrystals was made from a comparison of the shape and positions of individual lines in the x-ray diffraction patterns with those of the corresponding lines for the CsPbBr₃ and Cs₄PbBr₆ phases [20].

In our opinion, it is these nanocrystals that serve as centers of green luminescence in CsBr : Eu crystals, whereas the EuBr₂-type precipitates play the role of aggregate centers responsible for the photoluminescence and photostimulated luminescence in the wavelength range 436–443 nm. Note that the luminescence of EuBr₂-type precipitates in ABr : Eu (A = Na, K, Rb) crystals was observed in this spectral range by Medrano *et al.* [11].

Novosad and Streletska [12] proposed an alternative model for the aforementioned aggregate centers of luminescence. According to their model, Eu²⁺–O²⁻ pair centers with oxygen impurities compensating for the excess charge of Eu²⁺ ions are formed in CsBr : Eu crystals. However, this model allows neither for the complex dependences of the photoluminescence and photostimulated luminescence spectra on the activator content nor the formation of different types of aggregate centers of luminescence in CsBr : Eu crystals.

ACKNOWLEDGMENTS

We would like to thank M.M. Batentschuk (University of Erlangen–Nuremberg, Germany) for recording the photostimulated luminescence spectra.

REFERENCES

1. M. Sonoda, M. Takano, J. Migahara, and H. Kato, *Radiology* **148**, 833 (1983).
2. A. R. Laksman, *Phys. Status Solidi A* **153** (3), 3 (1996).
3. S. S. Novosad, B. O. Belikovitch, S. D. Martiniv, and I. I. Kukhars'kiĭ, *Ukr. Fiz. Zh.* **40** (11–12), 1212 (1995).
4. J. M. Spaeth, *Radiat. Meas.* **33**, 527 (2001).
5. S. Schweizer, U. Rogulis, S. Assmann, and J. M. Spaeth, *Radiat. Meas.* **33**, 483 (2001).
6. P. Hackenschmied, G. Zeitler, M. Batentschuk, A. Winnacker, B. Schmitt, M. Fuchs, and W. Knupfer, *Nucl. Instrum. Methods Phys. Res. B* **191**, 163 (2002).

7. E. A. Shuraleva, P. A. Parfianovich, and P. S. Ivakhnenko, *Spectroscopy of Crystals* (Nauka, Moscow, 1975).
8. G. D. Varenko, V. P. Avdonin, and B. G. Plachenov, *Opt. Spektrosk.* **28** (1), 72 (1970).
9. V. P. Savel'ev, V. P. Avdonin, L. D. Dugarova, A. P. Nedashkovskii, and B. T. Plachenov, *Fiz. Tverd. Tela (Leningrad)* **16** (4), 1090 (1974) [*Sov. Phys. Solid State* **16**, 700 (1974)].
10. P. Hackenschmied, G. Schierning, M. Batentschuk, and A. Winnacker, *J. Appl. Phys.* **93** (9), 5109 (2003).
11. C. P. Medrano, H. S. Murrieta, and J. P. Rubio, *J. Lumin.* **29**, 223 (1984).
12. S. S. Novosad and N. M. Streletska, *Funkts. Mater.* **9**, 190 (2002).
13. *Chemistry and Technology of Rare and Trace Elements*, Ed. by K. A. Bol'shakov, 2nd ed. (Vysshaya Shkola, Moscow, 1976), Part 2, p. 72.
14. L. A. Parfianovich and E. E. Penzina, *Electron-Type Color Centers in Ionic Crystals* (Vost.-Sib. Kn. Izd., Irkutsk, 1977).
15. S. Chernov, A. R. Melendes, T. M. Ritters, and M. Barbosa-Flores, *Radiat. Meas.* **33**, 797 (2001).
16. *Phosphors Handbook*, Ed. by Sh. Shinoya and W. M. Yen (CRC Press, New York, 2000).
17. P. M. Jaffe, *J. Electrochem. Soc.* **117** (7), 918 (1970).
18. M. Nikl, K. Nitsch, and K. Polak, *Phys. Rev. B* **51** (8), 5192 (1995).
19. S. V. Myagkota, *Opt. Spektrosk.* **87** (2), 311 (1999) [*Opt. Spectrosc.* **87**, 290 (1999)].
20. M. Nikl, K. Nitsch, E. Mihokova, K. Polak, G. P. Pazzi, P. Fabeni, M. Gurioli, F. Somma, S. Zazubovich, V. Babin, A. Scacco, S. Santucci, R. Phani, R. Aceves, M. Barboza-Flores, and R. Peres-Salas, *Proc. Electrochem. Soc.* **98-25**, 250 (1998).

Translated by O. Borovik-Romanova

SEMICONDUCTORS
AND DIELECTRICS

On the Theory of Thermal Conductivity of Dielectrics with Inclusion of the Interaction with a Thermostat (Theory and Numerical Experiment)

S. O. Gladkov and I. V. Gladyshev

Moscow State Institute of Radioengineering, Electronics, and Automation (Technical University),
pr. Vernadskogo 78, Moscow, 119454 Russia

Received December 1, 2003

Abstract—This paper reports on the results of investigations into the internal microscopic dissipative phenomena occurring in crystalline dielectrics in which the interaction of all subsystems with a thermostat plays a dominant role. It is shown that, in realistic physical situations where allowance is made not only for the coupling between interacting phonon subsystems of a dielectric but also for the interaction with a thermostat, the umklapp processes proceeding in samples with a size smaller than the critical value L_0 play an insignificant role. For these situations, it is proved that the phonon gas superflows through the volume without retardation and comes to rest only due to the interaction with immobile surface phonons of the thermostat. Numerical calculations demonstrate that the umklapp processes manifest themselves solely at high temperatures T (exceeding a temperature approximately equal to $\Theta_D/4$, where Θ_D is the Debye temperature) and for samples with a size $L > L_0$, which, according to our estimates, should be of the order of 10 cm. © 2004 MAIK “Nauka/Interperiodica”.

1. INTRODUCTION

As is known, the dissipative processes associated with the attainment of an internal thermal equilibrium in relaxing subsystems are of fundamental importance in constructing the theory of thermal conductivity of crystals.

It is generally believed that the final stage in attaining equilibrium in dielectrics proceeds through the umklapp mechanism [so-called umklapp processes (see, for example, the monographs by Akhiezer *et al.* [1] and Gurevich [2])] responsible for the relaxation of the momentum of the phonon system. This mechanism was first proposed by R. Peierls in 1929. The umklapp processes are actually of utmost importance but only for bulk samples. Indeed, we can easily imagine a situation in which the sample has a relatively small size L and the time τ_0 of the phonon mean free path between the sample boundaries is equal to L/c_s , where c_s is the mean acoustic velocity (the so-called Knudsen case). Since the relaxation time associated with the umklapp process is exponentially long [1, 2], we can state with assurance that there can frequently occur a situation where the inequality $\tau_u < L/c_s$ is violated and becomes reverse beginning from sizes $L < \tau_u c_s$. Qualitatively, this means that the phonons have no time to be retarded by the umklapp processes and gain the very interesting capacity to superflow. The final retardation should be accomplished only through the interaction with a thermostat, because, in actual conditions, the sample (as a rule) should be in contact with a heat reservoir at a constant temperature T_0 . This implies that, in a layer δ , the

bulk nonequilibrium superflowing phonons interact with surface equilibrium immobile phonons (being in direct contact with the heat reservoir) and, hence, will be retarded by them. As a result, the momentum relaxation will cease. It is this case that will be considered in the present work.

2. THEORY AND NUMERICAL CALCULATIONS

Let us assume that an external action (an acoustic wave or pulsed laser radiation) disturbs an internal phonon subsystem of a dielectric from equilibrium. Then, the dielectric is instantaneously placed in a thermostat at a temperature T_0 . We seek to describe the attainment of an internal relaxation with allowance made for the interaction of all phonon subsystems with the thermostat in a surface layer δ .

Owing to contact between the surface of the dielectric and a heat reservoir (Fig. 1), the system of surface (but three-dimensional) phonons in the region δ for a time $\tau_{\min} = \delta/c_l$ (here, c_l is the longitudinal acoustic velocity, which is always higher than the transverse acoustic velocity c_t) reaches an equilibrium Bose distribution: $\bar{N}_s = [\exp(\hbar\omega_{t,k}/T_0) - 1]^{-1}$, where $\omega_{t,l} = c_{t,l}k$ is the phonon dispersion and k is the wave vector. In what follows, the Boltzmann constant k_B will be taken equal to unity. It is necessary to stress that we are dealing here with not very low temperatures, which should at least be higher than the liquid-helium temperature. The description of the attainment of thermodynamic equi-

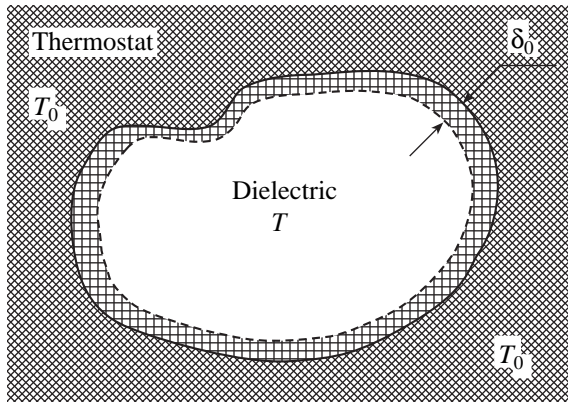


Fig. 1. Schematic drawing of the region δ involved in the interaction responsible for the attainment of equilibrium in the system of bulk nonequilibrium phonons for a sample with size $L < L_0$ (for explanation of the parameter L_0 , see text).

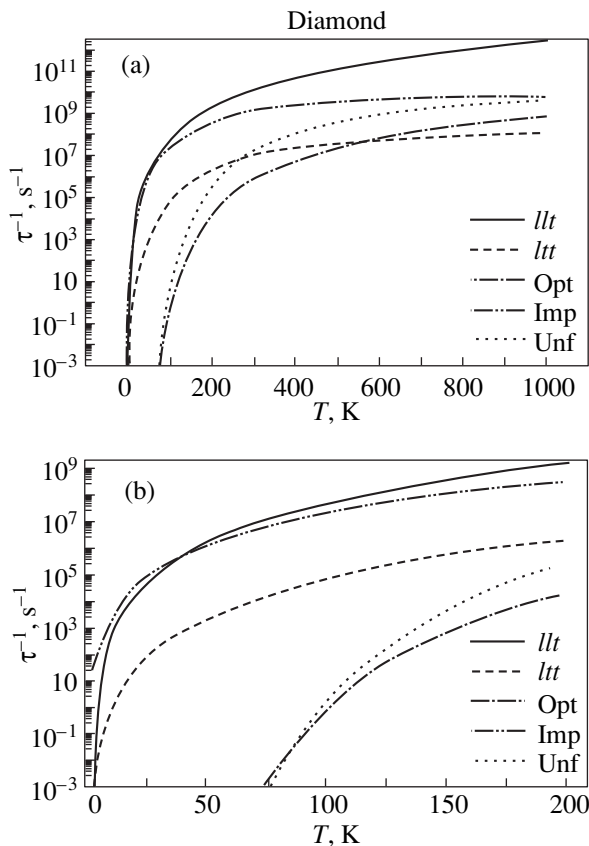


Fig. 2. Numerically calculated inverse relaxation times for diamond. Designations: llt is the inverse relaxation time for processes with two longitudinal and one transverse phonons, ltt is the inverse relaxation time for processes with one longitudinal and two transverse phonons, Opt is the inverse relaxation time for the process of coupling of two longitudinal phonons into one optical phonon, Imp is the inverse relaxation time for the process of transformation of a longitudinal phonon into a transverse phonon due to impurity scattering, and Unf is the inverse relaxation time for umklapp processes involving longitudinal phonons.

librium at temperatures close to absolute zero is a special problem.

The interaction between the bulk and surface phonons leads to equalization of the nonequilibrium parameters ($T \rightarrow T_0$, $\mu_l \rightarrow 0$, $V_l \rightarrow 0$) and complete thermalization of the internal subsystems. Running a little ahead, it should be noted that this situation becomes obvious after comparing the inverse relaxation times with the inverse time of the umklapp process, which is illustrated clearly in Fig. 2 with the results of numerical calculations. It can be seen from Fig. 2 that, at temperatures below the Debye temperature Θ_D , the umklapp processes are suppressed and become ineffective; consequently, the phonon gas superflows toward the sample boundaries. In some sense, this situation is similar to a ballistic flow of electrons in metals under conditions of their weak interaction with phonons.

In bulk samples (their size estimates are given below), the umklapp processes play a dominant role and the nonequilibrium phonon gas is retarded before it reaches the boundaries of the dielectric.

In our model, we assume that the time $\tau_{\max} = \delta/c_l$ is shorter than any one of the possible relaxation times in the systems under consideration ($\tau_{\max} < \tau_{\text{rel}}$). This condition imposes a specific restriction on the size δ of the region of the surface contact. For example, at a temperature $T \cong 100$ K, we have $\tau_{\text{rel}} = \tau_{llt} = 5 \times 10^{-9}$ s (Fig. 2) and the condition $\delta < 10^{-2}$ cm is satisfied at a longitudinal acoustic velocity $c_l = 1.8 \times 10^6$ cm/s (taken for diamond).

As the temperature increases, the relaxation times τ_{rel} become shorter and, hence, the quantity δ should also decrease. In this case, phonons in the immediate vicinity of the surface become completely two-dimensional. The interaction between the surface and bulk phonons results in thermalization of bulk phonons. Note that the temperature dependence of the relaxation time radically changes if the interaction with two-dimensional phonons is taken into account.

When analyzing the internal thermal equilibrium in the dielectric, we considered the following four subsystems: (i) the subsystem of longitudinal (l) phonons, (ii) the subsystem of transverse (t) phonons, (iii) the subsystem of optical (o) phonons, and (iv) the thermostat (T) with a temperature $T_0 = \text{const}$.

Reasoning from the principles developed, for example, in monograph [2] (see also [3, 4]), we can make the inference that three-particle scattering in the subsystem of transverse phonons is characterized by a shortest relaxation time τ_{llt} . Next in the hierarchical chain of relaxation times is the time τ_{llt} corresponding to the interaction $b_{lk}^+ b_{lk_1} b_{lk_2}^+$, where b_{lk}^+ (b_{lk}) is the operator of creation (annihilation) of a longitudinal phonon with wave vector \mathbf{k} and b_{tk}^+ (b_{tk}) is the operator of creation

(annihilation) of a transverse phonon with wave vector \mathbf{k} . The process competing with this interaction is impurity scattering of a longitudinal phonon, followed by its transformation into a transverse phonon. The relaxation time of this process is designated as $\tau_{\text{imp}l}$. The time τ_{ill} required to attain a quasi-equilibrium distribution of longitudinal phonons appears to be the longest among the aforementioned relaxation times; however, it is shorter than the time of longitudinal phonon relaxation due to the process $b_{l\mathbf{k}}^+ b_{o\mathbf{k}_1}^+ b_{o\mathbf{k}_2}$ with the participation of optical phonons. This time is denoted as τ_{loo} . The last process in the above hierarchical chain is the slowest relaxation process, namely, the umklapp process with a characteristic time τ_u . However, the results of the numerical analysis indicate that, in the T - L plane, there exists a region inside which the umklapp processes play a dominant role (Fig. 3) (we do not deal with this case in the present study). Therefore, all the aforementioned relaxation times satisfy the following inequalities: $\tau_{\text{ill}} \ll \tau_{\text{ill}} \leq \tau_{\text{imp}l} < \tau_{\text{ill}} \ll \tau_{\text{loo}} < \tau_u$. Under the assumption that these inequalities hold true, it is easy to elucidate qualitatively how all the subsystems reach thermodynamic equilibrium.

Making allowance for the interaction with the thermostat (which is important for our problem), we can write the following inequalities: $\tau_{TT} < \tau_{\text{ill}} \leq \tau_{\text{ill}T} \ll \tau_{\text{ill}T}$ and $\tau_{\text{imp}lT} \ll \tau_u$, where the subscript T indicates the interaction with the thermostat. As was noted above, the role of a thermostat is played by immobile surface phonons in the contact region δ (see scheme in Fig. 1). The approximate relationships for the relaxation times can be represented in the form

$$\begin{aligned}\tau_{\text{ill}T} &= \left(\frac{L}{2\delta}\right)\tau_{\text{ill}}, \\ \tau_{\text{ill}T} &= \left(\frac{L}{2\delta}\right)\tau_{\text{ill}T}, \\ \tau_{\text{imp}lT} &= \left(\frac{L}{2\delta}\right)\tau_{\text{imp}l}.\end{aligned}\quad (1)$$

Now, it is easy to write a kinetic equation that, in the τ approximation, turns out to be quite sufficient for our purposes. By linearizing this equation with respect to the independent parameters \mathbf{V}_l , μ_l , and $\delta T = T_l - T_0$ (where μ_l is the chemical potential of longitudinal phonons), we obtain the equations describing the relaxation of these parameters:

$$\begin{aligned}\delta\dot{T} &= -\frac{1}{\tau_1}\delta T, \\ \dot{\mu}_l &= -\frac{1}{\tau_2}\mu_l, \\ \dot{\mathbf{V}}_l &= -\left(\frac{1}{\tau_3} + \frac{1}{\tau_u}\right)\mathbf{V}_l.\end{aligned}\quad (2)$$

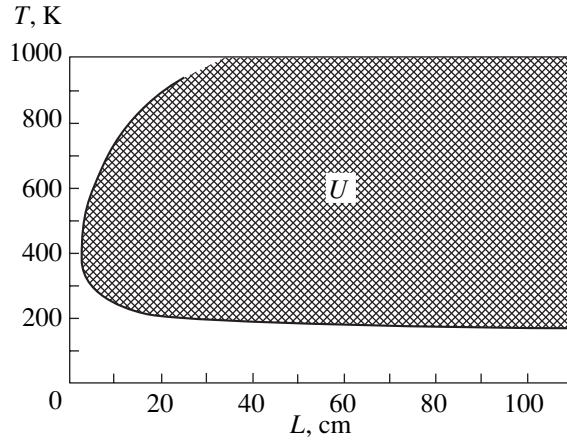


Fig. 3. Hatched region in the T - L plane (L is the sample size) in which the umklapp processes play an important role. Calculations are performed for a fixed parameter $\delta = 0.18$ cm under the assumption that δ does not depend on T .

Here, the inverse relaxation times are defined by the formulas

$$\frac{1}{\tau_1} = \frac{\int \frac{\hbar\omega_{lk}}{\tau_{lT,lk}} \frac{\partial \bar{N}_{lk}}{\partial T_l} \Big|_{T_l=T_0, \mu_l=\mathbf{V}_l=0} d^3k}{\int \hbar\omega_{lk} \frac{\partial \bar{N}_{lk}}{\partial T_l} \Big|_{T_l=T_0, \mu_l=\mathbf{V}_l=0} d^3k}, \quad (3)$$

$$\frac{1}{\tau_2} = \frac{\int \frac{1}{\tau_{lT,lk}} \frac{\partial \bar{N}_{lk}}{\partial(\hbar\omega_{lk})} \Big|_{T_l=T_0, \mu_l=\mathbf{V}_l=0} d^3k}{\int \frac{\partial \bar{N}_{lk}}{\partial(\hbar\omega_{lk})} \Big|_{T_l=T_0, \mu_l=\mathbf{V}_l=0} d^3k}, \quad (4)$$

$$\frac{1}{\tau_3} = \frac{\int \frac{k^2}{\tau_{lT,lk}} \frac{\partial \bar{N}_{lk}}{\partial(\hbar\omega_{lk})} \Big|_{T_l=T_0, \mu_l=\mathbf{V}_l=0} d^3k}{\int k^2 \frac{\partial \bar{N}_{lk}}{\partial(\hbar\omega_{lk})} \Big|_{T_l=T_0, \mu_l=\mathbf{V}_l=0} d^3k}. \quad (5)$$

The system of equations (2) is determined in the following way. The first equation representing the law of conservation of energy is derived by multiplying both sides of the kinetic equation into $\hbar\omega_{lk}$, followed by integration over d^3k . The second equation describes the law of conservation of the number of longitudinal phonons and is deduced through integration of both sides of the kinetic equation. Finally, the third equation (for the evolution of the drag velocity \mathbf{V}_l) represents the law of conservation of momentum of quasiparticles and is obtained by multiplying the kinetic equation into \mathbf{k} , followed by integration. As should be expected, this equation includes the relaxation time associated with the thermostat and the characteristic relaxation time of the umklapp process τ_u .

In the most interesting (theoretically and experimentally) temperature range, namely, at $T < \Theta_D$, and for not too large samples with a linear size L (Fig. 3), the inequality $1/\tau_3 \gg 1/\tau_u$ (Fig. 2) must be satisfied. This implies that the attainment of a final equilibrium in all the subsystems is characterized by the relaxation time $\tau_{lT,t} \approx (L/2\delta)\tau_{llt}$. For small-sized samples at $L \geq 2\delta$, we obtain $\tau_{lT,t} \geq \tau_{llt}$. In the case of bulk samples, we have $L \gg 2\delta$ and $\tau_{lT,t} \gg \tau_{llt}$. In order to compare the relaxation times τ_3 and τ_u , it is necessary to use an analytical expression for the time τ_u . The relaxation time τ_u for the three-particle interaction of longitudinal phonons can be written in the form

$$\frac{1}{\tau_{uk}} = \frac{\tilde{\gamma}}{4\pi} \frac{\Theta_D^2 \hbar a^3 k^6}{M^3 c_l^4 |\mathbf{k} + \mathbf{g}|} \int_{\frac{|\mathbf{k} + \mathbf{g}| - k}{2k}}^{\pi/ak} x^2 \left\{ 37(x+1)^2 + \frac{3}{x^2} \left[x^2 + (x+1)^2 - \frac{(\mathbf{k} + \mathbf{g})^2}{k^2} \right] \right\} \times [\bar{N}(\hbar\omega_{lk}) - \bar{N}(\hbar\omega_{lk}(x+1))] dx. \tag{6}$$

The averaging of the inverse time τ_{uk}^{-1} over the equilibrium Bose distribution function of longitudinal phonons is performed according to the formula

$$\frac{1}{\tau_u} = \frac{\int k^2 \bar{N}_{lk} \frac{dk}{\tau_{uk}}}{\int k^2 \bar{N}_{lk} dk}.$$

Substitution of the explicit expression (6) for $1/\tau_{uk}$ into the above formula gives

$$\frac{1}{\tau_u} = G \frac{\hbar \Theta_D^2}{g_1(\beta) M^3 c_l^4 a^2} \int_{-1}^1 dz \int_0^\pi y^3 \bar{N}(\beta y) \varphi(y, z) dy \times \int_{\frac{\varphi(y, z) - y}{2}}^\pi S(x, y) [\bar{N}(\beta x) - \bar{N}(\beta(x+y))] dx, \tag{7}$$

where $G = \tilde{\gamma}^2 \times 2.44 \times 10^{-5}$, $\beta = \Theta_D^*/(\pi T)$, and the functions have the form $\varphi(y, z) = \sqrt{y^2 + yz \times 4\pi + 4\pi^2}$, $S(x, y) = 37x^2(x+y)^2 + 3[x^2 + (x+y)^2 - \varphi(y, z)]^2$, $g_1(\beta) = \int_0^\pi y^2 \bar{N}(\beta y) dy$, and $\bar{N}(y) = \frac{1}{e^y - 1}$.

All the other mean relaxation times for a crystalline dielectric with cubic symmetry are derived as follows. The inverse relaxation time for the longitudinal phonon interacting with one longitudinal virtual phonon and

one transverse virtual phonon can be described by the relationship

$$\frac{1}{\tau_{llt}} = 3.9 \times 10^{-4} \tilde{\gamma}^2 \frac{c_l^7}{ac_s^6 g_1(\beta)} \times \left(\frac{\hbar}{\rho a^4 c_l} \right)^3 \frac{\lambda^2 (\lambda^2 - 1)}{(1 + 2\lambda^3)^2} \int_0^\pi \frac{\bar{N}(\beta y)}{y^4} dy \times \int_y^{\alpha y} (x-y)^2 \varphi_1(x, y) [\bar{N}(\beta(x-y)) - \bar{N}(\beta x)] dx, \tag{8}$$

where $\alpha = \frac{\lambda + 1}{\lambda - 1}$, $\lambda = c_l/c_t > 1$, $\Theta_D^* = \frac{\pi \hbar c_l}{a}$, $\Theta_D = \frac{\pi \hbar c_s}{a}$, and $c_s = \sqrt{\frac{3}{1 + 2\lambda^3}} c_l$ are the dimensionless parameters and the function has the form $\varphi_1(x, y) = y^4 [x^2 + y^2 - (x-y)^2 \lambda^2] [(x+y)^2 - \lambda^2(x-y)^2] + 6(\lambda^2 - 1)y^2(x-y)^2 [x^2 + y^2 - \lambda^2(x-y)^2]^2 + 36(x-y)^2 [(x+y)^2 - \lambda^2(x-y)^2]^3$. The inverse time of the relaxation process with the participation of the optical phonon is determined by the equality

$$\frac{1}{\tau_{loo}} = 0.04 \tilde{\gamma}^2 \frac{c_l^2}{ac_s g_1(\beta)} \left(\frac{\hbar}{\rho a^4 c_l} \right)^3 (1 + 2\lambda^3)^{2/3} \left(\frac{T}{\Theta_D} \right)^3 \times \exp\left(-\frac{2\Theta_D}{\pi T}\right) \int_0^\pi (1 - \exp(-\beta y)) \bar{N}(\beta y) y^2 dy \times \int_{x_H(y)}^\infty \sqrt{x} \exp(-x) \varphi_3(x, y) dx, \tag{9}$$

where the lower limit of integration is written as $x_H(y) = \frac{b}{4} \left(\beta y \frac{1}{b} \right)^2$, $b = \frac{3\pi}{4(1 + 2\lambda^3)^{2/3} \Theta_D} T$, and the function has

$$\text{the form } \varphi_3(x, t) = x^2 - xy\beta - \frac{20}{49} bx(\beta y)^2 + \frac{5}{49} (by\beta)^2 \left(\beta y + \frac{1}{b} \right)^2.$$

The inverse relaxation time for impurity scattering is represented by the formula

$$\frac{1}{\tau_{imp lt}} = c_l \tilde{B} \frac{c_l^6}{a\pi^4 c_s^5 g_1(\beta)} \int_0^\pi y^6 \bar{N}(\beta y) dy, \tag{10}$$

where c_i is the concentration of impurity atoms and $\tilde{B} = \frac{\pi^5}{18} \tilde{\gamma}^2 \lambda^5 \left(\frac{\Theta_D}{M c_l} \right)^2$. Here, $\tilde{\gamma}$ is the phenomenological dimensionless constant of the interaction between phonons and impurity atoms.

Finally, the last relaxation time is determined by the expression

Experimental parameters of dielectrics

Material	Symmetry group	Lattice constant, 10^{-8} cm	Number of atoms per unit cell	$A, 10^{-8}$ cm*	$\rho, \text{g/cm}^3$ [10]	$\bar{c}_l, 10^5$ cm/s [10]	$\bar{c}_t, 10^5$ cm/s [10]	$c_s, 10^5$ cm/s	λ^*	Θ_D, K	$C_{11111}, 10^{-12} \text{ cm}^3/\text{dyn}$ [15]	$ \bar{\gamma}_e , 10^{12} \text{ dyn/cm}^3$
C (diamond)	$m\bar{3}m$	3.57 [11]	8	1.785	3.51	18.1	12.1	13.22	1.5	1850 [10] 1860 [10] 2250 [10] 2196*	–	135
NaCl	$m\bar{3}m$	5.64 [11]	6	3.1	2.17	4.57	2.69	2.98	1.7	320 [10] 275 [10] 285*	–8.43	7
SiO ₂ (α -quartz)	32	$a, b = 4.913$ $c = 5.404$ [12]	9	2.438	2.65	5.96	4.44	4.77	1.34	580*	–2.1 –8.15 (C_{333333})	25

* Calculated from the data presented in the table.

$$\frac{1}{\tau_{lt}} = 5.9 \times 10^{-4} \bar{\gamma}^2 \frac{c_l^7}{ac_s^6 g_1(\beta)} \times \left(\frac{\hbar}{\rho a^4 c_l} \right)^3 \frac{\lambda^3 (\lambda^2 - 1)^2 \pi}{(1 + 2\lambda^3)^2} \int_0^\pi y^2 \bar{N}(\beta y) dy \quad (11)$$

$$\times \int_{B_1}^{B_2} \varphi_2(x, y) \left[1 + \bar{N}\left(\beta \frac{x}{\lambda}\right) + \bar{N}\left(\beta \left(y - \frac{x}{\lambda}\right)\right) \right] dx,$$

where the limits of integration with respect to x are written in the form $B_1 = \left(\frac{\lambda-1}{2}\right)y$ and $B_2 = \left(\frac{\lambda+1}{2}\right)y$ and the function $\varphi_2(x, y)$ is defined by the relationship

$$\varphi_2(x, y) = \left[\left(x - \frac{\lambda}{2}y\right)^2 - \left(\frac{y}{2}\right)^2 \right].$$

The mean relaxation time τ_3 can be estimated from the formula

$$\frac{1}{\tau_3} = \frac{2\delta}{L g_1^*} \int_0^{\Theta_D^*/T} \frac{1}{\tau_{lty}} y^4 \bar{N}(y) (1 + \bar{N}(y)) dy, \quad (12)$$

where $g_1^* = \int_0^{\Theta_D^*/T} y^4 \bar{N}(y) (1 + \bar{N}(y)) dy$ is the normalization function.

In the explicit form, we obtain

$$\frac{1}{\tau_3} = \frac{2\delta}{L g_1^*} \int_0^{\Theta_D^*/T} y^4 \bar{N}(y) (1 + \bar{N}(y)) dy \times \left\{ 0.12 \bar{\gamma}^2 \frac{c_l^2}{ac_s} \left(\frac{\hbar}{\rho a^4 c_l} \right)^3 \frac{\lambda^2 (\lambda^2 - 1) \left(\frac{T}{\Theta_D}\right)^5}{(1 + 2\lambda^3)^2} \right. \quad (13)$$

$$\left. \times \int_1^\alpha (x-1)^2 \varphi_1(x) [\bar{N}(y(x-1)) - \bar{N}(xy)] dx \right\}.$$

It should be noted that all the above expressions for the relaxation times were necessary for numerical calculations. The results of these calculations are presented in Fig. 2. The interested reader can verify the validity of the relationships between the relaxation times by way of numerical integration.

Before proceeding to the description of the thermal conductivity coefficient, a number of points regarding the parameter δ need to be made. By definition, the surface layer of the dielectric is the thermostat and its thickness is determined by the time of elastic relaxation of surface (but three-dimensional) phonons due to their scattering directly from the dielectric boundary. It can be seen from the numerical estimates of the relaxation times (Fig. 2) that, for diamond, the elastic relaxation time corresponds to the time $\tau_{lt}(T_0)$; i.e., the quantity δ should be less than $c_l \tau_{lt}(T_0)$. At $\tau_{lt} \sim 10^{-7}$ s, we obtain $\delta < 1.8 \times 10^6 \times 10^{-7} = 0.18$ cm. For samples with a linear size $L \cong 0.5$ cm, the small parameter relating the relaxation times τ_{lt} and τ_{lT} , according to relationships (1), is determined to be $\varepsilon = 2\delta/L = 0.72$. As model parameters (a, ρ, Θ_D , etc.) in our calculations, we used the reference experimental data presented in the table.

The calculations of the inverse relaxation times τ_3^{-1} (coinciding in order of magnitude with the inverse relaxation time τ_{lT}^{-1}) and τ_u^{-1} demonstrated that the interaction of longitudinal phonons with transverse phonons of the thermostat is dominant for samples with a size $L < L_0 = 3-10$ cm. However, for bulk samples ($L > L_0$) and in some regions in the $T-L$ plane (Fig. 3), the umklapp processes come into play.

It should also be noted that the temperature dependence of the thermal conductivity coefficient $\kappa(T)$ at any temperatures T , including the range to the right of the maximum, cannot be represented in analytical form, even though this dependence is of particular

interest. Nonetheless, the problem can be solved using the methods of numerical integration.

The analysis of the dependence $\kappa(T)$ will be started with the general expression for the tensor κ_{ij} , where $i, j = x, y, \text{ and } z$. Within the standard gas kinetic approximation [2], the tensor κ_{ij} can be represented in the following from:

$$\begin{aligned} \kappa_{ij} = & \int \hbar \omega_{lk} v_i v_j \frac{\partial \bar{N}_l(k)}{\partial T} \tau_{lk} \frac{d^3 k}{(2\pi)^3} \\ & + \int \hbar \omega_{tk} v_i v_j \frac{\partial \bar{N}_t(k)}{\partial T} \tau_{tk} \frac{d^3 k}{(2\pi)^3}, \end{aligned} \quad (14)$$

where $\omega_l(k) = c_l k$ is the phonon dispersion.

By averaging tensor (14) over the traveling directions of phonons and retaining the components corresponding to the fastest longitudinal relaxation process, we obtain

$$\bar{\kappa} = \xi \frac{\hbar c_l^2}{(2\pi)^3} \int \omega_l(k) \frac{\partial \bar{N}_l(k)}{\partial T} \tau_{lk} d^3 k, \quad (15)$$

where ξ^{-1} is the parameter defined by the relationship $\xi^{-1} = 3^{1/3}(1 + 2\lambda^3)^{2/3}$. In order not to overload the text, hereafter the bar over κ will be omitted.

Despite the simplicity of the derived formula, it can be used to analyze the temperature dependence of the thermal conductivity coefficient κ over the entire range of temperatures T . The problem is reduced to estimating the relaxation times τ_{lk} . It can be shown that the laws of conservation of energy and momentum allow only for the following four dissipative processes: (1) $b_{lk}^+ b_{tk_1}^+ b_{lk_2}$, (2) $b_{lk}^+ b_{tk_1} b_{tk_2}$, (3) $b_{lk}^+ b_{tk}$, and (4) $b_{lk}^+ b_{ok_1} b_{ok_2}$. In the case of process (1), the allowable magnitudes of the virtual wave vector are determined by the inequality $k_1 \geq \frac{c_l - c_t}{2c_l}$. For process (2), we have the inequality $\frac{k}{2} \left(\frac{c_l}{c_t} - 1 \right) \leq k_1 \leq \frac{k}{2} \left(\frac{c_l}{c_t} + 1 \right)$. For process (3), there are no restrictions. In the case of process (4), we can write the inequality $k_1 \geq \frac{1}{2} \left(\frac{c_l}{\beta} + k \right) k$, where β is derived from the mathematical definition of the spectrum of optical phonons $\omega_{ok} = \omega_o - \beta k^2$, which holds good for the long-wavelength approximation: $\omega_o \approx 2(c_s/a)$ and $\beta \approx ac_s/4$.

As a result, we found that the inverse relaxation time can be represented as the sum

$$\frac{1}{\tau_{lk}} = \frac{1}{\tau_{1lk}} + \frac{1}{\tau_{2lk}} + \frac{1}{\tau_{3lk}} + \frac{1}{\tau_{\text{imp}k}} + \frac{c_l}{L}. \quad (16)$$

In sum (16), the relaxation times are determined by the relationships

$$\begin{aligned} \frac{1}{\tau_{1lk}} = & \tilde{\gamma}_1 \frac{\Theta_D^2 \hbar a^3 \alpha k}{M^3 c_l^2 c_t^2} \int dk_1 [\bar{N}_{l(k_1-k)} - \bar{N}_{lk_1}] \\ & \times \{ k_1^2 A^2 [(k_1 - k)^2 \lambda^2 - (k_1 A - k)^2] \\ & + 6k_1^4 (1 - A)^2 + 36k_1^2 (1 - A^2) (k_1 A - k)^2 \}, \end{aligned} \quad (17)$$

$$\begin{aligned} \frac{1}{\tau_{2lk}} = & \tilde{\gamma}_2 \frac{\Theta_D^2 \hbar a^3}{M^3 c_l c_t^3} \\ & \times \int_{z_2 k}^{z_1 k} k_1^4 (1 - B^2) dk_1 [1 + \bar{N}_{tk_1} - \bar{N}(\omega_{lk} - \omega_{tk_1})], \end{aligned} \quad (18)$$

$$\begin{aligned} \frac{1}{\tau_{3lk}} = & \tilde{\gamma}_3 \frac{\Theta_D^2 \hbar a^3}{M^3 c_l \beta \omega_o^2} \int_{z_3}^{\infty} k_1 [\bar{N}_{ok_1} - \bar{N}_o(\omega_{lk} - \omega_{ok_1})] \\ & \times \left\{ k_1^4 - \frac{c_l}{\beta} k k_1^2 + \frac{6}{49} k^2 \left(\frac{c_l}{\beta} + k \right)^2 - \frac{20}{49} k^2 k_1^2 \right\} dk_1, \end{aligned} \quad (19)$$

$$\frac{1}{\tau_{\text{imp}k}} = \frac{\pi c_l \tilde{\gamma}_{\text{imp}} \Theta_D^2 a^3 \lambda^4 k^4}{18 M^2 c_l^2 c_t}, \quad (20)$$

where $\tilde{\gamma}_1 = \tilde{\gamma}^2 \frac{1}{39^2 \times 108\pi} = 1.94 \times 10^{-6} \tilde{\gamma}^2$, $A = \frac{k^2 + k_1^2 - \lambda^2 (k - k_1)^2}{2kk_1}$ (where $A \leq 1$), $\lambda = c_l/c_t \geq 1$, $\alpha = (\lambda + 1)/(\lambda - 1)$, $\tilde{\gamma}_2 = \tilde{\gamma}^2 \frac{49}{39^2 \times 108\pi} = 9.5 \times 10^{-5} \tilde{\gamma}^2$, $B = \frac{k(1 - \lambda^2) + 2k_1 \lambda}{2k_1}$, $z_1 = (\lambda - 1)/2$, $z_2 = (\lambda + 1)/2$, $z_3 = \frac{1}{2} \left(k + \frac{c_l}{\beta} \right)$, and $\tilde{\gamma}_3 = \tilde{\gamma}^2 \frac{49}{39^2 \times 32 \times 27} = 3.7 \times 10^{-5} \tilde{\gamma}^2$.

The relaxation time L/c_l accounts for the Knudsen scattering of longitudinal phonons from the sample boundaries. This relaxation time is predominantly responsible for the broadening of the maximum in the dependence $\kappa(T)$ and plays a significant role only at low temperatures.

With the use of formulas (16)–(20), the thermal conductivity coefficient κ (15) can be represented in the following compact form:

$$\begin{aligned} \kappa(T, \lambda, R) = & \frac{L}{a} \left(\frac{T}{\Theta_D} \right)^3 \frac{\pi}{2 \times 3^{1/3}} \frac{c_l}{a^2 (1 + 2\lambda^3)^{2/3}} \\ & \times \int_0^{\Theta_D^*/T} \frac{y^4 \bar{N}_y (1 + \bar{N}_y)}{1 + F(y)} dy, \end{aligned} \quad (21)$$

where $\Theta_D^* = \Theta_D \left(\frac{3}{1 + 2\lambda^3} \right)^{1/3}$ and the function in the denominator is the sum $F(y) = F_1(y) + F_2(y) + F_3(y) + F_{\text{imp}}(y)$. The functions entering into this sum are given in the Appendix.

Numerical integration of expression (21) with allowance made for formulas (A1)–(A4) was carried out using methods that have been widely covered in the literature (see, for example, [5–7]), and, hence, we will not dwell on their description. We note only that, as the parameters, we used the experimental data presented in the table (it was assumed that $c_l = \bar{c}_l$). The effective constant $\bar{\gamma}$ was chosen so that the results of numerical integration would be consistent with the experimental data. The last column of the table lists the dimensional constants $\bar{\gamma}_e$ related to the effective constant $\bar{\gamma}$ through the simple expression $\bar{\gamma}_e = \bar{\gamma} \Theta_D / a^3$ (the dimensional constant $\bar{\gamma}_e$ is given for diamonds of the *IIa* type). Since relationships (A1)–(A4) include the quantity $\bar{\gamma}^2$, the dimensional constant $\bar{\gamma}_e$ can be determined only in magnitude. The constant γ_{imp} is taken equal to 10^2 . However, there arises a problem with the choice of the Debye temperature. The point is that, according to different publications (and sometimes even in the same publication), the Debye temperature Θ_D for the same material has different values (the difference can be as much as 20%; see table). In our calculations for the diamond and NaCl, we used the Debye temperatures taken from [8]: $\Theta_D = 2250$ K for the diamond and $\Theta_D = 275$ K for NaCl. These data are in best agreement with the Debye temperatures determined from the relationship $\Theta_D = \hbar c_s (6\pi^2 N/V)^{1/3}$. Since the value of Θ_D for quartz is not given in [8], we used the Debye temperature calculated from the above formula and the experimental data presented in the table ($\Theta_D = 580$ K for quartz). Note that, in our case, the difference in the Debye temperatures for the same material leads to an insignificant change in the dependence $\kappa(T)$. The experimental data on the thermal conductivity were obtained for samples of the following sizes: ≈ 0.5 cm for the diamond and NaCl (in the calculation, the value of L was taken equal to 0.5 cm) and $0.5 \times 0.5 \times 4$ cm for quartz (the thermal conductivity coefficient κ was measured along the C axis, and, hence, the size was taken to be $L = 4$ cm).

As can be seen from Figs. 4 and 5, the results of numerical integration of the theoretical expression derived for the thermal conductivity coefficient of dielectrics are in good agreement with the experimental data. It should be noted that, in this case, the contribution of impurity scattering cannot be ignored even for the purest diamond of the *IIa* type (Fig. 4a), because perfect diamond crystals do not occur in nature and, moreover, synthetic (artificial) diamonds contain even a greater amount of defects than natural diamonds. In the

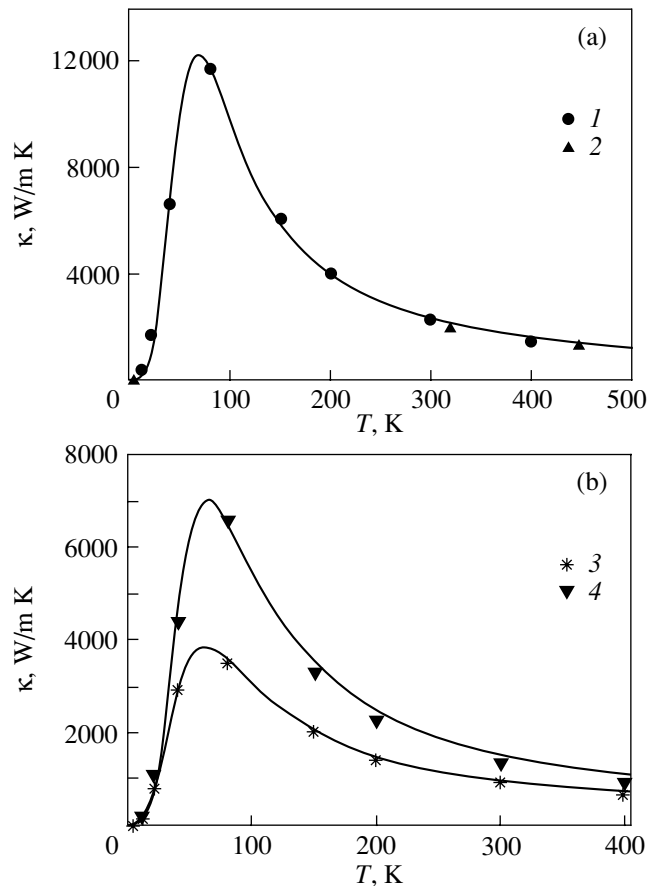


Fig. 4. Temperature dependences of the thermal conductivity coefficient for diamonds of the (a) (1, 2) *IIa*, (b) (3) *I*, and (4) *IIb* types. Points are the experimental data taken from (1, 3, 4) [10] and (2) [13]. Solid lines represent the results of theoretical calculations.

calculation performed for diamonds of the *IIa* type with the aforementioned integration parameters, we obtained the dimensional constant $\bar{\gamma}_e \approx 1.35 \times 10^{14}$ erg/cm³ and the concentration $c_i \approx 3 \times 10^{-6}$, which corresponds to an impurity concentration of the order of 5×10^{17} cm⁻³. Here, it should be specially emphasized that, first, a change in the value of γ_{imp} would lead to a change in the concentration of impurity atoms c_i and, second, an impurity concentration of 10^{17} cm⁻³ is not too high for diamonds. According to Plotnikova [9], in the purest diamonds (*IIa* type), the concentration of only nitrogen in the *A* form is less than 10^{18} cm⁻³. Furthermore, up to 50 types of different defects (including impurity and intrinsic point defects) are revealed in diamonds. However, to the best of our knowledge, only averaged data, as a rule, are available in the literature. In this respect, it is more difficult to compare the theoretical and experimental data for diamonds of the *I* and *IIb* types (Fig. 4b), because some diamonds of the *IIb* type exhibit semiconductor properties [9, 10] and diamonds of the *I* type are usually divided into subclasses

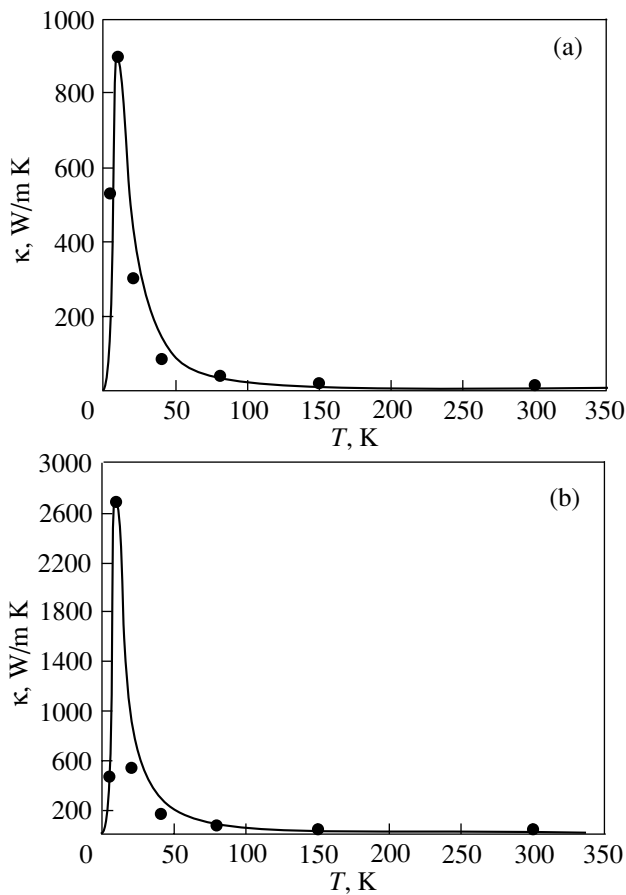


Fig. 5. Temperature dependences of the thermal conductivity coefficient for (a) NaCl and (b) SiO₂. Points are the experimental data taken from [10]. Solid lines represent the results of theoretical calculations.

depending on the type and amount of defects and impurities [9]. There are also diamonds in which the impurity concentration is higher than 10^{20} cm^{-3} . Moreover, an increase in the impurity concentration to high values should result in a change in the density, acoustic velocity, and other parameters of the material, which, in turn, can substantially change the dependence $\kappa(T)$. With the aim of simplifying our calculations and making allowance for the fact that the experimental data are averaged, all the integration parameters for diamonds of the *I* and *I**b*** types were taken to be constant (as was the case with diamonds of the *I**a*** type) and only the quantities $\bar{\gamma}$ and c_i were varied in computations. The results of the calculations are as follows: $\bar{\gamma}_e \approx 1.7 \times 10^{14} \text{ erg/cm}^3$ and $c_i \approx 1.5 \times 10^{-5}$ for diamonds of the *I**b*** type and $\bar{\gamma}_e \approx 2 \times 10^{14} \text{ erg/cm}^3$ and $c_i \approx 6 \times 10^{-5}$ for diamonds of the *I* type.

In the numerical experiment for NaCl and SiO₂, we took into account the mechanism of scattering of acoustic phonons by optical phonons. However, the impurity concentration in these compounds was assumed to be

negligible ($c_i = 0$), because grown crystals of NaCl and SiO₂, as a rule, are of sufficiently high quality. From analyzing the temperature dependences of the thermal conductivity coefficient $\kappa(T)$ presented in Fig. 5, we can draw the evident conclusion that, although NaCl is an ionic crystal and quartz is a piezoelectric crystal, the main contribution to the dependences $\kappa(T)$ for these crystals, as for diamonds, is made by the phonon relaxation mechanism. This mechanism is associated with the retardation of bulk phonons (traveling with drag velocity \mathbf{V}) by immobile thermalized phonons in the boundary layer δ . In this case, optical phonons play a very important role. As regards the dimensional constant $\bar{\gamma}_e$ for quartz, we assume that its value should differ from those for NaCl and diamonds. This can be explained by the fact that α -quartz belongs to the symmetry group 32, for which the tensor γ_{iklmnp} has not six but fourteen independent components.

It turned out that an increase in the impurity concentration leads to a drastic decrease in the thermal conductivity coefficient. This theoretical result is in agreement with the experimental data. The dependence $\kappa(T)$ becomes flatter, and the maximum of the thermal conductivity coefficient shifts toward the high-temperature range. This means that, in principle, there can occur a situation where the thermal conductivity coefficient $\kappa(T)$ will not reach its maximum up to the temperature of the phase transition (for example, melting). A similar dependence has been observed for a number of glasses [10] (see also [11–15]). The dependence $\kappa(T)$ for glasses has defied explanation in such a simple way, because relationship (21) for highly defective and non-crystalline materials provides a means for evaluating only the qualitative behavior of the thermal conductivity coefficient, even though the general tendency is quite clear.

Figure 6 illustrates how the effective interaction constant affects the thermal conductivity coefficient. Curves 1 and 3 are plotted for the effective interaction constants $\bar{\gamma}_e = 1.5 \times 10^{14} \text{ erg/cm}^3$ and $\bar{\gamma}_e = 3.5 \times 10^{14} \text{ erg/cm}^3$, respectively. An increase in the effective constant $\bar{\gamma}_e$ leads to a decrease in the thermal conductivity coefficient κ and a shift of the maximum in the dependence $\kappa(T)$ toward the low-temperature range. The rate of change in $\kappa(\bar{\gamma}_e)$ indicates that the nonlinear interaction constant has a profound effect on the maxima of the thermal conductivity coefficient. The positions of these maxima virtually coincide for the diamond, NaCl, and quartz (Fig. 7). The positions of the extrema in the dependences shown in Fig. 7 are as follows: $\lambda \approx 1.35$ for extremum *a*, $\lambda \approx 3.25$ for extremum *b*, $\lambda \approx 1.65$ for extremum *c*, and $\lambda \approx 7.8$ for extremum *d*. It is of interest to note that, according to the experimental data taken from [10], the parameters λ for crystalline and vitreous dielectrics, for the most part, fall in the range 1.34–3.10.

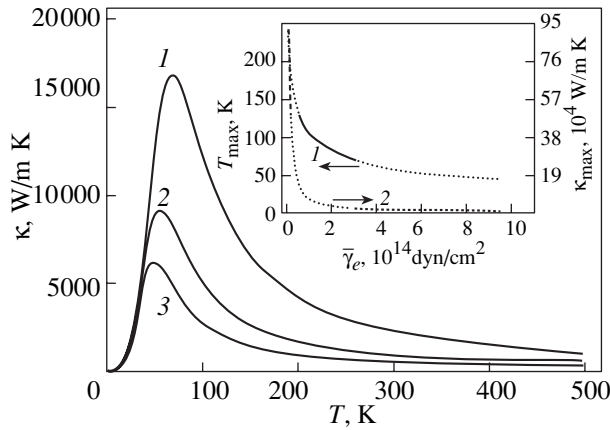


Fig. 6. Dependences $\kappa(T)$ for different nonlinear interaction constants (1) $\tilde{\gamma}_{e1} < (2) \tilde{\gamma}_{e2} < (3) \tilde{\gamma}_{e3}$. The inset shows the dependences of (1) the temperature T_{\max} and (2) the height κ_{\max} of the maximum in the dependence $\kappa(T)$ on the nonlinear interaction constant $\tilde{\gamma}_e$.

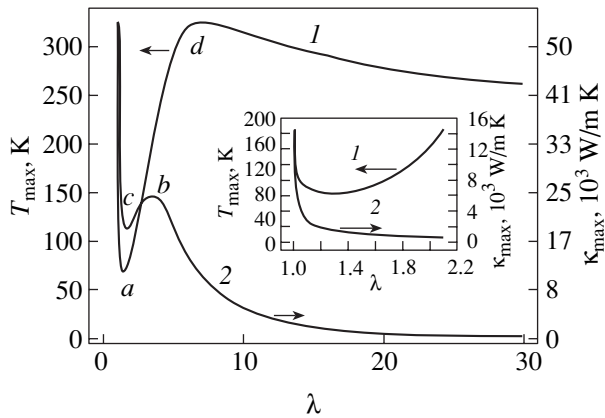


Fig. 7. Dependences of (1) the temperature T_{\max} and (2) the height κ_{\max} of the maximum in the dependence $\kappa(T)$ on the ratio λ of the longitudinal acoustic velocity to the transverse acoustic velocity. The inset shows the same dependences on a reduced scale (1 : 10). Letters *a*, *b*, *c*, and *d* indicate the extreme points observed in the dependences depicted on an enlarged scale.

3. CONCLUSIONS

Thus, the main results obtained in this study can be summarized as follows.

(1) The problem concerning the role of surface phonons of a thermostat in the theory of internal microscopic relaxation in crystalline dielectrics was correctly formulated for the first time.

(2) The relaxation theory was constructed with allowance made for the interaction of four main subsystems: (i) the subsystem of longitudinal acoustic phonons, (ii) the subsystem of transverse acoustic phonons, (iii) the subsystem of optical phonons, and (iv) the subsystem of thermalized surface phonons. An

exact relationship between the relaxation times was obtained by numerical integration. Within strictly analytical approaches, it would be impossible to derive this relationship and, hence, to elucidate the hierarchy of relaxation times.

(3) In the framework of the relaxation theory constructed in this work, it became possible to describe exactly the thermal conductivity coefficient with inclusion of only the most important mechanisms of interactions.

(4) The exact theoretical dependences $\kappa(T)$ for a number of crystalline dielectrics (diamond, NaCl, SiO₂) were determined using numerical integration. Satisfactory explanations were offered for the numerous available experimental data over the entire range of temperatures, except for the range of ultralow temperatures. Analysis of the above dependences in this temperature range will be the subject of a separate study.

(5) The dependences $\kappa(T)$ were constructed using only the experimentally determined parameters. Our analysis did not include adjustable parameters, except for the constant of nonlinear phonon interaction and the width δ of the contact region. Since the sample size L was small, the quantities δ and L were of the same order of magnitude; hence, the parameter δ/L was not involved in the final relationships (see the above estimates). The constant of nonlinear phonon interaction was estimated at 10^{13} erg/cm³ from the best fitting to the experimental data.

It should also be noted that examination of the region of contact with a thermostat and the temperature dependence $\delta(T)$ is an important problem from both the theoretical and experimental standpoints.

ACKNOWLEDGMENTS

We would like to thank A.S. Sigov for helpful remarks.

APPENDIX

Expression (21) involves the functions $F_1(y)$, $F_2(y)$, $F_3(y)$, and $F_{\text{imp}}(y)$. The function $F_1(y)$ has the form

$$F_1(y) = \tilde{\gamma}_1^* \frac{L}{a} \left(\frac{\hbar}{\rho a^4 c_l} \right)^3 \frac{\lambda^2 (\lambda^2 - 1)}{(1 + 2\lambda^3)^2} y^5 \left(\frac{T}{\Theta_D} \right)^5 \left(\frac{c_l}{c_s} \right) \times \int_1^\alpha (x-1)^2 \varphi_1(x) [\bar{N}(y(x-1)) - \bar{N}(xy)] dx, \quad (\text{A1})$$

where $\tilde{\gamma}_1^* = \frac{3\pi\tilde{\gamma}^2}{39^2 \times 16} = 0.12\tilde{\gamma}^2$ is the nonlinear interaction constant and the function $\varphi_1(x)$ is defined by the relationship

$$\begin{aligned} \varphi_1(x) = & [x^2 + 1(x-1)^2\lambda^2][(x+1)^2 - \lambda^2(x-1)^2] \\ & + 6(x-1)^2(\lambda^2 - 1)[x^2 + 1 - \lambda^2(x-1)^2]^2 \\ & + 36(x-1)^2[(x+1)^2 - \lambda^2(x-1)^2]^3. \end{aligned}$$

The function $F_2(y)$ is represented in the form

$$\begin{aligned} F_2(y) = & \tilde{\gamma}_2^* \frac{L}{a} \left(\frac{\hbar}{\rho a^4 c_l} \right)^3 \frac{\lambda^3 (\lambda^2 - 1)^2}{(1 + \lambda^3)^2} y^5 \left(\frac{T}{\Theta_D} \right)^5 \left(\frac{c_l}{c_s} \right) \\ & \times \int_{z_1}^{z_2} \varphi_2(x) \left[1 + \bar{N} \left(\frac{xy}{\lambda} \right) - \bar{N} \left(y \left(1 - \frac{x}{\lambda} \right) \right) \right] dx, \end{aligned} \quad (\text{A2})$$

where $\tilde{\gamma}_2^* = \frac{49}{32} \tilde{\gamma}_1^*$, $\varphi_2(x) = \left(x - \frac{\lambda+1}{2} \right)^2 \left(x - \frac{\lambda-1}{2} \right)^2$, and z_1 and z_2 are the same as in expression (16). By using the expression $F_3(y) = (L/c_s)(1/\tau_{3k})$ and taking into account relationship (12) and the dispersion of optical phonons at $T < \Theta_D$, we obtain

$$\begin{aligned} F_3(y) \cong & \tilde{\gamma}_3^* \frac{L}{a} \left(\frac{\hbar}{\rho a^4 c_l} \right)^3 (1 + 2\lambda^3)^{2/3} \left(\frac{T}{\Theta_D} \right)^3 \\ & \times (1 - \exp(-y)) \exp \left(-\frac{2\Theta_D}{\pi T} \right) \left(\frac{c_l}{c_s} \right) \\ & \times \int_{x_H(y)}^{\infty} \varphi_3(x) \sqrt{x} \exp(-x) dx. \end{aligned} \quad (\text{A3})$$

Here, the lower limit of integration is written as $x_H(y) = \frac{f}{4} \left(y + \frac{1}{f} \right)^2$ and the function $\varphi_3(x, y)$ has the form

$$\begin{aligned} \varphi_3(x, y) = & x^2 - xy - \frac{20}{49} fxy^2 + \frac{5}{49} (fy)^2 \left(y + \frac{1}{f} \right)^2, \\ f = & \frac{3\pi}{4(1 + 2\lambda^2)} \frac{T}{\Theta_D}, \quad \tilde{\gamma}_3^* = \frac{49\pi^4 \tilde{\gamma}^2}{81 \times 39^2} = 0.04\tilde{\gamma}^2. \end{aligned}$$

The function $F_{\text{imp}}(y)$ is given by the formula

$$F_{\text{imp}}(y) = c_i B_i y^4 \left(\frac{T}{\Theta_D} \right)^4 \left(\frac{c_l}{c_s} \right), \quad (\text{A4})$$

where $B_i = \frac{\pi L}{18a} \lambda^5 \left(\frac{\tilde{\gamma}_{\text{imp}} \Theta_D}{M c_l^2} \right)^2$.

REFERENCES

1. A. I. Akhiezer, V. G. Bar'yakhtar, and S. V. Peletminskii, *Spin Waves* (Nauka, Moscow, 1967; North-Holland, Amsterdam, 1968).
2. V. L. Gurevich, *Kinetics of Photon Systems* (Nauka, Moscow, 1980).
3. S. O. Gladkov, *Fiz. Tverd. Tela (Leningrad)* **23** (9), 2686 (1981) [*Sov. Phys. Solid State* **23**, 1575 (1981)].
4. S. O. Gladkov, *Zh. Éksp. Teor. Fiz.* **83**, 806 (1982) [*Sov. Phys. JETP* **56**, 452 (1982)].
5. G. M. Fikhtengol'ts, *Course of Differential and Integral Calculus*, 6th ed. (Nauka, Moscow, 1966), Vol. 2.
6. L. Z. Rumshinskii, *Mathematical Processing of Experimental Results* (Nauka, Moscow, 1971).
7. R. P. Fedorenko, *Introduction to Computational Physics* (Mosk. Fiz.-Tekh. Inst., Moscow, 1994).
8. *Handbook of Physical Quantities*, Ed. by I. S. Grigor'ev and E. Z. Meilikhov (Énergoatomizdat, Moscow, 1991).
9. S. P. Plotnikova, in *Diamond in Electronic Engineering* (Énergoatomizdat, Moscow, 1990), p. 156.
10. *Physical Encyclopedia*, Ed. by A. M. Prokhorov (Sovetskaya Éntsiklopediya, Moscow, 1983).
11. M. P. Shaskol'skaya, *Crystallography* (Vysshaya Shkola, Moscow, 1976).
12. *Minerals: Handbook* (Nauka, Moscow, 1965), Vol. 2, No. 2, p. 136.
13. V. I. Nepsha and Yu. A. Klyuev, in *Diamond in Electronic Engineering* (Énergoatomizdat, Moscow, 1990), p. 140.
14. N. V. Novikov and A. G. Gontar', in *Diamond in Electronic Engineering* (Énergoatomizdat, Moscow, 1990), p. 57.
15. Yu. I. Sirotin and M. P. Shaskol'skaya, *Principles of Crystal Physics* (Nauka, Moscow, 1975).

Translated by O. Borovik-Romanova

**MAGNETISM
AND FERROELECTRICITY**

Effect of Isovalent Doping of Manganite $(\text{La}_{1-x}\text{Pr}_x)_{0.7}\text{Ca}_{0.3}\text{MnO}_3$ Films ($0 \leq x \leq 1$) on Their Optical, Magneto-optical, and Transport Properties near the Metal–Insulator Transition

Yu. P. Sukhorukov*, N. N. Loshkareva*, E. A. Gan'shina, A. R. Kaul'**, O. Yu. Gorbenko**,
E. V. Mostovshchikova*, A. V. Telegin*, A. N. Vinogradov**, and I. K. Rodin****

**Institute of Metal Physics, Ural Division, Russian Academy of Sciences,
ul. S. Kovalevskoi 18, Yekaterinburg, 620219 Russia*

e-mail: suhorukov@imp.uran.ru

***Faculty of Physics, Moscow State University, Vorob'evy gory, Moscow, 119899 Russia*

Received October 28, 2003

Abstract—The optical, magneto-optical, and electric properties of epitaxial $(\text{La}_{1-x}\text{Pr}_x)_{0.7}\text{Ca}_{0.3}\text{MnO}_3$ films ($0 \leq x \leq 1$) grown by MOCVD on LaAlO_3 and SrTiO_3 substrates were studied. It is shown that the decrease in the average cation radius resulting from isovalent substitution of the Pr for La ions brings about a lowering of the Curie temperature, the metal–insulator transition temperature, and the temperatures of the maxima in magnetotransmission (MT) and magnetoresistance (MR). These temperatures depend only weakly on the substrate type. Substitution of La by Pr does not change the shape of the spectral response of the transverse Kerr effect. For concentrations $x \leq 0.50$, the maximum values of the Kerr effect and of the MT vary insignificantly, which should be assigned to the existence of a singly connected ferromagnetic metallic region at low temperatures. In films with $x = 0.75$, the presence of ferromagnetic metallic drops in an antiferromagnetic insulating matrix was revealed. The totality of the experimental data obtained suggest that nanoscopic magnetic and electronic non-uniformities exist both in films with a singly connected metallic region and in an $x = 1$ film, which is an antiferromagnetic insulator. © 2004 MAIK “Nauka/Interperiodica”.

1. INTRODUCTION

The phenomena of colossal magnetoresistance (MR) and giant magnetotransmission (MT) observed in lanthanum manganites with perovskite structure offer a broad potential for these materials in designing new recording media, electromagnetic radiation sensors [1], and IR optoelectronic devices controlled by magnetic or thermal fields [2]. These phenomena are related to the metal–insulator (MI) transition observed to occur near the Curie temperature and can be used to gain valuable information in studies on nonuniform charge distributions in manganites [3]. Deviations from stoichiometry [3] and nonisovalent doping of the antiferromagnetic dielectric LaMnO_3 by Ca^{2+} and Sr^{2+} ions bring about an increase in the volume of the ferromagnetic phase, the Curie temperature (T_C), and the metal–insulator transition temperature (T_{MI}). The actual variations in the magnetic and electric properties of the manganites depend on the vacancy concentration and doping level, i.e., on the $\text{Mn}^{4+}/\text{Mn}^{3+}$ ion concentration ratio.

Isovalent doping also noticeably affects the Curie temperature and the fractional volumes of the ferromagnetic (FM) and antiferromagnetic (AFM) phases. Indeed, substitution of Pr^{3+} for La^{3+} in an optimally doped manganite $\text{La}_{0.7}\text{Ca}_{0.3}\text{MnO}_3$ initiates transition from the FM metallic to the AFM insulating state [4].

In this system, $(\text{La}_{1-x}\text{Pr}_x)_{0.7}\text{Ca}_{0.3}\text{MnO}_3$ ($0 \leq x \leq 1$), an increase in the praseodymium concentration reduces the Mn–O–Mn valence angles because the ionic radius of Pr^{3+} is smaller than that of La^{3+} , while the $\text{Mn}^{4+}/\text{Mn}^{3+}$ ratio remains unchanged [5]. The phase diagram constructed from neutron diffraction data [4] defines the concentration region $x < 0.6$ as the region of existence of a uniform FM metal, while the region $x > 0.8$ is identified with a uniform insulator with a canted AFM structure. Within the concentration interval $0.6 \leq x \leq 0.8$, a macroscopically nonuniform magnetic state prevails, which is essentially a mixture of the FM and AFM phases.

The present study dealt primarily with the effect of Pr doping on the magnetic and electronic subsystems of epitaxial $(\text{La}_{1-x}\text{Pr}_x)_{0.7}\text{Ca}_{0.3}\text{MnO}_3$ films ($0 \leq x \leq 1$) and with the effect of the substrate on the magnetoresistance and magnetotransmission of films. This study is based on an integrated approach combining electrical, optical, and magneto-optical measurements. The first of them yield volume-averaged characteristics of the material, the second permit isolation of the contribution from regions with enhanced conductivity to light absorption, and magneto-optical measurements offer information concerning the magnetic subsystem.

Reduced lattice parameters a' , b' , c' and average unit cell volume $(a'b'c')^{1/3}$ of films, maximum values of the MT at $\lambda = 6.7 \mu\text{m}$ and of the MR in a magnetic field of 8 kOe, effective Curie temperature T_C^* , and temperatures of the maxima in MT and MR of films of various composition grown on LaAlO_3 (LAO), SrTiO_3 (STO), and $\text{Zr}_{0.85}\text{Y}_{0.15}\text{O}_{1.925}$ (ZYO) single crystal substrates

Film/substrate	a' , b' , Å	c' , Å	$(a'b'c')^{1/3}$, Å	MT, %	MR, %	T_C^* , K	$T_{\text{MT}}^{\text{max}}$, K	$T_{\text{MR}}^{\text{max}}$, K
$\text{La}_{0.7}\text{Ca}_{0.3}\text{MnO}_3/\text{LAO}$	3.862	3.872	3.865 ± 1	26	44	273	249	250
$\text{La}_{0.7}\text{Ca}_{0.3}\text{MnO}_3/\text{STO}$	3.868	3.859	3.865 ± 2	25	33	259	259	255
$(\text{La}_{0.75}\text{Pr}_{0.25})_{0.7}\text{Ca}_{0.3}\text{MnO}_3/\text{LAO}$	3.856	3.869	3.860 ± 1	30	68	211	213	211
$(\text{La}_{0.75}\text{Pr}_{0.25})_{0.7}\text{Ca}_{0.3}\text{MnO}_3/\text{STO}$	3.864	3.855	3.861 ± 2	25	45	214	215	214
$(\text{La}_{0.75}\text{Pr}_{0.25})_{0.7}\text{Ca}_{0.3}\text{MnO}_3/\text{ZYO}$	3.864	3.858	3.861 ± 1	25	19	211	211	211
$(\text{La}_{0.5}\text{Pr}_{0.5})_{0.7}\text{Ca}_{0.3}\text{MnO}_3/\text{LAO}$	3.848	3.869	3.855 ± 1	26	65	176	176	175
$(\text{La}_{0.5}\text{Pr}_{0.5})_{0.7}\text{Ca}_{0.3}\text{MnO}_3/\text{STO}$	3.861	3.848	3.856 ± 1	23	60	179	180	177
$(\text{La}_{0.25}\text{Pr}_{0.75})_{0.7}\text{Ca}_{0.3}\text{MnO}_3/\text{LAO}$	3.841	3.866	3.850 ± 2	4	21	79	103	<95
$(\text{La}_{0.25}\text{Pr}_{0.75})_{0.7}\text{Ca}_{0.3}\text{MnO}_3/\text{STO}$	3.858	3.835	3.850 ± 1	4		85	108	<95
$\text{Pr}_{0.7}\text{Ca}_{0.3}\text{MnO}_3/\text{LAO}$	3.839	3.858	3.845 ± 2					
$\text{Pr}_{0.7}\text{Ca}_{0.3}\text{MnO}_3/\text{STO}$	3.852	3.835	3.846 ± 2					
Unannealed								
$(\text{La}_{0.25}\text{Pr}_{0.75})_{0.7}\text{Ca}_{0.3}\text{MnO}_3/\text{LAO}$	3.841	3.867	3.850 ± 2	10	45	97	120	115
$(\text{La}_{0.25}\text{Pr}_{0.75})_{0.7}\text{Ca}_{0.3}\text{MnO}_3/\text{STO}$	3.860	3.834	3.851 ± 1	2	40	97	120	137

2. SAMPLES AND EXPERIMENTAL CONDITIONS

$(\text{La}_{1-x}\text{Pr}_x)_{0.7}\text{Ca}_{0.3}\text{MnO}_3$ (LPC) epitaxial films ($x = 0, 0.25, 0.5, 0.75, 1$) 300 nm thick were MOCVD grown on single crystal, (001)-oriented perovskite SrTiO_3 (STO) and LaAlO_3 (LAO) substrates at a substrate temperature of 750°C and a partial oxygen pressure $P = 0.003$ atm. The film with $x = 0.25$ was grown on a fluorite-structure $\text{Zr}_{0.85}\text{Y}_{0.15}\text{O}_{1.925}$ (ZYO) substrate. The film thickness was the same because of the equal reagent supply rates under diffusive deposition. To obtain homogeneous oxygen stoichiometry, the films were annealed for an hour in an oxygen flow under atmospheric pressure at a temperature of 750°C. In order to elucidate the part played by annealing in the formation of the properties of films close in composition to the percolation threshold, the characteristics of unannealed films with $x = 0.75$ grown on LAO and STO substrates were additionally studied. The table contains the reduced lattice parameters (a' , b' , c') and the pseudocubic perovskite parameter $(a'b'c')^{1/3}$ of films grown on STO substrates (cubic structure, $a = 3.903$ Å), pseudocubic LAO substrates ($a = 3.788$ Å), and, for the $x = 0.25$ composition, on ZYO substrates (cubic structure, $a = 5.14$ Å, which corresponds to the perovskite cube face diagonal, $a/(2)^{1/2}$). The orientation of the films relative to the substrates was derived from x-ray diffraction measurements and is (001)[100]STO || (001)[100]LPC, (001)[100]LAO || (001)[100]LPC, and (001)[110]ZYO || 010[111]LPC. The reduced parameters are related to the parameters of the orthorhombic cell (a , b , c) as follows: $c' = c/2$, $(a' + b')/2 = (a + b)/(2 \times$

$2^{1/2})$ for films on STO; $(a' + b')/2 = (a + b)/(4 \times 2^{1/2}) + c/4$, $c' = (a + b)/2 \times 2^{1/2}$ for films on LAO; and $c' = (a + b)/2 \times 2^{1/2}$, $(a' + b') = (a + b)/(4 \times 2^{1/2}) + c/4$ for the film on ZYO. The fact that the values of a , b , c for films on different substrates are different indicates the existence of residual strains between the film and the substrate; these strains are elastic, because the average volume of the perovskite cube $(a'b'c')^{1/3}$ in films grown on different substrates is practically the same (see table). Annealing in oxygen relieves strains in the films and, possibly, slightly changes the oxygen stoichiometry. The film preparation conditions are described in [6], where one can also find x-ray diffraction, Raman spectroscopy, and electron microscopy data indicating the structural and chemical homogeneity of the samples. As a reference in the determination of the chemical composition of the films, a ceramic of identical composition was used.

The transverse Kerr effect (TKE) was measured in the energy range 1.0–3.8 eV and the temperature interval 20–300 K for in-plane magnetic fields of up to 3.5 kOe. The relative change in the reflected light intensity $\delta = [I_H - I_0]/I_0$ was determined experimentally, where I_H and I_0 are the reflected light intensities with and without the magnetic field applied, respectively. The technique employed to measure the TKE is described in some detail in [7]. The electrical resistivity of the films was measured by the two-probe method in the temperature interval 77–300 K under magnetic fields of up to 10 kOe directed perpendicular to the current and along or perpendicular to the film plane. Silver

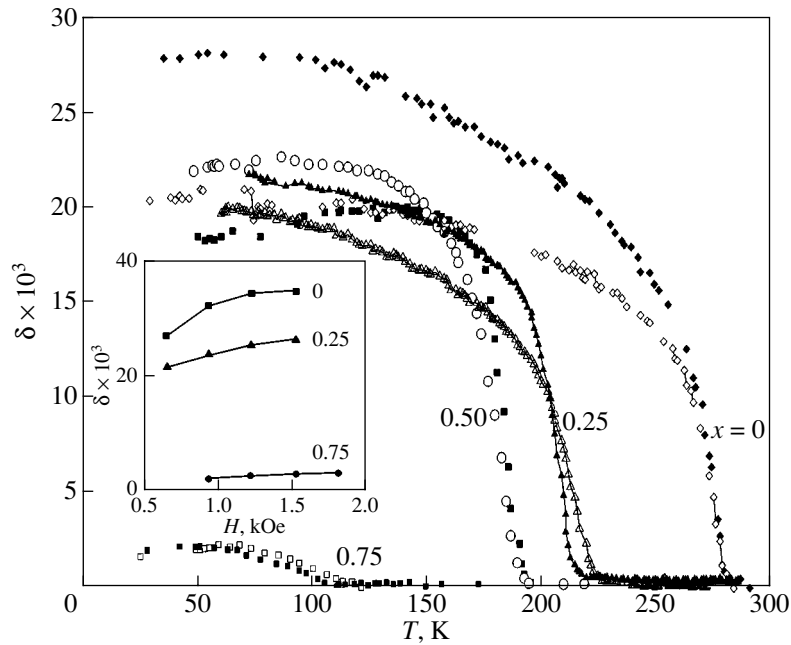


Fig. 1. Temperature dependences of the TKE of $(\text{La}_{1-x}\text{Pr}_x)_{0.7}\text{Ca}_{0.3}\text{MnO}_3$ films ($0 \leq x \leq 0.75$) grown on STO (open symbols) and LAO (filled symbols) obtained at an energy of 2.8 eV in a magnetic field of 380 Oe. Inset shows field dependences of the TKE measured at 2.8 eV and 77 K on LAO-grown films with different Pr concentrations.

contacts were ultrasonically applied to the films with indium-based solder.

The absorption spectra of films in the energy range 0.1–1.4 eV were studied with a high-sensitive IR spectrometer in the temperature interval 80–295 K and magnetic fields of up to 8 kOe directed both along the film plane and perpendicular to it. The TKE, light intensity transmitted through the film, MT, electrical resistivity, and MR were measured as a function of temperature in the heating mode at a rate of $\sim 1\text{--}3$ K/min in the temperature range 77–295 K. The field dependences of the MT and MR were measured at the temperatures of their maximum values in fields of up to 10 kOe.

3. EXPERIMENTAL RESULTS

3.1. The Kerr Effect

Figure 1 displays the temperature dependences of the TKE taken at an energy of 2.8 eV in a magnetic field of 380 Oe. Increasing the Pr concentration results in a decrease in the ferromagnetic ordering temperature T_C^* (see table). The effective Curie temperature T_C^* was determined as the point of the minimum of derivative $d(\delta)/dT$, because $\delta(T)$ reflects the temperature dependence of the magnetization. The effective Curie temperatures found in this way turn out to be slightly higher in the films grown on STO substrates than in the films grown on LAO and ZYO. The temperature dependences of the TKE obtained in the cooling–heating mode exhibit hysteretic behavior for all films. The

actual pattern of the hysteresis and its sign and width depend on the Pr concentration, film microstructure, and the kind of substrate used [8, 9]. This behavior may indicate that the transition to a magnetically ordered state in the LPC system is a first-order transition.

The spectral dependences of the TKE obtained in the low-temperature domain, i.e., after the transition to a metallic state, were similar for all films and mimicked the spectra measured on ceramic samples [10]. The magneto-optical activity of the manganites was shown [11] to originate from the transitions in the Mn^{3+} and Mn^{4+} octahedral complexes, which are responsible for the unique properties of these oxides. Substitution of Pr for La leads to rotation and tilting of the $[\text{MnO}_6]^{9-}$ octahedra rather than to their deformation and does not change the $\text{Mn}^{4+}/\text{Mn}^{3+}$ ratio, which correlates with the isovalent doping of the manganite. The magnitude of the TKE decreases strongly in annealed and unannealed samples with $x = 0.75$. The magnitude of the effect and the pattern of the TKE spectral response are different for unannealed films grown on different substrates (Fig. 2). All samples with $x = 0.75$ exhibited an inverse temperature hysteresis; in other words, the effect was smaller under cooling.

The field dependence of the TKE measured on films with $x \leq 0.5$ at 77 K shows saturation in weak fields of ~ 1.2 kOe, a feature characteristic of ferromagnets (see, e.g., inset to Fig. 1 for films with $x = 0$ and 0.25 grown on LAO). The nearly linear $\delta(H)$ relation obtained on the film with $x = 0.75$ attests to a predominantly AFM

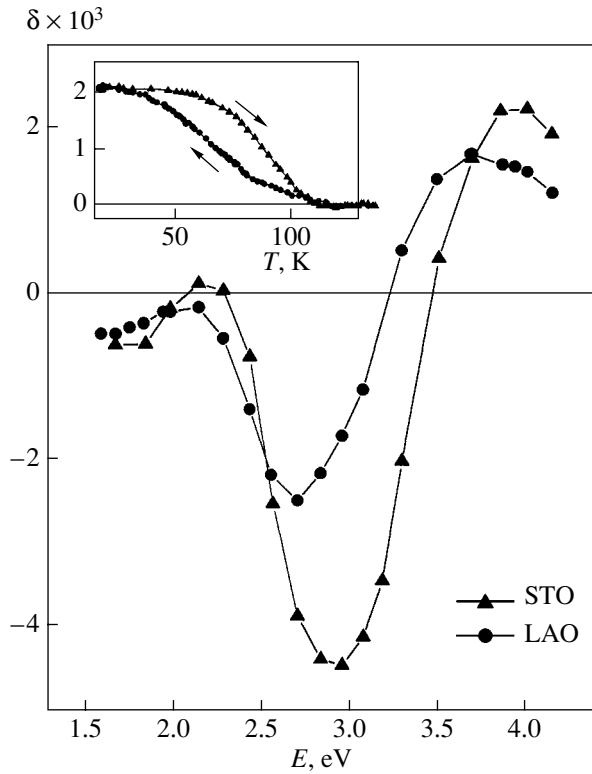


Fig. 2. Spectral response of the TKE in unannealed $(\text{La}_{0.25}\text{Pr}_{0.75})_{0.7}\text{Ca}_{0.3}\text{MnO}_3$ films grown on LAO and STO. Inset shows the temperature dependence of the TKE for a film grown on STO; the direction in which the temperature is varied is specified by arrows.

ordering in these films, while the fairly large amplitude of the TKE in weak fields indicates the existence of a fraction of the FM phase.

3.2. The Electrical Resistivity and Magnetoresistance

The temperature behavior of the electrical resistivity $\rho(T)$ of the LPC films displayed in Fig. 3 is evidence of the MI transition in compositions with $x \leq 0.5$, in unannealed films with $x = 0.75$ on both types of substrates, and in the annealed film with $x = 0.75$ on STO, which shows that the metallic behavior of $\rho(T)$ below T_C switches to a semiconductor pattern above T_C . The MI transition temperature decreases with increasing Pr concentration and is higher in films grown on STO substrates. The difference in the MI transition temperature between films grown on different substrates is the strongest for the $x = 0.75$ composition. The annealed film with $x = 0.75$ on LAO and the $x = 1$ films do not exhibit the MI transition in the temperature interval covered in our study. At 150 K, the $\rho(T)$ dependence measured in the $x = 0.25$ film on LAO reveals a weak anomaly. The film with $x = 0.25$ grown on ZYO has a higher resistivity than the films grown on LAO and STO perovskite substrates (particularly in the region of FM ordering) and undergoes a diffuse MI transition.

The temperature dependences of the absolute value of MR measured in LPC films in a field of 8 kOe perpendicular to the film plane have maxima near T_C

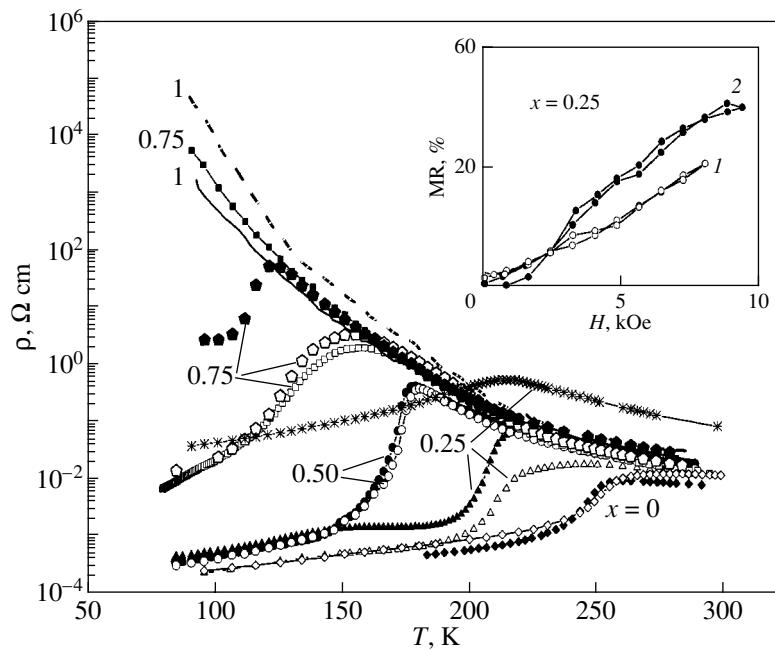


Fig. 3. Temperature dependences of the electrical resistivity of $(\text{La}_{1-x}\text{Pr}_x)_{0.7}\text{Ca}_{0.3}\text{MnO}_3$ films ($0 \leq x \leq 1$) grown on STO (open symbols, solid line for $x = 1$), LAO (filled symbols, dashed line for $x = 1$), and ZYO (asterisks, $x = 0.25$) and of unannealed films (pentagons, $x = 0.75$). Inset shows field dependences of magnetoresistance at the maximum of $\text{MR}(T)$ measured in a film with $x = 0.25$ on STO in a field oriented in the film plane (curve 1) and perpendicular to this plane (curve 2).

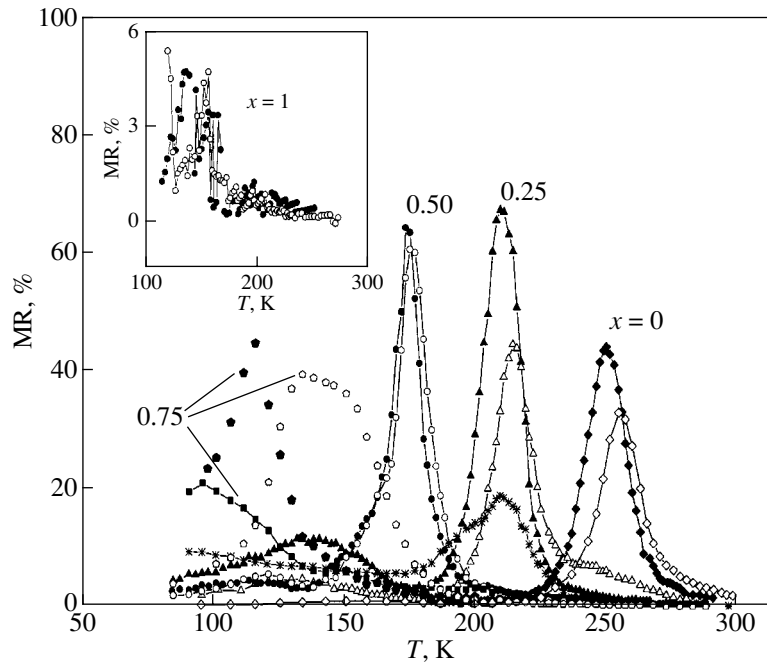


Fig. 4. Temperature dependences of the MR of $(\text{La}_{1-x}\text{Pr}_x)_{0.7}\text{Ca}_{0.3}\text{MnO}_3$ films ($0 \leq x \leq 0.75$) grown on STO (open symbols), LAO (filled symbols), and ZYO (asterisks, $x = 0.25$) and of unannealed films (pentagons, $x = 0.75$) in a magnetic field of 8 kOe directed perpendicular to the surface of the films. Inset shows the MR(T) dependence for films with $x = 1$.

(Fig. 4, table). The temperature of the maximum in magnetoresistance, $T_{\text{MR}}^{\text{max}}$, in films grown on STO substrates is higher than that in films grown on LAO. An increase in the Pr concentration to $x = 0.50$ leads to an increase in MR and a decrease in the temperature $T_{\text{MR}}^{\text{max}}$. For the $x = 0.25$ composition, the maximum MR $\sim 70\%$ is reached in films prepared on LAO substrates and the minimum MR ($\sim 19\%$) is reached in films grown on ZYO. The decrease in the magnitude of MR observed in films with $x = 0.75$, as well as the decrease in the maximum value of TKE in the $\delta(T)$ dependence of these films (Fig. 1), is connected with the decrease in the fractional volume of the FM phase in these films. The presence of a small fraction of the FM phase in the $x = 1$ composition is indicated by the appreciable magnitude of MR in the temperature interval 110–150 K (see inset to Fig. 4). Note the jumpy pattern that the MR(T) curve acquires as the temperature is lowered to 150 K, exhibiting high jumps and abrupt drops to zero.

Besides the main maximum near T_C , the MR(T) dependence of films with $x \leq 0.50$ has a weaker, diffuse satellite peak (Fig. 4). The satellite amplitude is the largest ($\sim 12\%$) in the film with $x = 0.25$ grown on LAO and is observed at $T \sim 135$ K; in films with $x = 0.50$ and 0.25 on STO, the satellite peak is $\sim 4.5\%$ at ~ 125 K, and the smallest satellite peak, $\sim 0.5\%$, was measured at ~ 165 K in $x = 0$ films. Besides the maximum in the MR(T) relation, the film with $x = 0.25$ grown on ZYO exhibits monotonic growth of MR with decreasing tem-

perature for $T < 170$ K. The MR reaches $\sim 10\%$ at 80 K in a field of 8 kOe.

The field dependences of MR of the films with $x \leq 0.50$ (see, for instance, inset to Fig. 3 for composition $x = 0.25$) measured near T_C show no hysteresis and no saturation under application of a magnetic field either perpendicular or parallel to the film plane. The magnetoresistance in an in-plane field is slightly larger than the MR measured in a field perpendicular to the film surface.

3.3. Optical Properties

A common feature of optical absorption spectra of the films studied here (Fig. 5) is an increase in light absorption at wavelengths $\lambda < 4 \mu\text{m}$ ($E > 0.32$ eV), which can be identified with the onset of interband transitions. At the fundamental absorption edge for compositions with $x = 0.5$ and 0.75 (annealed films), a band appears at $1.15 \mu\text{m}$ (~ 1.08 eV), whose intensity is higher in STO-grown films. As the samples are cooled to $\sim T_C$, the band shifts toward shorter wavelengths, and below T_C , it shifts toward longer wavelengths (inset to Fig. 5). No such band is seen in the spectra of films with $x = 0$ and 1 .

The absorption in the mid-IR range of films with $x = 1$ decreases under cooling from 295 to 80 K, as it does in conventional semiconductors (Fig. 5). The absorption of films with $x \leq 0.75$ behaves differently with temperature; namely, down to T_C it falls off, while below T_C the absorption undergoes a substantial growth. Appli-

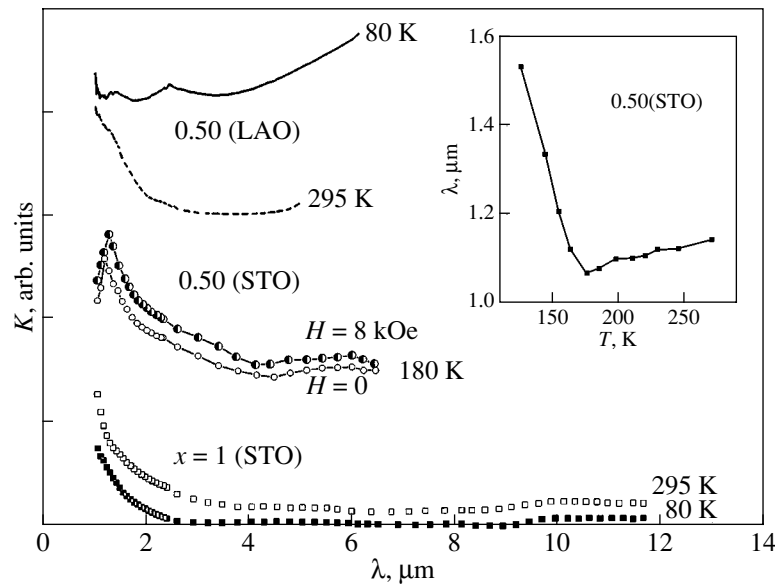


Fig. 5. Absorption spectra of $(\text{La}_{1-x}\text{Pr}_x)_{0.7}\text{Ca}_{0.3}\text{MnO}_3$ films grown on different substrates and measured at different temperatures. Inset shows the temperature dependence of the position of the band at $1.15 \mu\text{m}$ in the spectrum of the film with $x = 0.50$ grown on STO.

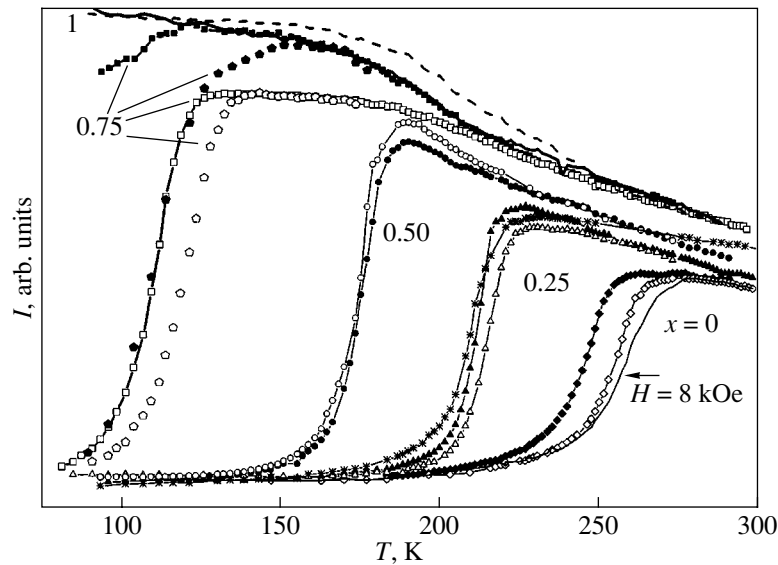


Fig. 6. Temperature dependences of light transmission at $\lambda \sim 6.7 \mu\text{m}$ in a field $H = 0$ obtained on $(\text{La}_{1-x}\text{Pr}_x)_{0.7}\text{Ca}_{0.3}\text{MnO}_3$ films ($0 \leq x \leq 1$) grown on STO (open symbols, bold solid line for $x = 1$), LAO (filled symbols, dashed line for $x = 1$), and ZYO (asterisks, $x = 0.25$) and of unannealed films (pentagons, $x = 0.75$); the thin solid line for the $x = 0$ composition is obtained in a field $H = 8 \text{ kOe}$.

cation of a magnetic field near T_C enhances the absorption in films with $x \leq 0.75$ even further and shifts the band at $\sim 1.15 \mu\text{m}$ to longer wavelengths (Fig. 5). No noticeable effect from the application of a magnetic field (up to 8 kOe) was observed in the absorption spectra of films with $x = 1$.

The character of the variation in the IR absorption in films with temperature near T_C and under application of a magnetic field is clearly illustrated by the temperature

dependence of the transmitted light intensity $I(T)$ measured at a fixed wavelength $\lambda \sim 6.7 \mu\text{m}$ (Fig. 6). For all compositions, except the annealed films with $x = 0.75$, the $I(T)$ curves correlate well in behavior with the $\rho(T)$ dependences (Fig. 3). In films with $x \leq 0.5$ and unannealed films with $x = 0.75$, the $I(T)$ dependence undergoes a sharp change in behavior with increasing temperature near the Curie point, which is an optical counterpart of the metal-insulator transition in the $\rho(T)$

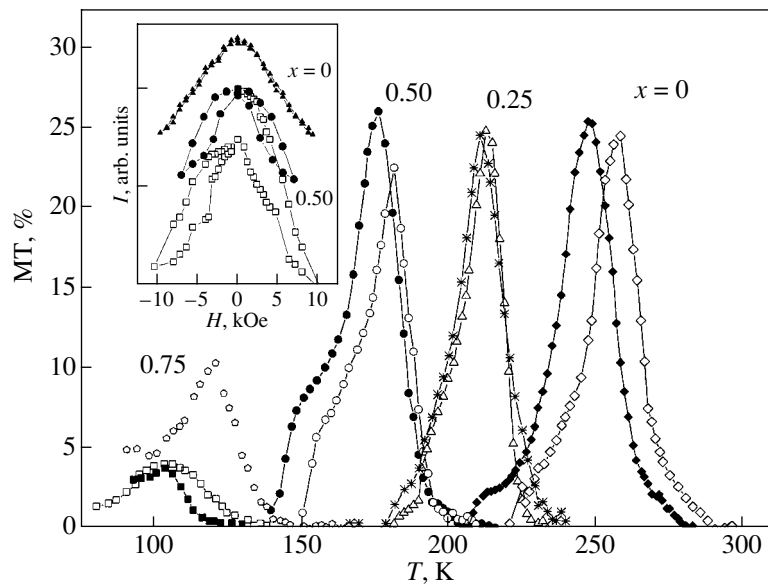


Fig. 7. Temperature dependences of the magnetotransmission at $\lambda \sim 6.7 \mu\text{m}$ of $(\text{La}_{1-x}\text{Pr}_x)_{0.7}\text{Ca}_{0.3}\text{MnO}_3$ films ($0 \leq x \leq 0.75$) obtained in a magnetic field of 8 kOe directed perpendicular to the surface of the films grown on STO (open symbols), LAO (filled symbols), and ZYO (asterisks, $x = 0.25$) and of an unannealed film with $x = 0.75$ (pentagons). Inset shows field dependences of light transmission at $\lambda \sim 6.7 \mu\text{m}$ of films with $x = 0.50$ obtained in a magnetic field perpendicular to the film plane (open squares) and in an in-plane field (filled circles). The curve corresponding to the $x = 0$ composition is offset upwards for clarity (filled triangles).

dependence. In the vicinity of the MI transition, the IR transmission drops by a factor of more than 4000. The MI transition temperature in the $I(T)$ dependence decreases with increasing Pr concentration and, as in the $\rho(T)$ dependence, is higher in films grown on STO substrates. In annealed films with $x = 0.75$, the MI transition in the $I(T)$ dependence is observed to occur in films on both types of substrates, despite its absence in the $\rho(T)$ dependence for the film grown on LAO (Fig. 3). The $I(T)$ and $\rho(T)$ dependences exhibit a semi-conducting behavior in samples with $x = 1$ throughout the temperature range covered.

Application of a magnetic field, as well as a decrease in temperature, brings about a decrease in film transparency near the MI transition (see, for instance, the solid line in Fig. 6 for the $x = 0$ film on STO), i.e., the onset of negative magnetotransmission, which is an analog of magnetoresistance. Magnetotransmission is a relative magnetic field-induced change in the intensity of the light transmitted through a film, $\text{MT} = [I_H - I_0]/I_0$, where I_H and I_0 are the values of transmission with and without a magnetic field present, respectively. The temperature dependence of the absolute values of the film MT (Fig. 7) follows the same pattern as that of the MR (Fig. 4). Just as the MR, magnetotransmission reaches a maximum near T_C . As the Pr concentration is increased to $x = 0.50$, the temperature at which the maximum in magnetotransmission is observed ($T_{\text{MR}}^{\text{max}}$) decreases, but the value of MT changes insignificantly ($\sim 25\%$), in contrast to MR. The asymmetry in the $\text{MT}(T)$ curves for films with $x = 0.50$ should be

assigned to the appearance of an additional magnetotransmission band in the form of a shoulder near 150 K. The value of MT in annealed samples with $x = 0.75$ is smaller than that in unannealed samples. Films grown on STO substrates feature higher temperatures of the maximum in MT than films grown on LAO and ZYO ($x = 0.25$). Practically no MT is observed in films with $x = 1$ (less than 0.5%).

For films with $x = 0$, the field dependence of the transmission has no hysteresis and no saturation and the $I(H)$ dependence is close to linear in fields above 1.5 kOe (inset to Fig. 7). Magnetotransmission, as well as magnetoresistance, is an effect that is an even function of field. Films with $x = 0.25, 0.50$, and 0.75 (unannealed) on either type of substrate reveal a hysteresis in the $I(H)$ relation in fields of up to 10 kOe. After removal of the field oriented perpendicular to the film plane, the transmission does not regain its original value. The new value of transmission, for instance, in films with $x = 0.50$, decreases by $\sim 17\%$ compared to the original level (inset to Fig. 7); in films with $x = 0.75$ (unannealed), by $\sim 25\%$; and in films with $x = 0.25$, by $\sim 3\%$. Demagnetizing the films by switching the field polarity does not restore the original level of light transmission. The film with $x = 0.50$ placed in an in-plane field of up to 8 kOe exhibits hysteresis, and the transmission recovers its original value as the magnetic field is cyclically switched.

4. DISCUSSION OF THE RESULTS

Let us compare the results of our study on the optical and magneto-optical properties and the electrical resistivity of $(\text{La}_{1-x}\text{Pr}_x)_{0.7}\text{Ca}_{0.3}\text{MnO}_3$ epitaxial films ($0 \leq x \leq 1$) with the data from [4], where a phase diagram for bulk polycrystals of this system is presented. As in [4], an increase in the concentration of Pr^{3+} ions substituting for La^{3+} brings about a decrease in T_C that is practically linear in x because of the decrease in the cation radius. The Goldschmidt radius of the La^{3+} ion is 1.06 Å, and that of Pr^{3+} is 1.01 Å. The decrease in the average cation radius $\langle r_a \rangle$ with the Pr concentration increasing to $x = 0.50$ is accompanied by enhanced carrier localization, which entails a decrease in T_C and in the MI transition temperature in the $\rho(T)$ and $I(T)$ dependences and an increase in the electrical resistivity and MR (see table, Figs. 3, 4, 6). Importantly, one of the most essential conclusions reached in [4] is the existence of praseodymium concentration ranges within which the magnetic and charge states are uniform ($x > 0.8$, $x < 0.6$).

The values of T_C of films with $x \leq 0.50$ (see table) insignificantly exceed those for polycrystals of corresponding composition [4]. The enhanced T_C may be due to different oxygen off-stoichiometries of films and bulk polycrystals and to a specific feature of the film state due to the strains generated at the film–substrate interface and to the stress gradient across the film thickness. The latter may also account for the differences in the magnitude and temperature of the maxima of MT and MR and in the values of the TKE between LPC films grown on STO and LAO.

Compressive (in the case of LPC–LAO and LPC–ZYO) or tensile (LPC–STO) strains arising at the film–substrate interface give rise to the formation of strain components normal to this interface. The maximum amplitude of potential energy at the interface is $E_0 = (\mu c')/(2\pi^2) \approx 530 \text{ erg/cm}^2$, where c' is the reduced lattice parameter along the film surface normal and μ is the interface rigidity modulus ($2.6 \times 10^{11} \text{ dyn/cm}^2$ [12]). In general, the interface potential energy depends on the parameter $\beta = 2\pi(c/p)(\lambda_+/\mu)$, where the ratio $c/p = (a-b)/(1/2)(a+b)$ characterizes the lattice parameter misfit between the substrate (b) and film (a), $\lambda_+ = (1 - \sigma_a)/\mu_a + (1 - \sigma_b)/\mu_b$, and σ is the Poisson ratio [12]. Estimates of β made for $x = 0.25$, $\sigma = 0.3$, and $\mu_a/\mu_b = 1$ yield 0.054 for LPC–STO, 0.093 for LPC–LAO, and 0.264 for LPC–ZYO. For all the substrates, the condition $\beta \ll 1$ is met. A rough relation connecting the critical film thickness h/a with the critical lattice misfit $f_c = (a-b)/a$ can be derived from the equation [12]

$$\ln[2\pi f_c e/(1 - \sigma) + 2\pi(1 - \sigma)^2 h f_c/(1 - 2\sigma)a] = 0, \quad (1)$$

where f_c is ~ 0.01 for the LPC–STO combination, 0.02 for LPC–LAO, and 0.06 for LPC–ZYO. As follows from Eq. (1), the largest pseudomorphic layer is in films

grown on STO, $h/a = 20$. In films grown on LAO, this value is smaller than 10, and the smallest value, 2, corresponds to films grown on ZYO. These values are noticeably smaller than the thicknesses of the films themselves, which implies that this difference cannot produce an appreciable change in the critical temperatures. At the same time, one may conceive of a small contribution due to thermal stresses arising because of the different coefficients of thermal expansion of the film and the substrate.

LPC films 300-nm thick with $x = 0.50$ and 0.25 exhibit a slight difference in the critical temperature T_C^* , the MI transition temperature, T_{MT}^{\max} , and T_{MR}^{\max} depending on the substrate material. There are a number of publications on $\text{La}_{0.7}\text{Ca}_{0.3}\text{MnO}_3$ films in which substitution of an STO by a LAO substrate resulted in a shift in T_C , the MI transition temperature, and T_{MR}^{\max} toward (i) higher temperatures up to 30°C [13–15], (ii) lower temperatures [16, 17], or (iii) remained practically unaffected [18, 19]. In the first and second cases, the values of T_C of the films differed appreciably from those in the phase diagram constructed for bulk samples [4]. In the third case, as in our studies, the values of T_C of films and bulk samples are similar. All publications mentioned above pointed out the substantial effect of strains at the film–substrate interface and of twinning on the position of the critical temperatures. Deviation from oxygen stoichiometry was also found to have a considerable effect on the critical temperatures [17]. We believe that, because of the large thickness (300 nm) of the (001)LPC films with $x \leq 0.50$, their deviation from oxygen stoichiometry (as well as the substrate type) does not affect the position of critical temperatures for films grown on different substrates.

The maximum sensitivity of the critical temperatures and of the magnitude of MT to the oxygen stoichiometry of films and the substrate type is observed when comparing the properties of annealed and unannealed films with the Pr concentration $x = 0.75$, which corresponds to separation into the FM metallic and AFM insulating phases ($T_N > T_C$ [4]). In unannealed films, most likely, the $\text{Mn}^{4+}/\text{Mn}^{3+}$ concentration ratio changes from that of the annealed composition. Such nonisovalent doping can result in higher Curie temperatures than for the annealed films and in the MI transition in films on both types of substrates (Figs. 3, 6). The values of MT (for films grown on LAO) and of MR also turn out to be higher than those for the films annealed in oxygen (see table). The difference in the MT value and in the magnitude and shape of the spectral response of TKE between unannealed films with $x = 0.75$ grown on LAO and STO substrates suggests different deviations from oxygen stoichiometry, and this deviation is probably higher in the film grown on LAO. The magnitude of the TKE in this film is higher because of the larger ferromagnetic contribution. Annealing in an oxygen flow results in a more uniform film stoichiometry. The criti-

cal temperatures decrease, and the values of the MT (~4%) and TKE level off. At the same time, in annealed films with $x = 0.75$, the MI transition is seen in the $\rho(T)$ dependence (Fig. 3) only in the film grown on an STO substrate, while in the $I(T)$ relation (Fig. 6) the MI transition manifests itself in films grown on both type of substrates. As we have shown for manganites with weakly nonisovalent doping [3, 20], this observation is a compelling argument for the presence of metallic drops that are not connected with one another in an insulating matrix. The existence of a fairly strong Kerr effect in films with $x = 0.75$ (Fig. 1), whose appearance temperature is close to the temperature of the MI transition observed in the $I(T)$ dependence, suggests that the metallic regions are ferromagnetic. Thus, films with $x = 0.75$ undergo phase separation just as polycrystalline samples do [4]. Tensile stresses in films grown on STO substrates are conducive to the formation of metallic regions of a more elongated shape, giving rise to through conduction in such films, which does not occur in films grown on LAO.

In films with $x = 1$, only the magnetoresistance data (see inset to Fig. 4) attest to the existence of charge and magnetic small-scale nonuniformities. Quite possibly, nonuniformities form in this composition in the layer close to the interface, where conduction channels terminate and current instabilities similar to the pinching effect in semiconductors set in. As already mentioned, the thickness h/a of this layer is small; therefore, field-induced changes in transmission manifest themselves here only weakly (MT < 0.5%).

Optical and magneto-optical studies show that LPC films are also nonuniform, both magnetically and in charge distribution, in the concentration range $x \leq 0.50$, where a singly connected metallic region forms. As follows from the $\rho(T)$ relations obtained for LPC films (Fig. 3), the percolation threshold, i.e., the transition from isolated metallic drops to through conduction in the crystal, occurs in the concentration range $0.5 < x < 0.75$. Near the percolation threshold, at $x = 0.50$, the MR reaches its maximum value (Fig. 4). As the film conductivity increases ($x < 0.5$), the MR decreases. This behavior of the MR is characteristic of nonuniform systems and doped magnetic semiconductors. An exclusion is the minimum value of MR in a completely relaxed $x = 0.25$ film grown on a ZYO substrate, which has the lowest conductivity. The higher electrical resistivity of the film grown on ZYO (Fig. 3) compared to those grown on LAO and STO perovskite substrates should be assigned to the resistance of large-angle boundaries separating regions with different crystallographic orientations, which form in a lanthanum manganite film grown on ZYO [21]. The growth in the MR in the film grown on ZYO observed to occur with decreasing temperature (Fig. 4) can be accounted for by the tunneling of spin-polarized carriers through the boundaries between these regions [21].

Nonuniformities are also possibly responsible for the satellites in the MR(T) dependences and for the asymmetry in the MT(T) curves (Fig. 7) for compositions with $x \leq 0.50$. Structural changes may serve as another explanation for the appearance of the satellites and of the anomaly in $\rho(T)$ at 150 K observed in the $x = 0.25$ film. Studies of this system performed over a broad range of temperatures [22, 23] did not uncover indications of structural transformations but revealed only a jump in volume for a polycrystal with $x = 0.5$ at a temperature of 150 K, which is associated with the MI transition. In films with $x = 0.5$, a satellite in the MR(T) relation is observed at 125 K.

Under application of a magnetic field, transmission is strongly reduced only in the FM regions, while in the AFM matrix it remains unchanged; therefore, the MT is actually proportional to the relative change in transmission in the FM regions and, unlike the MR, reaches a maximum when a singly connected metallic region forms in the sample below T_C [3].

In our case, substitution of Pr^{3+} for La^{3+} does not change the $\text{Mn}^{3+}/\text{Mn}^{4+}$ ratio and the singly connected metallic FM region persists up to the Pr concentration $x = 0.5$. This is what accounts for the similarity of the values of TKE at 70 K (Fig. 1) and of the maximum values of the MT, ~25%, between films with $x \leq 0.50$ grown on different substrates (Fig. 7).

Below the percolation threshold $x > 0.6$ [4], the values of the TKE and MT decrease noticeably, which suggests a decrease in the fractional volume of the FM phase. Because it is sensitive to even a small concentration of metallic drops, the MT effect is fairly large, ~10%, for the unannealed $x = 0.75$ film grown on STO (Fig. 7).

The charge and magnetic nonuniformities also become manifest in absorption spectra in the form of a resonance-like line at ~1.15 μm , whose position depends on the magnetic ordering (Fig. 5). This band probably originates from the overlap between electronic transitions and the geometric resonance (the Mie resonance) [3], i.e., from the appearance of a feature in the absorption spectrum resulting from surface plasmon excitation at the boundary of nonuniformities. This effect is accompanied by the onset of forbidden or weakly allowed transitions. The shift in the line toward longer wavelengths for $T < T_C$ or under application of a magnetic field (in the vicinity of T_C) may be due to a change in the resonance conditions near T_C .

Field dependences of the TKE at low temperatures show saturation for compositions with $x \leq 0.50$ (inset to Fig. 1). The absence of saturation in the $I(H)$ and $\rho(H)$ dependences near T_C under application of a magnetic field in the film plane and perpendicular to it should be assigned to magnetic moment fluctuations becoming maximum near T_C (Figs. 3, 7). The hysteresis in the $I(H)$ dependences near T_C observed under application of a magnetic field perpendicular to the film plane (the

case of the maximum demagnetizing factor) is similar to that in the $\rho(H)$ relation at 75 K [13] and is observed for compositions close to the percolation threshold. The residual transmission in the hysteretic $I(H)$ dependence (Fig. 7) cannot be removed by demagnetizing the films and is probably associated with the magnetic field-induced melting of the charge-ordered state (the transition to the charge-ordered state occurs at $T_{CO} = 180$ K [23]). The melting of the charge-ordered state is argued for by the decrease in film transmission after the first cycle of field variation. The residual transmission reaches a maximum value of $\sim 25\%$ at $x = 0.75$ (for the unannealed film; the annealed films were not measured because of the weak MT effect), where the fractional volume of the AFM charge-ordered phase exceeds that of the FM phase, and reaches a minimum level of $\sim 3\%$ in the $x = 0.25$ films. There is no residual transmission in the $I(H)$ dependence when an in-plane magnetic field is applied (the case of the minimum demagnetizing factor). The difference in the $I(H)$ behavior between different field geometries can be due to anisotropic magnetic nonuniformities. The MT hysteresis itself is apparently caused by a hysteresis of the magnetic structure in the transition layer separating the AFM matrix from FM drops, because it is not seen in the $MR(T)$ dependences near T_C (Fig. 3). The MT hysteresis is determined by the ratio of the fractional volumes of the AFM and FM regions at a given Pr concentration and by the shape of the FM regions in films grown on different substrates. The shape of the FM regions depends on the character of strains at the film-substrate interface, which define the shape of charge-disordered regions [24]. The absence of MT hysteresis at $x = 0$ is due to the small fraction of magnetic nonuniformities in these films. The TKE hysteresis observed in all films in the heating-cooling mode also attests to the existence of magnetic nonuniformities.

The high values of magnetotransmission in the IR range suggest that $(La_{1-x}Pr_x)_{0.7}Ca_{0.3}MnO_3$ films may potentially be applied as a new functional material for magnetically controlled optoelectronic devices intended for operation in the temperature range from 170 to 260 K. A number of conceivable optoelectronic devices were briefly described in [2]. The film with $x = 0.25$ grown on a LAO substrate has a high value of MR, $\sim 70\%$, in a field of 8 kOe at 211 K, which makes it promising for applications.

5. CONCLUSIONS

Isovalent substitution of La^{3+} by the smaller radius Pr^{3+} ions in $(La_{1-x}Pr_x)_{0.7}Ca_{0.3}MnO_3$ films brings about a decrease in the Curie temperature, in the temperatures of the maxima in magnetotransmission and magnetoresistance, and in the MI transition point. The nature of the substrate does not noticeably affect the Curie temperature and the temperatures of the maxima in the magnetotransmission and magnetoresistance. The

slight changes in the maximum values of the Kerr effect and magnetotransmission for concentrations $x \leq 0.50$ argue for the formation of a singly connected ferromagnetic metallic region in films at low temperatures. The totality of the magneto-optical and optical data obtained indicates, however, that nanoscopic magnetic and electronic nonuniformities exist both in films with a singly connected region and in a film with $x = 1$, which is an antiferromagnetic insulator. It has been shown that films with $x = 0.75$ undergo separation into an antiferromagnetic insulating matrix and ferromagnetic metallic drops.

ACKNOWLEDGMENTS

This study was supported by the federal research program (project no. 40.012.1.1.1153-7/03), the Russian Foundation for Basic Research (project nos. 02-02-16429, 03-02-06032, 03-02-06301, 02-03-33258), and by the program of the Department of Physical Sciences, Russian Academy of Sciences.

REFERENCES

1. J. H. Hao, X. T. Zeng, and H. K. Wong, *J. Appl. Phys.* **79** (3), 1810 (1996).
2. Yu. P. Sukhorukov, N. N. Loshkareva, E. A. Gan'shina, A. R. Kaul', O. Yu. Gorbenko, and K. A. Fatieva, *Pis'ma Zh. Tekh. Fiz.* **25** (14), 6 (1999) [*Tech. Phys. Lett.* **25**, 551 (1999)].
3. Yu. P. Sukhorukov, N. N. Loshkareva, E. A. Gan'shina, E. V. Mostovshchikova, I. K. Rodin, A. R. Kaul', O. Yu. Gorbenko, A. A. Bosak, A. S. Moskvina, and E. V. Zenkov, *Zh. Éksp. Teor. Fiz.* **123** (1), 293 (2003) [*JETP* **96**, 257 (2003)].
4. A. M. Balagurov, V. Yu. Pomjakushin, D. V. Sheptyakov, V. L. Aksenov, P. Fischer, L. Keller, O. Yu. Gorbenko, A. R. Kaul, and N. A. Babushkina, *Phys. Rev. B* **64** (2), 024420 (2001).
5. A. M. Balagurov, V. Yu. Pomjakushin, D. V. Sheptyakov, V. L. Aksenov, N. A. Babushkina, L. M. Belova, O. Yu. Gorbenko, and A. R. Kaul, *Eur. Phys. J. B* **19**, 215 (2001).
6. O. Yu. Gorbenko, A. A. Bosak, and A. R. Kaul, *Mater. Res. Soc. Symp. Proc.* **495**, 333 (1998).
7. E. A. Balykina, E. A. Gan'shina, and G. S. Krinchik, *Zh. Éksp. Teor. Fiz.* **93**, 1879 (1987) [*Sov. Phys. JETP* **66**, 1073 (1987)].
8. E. A. Gan'shina, I. K. Rodin, N. N. Loshkareva, Yu. P. Sukhorukov, and E. V. Mostovshchikova, *Izv. Ross. Akad. Nauk, Ser. Fiz.* **66** (6), 767 (2002).
9. E. A. Gan'shina, O. Yu. Gorbenko, A. G. Smechova, A. R. Kaul, N. A. Babushkina, and L. M. Belova, in *Non-Linear Electromagnetic Systems*, Ed. by V. Kose and J. Sievert (IOP Press, Amsterdam, 1998), p. 325.
10. E. A. Gan'shina, O. Yu. Gorbenko, A. R. Kaul, and A. N. Vinogradov, *J. Phys.: Condens. Matter.* **12**, 2857 (2000).
11. E. A. Balykina, E. A. Gan'shina, G. S. Krinchik, and A. Yu. Trifonov, *J. Magn. Mater.* **117**, 259 (1992).

12. J. H. Van-der-Merve, in *Single-Crystal Films*, Ed. by M. H. Francombe and H. Sato (Macmillan, New York, 1964; Mir, Moscow, 1966).
13. O. Yu. Gorbenko, A. R. Kaul, N. A. Babushkina, and L. M. Belova, *J. Mater. Chem.* **7**, 747 (1997).
14. W. Prellier, Ph. Lecocur, and B. Merecy, *J. Phys.: Condens. Matter* **13**, K915 (2001).
15. R. A. Rao, D. Lavric, T. K. Nath, C. B. Eom, L. Wu, and F. Tsui, *J. Appl. Phys.* **85**, 4794 (1999).
16. F. Martin, G. Jakob, W. Westerberg, and H. Adrian, *J. Magn. Magn. Mater.* **196–197**, 509 (1999).
17. A. P. Nosov and P. Strobel', *Fiz. Met. Metalloved.* **93** (3), 50 (2002).
18. B. Vengalis, F. Maneikis, F. Anisimovas, R. Butkute, L. Dapkus, and A. Kindurys, *J. Magn. Magn. Mater.* **211**, 35 (2000).
19. M. G. Blamire, B.-S. Teo, J. H. Durrel, N. D. Mathur, Z. H. Barber, J. L. McManus Driscoll, L. F. Cohen, and J. E. Evetts, *J. Magn. Magn. Mater.* **191**, 359 (1999).
20. N. N. Loshkareva, Yu. P. Sukhorukov, S. V. Naumov, N. I. Solin, I. B. Smolyak, and E. V. Panfilova, *Pis'ma Zh. Éksp. Teor. Fiz.* **68** (1), 89 (1998) [*JETP Lett.* **68**, 97 (1998)].
21. L. I. Koroleva, A. I. Abramovich, A. V. Michurin, O. Yu. Gorbenko, I. E. Graboy, A. R. Kaul, R. Szymczak, S. Deyev, and H. W. Zandbergen, *J. Phys.: Condens. Matter.* **13**, 5901 (2001).
22. A. M. Balagurov, V. Yu. Pomyakushin, V. L. Aksenov, N. A. Babushkina, L. M. Belova, O. Yu. Gorbenko, A. R. Kaul', N. M. Plakida, P. Fischer, M. Gutmann, and L. Keller, *Pis'ma Zh. Éksp. Teor. Fiz.* **67** (9), 672 (1998) [*JETP Lett.* **67**, 705 (1998)].
23. P. G. Radaelli, M. Marezio, H. Y. Hwang, S.-W. Cheong, and B. Batlogg, *Phys. Rev. B* **54**, 8992 (1996).
24. A. S. Moskvina, E. V. Zenkov, Yu. P. Sukhorukov, E. V. Mostovshchikova, N. N. Loshkareva, A. R. Kaul, and O. Yu. Gorbenko, *J. Phys.: Condens. Matter* **15**, 2635 (2003).

Translated by G. Skrebtsov

**MAGNETISM
AND FERROELECTRICITY**

Anomalies in the Magnetic and Magnetoelastic Properties of $\text{Sm}_{1-x}\text{Sr}_x\text{MnO}_3$ Single Crystals ($x \sim 0.5$) at Phase Transitions

Yu. F. Popov*, A. M. Kadomtseva*, G. P. Vorob'ev*, A. A. Mukhin, V. Yu. Ivanov**,
K. I. Kamilov*, Ya. S. Shtofich*, and A. M. Balbashov*****

*Moscow State University, Vorob'evy gory, Moscow, 119992 Russia
e-mail: kadomts@plms.phys.msu.ru

**General Physics Institute, Russian Academy of Sciences, ul. Vavilova 38, Moscow, 117942 Russia

***Moscow Power Institute, Moscow, 111250 Russia

Received November 12, 2003

Abstract—By studying the magnetic and magnetoelastic properties, it is established that, as the temperature is lowered, $\text{Sm}_{1-x}\text{Sr}_x\text{MnO}_3$ single crystals ($x = 0.5, 0.55$) undergo spontaneous phase transitions from the paramagnetic to a local charge-ordered state at $T_{\text{co}} = 220$ K and to an *A*-type antiferromagnetic state at $T_{\text{N}} = 175$ K. It is shown that strong magnetic fields ($H_{\text{cr}} \sim 200$ kOe) break up the antiferromagnetic order and charge ordering and drive a phase transition to a conducting ferromagnetic state. H – T phase diagrams are constructed for single crystals with $x = 0.5$ and 0.55 . © 2004 MAIK “Nauka/Interperiodica”.

1. INTRODUCTION

The $R_{1-x}M_x\text{MnO}_3$ substituted manganites ($R = \text{La}, \text{Pr}, \text{Nd}, \text{Sm}$; $M = \text{Ca}, \text{Sr}$) have attracted considerable interest over the past decade, largely due to the discovery of the colossal magnetoresistance effect in these compounds within a certain concentration interval [1, 2]. Substituted manganites are also remarkable for the strong correlation between their spin–charge lattice degrees of freedom and for the variety of T – x phase diagrams. The phase diagrams differ appreciably depending on the actual type of rare-earth ion involved. As the tolerance factor decreases as the atomic number of R increases or as one goes from Sr to Ca, the band width decreases, which enhances the localization effects and drives the transition from the ferromagnetic to antiferromagnetic and charge ordering state.

Among the various $R_{1-x}M_x\text{MnO}_3$ substituted manganites, the compounds with $x = 0.5$ are of particular interest, because it is in them that states with various types of magnetic, orbital, and charge ordering were discovered. Of these compounds, $\text{Sm}_{0.5}\text{Sr}_{0.5}\text{MnO}_3$ is the least studied; the information on the character of its ordering is fairly contradictory. A study [3] performed on polycrystalline samples yielded a T – x phase diagram according to which the $x = 0.5$ composition should be a ferromagnet with local charge ordering. Measurements carried out on a $\text{Sm}_{0.5}\text{Sr}_{0.5}\text{MnO}_3$ single crystal revealed antiferromagnetic ordering [4]. In order to straighten out these contradictions, we carried out an investigation of both spontaneous phase transitions and phase transitions induced by a strong magnetic field in these single crystals with $x = 0.5$ and 0.55 .

Our study of the magnetic and magnetoelastic properties revealed, in contrast to [3], that these compounds have no spontaneous magnetic moment and that they undergo two spontaneous phase transitions, namely, local charge ordering at $T_{\text{co}} = 220$ K and antiferromagnetic ordering at $T_{\text{N}} = 175$ K. We showed that a strong magnetic field (~ 200 kOe) suppresses the weakly magnetic, low-conducting state and drives a phase transition to the ferromagnetic conducting state.

2. EXPERIMENTAL RESULTS AND DISCUSSION

Single crystals of $\text{Sm}_{1-x}\text{Sr}_x\text{MnO}_3$ ($x = 0.5, 0.55$) were grown by zone melting with radiative heating. The magnetic and magnetoelastic properties were measured in the temperature range 10–300 K. In weak magnetic fields, the magnetic susceptibility passes through a broad maximum near $T_{\text{co}} = 220$ K (Fig. 1a), followed by a drop as the temperature decreases to $T_{\text{N}} = 175$ K. We believe that at $T_{\text{co}} = 220$ K local charge ordering sets in, in full agreement with [3], while at $T_{\text{N}} = 175$ K, as opposed to [3], antiferromagnetic ordering takes place, which is indicated by the absence of a spontaneous moment in the $M(H)$ curves (inset to Fig. 1a). As seen from Fig. 1b, at $T_{\text{N}} = 175$ K a local maximum appears in the temperature dependence of electrical resistivity, while on the whole the $\rho(T)$ graph features semiconducting behavior typical of manganites with a fairly large degree of localization. The temperature dependence of thermal expansion likewise exhibited an anomaly at $T_{\text{N}} = 175$ K (Fig. 1c), while at $T_{\text{co}} = 220$ K

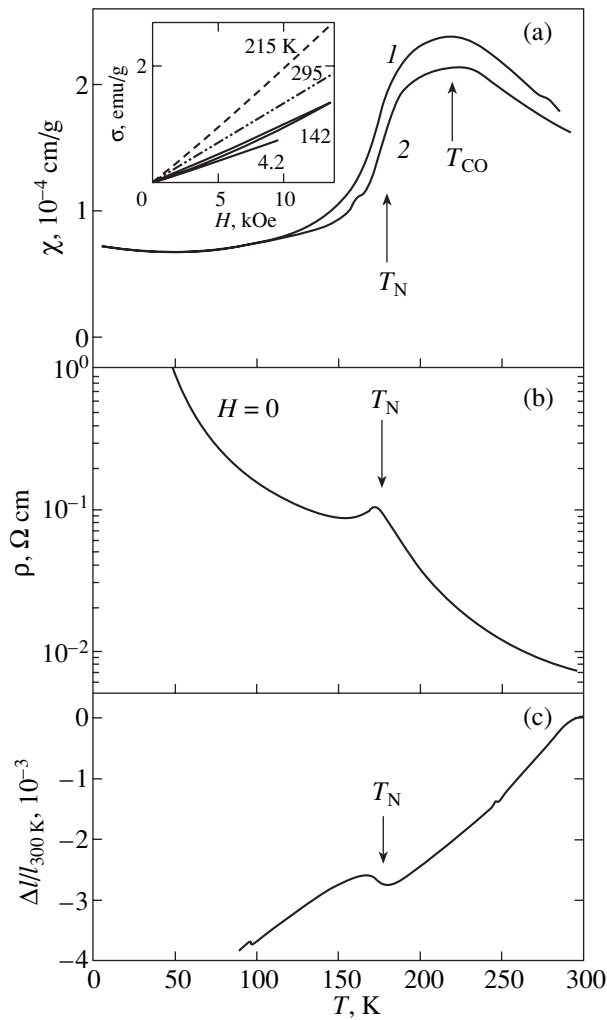


Fig. 1. Temperature dependences for $\text{Sm}_{1-x}\text{Sr}_x\text{MnO}_3$ single crystals (a) with magnetic susceptibility measured at $H = 5.75$ kOe for compositions (1) $x = 0.5$ and (2) 0.55 , (b) electrical resistivity measured for $x = 0.5$, and (c) thermal expansion for $x = 0.5$. Inset shows magnetization curves obtained in weak magnetic fields.

no anomaly was observed, probably because of the charge ordering bearing a local character [3]. We believe that $\text{Sm}_{0.5}\text{Sr}_{0.5}\text{MnO}_3$ has an A-type antiferromagnetic structure; i.e., it consists of antiferromagnetically coupled ferromagnetic layers.

Magnetization curves measured in a strong magnetic field revealed an increase in magnetization with jumps at $T \leq T_N = 175$ K, which switched to a diffuse behavior in the temperature range $175 < T < 220$ K. The strong rise in magnetization in threshold fields H_{cr} is obviously due to a transition to a ferromagnetic state with suppression of antiferromagnetic ordering for $T < T_N$ and suppression of local charge ordering in the range $175 < T < 220$ K (we assumed the average charge ordering temperature to be $T_{\text{co}} = 220$ K). The threshold field for $T = 10$ K was $H_{\text{cr}} = 240$ kOe. The magnetiza-

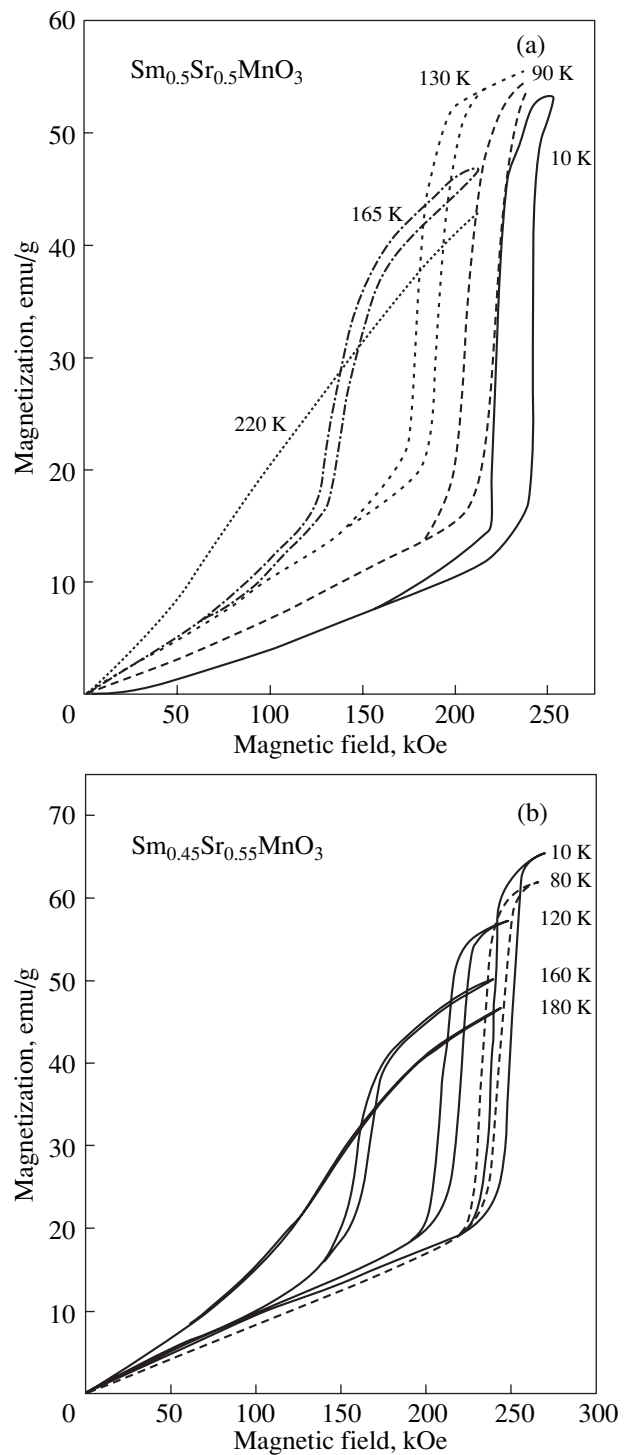


Fig. 2. Magnetization vs. magnetic field obtained at different temperatures for single crystals of (a) $\text{Sm}_{0.5}\text{Sr}_{0.5}\text{MnO}_3$ and (b) $\text{Sm}_{0.45}\text{Sr}_{0.55}\text{MnO}_3$.

tion curves of the composition with $x = 0.55$ obtained in a strong magnetic field exhibited a similar behavior (Fig. 2b). The threshold fields driving the phase transition to the ferromagnetic state at different temperatures

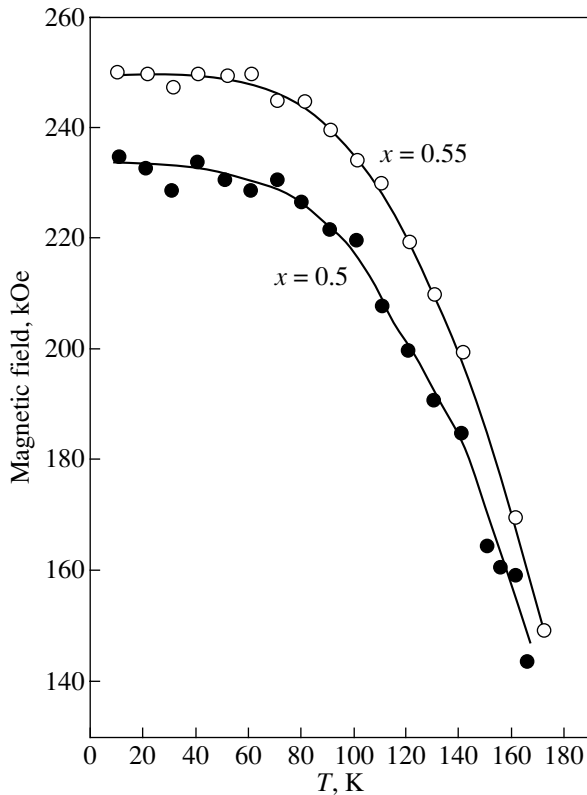


Fig. 3. $H_{cr}(T)$ diagrams for $x = 0.5$ and 0.55 .

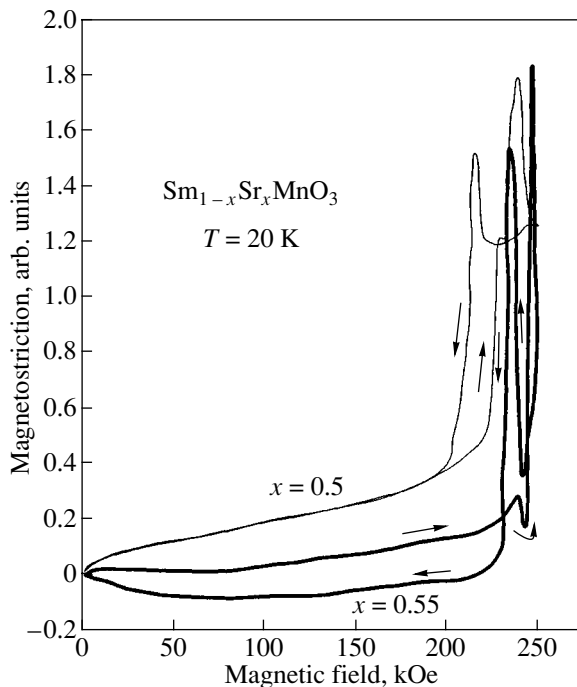


Fig. 4. Magnetostriction vs. magnetic field at $T = 20$ K for compositions $x = 0.5$ and 0.55 .

were used to construct H - T phase diagrams for both compositions (Fig. 3). The difference between the data on the magnetic structure of $\text{Sm}_{0.5}\text{Sr}_{0.5}\text{MnO}_3$ single crystals and polycrystals should possibly be assigned to single crystals having a better oxygen stoichiometry.

We also found that the phase transition from the antiferromagnetic to the ferromagnetic state is accompanied by a magnetostrictive deformation $\frac{\Delta l}{l} \sim 10^{-3}$.

Note that the transition is so steep that after the first measurement the sample partially breaks down, so the subsequent values of the magnetostriction turn out to be an order of magnitude smaller. For this reason, the magnetostriction is plotted in Fig. 4 in arbitrary units. Note that the magnetostrictive deformation is accompanied by strong hysteresis having complex character.

3. CONCLUSIONS

We have established that $\text{Sm}_{1-x}\text{Sr}_x\text{MnO}_3$ single crystals ($x = 0.5, 0.55$) are not ferromagnets as was reported in [3]. Our measurements revealed that two spontaneous phase transformations occur with decreasing temperature, namely, a transition to a state with local charge ordering at $T_{co} = 220$ K and a transition to the pure antiferromagnetic state, tentatively identified as A type, at $T_N = 175$ K. Thus, the T - x phase diagram presented in [3] for a composition close to $x = 0.5$ apparently needs to be refined. A strong magnetic field (~ 200 kOe) suppresses the antiferromagnetic and charge-ordered phases and drives a phase transition to the ferromagnetic conducting state.

ACKNOWLEDGMENTS

This study was supported by the Russian Foundation for Basic Research, project no. 03-02-16445a.

REFERENCES

1. Y. Tokura and Y. Tomioka, *J. Magn. Magn. Mater.* **200**, 1 (1999).
2. M. B. Salamon and M. Jaime, *Rev. Mod. Phys.* **73**, 583 (2001).
3. C. Martin, A. Maignan, M. Hervieu, and B. Raveau, *Phys. Rev. B* **60**, 12191 (1999).
4. Y. Tomioka, H. Kuwahara, A. Asamitsu, and M. Kasai, *Appl. Phys. Lett.* **70**, 3609 (1997).

Translated by G. Skrebtsov

MAGNETISM AND FERROELECTRICITY

Crystallographic, Magnetic, and Electrical Properties of Thin $Re_{0.6}Ba_{0.4}MnO_3$ Epitaxial Films ($Re = La, Pr, Nd, Gd$)

O. Yu. Gorbenko*, R. V. Demin*, A. R. Kaul'*, L. I. Koroleva*, R. Szymczak**,
H. Szymczak**, and M. Baran**

*Moscow State University, Vorob'evy gory, Moscow, 119992 Russia

e-mail: koroleva@ofef343.phys.msu.su

**Institute of Physics, Polish Academy of Sciences, Warsaw, 02-668 Poland

Received July 21, 2003; in final form, November 20, 2003

Abstract—Thin $Re_{0.6}Ba_{0.4}MnO_3$ epitaxial films ($Re = La, Pr, Nd, Gd$) grown on (001)SrTiO₃ and (001)ZrO₂(Y₂O₃) single crystal substrates have been prepared and studied. All the films were found to have a cubic perovskite structure, with the exception of the film with $Re = La$, which revealed rhombohedral distortion of the perovskite cell. The temperature dependences of the electrical resistivity and magnetoresistance pass through a maximum near the Curie point T_C , where the magnetoresistance reaches a colossal value. The magnetization isotherms $M(H)$ are superpositions of a magnetization that is linear in field (like that of an antiferromagnet) and a weak spontaneous magnetization. The magnetic moment per formula unit is substantially smaller than that expected under complete ferro- or ferrimagnetic ordering. The magnetizations of samples cooled in a magnetic field (FC samples) and with no field applied (ZFC samples) differ by an amount that persists up to the highest measurement fields (50 kOe). The $M(T)$ dependence obtained in strong magnetic fields is close to linear. Hysteresis loops of the FC samples are shifted along the field axis. The above magnetic and electric properties of thin films are explained in terms of two coexisting magnetic phases, which are due to strong s - d exchange coupling. © 2004 MAIK "Nauka/Interperiodica".

1. INTRODUCTION

The $Re_{1-x}A_xMnO_3$ manganites (Re is a rare earth ion; $A = Ca, Sr, Ba$) are currently attracting considerable interest because of the colossal magnetoresistance exhibited by some of them at room temperature. The best studied thus far are the compositions with Sr and Ca. Much less information is available on the $Re_{1-x}Ba_xMnO_3$ compounds, particularly, on their thin films. Only $La_{1-x}Ba_xMnO_3$ thin films with $x = 0.2$ and 0.33 have been investigated [1–3]; their room-temperature magnetoresistance R_0/R_H was observed to reach ~50% in a magnetic field $H = 0.8$ T for the former composition and $H = 5$ T for the latter. It has been pointed out that the magnetoresistance of the composition with $x = 0.33$ depends strongly on the deviation of oxygen from stoichiometry [4]. The $La_{1-x}Ba_xMnO_3$ system is obviously of considerable interest, because it exhibits very high Curie temperatures T_C (up to 362 K in the $x = 0.3$ composition) [5–7]. Such high values of T_C are due to the relatively large average radius of the A cation ($\langle r_A \rangle$); indeed, it is known that in the ABO_3 manganites T_C grows with increasing $\langle r_A \rangle$ [8, 9]. However, the misfit in size between the A cations (Re^{3+} and Ba^{2+}) reduces T_C [10].

There is currently no consensus on the crystal structure of the $Re_{1-x}Ba_xMnO_3$ compounds. For instance, in compositions with $0.2 \leq x \leq 0.4$ of the $La_{1-x}Ba_xMnO_3$

system, the hexagonal structure $R\bar{3}c$ was observed in [6], whereas stoichiometric samples of $Re_{1-x}Ba_xMnO_3$ ($Re = La, Pr$) exhibited a more complex crystal structure (according to the data from [7]), which correlates with neutron diffraction data [11]. At the same time, investigation of Raman and x-ray spectra showed that polycrystalline samples of $La_{1-x}Ba_xMnO_3$ with $x \geq 0.35$ undergo separation into the cubic phase $La_{0.65}Ba_{0.35}MnO_3$ and the hexagonal phase $BaMnO_3$ [12]. This is believed to be due to the size of the Ba^{2+} ions being too large for the cubic structure to be able to accommodate them for $x \geq 0.35$ [12].

This communication reports on a study of the crystallographic, magnetic, and electrical properties of thin $Re_{1-x}Ba_xMnO_3$ epitaxial films ($Re = La, Pr, Nd, Gd$) and interpretation of their features based on the theory of magnetic semiconductors. $Re_{1-x}Ba_xMnO_3$ films ($Re = Pr, Nd, Gd$) were obtained and characterized by us for the first time.

2. THIN-FILM PREPARATION AND EXPERIMENTAL TECHNIQUE

All the films were grown by MOCVD with an aerosol source of vapors of volatile metalorganic compounds. The aerosol was prepared by the ultrasonic method from a solution in diglyme (the total concentration of the metalorganic compounds in the solution was

0.02 mol/l). The starting volatile compounds were $Re(\text{thd})_3$ ($Re = \text{La, Pr, Nd, Gd}$), $\text{Mn}(\text{thd})_3$, and $\text{Ba}(\text{thd})_2(\text{Phen})_2$, where thd stands for 2,2,6,6-tetramethylheptane-3,5-dionate and Phen, for *o*-phenanthroline. Deposition was performed in a reactor with the substrate holder inductively heated to 800°C at an oxygen partial pressure of 3 mbar and a total pressure of 6 mbar. The deposition rate was 1 $\mu\text{m/h}$. The film thickness was varied in the range 300–400 nm. We used (001)SrTiO₃ and (001)ZrO₂(Y₂O₃) single crystal substrates. The films thus prepared were characterized by scanning electron microscopy complemented with x-ray microprobe analysis and x-ray diffraction.

The thin-film magnetization was measured with a SQUID magnetometer, and the electrical resistivity, by the four-probe technique.

3. EXPERIMENTAL RESULTS AND DISCUSSION

3.1. Structural Characteristics

X-ray diffraction measurements of the films deposited on (001)SrTiO₃ showed them to be cube-on-cube epitaxially grown single-phase perovskites. The pseudocubic lattice parameter of the perovskite phase decreased monotonically with decreasing Re^{3+} ionic radius. Only a La_{0.6}Ba_{0.4}MnO₃ film revealed the weak superstructural reflections and pseudocubic-reflection splitting expected to be observed in a rhombohedrally distorted perovskite structure (space group $R\bar{3}c$), which correlated with the behavior of this material in the ceramic state [7]. The other $Re_{0.6}\text{Ba}_{0.4}\text{MnO}_3$ films did not exhibit either peak splitting or the appearance of superstructural reflections characteristic of the rhombohedral, tetragonal, and orthorhombic distortions that can be met in the rare-earth (RE) perovskite manganites described in the literature. The rise in the symmetry to cubic can be attributed to the disorder parameter increasing with decreasing RE ion radius (and, accordingly, to the increased difference between the ionic radii of the RE element and barium, which fill the *A* sublattice of the perovskite structure in a random manner). This effect should be most pronounced for compositions with barium doping levels approaching 0.5.

A film on the (001)ZrO₂(Y₂O₃) substrate grew simultaneously in two orientations, (001) and (110). Our earlier studies of perovskite manganite films grown on (001)ZrO₂(Y₂O₃) revealed, as a rule, one orientation type only, (110) [13, 14]. We assign the appearance of the second orientation to the increase in the perovskite lattice constant caused by barium doping, which changes the lattice misfit between the film and the substrate.

3.2. Magnetic Properties

Figure 1 gives the temperature dependences of magnetization $M(T)$ of all the films studied [except the NdBaMnO film on the ZrO₂(Y₂O₃) substrate] in different magnetic fields. For the NdBaMnO film on ZrO₂(Y₂O₃), this dependence is similar to that shown in Fig. 1c. As seen from Fig. 1, at temperatures below a certain characteristic temperature T_f , each $M(T)$ curve splits in two at a certain field. The upper part of the curve was obtained in the following way. At this field, the sample was cooled from 300 down to 5 K (FC sample), after which its magnetization was measured under heating in the same field. The lower part of the curve was obtained in the same magnetic field under heating, but its cooling before the measurement proceeded differently; namely, the sample was cooled from 300 to 5 K with no field applied (ZFC sample). For $T < T_f$ the magnetization of the FC sample was higher than that of the ZFC sample; this difference was the larger, the lower the temperature and the magnetic field in which the magnetization was measured. In weak fields, the $M(T)$ curves of the ZFC sample exhibit a maximum at the temperature T_f , while for $T > T_f$ the $M(T)$ curves of the ZFC and FC samples merge. In strong fields, no maximum is observed in the $M(T)$ curves of the ZFC sample; nevertheless, the difference between the ZFC and FC curves persists up to the highest fields used, $H = 50$ kOe (except for the GdBaMnO film, for which the difference disappears for $H \leq 6$ kOe). Note that the $M(T)$ curves obtained for the NdBaMnO film on ZrO₂(Y₂O₃) in different magnetic fields are close to those observed for the film of the same composition on the SrTiO₃ substrate (Fig. 1c).

Figure 2 presents magnetization isotherms of the FC samples of GdBaMnO and NdBaMnO films grown on SrTiO₃ substrates. The isotherms of the other films studied in this work are similar to those depicted in Fig. 2. One immediately sees that the $M(H)$ curves actually represent a superposition of a weak spontaneous magnetization and a magnetization that is linear in field (like that of an antiferromagnet). Extrapolation of the linear part of the $M(H)$ curves to the point of its intersection with the M axis yielded this spontaneous magnetization, which was used to calculate the magnetic moment μ_{ex} (in $\mu_B/\text{f.u.}$). The values of μ_{ex} at 5 K are listed in the table for all the films studied in this work. The table also presents the theoretical magnetic moments μ_{th} (in $\mu_B/\text{f.u.}$) calculated for three cases of spin ordering of the Mn³⁺, Mn⁴⁺, and Re³⁺ ions; the first value was obtained taking into account ferromagnetic (FM) ordering of the Mn³⁺ and Mn⁴⁺ ions only; the second, taking into account the FM ordering of the Mn³⁺, Mn⁴⁺, and Re³⁺ spins; and the third, when the coupling between the Re³⁺ spins and the ferromagnetically ordered Mn³⁺ and Mn⁴⁺ ions is antiferromagnetic. We used the purely spin values of the ion magnetic moments: 2 μ_B for Pr³⁺, 3 μ_B for Nd³⁺, and 7 μ_B for

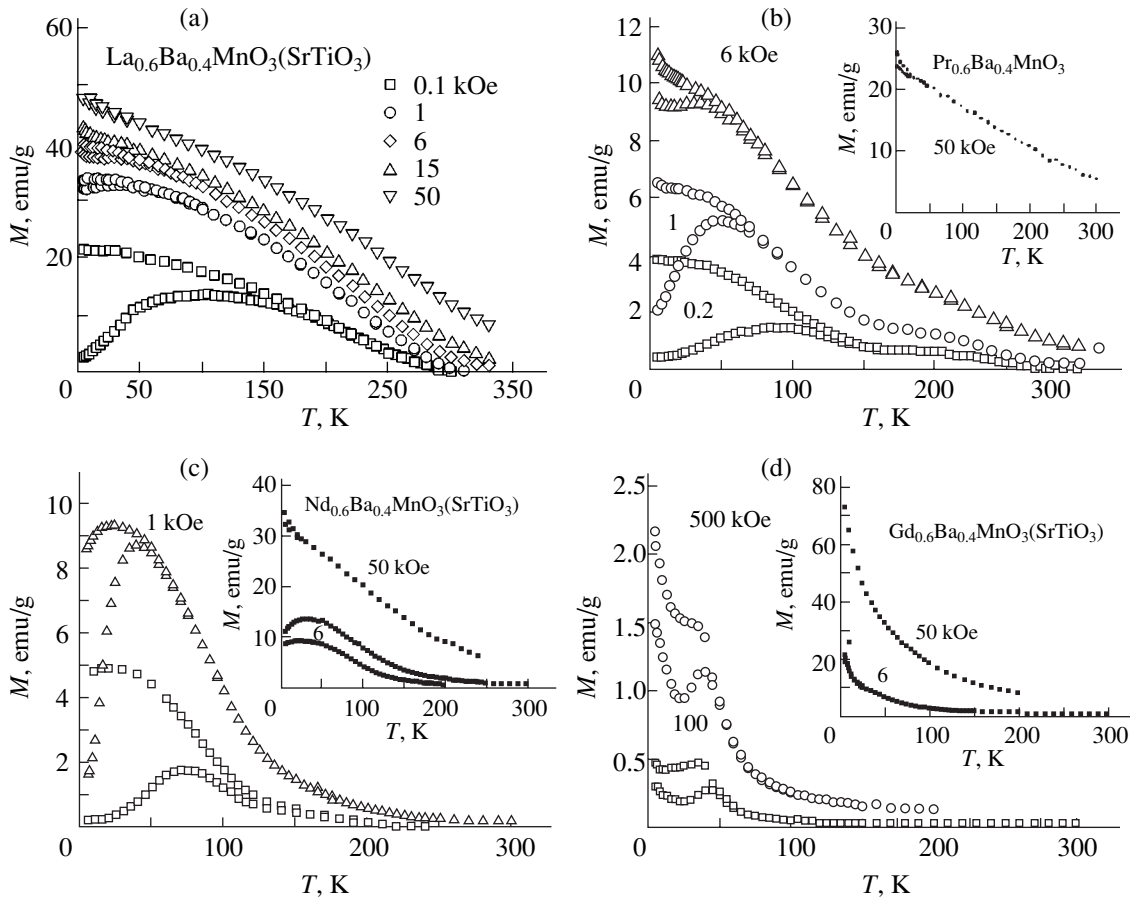


Fig. 1. Temperature dependences of the magnetization of thin $Re_{0.6}Ba_{0.4}MnO_3$ films ($Re = La, Pr, Nd, Gd$) on $SrTiO_3$ substrates measured in different magnetic fields. In the temperature region where the curves bifurcate, upper curves relate to FC samples and lower curves, to ZFC samples.

Gd^{3+} . As is evident from the table, μ_{ex} is far smaller than μ_{th} for all the films studied. This observation also argues for the coexistence of two magnetic phases in the films under study.

As seen from Figs. 1a–1c, the $M(T)$ dependence for films with $Re = La, Pr,$ and Nd in strong fields is close to linear, a feature not typical of ferromagnets. For ferromagnets, the $M(T)$ dependence is known to follow the Brillouin function [15]. The exact value of the Curie temperature T_C can obviously be extracted only from experiments performed with no external magnetic field applied, because a magnetic field suppresses and broadens the phase transition. In practice, however, the Curie point is customarily determined by extrapolating the steepest part of the $M(T)$ curve to the temperature axis, although this procedure yields, generally speaking, a certain characteristic temperature T_C' close to T_C . If the Curie temperature of the films studied here is determined in this way, T_C' will depend strongly on the field in which it is measured. The values of T_C' obtained by this technique are given in the table. From the table, it follows that the magnitude of T_C' of our films grows

strongly with increasing H . For instance, T_C' of the $LaBaMnO$ film measured in fields of 100 Oe and 50 kOe is 283 and 373 K, respectively. In magnetically uniform magnets with spontaneous magnetization, for example, in ferromagnets, this difference does not exceed 10 K.

As seen from Fig. 1d, the magnetizations of the FC and ZFC $GdBaMnO$ films differ only in weak fields and disappear altogether in $H = 6$ kOe. The shape of the $M(T)$ curves for this film differs from that for the other films studied (Figs. 1a–1c). In weak fields, as is evident from Fig. 1d, the $M(T)$ curves of the ZFC sample pass through a maximum and then exhibit a minimum followed by a steep rise. In place of the minimum seen in the curve for the ZFC sample, the $M(T)$ curve of the FC sample shows an inflection, after which a rapid rise sets in as the temperature is lowered still further. For $H \geq 6$ kOe, there is no difference between the FC and ZFC magnetizations and the magnetization falls off monotonically with increasing temperature without any of the features observed in lower fields. The magnetic moment in a field of 50 kOe at 5 K is $3.28 \mu_B/f.u.$ At the same time, the $M(T)$ curves obtained in fields $H < 6$ kOe

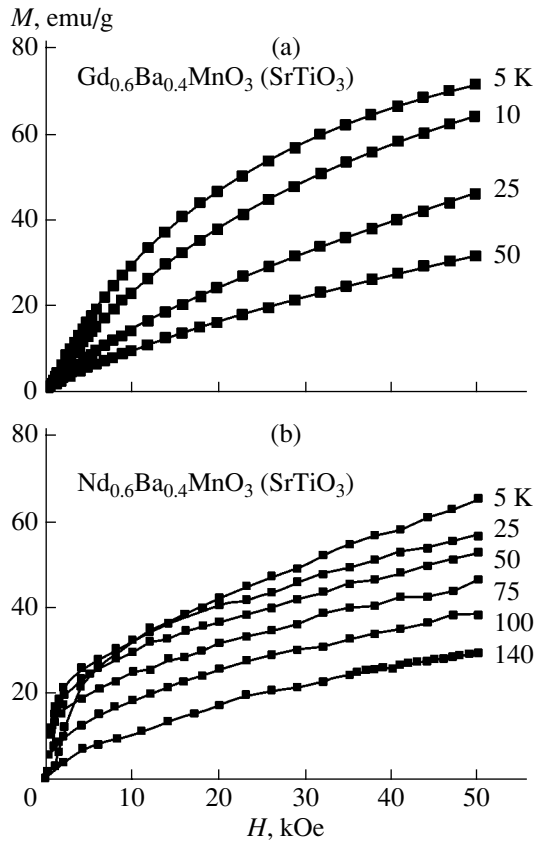


Fig. 2. Magnetization isotherms of FC thin films grown on SrTiO₃ substrates. (a) Gd_{0.6}Ba_{0.4}MnO₃ and (b) Nd_{0.6}Ba_{0.4}MnO₃.

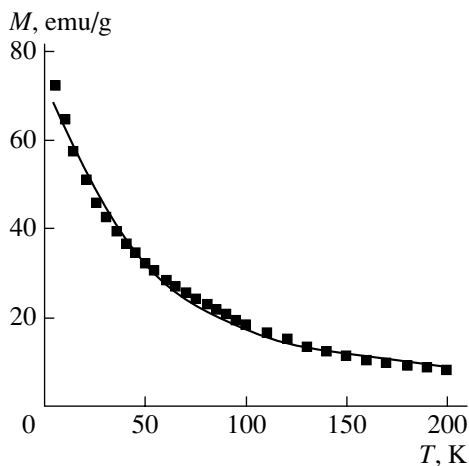


Fig. 3. Temperature dependence of the magnetization of a thin Gd_{0.6}Ba_{0.4}MnO₃ film on SrTiO₃ measured in a magnetic field of 50 kOe (points). Solid line is the Langevin function for an ensemble of superparamagnetic clusters with magnetic moments $\mu = 22 \mu_B$ and true magnetization $M_0 = 73.6$ emu/g.

resemble those characteristic of a ferrimagnet with a compensation point. In this case, μ_{th} at low temperatures should be equal to the difference between the magnetic moments of the Gd³⁺ and manganese ions, i.e., $0.6 \mu_B/f.u.$ The experimentally observed magnetic moment at $H = 500$ Oe, where the compensation point is still seen, does not exceed $0.08 \mu_B/f.u.$ (i.e., 7.5 times smaller than μ_{th}). This means that only part of the sample (about 13%) is ferrimagnetic; the remainder resides in the antiferromagnetic (AFM) state. Note that the ferrimagnetic state with a compensation point was observed earlier in a related compound, Gd_{0.67}Ca_{0.33}MnO₃ [16]. The existence of the AFM phase in the GdBaMnO film, as mentioned above, is indicated by its magnetization isotherms, shown in Fig. 2a. For $H \geq 6$ kOe, the compensation point on the $M(T)$ curves is no longer discernible and the film magnetization increases strongly, with the magnetic moment in a field of 50 kOe at 5 K becoming $\mu = 3.28 \mu_B/f.u.$ This magnetic moment is substantially larger than the value that should be expected under complete ferrimagnetic ordering of the sample ($0.6 \mu_B/f.u.$) but noticeably smaller than what should be expected in the case of complete FM ordering ($7.8 \mu_B/f.u.$). It may be conjectured that in these fields the moments of the Gd³⁺ and manganese ions are ferromagnetically ordered but the FM phase occupies only part of the sample. It thus follows that, in the GdBaMnO film residing in a state with two magnetic phases, the spontaneously magnetized phase undergoes a magnetic field-induced transition from the ferrimagnetic to FM ordering. The experimental $M(T)$ curve obtained in a field of 50 kOe can be fitted well by the Langevin function for an ensemble of superparamagnetic clusters with an FM cluster moment $\mu = 22 \mu_B$ and a true magnetization $M_0 = 73.6$ emu/g (Fig. 3):

$$M/M_0 = \coth(\mu H/kT) - kT/\mu H, \quad (1)$$

where M is the magnetization at the given temperature and M_0 is the true magnetization. Assuming the spins of the Gd³⁺ and manganese ions in a cluster to be ferromagnetically ordered, a cluster should contain ~ 3 chemical formulas. This argues for the existence of two, FM and AFM, magnetic phases in the GdBaMnO film, with the FM cluster moment being $\sim 22 \mu_B$.

The existence of a state with two magnetic phases in the films under study is corroborated by the hysteresis loops of the FC samples being displaced along the H axis. Figure 4 illustrates the displaced loops for the GdBaMnO and PrBaMnO films. A similar shift of the hysteresis loop was first observed in partially oxidized cobalt and was attributed to the exchange interaction between the ferromagnetic Co particles and their AFM shells of CoO [17]. This phenomenon was subsequently called exchange anisotropy. Observation of shifted hysteresis loops in a sample cooled in a weak magnetic field was later considered evidence of the

Magnetic properties of thin $Re_{0.6}Ba_{0.4}MnO_3$ films ($Re = La, Pr, Nd, Gd$) grown on (001)SrTiO₃ or (001)ZrO₂(Y₂O₃)

Parameter	La (SrTiO ₃)	Pr (SrTiO ₃)	Nd (SrTiO ₃)	Nd (ZrO ₂ (Y ₂ O ₃))	Gd (SrTiO ₃)
$\mu_{ex}, \mu_B/f.u.$	1.93	1.15	1.52	1.35	3.28
$\mu_{th}, \mu_B/f.u.$	3.6	3.6, 4.8, 2.4	3.6, 5.4, 1.8	3.6, 5.4, 1.8	3.6, 7.8, 0.6
$\Delta H, Oe$	57	400	230	300	380
$K_u \times 10^{-4}$	1	1.9	1.2	3.2	2.7
$T'_C, K (H = 100 Oe)$	283	160	142	145	75
$T'_C, K (H = 6 kOe)$	308	213	170	210	26
$T'_C, K (H = 50 kOe)$	373	369	260		50
$T_f, K (H = 100 Oe)$	100	95	73	75	
$T_f, K (H = 6 kOe)$	50	50	41	38	
$T_f, K (H = 50 kOe)$	30	33		33	
$T_{\rho(max)}, K$	284	116			

Note: μ_{ex} is the magnetic moment per formula unit calculated from spontaneous magnetization at 5 K, μ_{th} is the theoretical magnetic moment per formula unit, ΔH is the displacement of the hysteresis loop along the H axis measured at 5 K, K_u is the exchange anisotropy constant, T'_C is the Curie temperature determined by extrapolating the steepest part of the magnetization vs. temperature curve to intercept with the temperature axis, T_f is the temperature of the maximum in the temperature dependence of magnetization of the FC sample, and $T_{\rho(max)}$ is the temperature of the maximum in the temperature dependence of resistivity.

existence of a spin-glass-like state in the sample. Nevertheless, this phenomenon finds explanation only for the cluster spin glasses and should not exist in a true spin glass consisting only of randomly oriented spins. Kouvel [18] explained the shifted hysteresis loops that he observed in CuMn and AgMn spin glasses in terms of a nonuniform distribution of the Mn ions; he believed that the Mn-depleted regions are ferromagnetic and the Mn rich ones are antiferromagnetic, with the two being coupled by exchange interaction. The shifted hysteresis loops observed by us indicate unambiguously the presence of two magnetic phases, FM and AFM, in the films under study, with the FM and AFM regions exchange coupled. From the shift of the hysteresis loops

$$\Delta H = K_u/M_s, \quad (2)$$

where K_u is the exchange anisotropy constant and M_s is the saturation magnetization, we calculated K_u for all the above films. This constant was found to be on the order of 10^4 erg/cm³ (see table). Given the value of K_u , one can derive the exchange integral J describing one Mn–O–Mn bond through the FM/AFM interface between the phases in the film for a known surface area of this interface. Unfortunately, these data are currently lacking.

3.3. Electrical Properties

The electrical resistivity ρ and magnetoresistance $\Delta\rho/\rho = (\rho_H - \rho_{H=0})/\rho_{H=0}$ of LaBaMnO, PrBaMnO, and

NdBaMnO films on SrTiO₃ substrates were studied for $T > 78$ K in fields $H \leq 8.2$ kOe. Because of their small thickness, the GdBaMnO and NdBaMnO films on SrTiO₃ and ZrO₂(Y₂O₃) substrates, respectively, had such a high electrical resistivity that we succeeded in measuring it by the four-probe technique above T_C only. Figure 5 displays $\rho(T)$ curves for all the films on SrTiO₃ substrates studied by us, and Fig. 6 shows $(\Delta\rho/\rho)(T)$ curves for the PrBaMnO and LaBaMnO films. The magnetoresistance is negative. We see from Figs. 5 and 6 that

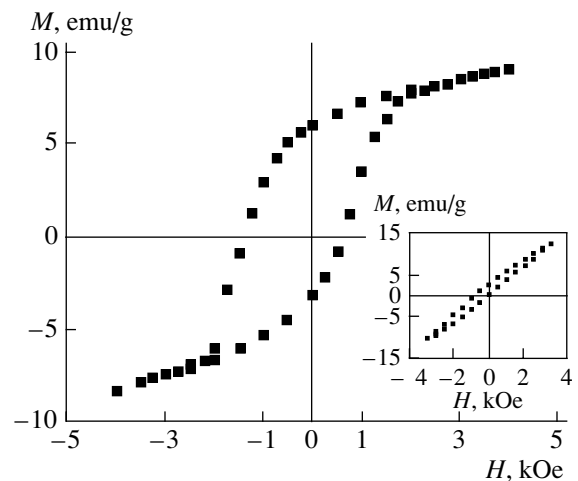


Fig. 4. Hysteresis loop of a thin Pr_{0.6}Ba_{0.4}MnO₃ film on a SrTiO₃ substrate obtained at 5 K after cooling in a magnetic field of 4 kOe. Inset: same for a thin Gd_{0.6}Ba_{0.4}MnO₃ film grown on SrTiO₃.

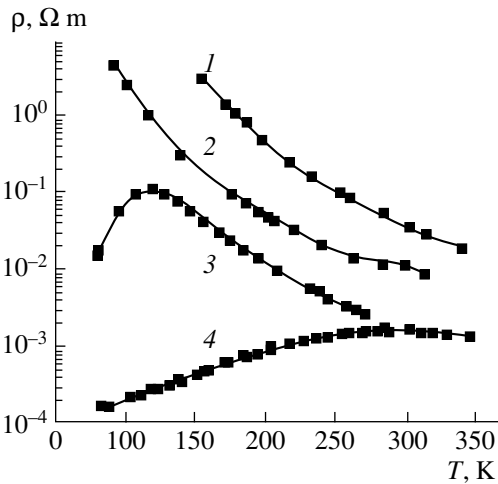


Fig. 5. Temperature dependence of the resistivity of thin $Re_{0.6}Ba_{0.4}MnO_3$ films grown on $SrTiO_3$ substrates. Re stands for (1) Gd, (2) Nd, (3) Pr, and (4) La.

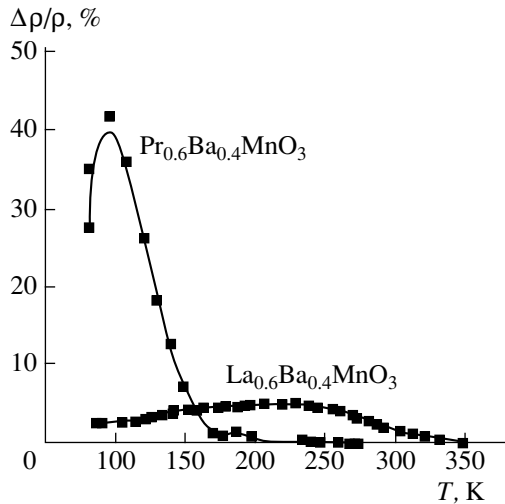


Fig. 6. Temperature dependence of the magnetoresistance of thin $Pr_{0.6}Ba_{0.4}MnO_3$ and $La_{0.6}Ba_{0.4}MnO_3$ films measured in a magnetic field of 8.5 kOe.

the $\rho(T)$ and $|\Delta\rho/\rho|(T)$ curves pass through a maximum, and the temperatures of the maximum for the latter curves are lower than those for the former curves, a situation typical of magnetic semiconductors. These temperatures are listed in the table. The maximum values of ρ are $\sim 10^{-3} \Omega \text{ cm}$ for $PrBaMnO$ and $NdBaMnO$ and $\sim 10^{-5} \Omega \text{ cm}$ for $LaBaMnO$. The magnetoresistance at the maximum is very high; as seen from Fig. 6, it is 43% for the $PrBaMnO$ films.

The presence of maxima in the $\rho(T)$ and $|\Delta\rho/\rho|(T)$ curves and the colossal magnetoresistance imply that our films are in a state with two coexisting magnetic phases induced by strong $s-d$ exchange. Obviously enough, these compositions are actually AFM semicon-

ductors $LaMnO_3$, $PrMnO_3$, $NdMnO_3$, and $GdMnO_3$ doped by Ba^{2+} ions. Judging from the value of ρ of the $LaBaMnO$, $PrBaMnO$, and $NdBaMnO$ films grown on $SrTiO_3$ substrates, their state is conducting, with the conducting FM matrix containing AFM clusters free of charge carriers (holes). This conducting state with two magnetic phases originates from a strong $s-d$ exchange and is described in review [19]. The conducting state with two magnetic phases is characterized by a strongly increased resistivity in the vicinity of the Curie temperature. One can conceive here of two mechanisms through which the magnetic impurity interaction can affect the resistivity, namely, the scattering of carriers, which reduces their mobility, and the formation of a tail of their band, which consists of localized states. Near the Curie point, the mobility of carriers decreases dramatically and they localize partially in the band tail, which accounts for the maximum in the $\rho(T)$ curve near T_C . A magnetic field delocalizes the carriers from the band tails and increases their mobility, thereby giving rise to the colossal magnetoresistance.

3.4. Experimental Evidence of the Existence of a Ferromagnetic–Antiferromagnetic Two-Phase State in Thin $Re_{0.6}Ba_{0.4}MnO_3$ Films ($Re = La, Pr, Nd, Gd$)

The above-mentioned magnetic properties resemble those of cluster spin glasses. For instance, the FC and ZFC samples have different magnetizations (Fig. 1), the magnetic moment per formula unit at 5 K is very small (see table), and the $M(T)$ curves differ in shape from the Brillouin function. Nevertheless, there are also substantial differences. Indeed, in spin glasses, the value of M of an FC sample does not depend on T for $T < T_f$, provided that the cluster size does not vary with T , which is frequently observed in spin glasses. In the case under study, the magnetization of an FC sample grows with decreasing temperature. In spin glasses, the magnetizations of FC and ZFC samples remain different only in weak fields, not over a few kilooersteds; by contrast, in the films studied by us, this difference persists up to the maximum fields used, 50 kOe (except for the $GdBaMnO$ film). These observations can be assigned to the FM phase of a two-phase sample increasing in volume with decreasing temperature. The difference in the shape of the $M(T)$ curves from that of the Brillouin function can be attributed to the same factor. The magnetization isotherms of spin glasses are nonlinear; as can be seen from Fig. 2, the films under study represent a superposition of a small spontaneous magnetization with a magnetization that is linear in field and characteristic of antiferromagnets.

The H -shifted hysteresis loops of the FC samples are not unambiguous evidence of the coexistence of two magnetic phases in them. Although this property is also observed in spin glasses, it implies only the existence of FM and AFM regions in them coupled by

exchange interaction [18]. In our earlier study [20], we estimated from this shift ΔH the exchange integral J describing one Mn–O–Mn bond through the FM/AFM interface for a number of manganites residing in the insulating FM/AFM two-phase state. It was found that $|J| \sim 10^{-6}$ eV; i.e., this value was two orders of magnitude smaller than the absolute value of the negative exchange integral between the FM layers in LaMnO_3 , $|J_1| = 5.8 \times 10^{-4}$ eV derived from neutron scattering experiments [21]. This means that the presence of a transition layer with canted spins at the above interface is unlikely. Because the charge carriers in such a two-phase sample are concentrated in its FM phase and are absent from the AFM phase, the topology of the two-phase-state is determined by Coulomb forces and the surface interface energy. As is evident from the table, the volume of the FM phase is comparable to that occupied by the AFM phase in LaBaMnO , PrBaMnO , and NdBaMnO films grown on SrTiO_3 substrates. Judging from the magnitude of ρ , the magnetic-two-phase state of these films is conducting, with the FM phase filling the space between the AFM insulating spheres. The values of K_u for the films studied by us (part of which are in the conducting two-phase state) and for the manganites studied in [20] and residing in the insulating two-magnetic-phase state are of the same order of magnitude. This fact suggests that the areas of the FM/AFM interfaces in these cases are likewise of the same order of magnitude and that the conclusions drawn in [20] can be extended to the films studied here; in other words, it is unlikely that a canted spin layer is present at the above interface.

The GdBaMnO film is apparently in the insulating magnetic-two-phase state; using the Langevin function (1), we estimated the FM cluster moment for this film at $H = 50$ kOe to be $22 \mu_B$, which shows that this cluster includes 3 formula units.

ACKNOWLEDGMENTS

This study was supported by the Russian Foundation for Basic Research, project no. 03-02-16100.

REFERENCES

1. R. von Helmolt, J. Wecker, B. Holzapfel, L. Schultz, and K. Zamwer, *Phys. Rev. Lett.* **71** (14), 2331 (1993).
2. G. C. Xiong, W. Li, H. L. Ju, R. L. Greene, and T. Venkatesan, *Appl. Phys. Lett.* **66** (13), 1689 (1995).
3. T. Kanki, H. Tanaka, and T. Kawai, *Phys. Rev. B* **64**, 224418 (2001).
4. H. L. J. Ju, J. Gopalakrishnan, J. L. Peng, Q. Li, G. C. Xiong, T. Venkatesan, and R. L. Greene, *Phys. Rev. B* **51** (9), 6143 (1995).
5. G. H. Jonker and J. H. van Santen, *Physica (Amsterdam)* **16** (2), 337 (1950); G. H. Jonker, *Physica (Amsterdam)* **22** (4), 702 (1956).
6. P. G. Radaelli, M. Marezio, H. Y. Hwang, and C. W. J. Cheong, *Solid State Chem.* **122** (3), 444 (1996).
7. A. Barnabe, F. Millange, A. Maignan, M. Hervieu, and B. Raveau, *Chem. Mater.* **10** (2), 252 (1998).
8. F. Millange, A. Maignan, V. Caignaert, Ch. Simon, and B. Raveau, *Z. Phys. B* **101** (2), 169 (1996).
9. A. Maignan, Ch. Simon, V. Caignaert, M. Hervieu, and B. Raveau, *Z. Phys. B* **99** (3), 305 (1996).
10. L. M. Rodriguez-Martinez and J. P. Attfield, *Phys. Rev. B* **54** (22), R15622 (1996).
11. Z. Jirak, E. Pollet, A. F. Andersen, J. C. Grenier, and P. Hagemuller, *Eur. J. Solid State Inorg. Chem.* **27** (3), 421 (1990).
12. C. Roy and R. C. Budhani, *J. Appl. Phys.* **85** (6), 3124 (1999).
13. O. Yu. Gorbenko, R. V. Demin, A. R. Kaul', L. I. Koroleva, and R. Szymczak, *Fiz. Tverd. Tela (St. Petersburg)* **40** (2), 290 (1998) [*Phys. Solid State* **40**, 263 (1998)].
14. A. I. Abramovich, L. I. Koroleva, A. V. Michurin, R. Szymczak, and S. Deev, *Zh. Éksp. Teor. Fiz.* **118** (2), 455 (2000) [*JETP* **91**, 399 (2000)].
15. S. V. Vonsovskii, *Magnetism* (Nauka, Moscow, 1971; Wiley, New York, 1974).
16. G. J. Snyder, C. H. Booth, F. Bridges, R. Hiskes, S. DiCarolis, M. R. Beasley, and T. H. Geballe, *Phys. Rev. B* **55** (10), 6453 (1997).
17. W. H. Meiklejohn and C. P. Bean, *Phys. Rev.* **105** (3), 904 (1957).
18. J. S. Kouvel, *J. Phys. Chem. Solids* **21**, 57 (1961); *J. Phys. Chem. Solids* **24**, 795 (1963).
19. É. L. Nagaev, *Usp. Fiz. Nauk* **166** (8), 833 (1996) [*Phys. Usp.* **39**, 781 (1996)]; *Phys. Rep.* **346**, 381 (2001).
20. R. V. Demin, L. I. Koroleva, R. Szymczak, and H. Szymczak, *Pis'ma Zh. Éksp. Teor. Fiz.* **75** (7), 402 (2002) [*JETP Lett.* **75**, 331 (2002)].
21. F. Moussa, M. Hennion, and J. Rodriguez-Carvajal, *Phys. Rev. B* **54** (21), 15149 (1996).

Translated by G. Skrebtsov

**MAGNETISM
AND FERROELECTRICITY**

The Vogel–Fulcher Law as a Criterion for Identifying a Mixed Ferroelectric–Glass Phase in Potassium Tantalate Doped with Lithium

V. V. Laguta, M. D. Glinchuk, and I. V. Kondakova

*Frantsevich Institute of Materials Science Problems, National Academy of Sciences of Ukraine,
ul. Krzhizhanovskogo 3, Kiev, 03680 Ukraine*

e-mail: dep4@materials.kiev.ua

Received October 31, 2003

Abstract—The dynamic dielectric response and the nonlinear dielectric susceptibility of $K_{1-x}Li_xTaO_3$ ($x = 0.010, 0.016, 0.030$) compounds are measured in a dc electric field in the temperature range $4 \leq T \leq 150$ K. It is found that the permittivity ϵ' of $K_{1-x}Li_xTaO_3$ samples with two lower concentrations of lithium impurities decreases in an electric field E . For samples with a lithium concentration $x = 0.030$, the permittivity ϵ' decreases in electric fields $E > 1$ kV/cm and increases in fields $E < 0.5$ kV/cm. The observed dependences of the maximum of the permittivity on the temperature and the frequency of the measuring field obey the Arrhenius law for samples with lower concentrations of lithium impurities ($x = 0.010, 0.016$) and the Vogel–Fulcher law for samples with a higher lithium concentration ($x = 0.030$). The results of the theoretical treatment performed in the framework of the random-field theory are consistent with the experimental data. It is established that the Arrhenius law is valid for dipole glass phases, whereas the Vogel–Fulcher law holds true for a mixed ferroelectric–glass phase in which the short-range and long-range polar orders coexist. The inference is made that the results of measurements of the dielectric response can be used to identify a mixed ferroelectric–glass phase in any disordered ferroelectric material. © 2004 MAIK “Nauka/Interperiodica”.

1. INTRODUCTION

Disordered ferroelectrics have attracted the particular attention of researches owing to their unusual properties. Potassium tantalate with lithium and niobium impurity ions occupying off-center positions in the crystal lattice has been frequently used as a model disordered ferroelectric material. All properties of $K_{1-x}Li_xTaO_3$ (KLT) and $KTa_{1-x}Nb_xO_3$ (KTN) compounds substantially depend on the concentration of Li^+ or Nb^{5+} off-center ions even at small $x < 0.1$ [1, 2]. In particular, the dipole glass phase with short-range polar clusters is observed at low impurity concentrations ($x < x_c$, where x_c is the critical concentration). At higher impurity concentrations ($x_0 \geq x \geq x_c$), there exists a mixed ferroelectric–glass phase in which the short-range and long-range polar orders occur simultaneously. A further increase in the impurity concentration ($x \geq x_0$) leads to the formation of a ferroelectric phase. The critical concentrations measured in the experiments are as follows: $x_c = 0.022$ for $K_{1-x}Li_xTaO_3$ ferroelectrics and $x_c = 0.008$ for $KTa_{1-x}Nb_xO_3$ ferroelectrics (see, for example, [3]). According to theoretical calculations, the critical concentration x_c and the phase diagram of disordered ferroelectrics, as a whole, are governed by the type and parameters of the distribution function of random electric fields, namely, the ratio of the most probable field E_0 to the half-width ΔE_i . The

most probable field E_0 is completely determined by the contribution of electric dipoles and is proportional to their concentration ($E_0 \sim x$) [1]. However, apart from the above contribution, the half-width ΔE_i depends on the contribution from other sources of random electric fields, for example, point charges and dilatation centers [4]. Note that the inclusion of contributions from these additional sources of random electric fields provides an explanation for the relatively high critical concentration of impurities in $K_{1-x}Li_xTaO_3$ ferroelectrics.

In the general case, the dipole glass, mixed ferroelectric–glass, and ferroelectric phases are characterized by the following ratios of the field parameters: $E_0/\Delta E_i < 1$, $E_0/\Delta E_i \geq 1$, and $E_0/\Delta E_i \gg 1$, respectively. Up to now, the problem of separating and identifying the dipole glass phase and mixed ferroelectric–glass phase in many disordered ferroelectrics, specifically in relaxors, has been extremely complicated. Although the non-ergodic behavior and processes with long relaxation times are typical of both the dipole glass and mixed ferroelectric–glass phases, these characteristics have been initially used for describing only the glass state. On the other hand, theoretical analysis of the effect of an external dc electric field on the dielectric susceptibility has demonstrated that the applied dc electric field always decreases the dielectric response in the dipole glass phase and either decreases or increases this response in the ferroelectric–glass phase [5, 6]. Therefore, the

results of measuring the nonlinear dielectric susceptibility make it possible to identify a mixed ferroelectric–glass phase. It is known that, in the model disordered ferroelectric compounds $K_{1-x}Li_xTaO_3$, the dipole glass and ferroelectric phases exist at impurity concentrations $x < x_c = 0.022$ [7] and $x \geq x_0 = 0.05$ [8], respectively. Hence, we can expect the formation of a mixed ferroelectric–glass phase in samples with intermediate concentrations of impurities. Thus, the results of measuring the nonlinear dielectric response in samples with impurity concentrations lying in the above range can be used to identify a mixed ferroelectric–glass phase. Moreover, it is reasonable to compare the experimental and theoretical dependences of the dynamic dielectric susceptibility in the lithium concentration ranges corresponding to the dipole glass and mixed ferroelectric–glass phases.

In the present work, we measured the dynamic dielectric response and the nonlinear permittivity of $K_{1-x}Li_xTaO_3$ compounds in an external dc electric field with the aim of identifying a mixed ferroelectric–glass phase. Furthermore, we proposed a new approach to the identification of the dipole glass and mixed ferroelectric–glass phases on the basis of analyzing the temperature dependence of the dynamic dielectric response. In this work, we demonstrated both experimentally and theoretically that the temperatures of the maximum of the permittivity at different frequencies of measurement obey the Arrhenius law for dipole glass phases and the Vogel–Fulcher law for a mixed ferroelectric–glass phase. Since the temperature and frequency dependences of the permittivity, as a rule, are measured in the study of disordered ferroelectrics, the proposed method for identifying the dipole glass and mixed ferroelectric–glass phases seems very promising.

2. EXPERIMENTAL TECHNIQUE AND RESULTS

We studied single crystals of the $KTaO_3$ compound doped with lithium ions at contents of 1.0, 1.6, and 3.0 at. %. The faces of crystals $3 \times 2 \times 1$ mm in size were parallel to the (001) planes. Electrodes were applied to the opposite faces of the crystal sample with the use of a silver paste.

The dielectric response was measured as a function of the frequency and temperature in an external dc electric field with a strength of up to 2000 V/cm. The measurements were performed on an HP 4275A bridge. The frequency of the ac electric field ranged from 10 kHz to 2 MHz. The temperature was varied from 300 to 4.2 K. The heating rate was 0.2–0.3 K/min.

Figures 1 and 2 show the temperature dependences of the permittivity and the dielectric loss measured at different frequencies for $KTaO_3$ samples with lithium contents of 1.0 and 1.6 at. % in a zero dc electric field. These dependences are characteristic of crystals doped with lithium at these contents. The temperature depen-

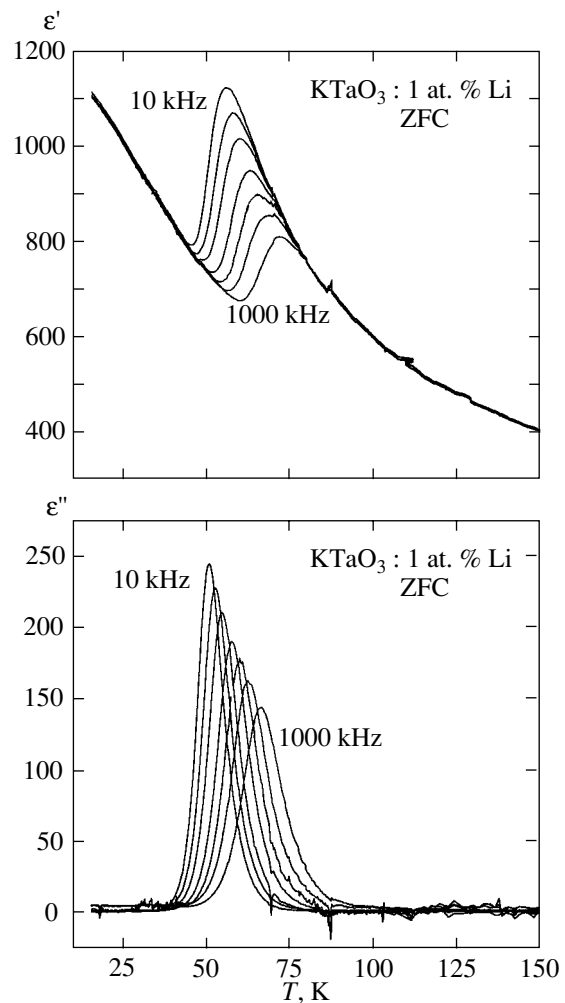


Fig. 1. Temperature dependences of the real part ϵ' and the imaginary part ϵ'' of the permittivity of $KTaO_3$: 1.0 at. % Li and their frequency dispersion.

dences of the permittivity and the dielectric loss measured at different frequencies for the $KTaO_3$: 3.0 at. % Li sample are plotted in Fig. 3. At temperatures $T < T_m$ (where T_m is the temperature of the maximum of the permittivity), the experimental dependences are characterized by a specific anomaly, namely, a stepwise decrease in the real part ϵ' and in the imaginary part ϵ'' of the permittivity at $T \approx 50$ K (see insets to Fig. 3). It can also be seen that this anomaly exhibits a hysteresis upon heating and cooling. Note that the temperature of the principal peak of the permittivity does not depend on the order in which the sample is subjected to heat treatment; i.e., it is identical upon heating and cooling. The second distinguishing feature of the anomaly at $T \approx 50$ K is that it is dispersionless. This means that, at least in the frequency range 10^4 – 2×10^6 Hz, the temperature of the jump in the permittivity ϵ does not depend on the frequency of the ac electric field.

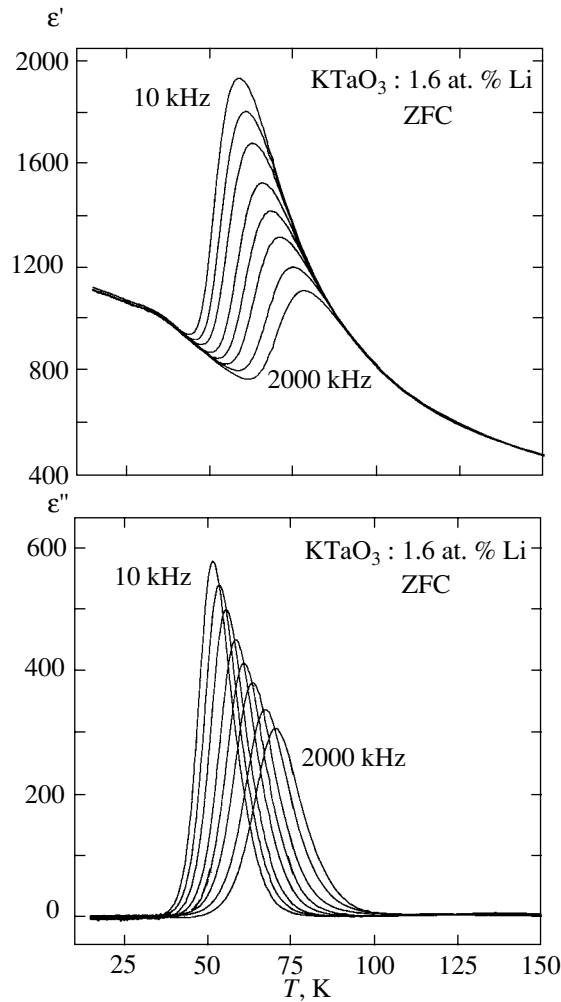


Fig. 2. Temperature dependences of the real part ϵ' and the imaginary part ϵ'' of the permittivity of KTaO_3 : 1.6 at. % Li and their frequency dispersion.

For samples doped with lithium at the three above contents, we analyzed the temperature dependences of the dispersion of the permittivity at temperatures close to T_m under the assumption that the relaxation of lith-

Dynamic characteristics of the dielectric response of $\text{K}_{1-x}\text{Li}_x\text{TaO}_3$ compounds

Parameter	x					
	0.010		0.016		0.030	
	experiment	theory	experiment	theory	experiment	theory
U , K	970	1109	994	1150	918	860
ν_0 , Hz	2.4×10^{12}	4×10^{12}	2.9×10^{12}	4×10^{12}	3.9×10^{12}	4×10^{12}
T_g , K	0	0	0	0	12	15

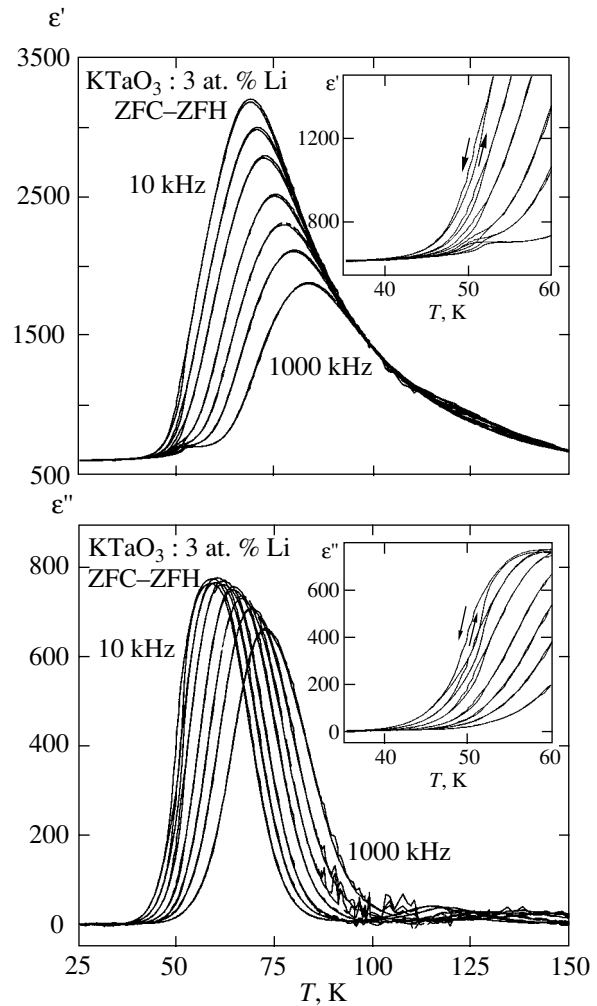


Fig. 3. Temperature dependences of the real part ϵ' and the imaginary part ϵ'' of the permittivity of KTaO_3 : 3.0 at. % Li and their frequency dispersion. The insets show the anomaly of the dielectric response at $T \approx 50$ K.

ium dipoles has a Debye character and that the frequency of dipole reorientations obeys either the Arrhenius law

$$\nu = \nu_0 \exp(-U/T_m) \quad (1)$$

or the Vogel-Fulcher law

$$\nu = \nu_0 \exp[-U/(T_m - T_g)]. \quad (2)$$

Here, the preexponential factor ν_0 , the activation barrier U , and the freezing temperature T_g are adjustable parameters. These parameters are listed in the table. Their values indicate that the dispersion of the permittivity ϵ for samples with low lithium contents (1.0, 1.6 at. %) is determined by the dynamics of individual (isolated or weakly interacting) lithium dipoles and is adequately described by the Arrhenius law, which is in good agreement with the ^7Li NMR data [1]. For samples with a higher lithium content (3.0 at. %), the dis-

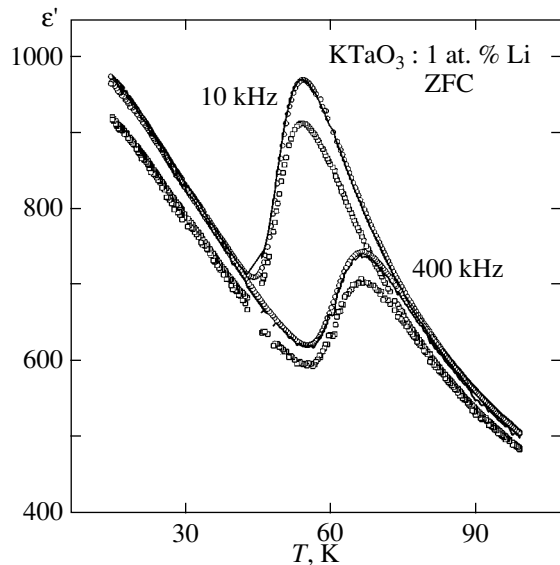


Fig. 4. Temperature dependences of the real part ϵ' of the permittivity of $\text{KTaO}_3 : 1.0 \text{ at. \% Li}$ measured under zero-field cooling (ZFC) conditions before (circles) and after (squares) application of a dc electric field $E_0 = 1.4 \text{ kV/cm}$. Solid lines represent experimental data corrected for the space-charge effect.

persion of the permittivity ϵ ceases to obey the Arrhenius law. In this case, the use of the Vogel–Fulcher law for describing the temperature dependence of the frequency of dipole reorientations leads to better agreement with the experimental data at reasonable adjustable parameters. It is this approach that is most frequently applied to the description of the dynamics of compounds containing the dipole glass phase or mixed ferroelectric–glass phase with allowance made for collective interactions.

The nonlinear effects of the permittivity were examined in an external dc electric field E . The permittivity was measured under the “field cooling” (FC) and “field cooling–zero-field heating” (FC–ZFH) conditions. After each measurement in an external dc electric field, the sample was heated to room temperature in order to eliminate the space charge. The space charge was accumulated in the immediate vicinity of the electrodes, which led to a decrease in the measured capacitance of the sample. On the other hand, the space-charge effect at low temperatures (4–150 K) can be taken into account under the assumption that there exists a temperature-independent capacitor connected in series with a capacitor of an “ideal” sample. It is evident that this additional capacitance, which depends on the electric field strength, can be determined by comparing the values of $\epsilon'(T)$ measured in the zero-field cooling (ZFC) mode immediately after applying a dc electric field and after slow heating (for 4–6 h) to 400–500 K. As an example, the temperature dependences of the permittivity $\epsilon'(T)$ measured with and without a dc electric field and experimental data, including the correction to $\epsilon'(T)$

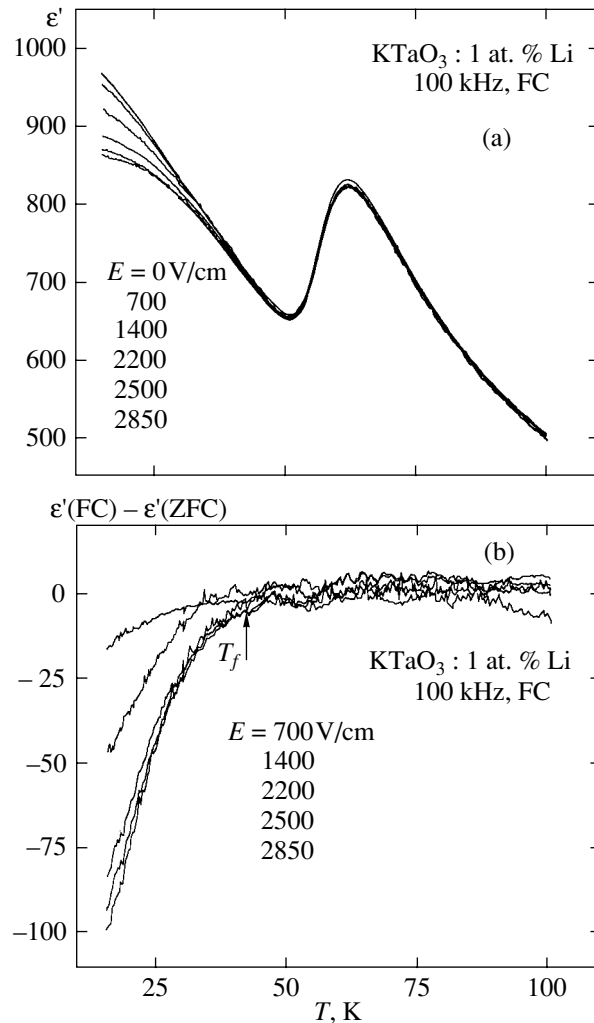


Fig. 5. (a) Effect of the dc electric field on the temperature dependence of the real part ϵ' of the permittivity of $\text{KTaO}_3 : 1.0 \text{ at. \% Li}$ measured under field-cooling (FC) conditions at a frequency of 100 kHz. (b) Temperature dependences of the nonlinear part of the permittivity ϵ' .

through the introduction of the series-connected capacitor C_0 , are presented in Fig. 4. It can be seen from this figure that the introduction of the series-connected capacitor into the circuit makes it possible to take into account the space-charge effect to sufficient accuracy.

The results of dielectric measurements under the FC conditions for the $\text{KTaO}_3 : 1.0 \text{ at. \% Li}$ compound with due regard for the space-charge effect are presented in Fig. 5a. The temperature dependence of the nonlinear part of the permittivity ϵ' , i.e., the difference $\epsilon'(T, E) - \epsilon'(T, 0)$, is depicted in Fig. 5b. It can be seen from Fig. 5 that the permittivity of the sample in an external dc electric field decreases at temperatures below the temperature T_g , which is usually referred to as the temperature of freezing of the dipole glass. It is at this temperature that the dipole system loses its ergodicity. A similar dependence $\epsilon'(T)$ is observed for the $\text{KTaO}_3 : 1.6 \text{ at. \% Li}$

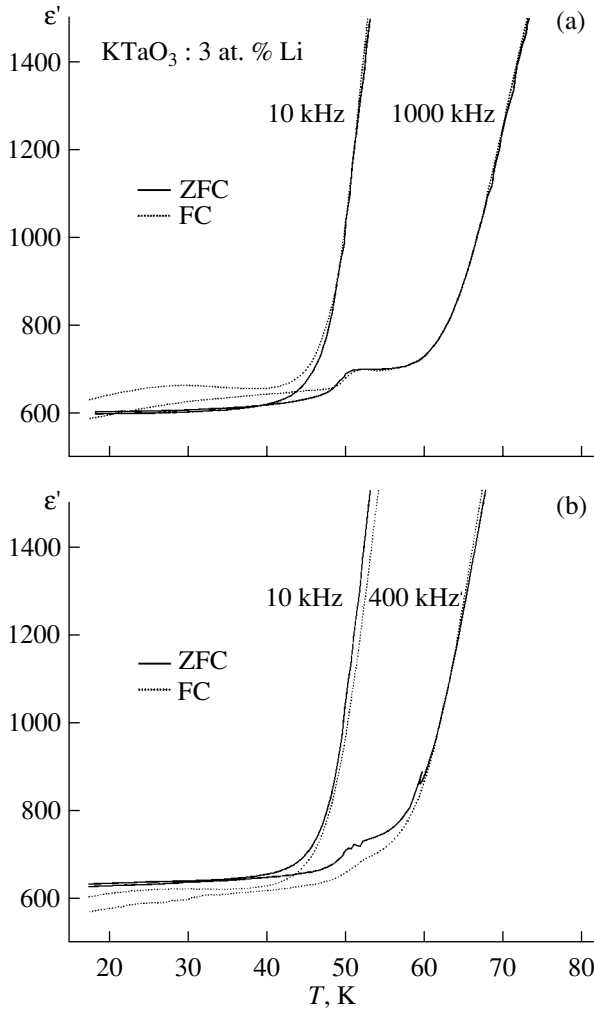


Fig. 6. Temperature dependences of the real part ϵ' of the permittivity of KTaO_3 : 3.0 at. % Li measured under ZFC (solid lines) and FC (dotted lines) conditions in dc electric fields of (a) 0.5 and (b) 2 kV/cm.

compound. For the KTaO_3 : 3.0 at. % Li sample, the dc electric field has a radically different effect on the permittivity. A profound effect of the dc electric field on the permittivity is observed only at temperatures $T < 50$ K. The permittivity ϵ' increases in weak electric fields ($E \leq 0.5$ kV/cm) at $T \leq 50$ K. However, in stronger fields $E \geq 1$ kV/cm, the permittivity ϵ' decreases; i.e., the difference $\epsilon'(T, E) - \epsilon'(T, 0)$ can be both positive and negative in sign (Figs. 6a, 6b). Moreover, the temperature dependence of the permittivity ϵ' exhibits a broad maximum in the temperature range $T < 50$ K. It is quite possible that this maximum shifts toward the high-temperature range with an increase in the frequency. However, we will not analyze this effect, because the position of the maximum cannot be determined to sufficient accuracy. Furthermore, the dc electric field substantially affects the jump in the permittivity ϵ' at $T \approx 50$ K. This anomaly decreases and completely disappears in electric fields with a strength of the order of 1–2 kV/cm.

3. DIELECTRIC SUSCEPTIBILITY IN THE FRAMEWORK OF THE RANDOM-FIELD THEORY

Let us consider the temperature and frequency dependences of the dielectric susceptibility of disordered ferroelectrics. In the general case, the dielectric susceptibility is determined by the reorientational motion of electric dipoles. In disordered ferroelectrics, the reorientation rate of electric dipoles strongly depends on random electric fields at their sites, because these fields affect the barrier between equivalent equilibrium positions of the dipoles with different orientations of the dipole moment [9]. It is obvious that the observed dielectric response can be obtained by averaging over random electric fields with allowance made for their distribution function. In [5], for electric dipoles with two possible orientations, the averaging was performed with a distribution function accounting for both the linear and nonlinear effects in external and internal (random) electric fields [10]. The relationship thus derived for the dielectric susceptibility is as follows:

$$\frac{4\pi}{\epsilon_0} \chi = \frac{Q}{1-Q}, \quad (3)$$

$$Q = \frac{2E_0}{\pi} \int_0^\infty \int_0^\infty \tanh\left(\frac{E_i}{kT}\right) \exp(-A\rho^{3/2} - C\rho^2) \times \sin(\rho E_i) \frac{\rho \cos(\rho(E + E_0L))}{1 + i\omega\tau_1(E_i)} dE_i d\rho, \quad (4)$$

$$A = \frac{32}{15} \left(\frac{\pi Ze}{2\epsilon_0}\right)^{3/2} n_1, \quad C = \frac{16\pi}{15} \left(\frac{d^*}{\epsilon_0 r_c^3}\right)^2 n r_c^3, \quad (5)$$

$$E_0 = \frac{4\pi n d^{*2}}{\epsilon_0}, \quad \tau_1 = \bar{\tau} \frac{\cosh(2E_i/kT)}{\cosh(E_i/kT)}.$$

Here, E is the external dc electric field (the ac measuring field is assumed to be very weak and tends to zero), n is the concentration of electric dipoles with dipole moment d , $d^* = d\gamma(\epsilon_0 - 1)/3$, γ is the Lorentz factor, ϵ_0 is the static permittivity of KTaO_3 as the host lattice, L is the ferroelectric order parameter (dimensionless polarization) characterizing the number of coherently oriented dipoles, n_1 is the concentration of point defects with charge Ze , r_c is the correlation length of the host lattice, and E_i stands for the internal random electric fields with a distribution function obtained in the framework of the statistical theory (see [4]). The time $\bar{\tau}$ obeys the Arrhenius law for the reorientational motion of electric dipoles between two equivalent positions separated by a barrier with height U : $\bar{\tau} = \tau_0 \exp(U/kT)$. Expression (4) was derived under the assumption that each isolated electric dipole attains equilibrium through Debye relaxation.

Therefore, relationships (3)–(5) describe the dependences of the dielectric susceptibility on the tempera-

ture, frequency, external dc electric field, parameters of the host lattice, and sources of random electric fields.

In [5], the dielectric susceptibility (nonlinear with respect to the external dc electric field) was calculated from formulas (3) and (4). These calculations demonstrated that, for parameters corresponding to a mixed ferroelectric–glass phase, the external dc electric field either decreases or increases the dielectric response, depending on the field strength and temperature. In the dipole glass phase, an external dc electric field of any strength leads only to a decrease in the dielectric response over the entire range of temperatures.

The theoretical inference made in [5] is confirmed by the experimental data presented in Figs. 5 and 6. In actual fact, the permittivity of $K_{1-x}Li_xTaO_3$ compounds with lithium concentrations $x = 0.010$ and 0.016 , which correspond to the dipole glass phase (because $x < x_c = 0.022$), decreases in an external electric field (Fig. 5). For samples with $x = 0.03$, i.e., in the mixed ferroelectric–glass phase, the external dc electric field E has a substantially different effect on the permittivity (Fig. 6). It can be seen from Fig. 6 that the permittivity ϵ' increases in weak electric fields $E \leq 0.5$ kV/cm at temperatures $T \leq 50$ K and decreases in stronger fields $E > 1$ kV/cm. This implies that the difference $\epsilon'(T, E) - \epsilon'(T, 0)$ can be both positive and negative in sign.

Now, we analyze the frequency and temperature dependences of the dielectric susceptibility in the absence of an external dc electric field ($E = 0$). The calculations were performed according to formulas (3) and (4) for the following parameters obtained earlier by the NMR technique for individual lithium ions in $K_{1-x}Li_xTaO_3$ compounds [11]: $U = 1000$ K; $\tau_0 = 10^{-13}$ s; and $x = 0.010, 0.016,$ and 0.030 . The temperature-dependent correlation lengths involved in relationships (5) were determined from an expression for the static permittivity of pure potassium tantalate (whose magnitude is proportional to the soft-mode frequency according to the Barrett formula) with the parameters taken from [12]. The values of ϵ_0 in relationships (4) and (5) were obtained from the phenomenological expression for pure $KTaO_3$: $\epsilon_0 = 48 + C/(T - T_0)$, where $C = 5 \times 10^4$ K and $T_0 \cong 12.9$ K. We also assumed that impurity point charges make a considerable contribution to the width of the random-field distribution. Since nothing is *a priori* known about the concentration and other characteristics of point defects in $K_{1-x}Li_xTaO_3$ ferroelectrics, the parameter A determined by these defects can be used as an adjustable parameter of theory and experiment. It should be emphasized that changes in the parameter A do not lead to a shift in the maximum of the dependence $\epsilon'(T)$ (i.e., $T_m = \text{const}$) and only broaden the distribution and decrease its maximum (Fig. 7). Since the temperature T_m of the maximum of the permittivity is the most important characteristic responsible for the temperature dependence of the

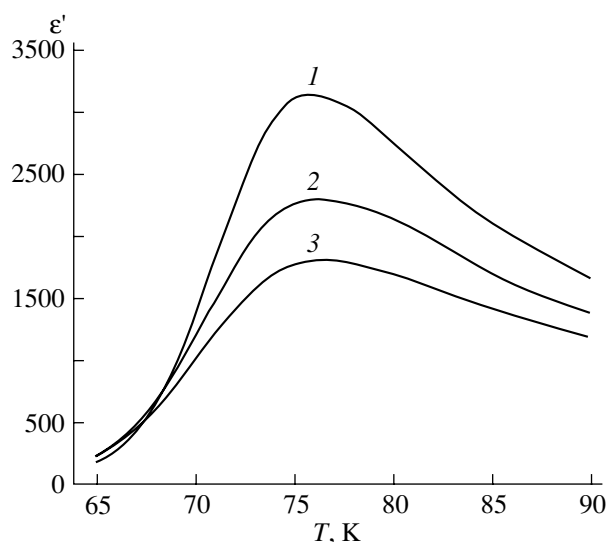


Fig. 7. Theoretical temperature dependences of the real part ϵ' of the permittivity of a $K_{1-x}Li_xTaO_3$ ferroelectric at a frequency of 10^6 Hz for different concentrations A of point charges: (1) A_1 , (2) $2A_1$, and (3) $3A_1$ (where A_1 is an arbitrary relative concentration of point charges).

relaxation rate, it is clear that the choice of the parameter A does not affect the relaxation behavior.

Figures 8a–8c present the results of calculating the permittivity $\epsilon'(\omega, T)$ according to relationships (3) and (4) for $x = 0.010, 0.016,$ and 0.030 . The temperatures $T_m(\nu)$ of the maxima of the permittivity are described by the Arrhenius law with high accuracy for the following parameters: $U = 1100$ K and $\nu_0 = 4 \times 10^{12}$ Hz for $x = 0.01$ and $U = 1150$ K and $\nu_0 = 4 \times 10^{12}$ Hz for $x = 0.016$. Our attempts to describe the dependence $T_m(\nu)$ for $x = 0.03$ in terms of the Arrhenius law with reasonable values of the parameter ν_0 were not successful. The experimental data were described only using the Vogel–Fulcher law (2) for parameters $\nu_0 = 4 \times 10^{12}$ Hz and $T_g = 15$ K.

A comparison of the calculated data with the results of dielectric measurements shows that theory adequately describes experiment and that the theoretical and experimental parameters of the Arrhenius and Vogel–Fulcher laws are close to each other (see table). Thus, the experimental investigation and theoretical analysis proved that, for $K_{1-x}Li_xTaO_3$ compounds, the Arrhenius law is valid for the dipole glass phase ($x = 0.010, 0.016$), whereas the Vogel–Fulcher law holds true for the mixed ferroelectric–glass phase ($x = 0.030$).

4. DISCUSSION

Investigations into the model disordering of $K_{1-x}Li_xTaO_3$ ferroelectrics demonstrated that the relaxation rates are adequately described by the Arrhenius law at $x < x_c$ (the dipole glass phase) and the Vogel–

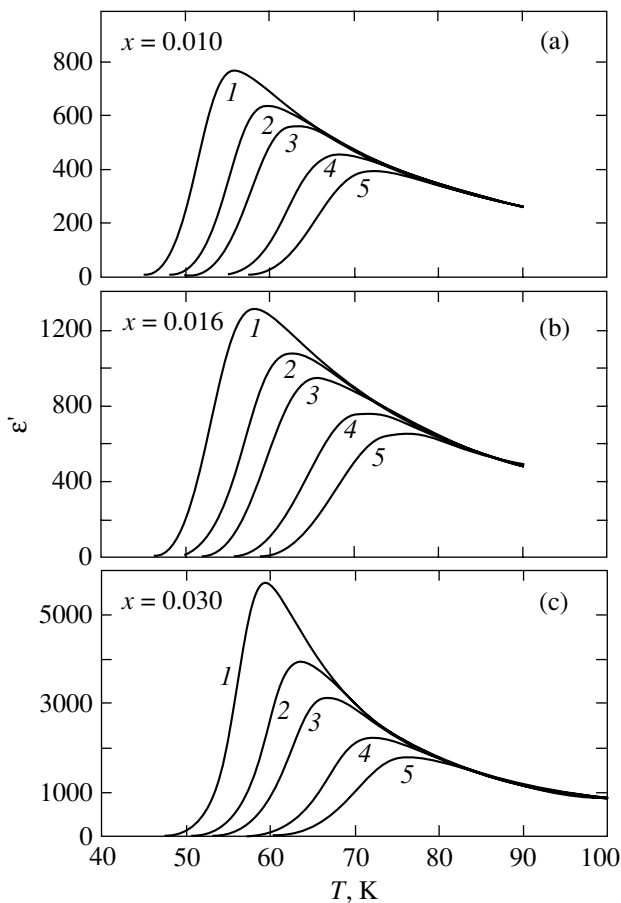


Fig. 8. Theoretical temperature dependences of the real part ϵ' of the permittivity of $K_{1-x}Li_xTaO_3$ ferroelectrics at frequencies of (1) 10^4 , (2) 4×10^4 , (3) 10^5 , (4) 4×10^5 , and (5) 10^6 Hz for lithium contents of (a) 1.0, (b) 1.6, and (c) 3.0 at. %.

Fulcher law at $x > x_c$ (the mixed ferroelectric–glass phase). It should be noted that the rate of dielectric relaxation in $K_{1-x}Li_xTaO_3$ compounds (at $x > x_c$) has already been described theoretically by the Vogel–Fulcher law in [13]. However, for many years, the dielectric spectra of $K_{1-x}Li_xTaO_3$ compounds, as a rule, were described by the Arrhenius law over the entire range of lithium concentrations [1, 2]. Therefore, the experimental data obtained in the present work for the first time confirmed the validity of the Vogel–Fulcher law for $K_{1-x}Li_xTaO_3$ compounds with lithium concentrations $x_0 > x > x_c$. Note also that a similar situation occurs with investigations into the properties of $KTa_{1-x}Nb_xO_3$ compounds. Samara [14] was the first to demonstrate that the relaxation processes in these compounds at $x > x_c = 0.008$, i.e., in the ferroelectric–glass phase, can be described by the Vogel–Fulcher law rather than by the Arrhenius law, which holds true only at low lithium concentrations, i.e., in the dipole glass phase (see [1–3] and references therein). In the study of the specific features in the properties of the dipole glass

and mixed ferroelectric–glass phases, the significant advantage of $K_{1-x}Li_xTaO_3$ and $KTa_{1-x}Nb_xO_3$ compounds over more complex disordered ferroelectrics, such as relaxors $PbMg_{1/3}Nb_{2/3}O_3$, is that the aforementioned phases can be prepared by varying the concentration of lithium or niobium ions. Taking into account that the phases of all disordered ferroelectrics are of similar nature, the results of our investigations into the dielectric properties of $K_{1-x}Li_xTaO_3$ compounds open up possibilities for identifying the dipole glass and mixed ferroelectric–glass phases in any disordered ferroelectrics, including relaxors. In particular, since the Vogel–Fulcher law has been successfully used for describing the dielectric relaxation in all relaxors (see, for example, [15, 16]), we can conclude that all ferroelectric relaxors are in a mixed ferroelectric–glass phase in which the short-range and long-range polar orders coexist. This inference is in good agreement with experimental data on the nonlinear dielectric susceptibility of $PbMg_{1/3}Nb_{2/3}O_3$ ferroelectrics, according to which an external dc electric field can lead to both a decrease and an increase in the dielectric susceptibility [6]. In our case, the same situation was observed for the $K_{1-x}Li_xTaO_3$ compound at $x = 0.03$. Furthermore, a similar effect of the external electric field E on the dielectric susceptibility, namely, an increase in the dielectric response at some temperatures T and electric field strengths E , was observed earlier for $K_{1-x}Li_xTaO_3$ compounds with $x = 0.026$ [17] and 0.035 [18].

The origin of the weak maximum in the dependence $\epsilon'(T, \nu)$ of the $K_{1-x}Li_xTaO_3$ compound ($x = 0.030$) at $T \approx 50$ K remains unclear. Similar anomalies with a hysteresis in the experimental dependences $\epsilon'(T)$ were previously observed for the $K_{1-x}Li_xTaO_3$ ferroelectric at $x = 0.026$ [7]. We cannot rule out the possibility that these anomalies in the mixed ferroelectric–glass phase are associated with the first-order phase transition in long-range order regions. Earlier [12], two types of anomalies in the dielectric response of disordered ferroelectrics in the mixed ferroelectric–glass phase were predicted theoretically. At present, we are performing further investigations with the aim of elucidating the nature of the anomalies in the dielectric response of the model disordered ferroelectrics $K_{1-x}Li_xTaO_3$.

REFERENCES

1. B. E. Vugmeister and M. D. Glinchuk, *Rev. Mod. Phys.* **62** (4), 993 (1990).
2. U. T. Hochli, K. Knorr, and A. Loidl, *Adv. Phys.* **39** (5), 405 (1990).
3. W. Kleemann, *Int. J. Mod. Phys.* **7** (13), 2469 (1993).
4. M. D. Glinchuk and V. A. Stephanovich, *J. Phys.: Condens. Matter* **6**, 6317 (1994).
5. M. D. Glinchuk and V. A. Stephanovich, *J. Phys.: Condens. Matter* **10**, 11081 (1998).
6. A. E. Glazunov and A. K. Tagansev, *Ferroelectrics* **201**, 305 (1997).

7. W. Kleemann, S. Kutz, and D. Rytz, *Europhys. Lett.* **4** (2), 239 (1987).
8. S. R. Andrews, *J. Phys.: Condens. Matter* **18**, 1357 (1985).
9. M. D. Glinchuk, E. A. Eliseev, and V. A. Stefanovich, *Fiz. Tverd. Tela (St. Petersburg)* **44** (5), 912 (2002) [*Phys. Solid State* **44**, 953 (2002)].
10. M. D. Glinchuk, R. Farhi, and V. A. Stephanovich, *J. Phys.: Condens. Matter* **9**, 10237 (1997).
11. J. J. van der Klink, D. Rytz, F. Borsa, and U. T. Hochli, *Phys. Rev. B* **27** (1), 89 (1983).
12. M. D. Glinchuk and V. A. Stephanovich, *Ferroelectrics* **169**, 281 (1995).
13. M. D. Glinchuk and V. A. Stephanovich, *Ferroelectr. Lett. Sect.* **22**, 113 (1997).
14. G. A. Samara, *Phys. Rev. Lett.* **53** (2), 298 (1984).
15. B. D. Viehland, S. Jang, and L. E. Cross, *Philos. Mag. B* **64** (3), 335 (1991).
16. E. Glazunov and A. K. Tagansev, *Appl. Phys. Lett.* **73** (6), 856 (1998).
17. U. T. Hochli, D. Rytz, J. J. Van der Klink, and F. Borsa, *Solid State Commun.* **49** (9), 863 (1984).
18. Y. Yacoby, A. Agranat, and I. Ohana, *Solid State Commun.* **45** (8), 757 (1983).

Translated by O. Borovik-Romanova

**MAGNETISM
AND FERROELECTRICITY**

Dielectric Response of a (1000 nm)SrTiO₃ Layer Epitaxially Grown on (001)La_{0.67}Ca_{0.33}MnO₃ to Temperature Variation and Electric Field

Yu. A. Boikov* and T. Claeson**

*Ioffe Physicotechnical Institute, Russian Academy of Sciences, Politekhnikeskaya ul. 26, St. Petersburg, 194021 Russia
e-mail: Yu.Boikov@mail.ioffe.ru

**Chalmers Technical University, Göteborg, 41296 Sweden

Received September 18, 2003; in final form, November 11, 2003

Abstract—The structure and dielectric characteristics of the (1000 nm)SrTiO₃ spacer in a (001)SrRuO₃ || (001)SrTiO₃ || (001)La_{0.67}Ca_{0.33}MnO₃ trilayer heterostructure grown on a (001)(LaAlO₃)_{0.3} + (Sr₂AlTaO₆)_{0.7} substrate have been studied. Both oxide electrodes, as well as the strontium titanate layer, were cube-on-cube epitaxially grown. The unit cell parameter in the SrTiO₃ layer measured in the substrate plane (3.908 ± 0.003 Å) practically coincided with that determined along the normal to the substrate surface (3.909 ± 0.003 Å). The temperature dependence of the real part of the permittivity ϵ' of the SrTiO₃ layer in the range 70–180 K fits the relation $(\epsilon')^{-1} \sim \epsilon_0^{-1} C_0^{-1} (T - T_C)$ well, where C_0 and T_C are the Curie constant and the Curie–Weiss temperature, respectively, for bulk strontium titanate crystals and ϵ_0 is the free-space permittivity. The data obtained on the temperature dependence of the permittivity of SrTiO₃ films enabled us to evaluate the effective depth of electric field penetration into the manganite electrode ($L_e \approx 0.5$ nm) and the corresponding capacitance ($C_e \approx 1 \times 10^{-6}$ F/cm²) of the interface separating the (001)SrTiO₃ layer from the (001)La_{0.67}Ca_{0.33}MnO₃ bottom electrode. © 2004 MAIK “Nauka/Interperiodica”.

1. INTRODUCTION

Thin layers of (Ba,Sr)TiO₃ (BSTO) are a promising material for application in microelectronics (RAM cells [1]) and microwave technologies (tunable filters, phase shifters, delay lines, etc. [2]). The permittivity $\epsilon = \epsilon' - i\epsilon''$ (ϵ' and ϵ'' are the real and imaginary parts of permittivity), the leakage current, and the loss tangent $\tan \delta = \epsilon''/\epsilon'$ of a BSTO film depend strongly on its microstructure, which is determined by the growth conditions and parameters of the substrate and the conducting material employed for the electrodes. The response of ϵ' of a thin BSTO film to an electric field and temperature variation is, as a rule, substantially weaker than that of a single crystal. The strong difference in the temperature and field dependences of ϵ' between thin film and bulk BSTO samples can originate, besides from microstructure degradation, from (i) the formation of an off-stoichiometric spacer at the film/electrode interface [3], (ii) a strong electric field in the bulk of the ferroelectric layer [4], (iii) biaxial mechanical strains [5] caused by lattice misfit and different temperature coefficients of linear expansion of the film and the substrate, etc.

BSTO epitaxial films are more attractive for applications than polycrystalline layers, because they are distinctly oriented (the parameters of the BSTO para- and ferroelectric phases are anisotropic [6, 7]), both with respect to the surface normal and azimuthally; in

addition, these films have no large-angle grain boundaries in the bulk, near which one usually observes deviations from stoichiometry (primarily, in oxygen). To fabricate plane-parallel film capacitors with an epitaxial BSTO spacer, thin layers of conducting perovskite-like oxides SrRuO₃ (SRO), (La,Sr)CoO₃, and YBa₂Cu₃O_{7- δ} have been employed to advantage for the bottom electrode [4, 8].

We report here on a study of the structure and dielectric parameters of a SrTiO₃ (STO) layer grown on the surface of a conducting film of manganite (120 nm)La_{0.67}Ca_{0.33}MnO₃ (LCMO). Thin films of perovskite-like manganites can be employed to advantage as electrodes in capacitive heterostructures that include a ferroelectric layer, because the effective hole concentration in their bulk at temperatures close to the ferromagnetic phase transition point is strongly magnetic-field dependent, which is conducive to the development of tunable devices (we have in mind controlling the impedance of a heterostructure with a magnetic field). There is only a very small number of publications dealing with studies of epitaxial heterostructures that include thin layers of manganites and ferroelectrics [9].

The material used for the top electrode was strontium ruthenate. As we showed earlier [10], the stray capacitance per unit area of the BSTO/SRO interface is

substantially larger than that of the BSTO/noble-metal contact.

2. EXPERIMENTAL

An excimer laser (ComPex 205, KrF, $\lambda = 248$ nm, $\tau = 30$ ns) was used for successive evaporation of the starting stoichiometric targets, LCMO \rightarrow STO \rightarrow SRO, prepared by standard ceramic technology. Trilayer heterostructures (100 nm)SRO/(1000 nm)STO/(120 nm)LCMO were grown on the surface of a single-crystal substrate (001)(LaAlO₃)_{0.3} + (Sr₂AlTaO₆)_{0.7} (LSATO) at an oxygen pressure $P_O = 0.3$ mbar. The laser radiation density on the target surface was within the limits (1.8–2.0) J/cm². In the course of the electrode preparation (LCMO, SRO), the substrate temperature was maintained at $T_s = 760^\circ\text{C}$. The temperature T_s was raised to 780°C when depositing the STO layer.

The phase composition of the heterostructures thus grown, the orientation of the films making up these heterostructures, and the lattice parameters of the electrodes and the STO spacer were studied by x-ray diffraction (Philips X'pert MRD, CuK _{α 1}, $\omega/2\theta$ and ϕ scans, rocking curves). To estimate the average grain size and the lattice distortions in the heterostructure layers, the first four Bragg peaks (of each of the layers) in the $\omega/2\theta$ scans were visualized with a four-crystal germanium monochromator ({220}Ge) forming the incident x-ray beam and a plane graphite monochromator (to measure 2θ).

The morphology of the free surface of the grown films was studied with an atomic force microscope (NanoScope-IIIa, tapping mode).

Square contact pads ($S = 200 \times 200$ μm) on the top SRO electrode, as well as windows in the STO spacer (intended for providing electrical contact with the common bottom LCMO electrode), were made by photolithography and ion milling (Ar, 500 V, 0.2 mA).

The capacitance $C = \epsilon S/d$ and the loss tangent $\tan \delta$ of the plane-parallel SRO/STO/LCMO capacitor structures (Fig. 1) were measured with an hp 4263A LCR meter ($f = 100$ kHz) at a constant bias $V_b = \pm 2.5$ V applied to the oxide electrodes and with no bias. The same LCR meter was employed to measure the resistance R of the conducting oxide electrodes in the van der Pauw geometry. The electrical resistivity ρ of the film electrodes was calculated from the relation $\rho = R\pi d_1/\ln 2$ [11], where d_1 is the conducting oxide layer thickness.

3. EXPERIMENTAL RESULTS AND DISCUSSION

The structure and dielectric and electronic properties of heteroepitaxial films of perovskite-like oxides depend strongly on the conditions of their growth and the substrate characteristics. The difference in the tem-

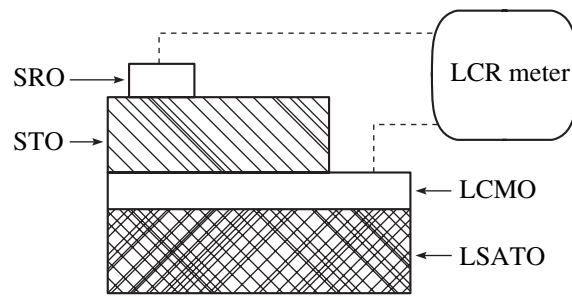


Fig. 1. Schematic of a plane-parallel capacitive heterostructure used to study the dielectric parameters of a (1000 nm)STO layer grown on the (001)LCMO || (001)LSATO surface.

perature coefficients of linear expansion and the misfit m between the lattice parameters of the deposited layer material a_L and the material of the substrate a_s [$m = (a_L - a_s)/a_s \times 100\%$] are the major factors responsible for the biaxial mechanical strains, which exert a pronounced influence on the electron transport, ferroelectricity, and ferromagnetism in thin layers of perovskite-like oxides.

The temperature coefficients of linear expansion of SRO, STO, LCMO, and LSATO are very close to one another [4]. The lattice parameters of LCMO (pseudocubic, $a_1 = 3.858$ \AA [12], $T = 300$ K) and LSATO (pseudocubic, $a_2 = 3.868$ \AA [13], $T = 300$ K) differ only slightly, $m = -0.3\%$. This was a decisive factor in choosing LSATO as the substrate material. The STO cubic cell parameter ($a_3 = 3.905$ \AA [14]) is larger than that of the LCMO ($m \approx 1\%$), which accounts for the manganite film grown on a strontium titanate substrate being acted upon by tensile in-plane mechanical stresses. Thin epitaxial LCMO films grown on the surface of strontium titanate single crystals have typically high electrical resistivities ρ and low ferromagnetic phase transition temperatures [15] (compared to those for magnetic films grown on (001)LSATO). To fabricate the top electrode with a high conductivity throughout the temperature range covered in our study (4.2–300 K), an epitaxial film of strontium ruthenate (SRO pseudocubic cell parameter 3.923 \AA [16], $T = 300$ K) was grown on the STO/LCMO/LSATO surface. Application of different conducting oxides for the bottom and top electrode materials made it possible for us to estimate (using x-ray measurements) the lattice parameters, both in the substrate plane and along its surface normal, for all layers in the trilayer heterostructures prepared.

We analyze first the data obtained on the structure and surface morphology of the layers making up the SRO/STO/LCMO/(001)LSATO heterostructure and then the data on the electrical parameters of the electrodes and the dielectric properties of the STO layer.

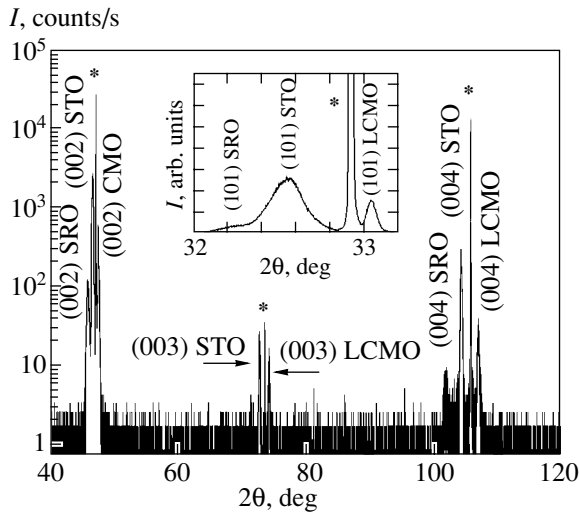


Fig. 2. X-ray diffractogram ($\text{CuK}\alpha_1$, $\omega/2\theta$) of the (001)SRO || (001)STO || (001)LCMO || (001)LSATO heterostructure obtained in the case where the plane containing the incident and reflected x-ray beams was oriented perpendicular to the substrate plane; the asterisk denotes substrate peaks. Inset shows a fragment of the diffractogram obtained from the same heterostructure in the case where the plane containing the incident and reflected x-ray beams was oriented perpendicular to (101)LSATO.

3.1. Layer Structure in the SRO/STO/LCMO Trilayer System

Our analysis of the x-ray diffractograms of the SRO/STO/LCMO heterostructure did not reveal any peaks that would indicate the presence of macroinclusions of secondary phases in its bulk or on the free surface (Fig. 2). As seen from Fig. 2, the reflections due to the electrodes (SRO and LCMO), the STO layer, and the substrate in the x-ray scans obtained were reliably resolved. The x-ray measurements ($\omega/2\theta$ and ϕ scans) suggest that the ferroelectric film and the oxide electrodes in the grown heterostructures were preferentially oriented (both azimuthally and relative to the normal to the substrate plane) with the (001) plane and the [010] direction in SRO, STO, and LCMO parallel to the (001) plane and the [010] direction in the LSATO substrate, respectively.

The lattice parameter of the (120 nm)LCMO layer in the SRO/STO/LCMO/LSATO heterostructure, which was measured along the normal to the substrate plane ($a_{\perp} = 3.837 \pm 0.003 \text{ \AA}$), was less than that in the substrate plane ($a_{\parallel} = 3.866 \pm 0.003 \text{ \AA}$) (see table). The measured parameter a_{\parallel} in the manganite layer coincided with the parameter of the pseudocubic LSATO unit cell, which implies that the LCMO film was grown coherently on the substrate surface. Because of the negative value of m , the (001)LCMO || (001)LSATO films were subjected to weak in-plane tensile stresses. An analysis of the measured diffractograms ($2\theta = 20^{\circ}$ – 120°) did not reveal any complex structure in the

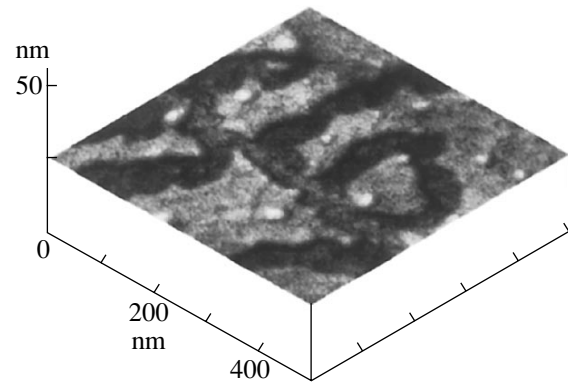


Fig. 3. AFM image of the free surface of the (120 nm)LCMO film grown coherently on (001)LSATO. The film surface clearly reveals growth steps with a height that is a multiple of the LCMO lattice parameter.

(00n)LCMO peaks that would indicate strain relaxation in the 120-nm-thick manganite film (or in part of it).

The effective cell volume $V_{\text{eff}} = a_{\perp} a_{\parallel}^2 \approx 57.32 \text{ \AA}^3$ in the LCMO layer of the SRO/STO/LCMO heterostructure differed only slightly from those for the bulk stoichiometric LCMO samples ($V_{\text{eff}} = 57.42 \text{ \AA}^3$ [12], see table).

The LCMO films grown on (001)LSATO substrates had a smooth surface (Fig. 3). The AFM image of the free surface of the manganite film clearly shows growth steps, whose height is a multiple of the LCMO lattice parameter. Unlike the thin LCMO films grown on the surface of substrates with an appreciable negative (for instance, STO) or positive (LaAlO_3) lattice misfit, on the surface of the (001)LCMO || (001)LSATO layers prepared in this study we did not see the characteristic hollows [17] decorating small-angle grain boundaries in the manganite layer.

The lattice parameter of the strontium titanate layer in the SRO/STO/LCMO heterostructure measured in the substrate plane practically coincided with that determined along the normal to the substrate surface (see table). The strain relaxation in the STO layer occurred in the course of its deposition and cooling to room temperature.

The (100 nm)SRO film in the SRO/STO/LCMO/LSATO heterostructure was subjected to in-plane compressive strains. The lattice misfit is $\sim 0.7\%$ in the case of an SRO film grown on the STO surface. The lattice parameter measured in the strontium ruthenate layer along the normal to the substrate plane ($3.973 \pm 0.003 \text{ \AA}$) was substantially larger than that in the substrate plane ($3.915 \pm 0.003 \text{ \AA}$). Epitaxial SRO films tend to grow coherently on the substrate surface even in the case of a fairly large m [18].

To estimate the average grain size in the conducting electrodes and the ferroelectric spacer in the SRO/STO/LCMO heterostructure, we made use of the data on the dependence of the FWHM ϑ of the peaks in

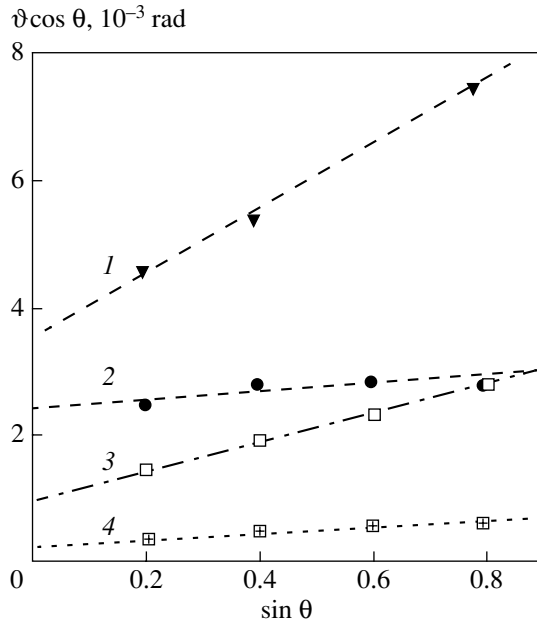


Fig. 4. $\vartheta \cos \theta$ vs. $\sin \theta$ for (1) the top SRO electrode, (2) STO spacer, (3) bottom LCMO electrode, and (4) the LSATO substrate in the (100 nm)SRO/(1000 nm)STO/(120 nm)LCMO/(500 μm)LSATO heterostructure.

the x-ray diffractograms on θ (Fig. 4). The dependence of ϑ on the effective grain size t and the average lattice distortion $\Delta a/a$ in a film can be written as [19]

$$\vartheta \cos \theta = 0.9\lambda_1/t + 2\Delta a/a \sin \theta, \quad (1)$$

where $\lambda_1 = 1.54056 \text{ \AA}$ is the x-ray wavelength. We used Eq. (1) and the $\vartheta \cos \theta$ vs. $\sin \theta$ relations extracted from x-ray measurements to derive (from the intercept that the straight line makes on the ordinate axis) the values of t for all layers in the heterostructure (see table). The slope of the graphs in Fig. 4 yielded the relative lattice distortions in the oxide electrodes and the ferroelectric spacer (see table). The largest value, $t \sim 150 \text{ nm}$, was obtained for the bottom electrode in the SRO/STO/LCMO heterostructure; this value differs little from the thickness of the manganite layer. Thus, if the LCMO layer in the SRO/STO/LCMO heterostructure consists of crystalline grains, their average size is 150 nm. The mechanisms responsible for the formation of grain boundaries in coherently grown epitaxial films were considered by us in [20]. The average grain size in

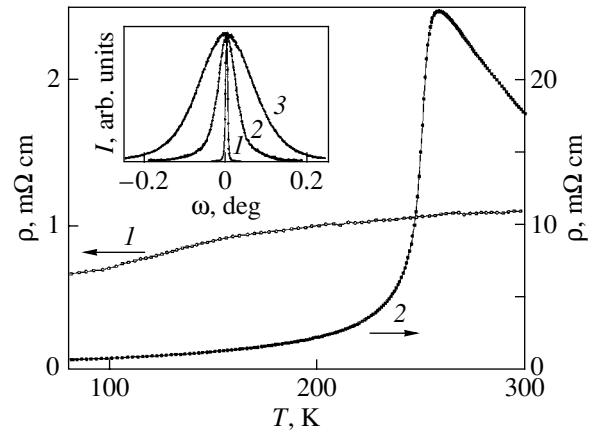


Fig. 5. Temperature dependences of the electrical resistivity ρ (1) for the (100 nm)SRO layer grown on (1000 nm)STO/(120 nm)LCMO/LSATO and (2) for the LCMO layer in the heterostructure (1000 nm)STO/(120 nm)LCMO/LSATO; $f = 100 \text{ Hz}$. Inset shows rocking curves for the (002) x-ray peak due to (1) the LSATO substrate, (2) bottom LCMO electrode, and (3) STO spacer in the SRO/STO/LCMO/LSATO heterostructure.

the STO film grown on LCMO/LSATO was 60 nm, which fits well with the corresponding data for the (700 nm) $\text{Ba}_{0.25}\text{Sr}_{0.75}\text{TiO}_3$ layer grown on the SRO/LSATO surface [4]. The values of $\Delta a/a$ were the largest for the top electrode (SRO) in the SRO/STO/LCMO heterostructure, which consisted of crystalline grains of the smallest size (see table).

The structure of the STO spacer in the SRO/STO/LCMO trilayer system obtained under the above growth conditions is governed to a considerable extent by the quality of the structure and morphology of the free surface of the manganite electrode. The small lattice misfit between LCMO and LSATO favors the formation of high-perfection epitaxial (001)LCMO films on the (001)LSATO surface [21]. The halfwidth of the rocking curve for the (002) x-ray reflection produced by the (120 nm)LCMO film in a (001)SRO || (001)STO || (001)LCMO || (001)LSATO heterostructure was in the range 0.06° – 0.09° , which is about one-half that for the STO (002) x-ray peak from the same heterostructure (see inset to Fig. 5). A rocking curve for the (002) x-ray peak from a single crystal LSATO substrate is shown for comparison in the same figure.

Parameters of layers in the heterostructure (001)SRO || (001)STO || (001)LCMO || (001)LSATO ($T = 300 \text{ K}$)

Layer	$d, \text{ nm}$	$a_{\perp}, \text{ \AA}$	$a_{\parallel}, \text{ \AA}$	$V_{\text{eff}}, \text{ \AA}^3$	$t, \text{ nm}$	$(\Delta a/a) \times 10^4$
LCMO	120	3.837	3.866	57.32	150	11
STO	1000	3.908	3.909	59.72	60	3
SRO	100	3.973	3.915	60.89	40	26

Note: The pseudocubic lattice parameter in the LSATO substrates used here was $3.867 \pm 0.003 \text{ \AA}$ (calculated from our x-ray data).

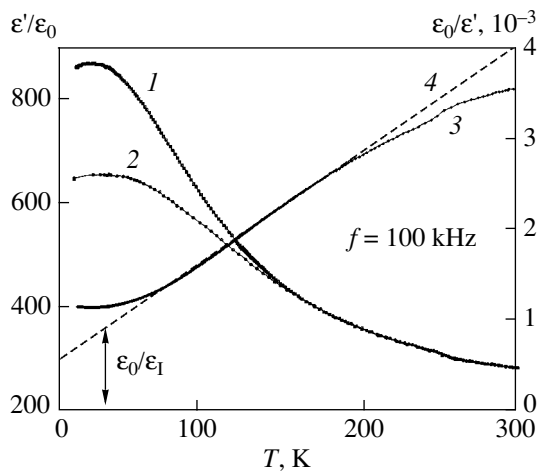


Fig. 6. Temperature dependences of (1, 2) ϵ'/ϵ_0 and (3) ϵ_0/ϵ' obtained for the STO layer in the SRO/STO/LCMO heterostructure. (1, 3) $V_b = 0$ and (2) $V_b = -2.5$ V. In the temperature interval 70–180 K, ϵ_0/ϵ' increased linearly with temperature (dashed straight line 4).

3.2. Electrical Resistivity of SRO and LCMO Films in an SRO/STO/LCMO Heterostructure

Figure 5 presents temperature dependences of ρ for the LCMO layer in the (1000 nm)STO/(120 nm)LCMO/LSATO and the (100 nm)SRO layer grown on the (1000 nm)STO/(120 nm)LCMO/(001)LSATO surface. A sharp peak on the $\rho(T)$ curve for the (120 nm)LCMO film was observed at $T_R \approx 225$ K, which fits well with the corresponding available data on bulk stoichiometric LCMO samples [22]. We did not find any systematic difference in the values of ρ for the manganite film (120 nm)LCMO/LSATO before and after the formation of a (1000 nm)STO layer on its surface. Ferromagnetic spin ordering in the SRO layer accounts for the change in the slope of the $\rho(T)$ curve at $T \sim 150$ K (Fig. 5). The absolute values of the electrical resistivity of the SRO layer in the grown heterostructures were several times those for the strontium ruthenate film grown on a single crystal substrate of strontium titanate. This should be assigned to the high density of grain boundaries and oxygen vacancies in the SRO layer grown on STO/LCMO/LSATO. For $T < 200$ K, the conductivity of both the top (SRO) and the bottom (LCMO) electrode in the SRO/STO/LCMO heterostructure was in excess of $500 \Omega^{-1} \text{ cm}^{-1}$ (Fig. 5).

3.3. Dielectric Parameters of STO Films

The temperature dependences of ϵ' of the STO layer in the SRO/STO/LCMO heterostructure measured at $V_b = 0$ and -2.5 V are presented in graphical form in Fig. 6. The maximum in the $\epsilon'(T)$ curve for $V_b = 0$ was observed at temperature $T_M \approx 25$ K. The response of ϵ' of the STO layer in the SRO/STO/LCMO heterostructure to electric field ($E \leq 25$ kV/cm) was seen to persist

up to 150 K. In bulk single-domain STO single crystals, noticeable suppression of ϵ' by the electric field was observed at temperatures below the structural phase transition point T_S (~ 65 K [7]). Nonuniform biaxial stresses may account for the substantial T_S fluctuations in the grains making up the STO layer.

The $\epsilon'(T)$ relation measured in the range 70–180 K for the STO layer in the SRO/STO/LCMO/LSATO heterostructure was fitted well by the relation

$$(\epsilon')^{-1} = \epsilon_0^{-1} C_0^{-1} (T - T_C) + \epsilon_1^{-1}, \quad (2)$$

where $T_C = 30$ K is the Curie–Weiss temperature for STO single crystals [7]; $C_0 = 0.86 \times 10^5$ K is a constant, which practically coincides with the Curie constant for bulk strontium titanate samples [23]; and $\epsilon_1 \approx 1100\epsilon_0$.

It appears natural to relate the second term in Eq. (2) to the effect of STO/electrode interfaces on the effective permittivity of the strontium titanate spacer measured in the experiment, or rather, to the stray capacitance $C_1 = \epsilon_1 S/d$ created by electric field penetration into the top and bottom electrodes, which, according to [24, 25], does not depend on either the electric field or temperature. The capacitance (per unit STO/electrode interface area) $C_e = C_1/S \approx 1 \times 10^{-6}$ F/cm² induced by the penetration of an electric field into an electrode can be cast as [24]

$$C_e = \epsilon_e / 2.3 L_e, \quad (3)$$

where ϵ_e is the permittivity of the electrode material and L_e is the characteristic depth of electric field penetration into the electrode. We could not find any literature data on the value of the low-frequency ($f < 1$ MHz) permittivity of LCMO. A rough estimate of L_e in a film of a perovskite-like manganite can be gained from the high-frequency permittivity $\epsilon \approx 8.5\epsilon_0$ reported in [26]. Assuming the contributions to C_e from the top and bottom ferroelectric/electrode interfaces in the SRO/STO/LCMO heterostructure to be approximately equal and using Eq. (3) for the characteristic electric field penetration depth into the manganite electrode, we obtained $L_e \approx 5$ Å. The characteristic electric field penetration depth into the manganite electrode exceeds the value of L_e for noble metals by nearly an order of magnitude [24]. According to [24], L_e can be cast as

$$L_e^2 = 2\epsilon_e E_F / 3ne^2, \quad (4)$$

where E_F is the Fermi energy and n is the carrier concentration in the electrode. With $n \approx 6 \times 10^{21} \text{ cm}^{-3}$ (hole concentration in the LCMO electrode in accordance with the chemical formula) and the effective hole mass $m^* \approx 2.5m_0$ [22] (this value of m^* was used to estimate E_F ; m_0 is the free electron mass), Eq. (4) yields for L_e a value of 1.5 Å. The fairly large difference (three to four times) between the value of L_e derived from the exper-

imental data on the temperature dependence of ϵ' for the STO spacer and that calculated using Eq. (4) indicates that the hole concentration in the LCMO layer near the interface with the ferroelectric layer is substantially lower than that in the bulk of the manganite layer. The decrease in the hole concentration in the LCMO layer near the STO/LCMO interface may be associated with its depletion in oxygen. It is the high concentration of oxygen vacancies in the near-surface layer that accounted for the drop in the magnetization of thin (<50 Å) LCMO films with a decrease in their thickness [27].

As the temperature increased in the range 200–255 K, ϵ' of the STO layer in the SRO/STO/LCMO heterostructure decreased more slowly than predicted by Eq. (2) (Fig. 6). Among the factors responsible for the features in the $\epsilon'(T)$ relation appearing at temperatures close to the ferromagnetic phase transition point, one could mention, in addition to the variation in the effective hole concentration, that (i) the lattice parameters in the LCMO layer undergo a sharp change in this temperature interval (the Jahn–Teller distortion), which cannot but affect the effective permittivity of the manganite electrode; (ii) the walls separating the ferromagnetic from antiferromagnetic domains in the LCMO layer and polarons may contribute to ϵ'_1 ; and (iii) the inductance of the bottom electrode changes strongly in the above temperature interval, which may influence the measured effective capacitance of the SRO/STO/LCMO heterostructure.

The suppression of ϵ' by an electric field was observed to be most pronounced at temperatures close to T_M (see Fig. 6 and inset to Fig. 7). No hysteresis was observed in the measured $\epsilon'(V_b)$ relations within the 4.2- to 150-K interval (V_b was varied in the order $0 \rightarrow +2.5 \text{ V} \rightarrow 0 \rightarrow -2.5 \text{ V} \rightarrow 0$ in steps of 0.05 V; see inset to Fig. 7). The maximum in the $\epsilon'(V_b)$ relations obtained for STO films in the SRO/STO/LCMO heterostructures grown was found to be slightly shifted toward positive values of V_b . The lack of symmetry in the $\epsilon'(V_b)$ curve with respect to the point $V_b = 0$ is partially associated with the existence of a built-in electric field in the bulk of the ferroelectric layer, which formed because the work functions of the bottom (LCMO) and top (SRO) electrodes were different.

For $T < 200 \text{ K}$, $\tan \delta (V_b = 0)$ for the STO spacer did not exceed 0.03 and increased approximately linearly with temperature (Fig. 7). Application of a bias of $\pm 2.5 \text{ V}$ to the oxide electrodes brought about a slight decrease in $\tan \delta$ (see inset to Fig. 7). The sharp peak in the $\tan \delta (T)$ curve is due to the low conductivity of the manganite electrode at temperatures close to the ferromagnetic phase transition point. The maximum values of the loss tangent were measured on the SRO/STO/LCMO capacitive heterostructure at the

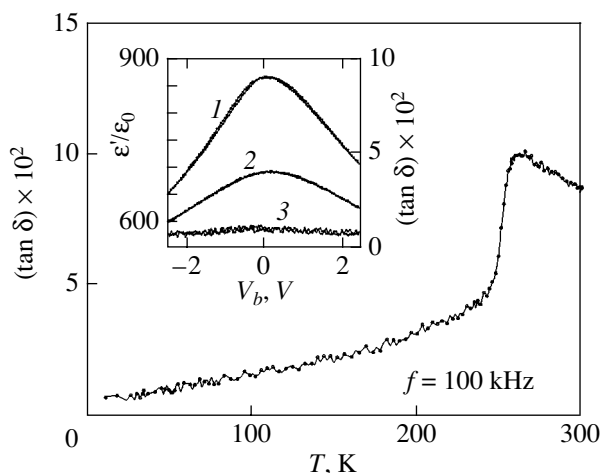


Fig. 7. Temperature dependence of $\tan \delta$ for a plane-parallel SRO/STO/LCMO capacitive structure. Inset shows the (1, 2) $\epsilon'/\epsilon_0(V_b)$ and (3) $\tan \delta (V_b)$ dependences measured for the STO layer in the SRO/STO/LCMO heterostructure at temperature T equal to (1) 25 and (2, 3) 77 K.

same transition temperature at which the maximum in the $\rho(T)$ dependence for the LCMO electrode was observed.

4. CONCLUSIONS

The strontium titanate layer ($d \leq 1000 \text{ nm}$) grown at $T_s = 780^\circ\text{C}$ and $P_O = 0.3 \text{ mbar}$ on the surface of a (001)LCMO || (001)LSATO epitaxial film consists of grains with a lateral size of $\sim 60 \text{ nm}$. The crystal grains in the STO layer show distinct preferential orientation (both azimuthal and relative to the normal to the substrate surface). Mechanical strains in the (1000 nm)STO spacer in the SRO/STO/LCMO/LSATO heterostructure relax to a considerable extent in the course of deposition and cooling of the heterostructure from T_s to 300 K. For $T < 180 \text{ K}$, the characteristic electric field penetration depth into the manganite (LCMO) electrode is about 5 \AA . Because of the relatively large value of L_e , the stray capacitance of the STO/LCMO interface may exert considerable influence on the pattern of the temperature dependence of ϵ' of the ferroelectric layer.

ACKNOWLEDGMENTS

This study was supported in part by the program “Low-Dimensional Quantum Nanostructures.”

REFERENCES

1. C. S. Hwang, Mater. Sci. Eng. B **56** (2–3), 178 (1998).
2. J. P. Hong and J. S. Lee, Appl. Phys. Lett. **68** (21), 3034 (1996).

3. S. K. Streiffer, C. Basceri, C. B. Parker, S. E. Lash, and A. I. Kingon, *J. Appl. Phys.* **86** (8), 4565 (1999).
4. Y. A. Boikov and T. Claeson, *Physica B (Amsterdam)* **311** (3–4), 250 (2002).
5. N. A. Pertsev, A. K. Tagantsev, and N. Setter, *Phys. Rev. B* **61** (2), R825 (2000).
6. W. J. Merz, *Phys. Rev.* **91** (3), 513 (1953).
7. R. C. Neville, B. Hoeneisen, and C. A. Mead, *J. Appl. Phys.* **43** (5), 2124 (1972).
8. Yu. A. Boikov and T. Claeson, *Physica C (Amsterdam)* **336** (3–4), 300 (2000).
9. M. Tachiki, M. Noda, K. Yamada, and T. Kobayashi, *J. Appl. Phys.* **83** (10), 5351 (1998).
10. Yu. Boikov and T. Claeson, *Appl. Phys. Lett.* **80** (24), 4603 (2002).
11. T. I. Kamins, *J. Appl. Phys.* **42** (9), 4357 (1971).
12. C. J. Lu, Z. L. Wang, C. Kwon, and Q. X. Jia, *J. Appl. Phys.* **88** (7), 4032 (2000).
13. Specification of the Kristek Company Supplying the LSATO Sublayers.
14. R. W. J. Wyckoff, *Crystal Structure*, 2nd ed. (Interscience, New York, 1964), Vol. 2, p. 394.
15. Yu. A. Boikov, D. Erts, and T. Claeson, *Mater. Sci. Eng. B* **79** (2), 133 (2001).
16. J. C. Jiang, W. Tian, X. Pan, Q. Gan, and C. B. Eom, *Mater. Sci. Eng. B* **56** (2–3), 152 (1998).
17. Yu. A. Boïkov, T. Claeson, and A. Yu. Boïkov, *Fiz. Tverd. Tela (St. Petersburg)* **45** (6), 1040 (2003) [*Phys. Solid State* **45**, 1090 (2003)].
18. R. A. Rao, Q. Gan, and C. B. Eom, *Appl. Phys. Lett.* **71** (9), 1171 (1997).
19. E. D. Specht, R. E. Clausing, and L. Heatherly, *J. Mater. Res.* **5** (11), 2351 (1990).
20. Yu. A. Boïkov, V. A. Danilov, and A. Yu. Boïkov, *Fiz. Tverd. Tela (St. Petersburg)* **45** (4), 649 (2003) [*Phys. Solid State* **45**, 681 (2003)].
21. Yu. A. Boïkov, T. Claeson, and A. Yu. Boïkov, *Zh. Tekh. Fiz.* **71** (10), 54 (2001) [*Tech. Phys.* **46**, 1260 (2001)].
22. Y. Tokura, in *Colossal Magnetoresistive Oxides*, Ed. by Y. Tokura (Gordon and Breach, Amsterdam, 2000), p. 1.
23. A. D. Hilton and B. W. Ricketts, *J. Phys. D: Appl. Phys.* **29** (5), 1321 (1996).
24. H. Y. Ku and F. G. Ullman, *J. Appl. Phys.* **35** (2), 265 (1964).
25. J. G. Simmons, *Appl. Phys. Lett.* **6** (3), 54 (1965).
26. A. V. Boris, N. N. Kovaleva, A. V. Bazhenov, A. V. Samoilov, N.-C. Yeh, and R. P. Vasquez, *J. Appl. Phys.* **81** (8), 5756 (1997).
27. U. P. Wad, A. S. Ogale, S. B. Ogale, and T. Venkatesan, *Appl. Phys. Lett.* **81** (18), 3422 (2002).

Translated by G. Skrebtsov

MAGNETISM AND FERROELECTRICITY

Theory of Switching of Multiaxial Ferroelectrics (Initial Stage)

M. A. Zakharov*, S. A. Kukushkin**, and A. V. Osipov**

* Novgorod State University, Novgorod, 173003 Russia

** Institute of Problems of Mechanical Engineering, Russian Academy of Sciences,
Vasil'evskii Ostrov, Bol'shoi pr. 61, St. Petersburg, 199178 Russia

e-mail: ksa@math.ipme.ru

Received November 24, 2003

Abstract—The classical theory of nucleation and growth is used to study the thermodynamics and kinetics of switching of multiaxial ferroelectrics. The initial stage of 180° - and 90° -domain switching is studied in the tetragonal, orthorhombic, and trigonal phases. The multidimensional kinetic theory of first-order phase transitions is applied to describe the initial stage of switching of ferroelectric crystals in the general case where three-dimensional growth (along the radius and height) of repolarized domains occurs. The energy of nucleus formation is calculated in the vicinity of the saddle point of an activation barrier in the space of sizes and shapes, and the dependence of the critical domain size on the switching field is found. The two-dimensional Fokker–Planck kinetic equation is reduced to a one-dimensional Zel'dovich equation, and a stationary solution to the Zel'dovich equation is obtained. The diffusion coefficients are derived in the size space for the normal and layer-by-layer mechanisms of domain growth. The main characteristic of the initial switching stage, namely, the steady-state flux of repolarized domains, is found as a function of the applied field. © 2004 MAIK “Nauka/Interperiodica”.

1. INTRODUCTION

This work is the continuation of our studies [1, 2] dealing with the development of a kinetic theory of switching of ferroelectrics and related materials. In those papers, we showed that the role of an applied electric field during the switching of ferroelectrics is analogous to that of supersaturation or supercooling during conventional phase transitions in solutions and melts. This analogy allows us to apply the classical theory of nucleation and growth to develop a theory of switching of ferroelectrics.

This work deals with the thermodynamic and kinetic description of the initial switching stage in multiaxial ferroelectrics, i.e., the stage of the fluctuation formation of nucleation centers of a new repolarized phase. An important feature of such crystals (typically represented by barium titanate BaTiO_3) is that the order parameter that appears has several components. As a consequence, during the repolarization of a ferroelectric, both 180° and 90° domains can form depending on the direction of the applied field. The kinetic description of the nucleation and growth of 180° domains in multiaxial ferroelectrics does not differ radically from the description of repolarization of uniaxial ferroelectrics [1]. Therefore, in this work, particular attention is given to the thermodynamics and kinetics of nucleation of 90° domains.

Another specific feature of the theory described below is the consideration of the general case of three-dimensional domain growth. In our previous studies [1, 2], the growth of nucleation centers was implicitly

assumed to be two-dimensional, since we took into account only radial domain growth. The presence of two degrees of freedom for repolarized domains does not allow us to apply the “traditional” one-dimensional kinetic theory; it requires a two-dimensional Fokker–Planck kinetic equation. To analyze and solve the corresponding equations, we use the multidimensional kinetic theory of first-order phase transitions proposed by Shneĭdman [3] and then developed in [4, 5].

This paper is organized as follows. In Section 2, we study the thermodynamics of switching of a multiaxial ferroelectric, making allowance for various symmetry types of the pyroelectric phase. In particular, we consider switching in the tetragonal, orthorhombic, and trigonal low-symmetry phases. In Section 3, the kinetics of the initial switching stage is studied using the multidimensional kinetic theory of first-order phase transitions. We introduce a two-dimensional nonequilibrium distribution function of repolarized domains over the number of unit cells and the corresponding two-dimensional Fokker–Planck (Zel'dovich) kinetic equation and find the domain critical size as a function of the switching field. The two-dimensional kinetic equation is reduced to a one-dimensional Zel'dovich equation, and the main kinetic characteristic of the initial switching stage, namely, the steady-state flux of repolarization centers, is determined. In Section 4, we discuss the results and compare them qualitatively with the experimental data on barium titanate.

2. THERMODYNAMICS OF SWITCHING

Let us consider a multiaxial ferroelectric crystal in a spatially uniform (single-domain) state at a temperature below the Curie point. For definiteness, the high-symmetry phase of the crystal is assumed to belong to point symmetry group $m3m$. A typical example of a ferroelectric whose paraelectric phase has this symmetry is barium titanate BaTiO_3 .

Let the crystal be placed in an external electric field \mathbf{E} . The Cartesian coordinate system is chosen so that the x , y , and z axes are directed along the corresponding fourfold rotation axes of the cubic group $m3m$ of the initial high-symmetry phase of the crystal. In this case, the incomplete thermodynamic potential of the multiaxial ferroelectric in the external electric field at a temperature near the Curie point has the form [6]

$$\begin{aligned} \Phi = & \Phi_0(p, T) + \frac{1}{2}\alpha(T - T_C)\eta^2 + \frac{1}{4}\beta_1\eta^4 \\ & + \frac{1}{2}\beta_2(\eta_x^2\eta_y^2 + \eta_y^2\eta_z^2 + \eta_z^2\eta_x^2) - a\eta\mathbf{E}, \end{aligned} \quad (1)$$

where $\boldsymbol{\eta} = \{\eta_x, \eta_y, \eta_z\}$ is the order parameter of the proper ferroelectric phase transition, which transforms like a polar vector; $\Phi_0(p, T)$ is the part of the thermodynamic potential that is independent of the order parameter; p and T are the pressure and temperature of the medium where the crystal is placed, respectively; α , β_1 , and β_2 are the coefficients of expansion of the thermodynamic potential in powers of η ; T_C is the Curie temperature; and a is a positive constant.

Minimizing thermodynamic potential (1), we obtain the following relation between the order-parameter components and the external field:

$$\begin{aligned} \frac{\partial\Phi}{\partial\eta_i} = & \alpha(T - T_C)\eta_i + \beta_1\eta^2\eta_i \\ & + \beta_2(\eta^2 - \eta_i^2)\eta_i - aE_i = 0, \end{aligned} \quad (2)$$

$i = x, y, z.$

Using the explicit form of Gibbs potential (1), we can derive a relation between the polarization vector \mathbf{P} and the order parameter $\boldsymbol{\eta}$,

$$P_i = -\frac{\partial\Phi}{\partial E_i} = a\eta_i, \quad i = x, y, z, \quad (3)$$

where the equilibrium values of the order-parameter components are determined by the solutions to system (2).

We first consider the case of a zero external field ($\mathbf{E} = 0$). It follows from system (2) that, in the absence of an electric field at temperatures above the Curie point, the high-symmetry phase is stable ($\eta = 0$). When studying switching, we are interested in the temperature range below the Curie point, where a stable state is characterized by a nonzero order parameter (low-symmetry phase) and, hence, a nonzero polarization. It

should be noted that, unlike uniaxial ferroelectrics, which have a single low-symmetry phase, multiaxial ferroelectrics can have two or more low-symmetry phases, each of which is stable in the corresponding temperature range. For example, at $T < T_C$, thermodynamic potential (1) allows the existence of three different low-symmetry phases [6]. One low-symmetry phase, which will be called phase I, corresponds to the following solutions to system (2):

$$\begin{aligned} \eta_{i1,20}^2 = \eta_{j1,20}^2 = 0, \quad \eta_{k1,20}^2 = & \frac{\alpha(T_C - T)}{\beta_1}, \\ P_{i1,20}^2 = P_{j1,20}^2 = 0, \quad P_{k1,20}^2 = & a^2 \frac{\alpha(T_C - T)}{\beta_1}, \end{aligned} \quad (4)$$

$$i, j, k = x, y, z.$$

The second low-symmetry phase (phase II) corresponds to a different type of solutions to system (2):

$$\begin{aligned} \eta_{i1,20}^2 = \eta_{j1,20}^2 = \frac{\alpha(T_C - T)}{2\beta_1 + \beta_2}, \quad \eta_{k1,20}^2 = 0, \\ P_{i1,20}^2 = P_{j1,20}^2 = a^2 \frac{\alpha(T_C - T)}{2\beta_1 + \beta_2}, \quad P_{k1,20}^2 = 0, \end{aligned} \quad (5)$$

$$i, j, k = x, y, z.$$

Finally, solutions of the type

$$\begin{aligned} \eta_{x1,20}^2 = \eta_{y1,20}^2 = \eta_{z1,20}^2 = \frac{\alpha(T_C - T)}{3\beta_1 + 2\beta_2}, \\ P_{x1,20}^2 = P_{y1,20}^2 = P_{z1,20}^2 = a^2 \frac{\alpha(T_C - T)}{3\beta_1 + 2\beta_2} \end{aligned} \quad (6)$$

are related to the third possible low-symmetry phase (phase III).

The appearance of a nonzero order parameter below the Curie point is caused by a change (lowering) of the symmetry of the ferroelectric crystal. In particular, solutions (4) correspond to the tetragonal point group $4mm$; solutions (5), to the orthorhombic point group $mm2$; and phase III [solutions (6)] belongs to the trigonal point group $3m$ [6]. The stability of a low-symmetry phase in a certain temperature range is determined by the relations between the expansion coefficients of thermodynamic potential (1). Therefore, to describe the switching of a multiaxial ferroelectric, one has to take into account the specific features of the low-symmetry phase that exists under given thermodynamic conditions.

Under given thermodynamic conditions, the quantitative measure of the metastability of a system undergoing a first-order phase transition is the difference in chemical potential between the parent and new phases; the time evolution of this quantity allows complete description of the transition kinetics. For first-order phase transitions occurring in solutions or melts, this quantity is called supersaturation or supercooling. To develop a kinetic theory of phase transformation in an

arbitrary metastable condensed system (e.g., in the course of repolarization of a ferroelectric, magnetization reversal of a ferromagnet, martensitic transformations, etc.), it is necessary to define the corresponding analog of supersaturation or supercooling. In particular, in the kinetic theory of switching of uniaxial ferroelectrics [1], where a phase transition is described by a one-component order parameter, we introduced quantities $\Delta P = |P_z - P_{z10}|$ and $\xi_P = |P_z - P_{z10}|/|P_{z10}| = \Delta P/|P_{z10}|$, which we call repolarization and relative repolarization, respectively. To describe the switching of uniaxial ferroelastic ferroelectrics, we also introduced reformation in addition to repolarization [2].

To thermodynamically describe the switching of multiaxial ferroelectrics where an order parameter has several components, it is necessary to generalize the concepts of repolarization and relative repolarization introduced earlier. To this end, we introduce the following quantities characterizing the metastability of a multiaxial ferroelectric:

$$\Delta\eta = |\eta - \eta_{10}|, \quad \xi_\eta = \frac{|\eta - \eta_{10}|}{|\eta_{10}|} = \frac{\Delta\eta}{|\eta_{10}|}. \quad (7)$$

These quantities will be called reorientation and relative reorientation, respectively. Taking into account relation (3) between the order parameter η and the polarization vector \mathbf{P} , we introduce generalized repolarization and relative repolarization as follows:

$$\Delta P \equiv |\mathbf{P} - \mathbf{P}_{10}| = a|\eta - \eta_{10}|, \quad (8)$$

$$\xi_P \equiv \frac{|\mathbf{P} - \mathbf{P}_{10}|}{|\mathbf{P}_{10}|} = \frac{\Delta P}{|\mathbf{P}_{10}|} = \xi_\eta.$$

Now, let us consider the case of a weak field applied to the crystal. The repolarization and relative repolarization can easily be determined as functions of this field. To this end, we expand the left-hand side of Eq. (2) in powers of $(\eta - \eta_{10})$

$$\begin{aligned} & [\alpha(T - T_C)\eta + \beta_1(3\eta_{x10}^2 + \eta_{y10}^2 + \eta_{z10}^2) \\ & + \beta_2(\eta_{y10}^2 + \eta_{z10}^2)]\Delta\eta_x + 2(\beta_1 + \beta_2)\eta_{y10}\eta_{x10}\Delta\eta_y \\ & + 2(\beta_1 + \beta_2)\eta_{z10}\eta_{x10}\Delta\eta_{zx} = aE_x, \\ & 2(\beta_1 + \beta_2)\eta_{x10}\eta_{y10}\Delta\eta_x + [\alpha(T - T_C)\eta \\ & + \beta_1(\eta_{x10}^2 + 3\eta_{y10}^2 + \eta_{z10}^2) + \beta_2(\eta_{x10}^2 + \eta_{z10}^2)]\Delta\eta_y \quad (9) \\ & + 2(\beta_1 + \beta_2)\eta_{z10}\eta_{y10}\Delta\eta_{zy} = aE_y, \\ & 2(\beta_1 + \beta_2)\eta_{x10}\eta_{z10}\Delta\eta_x + 2(\beta_1 + \beta_2)\eta_{y10}\eta_{z10}\Delta\eta_y \\ & + [\alpha(T - T_C)\eta + \beta_1(\eta_{x10}^2 + \eta_{y10}^2 + 3\eta_{z10}^2) \\ & + \beta_2(\eta_{x10}^2 + \eta_{y10}^2)]\Delta\eta_{zz} = aE_z, \end{aligned}$$

where $\Delta\eta_x = \eta_x - \eta_{x10}$, $\Delta\eta_y = \eta_y - \eta_{y10}$, and $\Delta\eta_z = \eta_z - \eta_{z10}$.

With definitions (7) and (8), Eqs. (9) allow one to derive the general relation between the repolarization ΔP and the external field \mathbf{E} and, hence, open the way for thermodynamic and kinetic description of the switching of multiaxial ferroelectrics using well-developed methods from the classical theory of nucleation and growth. It should be noted that the generality of this approach consists in the fact the thermodynamics and kinetics of switching of a ferroelectric from any possible low-symmetry phase can be studied using a universal model, which is based on the concept of repolarization as an analog of supersaturation. Therefore, we will discuss in more detail the specific features of the description of the switching thermodynamics with allowance for the symmetry of possible pyroelectric phases of the multiaxial ferroelectric crystal under study.

For convenience in the further thermodynamic description of switching, we consider the following temperature ranges separately. Let us assume that phase I is stable in the range $T_1 < T < T_C$; phase II, in the range $T_2 < T < T_1$; and that phase III is stable at $T < T_2$. Note that this situation takes place in BaTiO₃ crystals [6].

First, we consider the temperature range $T_1 < T < T_C$, where the tetragonal $4mm$ phase (phase I) is stable. Let the order parameter and the spontaneous polarization of the this single-domain low-symmetry phase be $\eta = \{0, 0, \eta_z\}$ and $\mathbf{P} = \{0, 0, P_z\}$, respectively. We place the ferroelectric in an external electric field, which is either opposite to the initial polarization of phase I, $\mathbf{E} = \{0, 0, -E_z\}$, or perpendicular to it, $\mathbf{E} = \{0, E_y, 0\}$. As a result of the application of the external field, the ferroelectric initial phase has a certain excess energy and does not correspond to the absolute minimum of thermodynamic potential (1); thus it is a metastable phase. A stable phase should have a polarization directed along the external field. As a consequence, nucleation centers of a new energetically favorable phase form in the crystal and there appear either 180° domains, when the applied field is opposite to the initial polarization, or 90° domains, when the switching field is normal to it. The former case (homogeneous formation of 180° domains) was studied earlier when analyzing the switching of uniaxial ferroelectrics [1] and uniaxial ferroelastic ferroelectrics [2]. Therefore, we will consider only the nucleation and growth of 90° domains.

Substituting the order parameter $\eta_{10} = \{0, 0, \eta_{z10}\}$ and the field $\mathbf{E} = \{0, E_y, 0\}$ into Eqs. (9), we obtain

$$\begin{aligned} \Delta\eta_x &= 0, \\ \Delta\eta_y &= \frac{aE_y}{\alpha(T - T_C) + (\beta_1 + \beta_2)\eta_{z10}^2} = \frac{\chi_{yy}E_y}{a}, \quad (10) \\ \Delta\eta_z &= 0, \end{aligned}$$

where $\chi_{yy} = a^2(\beta_1/\beta_2)/\alpha(T_C - T)$ is the yy component of the dielectric susceptibility tensor. It follows that

$$\begin{aligned}\Delta\eta &= \Delta\eta_y = \frac{\chi_{yy}E_y}{a}, \quad \Delta P = a\Delta\eta = \chi_{yy}E_y, \\ \xi_\eta &= \xi_P = \frac{\Delta\eta}{|\eta_{10}|} = \frac{\chi_{yy}E_y}{a\eta_{z10}} = \frac{\chi_{yy}E_y}{P_{z10}}.\end{aligned}\quad (11)$$

These expressions determine the reorientation $\Delta\eta$ and repolarization ΔP as a function of the applied field for switching the ferroelectric from the tetragonal pyroelectric phase. As seen from Eqs. (11), in the case of nucleation of 90° domains in the ferroelectric, the role of supersaturation during conventional first-order phase transitions is played by the electric field applied perpendicular to the polarization axis of the crystal. It should be noted that, for repolarization of the initial sample with the formation of 180° domains, the analog of supersaturation is a field directed parallel to the polarization axis [1].

Now, we consider the temperature range $T_2 < T < T_1$, where the orthorhombic $mm2$ phase of the model ferroelectric under study is stable. For definiteness, the order parameter is taken to be $\eta_{10} = \{\eta_{x10}, \eta_{y10}, 0\}$, where $\eta_{x10} = \eta_{y10}$, which agrees with one of the possible solutions from (5) corresponding to the point symmetry of this pyroelectric phase. Using general relations (9), it is easy to show that [6]

$$\begin{aligned}\Delta P_x &= \chi_{xx}E_x + \chi_{xy}E_y = \chi_1E_x + \chi_2E_y, \\ \Delta P_y &= \chi_{yx}E_x + \chi_{yy}E_y = \chi_2E_x + \chi_1E_y,\end{aligned}\quad (12)$$

where $\chi_1 \equiv \chi_{xx} = \chi_{yy}$, $\chi_2 \equiv \chi_{xy} = \chi_{yx}$.

Depending on the direction of the external field, both 90° and 180° repolarization centers can form. In particular, in the switching field $\mathbf{E} = \{-E_x, E_y, 0\}$ with $E_x = E_y = E/\sqrt{2}$ (which causes the formation of 90° domains in the orthorhombic phase), the reorientation $\Delta\eta$ and repolarization ΔP are

$$\begin{aligned}\Delta\eta &= \sqrt{\Delta\eta_x^2 + \Delta\eta_y^2} = \frac{E|\chi_1 - \chi_2|}{a}, \\ \Delta P &= a\Delta\eta = E|\chi_1 - \chi_2|, \\ \xi_\eta &= \xi_P = \frac{E|\chi_1 - \chi_2|}{\sqrt{P_{x10}^2 + P_{y10}^2}} = \frac{E|\chi_1 - \chi_2|}{P_{10}},\end{aligned}\quad (13)$$

where $E = \sqrt{E_x^2 + E_y^2} = E_x\sqrt{2}$ and $P_{10} = \sqrt{P_{x10}^2 + P_{y10}^2} = P_{x10}\sqrt{2}$.

On the other hand, when 180° domains nucleate in the field $\mathbf{E} = \{-E_x, -E_y, 0\}$ with $E_x = E_y$, the reorienta-

tion and repolarization in the orthorhombic phase are different:

$$\begin{aligned}\Delta\eta &= \frac{E(\chi_1 + \chi_2)}{a}, \quad \Delta P = E(\chi_1 + \chi_2), \\ \xi_\eta &= \xi_P = \frac{E(\chi_1 + \chi_2)}{P_{10}}.\end{aligned}\quad (14)$$

The thermodynamics of switching from the trigonal phase is studied similarly. It is obvious that the consideration given above can easily be applied to a pyroelectric phase of any allowable symmetry. In other words, the application of an external electric field in a certain direction makes the initial pyroelectric phase metastable. The reorientation introduced above can serve as a quantitative characteristic of the metastability of the ferroelectric crystal. The type of repolarization centers forming in the parent multiaxial ferroelectric is specified by the direction of the applied field, while the metastability of the system is fully determined by the magnitude of the applied field.

3. KINETICS OF THE INITIAL STAGE OF SWITCHING

To describe the kinetics of switching of multiaxial ferroelectrics, we introduce, in addition to the polarization $\mathbf{P} = \{P_x, P_y, P_z\}$ used above, the corresponding specific quantity $\mathbf{p} = \{p_x, p_y, p_z\}$ per unit cell of the crystal, i.e., the dipole moment of the unit cell, $\mathbf{p} = \mathbf{P}\omega$, where ω is the unit cell volume.

Then, we make an assumption about the shape of the nucleating ferroelectric domains. Note that the shape of domains, as well as their orientation, cannot be arbitrary, since the continuity condition of the tangential component of an electric-field vector must be met at the nucleation center-medium interface in a ferroelectric [7]. Nucleation centers can be, for example, cylindrical in shape (with the lateral surface oriented parallel to the field) or, in a more general case, ellipsoidal, with one of the principal axes oriented along the field. In [1, 2], the growth of cylindrical domains with a constant height and a variable base radius was studied; in other words, it was implicitly assumed that domains had a single degree of freedom that could affect the kinetics of switching of a ferroelectric. In what follows, we study the general case of the kinetics of the early switching stage, where repolarization centers have two degrees of freedom.

Let us analyze the nucleation of a cylindrical domain with height H and base radius R . Elementary building blocks of such domains are assumed to be unit cells of the crystal with polarization \mathbf{p} . When a repolarization center forms, the free energy of the ferroelectric crystal changes by ΔF , which, according to the classical

theory of nucleation and growth, can be determined from the relation

$$\begin{aligned}\Delta F &= -\frac{V}{\omega}(f_1 - f_2) + \sigma S \\ &= -\frac{\pi R^2 H}{\omega} \Delta f + \sigma(2\pi R^2 + 2\pi RH),\end{aligned}\quad (15)$$

where f_1 and f_2 are the free energies per unit cell of the medium and nucleation center, respectively; $\Delta f = f_1 - f_2$; $V = \pi R^2 H$ and $S = 2\pi R^2 + 2\pi RH$ are the volume and surface area of the cylindrical domain; and σ is the surface tension coefficient of the domain wall.

The quantity Δf can be interpreted as the effective driving force that leads to the growth of energetically favorable domains with polarization directed along the applied field. To find Δf , we write the initial thermodynamic potential (1) in the form $\Phi = \tilde{\Phi}_0 - \mathbf{E}\mathbf{P}$, where $\tilde{\Phi}_0$ is the field-independent part of the potential. Then, the free energies of the unit cells with polarization directed along the field, opposite to the field, and perpendicular to it are $\Phi = \tilde{\Phi}_0 - Ep$, $\Phi = \tilde{\Phi}_0 + Ep$, and $\Phi = \tilde{\Phi}_0$, respectively (p is the specific polarization introduced earlier). It follows that, in the case of switching of the ferroelectric crystal with the formation of 180° domains, the energy of the system decreases by $\Delta f = 2E_p$ [1] and the gain in energy due to the formation of 90° domains is $\Delta f = Ep$.

It should be noted that the process of repolarization of a ferroelectric is inevitably accompanied by processes that decrease the effective driving force Δf of the phase transformation. In particular, the effect of the elastic energy related to the critical phenomenon and the depolarizing field can be of importance. Note also that the elastic stresses caused by deformation of the crystal lattice can result in a ferroelastic transition, which is observed in ferroelastic ferroelectrics.

Instead of the parameters R and H of a cylindrical nucleation center, we introduce new variables n and α , where n is the number of unit cells in a nucleation center of volume V and $\alpha = H/R$ is the characteristic ratio of the linear dimensions of a domain. The free energy of the nucleation center expressed in terms of the new variables takes the form

$$\Delta F(n, \alpha) = -n\Delta f + 2\pi\sigma\left(\frac{\omega}{\pi}\right)^{2/3}\left(\frac{1+\alpha}{\alpha^{2/3}}\right)n^{2/3}. \quad (16)$$

The critical domain size is determined by the saddle point (n_c, α_c) in the energy surface $\Delta F = \Delta F(n, \alpha)$, where

$$\frac{\partial \Delta F(n, \alpha)}{\partial n} = 0, \quad \frac{\partial \Delta F(n, \alpha)}{\partial \alpha} = 0. \quad (17)$$

From Eqs. (17), we obtain

$$n_c = 16\pi\frac{\sigma^3\omega^2}{(\Delta f)^3}, \quad \alpha_c = 2, \quad V_c = \pi\left(\frac{\sigma\omega}{\Delta f}\right)^2. \quad (18)$$

Therefore, the minimum energy for the formation of a critical nucleus is

$$R_{\min} = \Delta F(n_c, \alpha_c) = 8\pi\frac{\sigma^3\omega^2}{(\Delta f)^2}. \quad (19)$$

The critical domain size and the minimum energy for nucleus formation are functions of the applied field and can be calculated directly. Note also that these dependences can be applied for studying both 180° domains (at $\Delta f = 2E_p$) and 90° domains (at $\Delta f = Ep$).

To describe the kinetics of switching of the ferroelectric crystal with allowance for the three-dimensional growth of new-phase nucleation centers, we introduce the two-dimensional nonequilibrium distribution function of repolarized domains over the number of unit cells and their shapes $f(n, \alpha, t)$ normalized to the number of domains $N(t)$ per unit volume of the crystal:

$$\int_0^\infty \int_0^\infty f(n, \alpha, t) dn d\alpha = N(t).$$

The time evolution of the two-dimensional nonequilibrium distribution function is determined by the solution to the corresponding two-dimensional Fokker–Planck kinetic equation [5]

$$\begin{aligned}& \frac{\partial f(n, \alpha, t)}{\partial t} \\ &= \frac{\partial}{\partial n} D_n \left[\frac{\partial f(n, \alpha, t)}{\partial n} + \frac{1}{k_B T} \frac{\partial \Delta F(n, \alpha)}{\partial n} f(n, \alpha, t) \right] \\ &+ \frac{\partial}{\partial \alpha} D_\alpha \left[\frac{\partial f(n, \alpha, t)}{\partial \alpha} + \frac{1}{k_B T} \frac{\partial \Delta F(n, \alpha)}{\partial \alpha} f(n, \alpha, t) \right],\end{aligned}\quad (20)$$

where D_n and D_α are the diffusion coefficients in the space of sizes and shapes, respectively, and k_B is the Boltzmann constant.

Kinetic equation (20) can be solved using the multidimensional kinetic theory of first-order phase transitions [3–5]. In this theory, the multidimensional kinetic equation is linearized in the vicinity of a saddle point (i.e., the Fokker–Planck approximation is used, as is normally done for studying the kinetics of first-order phase transitions) and then a linear transformation is performed in order to pass to new, separable variables characterizing the state of a nucleation center [4]. The Fokker–Planck equation linearized in the vicinity of the saddle point corresponds to constant (i.e., independent of the variables characterizing a nucleation center) diffusion coefficients in the space of sizes and shapes; their values are calculated at the saddle point.

Let us find a stationary solution to kinetic equation (20), which describes the initial stage of switching of the ferroelectric crystal under study. First, following [4, 5], we analyze the energy for nucleus formation $\Delta F = \Delta F(n, \alpha)$, which is determined by Eq. (16) in the vicinity of the saddle point (n_c, α_c) . In the vicinity of this point, we can use the quadratic approximation to the quantity ΔF

$$\Delta F(n, \alpha) = \Delta F_c - A(n - n_c)^2 + B(\alpha - \alpha_c)^2, \quad (21)$$

where ΔF_c is the minimum energy for the formation of a critical nucleus (19), $A = (\Delta f)^4/96\pi\sigma^3\omega^2$, and $B = 2\pi\sigma^3\omega^2/3(\Delta f)^2$.

As can be seen from the structure of Eq. (21), n is a thermodynamically unstable variable and α is thermodynamically stable. Note that the presence of a thermodynamically unstable variable describing a nucleation center is a characteristic feature of all multidimensional first-order phase transitions [4].

Using the Gibbs formula and the energy for nucleus formation (21), we can obtain the equilibrium distribution of domains over their sizes and shapes:

$$\begin{aligned} f_{\text{eq}}(n, \alpha) &= \exp\left(-\frac{\Delta F(n, \alpha)}{k_B T}\right) \\ &= \exp\left(-\frac{\Delta F_c}{k_B T}\right) \exp\left(\frac{A(n - n_c)^2}{k_B T}\right) \exp\left(-\frac{B(\alpha - \alpha_c)^2}{k_B T}\right). \end{aligned} \quad (22)$$

Using this equilibrium distribution function for domains, kinetic equation (20) can be supplemented with the standard initial and boundary conditions

$$\begin{aligned} f(n, \alpha, 0) &= 0, \\ \frac{f(n, \alpha, t)}{f_{\text{eq}}(n, \alpha)} \Big|_{n \rightarrow 0} &\rightarrow 1, \quad \frac{f(n, \alpha, t)}{f_{\text{eq}}(n, \alpha)} \Big|_{n \rightarrow \infty} \rightarrow 0, \\ \frac{f(n, \alpha, t)}{f_{\text{eq}}(n, \alpha)} \Big|_{\alpha \rightarrow 0} &\rightarrow 1, \quad \frac{f(n, \alpha, t)}{f_{\text{eq}}(n, \alpha)} \Big|_{\alpha \rightarrow \infty} \rightarrow 0. \end{aligned} \quad (23)$$

We seek a solution to Eq. (20) in the form

$$f(n, \alpha, t) = C \exp\left(-\frac{B(\alpha - \alpha_c)^2}{k_B T}\right) \varphi(n, t), \quad (24)$$

where the normalizing constant C is chosen such that

$$C \int_0^{\infty} \exp\left(-\frac{B(\alpha - \alpha_c)^2}{k_B T}\right) d\alpha = 1.$$

With this constant C , the distribution function $\varphi(n, t)$ is normalized to the number of domains per unit volume of the crystal, i.e.,

$$\int_0^{\infty} \varphi(n, t) dn = N(t).$$

By substituting Eq. (24) into Eq. (20), the two-dimensional kinetic equation is reduced to an ordinary one-dimensional Zel'dovich equation,

$$\frac{\partial \varphi(n, t)}{\partial t} = D_n \frac{\partial}{\partial n} \left[\frac{\partial \varphi(n, t)}{\partial n} - \frac{2A(n - n_c)}{k_B T} \varphi(n, t) \right] \quad (25)$$

with the initial and boundary conditions

$$\begin{aligned} \varphi(n, 0) &= 0, \\ \frac{\varphi(n, t)}{\Phi_{\text{eq}}(n)} \Big|_{n \rightarrow 0} &\rightarrow 1, \quad \frac{\varphi(n, t)}{\Phi_{\text{eq}}(n)} \Big|_{n \rightarrow \infty} \rightarrow 0. \end{aligned} \quad (26)$$

Knowing the energy for the formation of a critical nucleus (19) and using the expression for the diffusion coefficient D_n in the space of sizes, we can determine the steady-state flux of repolarization centers (the main kinetic characteristic of the initial stage of switching of the ferroelectric). According to [1, 8], the steady-state flux is given by

$$I = N_v D_n \frac{1}{\sqrt{\pi}} \sqrt{\frac{1}{2k_B T} \left| \frac{\partial^2 \Delta F(n, \alpha)}{\partial n^2} \right|_{n=n_c}} \times \exp\left[-\frac{\Delta F_c}{k_B T}\right], \quad (27)$$

where N_v is the number of unit cells per unit volume of the crystal, which can be estimated as $N_v \sim 1/\omega$.

Substituting Eq. (21), we obtain

$$\begin{aligned} I &= N_v D_n \sqrt{\frac{A}{\pi k_B T}} \exp\left[-\frac{8\pi\sigma^3\omega^2}{k_B T (\Delta f)^2}\right] \\ &= \frac{N_v D_n (\Delta f)^2}{4\pi\omega\sigma^{3/2} \sqrt{6k_B T}} \exp\left[-\frac{8\pi\sigma^3\omega^2}{k_B T (\Delta f)^2}\right]. \end{aligned} \quad (28)$$

To determine the steady-state flux I , we need to know the diffusion coefficient in the size space D_n . The explicit form of this coefficient significantly depends on the growth mechanism of repolarized regions in the crystal. In [1], two mechanisms of domain growth, namely, the normal and layer-by-layer mechanisms, were studied. Using the technique developed in [1], we can easily find the diffusion coefficient with allowance for the three-dimensional growth of repolarized regions for both growth mechanisms. In the case of the normal mechanism, we obtain

$$D_n^{(1)} = 6\pi\beta_0 \left(\frac{2\sigma\omega}{\Delta f}\right)^2, \quad (29)$$

where β_0 is the kinetic coefficient.

Following [1] in the case of the layer-by-layer growth mechanism, we obtain

$$D_n^{(2)} = 6\pi\beta_{\text{st}0} \frac{\Delta f}{\sigma_{\text{st}}\omega} \left(\frac{2\sigma\omega}{\Delta f}\right)^3, \quad (30)$$

where β_{st0} and σ_{st} are the step-related kinetic coefficient and surface tension coefficient, respectively.

With these expressions, the steady-state fluxes of repolarization centers take the form

$$I^{(1)} = \beta_0 N_v \omega \sqrt{\frac{6\sigma}{k_B T}} \exp\left[-\frac{8\pi\sigma^3 \omega^2}{k_B T (\Delta f)^2}\right], \quad (31)$$

$$I^{(2)} = 2\beta_{st0} N_v \omega \frac{\sigma}{\sigma_{st}} \sqrt{\frac{6\sigma}{k_B T}} \exp\left[-\frac{8\pi\sigma^3 \omega^2}{k_B T (\Delta f)^2}\right],$$

where superscripts 1 and 2 refer to the normal and layer-by-layer growth mechanisms, respectively.

Let us express the steady-state fluxes in terms of the electric field applied to the crystal. For the flux of 180° domains, we obtain

$$I^{(1)} = \beta_0 N_v \omega \sqrt{\frac{6\sigma}{k_B T}} \exp\left[-\frac{2\pi\sigma^3 \omega^2}{k_B T (\mathbf{pE})^2}\right], \quad (32)$$

$$I^{(2)} = 2\beta_{st0} N_v \omega \frac{\sigma}{\sigma_{st}} \sqrt{\frac{6\sigma}{k_B T}} \exp\left[-\frac{2\pi\sigma^3 \omega^2}{k_B T (\mathbf{pE})^2}\right],$$

and, for the flux of 90° domains, we have

$$I^{(1)} = \beta_0 N_v \omega \sqrt{\frac{6\sigma}{k_B T}} \exp\left[-\frac{8\pi\sigma^3 \omega^2}{k_B T (\mathbf{pE})^2}\right], \quad (33)$$

$$I^{(2)} = 2\beta_{st0} N_v \omega \frac{\sigma}{\sigma_{st}} \sqrt{\frac{6\sigma}{k_B T}} \exp\left[-\frac{8\pi\sigma^3 \omega^2}{k_B T (\mathbf{pE})^2}\right].$$

For comparison with the experimental data, the following approximate expressions can be conveniently used for the domain fluxes as a function of the electric field:

$$\ln I^{(1,2)} = C_{1,2} - \frac{8\pi\sigma^3 \omega^2}{k_B T (\mathbf{pE})^2}, \quad (34)$$

for 90° domains and

$$\ln I^{(1,2)} = C_{1,2} - \frac{2\pi\sigma^3 \omega^2}{k_B T (\mathbf{pE})^2}, \quad (35)$$

for 180° domains. Here, the constants $C_{1,2}$ depend on the domain-growth mechanism and are determined by the preexponential factors in Eqs. (32) and (33).

Finally, the time required for the domain flux to reach a steady-state value and the lifetime of the steady-state flux can be estimated from the formulas obtained in [1].

4. DISCUSSION OF THE RESULTS

Now, we present some estimates for the critical nucleus size and the steady-state repolarization flux.

We use the experimental data for the best studied multiaxial ferroelectric, barium titanate. According to [6, 9, 10], the Curie temperature of barium titanate is $T_C \sim 393$ K; the equilibrium spontaneous polarization at $T \sim 373$ K is $P_{x10} \sim 1.2 \times 10^{-1}$ C m $^{-2}$; the dielectric susceptibilities along and perpendicular to the polar axis are $\chi_c \sim 60$ and $\chi_a \sim 300$, respectively; the molecular weight is $M \sim 0.233$ kg mol $^{-1}$; and the density is $\rho \sim 6.02 \times 10^3$ kg cm $^{-3}$. The unit cell volume of barium titanate is estimated as $\omega \sim M/\rho N_A = 0.64 \times 10^{-28}$ m 3 (N_A is Avogadro's number); therefore, $N_v \sim \omega^{-1} = 1.6 \times 10^{28}$ m $^{-3}$. The kinetic coefficient β_0 depends on the activation energy for atomic displacement in the ferroelectric; according to [1], it can be estimated as $\beta_0 \sim 10^{31}$ m $^{-2}$ s $^{-1}$.

To estimate the critical nucleus size and the repolarization flux, it is necessary to know the surface tension coefficient σ of a domain wall and, in the case of layer-by-layer growth, the surface tension coefficient of the step. The experimental (as well as theoretical) estimates of the surface tension coefficients are highly contradictory [11–14]. For example, according to Miller and Weinreich, $\sigma \sim 0.56 \times 10^{-3}$ J m $^{-2}$, whereas Zhirnov's calculations give $\sigma \sim (2-4) \times 10^{-3}$ J m $^{-2}$ for a 180° wall and $\sigma \sim 10 \times 10^{-3}$ J m $^{-2}$ for a 90° wall [10]. Following [15], we can assume that the coefficient of surface tension of a domain wall in barium titanate lies in the range from $\sigma \sim 0.1 \times 10^{-3}$ to $\sim 10 \times 10^{-3}$ J m $^{-2}$. This scatter in the values of σ makes it difficult to make strict quantitative estimations using Eqs. (18) and (31)–(35), and the further consideration is qualitative in character.

Note that, in general, the coefficient of surface tension should be determined from the nucleation rate of a new phase, namely, from Eqs. (31)–(35). Therefore, it is necessary to find the nucleation rate experimentally and to compare it with theoretical dependences (31)–(35). Only in this case can one find the exact value of the surface interphase energy. It should be noted that the process of repolarization, as a rule, begins at the surface of a ferroelectric, specifically, at the places where electrodes are applied or at defects, which are always present in crystals. In this case, the energy for nucleus formation decreases significantly and the process of switching acquires features that are inherent to the heterogeneous formation of nucleation centers on a substrate. Therefore, in general, Eqs. (31)–(35) should contain a coefficient γ ($0 \leq \gamma \leq 1$) taking into account the decrease in the energy for the formation of a repolarization center.

For the normal growth mechanism, the numerical calculation by Eqs. (18) and (31)–(35) with $\sigma \sim 0.56 \times 10^{-3}$ J m $^{-2}$ indicates that, with applied fields $E_x < E_{cx}$ or $E_y < E_{cy}$ (where $E_{cx} \sim 4 \times 10^5$ V m $^{-1}$ and $E_{cy} \sim 0.8 \times 10^6$ V m $^{-1}$), the steady-state repolarization fluxes are zero; hence, the crystal is not switched. This estimation

of the lower value of the applied field agrees with the experimental values of the coercive field for barium titanate [16]. We think that the slightly overestimated values can be explained by the rough assumption regarding the cylindrical shape of domains. More accurate estimates can be obtained assuming an ellipsoidal shape of nucleation centers and taking into account the depolarizing fields and lattice defects. In fields $E_x > E_{cx}$ or $E_y > E_{cy}$, it is easy to estimate the main characteristics of the initial repolarization stage. For example, in a field $E_x = 7 \times 10^5 \text{ V m}^{-1}$, the dimensions of the critical nucleation center of a 180° domain are $R_c, H_c \sim 10^{-8} \text{ m}$ and the steady-state flux is $I \sim 10^{32}$. Similar linear dimensions of critical nucleation centers for 90° domains are reached in a field $E_y = 0.8 \times 10^7 \text{ V m}^{-1}$, and the steady-state flux under these conditions is $I \sim 10^{40}$.

5. CONCLUSIONS

Let us briefly formulate the basic result of this work and directions for further developing our approach. In the context of the classical theory of nucleation and growth, we have considered the thermodynamics and kinetics of the initial stage of switching of multiaxial ferroelectrics. The switching kinetics has been described in the most general case, where repolarized domains have two degrees of freedom and their growth is not limited by any formal relations. However, we considered only the initial stage of the switching kinetics, where the fraction of a crystal involved in the phase transformation is very small. Therefore, there is virtually no switching current at this stage. In this connection, it is interesting to study the second and third stages of the phase transformation, i.e., the stages of bulk polarization and Ostwald ripening. These problems will be discussed in a future publication.

ACKNOWLEDGMENTS

This study was partly supported by the Russian Foundation for Basic Research (project no. 03-01-00574), the Russian Federal Research Center "Integration" (project nos. A0151, B0056), the program "Control of Nonlinear Mechanical Systems under Conditions of Uncertainty and Chaos" (project no. 19), the Ministry of Industry, Science, and Technology of the Russian Federation (project no. 40.010.1.1195), state contract nos. NFM-1/03 and NSh-2288.2003.1,

the program "Universities of Russia" (project no. UR.01.01.024), and the RFBR-NWO program (project no. 047.011.2001.011).

REFERENCES

1. S. A. Kukushkin and A. V. Osipov, *Fiz. Tverd. Tela* (St. Petersburg) **43** (1), 80 (2001) [*Phys. Solid State* **43**, 82 (2001)]; *Fiz. Tverd. Tela* (St. Petersburg) **43** (1), 88 (2001) [*Phys. Solid State* **43**, 90 (2001)]; *Fiz. Tverd. Tela* (St. Petersburg) **43** (2), 312 (2001) [*Phys. Solid State* **43**, 325 (2001)].
2. S. A. Kukushkin and M. A. Zakharov, *Fiz. Tverd. Tela* (St. Petersburg) **44** (2), 332 (2002) [*Phys. Solid State* **44**, 345 (2002)]; *Fiz. Tverd. Tela* (St. Petersburg) **44** (12), 2193 (2002) [*Phys. Solid State* **44**, 2298 (2002)].
3. V. A. Shneĭdman, *Zh. Ėksp. Teor. Fiz.* **91** (2), 520 (1986) [*Sov. Phys. JETP* **64**, 306 (1986)].
4. F. M. Kuni and A. A. Melikhov, *Teor. Mat. Fiz.* **81** (2), 247 (1989).
5. S. A. Kukushkin and A. V. Osipov, *Fiz. Tverd. Tela* (St. Petersburg) **36** (5), 1258 (1994) [*Phys. Solid State* **36**, 687 (1994)].
6. B. A. Strukov and A. P. Livanyuk, *Physical Principles of Ferroelectric Phenomena in Crystals* (Nauka, Moscow, 1995).
7. L. D. Landau and E. M. Lifshitz, *Course of Theoretical Physics, Vol. 8: Electrodynamics of Continuous Media*, 2nd ed. (Nauka, Moscow, 1982; Pergamon, Oxford, 1984).
8. Ya. B. Zel'dovich, *Zh. Ėksp. Teor. Fiz.* **12** (11/12), 525 (1942).
9. F. Jona and G. Shirane, *Ferroelectric Crystals* (Pergamon, Oxford, 1962; Mir, Moscow, 1965).
10. J. Burfoot, *Ferroelectrics: an Introduction to the Physical Principles* (Van Nostrand, London, 1967; Mir, Moscow, 1970).
11. M. Hayashi, *J. Phys. Soc. Jpn.* **33**, 616 (1972).
12. E. V. Burtsev and S. P. Chervonobrodov, *Ferroelectrics* **45**, 97 (1982).
13. M. Molotskii, R. Kris, and G. Rosenmann, *J. Appl. Phys.* **88** (9), 5318 (2000).
14. A. K. Tagantsev, I. Stolichnov, E. L. Colla, and N. Setter, *J. Appl. Phys.* **90** (3), 1387 (2001).
15. R. E. Nettleton, *J. Appl. Phys.* **38** (7), 2775 (1967).
16. A. S. Sonin and B. A. Strukov, *Introduction to Ferroelectricity* (Vysshaya Shkola, Moscow, 1970).

Translated by K. Shakhlevich

**MAGNETISM
AND FERROELECTRICITY**

Pyroelectric, Piezoelectric, and Polarization Responses of Glycine Phosphite Crystals with an Admixture of Glycine Phosphate

V. V. Lemanov*, S. G. Shul'man*, V. K. Yarmarkin*, S. N. Popov*, and G. A. Pankova**

*Ioffe Physicotechnical Institute, Russian Academy of Sciences,
Politekhnicheskaya ul. 26, St. Petersburg, 194021 Russia
e-mail: lemanov@mail.ioffe.ru

**Institute of Macromolecular Compounds, Russian Academy of Sciences,
Bol'shoi proezd 31, St. Petersburg, 119034 Russia

Received December 16, 2003

Abstract—Temperature dependences of the pyroelectric, piezoelectric, and polarization responses of glycine phosphite crystals containing different amounts of glycine phosphate were studied in the range 120–320 K. The experimental data obtained suggest the presence of a built-in bias field oriented along the twofold symmetry axis in these crystals. This field was found to be 5 kV/cm. It is suggested that the built-in bias plays a decisive role in the formation of the pyroelectric and piezoelectric crystal responses in the temperature interval 225–280 K, which is significantly higher than the ferroelectric phase transition point in nominally pure glycine phosphite crystals (224 K). © 2004 MAIK “Nauka/Interperiodica”.

1. INTRODUCTION

Investigation of crystals of protein aminoacids and their derivatives, of which many belong to crystal groups lacking inversion symmetry (including polar groups) and may possess piezo-, pyro-, and ferroelectric properties, is of considerable interest both in the physics of crystals and biophysics (see reviews [1, 2] and references therein). The phase transition observed recently [3] in glycine phosphite ($\text{NH}_2\text{CH}_2\text{COOH}$) · H_3PO_3 ($\text{Gly} \cdot \text{H}_3\text{PO}_3$) at about 224 K from the paraelectric phase of symmetry C_{2h} to the ferroelectric state of symmetry C_2 raises interest in glycine phosphite crystals containing glycine phosphate ($\text{Gly} \cdot \text{H}_3\text{PO}_4$). The fact is that $\text{Gly} \cdot \text{H}_3\text{PO}_4$ crystals, which, like $\text{Gly} \cdot \text{H}_3\text{PO}_3$, have a centrosymmetric monoclinic structure C_{2h} at room temperature, retain this structure under cooling to at least 120 K and do not exhibit piezoelectric properties in this temperature interval [4].

2. EXPERIMENTAL TECHNIQUE

We studied single crystals grown from saturated aqueous solutions of $\text{Gly} \cdot \text{H}_3\text{PO}_3$ and $\text{Gly} \cdot \text{H}_3\text{PO}_4$ mixed in ratios of 90 : 10, 75 : 25, 60 : 40, and 10 : 90. The crystals were grown under slow cooling of the solutions from 25 to 8°C at a rate of 1 K/day to a volume of about 1 cm³. X-ray diffraction analysis of crystals of various compositions showed that the crystals on the glycine phosphite side have the structure of pure glycine phosphite and that the crystals on the glycine phosphate side have the structure of pure glycine phos-

phate, thus indicating low mutual solubility of the components in the solid phase (we estimated it to be no greater than 0.1%). The pyroelectric, piezoelectric, and dielectric properties were studied in most detail on crystals grown from solutions with a component ratio of 75 : 25.

$\text{Gly} \cdot \text{H}_3\text{PO}_3$ crystals belong to space group $P2_1/a-C_{2h}^5$ of the monoclinic system at room temperature [5]. The samples intended for investigation of the pyroelectric and dielectric properties were platelets $8 \times 3 \times 0.2$ mm in size cut from single crystals, with the major face oriented perpendicular to the twofold symmetry axis. Conducting electrodes were applied as a slurry of finely dispersed silver. Measurements were conducted in a vacuum of 10^{-5} bar in the temperature range from 200 to 293 K.

The pyroelectric response of the crystals was measured under stepped IR irradiation [6]. The IR radiation was produced by an incandescent lamp with a 0.2-mm-thick silicon filter. The voltage was fed from a load resistor of 10 GΩ to the input of a KR544-UD-1A-based operational amplifier with a voltage gain of unity and then supplied to a recorder. For illustration, Fig. 1 shows the typical time dependence of the pyroelectric response of the crystals studied (obtained for nominally pure glycine phosphite at 210 K) after the IR source was turned on. The quantitative characteristic of the pyroelectric response in this study was the maximum pyroelectric voltage, which is proportional to the pyroelectric coefficient of the material [6].

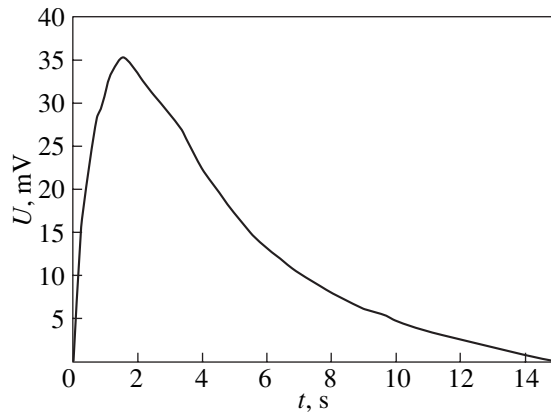


Fig. 1. Pyroelectric response of nominally pure glycine phosphite crystals plotted vs. time of IR illumination (at 210 K).

Dielectric hysteresis loops were measured in the standard Sawyer–Tower arrangement at 50 Hz, with the samples dc-biased from an external source within the voltage range from 0 to ± 200 V. The dielectric permittivity ϵ and the loss tangent $\tan \delta$ were studied in the frequency range from 1 kHz to 1 MHz for voltage amplitudes of 4 V and 100 mV measured with E7-8 and E7-12 bridges, respectively.

The integrated piezoelectric response of the crystals was measured in the temperature range 120–320 K on an IS-2 NQR setup [4]. The sample to be studied, in the form of a set of small crystallites, was placed in the capacitor of a circuit to which 4- μ s-long voltage pulses with a carrier frequency of 10 MHz were applied at a pulse repetition frequency of 12 Hz and a maximum voltage across the circuit of 4 kV. The piezoelectric response signals were measured with an AI-1024 multichannel pulse-height analyzer.

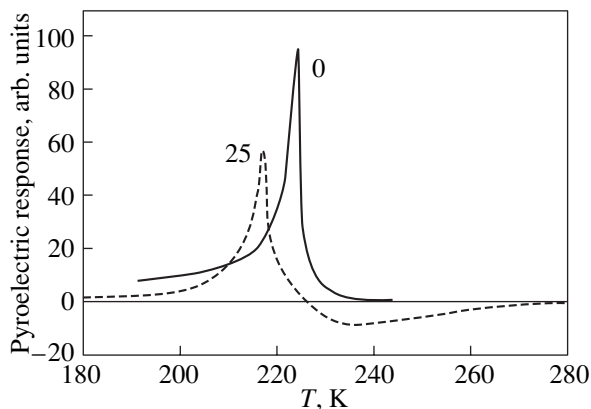


Fig. 2. Temperature behavior of the pyroelectric responses of nominally pure glycine phosphite (solid line) and of glycine phosphite doped with glycine phosphate (dashed line). Numbers on the curves denote the percentage of glycine phosphate impurity in the starting aqueous solution.

3. EXPERIMENTAL RESULTS AND DISCUSSION

Figure 2 displays temperature dependences of the pyroelectric response of nominally pure glycine phosphite and of glycine phosphite containing glycine phosphate measured under identical conditions; the data related to doped crystals were obtained on crystals grown from an aqueous solution of $\text{Gly} \cdot \text{H}_3\text{PO}_3$ and $\text{Gly} \cdot \text{H}_3\text{PO}_4$ taken in a ratio of 75 : 25. Introducing an impurity is seen to shift the pyroelectric response peak toward lower temperatures and reduce its intensity. In addition to this peak, $\text{Gly} \cdot \text{H}_3\text{PO}_3$ crystals doped with $\text{Gly} \cdot \text{H}_3\text{PO}_4$ exhibited a pyroelectric response signal of opposite polarity that was comparable in magnitude to this peak in the temperature region considerably in excess of the Curie temperature (up to 280 K). Prepolarization of the crystals with a field of ± 10 kV/cm did not change either the sign or the amplitude of the pyroelectric responses as the temperature was lowered from room temperature to 200 K. This gives us grounds to suggest that glycine phosphite crystals doped with glycine phosphate have a built-in bias field similar to that revealed earlier in crystals of natural colemanite [7] and later in triglycine sulfate doped with *L*-alanine [8] and some other materials.

Figure 3 displays temperature dependences of the integral piezoelectric response of $\text{Gly} \cdot \text{H}_3\text{PO}_3$ crystals grown with different concentrations of $\text{Gly} \cdot \text{H}_3\text{PO}_4$ in the original aqueous solution (the integral piezoelectric response is understood to mean the total piezoelectric-response signal intensity, which is determined both by the electromechanical coupling and by the sample ringing time, i.e., the damping time of elastic vibrations). As the temperature is lowered from the phase transition point of pure $\text{Gly} \cdot \text{H}_3\text{PO}_3$ (224 K [3]), the piezoelectric response is seen to vary nonmonotonically with tem-

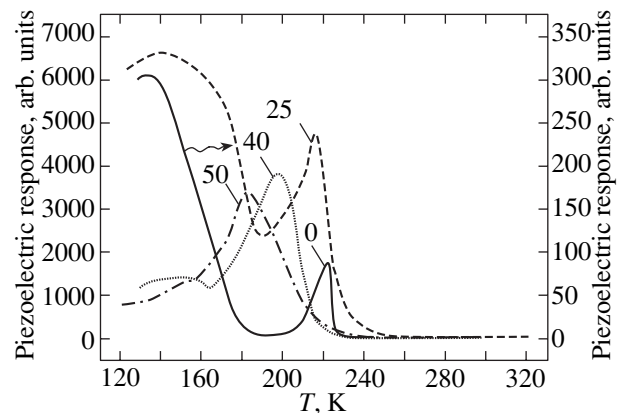


Fig. 3. Temperature behavior of the pyroelectric responses of nominally pure glycine phosphite and of glycine phosphite doped with different amounts of glycine phosphate. Numbers on the curves are the same as those in Fig. 2. The right-hand ordinate axis corresponds to pure crystals, and the left-hand ordinate axis, to doped crystals.

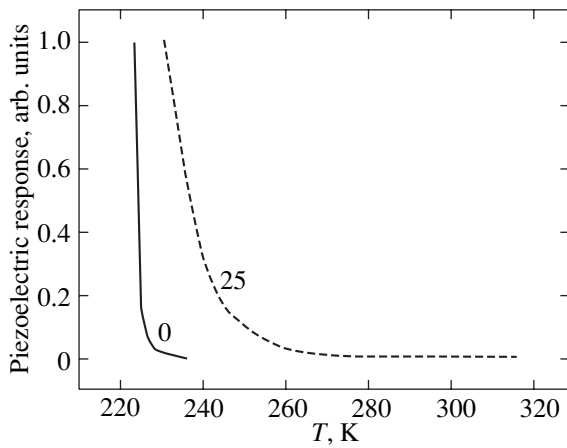


Fig. 4. Temperature behavior of the piezoelectric responses of nominally pure and doped glycine phosphite crystals. Numbers on the curves are the same as those in Fig. 3.

perature. Figure 3 also shows that, as the $\text{Gly} \cdot \text{H}_3\text{PO}_4$ concentration is increased, the maxima and minima of these dependences shift toward lower temperatures. Note also the relatively low piezoelectric response of pure crystals compared to the doped ones, which may be attributed to the higher damping of elastic vibrations in pure crystals.

Figure 4 presents temperature dependences of the integral piezoelectric response (in arbitrary units) of pure and doped glycine phosphite crystals obtained at temperatures close to the ferroelectric phase transition point of pure $\text{Gly} \cdot \text{H}_3\text{PO}_3$. These dependences clearly show the temperature interval of the piezoelectric response of doped crystals to spread noticeably toward higher temperatures as compared to the nominally pure samples. Possible reasons for this behavior will be discussed later.

Figures 5 and 6 display $P(E)$ hysteresis loops measured on crystals of nominally pure and doped glycine phosphite, respectively. A comparison of these relations obtained at the same temperature (220 K) with and without application of an external bias of both polarities suggests that, in the glycine phosphite crystal doped with glycine phosphate, there exists a built-in field of about 5 kV/cm oriented parallel to the C_2 crystallographic axis. This conclusion follows both directly from the strongly asymmetric shape of the hysteresis loops of the doped crystal measured without a bias and from the pattern of the variation in the dielectric hysteresis loop shape produced when a bias of either polarity is applied to the crystal from an external source. For instance, when a negative bias is applied to the top electrode connected directly to the ac voltage source in the Sawyer–Tower circuit and generates a field $E_b = -3$ kV/cm in the crystals, the change in polarization induced by the measuring voltage increases considerably, whereas a positive bias producing a field $E_b = +3$ kV/cm reduces the change in the polarization. It can

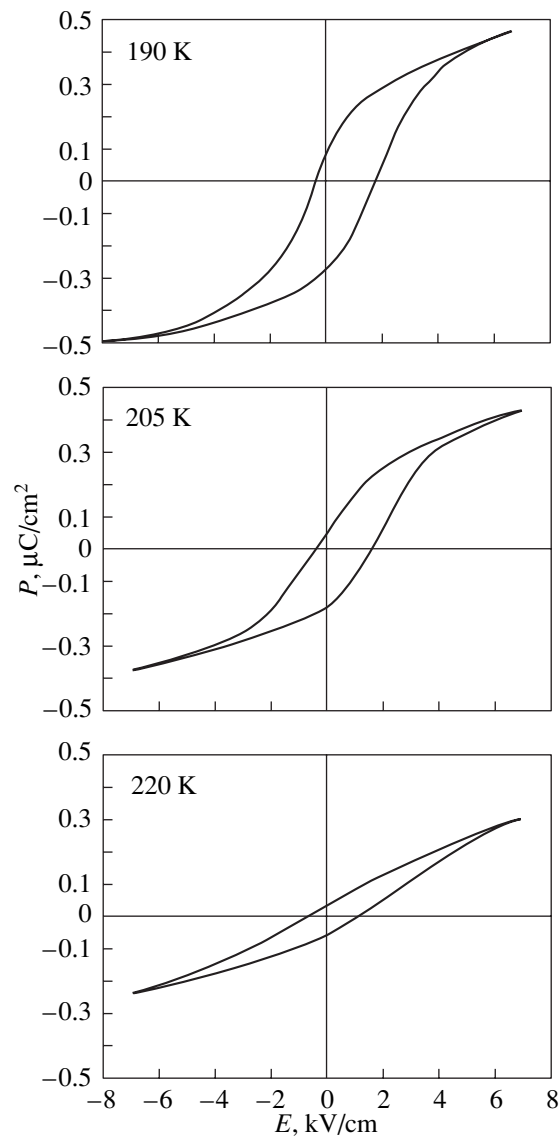


Fig. 5. Dielectric hysteresis loops of nominally pure glycine phosphite obtained at a frequency of 50 Hz at different temperatures.

be assumed that in the first case the external bias field is directed oppositely to the built-in field in the crystal and partially counterbalances it. By contrast, in the second case, the bias produced by the external source and aligned with the built-in field adds to the latter and further saturates the crystal polarization generated by the built-in field, thereby suppressing the polarization switching effected by the ac measuring voltage. Note that our crystals of pure glycine phosphite also have a built-in bias field, albeit a lower one than in the doped glycine phosphite (not over 500 V/cm), which is indicated by the relatively weak asymmetry of the hysteresis loops shown in Fig. 5 and is supported by data in the literature [9]; the generation of this field in nominally pure crystals should most probably be assigned to their containing residual impurities and defects.

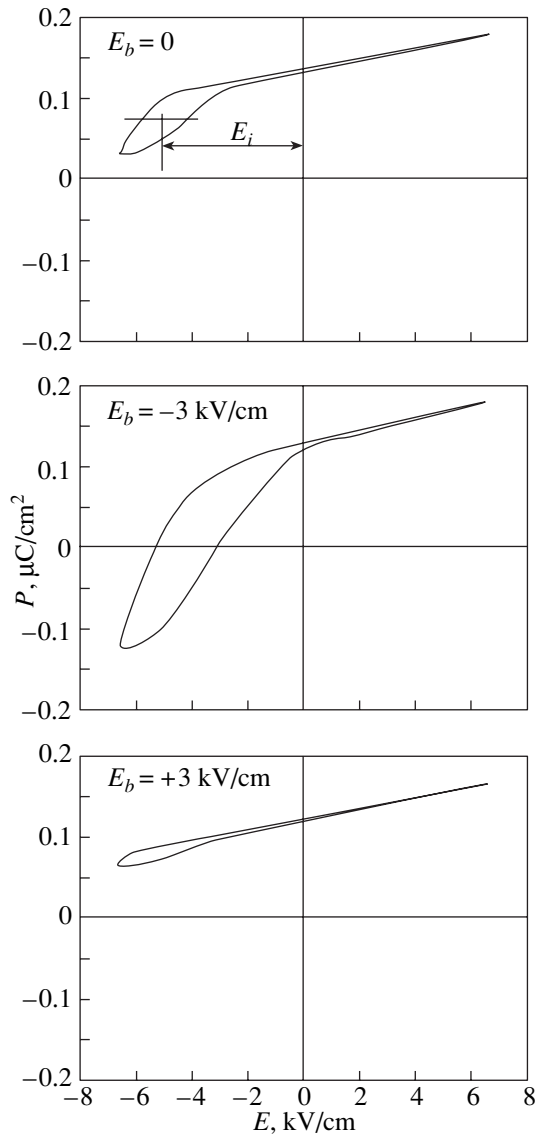


Fig. 6. Dielectric hysteresis loops of glycine phosphite doped with glycine phosphate (75 : 25 solution ratio) plotted vs. external bias E_b . Temperature 220 K, and measuring voltage frequency 50 Hz. The positive and negative values of the bias correspond to the field E_b parallel and antiparallel to the direction of the built-in bias field E_i , respectively.

Figures 7 and 8 illustrate the temperature behavior of the permittivity of pure and doped glycine phosphite crystals measured on the same samples with no external bias applied and with a bias of both polarities. Application of a bias voltage to samples of pure glycine phosphite is seen to entail approximately the same decrease in ϵ at the maximum of the temperature dependence for both voltage polarities (Fig. 7), whereas biasing crystals with the glycine phosphate impurity (Fig. 8) produces essentially different results when the voltage polarity is switched; indeed, with the external field opposing the built-in bias ($E_b = -7$ kV/cm), the ϵ peak

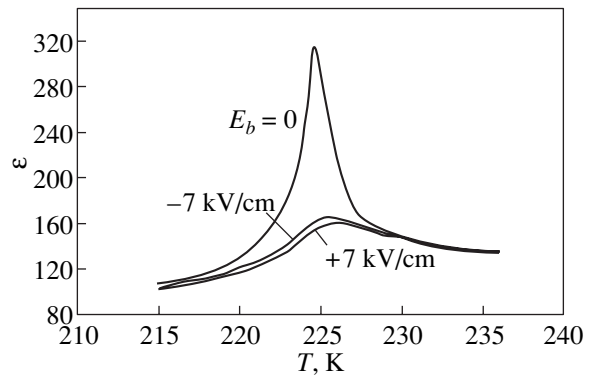


Fig. 7. Temperature behavior of the permittivity of nominally pure glycine phosphite crystals measured for different values of the external bias field E_b . Measuring voltage frequency 1 MHz, and field 5 V/cm. The interpretation of positive and negative values of the bias is the same as that in Fig. 6.

increases in amplitude, while for the opposite orientation ($E_b = +7$ kV/cm) it decreases.

Additional evidence of the existence of a strong built-in field in crystals doped with glycine phosphate is given by the temperature dependences of $\tan\delta$ of pure and doped (60 : 40) glycine phosphite crystals measured at 1 kHz and a measuring voltage amplitude of 4 V (i.e., in an electric field of 200 V/cm). We see that, in contrast to pure crystals, whose $\tan\delta$ grows strongly with decreasing temperature to reach a maximum at a temperature a few degrees below T_C , $\tan\delta$ in doped samples remains relatively small within the temperature range covered. In view of the contribution of molecular motions to the ferroelectric phase transition observed in glycine phosphite crystals [10], this may be accounted for by the hindering action that the built-in bias field in doped crystals exerts on these molecular motions, which are apparently responsible for the high values of $\tan\delta$ and the above-mentioned strong damping of elastic vibrations in pure crystals.

Thus, the totality of the results obtained suggests that, in glycine phosphite crystals doped with glycine phosphate, there exists a strong (about 5 kV/cm) built-in bias field aligned with the C_2 crystallographic axis. This internal bias field may account for the pyro- and piezoelectric response in crystals doped with glycine phosphate at temperatures substantially in excess of the ferroelectric phase transition temperature, thus causing a slight deformation of the glycine phosphite lattice, which is, however, large enough for the pyro- and piezoelectric activity to become observable in the temperature region from 225 to 280 K. To verify this conjecture experimentally, one should carry out an additional investigation, primarily, comprehensive x-ray diffraction characterization of doped glycine phosphite crystals in the above temperature region.

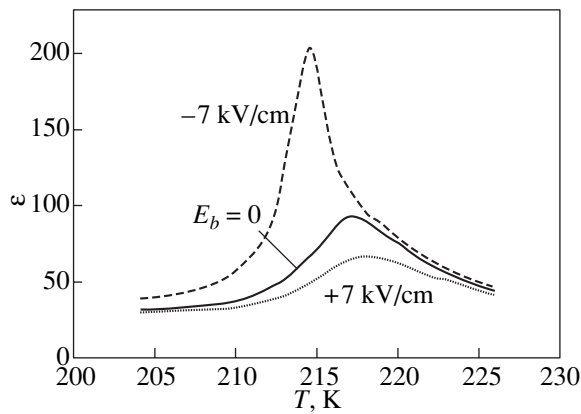


Fig. 8. Temperature behavior of the permittivity of glycine phosphite doped with glycine phosphate (75 : 25 solution ratio) measured for different values of the external bias field E_b . Conditions of measurement and notation of the curves are the same as those in Fig. 7.

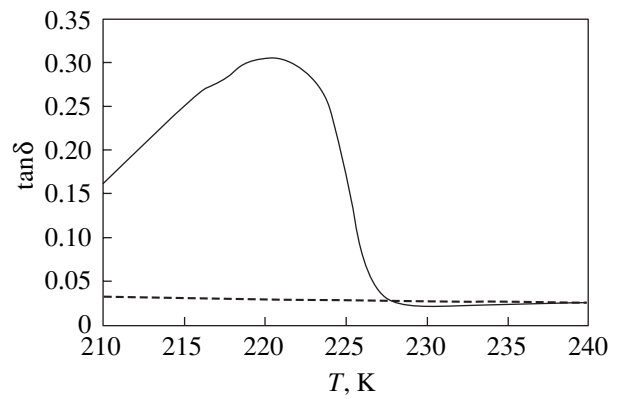


Fig. 9. Temperature behavior of loss tangent $\tan\delta$ of nominally pure glycine phosphite (solid line) and of glycine phosphite doped with glycine phosphate (60 : 40 solution ratio, dashed line). Measuring voltage frequency 1 kHz, and field 200 V/cm.

The existence of a built-in bias field in Gly · H₃PO₃ crystals doped with Gly · H₃PO₄ also makes it possible to explain (at least qualitatively) the above-mentioned reversal of the sign of the pyroelectric response observed to occur as one crosses the Curie temperature T_C . As in the colemanite crystals studied earlier, which revealed a shift in hysteresis loops in the absence of an external bias [7], in triglycine sulfate doped with *L*-alanine [8, 11], in deuterated glycine phosphite [12], and in BaTiO₃ ceramics doped by acceptor impurities [13], the formation of a built-in bias field E_i in doped glycine phosphite crystals is accounted for most probably by structural defects, which possess an electric dipole moment and are oriented appropriately with respect to the crystallographic axes. The preferential orientation of dipolar defects is usually related to the energy of their electrical and/or elastic interaction with the crystal lattice [7, 8, 11–15]. In Gly · H₃PO₃ crystals doped with Gly · H₃PO₄, complexes including differently charged anions [HPO₃]⁻² and [PO₄]⁻³, which also differ in terms of their spatial configuration and size, may serve as such dipolar defects. The preferential orientation of these defects most probably forming in the course of crystal growth creates a polarization P_i in the crystals at $T > T_C$. In a crystal cooled below T_C , this polarization adds algebraically to the spontaneous polarization P_s oriented along the C_2 symmetry axis to make the total polarization $P_\Sigma = P_i + P_s$ in the crystal at $T < T_C$, with the vectors \mathbf{P}_i and \mathbf{P}_s being either parallel or antiparallel to each other, depending on the absolute and relative magnitude of the electric and elastic interaction energies [13].

Figure 10 schematically shows the assumed orientation of the vectors \mathbf{P}_i , \mathbf{P}_s , \mathbf{P}_Σ , and \mathbf{E}_i in the crystals under study and the corresponding pattern of the temperature dependence of the pyroelectric coefficient dP/dT at temperatures above and below T_C . At $T > T_C$, because of

the continuity of the normal component of electric induction $\mathbf{D} = \epsilon_0\mathbf{E} + \mathbf{P}$, the dipole-induced polarization \mathbf{P}_i brings about a redistribution of free charges between the crystal electrodes connected through the load resistor in pyroelectric response measurements, so the sur-

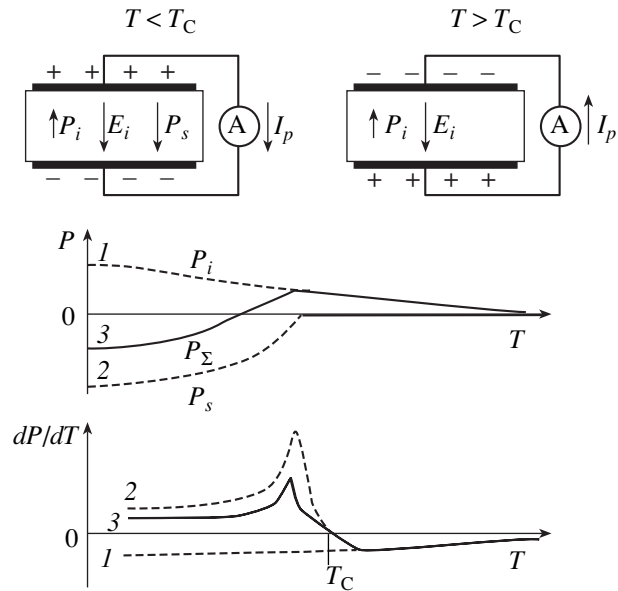


Fig. 10. Schematic image of glycine phosphate–doped glycine phosphite crystals connected in a circuit for measuring the pyroelectric response and temperature dependences of the polarization \mathbf{P} and the pyroelectric coefficient dP/dT . \mathbf{P}_i is the polarization induced by the oriented dipoles present in the crystal, \mathbf{E}_i is the dipole field (built-in bias field), \mathbf{P}_s is spontaneous polarization; \mathbf{P}_Σ is the total (net) polarization, and I_p is the pyroelectric current. Symbols + and – denote the polarity of free charges at the electrodes. Curves 1–3 are temperature dependences of \mathbf{P}_i , \mathbf{P}_s , and \mathbf{P}_Σ (and of their derivatives), respectively.

face charge density at the electrodes becomes equal to $|P_i|$. When the crystal is heated by IR radiation, P_i decreases in magnitude and a pyroelectric current appears in the measuring circuit; the pyroelectric response signal, which is proportional to dP_i/dT , varies comparatively weakly with temperature and, for the dipole orientation shown in Fig. 10, is negative at $T > T_C$. For the antiparallel orientation (with respect to P_i) of the spontaneous polarization vector P_s , which appears under cooling below T_C , and for $|P_s| > |P_i|$, the pyroelectric response (proportional to dP_Σ/dT) becomes negative at $T < T_C$.

ACKNOWLEDGMENTS

This study was supported in part by the Russian Foundation for Basic Research (project no. 02-02-17666), the state program of support for leading scientific schools (NSh-2168.2003.2), and the program of the Department of Physical Sciences, Russian Academy of Sciences.

REFERENCES

1. V. V. Lemanov, in *Piezoelectric Materials: Advances in Science, Technology and Applications*, Ed. by C. Galassi *et al.* (Kluwer Academic, Dordrecht, 2000).
2. V. V. Lemanov, *Ferroelectrics* **238**, 211 (2000).
3. S. Dacko, Z. Czapla, J. Baran, and M. Drozd, *Phys. Lett. A* **223**, 217 (1996).
4. V. V. Lemanov, S. N. Popov, and G. A. Pankova, *Fiz. Tverd. Tela (St. Petersburg)* **44**, 1840 (2002) [*Phys. Solid State* **44**, 1929 (2002)].
5. M.-T. Averbuch-Pouchot, *Acta Crystallogr. C* **49**, 815 (1993).
6. M. Simhony and A. Shaulov, *J. Appl. Phys.* **42**, 3741 (1971).
7. H. H. Wieder, *J. Appl. Phys.* **30**, 1010 (1959).
8. P. J. Lock, *Appl. Phys. Lett.* **19**, 390 (1971).
9. R. Tchukvinskyi, R. Cach, Z. Czapla, and S. Dacko, *Phys. Status Solidi A* **165**, 309 (1998).
10. P. Morawski, M. Gramza, J. Goslar, W. Hilczer, J. Szczepanska, and S. K. Hoffman, *Ferroelectr. Lett. Sect.* **23**, 121 (1998).
11. E. T. Keve, K. L. Bye, P. W. Whipps, and A. D. Annis, *Ferroelectrics* **3**, 39 (1971).
12. S. Dacko and Z. Czapla, *Ferroelectr. Lett. Sect.* **27**, 17 (2000).
13. G. Arlt and H. Neumann, *Ferroelectrics* **87**, 109 (1989).
14. A. P. Levanyuk, V. V. Osipov, A. S. Sigov, and A. A. Sobyanin, *Zh. Éksp. Teor. Fiz.* **76**, 345 (1979) [*Sov. Phys. JETP* **49**, 176 (1979)].
15. N. I. Lebedev, A. P. Levanyuk, and A. S. Sigov, *Zh. Éksp. Teor. Fiz.* **85**, 1423 (1983) [*Sov. Phys. JETP* **58**, 825 (1983)].

Translated by G. Skrebtsov

LATTICE DYNAMICS AND PHASE TRANSITIONS

Statistical Mechanics of Cation Ordering and Lattice Dynamics of $\text{PbZr}_x\text{Ti}_{1-x}\text{O}_3$ Solid Solutions

V. I. Zinenko and S. N. Sofronova

Kirensky Institute of Physics, Siberian Division, Russian Academy of Sciences,
Akademgorodok, Krasnoyarsk, 660036 Russia

e-mail: zvi@iph.krasn.ru

Received August 28, 2003

Abstract—An effective Hamiltonian for Zr–Ti cation ordering in $\text{PbZr}_x\text{Ti}_{1-x}\text{O}_3$ solid solutions is written out. To determine the parameters of the effective Hamiltonian, a nonempirical calculation is performed within an ionic-crystal model taking into account the deformation and dipole and quadrupole polarizabilities of ions. The thermodynamic properties of cation ordering are studied using the Monte Carlo method. The calculated phase transition temperatures (180 and 250 K for the concentrations $x = 1/3$ and $1/2$, respectively) are much lower than the melting temperature of the compound under study. At such temperatures, the ordering kinetics is frozen and, in reality, the phase transition to the ordered phase does not occur, in agreement with experimental observations. Within the same ionic-crystal model, we calculated the high-frequency permittivity, Born dynamic charges, and the lattice vibration spectrum for a completely disordered phase and certain ordered phases. It is shown that soft vibration modes, including ferroelectric ones, exist in the lattice vibration spectrum of both the completely disordered and the ordered phases. © 2004 MAIK “Nauka/Interperiodica”.

1. INTRODUCTION

Solid solutions of lead titanate and lead zirconate $\text{PbZr}_x\text{Ti}_{1-x}\text{O}_3$ (PZT) have been attracting research attention for many decades; a great number of experimental and theoretical studies have dealt with their physical properties. The PZT system has a complicated phase diagram and a number of interesting properties in terms of both theory and application (in particular, high values of the piezoelectric constants).

At high temperatures, PZT has a perovskite structure. As the temperature is decreased, this compound exhibits structural phase transitions to a rhombohedral, an orthorhombic, or a monoclinic phase with ferroelectric or antiferroelectric ordering, depending on the Zr/Ti content ratio (see, e.g., [1] and references therein). Phase transitions related to the ordering of tetravalent zirconium and titanium cations have not been observed experimentally at any concentration or temperature; however, there are experimental indications that, in the samples under study, there exist small regions with an ordered distribution of titanium and zirconium ions over the lattice sites [2]. Apparently, the presence of such ordered regions has a significant effect on lattice instability with respect to ferroelectric, antiferroelectric, and rotational distortions [3]. The properties of the solid solutions, in particular, the energies of different structures [4], some lattice vibration frequencies in the distorted phases [3], and Born effective charges in the disordered and ordered phases [5–8], were studied by performing *ab initio* calculations using different approaches in combination with the density functional method. However, the phase transitions

related to ordering of titanium and zirconium ions over the lattice sites were not discussed in the papers mentioned above; it was only noted that the energy of such ordering is small, because the valences of ions randomly distributed over the perovskite structure are equal.

In this paper, we perform a nonempirical calculation within an ionic-crystal model including the deformation and dipole and quadrupole polarizabilities of ions to study phase transitions related to ordering of titanium and zirconium ions and determine the entire vibration frequency spectrum of the disordered phase, the vibration frequencies at $q = 0$ for the ordered phases, the Born effective charges, and the high-frequency permittivity.

In Section 2, we introduce an effective Hamiltonian describing phase transitions of the order–disorder type in a model two-component Zr/Ti alloy. The parameters of the effective Hamiltonian, in which interactions within the first three coordination shells are taken into account, are determined by calculating the total energy of the crystal in different ordered phases. At certain values of the parameters of the effective Hamiltonian, using the Monte Carlo method, we study the thermodynamic properties of the system, namely, the phase transition temperatures and the temperature dependences of the heat capacity and of the long-range and short-range order parameters.

In Section 3, in the virtual-crystal approximation for different values of the Zr/Ti content ratio, we calculate the permittivity, Born effective charges, and the entire lattice vibration spectrum of the cubic phase of the dis-

ordered crystal for different concentrations x . Analogous calculations are also carried out for certain ordered phases of $\text{PbZr}_x\text{Ti}_{1-x}\text{O}_3$ with $x = 1/3$ and $1/2$; however, for brevity, we present here only the vibration frequencies at the center of the Brillouin zone.

Finally, in Section 4, we summarize the results of the study.

2. STATISTICAL MECHANICS OF B -CATION ORDERING

To describe phase transitions related to B -cation ordering in $\text{PbZr}_x\text{Ti}_{1-x}\text{O}_3$ solid solutions, we use the effective-Hamiltonian method in which only the degrees of freedom related to positional disorder of titanium and zirconium atoms at the sites of the crystal lattice (the b positions in the O_h space group) are taken into account. In this case, the problem of B -cation ordering in $AB'B''\text{O}_3$ solid solutions is equivalent to the problem of ordering in a two-component alloy and we can use a model based on the assumption that the atoms of a solution are placed at the sites of a certain rigid crystal lattice [9]. The configuration energy of the solution is expressed as the sum of all interatomic pair interaction potentials. In this model, the Hamiltonian of the system can be written as

$$H = \frac{1}{2} \sum_{k,j} [v_{B'B'}(\mathbf{r}_k, \mathbf{r}_j) n_k^{B'} n_j^{B'} + v_{B''B''}(\mathbf{r}_k, \mathbf{r}_j) n_k^{B''} n_j^{B''} + 2v_{B'B''}(\mathbf{r}_k, \mathbf{r}_j) n_k^{B'} n_j^{B''}] - \sum_j [n_j^{B'} \mu_{B'}(\mathbf{r}_j) + n_j^{B''} \mu_{B''}(\mathbf{r}_j)] + H_0, \quad (1)$$

where $v_{B'B'}$, $v_{B''B''}$, and $v_{B'B''}$ are the pair interaction potentials between B' atoms, between B'' atoms, and between B' and B'' atoms, respectively, at lattice sites \mathbf{r}_k and \mathbf{r}_j and $\mu_{B'}$ and $\mu_{B''}$ are the chemical potentials of the cations B' and B'' . The quantities $n_j^{B'}$ and $n_j^{B''}$ are random functions defined as follows: if site j is occupied by a B' atom, then $n_j^{B'} = 1$ and $n_j^{B''} = 0$, and if site j is occupied by a B'' atom, then $n_j^{B'} = 0$ and $n_j^{B''} = 1$. The quantities $n_j^{B'}$ and $n_j^{B''}$ satisfy the relation $n_j^{B'} + n_j^{B''} = 1$. Using this relation, we can rewrite Eq. (1) as [9]

$$H = \frac{1}{2} \sum_{k,j} v(\mathbf{r}_k, \mathbf{r}_j) n_k^{B'} n_j^{B''} - \mu \sum_j n_j^{B'} + H_0, \quad (2)$$

where

$$v(\mathbf{r}_k, \mathbf{r}_j) = v_{B'B'}(\mathbf{r}_k, \mathbf{r}_j) + v_{B''B''}(\mathbf{r}_k, \mathbf{r}_j) - 2v_{B'B''}(\mathbf{r}_k, \mathbf{r}_j)$$

is the effective interaction constant and

$$\mu = \mu_{B'}(\mathbf{r}_j) - \mu_{B''}(\mathbf{r}_j) + \sum_{i,k} (v_{B'B'}(\mathbf{r}_k, \mathbf{r}_j) - v_{B''B''}(\mathbf{r}_k, \mathbf{r}_j))$$

is the chemical potential of the system.

The effective interaction constants are evaluated by performing a nonempirical calculation of the total energy of the crystal in the Gordon–Kim model with inclusion of the dipole and quadrupole polarizabilities of ions [10, 11]. The total energy is

$$E = E_s + E_p + E_q + E_{pq} + E_{\text{self}}, \quad (3)$$

where

$$E_s = -\frac{1}{2} \sum_{i,j=1}^{N_a} Z_i C_{ij}^{(0)} Z_j + \sum_{i,j=1}^{N_a} \Phi_{ij}^{(00)}(V_i, V_j, |\mathbf{R}_i - \mathbf{R}_j|), \quad (4)$$

$$E_p = \frac{1}{2} \sum_{i,j=1}^{N_a} \sum_{\alpha,\beta=1}^3 P_i^\alpha \left(\frac{\delta_{ij}}{-\alpha_i^\beta(V_i)} + \Phi_{ij,\alpha\beta}^{(11)}(V_i, V_j, |\mathbf{R}_i - \mathbf{R}_j|) - C_{ij,\alpha\beta}^{(2)} \right) P_j^\beta \quad (5)$$

$$+ \sum_{i,j=1}^{N_a} \sum_{\alpha=1}^3 P_i^\alpha (\Phi_{ij,\alpha}^{(10)}(V_i, V_j, |\mathbf{R}_i - \mathbf{R}_j|) - C_{ij,\alpha}^{(1)} Z_j),$$

$$E_{qp} = \frac{1}{2} \sum_{i,j=1}^{N_a} \sum_{\alpha,\beta,\gamma,\delta=1}^3 q_i^{\alpha\beta} \left[\frac{\delta_{ij}}{-\alpha_i^\beta(V_i)} - \frac{1}{36} (\Phi_{ij,\alpha\beta\gamma\delta}^{(22)}(V_i, V_j, |\mathbf{R}_i - \mathbf{R}_j|) - C_{ij,\alpha\beta\gamma\delta}^{(4)}) \right] q_j^{\gamma\delta} \quad (6)$$

$$- \frac{1}{6} \sum_{i,j=1}^{N_a} \sum_{\alpha,\beta=1}^3 q_i^{\alpha\beta} (\Phi_{ij,\alpha\beta}^{(20)}(V_i, V_j, |\mathbf{R}_i - \mathbf{R}_j|) - C_{ij,\alpha\beta}^{(2)} Z_j),$$

$$E_q = -\frac{1}{6} \sum_{i,j=1}^{N_a} \sum_{\alpha,\beta,\gamma=1}^3 q_i^{\alpha\beta} (\Phi_{ij,\alpha\beta\gamma}^{(21)}(V_i, V_j, |\mathbf{R}_i - \mathbf{R}_j|) - C_{ij,\alpha\beta\gamma}^{(3)} P_j^\gamma). \quad (7)$$

Here, E_s is the interaction energy of spherically symmetric ions; E_p , E_q , and E_{pq} are the interaction energies of dipole and quadrupole moments; $E_{\text{self}} = \sum_{i=1}^{N_a} E_i^{\text{ion}}$ is the self-energy of ions; $C_{ij}^{(n)} = \nabla^n \frac{1}{|\mathbf{R}_i - \mathbf{R}_j|}$ is the long-range part of the interactions, which is calculated by the Ewald method; $\Phi_{ij,\alpha\beta\gamma}^{(mn)}(V_i, V_j, |\mathbf{R}_i - \mathbf{R}_j|)$ is the short-range part of the interaction; and $P_i^\alpha (q_i^{\alpha\beta})$ are the dipole (quadrupole) moments of ions, which can be found by minimizing the total energy of the crystal [11].

To find the crystal energy in the disordered phase, we use the virtual-crystal approximation. In this approximation, the short-range part of pair interactions of a virtual ion $\langle B \rangle$ with the other ions (i) is

$$\Phi_{iB}^{II'} = x\Phi_{iB'}^{II'} + (1-x)\Phi_{iB''}^{II'}. \quad (8)$$

The contribution from the virtual ion to the self-energy can be written as

$$E_B^{\text{ion}} = xE_{B'}^{\text{ion}} + (1-x)E_{B''}^{\text{ion}}. \quad (9)$$

The quadrupole and dipole polarizabilities of the virtual ion B are

$$\alpha_B^{d,q} = x\alpha_{B'}^{d,q} + (1-x)\alpha_{B''}^{d,q}. \quad (10)$$

The long-range part of the interaction remains the same as that for the pure components of the solutions.

Let us discuss the phase transition in a $\text{PbZr}_x\text{Ti}_{1-x}\text{O}_3$ solid solution related to ordering of the B cations in the case where $x = 1/2$ and $1/3$. Furthermore, in the effective Hamiltonian (2), we restrict ourselves to interactions within the first three coordination shells. To calculate the effective constants, we find the energies of several structures with different ordering of the titanium ions. For the ordered structures, we use the notation from [12], where an analogous calculation of the energies was performed for the $\text{PbSc}_{1/2}\text{Ta}_{1/2}\text{O}_3$ solid solution. Table 1 lists the configuration motif, the lattice parameters of the ordered structures, the energies per ABO_3 formula unit calculated without and with regard to relaxation of Pb and O ions, and expressions of the energy in terms of the effective constants defined in Eq. (2). The table also gives the energies of mixtures of pure substances PbTiO_3 (PTO) and PbZrO_3 (PZO) for concentrations $x = 1/2$ and $1/3$. It is seen from the Table 1 that at any concentration the most favorable ordered structure considered is the structure with Zr and Ti cations ordered along the body diagonal of the cubic unit cell of the disordered phase. However, without taking the relaxation of Pb and O ions into account, this structure has a somewhat greater energy than the mixture of the pure substances. For concentration $x = 1/2$, the result obtained agrees with calculations performed by other authors [4]. The difference in the energies of the two unrelaxed structures with ordering along the [111] and [100] directions obtained in this study (5.3 mRy) also agrees with the results obtained in other calculations (4.6 and 5.9 mRy [4]).

Since only the degrees of freedom related to positional disorder of B' and B'' atoms are taken into account in the effective Hamiltonian, the effective interaction constants are calculated using the energies of unrelaxed structures. The energy expressed in terms of the effective constants contains a constant energy E_0 , which is independent of the positions of B' and B'' ions and can be taken as the zero of energy. The calculated effective interaction constants are listed in Table 2.

To study the statistical properties of the phase transitions related to the ordering of B cations in the $\text{PbZr}_x\text{Ti}_{1-x}\text{O}_3$ compounds ($x = 1/2, 1/3$), in addition to using the effective Hamiltonian (2), we applied the standard Monte Carlo method [13].

The Monte Carlo procedure consists in the following. As the initial structure, we take one of the ordered structures or the completely disordered structure at a fixed temperature. One Monte Carlo step is sequential running over all lattice sites. For each site (s), one of the nearest neighbors is randomly chosen (s'). If the atoms at sites s and s' are of the same type, then the configuration remains unchanged. If the atoms at sites s and s' differ in type, then we calculate the energy difference between the initial configuration and the configuration in which the atoms in sites s and s' change places:

$$\Delta E^{\text{conf}} = \sum_{i=1}^3 2(m_{B'B'}^{(i)} - m_{B''B''}^{(i)} + \delta) v_i, \quad (11)$$

where $m_{B'B'}^{(i)}$ is the number of i th nearest B' -type neighbors of a B' -type atom, $m_{B''B''}^{(i)}$ is the number of i th nearest B'' -type neighbors of a B'' -type atom before the permutation, and $\delta = 1$ if $i = 1$ and $\delta = 0$ if $i = 2, 3$.

The latter condition means that the nearest neighbors change places. The permutation is accepted and the configuration is taken to be new in the following cases: (i) $\Delta E^{\text{conf}} \leq 0$ or (ii) $\Delta E^{\text{conf}} > 0$ if $\xi < \exp[-\Delta E^{\text{conf}}/kT]$, where ξ is a random number and $0 < \xi < 1$.

After each Monte Carlo step, we calculate the energy of the configuration, the short-range order parameter σ , and the long-range order parameter η . The short-range order parameter is defined by [14]

$$\sigma = \left| \frac{n_{B'B''} - n_{B'B''}(\text{disorder})}{n_{B'B''}(\text{order}) - n_{B'B''}(\text{disorder})} \right|, \quad (12)$$

where $n_{B'B''}(\text{disorder}) = \bar{Z}Nx(1-x)$ is the number of $B'B''$ pairs in the completely disordered solid solution, \bar{Z} is the coordination number, N is the number of atoms in the solution, and x is the concentration of atoms of type B' .

For concentration $x = 1/2$, the structures with ordering along the [111], [110], and [100] directions have the lowest energies; therefore, they are of greatest interest. For each of these structures, we calculate the short-range and long-range order parameters.

For different completely ordered structures in the case where $x = 1/2$, the values of $n_{B'B''}(\text{order})$ are

$$\begin{aligned} n_{B'B''}(111) &= 6N, & n_{B'B''}(110) &= 4N, \\ n_{B'B''}(100) &= 2N. \end{aligned}$$

Table 1. Energies of different ordered $\text{PbZr}_x\text{Ti}_{1-x}\text{O}_3$ structures

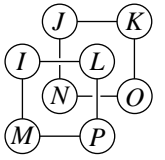
Configuration {IJKL} {MNOP} $B' = +1, B'' = -1$	Lattice parameters ($a_0 = 3.95 \text{ \AA}$)	Calculated energies without regard to the ion self-energy, eV		Expressions of the energy in terms of the effective constants v_i
		without relaxation	with relaxation	
				
$x = 1/2$				
{-1 1 -1 1}	$a = b = c = 2a_0$	-158.128282	-158.253272	$6v_1 + 8v_3 - \mu/2 + E_0$
{1 -1 1 -1}				
$B'B''$ along [111]				
{-1 1 -1 -1}	$a = b = c = 2a_0$	-158.074271	-158.180158	$3v_1 + 6v_2 + 8v_3 - \mu/2 + E_0$
{1 1 1 -1}				
{1 1 1 1}	$a = b = a_0,$	-158.056270	-158.227649	$2v_1 + 8v_2 + 8v_3 - \mu/2 + E_0$
{-1 -1 -1 -1}	$c = 2a_0$			
$B'B''$ along [100]				
{1 -1 1 -1}	$a = b = \sqrt{2}a_0,$	-158.091386	-158.210677	$4v_1 + 8v_2 - \mu/2 + E_0$
{1 -1 1 -1}	$c = a_0$			
$B'B''$ along [110]				
{-1 -1 -1 1}	$a = b = c = 2a_0$	-158.091829	-158.203578	$4v_1 + 6v_2 + 4v_3 - \mu/2 + E_0$
{1 1 1 -1}				
{1 -1 -1 -1}	$a = b = c = 2a_0$	-158.073826	-158.160574	$3v_1 + 8v_2 + 4v_3 - \mu/2 + E_0$
{1 1 1 -1}				
{1 1 1 1}	$a = b = a_0$	-158.012134	-158.900837	$v_1 + 4v_2 + 4v_3 - \mu/2 + E_0$
{1 1 1 1}+	$c = 4a_0$			
{-1 -1 -1 -1}				
{-1 -1 -1 -1}				
1/2PZO + 1/2PTO		-158.157773		
$x = 1/3$				
$B'B''$ along [100]	$a = b = a_0,$ $c = 3a_0$	-159.074277	-159.210991	$(4v_1 + 16v_2 + 16v_3 - 2\mu)/3 + E_0$
$B'B''$ along [111]	$a = b = \sqrt{2}a_0,$ $c = \sqrt{3}a_0$	-159.133164	-159.259862	$4v_1 + 4v_2 + 4v_3 - 2\mu/3 + E_0$
1/3PZO + 2/3PTO		-159.229638		

Table 2. Effective interaction constants (in meV)

v_1	v_2	v_3
-12.22	-1.61	-0.86

For concentration $x = 1/3$, two ordered structures were considered, namely, those with ordering along the [111] and [100] directions. The number of $B'B''$ pairs for the ordered structures in the case of $x = 1/3$ is

$$n_{B'B''}(111) = 4N, \quad n_{B'B''}(100) = 4/3N.$$

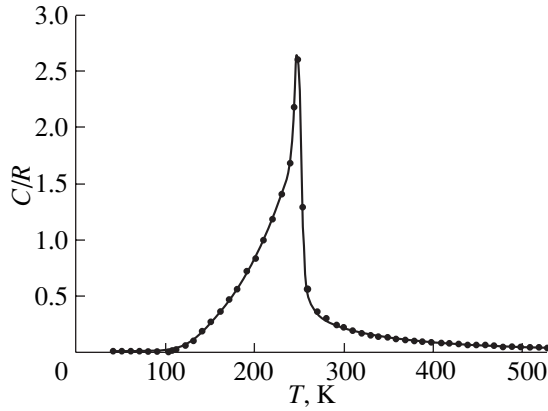


Fig. 1. Temperature dependence of the excess heat capacity related to B -cation ordering in the $\text{PbZr}_{1/2}\text{Ti}_{1/2}\text{O}_3$ solid solution.

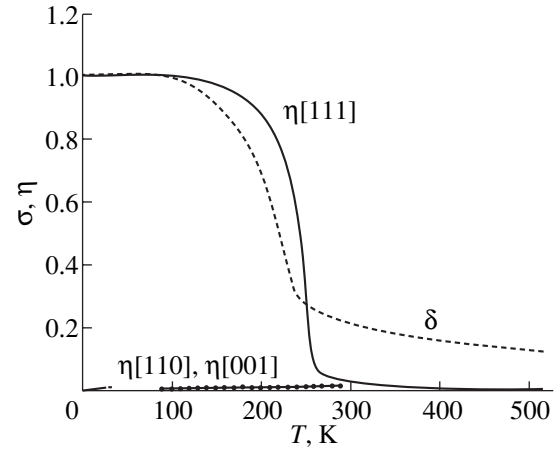


Fig. 2. Temperature dependence of the long-range and short-range order parameters in the $\text{PbZr}_{1/2}\text{Ti}_{1/2}\text{O}_3$ solid solution.

The long-range order parameter for $x = 1/2$ is defined as

$$\eta = \left| \frac{4R_B(B')}{N} - 1 \right|, \quad (13)$$

where $R_B(B')$ is the number of atoms of type B' at their “sites proper.”

For different types of ordering, the B' sites are defined by the following conditions:

$$\exp[i\pi(x + y + z)] = 1, \quad (14a)$$

for ordering along the [111] direction,

$$\exp[i\pi(x + y)] = 1, \quad (14b)$$

for ordering along the [110] direction, and

$$\exp[i\pi(x)] = 1, \quad (14c)$$

for ordering along the [100] direction, where x , y , and z are the site coordinates.

For concentration $x = 1/3$, the long-range order parameter is

$$\eta = \frac{1}{2} \left| \frac{9R_B(B')}{N} - 1 \right|. \quad (15)$$

The B' sites are defined by the following conditions:

$$\cos\left(\frac{2\pi}{3}(x + y + z)\right) = 1, \quad (16a)$$

for ordering along the [111] direction and

$$\cos\left(\frac{2\pi}{3}x\right) = 1, \quad (16b)$$

for ordering along the [100] direction.

We studied lattices $16 \times 16 \times 16$ in size for $x = 1/2$ and $18 \times 18 \times 18$ for $x = 1/3$ with periodic boundary conditions. The first 10 000 steps at each temperature are disregarded and are not included in averaging the quantities E^{conf} , η , and σ . The average values $\langle E^{\text{conf}} \rangle$,

$\langle (E^{\text{conf}})^2 \rangle$, $\langle \eta \rangle$, and $\langle \sigma \rangle$ are calculated in two steps. After $p = 50$ steps, the group averages are calculated:

$$\langle \eta \rangle_g = \frac{1}{p} \sum_{i=1}^p \eta_i, \quad \langle \sigma \rangle_g = \frac{1}{p} \sum_{i=1}^p \sigma_i, \quad (17)$$

$$\langle E^{\text{conf}} \rangle_g = \frac{1}{p} \sum_{i=1}^p E_i^{\text{conf}}, \quad \langle (E^{\text{conf}})^2 \rangle_g = \frac{1}{p} \sum_{i=1}^p (E_i^{\text{conf}})^2.$$

Then, the averaging over $M = 500$ groups is performed:

$$\begin{aligned} \langle \eta \rangle &= \frac{1}{M} \sum_{i=1}^M \langle \eta \rangle_g, & \langle \sigma \rangle &= \frac{1}{M} \sum_{i=1}^M \langle \sigma \rangle_g, \\ \langle E^{\text{conf}} \rangle &= \frac{1}{M} \sum_{i=1}^M \langle E^{\text{conf}} \rangle_g, & (18) \\ \langle (E^{\text{conf}})^2 \rangle &= \frac{1}{M} \sum_{i=1}^M \langle (E^{\text{conf}})^2 \rangle_g. \end{aligned}$$

The heat capacity of the system is defined as $C = \frac{1}{kT^2} (\langle (E^{\text{conf}})^2 \rangle - \langle E^{\text{conf}} \rangle^2)$.

The temperature dependences of the heat capacity and of the short-range and long-range order parameters for $x = 1/2$ are shown in Figs. 1 and 2. At low temperatures, the only stable structure is the structure with the ordering along the [111] direction, which appears both upon heating and cooling. The structures with other ordering types are unstable; this can be seen from Fig. 2. The long-range order parameters of the structures with ordering along the [110] and [100] directions are equal to zero throughout the entire temperature range. The phase transition from the ordered to the disordered state occurs at a temperature of about 250 K. As noted in Section 1, experimental data show that ordering does not occur in the $\text{PbZr}_{1/2}\text{Ti}_{1/2}\text{O}_3$ solid solution.

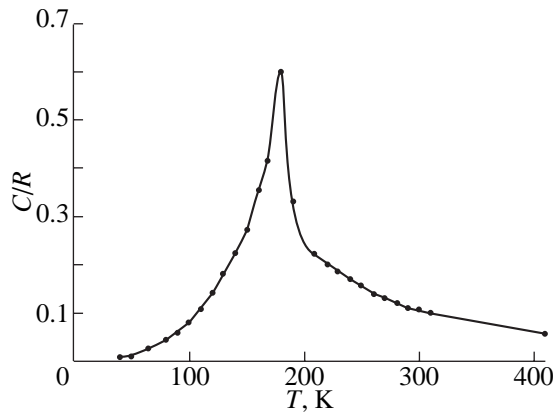


Fig. 3. Same as in Fig. 1 but for the $\text{PbZr}_{1/3}\text{Ti}_{2/3}\text{O}_3$ solid solution.

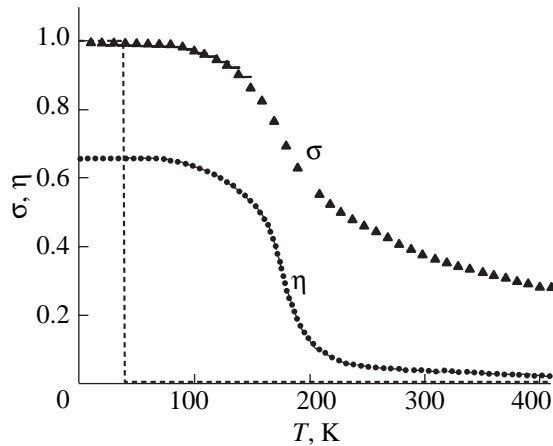


Fig. 4. Temperature dependence of the long-range and short-range order parameters for the $\text{PbZr}_{1/3}\text{Ti}_{2/3}\text{O}_3$ solid solution. Dashed lines show the order parameter for ordering along [111] with a B-cation ratio of 1 : 2, points represent the order parameter for ordering along [111] with a B-cation ratio of 1 : 1 in the heating and cooling modes, and triangles represent the short-range order parameter.

Since the ordering processes in solid solutions, as well as in metal alloys, are diffusive in character, the kinetics of these processes is frozen at the transition temperature obtained, $T = 250$ K, which is much smaller than the melting temperature of PZT ($T_{\text{melt}} \sim 1200$ K); therefore, the phase transition to an ordered state does not occur.

The temperature dependences of the heat capacity and of the short-range and long-range order parameters for concentration $x = 1/3$ are shown in Figs. 3 and 4. The structure with the 1 : 2 ratio and ordering along the [111] direction is metastable for this concentration. If we start the Monte Carlo procedure at a low temperature from this configuration, then the structure collapses with increasing temperature. Part of the solution

becomes ordered along the body diagonal to the Zr/Ti ratio of 1 : 1, and regions of pure Ti appear. With a further increase in temperature (near 180 K), the ordered regions with the 1 : 1 ratio become disordered. In the cooling regime, ordered regions with the 1 : 1 ratio appear at 180 K, and this structure survives down to low temperatures. A peak in the heat capacity is observed to occur at 180 K. There are experimental indications [2] that nanodomains with the ordering of Zr and Ti ions in a ratio of 1 : 1 exist in PZT solid solutions at low temperatures.

3. LATTICE DYNAMICS OF THE DISORDERED AND CERTAIN ORDERED PHASES

The frequency vibration spectrum, high-frequency permittivity, Born effective charges, and elastic moduli of the ordered phases of $\text{PbZr}_x\text{Ti}_{1-x}\text{O}_3$ solid solutions are calculated within the Gordon–Kim model of ionic crystals with regard to deformability and dipole and quadrupole distortions of the electronic density of ions. The corresponding formulas for calculations can be found in [15]. In the case of disordered solid solutions, we calculated the dynamic properties using the virtual-crystal approximation; i.e., in the dynamic matrix, all but the long-range Coulomb contributions are calculated by expanding the interaction energy of a virtual $\langle B \rangle$ ion with the other ions into a Taylor series in small displacements.

First, we discuss the case of disordered solid solutions, which, like the pure components, have a cubic perovskite structure and one molecule per unit cell.

Table 3 lists the calculated lattice cell parameters, high-frequency permittivity, Born effective charges, and elastic moduli for the pure components PbZrO_3 and PbTiO_3 and for solid solutions with concentrations $x = 1/3$, $1/2$, and $2/3$. For comparison, the results of other *ab initio* calculations [16, 17] are also presented. Figure 5 shows the calculated vibration spectrum of the disordered $\text{PbZr}_{1/2}\text{Ti}_{1/2}\text{O}_3$ solid solution for symmetry points and directions in the Brillouin zone, and Table 4 lists the calculated vibration frequencies at the $\Gamma(0, 0, 0)$ and $R(1/2, 1/2, 1/2)$ points for the pure components and for the disordered solutions with concentrations $x = 1/3$, $1/2$, and $2/3$. It is seen from Tables 3 and 4 that the results of our calculations agree (within 10–30%) with the results of other *ab initio* calculations (except for the value of ϵ_∞ for PbTiO_3 obtained in [17]). In solid solutions, as well as in the pure components, there are soft modes in the vibration spectrum. We note that, in addition to a polar vibration mode, our calculations for pure PbTiO_3 predict antiferroelectric lattice instability and that the vibration mode R_{25} , whose eigenvectors correspond to rotation of the TiO_6 octahedron, turns out to be hard. At the same time, in PbZrO_3 , in addition to the ferroelectric and antiferroelectric instabilities, there exists a soft mode R_{25} related to rotation of the ZrO_6 octahedron. All three types of instability exist in a solid

Table 3. Lattice parameter a_0 , permittivity ϵ_∞ , Born effective charge Z , and elastic moduli C_{ij} for crystals $\text{PbZr}_x\text{Ti}_{1-x}\text{O}_3$ in the virtual-crystal approximation

x	$a_0, \text{\AA}$	ϵ_∞	Z_{Pb}	$Z_{\langle B \rangle}$	Z_{O1}	Z_{O3}	$C_{11}, 10^2 \text{ GPa}$	$C_{12}, 10^2 \text{ GPa}$	$C_{44}, 10^2 \text{ GPa}$
0	3.83	4.90	2.78	5.67	-4.93	-1.76	2.58	1.16	1.14
	3.97*	8.24*	3.90**	7.06**	-5.83**	-2.56**			
1/3	3.91	5.21	2.78	5.78	-4.97	-1.79	2.45	0.99	0.96
1/2	3.95	4.87	2.77	5.62	-4.68	-1.86	2.34	0.91	0.90
	3.99***		3.92***	6.47***	-5.28***	-2.54***			
2/3	3.97	4.81	2.77	5.56	-4.53	-1.90	2.42	0.89	0.86
1	4.03	4.50	2.77	5.35	-4.15	-1.98	2.36	0.80	0.78
	4.12*	6.97*	3.92**	5.85**	-4.81**	-2.48**			

* Calculated by the pseudopotential method and the linear-response method [17].

** Calculated by the pseudopotential method and the frozen-phonon method [16].

*** Calculated by the pseudopotential method in the virtual-crystal approximation [6].

solution if the position of a tetravalent cation is occupied by the virtual atom $\langle B \rangle$.

It is seen from Table 1 that, for concentration $x = 1/2$, there are two ordered structures of lowest energies. The structure with the B' and B'' cations ordered along the $[001]$ direction has the $P4/mmm$ symmetry, and the structure with ordering along the $[111]$ direction (the elpasolite structure) has the $Fm3m$ symmetry. For both structures, there are adjustable parameters. In the tetragonal structure, the oxygen ions located between the Zr and Ti ions, as well as the Pb ions, can be displaced along the z axis. In the elpasolite structure, there is a degree of freedom related to “breathing” of the oxygen octahedron. We minimized the total energy with respect to the volume and the free parameters at a constant value of the ratio $c/a = 2.0$ for the tetragonal lattice. For the elpasolite structure, the oxygen octahedron is drawn to the Ti ion by 0.05 \AA . For the tetragonal structure, the

oxygen and lead ions are displaced along the z axis to the Ti ion by 0.11 \AA . The calculated unit cell parameters, high-frequency permittivity, and Born effective charges for these two ordered structures at $x = 1/3$ and $1/2$ are given in Tables 5 and 6; for comparison, the results of other calculations are also presented. It is seen from Tables 5 and 6 that the Born dynamic charges calculated in this study (especially for the lead ion) both in the disordered and in the ordered phases at concentrations $x = 1/2$ and $1/3$ are somewhat smaller than those obtained using the pseudopotential method [18]. It is interesting to note that, in the pure components of a solution, the effective charge of the titanium ion exceeds that of the zirconium ion, whereas for the ordered structures the effective charge of the zirconium ion either is approximately equal to or exceeds that of the titanium ion.

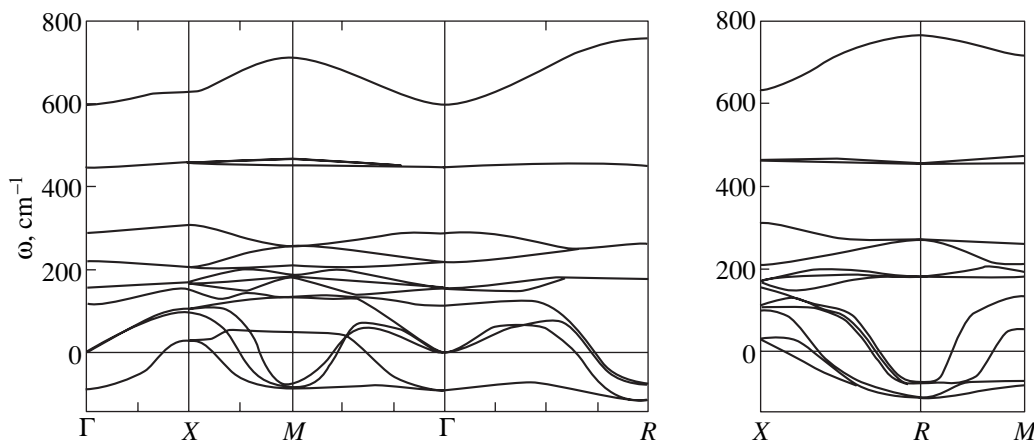

Fig. 5. Phonon spectrum of $\text{PbZr}_{1/2}\text{Ti}_{1/2}\text{O}_3$ calculated in the virtual-crystal approximation.

Table 4. Vibration frequencies (cm^{-1}) for $\text{PbZr}_x\text{Ti}_{1-x}\text{O}_3$ calculated for various concentrations in the virtual-crystal approximation (the mode degeneracy is indicated in parentheses)

x	$q = 0$						
	$TO1(2)$	$LO1$	$T_{2u}(3)$	$TO2(2)$	$LO2$	$TO3(2)$	$LO3$
0	87.3i 144i*	142.0 104*	180.8	236.7 121*	318.9 410*	437.8 497*	616.3 673*
1/3	88.3i	121.6	154.6	222.5	288.7	442.8	608.2
1/2	89.5i	114.7	156.4	219.7	289.6	448.4	600.7
2/3	88.4i	113.3	153.4	218.2	285.5	470.8	611.4
1	91.9i 131i* 140i**	104.9 90*	150.0 30**	214.1 63* 170**	283.5 310*	488.2 486* 600**	609.3 720**
x	$q = R$						
	$R_{15}(3)$	$R_{25}(3)$	$R_{15}(3)$	$R_{25}(3)$	$R_{12}(2)$	R_2	
0	110.5i	51.3	177.5	383.0	423.8	718.9	
1/3	119.4i	67.8i	171.8	365.7	438.6	691.2	
1/2	113.3i	77.5i	178.8	342.2	451.6	676.8	
2/3	110.9i	93.6i	181.5	328.5	483.9	677.5	
1	105.0i	113.3i	190.9	299.7	510.8	661.6	

* Calculated by the pseudopotential method and the frozen-phonon method [15].

** Calculated by the pseudopotential method and the linear-response method [16].

Table 5. Lattice parameters, Born effective charges, and permittivity for ordered $\text{PbZr}_{1/2}\text{Ti}_{1/2}\text{O}_3$ solid solutions with different ordering types (for the ordering along [001], the O1 ions lie between Zr and Ti ions, the O2 ions lie in the same plane as the Zr ions, and the O3 ions lie in the same plane as the Ti ions)

Ordering	$a_0, \text{\AA}$	ϵ_∞		Z_{Pb}		Z_{Ti}		Z_{Zr}		Z_{O1}		Z_{O2}		Z_{O3}	
		11	33	xx	zz	xx	zz	xx	zz	xx	zz	xx, yy	zz	xx, yy	zz
Along [111]	$a = 7.88$	4.97	4.97	2.78		5.48		5.77		-1.85	-4.71				
Along [001]	$a = 3.95,$ $c/a = 2.0$	5.01	4.85	2.78	2.84	5.52	6.02	6.10	5.53	-1.79	-4.98	-5.02	-2.12	-5.11,	-1.51
Along [001] (calculation data from [5])	$a = 3.99,$ $c/a = 2.07$	-	-		3.0		5.3		6.0		-4.6		-2.1		-2.1

We calculated the entire lattice vibration spectra in low-energy ordered PZT phases at concentrations $x = 1/3$ and $1/2$. The limiting optical vibration frequencies at $q = 0$ are given in Table 7. For comparison, the table also lists the results of *ab initio* LAPW calculations of limiting frequencies in the $\text{PbZr}_{1/2}\text{Ti}_{1/2}\text{O}_3$ phase ordered along the [111] direction [3]. We see from Table 7 that, for both values of the Zr/Ti ratio in the ordered phases, the crystal lattice is unstable with respect both to the ferroelectric mode ($100.6i$ and $115i \text{ cm}^{-1}$ in the phases $P\bar{3}m1$ and $P4mm$ for $x = 1/3$, respectively, and $87.3i$ and $103.5i \text{ cm}^{-1}$ in the phases $Fm\bar{3}m$ and $P4/mmm$ for $x = 1/2$, respectively) and to other vibration modes. We

note that, in the ordered $\text{Pb}_2\text{ZrTiO}_6$ with an elpasolite structure, in addition to the ferroelectric soft mode, there is a soft T_{1g} mode that is very close in energy ($87i \text{ cm}^{-1}$) and whose eigenvectors correspond to rotations of the TiO_6 (ZrO_6) octahedrons. Thus, for a Zr/Ti ratio close to $1/2$, we might expect both polar and rotational distortions of the crystal lattice. It is seen from Table 7 that the $\text{Pb}_3\text{ZrTi}_2\text{O}_9$ compound with ordering along the [111] and [001] directions is even more unstable with respect to a ferroelectric mode or other vibration modes that are close in energy. For these values of the Zr/Ti ratio, the pattern of lattice distortions during structural phase transitions can be more complicated.

Table 6. Permittivity and Born effective charges for ordered $\text{PbZr}_{1/3}\text{Ti}_{2/3}\text{O}_3$ solid solutions with different ordering types

Ion	Ordering along [001] (calculation data)				Ordering along [111] (our calculation data)	
	this study		[18]			
	ϵ_{11}	ϵ_{33}	ϵ_{11}	ϵ_{33}	ϵ_{11}	ϵ_{33}
	5.09	5.28	–	–	5.11	5.04
	Z_{xx}	Z_{zz}	Z_{xx}	Z_{zz}	Z_{xx}	Z_{zz}
Pb1	2.88	2.87	3.90	4.04	2.86	2.96
Pb2	2.81	2.92	3.88	3.53	2.93	2.65
Pb3	2.88	2.87	3.90	4.04	2.86	2.96
Ti1	5.50	6.52	6.77	6.65	5.63	5.07
Ti2	5.50	6.52	6.77	6.65	5.63	5.07
Zr	6.09	5.87	6.33	6.69	5.24	5.75
O1	-1.65	-5.32	-2.58	-5.39	-1.69	-5.23
O2	-5.16	-1.62	-5.58	-2.34	-1.57	-5.20
O3	-1.72	-1.62	-2.72	-2.34	-1.57	-5.20
O4	-1.55	-6.09	-2.53	-5.57	-1.65	-4.91
O5	-5.16	-1.62	-5.58	-2.34	-1.79	-4.93
O6	-1.72	-1.62	-2.72	-2.34	-1.65	-4.91
O7	-1.65	-5.32	-2.58	-5.39	-1.79	-4.93
O8	-5.06	-2.17	-5.17	-2.94	-1.65	-4.91
O9	-1.96	-2.17	-2.33	-2.94	-1.65	-4.91

Table 7. Vibration frequencies (cm^{-1}) at $q = 0$ for ordered PZT structures with concentration $x = 1/3$ and $1/2$ (the mode degeneracy is indicated in parentheses)

$\text{Pb}_3\text{ZrTi}_2\text{O}_9$				$\text{Pb}_3\text{ZrTiO}_6$			
ordering along [111], $P\bar{3}m1$ symmetry (our calculation data)		ordering along [001], $P4mm$ symmetry (our calculation data)		ordering along [111], $Fm\bar{3}m$ symmetry (calculation data)		ordering along [001], $P4/mmm$ symmetry (our calculation data)	
				this study	[3]		
100.6i	218.1	115.0i	185.6	87.3i(2)	125i	103.5i	379.7
98.9i	219.2	95.5i	186.6(2)	87.0i(3)		101.8i	398.6
94.6i(2)	237.4	67.5i(2)	195.5	58.2i(3)	16i	28.8(2)	431.9
66.7i	261.8	23.5i	202.0	117.0		75.9	453.3
52.8i	286.5	22.8i	203.9	157.3(3)		82.6	517.5
52.7i	299.6	63.3(2)	227.0	217.5(2)		106.3	625.6
16.9i(2)	332.2	91.4(2)	296.6	226.9(3)	158	119.4	626.1
3.6i	335.3(2)	97.6	319.5	276.5		120.8	
42.3	357.3	102.3	375.9	361.3(2)	326	158.9	
78.3	370.6	116.0	383.4(2)	372.2	357	159.4	
90.3(2)	372.1	138.7(2)	384.8	442.6(2)	538	164.8(2)	
120.9	459.8	141.8	442.9	456.6(2)		190.3	
147.9(2)	489.3(2)	160.3(2)	452.1	608.2		197.5	
156.8	491.8	167.5(2)	551.0	699.7	838	205.9	
207.4	622.2	172.5	628.7			210.6	
211.6	687.5	181.7	650.6			212.9	
214.7(2)	723.7	183.4	666.0			213.8	
215.2						293.3	

4. CONCLUSIONS

Thus, we have written out the effective Hamiltonian and studied the thermodynamic properties of cation ordering in $\text{PbZr}_x\text{Ti}_{1-x}\text{O}_3$ solid solutions using the Monte Carlo method. We have calculated the parameters of the effective Hamiltonian by performing nonempirical total-energy calculations for structures with different types of zirconium and titanium ion ordering. The energies were calculated using the ionic-crystal model with regard to deformability and dipole and quadrupole polarizabilities of the ions. By carrying out Monte Carlo calculations, we determined the cation-ordering phase transition temperatures $T_c \approx 180$ and ≈ 250 K for concentrations $x = 1/3$ and $1/2$, respectively. For the compound under study, these temperatures are much lower than the melting temperature ($T_{\text{melt}} \sim 1200$ K). Due to the alloy ordering being diffusive in character, the ordering kinetics at temperatures close to room temperature is frozen and in reality the phase transition in the ordered phase does not occur, in agreement with experiment.

Using the same ionic-crystal model, we have calculated the high-frequency permittivity, Born dynamic charges, and the lattice vibration spectra for the completely disordered and for the ordered phases of lowest energies. It was found that there are soft vibration modes, including ferroelectric modes, in the lattice vibration spectrum both in the completely disordered and in the ordered phases; moreover, a few soft modes of different symmetry have almost equal energies.

ACKNOWLEDGMENTS

This study was supported by the Russian Foundation for Basic Research (project nos. 03-02-16076, MAS 03-02-06911) and program no. 9 of the Presidium of the Russian Academy of Sciences.

REFERENCES

1. B. Noheda, J. A. Gonzalo, L. E. Cross, R. Guo, S.-E. Park, D. E. Cox, and G. Shirane, *Phys. Rev. B* **61**, 8687 (2000).
2. D. Viehland, *Phys. Rev. B* **52**, 778 (1995).
3. M. Fornari and D. J. Singh, cond-mat/0012126, Vol. 1 (2000).
4. G. Saghi-Szabo and R. E. Cohen, *Ferroelectrics* **194**, 287 (1997).
5. L. Bellaiche and D. Vanderbilt, *Phys. Rev. Lett.* **83**, 1347 (1999).
6. L. Bellaiche and D. Vanderbilt, *Phys. Rev. B* **61**, 7877 (2000).
7. G. Saghi-Szabo, R. E. Cohen, and H. Krakauer, *Phys. Rev. B* **59**, 12771 (1999).
8. H. Fu and O. Gülsereen, *Phys. Rev. B* **66**, 214114 (2002).
9. A. G. Khachatryan, *Theory of Phase Transformations and the Structure of Solid Solutions* (Nauka, Moscow, 1974).
10. O. V. Ivanov and E. G. Maksimov, *Zh. Éksp. Teor. Fiz.* **108**, 1841 (1995) [*JETP* **81**, 1008 (1995)].
11. V. I. Zinenko, N. G. Zamkova, and S. N. Sofronova, *Zh. Éksp. Teor. Fiz.* **123**, 846 (2003) [*JETP* **96**, 747 (2003)].
12. B. P. Burton and R. E. Cohen, *Ferroelectrics* **151**, 331 (1994).
13. N. Metropolis, A. Rosenbluth, M. Rosenbluth, A. Teller, and E. Teller, *J. Chem. Phys.* **21**, 1087 (1953).
14. L. Guttman, *J. Chem. Phys.* **34**, 1024 (1961).
15. N. G. Zamkova, V. I. Zinenko, O. V. Ivanov, E. G. Maksimov, and S. N. Sofronova, *Ferroelectrics* **283**, 49 (2003).
16. W. Zhong, R. D. King-Smith, and D. Vanderbilt, *Phys. Rev. Lett.* **72**, 3618 (1994).
17. P. Ghonsez, E. Cockrayne, U. V. Waghmare, and K. M. Rabe, *Phys. Rev. B* **60**, 836 (1999).
18. L. Bellaiche, J. Padilla, and D. Vanderbilt, cond-mat/9802209, Vol. 1 (1998).

Translated by I. Zvyagin

LATTICE DYNAMICS
AND PHASE TRANSITIONS

Hydrostatic Pressure–Induced Phase Transitions in RbMnCl₃: Raman Spectra and Lattice Dynamics

A. N. Vtyurin*, S. V. Goryainov**, N. G. Zamkova*, V. I. Zinenko*, A. S. Krylov*,
S. N. Krylova*, and A. D. Shefer*

*Kirensky Institute of Physics, Siberian Division, Russian Academy of Sciences,
Akademgorodok, Krasnoyarsk, 660036 Russia

e-mail: vtyurin@iph.krasn.ru

**Joint Institute of Geology, Geophysics, and Mineralogy, Siberian Division, Russian Academy of Sciences,
pr. Nauki 3, Novosibirsk, 630090 Russia

Received September 26, 2003

Abstract—Raman scattering spectra of RbMnCl₃ are measured at room temperature under high hydrostatic pressure. The results are interpreted based on first principles lattice dynamics calculations. The experimental data obtained correlate with the calculations in the low frequency domain but disagree slightly in the region of high-frequency vibrations. The transition from the hexagonal to the cubic perovskite phase observed earlier (near 0.7 GPa) was confirmed, and new transitions to lower symmetry distorted phases were discovered (at 1.1 and 5 GPa). © 2004 MAIK “Nauka/Interperiodica”.

1. INTRODUCTION

The RbMnCl₃ crystal belongs to the large family of perovskite-like structures with the general formula ABX₃. The smaller radius cations *B* (in this case, of manganese) surrounded by anions *X* form fairly rigid octahedral groups in these structures, with the larger radius cations *A* located in the voids between these groups. These octahedra can share corners to form a classical cubic perovskite lattice (*c*-type packing in Fig. 1a) or faces in the case of hexagonal structures (*h*-type packing in Fig. 1b). Most of the widely known oxygen-containing perovskites crystallize in the cubic packing, and their properties have been studied in considerable detail. Halogen-containing perovskites are capable of forming both cubic and hexagonal lattices, as well as mixed structural types consisting of combinations of these two types [1], as illustrated in Fig. 1c. These structures are exemplified by RbMnX₃ crystals, where *X* stands for a halogen. The fluoride RbMnF₃ has a cubic perovskite structure, the bromide RbMnBr₃ possesses a hexagonal structure, and the chloride RbMnCl₃ has a mixed structure (Fig. 1c) [1, 2]. The similarity in the chemical composition and structure of these crystals gives grounds to suggest that a change in the external conditions (temperature or pressure) may induce phase transitions between these structural types, which should inevitably manifest itself in anomalies in the lattice dynamics. Indeed, RbMnCl₃ exhibits a phase transition with decreasing temperature (which is accompanied by restoration of the soft mode in the Raman spectrum [3]), as well as another transition from

the hexagonal to cubic structure at high temperatures and pressures. In [4], a fine-grained RbMnCl₃ powder was subjected to a hydrostatic pressure of above 0.7 GPa and annealed under pressure (for half an hour at 700°C), after which the cubic structure stabilized in this way was studied under normal conditions. In [5], the cubic structure was observed to form in a part of the sample volume at comparable temperatures and pressures. Although it was pointed out that the actual annealing temperature affects the pressure of the transition to the cubic phase only slightly, this transition has nevertheless not been observed at room temperature to date.

Recent theoretical studies of this group of crystals [6] performed in an *ab initio* approach [7] revealed that the hexagonal structure of RbMnCl₃ should become unstable with increasing hydrostatic pressure, with the cubic modification of the crystal becoming energetically preferable (the calculated pressure at which the hexagonal lattice should lose stability is about 1 GPa, which correlates well with the experimental value of 0.7 GPa). According to those calculations, the onset of instability of the hexagonal lattice should be attributed to the high polarizability of the halogen ion and the breakdown of the fine balance between the multipole contributions to the energy of the hexagonal structure. Considering that the difference between the calculated energies of the cubic and hexagonal RbMnCl₃ lattices is very small and depends on pressure only weakly, those calculations obviously require experimental verification, both to test the validity of this approach for calculating the ion interaction potential as a whole and,

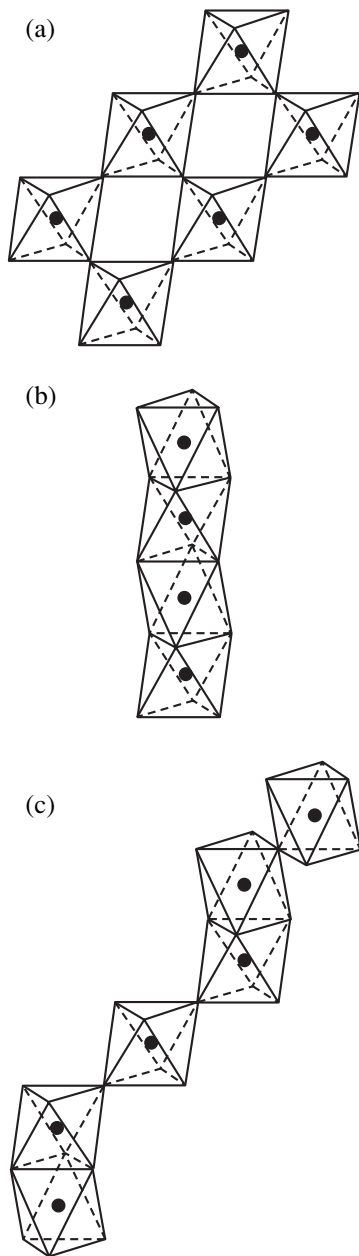


Fig. 1. Octahedral group packing in ABX_3 polytypes. (a) Cubic perovskite structure and (b) double-layer hexagonal and (c) six-layer hexagonal structures.

in particular, to look for the existence of a room temperature transition of the hexagonal to cubic structure in $RbMnCl_3$ under pressure.

This stimulated our present comparative experimental investigation of polarized Raman spectra in the hexagonal phase of $RbMnCl_3$ and of the vibrational spectrum calculated by the method proposed in [7] and by another technique similar to it [8] and a study of the effect of hydrostatic pressure on the Raman spectrum of this crystal.

2. STRUCTURE AND SYMMETRY OF THE CRYSTAL

The crystals intended for experimental study were Bridgman-grown in a quartz ampoule by multiple recrystallization. The grown bright red boules were 40 mm in diameter and up to 50 mm long and were inspected to select regions with no inclusions, crystallites, or other structural defects visible with a microscope. The samples fabricated for polarization measurements were rectangular parallelepipeds measuring $3 \times 4 \times 5$ mm, with two edges oriented along the a and c crystallographic axes. The orientation was performed using the x-ray technique to within $\pm 15'$ and using a polarization microscope; in the course of experiments conducted under normal conditions, the crystal orientation was checked periodically from the absence of birefringence in the sample and from the Rayleigh scattering background level. The techniques employed to grow the single crystals and prepare the samples are described in [3].

At room temperature, the structure of the crystal belongs to space group $P6_3/mmc$, $Z = 6$ [1, 9]. Each of the ions in the unit cell can occupy two symmetry-independent positions, with the five atomic coordinates not being fixed by crystal symmetry (Table 1). As follows both from experimental studies [9] and from calculations of the equilibrium crystal structure [6], the $MnCl_6$ octahedra differ slightly from the ideal shape; indeed, they are extended along the hexagonal axis.

The vibrational representation can be decomposed into irreducible representations at the center of the Brillouin zone for the hexagonal phase as

$$\Gamma = 5A_{1g}(xx, yy, zz) + 6E_{1g}(xz, yz, zx, zy) + 8E_{2g}(xx, yy, xy, yx) + A_{1u} + 7A_{2u} + 2B_{1u} + 6B_{2u} + 9E_{1u} + 7E_{2u} + 2A_{2g} + 6B_{1g} + B_{2g}, \quad (1)$$

with the Raman tensor components in which the vibrational modes of the corresponding symmetry are active being shown in parentheses. While this result differs somewhat from the expression given in [3], it agrees with the number of vibrational degrees of freedom per unit cell and is in accord with [8].

One can write a similar expression for the cubic phase ($Pm\bar{3}m$, $Z = 1$),

$$\Gamma = 4F_{1u} + F_{2u}. \quad (2)$$

This expression does not contain Raman active vibrations. As follows from a comparison of Eqs. (1) and (2), the selection rules for these structures are essentially different, which greatly simplifies their assignment by Raman spectroscopy.

3. EXPERIMENTAL TECHNIQUE AND RESULTS

3.1. Raman Scattering under Normal Conditions

The experiment under normal conditions was performed on a computerized DFS-24-based Raman spectrometer. The experimental techniques used, the design of the setup, and the data treatment chosen were described in considerable detail in [10]. Ar⁺ laser polarized radiation served for pumping (500 mW, 514.5 nm).

We obtained spectra in four scattering geometries: $y(xx)z$ with the expected lines, according to Eq. (1), $5A_{1g} + 8E_{2g}$; $y(xy)z$ with $8E_{2g}$ lines, $y(xz)x$ with $6E_{1g}$ lines; and $y(zz)x$ with $5A_{1g}$ lines. The results obtained are displayed in Fig. 2.

The $y(xz)x$ and $y(zz)x$ components are seen to be substantially weaker than the others (the spectra are plotted on an arbitrary scale, but the drop in scattering intensity is evident from the deteriorating signal/noise ratio). Obviously enough, this is due to a strong anisotropy in the crystal susceptibility. Out of the five expected A_{1g} lines, only two, at 55 and 178 cm⁻¹, can be reliably detected in Fig. 2c. To search for the others, the spectra in Figs. 2a and 2b need to be compared. In comparison with Fig. 2b, Fig. 2a reveals a strong increase in intensity in the region of 260 cm⁻¹ and a somewhat weaker, but still clearly pronounced increase near 138 cm⁻¹. The remaining maxima in Figs. 2a and 2b, namely, the maxima at 49, 60, 78, 154, 174, and 218 cm⁻¹, should be assigned to E_{2g} -type vibrations. Note that the strongest spectral line at 260 cm⁻¹ also manifests itself in the xy component, although at a substantially lower intensity, which may be due to either sample misorientation or to the radiation becoming depolarized by defects in the crystal structure. The remaining, weakest component of the xz spectrum is shown in Fig. 2d. Out of the six expected E_{1g} lines, one sees reliably only the maxima at 55, 111, and 153 cm⁻¹, with a tentative identification of a weak line near 80 cm⁻¹; its intensity is, however, comparable to the background level.

3.2. Raman Scattering under Pressure

Room temperature experiments under high hydrostatic pressure (up to 9 GPa) were carried out on a diamond anvil setup similar to the one employed in [11, 12]; the chamber containing the sample was 0.25 mm in diameter and 0.1 mm in height. The pressure was determined to within 0.05 GPa from the luminescence band shift of ruby [12, 13], a microcrystal of which was placed near the nonoriented sample measuring 50–70 μm. The pressure-transmitting medium was a highly dehydrated mixture of ethyl and methyl alcohols. The Raman spectra were also excited by an Ar⁺ laser (514.5 nm, 500 mW) and recorded with an OMARS 89 (Dilor) multichannel Raman spectrometer. Because of the small sample size and the strong diffuse scattering,

Table 1. Positions of atoms in the six-layer hexagonal structure of RbMnCl₃ (in units of $a_h = 7.1$ Å, $c_h = 19.0$ Å [8])

Ion	Position	x	y	z
Rb1	2(b)	0	0	1/4
Rb2	4(f)	1/3	2/3	z_1
Mn1	2(a)	0	0	0
Mn2	2(f)	1/3	2/3	z_2
Cl1	6(h)	y_1	$2y_1$	1/4
Cl2	12(k)	y_1	$2y_2$	z_3

only the high-frequency part of the spectrum (150–500 cm⁻¹) was recorded. Simultaneously, the domain structure and birefringence in the sample were observed with a polarization microscope.

The transformation of the spectrum with pressure is shown in Fig. 3. The high-frequency part of the spectrum observed under normal pressure coincides with that shown in Fig. 2a; namely, one clearly sees a strong peak at 260 cm⁻¹, a weak maximum at 218 cm⁻¹, and an increase in intensity as the 154–174 cm⁻¹ doublet is approached. A similar pattern (with a slight increase in the peak frequency) is observed when the pressure is increased to ~0.4 GPa, where the spectral intensity begins to gradually fall off. At the same time, the microscope reveals the appearance and growth of an optically isotropic region in the crystal. Note that the possible phase separation at the pressure-induced transition to the cubic phase was pointed out in [5]. At pressures above 0.75 GPa, there is no Raman scattering at all and the crystal becomes completely optically isotropic (with the exception of small regions on the surface, which may be due either to surface defects or to crystal interaction with the pressure-transmitting medium). This phase transition point agrees satisfactorily with the value of 1.1 GPa quoted in [6] and the transition pressure of 0.7 GPa reported in [4].

As the pressure increases above ~1.1 GPa, Raman scattering reappears, but its spectrum changes the pattern in that the 218 cm⁻¹ line is absent and a doublet forms in its place in the region of 200 cm⁻¹. On the whole, the pattern of the spectrum (in this high-frequency part, which derives primarily from stretch vibrations of the bonds forming the octahedral groups) closely resembles that of the spectra of “cubic” perovskites after transition to the rhombohedrally distorted phase (see, e.g., [14]). As the pressure increases, the intensity of the Raman lines and their frequencies increase. At pressures near 5 GPa, the frequency growth rate increases, while the line intensities start to wane noticeably, which may indicate the onset of one more phase transition (Fig. 4). No other transient phenomena are observed in the spectra as the pressure is increased still more (up to 9.65 GPa). As the pressure is relieved, the crystal recovers its original state by passing through the same sequence of changes. Multiple transitions

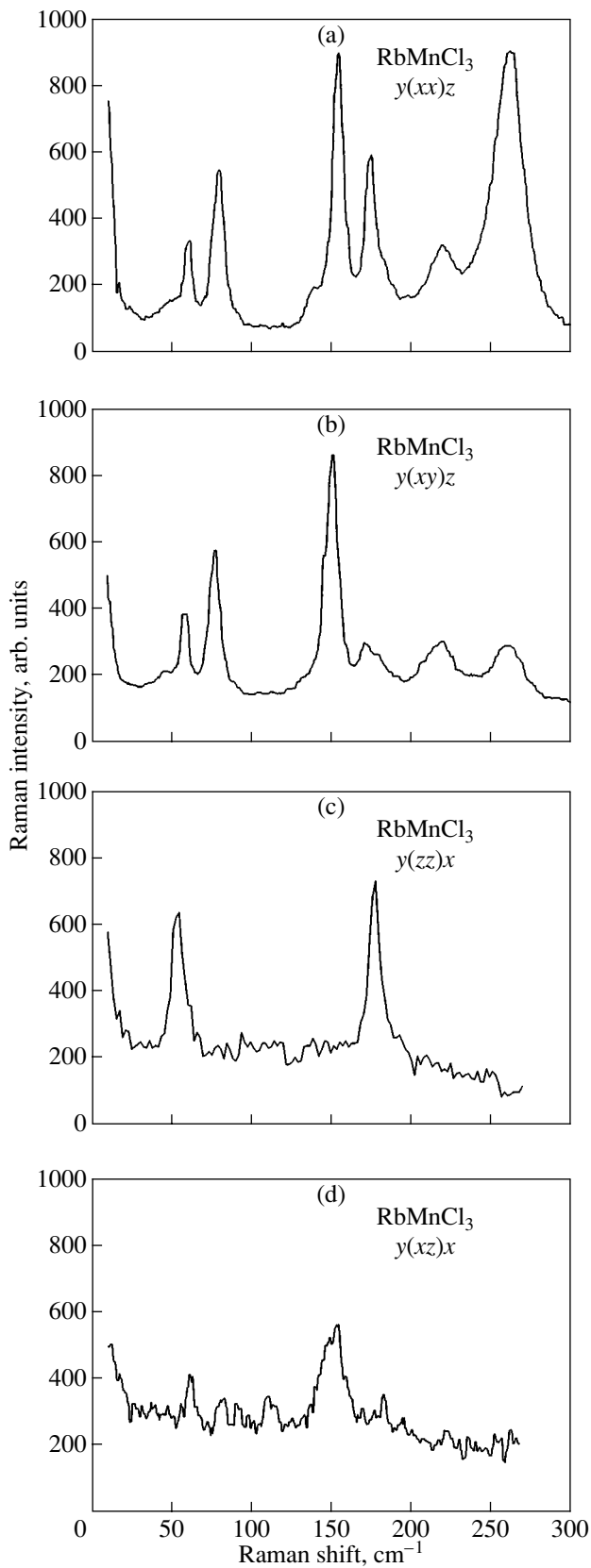


Fig. 2. Room-temperature polarized Raman spectra of RbMnCl_3 measured in different scattering geometries.

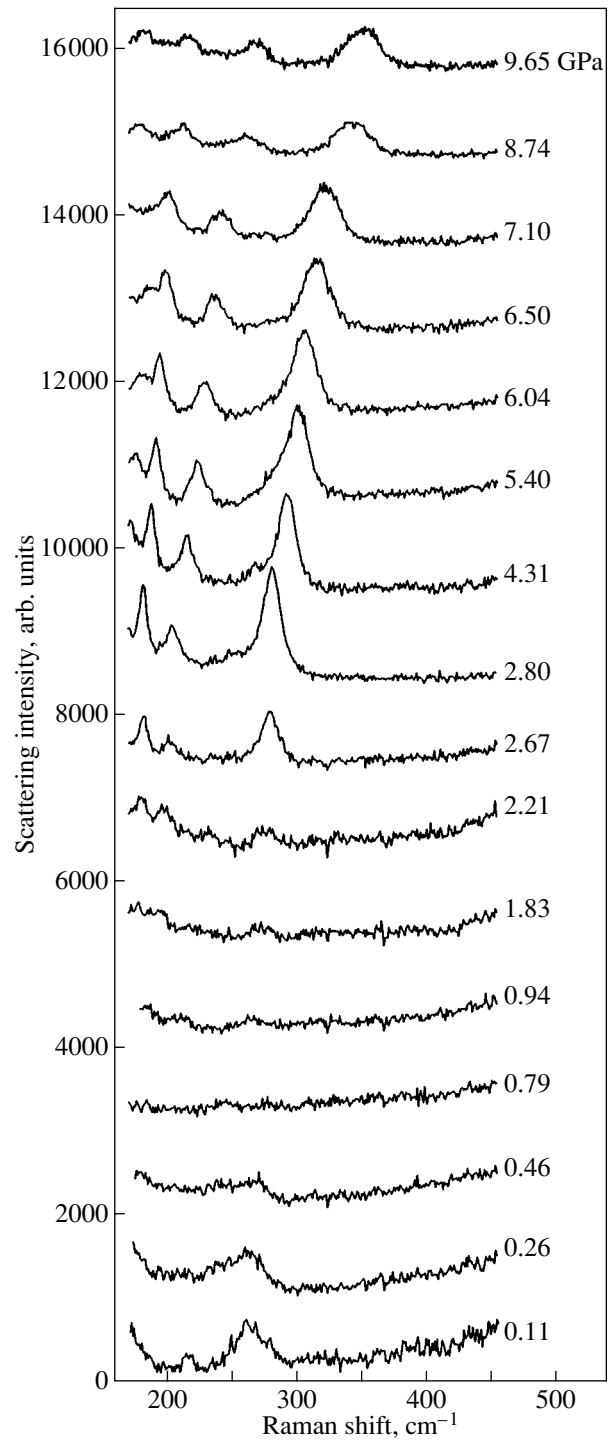


Fig. 3. Pressure-induced transformation of the high-frequency part of a Raman spectrum.

through the first detected point of transition from the hexagonal to the optically isotropic phase do not entail its displacement, nor are any hysteresis phenomena observed (within the measurement accuracy), in contrast with [4], where the annealed cubic phase persisted after the removal of pressure.

4. MODELING OF THE SPECTRUM

To calculate the vibrational spectrum, we used the Gordon–Kim model and took into account the ion electronic density distortion up to quadrupoles [7, 15]. The electronic density of the crystal in this model is represented as the sum of electronic densities of individual ions:

$$\rho_i(\mathbf{r}) = \sum_{l=0}^2 \sum_{m=-l}^l \rho_i^{(l)}(r) Y_{lm}(\theta, \phi), \quad (3)$$

where $\rho_i^{(1)}$ and $\rho_i^{(2)}$ are the dipole and quadrupole components of the ion electronic density, respectively. The electronic density of an ion was calculated in terms of the Watson sphere, which describes the effect of the crystal environment [7, 15]:

$$V(\mathbf{r}) = \begin{cases} -Z/R_W, & r < R_W \\ -Z/r, & r > R_W \end{cases}, \quad (4)$$

where Z is the ion charge and R_W is the radius of the Watson sphere. The total crystal energy can be written as

$$E = E_0 + E_{d-d} + E_{q-q} + E_{d-q} + E_{\text{self}}, \quad (5)$$

where E_{self} is the sum of the ion self-energies,

$$E_0 = -\frac{1}{2} Z \hat{C}^{(0)} Z + \Phi^{(00)} \quad (6)$$

is the interaction energy of spherically symmetric ions, and

$$E_{d-d} = \frac{1}{2} \mathbf{d} (\hat{\alpha}_d^{-1} + \hat{\Phi}^{(11)} - \hat{C}^{(2)}) \mathbf{d} + \mathbf{d} (\hat{\Phi}^{(10)} - \hat{C}^{(1)} Z),$$

$$E_{q-q} = \frac{1}{2} \mathbf{Q} \left[\hat{\alpha}_q^{-1} - \frac{1}{36} (\hat{\Phi}^{(22)} - \hat{C}^{(4)}) \right] \mathbf{Q} \quad (7)$$

$$- \frac{1}{6} \mathbf{Q} (\hat{\Phi}^{(20)} - \hat{C}^{(2)} Z),$$

$$E_{d-q} = -\frac{1}{6} \mathbf{Q} (\hat{\Phi}^{(21)} - \hat{C}^{(3)}) \mathbf{d}$$

are the energies of the dipole–dipole, quadrupole–quadrupole, and dipole–quadrupole interactions, respectively; $\hat{\alpha}_d$ and $\hat{\alpha}_q$ are the diagonal matrices of the dipole and quadrupole polarizabilities of single ions calculated by the Steinheimer method (for more details, see [7]). The short-range parts of the ion pair interactions $\Phi^{(ll')}$ are calculated in terms of the density functional theory as

$$\begin{aligned} \Phi_{ij}^{ll'} &= F(\rho_i^{(l)}(\mathbf{r}' - \mathbf{R}_i) + \rho_j^{(l')}(\mathbf{r} - \mathbf{R}_j)) \\ &\quad - F(\rho_i^{(l)}(\mathbf{r} - \mathbf{R}_i) - \rho_j^{(l')}(\mathbf{r} - \mathbf{R}_j)), \end{aligned} \quad (8)$$

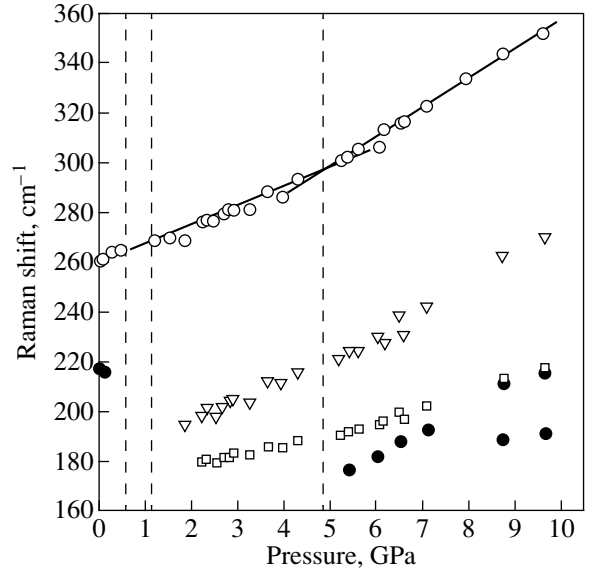


Fig. 4. Pressure dependences of the strongest spectral line frequencies. Dashed vertical lines indicate the tentative transition points, and solid straight lines are linear extrapolations.

and the long-range part of the interaction potential

$$C_{ij}^{(l+l')} = \nabla^{(l+l')} \frac{1}{|\mathbf{R}_{ij}|} \quad (9)$$

is calculated by Ewald's method. The fitting parameters of the structure (Table 1), as well as the dipole and quadrupole ion moments, were determined from the following energy minimum conditions:

$$\frac{\partial E}{\partial \mathbf{d}} = 0,$$

[whence it follows that

$$\begin{aligned} \mathbf{d} &= \hat{\mathbf{A}} [\hat{\Phi}^{(10)} - \hat{C}^{(1)} Z + \mathbf{Q} (\hat{\Phi}^{(21)} - \hat{C}^{(3)})], \\ \hat{\mathbf{A}} &= (\hat{\alpha}_d^{-1} + \hat{\Phi}^{(11)} - \hat{C}^{(2)})^{-1}, \end{aligned} \quad (10)$$

with $\hat{\mathbf{A}}$ being a matrix that is the inverse of that of the dipole–dipole interaction in Eq. (7)] and

$$\frac{\partial E}{\partial \mathbf{Q}} = 0,$$

which yields the equation

$$\mathbf{Q} = \hat{\mathbf{B}} (\hat{\Phi}^{(20)} - \hat{C}^{(2)} + \hat{\mathbf{A}}'),$$

where

$$\begin{aligned} \hat{\mathbf{B}} &= \left[\hat{\alpha}_q^{-1} - \frac{1}{36} (\hat{\Phi}^{(22)} - \hat{C}^{(4)}) \right. \\ &\quad \left. + (\hat{\Phi}^{(21)} - \hat{C}^{(3)}) \hat{\mathbf{A}} (\hat{\Phi}^{(21)} - \hat{C}^{(3)})^+ \right]^{-1}, \\ \hat{\mathbf{A}}' &= (\hat{\Phi}^{(10)} - \hat{C}^{(1)} Z) \hat{\mathbf{A}} (\hat{\Phi}^{(21)} - \hat{C}^{(3)})^+. \end{aligned} \quad (11)$$

Note that the structural parameters calculated in this way are almost identical to the figures derived experimentally [8]. Equations (3)–(11) are discussed in more detail in [6].

To calculate the vibrational spectrum of a crystal, one has to take into account the dependence of its energy (5) on the displacements of ions from their equilibrium positions. The corresponding expression for the dynamic matrix, including the electronic polarizability of ions and their breathing modes in the crystal environment, can be written in the form (for a crystal of arbitrary symmetry) [7]

$$D_{\alpha\beta}(\mathbf{q}, jj') = \frac{\exp(-i\mathbf{q}\mathbf{X}_{jj'})}{\sqrt{M_j M_{j'}}} \times \left\{ \frac{1}{2} Z_j C_{\alpha\beta}^{(2)}(\mathbf{q}, jj') Z_{j'} + \tilde{D}_{RR}^{\alpha\beta}(\mathbf{q}, jj') - \sum_{k, k'=1}^{N_a} \tilde{D}_{RV}^{\alpha}(\mathbf{q}, jk) \tilde{D}_{VV}(\mathbf{q}, kk') \tilde{D}_{RV}^{\beta*}(\mathbf{q}, j'k') \right\}. \quad (12)$$

The matrices entering Eq. (12) are defined as follows:

$$\begin{aligned} D_{RR}^{\alpha\beta}(\mathbf{q}, jj') &= \Phi_{RR, \alpha\beta}^{(00)}(\mathbf{q}, jj') \\ &- \sum_{\gamma\delta=1k, k'=1}^3 \sum_{N_a} [\Phi_{R, \alpha\gamma}^{(01)}(\mathbf{q}, jk) - C_{\alpha\gamma}^{(2)}(\mathbf{q}, jk) Z_k] \\ &\times A_{\alpha\gamma}(\mathbf{q}, kk') [\Phi_{R, \beta\delta}^{(01)}(\mathbf{q}, k'j') - C_{\beta\delta}^{(2)}(\mathbf{q}, k'j') Z_{k'}], \\ A_{\alpha\beta}(\mathbf{q}, jj') &= \left[\frac{\delta_{\alpha\beta} \delta_{jj'}}{\alpha_{d,j}} + \Phi_{\alpha\beta}^{(11)}(\mathbf{q}, jj') - C_{\alpha\beta}^{(2)}(\mathbf{q}, jj') \right], \\ D_{RV}^{\alpha}(\mathbf{q}, jj') &= \Phi_{RV, \alpha}^{(00)}(\mathbf{q}, jj') \\ &- \sum_{\gamma=1k, k'=1}^3 \sum_{N_a} \Phi_{R, \alpha}^{(01)}(\mathbf{q}, jk) A_{\alpha\gamma}(\mathbf{q}, kk') \Phi_{V, \gamma}^{*(01)}(\mathbf{q}, k'j'), \\ D_{VV}(\mathbf{q}, jj') &= \Phi_{VV}^{(00)}(\mathbf{q}, jj') \\ &- \sum_{\gamma\delta=1k, k'=1}^3 \sum_{N_a} \Phi_{V, \gamma}^{(01)}(\mathbf{q}, jk) A_{\gamma\delta}(\mathbf{q}, kk') \Phi_{V, \delta}^{*(01)}(\mathbf{q}, k'j'), \\ D_{RR}^{\alpha\beta}(\mathbf{q}, jj') &= \Phi_{RR}^{(00)}(\mathbf{q}, jj') \quad (13) \\ &\times \sum_{\gamma\delta=1}^3 \mathbf{P}_{j, \gamma\delta}^{(2)} (\Phi_{RR, \gamma\delta\alpha\beta}^{(20)}(\mathbf{q}, jj') - C_{\gamma\delta\alpha\beta}^{(4)}(\mathbf{q}, jj')) Z_j \\ &- \sum_{\gamma\delta=1k, k'=1}^3 \sum_{N_a} \left[Z_k (\Phi_{R, \alpha\gamma}^{(01)}(\mathbf{q}, jk) - C_{\alpha\gamma}^{(2)}(\mathbf{q}, jk)) \right. \end{aligned}$$

$$\begin{aligned} &- \sum_{\gamma\delta'=1}^3 \mathbf{P}_{j, \gamma\delta'}^{(2)} (\Phi_{R, \alpha}^{(21)}(\mathbf{q}, jk) - C_{\gamma\delta'\alpha\beta}^{(4)}(\mathbf{q}, jk)) Z_j \left. \right] \\ &\times A_{\gamma\delta}(\mathbf{q}, kk') \left[(\Phi_{R, \delta\beta}^{*(01)}(\mathbf{q}, k'j') - C_{\beta\delta}^{(2)}(\mathbf{q}, k'j')) Z_{k'} \right. \\ &- \left. \sum_{\gamma\delta'=1}^3 \mathbf{P}_{j, \gamma\delta'}^{(2)} (\Phi_{R, \beta}^{(21)}(\mathbf{q}, k'j') - C_{\gamma\delta'\beta\alpha}^{(4)}(\mathbf{q}, k'j')) Z_j \right], \end{aligned}$$

$$\mathbf{P}_{i, \alpha\beta}^{(2)} = -\frac{1}{6} \sum_{j=1}^{N_a} \sum_{\gamma\delta=1}^3 \tilde{B}_{ij}^{\alpha\beta, \gamma\delta}$$

$$\times \sum_{k=1}^{N_a} (\Phi_{jk, \gamma\delta}^{(20)}(V_i, V_j, \mathbf{R}_{ij}) - C_{jk, \gamma\delta}^{(1)} Z_k),$$

$$\tilde{B}_{ij}^{\alpha\beta, \gamma\delta} = \left[\frac{\delta_{\alpha\beta} \delta_{ij} \delta_{\gamma\delta}}{\alpha_{Q,i}} + \Phi_{ij, \alpha\beta\gamma\delta}^{(22)}(V_i, V_j, \mathbf{R}_{ij}) - C_{ij, \alpha\beta\gamma\delta}^{(4)} \right]^{-1},$$

where N_a is the number of atoms in a unit cell and the lattice sum matrices $C^{(2)}$ and $C^{(4)}$ describe the contributions from long-range Coulomb interactions to the dynamic matrix. The short-range interaction contributions can be cast as

$$\Phi_{RR, \alpha\beta}^{(ll')}(\mathbf{q}, jj') = \sum_n \frac{\partial^2 \Phi^{(ll')}(n0)}{\partial R_\alpha \binom{n}{j} \partial R_\beta \binom{0}{j'}} \exp(-i\mathbf{q}\mathbf{n}),$$

$$\Phi_{VV}^{(ll')}(\mathbf{q}, jj') = \sum_n \frac{\partial^2 \Phi^{(ll')}(n0)}{\partial V_j \partial V_{j'}} \exp(-i\mathbf{q}\mathbf{n}),$$

$$\Phi_{RV, \alpha}^{(ll')}(\mathbf{q}, jj') = \sum_n \frac{\partial^2 \Phi^{(ll')}(n0)}{\partial R_\alpha \binom{n}{j} \partial V_{j'}} \exp(-i\mathbf{q}\mathbf{n}), \quad (14)$$

$$\Phi_{R, \alpha\beta}^{(ll')}(\mathbf{q}, jj') = \sum_n \frac{\partial \Phi^{(ll')}(n0)}{\partial R_\beta \binom{n}{j}} \exp(-i\mathbf{q}\mathbf{n}),$$

$$\Phi_{V, \alpha}^{(ll')}(\mathbf{q}, jj') = \sum_n \frac{\partial \Phi^{(ll')}(n0)}{\partial V_{j'}} \exp(-i\mathbf{q}\mathbf{n}).$$

Note that this approach to calculating the frequencies and eigenvectors of lattice vibrations differs somewhat from the method proposed in [8], where the Gordon–Kim model was used to determine the Born–Mayer potential coefficients.

Table 2. Vibration frequencies in the hexagonal phase (in cm^{-1})

Vibration mode	Calc.	Data from [8]	Exp.	Vibration mode	Calc.	Data from [8]	Exp.
A_{1g}	52	40	55	E_{1g}	25	44	
A_{1g}	90	161		E_{1g}	53	120	55
A_{1g}	114	254	138	E_{1g}	69	157	80?
A_{1g}	149	339	178	E_{1g}	97	171	111
A_{1g}	189	368	260	E_{1g}	155	301	153
A_{1u}	87i	20i		E_{1g}	65i	51i	
A_{2g}	61	63		$E_{1u}(LO/TO)$	49i/73i	40	
A_{2g}	85i	71		$E_{1u}(LO/TO)$	0/0	0	
$A_{2u}(LO/TO)$	0/0	0		$E_{1u}(LO/TO)$	50/15	56	
$A_{2u}(LO/TO)$	42/36	35		$E_{1u}(LO/TO)$	53/51	64	
$A_{2u}(LO/TO)$	73/59	56		$E_{1u}(LO/TO)$	74/69	119	
$A_{2u}(LO/TO)$	86/83	146		$E_{1u}(LO/TO)$	98/80	171	
$A_{2u}(LO/TO)$	141/88	202		$E_{1u}(LO/TO)$	111/104	242	
$A_{2u}(LO/TO)$	157/144	271		$E_{1u}(LO/TO)$	136/128	244	
$A_{2u}(LO/TO)$	200/187	352		$E_{1u}(LO/TO)$	186/163	330	
B_{1g}	30	26		E_{2g}	24	39	
B_{1g}	70	62		E_{2g}	42	55	49
B_{1g}	77	99		E_{2g}	53	80	60
B_{1g}	83	174		E_{2g}	76	143	78
B_{1g}	155	296		E_{2g}	90	216	154
B_{1g}	185	356		E_{2g}	105	242	174
B_{1u}	61	74		E_{2g}	157	306	218
B_{1u}	88i	44i		E_{2g}	67i	39i	
B_{2g}	84i	53i		E_{2u}	86i	7	
B_{2u}	52	53		E_{2u}	27	42	
B_{2u}	57	112		E_{2u}	32	82	
B_{2u}	114	221		E_{2u}	80	135	
B_{2u}	148	276		E_{2u}	95	166	
B_{2u}	150	339		E_{2u}	119	215	
B_{2u}	202	391		E_{2u}	163	328	

To make a symmetry analysis of the eigenvectors of the normal lattice vibration modes obtained by diagonalizing the dynamic matrix (12), we made use of the projection operators to expand the eigenvectors in terms of a set of basis functions for irreducible representations of the crystal symmetry group. We constructed a complete vibrational representation $P(g)$ for the space group of the hexagonal phase and used it to calculate the projection operators [16]:

$$P_\rho = \frac{d(\rho)}{N(g)} \sum_{g \in G} \chi_\rho(g) P(g), \quad (15)$$

where $d(\rho)$ is the dimension of a representation ρ of a point symmetry operation, $N(g)$ is the dimension of the

symmetry group, $\chi_\rho(g)$ is the character of the matrix of the irreducible representation ρ , $P(g)$ is the vibrational representation of the symmetry operation of the given irreducible representation ρ of group G , P_ρ is the projection operator, and summation is performed over all symmetry group operations. An eigenvector \mathbf{f} of vibration transforms according to the irreducible representation ρ of group G provided it satisfies the criterion [16]

$$P_\rho \mathbf{f} = \frac{N(g)}{d(\rho)} \mathbf{f}. \quad (16)$$

This algorithm of expansion of the dynamic matrix eigenvectors in terms of irreducible representations was realized with the Mathematica 4.2 software package.

Table 3. Eigenvectors of fully symmetric lattice vibrations in the hexagonal phase

Atom	Coor- dinate	Frequency (cm ⁻¹)					Atom	Coor- dinate	Frequency (cm ⁻¹)				
		52	91	114	149	189			52	91	114	149	189
Rb	X	0.000	0.000	0.000	0.000	0.000	Cl	X	0.012	-0.016	0.024	-0.006	0.004
	Y	0.000	0.002	0.000	0.000	0.000		Y	0.012	-0.016	0.024	-0.006	0.004
	Z	0.000	0.000	0.000	0.000	0.000		Z	0.000	0.000	0.000	0.000	0.000
Rb	X	-0.001	0.000	0.000	0.000	0.000	Cl	X	-0.012	0.013	-0.024	0.006	-0.004
	Y	0.000	0.000	0.000	0.000	0.000		Y	0.000	0.000	0.000	0.000	0.000
	Z	0.000	0.000	0.000	0.000	0.000		Z	0.000	0.000	0.000	0.000	0.000
Rb	X	0.000	0.000	0.000	0.000	0.000	Cl	X	0.000	0.000	0.000	0.000	0.000
	Y	0.000	0.000	0.000	0.000	0.000		Y	-0.012	0.006	-0.024	0.006	-0.004
	Z	-0.012	0.001	0.005	-0.003	0.001		Z	0.000	0.000	0.000	0.000	0.000
Rb	X	0.000	0.000	0.000	0.000	0.000	Cl	X	-0.003	-0.005	-0.002	0.010	0.018
	Y	0.000	0.000	0.000	0.000	0.000		Y	-0.002	-0.005	-0.002	0.010	0.018
	Z	0.012	-0.001	-0.006	0.003	-0.001		Z	0.002	0.007	0.002	-0.001	0.003
Rb	X	0.000	0.000	0.000	0.000	0.000	Cl	X	0.003	0.005	0.002	-0.009	-0.019
	Y	0.000	0.000	0.000	0.000	0.000		Y	0.000	-0.001	0.000	0.000	0.000
	Z	-0.012	0.001	0.006	-0.003	0.001		Z	0.002	0.007	0.002	-0.001	0.003
Rb	X	0.000	0.000	0.000	0.000	0.000	Cl	X	0.000	-0.001	0.000	0.000	0.000
	Y	0.000	0.000	0.000	0.000	0.000		Y	0.002	0.002	0.002	-0.010	-0.018
	Z	0.012	-0.001	-0.005	0.003	-0.001		Z	0.002	0.007	0.002	-0.001	0.003
Mn	X	0.000	0.000	0.000	0.000	0.000	Cl	X	0.003	0.005	0.002	-0.009	-0.019
	Y	0.000	0.000	0.000	0.000	0.000		Y	0.002	0.006	0.002	-0.009	-0.019
	Z	0.000	0.000	0.000	0.000	0.000		Z	-0.002	-0.007	-0.002	0.001	-0.003
Mn	X	0.000	0.000	0.000	0.000	0.000	Cl	X	-0.003	-0.005	-0.002	0.010	0.018
	Y	0.000	0.000	0.000	0.000	0.000		Y	0.000	0.000	0.000	0.000	0.000
	Z	0.000	0.000	0.000	0.000	0.000		Z	-0.002	-0.007	-0.002	0.001	-0.003
Mn	X	0.000	0.001	0.000	0.000	0.000	Cl	X	0.000	-0.001	0.000	0.000	0.000
	Y	0.000	-0.005	0.000	0.000	0.000		Y	-0.002	-0.003	-0.002	0.010	0.018
	Z	-0.001	0.003	0.006	0.011	-0.005		Z	-0.002	-0.007	-0.002	0.001	-0.003
Mn	X	0.000	0.001	0.000	0.000	0.000	Cl	X	0.003	0.005	0.002	-0.009	-0.019
	Y	0.000	0.006	0.000	0.000	0.000		Y	0.002	0.006	0.002	-0.000	-0.019
	Z	0.001	-0.003	-0.005	-0.011	0.005		Z	0.002	0.007	0.002	-0.001	0.003
Mn	X	0.000	0.001	0.000	0.000	0.000	Cl	X	-0.003	-0.005	-0.002	0.010	0.018
	Y	0.000	0.006	0.000	0.000	0.000		Y	0.000	0.000	0.000	0.000	0.000
	Z	-0.001	0.003	0.005	0.011	-0.005		Z	0.002	0.007	0.002	-0.001	0.003
Mn	X	0.000	0.001	0.000	0.000	0.000	Cl	X	0.000	-0.001	0.000	0.000	0.000
	Y	0.000	-0.005	0.000	0.000	0.000		Y	-0.002	-0.003	-0.002	0.010	0.018
	Z	0.001	-0.003	-0.006	-0.011	0.005		Z	0.002	0.007	0.002	-0.001	0.003
Cl	X	-0.012	0.013	-0.025	0.006	-0.004	Cl	X	-0.003	-0.005	-0.002	0.010	0.018
	Y	-0.012	0.013	-0.025	0.006	-0.004		Y	-0.002	-0.005	-0.002	0.010	0.018
	Z	0.000	0.000	0.000	0.000	0.000		Z	-0.002	-0.007	-0.002	0.001	-0.003
Cl	X	0.012	-0.016	0.024	-0.006	0.004	Cl	X	0.003	0.005	0.002	-0.009	-0.019
	Y	0.000	0.001	0.000	0.000	0.000		Y	0.000	-0.001	0.000	0.000	0.000
	Z	0.000	0.000	0.000	0.000	0.000		Z	-0.002	-0.007	-0.002	0.001	-0.003
Cl	X	0.000	0.000	0.000	0.000	0.000	Cl	X	0.000	-0.001	0.000	0.000	0.000
	Y	0.012	-0.006	0.025	-0.006	0.004		Y	0.002	0.002	0.002	-0.010	-0.018
	Z	0.000	0.000	0.000	0.000	0.000		Z	-0.002	-0.007	-0.002	0.001	-0.003

5. RESULTS AND DISCUSSION

The results of the calculations of the eigenfrequencies and their assignment according to irreducible representations of the crystal symmetry group are compared in Table 2 with the results quoted in [8] and the frequencies of the experimentally observed Raman spectral lines; the eigenvectors of the fully symmetric (A_{1g}) vibrations are presented in Table 3.

The calculated and experimental frequencies for all vibration modes are seen to be in satisfactory agreement considering that the method of calculation did not employ fitting parameters. Some of the calculated frequencies turned out to be imaginary, which indicates the lattice of the hexagonal phase to be unstable at 0 K and is in accord with the phase transition in RbMnCl_3 observed to occur at 272 K [3] (a comprehensive analysis of the origin of this instability is given in [8] in terms of a similar approach; we do not dwell on it here). We did not succeed in observing the lowest frequency modes near 20 cm^{-1} , apparently because of the low-frequency dynamics undergoing strong rearrangement at this phase transition; this could also be associated, however, with the strong wing of Rayleigh scattering in this region. In accordance with experiment, the calculation shows that the highest frequency vibrations correspond to the irreducible representation A_{1g} ; an analysis of their eigenvectors (Table 3) suggests that such vibrations are primarily connected with the chlorine ions being displaced in the Mn–Cl bond direction (although they also have a small contribution from the manganese ions and even an insignificant contribution from the heavy rubidium ions). As seen from Table 2, the disagreement between the calculated and experimental frequencies is the largest in this spectral region.

In the middle frequency range, the agreement between the calculated and experimental frequencies is noticeably better; the dynamics is governed here apparently primarily by long-range Coulomb interactions of the ions. Interestingly, the heavy rubidium ions provide a substantial contribution to the eigenvectors of the fairly high-frequency modes at 114 and 149 cm^{-1} , which is even larger than that to the lower lying modes (Table 3).

Note that the calculation of the crystal lattice potential and of the phonon spectrum performed in [8] took into account only the Coulomb interaction of point ions and the short-range repulsion of spherically symmetric free ions. However, as shown in [7], the energetically preferable structure for RbMnCl_3 in this case is cubic rather than hexagonal. Stabilization of the latter structure is determined by the polarization energy, which is connected with the presence of dipole and quadrupole ion moments.

Note, however, that the frequency spectra obtained by the methods used in [7] and [8] are qualitatively similar; also similar are the numbers of imaginary frequencies corresponding to vibrations that are unstable at low

temperatures (the lowest positive frequency of 7 cm^{-1} , which was obtained with the Born–Mayer potential, turned out to be imaginary when the multipole distortions of the electronic density were included). This similarity suggests that an analysis of the origin of the lattice instability at low temperatures (which is determined primarily by the low-frequency dynamics) should yield similar results in both cases. Good qualitative agreement is also observed in the middle frequency range (up to $50\text{--}60 \text{ cm}^{-1}$). By contrast, in the region of high-frequency vibrations, which are associated primarily with the stretch vibrations of the Mn–Cl bonds, the results are in obvious disagreement. Apparently, this indicates overestimation of the force constants of these bonds with the Born–Mayer potential, whereas the multipole approximation underestimates them.

The agreement between the calculated (1.1 GPa) and experimental (0.7 GPa) pressures for the transition from the hexagonal to cubic phase should apparently be considered satisfactory. This is corroborated by the optical isotropy of the crystal and the absence of Raman scattering. Note that this phase transition, associated with a considerable rearrangement of the lattice, entails separation of the phases that coexist in the pressure interval $0.4\text{--}0.8 \text{ GPa}$ (and, possibly, at still higher pressures near the sample surface, where structural defects should play an appreciable role).

6. CONCLUSIONS

Thus, our study has revealed that the fitting parameter-free method proposed in [8, 15] permits efficient calculation of the lattice stability and dynamics of ionic crystals in fairly complex structures. A comparative analysis of Raman scattering and of the calculated lattice vibration spectrum for the RbMnCl_3 hexagonal phase made it possible to assign most of the Raman lines allowed by the selection rules and to determine the eigenvectors of the corresponding vibrations. Some differences between the experimental and calculated frequencies observed in the high-frequency part of the spectrum can be tentatively related to the covalency of the Mn–Cl bonds.

The pressure-induced transition from the hexagonal to cubic phase, which was earlier observed to occur only at high temperatures, has been detected at room temperature, in full agreement with calculations [5]. This transition takes place through separation of the phases that coexist in the range $0.4\text{--}0.8 \text{ GPa}$, which correlates with the calculated pressure of 1.1 GPa at which the hexagonal phase becomes unstable; the phase transition was found to be reversible and was not accompanied by noticeable hysteresis effects. A further increase in pressure was observed to drive transitions at 1.1 GPa and, tentatively, at 5 GPa.

ACKNOWLEDGMENTS

The authors are indebted to K.S. Aleksandrov for helpful discussions and to A.P. Shebanin for assistance in performing the spectral measurements under pressure.

This study was supported jointly by the Russian Foundation for Basic Research and Krasnoyarsk Science Foundation Enisei (project no. 02-02-97707) and the program of the Siberian Division of the Russian Academy of Sciences "Integration" (project no. 88).

REFERENCES

1. K. S. Aleksandrov, A. T. Anistratov, B. V. Beznosikov, and N. V. Fedoseeva, *Phase Transitions in Crystals of ABX₃ Haloid Compounds* (Nauka, Novosibirsk, 1981).
2. K. S. Aleksandrov and B. V. Beznosikov, *Perovskite-like Crystals* (Nauka, Novosibirsk, 1999).
3. K. S. Aleksandrov, A. T. Anistratov, S. V. Mel'nikova, V. I. Zinenko, L. A. Shabanova, and A. D. Shefer, *Fiz. Tverd. Tela (Leningrad)* **21**, 1119 (1979) [*Sov. Phys. Solid State* **21**, 650 (1979)].
4. J. M. Longo and J. A. Kafalas, *J. Solid State Chem.* **3**, 429 (1971).
5. I. P. Aleksandrova, V. F. Shabanov, A. K. Moskalev, *et al.*, *Structural Phase Transitions in Crystals at High Pressure* (Nauka, Novosibirsk, 1982).
6. V. I. Zinenko, N. G. Zamkova, and S. N. Sofronova, *Zh. Éksp. Teor. Fiz.* **123**, 846 (2003) [*JETP* **96**, 747 (2003)].
7. V. I. Zinenko, N. G. Zamkova, and S. N. Sofronova, *Zh. Éksp. Teor. Fiz.* **114**, 1742 (1998) [*JETP* **87**, 944 (1998)].
8. M. B. Smirnov and V. Yu. Kazimirov, *Kristallografiya* **48**, 480 (2003) [*Crystallogr. Rep.* **48**, 435 (2003)].
9. J. Goodyear, G. A. Steigmann, and E. M. Ali, *Acta Crystallogr. B* **33**, 256 (1977).
10. A. S. Krylov, A. D. Shefer, and A. N. Vtyurin, *Prib. Tekh. Éksp.*, No. 3, 146 (1995).
11. Q. Wang, G. Ripault, and A. Bulou, *Phase Transit.* **53**, 1 (1995).
12. S. V. Goryainov and I. A. Belitsky, *Phys. Chem. Miner.* **22**, 443 (1995).
13. R. G. Munro, G. J. Piermarini, S. Block, and W. B. Holzapfel, *J. Appl. Phys.* **57**, 165 (1985).
14. K. S. Aleksandrov, V. N. Voronov, A. N. Vtyurin, S. V. Goryainov, N. G. Zamkova, V. I. Zinenko, and A. S. Krylov, *Zh. Éksp. Teor. Fiz.* **121**, 1239 (2002) [*JETP* **94**, 977 (2002)].
15. O. V. Ivanov and E. G. Maksimov, *Zh. Éksp. Teor. Fiz.* **108**, 1841 (1995) [*JETP* **81**, 1008 (1995)].
16. H. Streitwolf, *Gruppentheorie in der Festkörperphysik* (Teubner, Leipzig, 1967; Mir, Moscow, 1971).

Translated by G. Skrebtsov

LATTICE DYNAMICS
AND PHASE TRANSITIONS

Lattice Dynamics and Raman Scattering Spectrum of Elpasolite Rb_2KScF_6 : Comparative Analysis

S. N. Krylova*, A. N. Vtyurin*, A. Bulou**, A. S. Krylov*, and N. G. Zamkova*

* Kirensky Institute of Physics, Siberian Division, Russian Academy of Sciences,

Akademgorodok, Krasnoyarsk, 660036 Russia

e-mail: slanky@iph.krasn.ru

** Universite du Maine, Le Mans, Cedex 9, 72085 France

Received September 26, 2003

Abstract—Raman scattering spectra of elpasolite Rb_2KScF_6 are studied in a wide temperature range including two phase transitions: from the cubic to the tetragonal phase and then to the monoclinic phase. The experimental Raman scattering spectrum is compared with the lattice vibration spectra of these phases calculated using an *ab initio* approach. A number of anomalies (caused by structural rearrangement during the phase transitions) are revealed and quantitatively analyzed in the ranges of both the intramolecular vibrations of the octahedron molecular ScF_6 ions and low-frequency intermolecular lattice vibrations. The interaction between low-frequency intramolecular vibrations and the intermolecular modes is found to be significant, and strong resonance interaction of the rotational soft modes (which are recovered below the phase transition points) with hard low-frequency vibrations of the rubidium ion sublattice is detected. These interactions are shown to substantially complicate the spectra. © 2004 MAIK “Nauka/Interperiodica”.

1. INTRODUCTION

The perovskite-like Rb_2KScF_6 crystal belongs to the family of $A_2B^{(1)}B^{(2)}X_6$ elpasolites, where A and B are metal cations or more complex molecular ions and X are oxygen or halogen anions [1]. As a rule, one of the highly polarized cations enters into the rather rigid octahedral molecular group BX_6 and the crystal structure can be considered a skeleton of these octahedra separated by cations with a strongly localized electron density. In many cases, phase transitions in elpasolites are related to changes in the octahedral skeleton, namely, small tilts of these octahedra or their orientation ordering. In particular, these changes manifest themselves experimentally in substantial anomalies in the crystal lattice dynamics, including the condensation of soft phonon modes during displacive transitions [1–5].

The Rb_2KScF_6 crystal undergoes phase transitions from the cubic to the tetragonal phase and then to the monoclinic phase [6]. The stability of these structures and the dynamics of their lattices were analyzed in [7, 8] by performing nonempirical calculations. It was shown that the instability of these structures is of phonon nature and that the mechanism of at least the first transition is related to the condensation of an optical phonon, which should appear again in the low-symmetry phases. Earlier searches for manifestations of such vibrations in Raman scattering spectra did not meet with success [9] (as in the cases of other fluorine-containing elpasolites [10]). Later, observation of the

recovery of soft phonon modes in the Rb_2KScF_6 crystal was reported in [11, 12]. However, the number of these modes is inconsistent with that predicted by group-theoretic analysis [13] and they can be observed experimentally only well below the phase transition point. Therefore, the purpose of this work is to analyze the experimental spectral data quantitatively, compare them with the results of numerical calculations, and establish the causes of discrepancies between the calculated and experimental data.

2. CRYSTAL STRUCTURE AND SYMMETRY

The unit cell of the high-symmetry cubic phase of the elpasolite $A_2BB^{3+}X_6$ can be represented as a cubic perovskite cell with doubled parameters in which the B and B^{3+} ions alternate along all three coordinate axes. The structure of the unit cell (space group $Fm\bar{3}m$, $Z = 4$) is shown in Fig. 1.

As the temperature decreases, the Rb_2KScF_6 crystal undergoes two sequential phase transitions: from the cubic to the tetragonal phase (space group $I114/m$, $Z = 2$) at $T_1 = 252$ K and then to the monoclinic phase (space group $P12_1/n1$, $Z = 2$) at $T_2 = 223$ K [6]. The calculated distortion of the structure [8] that is predicted to occur at the first phase transition is shown in Fig. 2. As is seen, this distortion is a rotation of the rigid ScF_6 octahedra.

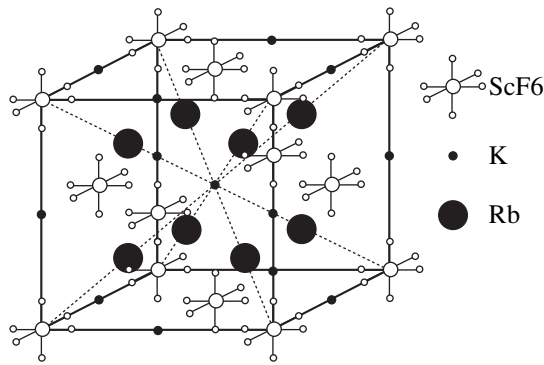


Fig. 1. Structure of the initial cubic phase of the Rb_2KScF_6 crystal.

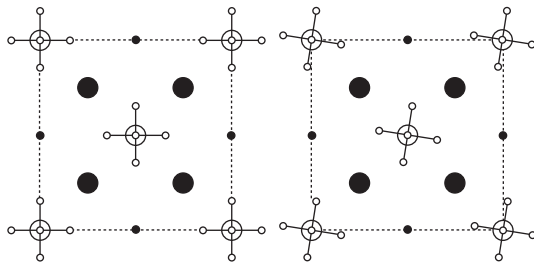


Fig. 2. Lattice distortions associated with the transition to the tetragonal phase.

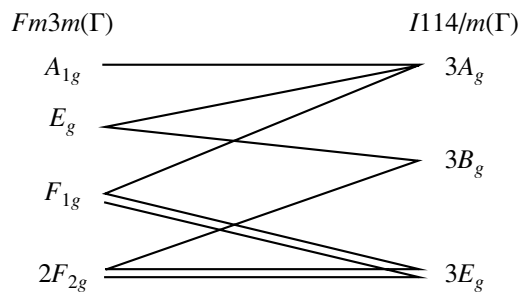


Fig. 3. Correlation diagrams for the Raman-active vibrations of the cubic and tetragonal phases.

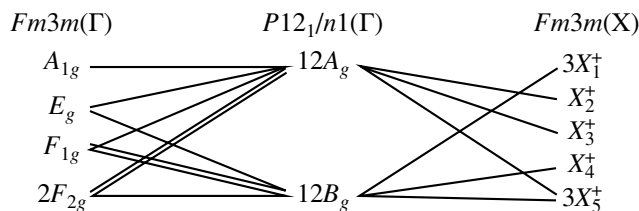


Fig. 4. Correlation diagrams for the Raman-active vibrations of the cubic and monoclinic phases.

In the high-symmetry cubic phase, the reduction of the oscillation representation at the center of the Brillouin zone is

$$\Gamma_{\text{vibr}}(Fm3m) = A_{1g}(xx, yy, zz) + E_g(xx, yy, zz) + 2F_{2g}(xz, yz, xy) + F_{1g} + 5F_{1u} + F_{2u}. \quad (1)$$

The Raman tensor components in which the corresponding vibrations are active are indicated in parentheses. The intramolecular modes related to the internal vibrational degrees of freedom in the ScF_6 octahedron in the crystal can be considered to interact only weakly with intermolecular lattice vibrations related to the rigid motion of the octahedron as a whole and to remain strongly localized, which agrees with the data from [10–13]. In this case, in the cubic phase, only the intermolecular mode F_{2g} is Raman-active; the other Raman-active modes are the intramolecular vibrations of this group.

Since the symmetry of the free octahedron coincides with the symmetry of the position of the ScF_6 groups in the crystal, the symmetry and shape of their intramolecular vibrations should remain unchanged in this approximation [14].

In the tetragonal phase, the reduction of the oscillation representation at the center of the Brillouin zone has the form

$$\Gamma_{\text{vibr}}(I114/m) = 3A_g(xx, yy, zz) + 3B_g(xx, yy, xy) + 3E_g(xz, yz) + 5A_u + B_u + 6E_u. \quad (2)$$

Figure 3 shows the correlation diagram for vibrations (1) and (2).

The structural distortions due to the first phase transition (Fig. 2) transform according to the triply degenerate irreducible representation F_{1g} . Therefore, the soft mode above the transition point should also transform according to this representation; this mode is inactive in the Raman scattering spectra (and the infrared absorption spectra).

From the correlation diagram in Fig. 3, it follows that, below the transition point to the tetragonal phase, the degeneracy of the intramolecular (E_g, F_{2g}) and intermolecular (F_{2g}) vibrations can be removed (i.e., splitting will occur) and two soft modes can split and become Raman-active.

In the low-symmetry monoclinic phase, the reduction of the oscillation representation of the symmetry group has the form

$$\Gamma_{\text{vibr}}(P12_1/n1) = 12A_g(xx, yy, zz, xy, yx) + 12B_g(xz, yz, zx, zy) + 18A_u + 18B_u. \quad (3)$$

The transition to the monoclinic phase is accompanied by a twofold increase in the unit cell volume. The modes at the $X(0, 0, \pi/a)$ point in the Brillouin zone, including the possible soft mode X_2^+ , are Raman-inactive; however, they can become Raman-active below

the second transition point (and the soft mode can also be recovered). The correlation between the Raman-active modes in the monoclinic phase and the modes in the cubic phase is shown in Fig. 4. As is seen, the mode X_2^+ is the only one in this structure and it corresponds to rotation of the octahedral groups. We might also expect further splitting of the modes that are degenerate in the tetragonal phase, including the recovering soft mode corresponding to the transition from the cubic to the tetragonal phase.

3. EXPERIMENTAL AND DATA PROCESSING TECHNIQUES

To study Raman spectra, we applied polarized 514.5-nm radiation from a 500-mW Ar⁺ laser as an excitation source. The spectra were recorded in the 180° geometry using a T-64000 spectrometer (I.S.A., Jobin Yvon) with matrix recording. Samples 2 × 2 × 4 mm in size were taken from the solidification batch used in [6, 11]; their edges were orientated along the crystallographic axes of the cubic phase. The samples are optically transparent and do not contain color defects or inclusions that are visible under a microscope. To weaken the wing of elastic scattering as much as possible to record low-frequency spectra, we applied a triple monochromator in the dispersion subtraction mode. Low frequencies were cut beginning from 8 cm⁻¹. To record high-resolution spectra of intramolecular vibrations (with minimum distortion of line contours), we applied the dispersion addition mode. The spectral size of the recording matrix cell was 650/1024 cm⁻¹ in the dispersion subtraction mode and 220/1024 cm⁻¹ in the dispersion addition mode; the counting time was 600 s. The temperature of a sample during the recording of spectra was maintained with an accuracy of better than 0.2 K. The Rb₂KScF₆ crystal was studied in the temperature range 50–600 K.

To determine the parameters of spectral lines, we processed the experimental data with the SigmaPlot 8.0 software package using the dispersion shape of a contour. Moreover, we took into account the frequency-dependent correction

$$I_s(\Omega_\alpha) \sim |Q_\alpha|^2 \sim n_\alpha + 1 = \frac{1}{1 - \exp(-\hbar\Omega_\alpha/k_B T)} \quad (4)$$

to the temperature dependence of the scattering intensity.

To correctly compare the experimental Raman spectra with the calculations carried out in [7, 8] and determine the eigenvectors of the observed vibrations, we performed a group-theoretic analysis of the eigenvectors of the calculated lattice vibrations. For this purpose, the calculated eigenvectors of the dynamic matrix are expanded in terms of the basis functions of the irreducible representations of the crystal symmetry group using projection operators. We constructed the com-

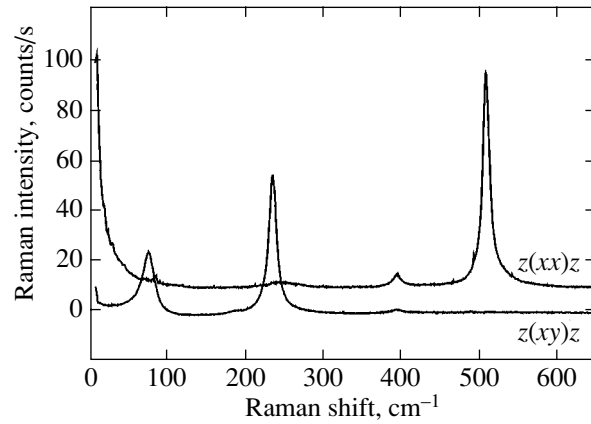


Fig. 5. Raman spectrum of the cubic phase of Rb₂KScF₆ ($T = 300$ K).

plete oscillation representation $P(g)$ of the space group of the hexagonal phase and then found the projection operators [15]:

$$P_\rho = \frac{d(\rho)}{N(g)} \sum_{g \in G} \chi_\rho(g) P(g). \quad (5)$$

Here, $d(\rho)$ is the dimension of the representation ρ of the point symmetry operation, $N(g)$ is the dimension of the symmetry group, $\chi_\rho(g)$ is the character of the matrix of the irreducible representation ρ , $P(g)$ is the oscillation representation of the symmetry operation for the irreducible representation ρ of the group G , and P_ρ is the projection operator. Summation is performed over all operations of the symmetry group. A vibration eigenvector \mathbf{f} is transformed according to the irreducible representation ρ of the group G if it satisfies the criterion [15]

$$P_\rho \mathbf{f} = \frac{N(g)}{d(\rho)} \mathbf{f}. \quad (6)$$

This algorithm of expansion of the eigenvectors of a dynamic matrix in terms of the irreducible representations is realized using the Mathematica 4.2 software package.

4. EXPERIMENTAL RESULTS AND DISCUSSION

4.1. Raman Scattering Spectrum of the Cubic Phase

The spectrum of the Rb₂KScF₆ cubic crystal far from the phase transition point is shown in Fig. 5. In Table 1, the calculated modes of the cubic phase [7] are assigned to the symmetry types and the experimental frequencies are compared with the corresponding calculated frequencies.

The number, frequencies, and polarization of the spectral lines of the cubic phase agree well with those observed earlier [9–13]. The lines are strongly polar-

Table 1. Experimental and calculated vibration frequencies (cm^{-1}) of Rb_2KScF_6 in the cubic phase

Vibration mode	Calculation [7]	Experiment
F_{1g}	66i	
F_{1u}	34i	
F_{2g}	26i	89
F_{1u}	0	
F_{1u}	80	
F_{2u}	99	
F_{1u}	135	
F_{2g}	152	230
F_{1u}	164	
F_{1u}	185	
F_{1u}	189	
E_g	343	390
A_{1g}	402	505
F_{1u}	404	
F_{1u}	462	

Note: Boldface type shows the calculated frequency of the soft mode corresponding to the first phase transition.

ized, which confirms the high quality of the sample. The calculated frequencies are somewhat lower than the experimental ones, which can be due to the fact that the calculations correspond to the absolute zero of temperature, where the cubic phase is unstable. This circumstance also explains the imaginary values of the frequencies of the low-frequency vibrations.

Table 2 gives examples for the eigenvectors of intramolecular vibrations of the ScF_6 octahedra. As was expected, the eigenvectors of the two highest frequency vibration modes (390 and 505 cm^{-1}) correspond to intramolecular vibrations of the free ScF_6 octahedra

(390 and 498 cm^{-1} for the free ScF_6 ion, respectively [14]). However, the low-frequency intramolecular vibration of the octahedral ion and the intermolecular vibration mode of the rubidium ion sublattice (both vibrations have the F_{2g} symmetry) are found to be mixed, although their vibration frequencies are rather far from each other (230 and 89 cm^{-1} , respectively). This finding indicates noticeable interaction between the intermolecular and the intramolecular vibrations even in the high-symmetry cubic phase.

4.2. Temperature Dependence of the Internal Vibration Modes

The correlation diagrams of the Raman-active internal modes are given in Fig. 6. It is seen that, below the transition to the monoclinic phase, an additional line corresponding to the Brillouin zone boundary can appear in the region of the fully symmetrical high-frequency vibration of the ScF_6 group.

The transformation of the spectrum in the frequency range in question is shown in Fig. 7, and the temperature dependences of the frequencies and half-widths of the observed lines are shown in Fig. 8. In Fig. 7, additional lines are clearly seen to appear in this spectral region at low temperatures, which agrees well with the selection rules (see the correlation diagram in Fig. 6). The temperature dependence of the frequency significantly changes in character near the phase transformation points. Extrapolating the temperature dependence of the frequency in the cubic phase using the well-known relation [12, 13] (see Fig. 8)

$$\Omega_\alpha(T) = \Omega_\alpha(0)\exp(-3\gamma_\alpha\alpha T) \quad (7)$$

gives the product of the Grüneisen parameter by the coefficient of thermal expansion, $\gamma_\alpha\alpha \approx 0.2 \times 10^{-5} \text{ K}^{-1}$. The frequency extrapolated to zero temperature is equal to 518 cm^{-1} . Such a low value of the Grüneisen param-

Table 2. Eigenvectors of the internal vibrations of the ScF_6 ion

Atom	E_g						A_{1g}		
	x	y	z	x	y	z	x	y	z
Rb	0	0	0	0	0	0	0	0	0
Rb	0	0	0	0	0	0	0	0	0
K	0	0	0	0	0	0	0	0	0
Sc	0	0	0	0	0	0	0	0	0
F	0	0	0.29	0	0	0.5	0	0	-0.41
F	0	0	-0.29	0	0	-0.5	0	0	0.41
F	0.29	0	0	0.5	0	0	0.41	0	0
F	-0.29	0	0	-0.5	0	0	-0.41	0	0
F	0	-0.58	0	0	0	0	0	-0.41	0
F	0	0.58	0	0	0	0	0	0.41	0

eter, even making allowance for its dependence on the frequency

$$\gamma_\alpha = \frac{B_T}{\Omega_\alpha} \left(\frac{d\Omega_\alpha}{dP} \right)_T \quad (8)$$

indicates that the effect of anharmonicity on this vibration is weak (Ω_α is the frequency of this vibration, B_T is the isothermal bulk modulus of elasticity, P is the hydrostatic pressure).

The frequency shift with respect to the extrapolated value below the transition to the tetragonal phase is shown in Fig. 9.

A small additional frequency shift appears even in the cubic phase in a rather wide (about 50 K) region above the phase transition point. The shift increases monotonically in the tetragonal phase and becomes virtually linear in the monoclinic phase, which corresponds to a second-order (or close-to-second-order) phase transformation.

The half-width of this line also changes with temperature. Its temperature dependence is shown in Fig. 10. The curve in Fig. 10 is the half-width in the cubic phase fitted by the expression

$$\sigma(\Omega_\alpha, T) = \sigma(\Omega_\alpha, 0) \left(1 + \frac{1}{\exp(\hbar\Omega_{\beta_1}/k_B T) - 1} + \frac{1}{\exp(\hbar\Omega_{\beta_2}/k_B T) - 1} \right) \quad (9)$$

which describes the line broadening caused by the decay into two phonons [16, 17]. The experimental dependence is seen to be correctly described by this expression; this fact indicates the absence of substantial contributions from other line-broadening mechanisms, e.g., structural disordering of the crystal in the high-temperature phase. The fitted frequencies of the phonons involved in the decay of this intramolecular vibration are found to be $\Omega_{\beta_1} \approx 413 \text{ cm}^{-1}$ and $\Omega_{\beta_2} = \Omega_\alpha - \Omega_{\beta_1}$, which correspond to a decay into two optical phonons with one of the phonons being close in frequency to the intramolecular vibration ν_2 [14] and the other falling in the region of high-frequency lattice vibrations. The line half-width extrapolated to zero temperature is 0.9 cm^{-1} .

As follows from Fig. 5, the intramolecular vibration ν_2 in the cubic phase is very weak; for this reason, we failed to reliably detect its splitting below the phase transition points. The temperature dependence of its frequency is also described well by Eq. (7) with $\gamma_\alpha \approx 0.4 \times 10^{-4} \text{ K}^{-1}$, which corresponds to a higher value of the Grüneisen parameter (i.e., greater anharmonicity of vibrations); the frequency extrapolated to zero temperature is equal to 407 cm^{-1} .

The temperature dependences of the frequencies and half-widths of the lines detected in the region of the intramolecular vibration ν_5 are shown in Fig. 11. The

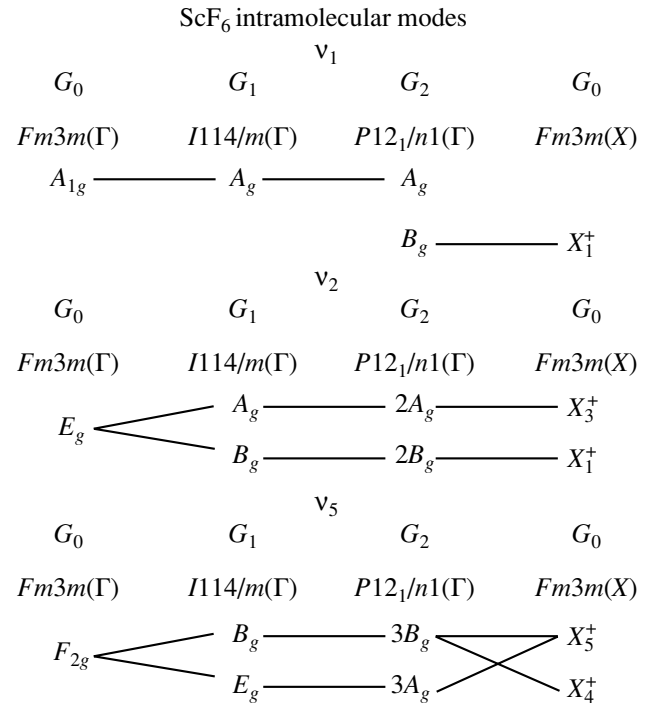


Fig. 6. Correlation diagrams for the Raman-active internal vibrations of the ScF₆ groups. The vibrations that are allowed in the spectrum by the selection rules are marked.

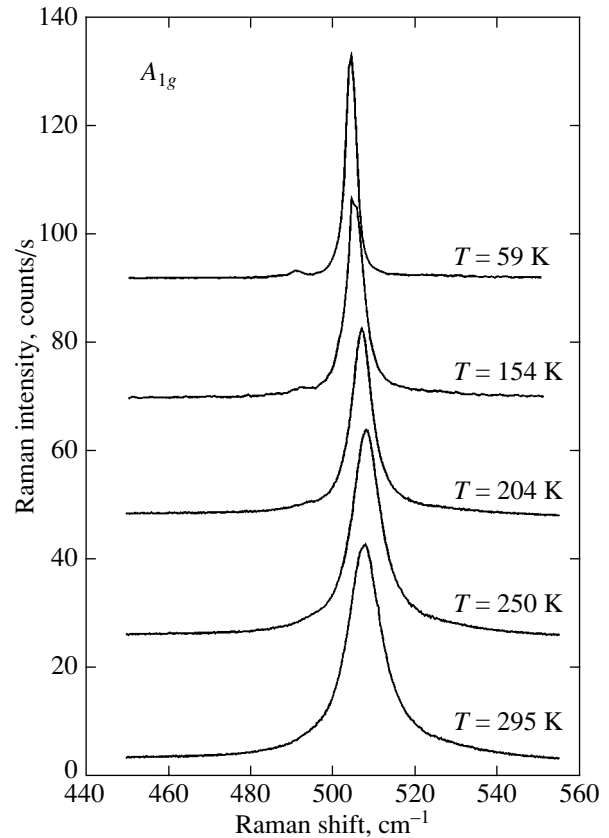


Fig. 7. Variation of the Raman spectrum in the region of the fully symmetrical internal vibration with temperature.

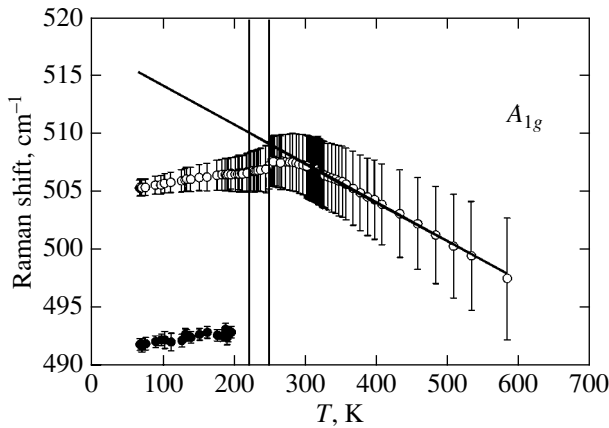


Fig. 8. Temperature dependences of the frequencies of the lines corresponding to the fully symmetrical internal vibration. The vertical bars show their half-widths at half-maximum (HWHM).

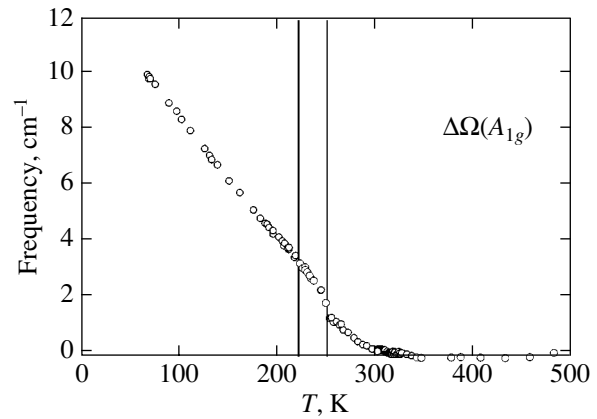


Fig. 9. Temperature dependence of the frequency shift of the fully symmetrical internal vibration with respect to the extrapolated value.

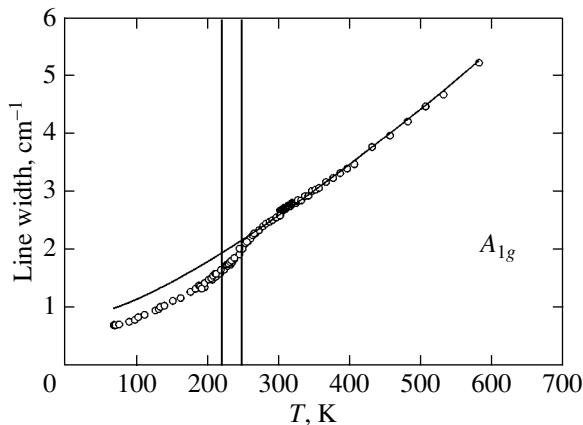


Fig. 10. Temperature dependence of the half-width at half-maximum (HWHM) of the internal vibration ν_1 . The curve is extrapolation by Eq. (9).

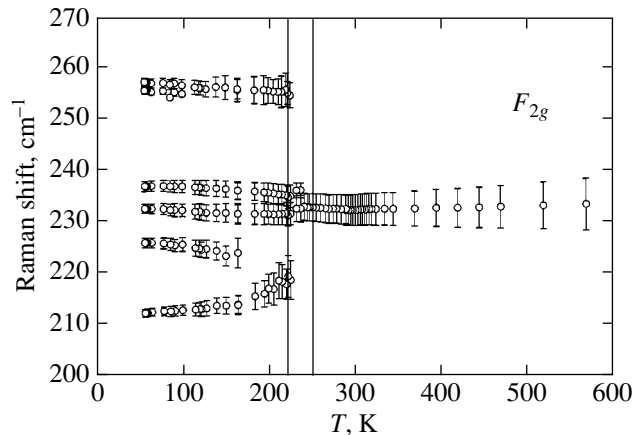


Fig. 11. Temperature dependences of the line frequencies in the region of the internal vibration ν_5 . The vertical bars show the line half-widths (HWHM).

number of the lines corresponds to the selection rules (Fig. 6), and their positions agree qualitatively with the calculations [7].

The frequency of the most intense line in this range (232 cm^{-1}) remains virtually unchanged in the cubic phase, which indicates that the contributions from thermal expansion and phonon–phonon interaction to the temperature dependence of the frequency compensate each other. Below the transition from the cubic to the tetragonal phase, the frequency of this line changes continuously and the line splits to form a doublet. At the transition to the monoclinic phase, the frequencies change in a jump and split further. The continuous variation of the spectrum during the first phase transition and the jumpwise change during the second transition agree with the data on the thermodynamics of these transitions [6]. The lines that appear in the monoclinic

phase and correspond to the Brillouin zone boundary of the cubic phase are very weak, and some of them can be detected only far below the transition to the monoclinic phase.

The temperature dependence of the half-width of the line at 232 cm^{-1} fitted by Eq. (9) gives a value of 0.1 cm^{-1} for the line half-width extrapolated to $T = 0$ and a frequency of 224 cm^{-1} for the phonon that forms during decay; this frequency corresponds to the decay into an optical and acoustic phonons at the Brillouin zone boundary.

4.3. Temperature Dependence of the Lattice Vibration Modes

The variation of the intermolecular vibration spectrum with temperature is shown in Fig. 12. The spec-

trum can be divided into two portions, above and below 60 cm^{-1} . The higher frequency spectrum corresponds to stable (hard) intermolecular vibration modes of the rubidium ion sublattice with a small admixture of the low-frequency intramolecular deformation vibration mode of the ScF_6 ions. (The eigenvector of this mode, as well as the eigenvector of the Raman-inactive soft mode in the cubic phase, is given in Table 3). In this range, the frequency of the intermolecular mode grows slowly (89 cm^{-1} at room temperature). Below the first transition point, this mode splits into two lines and then splits further below the second transition point and additional low-intensity lines appear upon deeper cooling. The temperature dependences of the frequencies and widths of these lines are shown in Fig. 13.

The total number of lines detected in this higher frequency range corresponds to the selection rules (see the correlation diagram in Fig. 14).

Note that new lines appear immediately after the phase transitions, which is related to the splitting of degenerate vibration modes in the high-symmetry phases. However, the additional lines caused by a two-fold increase in the unit cell volume appear far below the phase transition points. This finding can be explained by the fact that the phase transitions result in substantial changes in the crystal dynamics, which leads to shifts and splitting of the lines corresponding to Raman-active modes in the high-temperature phase. At the same time, the derivatives of the crystal dielectric susceptibility with respect to the atomic displacements change only weakly and the forbidden vibrations at the Brillouin zone boundary remain weak until their eigenvectors become sufficiently strongly distorted.

In the low-frequency portion of the spectrum ($<60 \text{ cm}^{-1}$), the central scattering peak grows and broadens as the temperature decreases in the region several degrees above the phase transition point. Below the first transition point, a wide wing (which can be interpreted as the excitation of a low-intensity broad

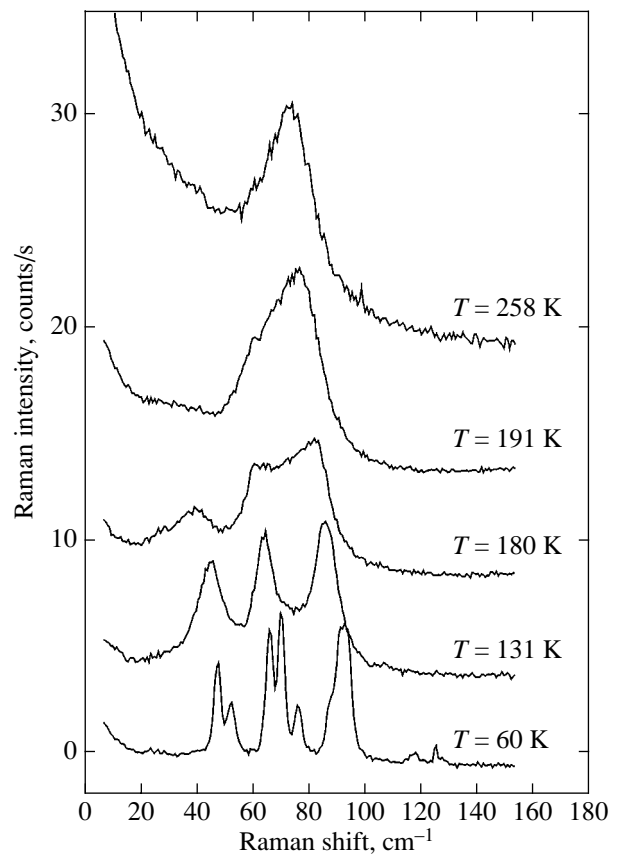


Fig. 12. Variation of the lattice vibration spectrum of Rb_2KScF_6 with temperature.

band) appears near the central peak (Fig. 15). At lower temperatures, this band exhibits two maxima, at 26 and 39 cm^{-1} . Figure 15 shows the temperature dependence of the squared frequencies of the maxima of these lines.

In the tetragonal phase, no significant shifts in the frequencies of these lines are observed (the accuracy of

Table 3. Eigenvectors of lattice vibration modes in the cubic phase

Atom	Hard F_{2g} mode, $\Omega = 89 \text{ cm}^{-1}$			Soft F_{1g} mode, $\Omega = 66i \text{ cm}^{-1}$		
	x	y	z	x	y	z
Rb	0.35	-0.52	0.18	0	0	0
Rb	-0.35	0.52	-0.18	0	0	0
K	0	0	0	0	0	0
Sc	0	0	0	0	0	0
F	-0.16	0.10	0	0.39	0.08	0
F	0.16	-0.10	0	-0.39	-0.08	0
F	0	-0.05	0.16	0	0.31	0.39
F	0	0.05	-0.16	0	-0.31	-0.39
F	0.05	0	0.10	0.31	0	-0.08
F	-0.05	0	-0.10	-0.31	0	0.08

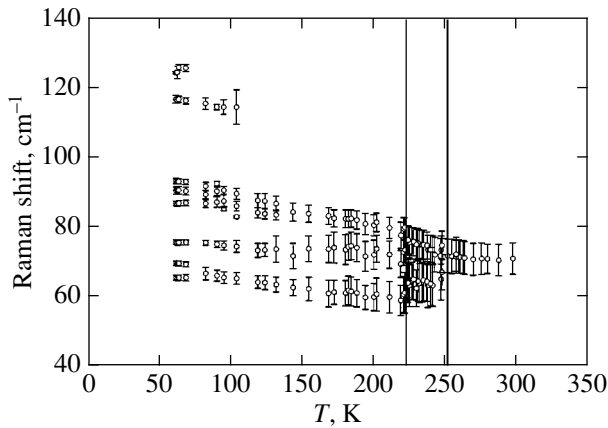


Fig. 13. Temperature dependences of the frequencies of the Rb_2KScF_6 hard lattice vibration modes. The vertical bars show the line half-widths (HWHM).

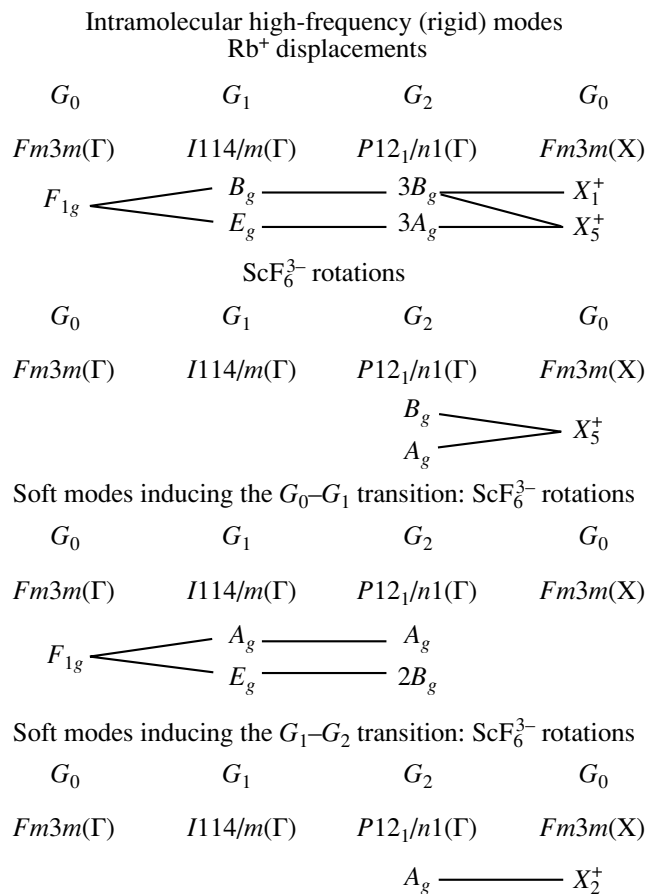


Fig. 14. Correlation diagrams for the Raman-active lattice vibrations. The vibrations that are allowed in the spectrum by the selection rules are marked.

determining the line positions is low, because the noise level is comparable to the line intensities). We note only a transfer of intensity to the high-frequency portion of this band and a decrease in the intensity of the central peak (which is likely due to rearrangement of the domain structure) with decreasing temperature.

When the second transition point is reached, the intensity of elastic scattering increases jumpwise and the intensity of the detected band is redistributed; namely, its high-frequency portion increases substantially. The frequency of this maximum increases monotonically upon cooling, and the temperature dependence of the frequency squared is almost linear, which is characteristic of the soft modes related to displacive second-order (or close-to-second-order) phase transitions. Below 100 K, where the lines become strongly narrower because of small anharmonicity at such temperatures, this maximum splits in two. As the temperature decreases further, the high-frequency component of the doublet formed continues to move upward, whereas the position of the low-frequency component remains virtually unchanged (47–48 cm^{-1}).

The position of the lowest frequency maximum also remains virtually unchanged (23–27 cm^{-1}). Its intensity decreases slowly, and, below 100 K, it can hardly be detected against the noise background.

The number of lines observed in the lattice vibration spectra is consistent with the selection rules (see the correlation diagram in Fig. 14). This diagram shows that, below the first transition point, the two modes will be observed that are formed as a result of the condensation and partial splitting of the earlier Raman-inactive F_{1g} phonon, which corresponds to rotational vibrations of the octahedron groups prior to the transition (Table 3). By analogy with the hard intermolecular modes, we might expect their intensities to be rather low. After the second phase transition, they should split to yield a triplet (the symmetry of the corresponding vibrations in the monoclinic phase is $A_g + 2B_g$). Simultaneously, the soft

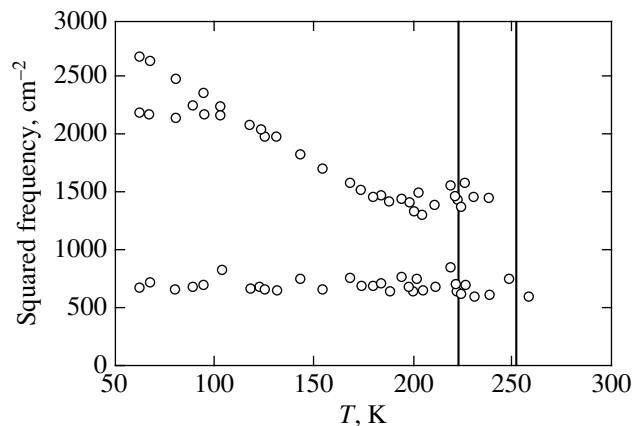


Fig. 15. Temperature dependence of the squared frequencies of the detected low-frequency lattice vibrations.

mode corresponding to this transition should begin to recover; this mode also has the A_g symmetry in the monoclinic phase and also corresponds to rotations of the octahedron groups in the high-temperature phase. The presence of the hard vibration modes of the rubidium ion sublattice of the same symmetry in the spectrum (Fig. 14; the calculated frequencies and eigenvectors of all lattice vibrations in the monoclinic phase can be found in [18]) leads to their resonance interaction with the recovering soft modes. This mode interaction is accompanied by strong mixing of their eigenvectors until the high-frequency component of the “soft multiplet” shifts toward sufficiently high frequencies, where it becomes observable in the experimental spectrum. Note that, according to the dynamics calculations of the monoclinic phase at $T = 0$ [7], the frequencies of the two lowest vibration modes in the spectrum are 22 and 31 cm^{-1} , which agrees well with the experimental position of the low-frequency maximum (23–27 cm^{-1}). However, calculations [18] show that the eigenvector of these vibrations is a superposition of the rotations of the rigid ScF_6 groups (without distortion) and the displacements of the rubidium atoms.

5. CONCLUSIONS

The phase transitions in Rb_2KScF_6 have been found to be accompanied by the recovery of soft phonon modes, which allows us to attribute them to displacive transitions [8, 9]. We did not detect any lattice disordering-induced anomalies in the lattice dynamics of the high-symmetry phase. The group-theoretic analysis shows that the eigenvectors of both soft modes above the phase transition points are connected with the rotations of the ScF_6^+ octahedron molecular ions. Below the transition to the monoclinic phase, a strong interaction between the recovering rotational soft modes and the displacements of the rubidium ions is observed. This interaction results in modification of the temperature dependences of the phonon frequencies and mixing of the phonon eigenvectors and complicates the vibration spectrum.

Anomalies in the temperature dependences of the parameters of the hard intermolecular modes and the intramolecular vibrations of the KScF_6 groups have been revealed and interpreted. Quantitative analysis of these anomalies supported the transition to the tetragonal phase being a second-order transition and the transition to the monoclinic phase being a first-order (close-to-second-order) transition. The small values of the line half-widths and their temperature dependences indicate that the vibration damping in the high-symmetry phase is determined by the decay of phonons due to their anharmonicity and is not related to structure disordering, except, possibly, for the pretransition region.

ACKNOWLEDGMENTS

The authors thank K.S. Aleksandrov, I.N. Flerov, and V.I. Zinenko for supplying the samples and for valuable discussions.

This work was supported jointly by the Russian Foundation for Basic Research and the Krasnoyarsk Science Foundation (project Enisei, no. 02-02-97707) and the Siberian Division of the Russian Academy of Sciences (project no. 88).

REFERENCES

1. K. S. Aleksandrov and B. V. Beznosikov, *Perovskite-like Crystals* (Nauka, Novosibirsk, 1997).
2. W. Buhner and H. U. Gudel, *J. Phys. C* **20**, 3809 (1987).
3. G. P. Knudsen, *Solid State Commun.* **49**, 1045 (1984).
4. F. Prokert and K. S. Aleksandrov, *Phys. Status Solidi B* **124**, 503 (1984).
5. G. Baldinozzi, Ph. Sciau, and A. J. Bulou, *J. Phys.: Condens. Matter* **7**, 8109 (1995).
6. I. N. Flerov, M. V. Gorev, S. V. Mel'nikova, S. V. Misyul', V. N. Voronov, and K. S. Aleksandrov, *Fiz. Tverd. Tela (St. Petersburg)* **34**, 2185 (1992) [*Sov. Phys. Solid State* **34**, 1168 (1992)].
7. V. I. Zinenko and N. G. Zamkova, *Fiz. Tverd. Tela (St. Petersburg)* **41**, 1297 (1999) [*Phys. Solid State* **41**, 1185 (1999)].
8. V. I. Zinenko and N. G. Zamkova, *Zh. Éksp. Teor. Fiz.* **118**, 359 (2000) [*JETP* **91**, 314 (2000)].
9. I. N. Flerov, M. V. Gorev, K. S. Aleksandrov, A. Tressaud, J. Grannec, and M. Cousi, *Mater. Sci. Eng. R* **24**, 81 (1998).
10. M. Cousi, S. Khairoun, and A. Tressaud, *Phys. Status Solidi A* **98**, 423 (1986).
11. A. N. Vtyurin, A. Bulou, A. S. Krylov, and V. N. Voronov, *Fiz. Tverd. Tela (St. Petersburg)* **43**, 2066 (2001) [*Phys. Solid State* **43**, 2154 (2001)].
12. A. S. Krylov, A. N. Vtyurin, A. Bulou, and V. N. Voronov, *Ferroelectrics* **284**, 47 (2003).
13. A. N. Vtyurin, A. Bulou, A. S. Krylov, and V. N. Voronov, Preprint No. 815F, IF SO RAN (Inst. of Physics, Siberian Division, Russian Academy of Sciences, Krasnoyarsk, 2002).
14. K. Nakamoto, *Infrared and Raman Spectra of Inorganic and Coordination Compounds* (Wiley, New York, 1986; Mir, Moscow, 1991).
15. H. Streitwolf, *Gruppentheorie in der Festkörperphysik* (Teubner, Leipzig, 1967; Mir, Moscow, 1971).
16. M. Balkanski, R. F. Wallis, and E. Haro, *Phys. Rev. B* **28**, 1928 (1983).
17. J. Gonzalez, E. Moya, and J. C. Chervin, *Phys. Rev. B* **54**, 4707 (1996).
18. S. N. Krylova, A. N. Vtyurin, A. Bulou, A. S. Krylov, and N. G. Zamkova, Preprint No. 821F, IF SO RAN (Inst. of Physics, Siberian Division, Russian Academy of Sciences, Krasnoyarsk, 2003).

Translated by K. Shakhlevich

LATTICE DYNAMICS AND PHASE TRANSITIONS

X-ray Study of $[\text{N}(\text{CH}_3)_4]_2\text{ZnCl}_4$ at Low Temperatures

A. U. Sheleg and A. M. Naumovets

*Institute of Solid State Physics and Semiconductors, National Academy of Sciences of Belarus,
ul. P. Brovki 17, Minsk, 220072 Belarus*

e-mail: sheleg@ifftp.bas-net.by

Received October 30, 2003

Abstract—The unit cell parameters a , b , and c of $[\text{N}(\text{CH}_3)_4]_2\text{ZnCl}_4$ have been measured by x-ray diffraction in the temperature range 80–293 K. Temperature dependences of the thermal expansion coefficients α_a , α_b , and α_c along the principal crystallographic axes and of the unit cell thermal expansion coefficient α_V were determined. It is shown that the $a = f(T)$, $b = f(T)$, and $c = f(T)$ curves exhibit anomalies in the form of jumps at phase transition temperatures $T_1 = 161$ K and $T_2 = 181$ K and that the phase transition occurring at $T_3 = 276$ K manifests itself in the $a = f(T)$ and $b = f(T)$ curves as a break. A slight anisotropy in the coefficient of thermal expansion of the crystal was revealed. The phase transitions occurring at $T_1 = 161$ K and $T_2 = 181$ K in $[\text{N}(\text{CH}_3)_4]_2\text{ZnCl}_4$ were established to be first-order. © 2004 MAIK “Nauka/Interperiodica”.

1. INTRODUCTION

The tetramethylammonium tetrachlorozincate $[\text{N}(\text{CH}_3)_4]_2\text{ZnCl}_4$ belongs to the $[\text{N}(\text{CH}_3)_4]_2\text{XB}_4$ family ($X = \text{Zn, Co, Cu, Mn, Fe, Cd, Ni}$; $B = \text{Cl, Br}$), which is characterized by the occurrence of phase transitions (PTs) in most of these crystals and by the manifestation of ferroelectric properties within a relatively narrow temperature interval [1]. In addition, some of these crystals exhibit an intermediate incommensurate phase at the crossover from the para- to the ferroelectric phase.

The $[\text{N}(\text{CH}_3)_4]_2\text{ZnCl}_4$ crystal is of interest because it undergoes a sequence of phase transitions. PTs were shown in [2] to occur in this crystal at 161, 181, 276.3, 279, and 293 K, with ferroelectric properties (spontaneous polarization along the a axis and a hysteresis loop) revealed in the range 276.3–279 K. The paraelectric phase crosses over to the ferroelectric phase in this crystal through an incommensurate phase with a modulation wave vector $q_i = 0.42c^*$, which is observed in the temperature interval 279–293 K.

At room temperature, $[\text{N}(\text{CH}_3)_4]_2\text{ZnCl}_4$ belongs to the orthorhombic crystal system (space group $Pm\bar{c}n$) and has unit cell parameters $a = 8.946 \pm 0.007$ Å, $b = 15.515 \pm 0.012$ Å, and $c = 12.268 \pm 0.007$ Å [4] or $a = 8.998$ Å, $b = 15.541$ Å, $c = 12.276$ Å and $Z = 4$ [5]. The crystal structure of this compound was studied by x-ray diffraction at 303, 333, and 363 K (normal phase) and 278.5 K (ferroelectric phase) [6]. The $[\text{N}(\text{CH}_3)_4]_2\text{ZnCl}_4$ crystal in the ferroelectric phase was shown to be monoclinic (space group $P2_1cn$). The crystal structure of the phases in the temperature intervals 276.3–181 K and 181–161 K is monoclinic (space groups $P112_1/n$ and $P12_1/c1$, respectively) and below 161 K, orthorhombic (space group $P2_12_12_1$) [3]. It was of interest to deter-

mine the variation in the unit cell parameters with temperature in the regions of these PTs.

In this study, measurements of the variation in the unit cell parameters of $[\text{N}(\text{CH}_3)_4]_2\text{ZnCl}_4$ with temperature and the coefficients of thermal expansion determined from them are given.

2. EXPERIMENTAL TECHNIQUES

X-ray measurements of the unit cell parameters were carried out on a DRON-3 diffractometer with CuK_α and MoK_α monochromatic radiation in the temperature interval 80–293 K. The measurements were performed on $4 \times 4 \times 3$ -mm single crystal platelets, whose faces were growth planes parallel to the (010), (001), and (110) crystallographic planes. The temperature dependences of the unit cell parameters were derived from measurements of the Bragg angles of the 080, 004, and 440 2θ reflections. The Bragg reflections at large angles obtained from this crystal were very weak. Therefore, we had to use reflections at comparatively small angles to determine the cell parameters. The parameters b and c were determined using samples whose major faces coincided with the (010) and (001) growth planes. The parameter a was derived from the temperature dependences $d_{010} = f(T)$ and $d_{110} = f(T)$. Because the maximum changes in the angles induced by monoclinic distortions in the $P112_1/n$ and $P12_1/c1$ phases do not exceed $\Delta\gamma \leq 0.6^\circ$ and $\Delta\beta \leq 0.06^\circ$, respectively [7] (thus yielding an error of $\Delta a \sim 10^{-4}$ Å in the calculation of the parameter a), we neglected the monoclinic distortions in its determination. The diffraction spectra were taken in the θ – 2θ arrangement. The reflection intensity profiles were scanned in steps of 0.01° over a constant pulse accumulation time $T_0 = 20$ s. The

2θ angles were determined from the centers of gravity of the reflections.

Samples were placed in a helium cryostat designed for x-ray measurements. The desired temperature was set and maintained automatically with a VRT-2 temperature control unit. The sample temperature was monitored by means of a chromel–alumel-0.15% Fe thermocouple, one of whose junctions was attached to the sample and the other was thermostatted in thawing ice. This system permitted us to set and maintain the sample temperature to within 0.1 K over the temperature region covered. Prior to each exposure, the sample was kept at the given temperature for 10–12 min.

The room-temperature unit cell parameters of the $[\text{N}(\text{CH}_3)_4]_2\text{ZnCl}_4$ crystal determined by us are $a = 8.993 \pm 0.009 \text{ \AA}$, $b = 15.533 \pm 0.008 \text{ \AA}$, and $c = 12.273 \pm 0.008 \text{ \AA}$, which is in satisfactory agreement with literature data.

The experimental temperature dependences of the unit cell parameters and volume were used to derive the corresponding coefficients of thermal expansion (TECs) $\alpha_a = f(T)$, $\alpha_b = f(T)$, and $\alpha_c = f(T)$ along the principal crystallographic axes, as well as the coefficient of thermal expansion of the cell volume $\alpha_v = f(T)$, in the temperature interval 80–293 K. In the intervals 80–161, 161–181, and 181–293 K, the $c = f(T)$ and $V = f(T)$ curves were fitted by three cubic polynomials of the type $L = A + \sum_i (-1)^i B_i T^i$. The $a = f(T)$ and $b = f(T)$ curves were fitted by four cubic polynomials of this type in the intervals 80–161, 161–181, 181–276, and 276–293 K because of an anomaly at $T_3 \approx 276 \text{ K}$, which was not observed in the $c = f(T)$ and $V = f(T)$ curves.

The fitting curves were divided into temperature sections 0.7–1.5-K long, within which the TECs were calculated using the relation $\alpha_L = \frac{1}{L} \frac{\Delta L}{\Delta T}$, where L is the unit cell parameter corresponding to the center of the ΔT section and ΔL is the change in the parameter within this section.

3. RESULTS AND DISCUSSION

Figures 1–4 plot the temperature dependences of the unit cell parameters and volume and of the coefficient of thermal expansion of the $[\text{N}(\text{CH}_3)_4]_2\text{ZnCl}_4$ crystal obtained in the range 80–293 K. From these figures, we see that the cell parameters a , b , and c and volume V grow smoothly with increasing temperature. In the phase transition regions at $T_1 \approx 161 \text{ K}$ and $T_2 \approx 181 \text{ K}$, however, the $a = f(T)$, $b = f(T)$, $c = f(T)$, and $V = f(T)$ curves exhibit anomalies in the form of jumps. Interestingly, the jumps seen at $T_1 = 161 \text{ K}$ in the temperature dependences of the cell parameters a , b , and c and of the cell volume V are small in amplitude, namely, ≈ 0.011 , ≈ 0.004 , $\approx 0.005 \text{ \AA}$, and $\approx 3.6 \text{ \AA}^3$, respectively. The changes in the parameters a , b , and c measured in

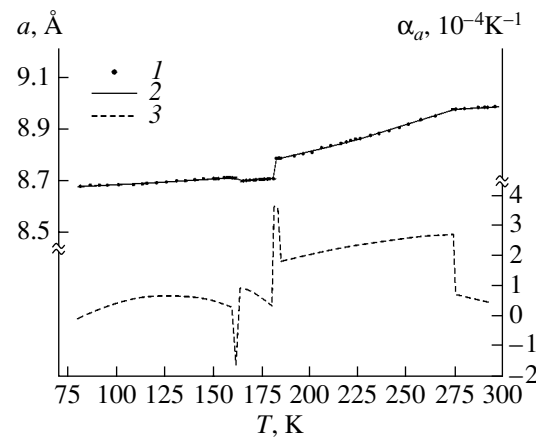


Fig. 1. Temperature dependences (1, 2) of unit cell parameter a [(1) experimental points, (2) fitting to experimental data] and (3) of TEC α_a .

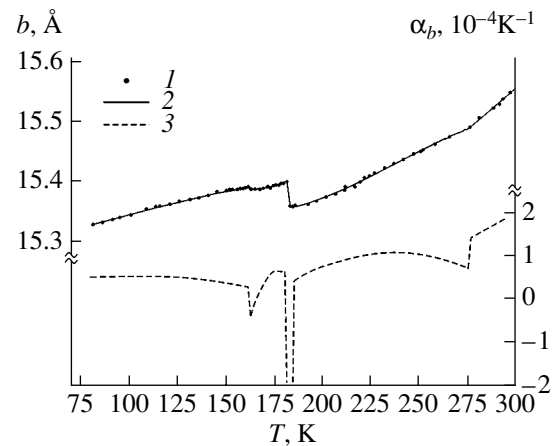


Fig. 2. Temperature dependences (1, 2) of unit cell parameter b [(1) experimental points, (2) fitting to the experimental data] and (3) of TEC α_b .

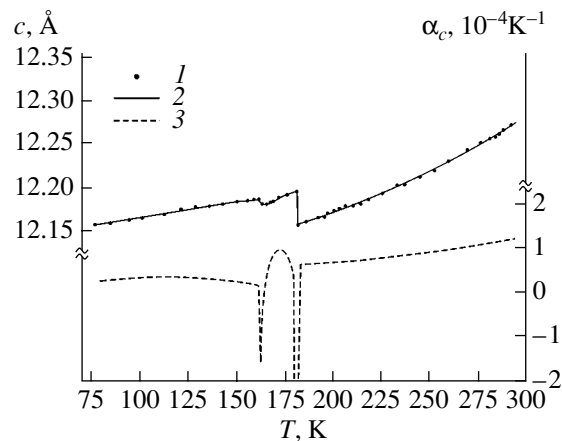


Fig. 3. Temperature dependences (1, 2) of unit cell parameter c [(1) experimental points, (2) fitting to the experimental data] and (3) of TEC α_c .

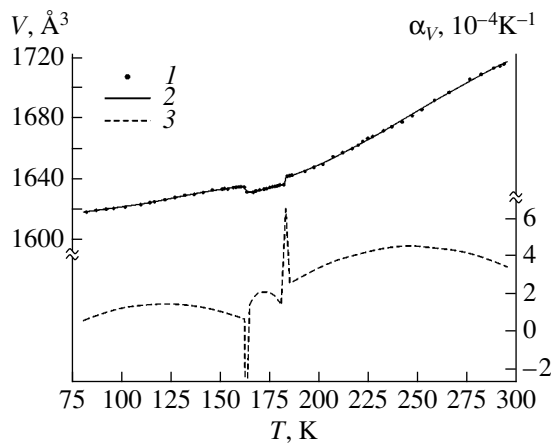


Fig. 4. Temperature dependences (1, 2) of the unit cell volume V [(1) experimental points, (2) fitting to the experimental data] and (3) of TEC α_V .

the PT region at $T_2 = 181$ K are fairly large: $\Delta a \approx 0.081$ Å, $\Delta b \approx 0.041$ Å, and $\Delta c \approx 0.04$ Å. Note, however, that while the parameters b and c drop abruptly by $\Delta b \approx 0.041$ Å and $\Delta c \approx 0.04$ Å at $T_2 = 181$ K, the parameter a increases by $\Delta a \approx 0.081$ Å. As a result, the cell volume changes insignificantly at this PT, $\Delta V \approx 5.3$ Å³, and these large changes in linear dimension do not lead to crystal breakup.

In the PT region at $T_3 \approx 276$ K, the $a = f(T)$ and $b = f(T)$ curves exhibit distinct anomalies in the form of breaks. As for the PT at $T_4 = 279$ K, it is practically impossible to separate this PT from the PT at T_3 because their temperatures are too close. Note that the cell parameters a , b , and c undergo slight changes as the temperature increases in the range 80–161 K. By contrast, after the phase transition at $T_2 = 181$ K, the three cell parameters suffer a stronger variation with increasing temperature, with the result that the TEC in the range 181–276 K is larger in magnitude than in the interval 80–161 K (Figs. 1–3).

As is evident from Figs. 1–4, the $\alpha_b = f(T)$ and $\alpha_c = f(T)$ curves feature a small maximum in the temperature interval between the PTs at $T_1 = 161$ K and $T_2 = 181$ K, while the TEC α_a decreases with increasing tempera-

ture. At the PT points $T_1 = 161$ K and $T_2 = 181$ K, the $\alpha_a = f(T)$ and $\alpha_c = f(T)$ curves pass through sharp minima, while the $\alpha_b = f(T)$ curve has a minimum at $T_1 = 161$ K and a maximum at $T_2 = 181$ K. In the PT region at $T_3 = 276$ K, the TEC drops along the a axis while undergoing a jump along the b axis. In the region of the phase transitions at $T_1 = 161$ K and $T_2 = 181$ K, the volume expansion coefficient α_V varies with temperature similarly to the TEC α_a .

As seen from the above data (Figs. 1–3), the thermal expansion of $[\text{N}(\text{CH}_3)_4]_2\text{ZnCl}_4$ is slightly anisotropic, with the relation between the TECs α_a , α_b , and α_c being different in different temperature intervals. In the range 80–161 K, $\alpha_a \approx \alpha_b \approx \alpha_c$, while in the temperature region 181–276 K, where the crystal structure is monoclinic, the thermal expansion anisotropy is more noticeable, $\alpha_a > \alpha_b > \alpha_c$. In the temperature interval 161–181 K, the TEC relation can be written as $\alpha_a \approx \alpha_b < \alpha_c$. Note that, in the ranges 80–161 and 181–276 K, the TECs along the three principal crystallographic axes vary little with increasing temperature. Above $T_3 = 276$ K, α_a and α_b vary more strongly, with α_b increasing and α_a decreasing.

The above data allow us to conclude that the phase transitions at $T_1 = 161$ K and $T_2 = 181$ K are first-order.

REFERENCES

1. K. Gesi, J. Phys. Soc. Jpn. **51** (1), 203 (1984).
2. Sh. Sawada, Y. Shiroishi, A. Yamamoto, M. Takashige, and M. Matsuo, J. Phys. Soc. Jpn. **44** (2), 687 (1978).
3. H. Mashiyama and S. Tanisaki, Phys. Lett. A **76** (3), 347 (1980).
4. B. Morosin and E. C. Lingafelter, Acta Crystallogr. **12** (8), 611 (1959).
5. J. R. Wiesner, R. C. Srivastava, C. H. L. Kennard, M. Di Vaira, and E. C. Lingafelter, Acta Crystallogr. **23** (4), 565 (1967).
6. K. Hasebe, H. Mashiyama, N. Koshiy, and S. Tanisaki, J. Phys. Soc. Jpn. **56** (10), 3543 (1987).
7. K. Deguchi, H. Motegi, and E. Nakamura, Jpn. J. Appl. Phys., Suppl. **24** (2), 761 (1985).

Translated by G. Skrebtsov

LATTICE DYNAMICS AND PHASE TRANSITIONS

Structural Phase Transition in $(1 - x)\text{SrTiO}_3 + x\text{SrMg}_{1/3}\text{Nb}_{2/3}\text{O}_3$ Solid Solutions

V. V. Lemanov*, E. P. Smirnova*, and E. V. Ukhin**

*Ioffe Physicotechnical Institute, Russian Academy of Sciences, Politekhnikeskaya ul. 26, St. Petersburg, 194021 Russia

**Voronezh State University, Universitetskaya pl. 1, Voronezh, 394006 Russia

Received December 4, 2003

Abstract—The temperature dependences of the shear modulus and internal friction in ceramic samples of $(1 - x)\text{SrTiO}_3 + x\text{SrMg}_{1/3}\text{Nb}_{2/3}\text{O}_3$ solid solutions were studied by the torsional vibration method in the range 80–300 K. It was established that the temperature T_a of the $O_h^1 - D_{4h}^{18}$ structural phase transition in these solid solutions increases with increasing x , although the lattice constant also increases. A discussion is presented of the contributions to the $T_a(x)$ dependence due to a change in the volume and changes caused by the presence of a second solid-solution component (the impurity contribution). It is also shown that the defect-induced relaxation revealed earlier in a study of the dielectric properties of these materials manifests itself in internal friction peaks. © 2004 MAIK “Nauka/Interperiodica”.

1. INTRODUCTION

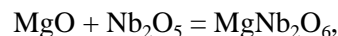
At a temperature $T_a = (105\text{--}110)$ K, strontium titanate SrTiO_3 undergoes an improper ferroelastic phase transition with doubling of the unit cell (soft mode at the Brillouin zone edge) and with a $O_h^1 - D_{4h}^{18}$ symmetry change (this transition is also referred to as antiferrodistortive). In SrTiO_3 -based solid solutions of the $\text{Sr}_{1-x}\text{A}_x\text{TiO}_3$ type, the change in the transition temperature T_a correlates with the change in the lattice parameter [1]; indeed, for $A = \text{Ca}$ the temperature T_a increases [2] and the lattice parameter a decreases, whereas for $A = \text{Pb}$ and Ba the transition temperature T_a decreases [3, 4] while the lattice parameter increases. Note that the introduction of a small amount of the second component in the above solid solutions drives a ferroelectric phase transition at low temperatures [1].

It was of interest to explore the character of the $T_a(x)$ dependence in $\text{SrTi}_{1-x}(\text{Mg}_{1/3}\text{Nb}_{2/3})_x\text{O}_3$ solid solutions, in which Mg^{2+} and Nb^{5+} substitute for the Ti^{4+} ions. These solid solutions were also found to suffer a very strong dielectric relaxation [5], which raised the intriguing question of whether this relaxation is also seen in the elastic properties.

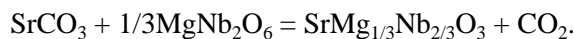
2. EXPERIMENT

$(1 - x)\text{SrTiO}_3 + x\text{SrMg}_{1/3}\text{Nb}_{2/3}\text{O}_3$ samples were prepared using standard ceramic technology [5]. The starting reagents were strontium carbonate and very-high-purity oxides of Ti, Mg, and Nb. The $\text{SrMg}_{1/3}\text{Nb}_{2/3}\text{O}_3$

ceramic was synthesized in two steps, with columbite MgNb_2O_6 prepared in the first step,



and $\text{SrMg}_{1/3}\text{Nb}_{2/3}\text{O}_3$, in the second,



The columbite was synthesized at 1000°C for 20 h. Samples were subjected to compression under 200 MPa (2 kbar) and sintered at 1460°C for 1.5 h. In contrast to the small samples 8 mm in diameter and 2 mm thick used in [5], the present study was carried out on large ceramic plates 1.5×4.5 cm in area and 0.4 to 1.4 cm thick, from which samples $1.5 \times 0.2 \times 0.2$ cm in size were cut for measurements. The density of all the samples was 94 to 97% of the density as determined from x-ray diffraction.

X-ray diffraction measurements were conducted on a DRON-2 diffractometer at room temperature. The lattice parameters were measured on powders with Ge as an internal reference.

The shear modulus G and the Q factor were determined on a reverse torsion pendulum [6]. A long twisting rod was attached to the sample, and the lower end of the rod was fixed. A special electromagnetic system periodically twisted the rod and, hence, the sample at the resonance frequency of the composite oscillator (the twisting rod–sample system), which was 25 Hz in our case. Photoelectric sensors were employed to measure small torsional strains. The internal friction (inverse Q factor, Q^{-1}) was derived from the decay rate of free oscillations. The shear modulus G was determined from the period (frequency) of resonance oscillations. The maximum shear stresses in a sample reached about 10 MPa. Such stresses corresponded to

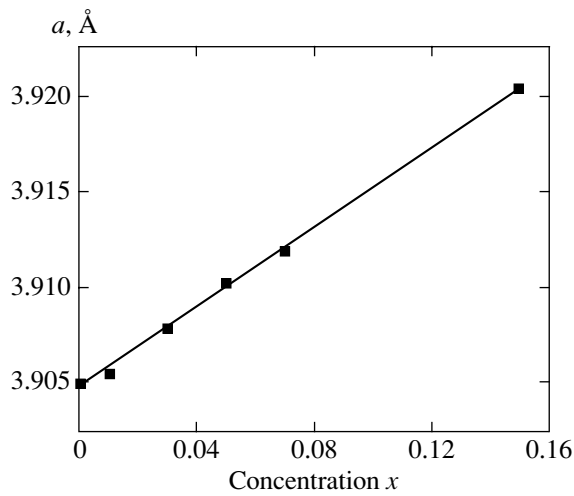


Fig. 1. Concentration dependence of the lattice parameter of $(1-x)\text{SrTiO}_3 + x\text{SrMg}_{1/3}\text{Nb}_{2/3}\text{O}_3$ solid solutions.

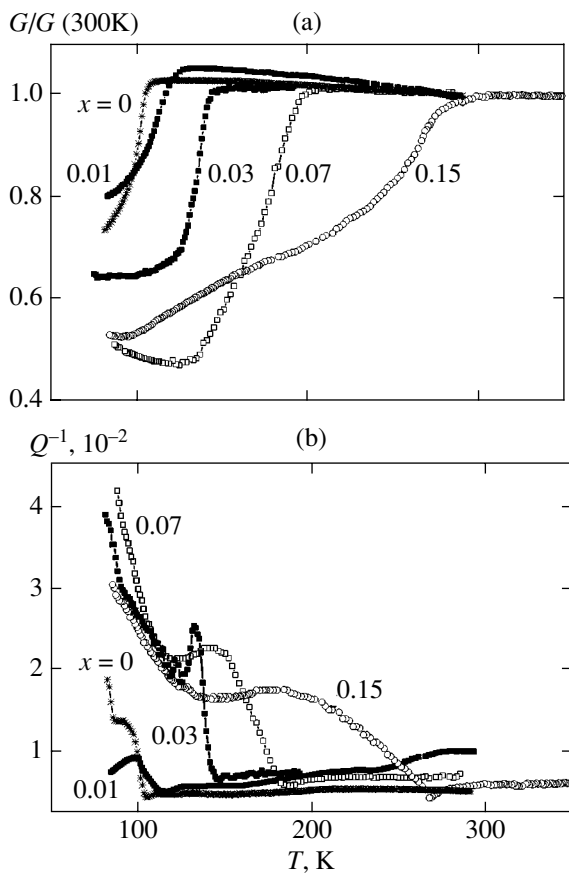


Fig. 2. Temperature dependences of (a) the relative shear modulus $G/G(300\text{ K})$ and (b) internal friction Q^{-1} in $(1-x)\text{SrTiO}_3 + x\text{SrMg}_{1/3}\text{Nb}_{2/3}\text{O}_3$ solid solutions for different values of x .

shear strains of the order of 10^{-4} and sample twisting angles of about 0.1° . All measurements were performed at strain amplitudes substantially smaller than their maximum values.

3. EXPERIMENTAL RESULTS AND DISCUSSION

Figure 1 plots the dependence of the lattice parameter of the $(1-x)\text{SrTiO}_3 + x\text{SrMg}_{1/3}\text{Nb}_{2/3}\text{O}_3$ solid solution on concentration x .

$\text{SrMg}_{1/3}\text{Nb}_{2/3}\text{O}_3$ belongs to the trigonal crystal system and space group D_{3d}^3 with unit cell parameters $a = 5.66\text{ \AA}$ and $c = 6.98\text{ \AA}$ [7]. The parameter of the reduced perovskite cell is $a_p = 4.01\text{ \AA}$. As seen from Fig. 1, the lattice parameter of the solid solution as a function of x varies from the SrTiO_3 parameter ($a = 3.905\text{ \AA}$) to the reduced lattice parameter of $\text{SrMg}_{1/3}\text{Nb}_{2/3}\text{O}_3$ ($a_p = 4.01\text{ \AA}$) following the linear Vegard law. The slope of the $a(x)$ graph is $da/dx = 0.1\text{ \AA}$. For concentrations $x > 0.15$, the linear $a(x)$ relation breaks down, and for $x = 0.2$ the samples become two-phase, which suggests that the solubility limit of $\text{SrMg}_{1/3}\text{Nb}_{2/3}\text{O}_3$ in SrTiO_3 lies at a value of x between 0.15 and 0.2.

Figure 2 illustrates the temperature behavior of the relative shear modulus $G/G(300\text{ K})$ and of internal friction Q^{-1} obtained for samples with $x = 0, 0.01, 0.03, 0.07,$ and 0.15 . We see that the temperature dependences of the shear modulus in the phase transition region behave as they do in SrTiO_3 single crystals subjected to torsional vibrations about the $[110]$ direction [8]. When a single crystal is oriented in this way, the domain wall motion provides a dominant contribution to the change in the shear modulus at the phase transition. In ceramic samples, this change turns out to be of the same magnitude or even slightly larger (for $x = 0.07, 0.15$) than in a single crystal of pure strontium titanate (note that the diffuse anomaly of the shear modulus in the sample with $x = 0.15$ is apparently due to this concentration being close to the solubility limit). Thus, the contribution from structural domains in a ceramic with an average grain size of about $10\text{ }\mu\text{m}$ to the elastic properties is not less than that in single crystals. The dominant contribution of domains to the change in the shear modulus in the region of the phase transition in single crystals was corroborated by experiments with static shear stresses [8]. Such stresses convert the sample to the single-domain state, with the phase transition-induced changes in the shear modulus decreasing by approximately one order of magnitude. Unfortunately, such experiments cannot be performed on ceramic samples because of their comparatively high brittleness.

Now, we consider the temperature dependence of the internal friction, $Q^{-1}(T)$. As seen from Fig. 2b, the $Q^{-1}(T)$ relation exhibits two anomalies, namely, an appreciable increase in internal friction at temperatures near 100 K and internal-friction peaks at about 130, 135, and 165 K for concentrations $x = 0.03, 0.07,$ and 0.15 , respectively. The origin of the first anomaly lies in the fact that alternating elastic stresses initiate domain wall motion, which accounts for the increased losses. As for the internal friction peaks, they may be due to

reorientation of $\{\text{Mg}^{2+}-V_{\text{O}}\}$ -type defects driven by elastic stresses [9]. These defects are actually electric and elastic dipoles consisting of the Mg^{2+} ion in the Ti^{4+} position in the SrTiO_3 lattice and of a nearby vacancy V_{O} of the O^{2-} ion, which provides charge neutrality. It appears [5] that it is reorientation of such defects by an ac electric field that accounts for the giant dielectric relaxation. The samples employed in this study also exhibit dielectric relaxation, albeit not so strong as that observed in [5]. Our suggestion that it is the reorientation of such defects that is responsible for the internal friction peaks is borne out by the following two experimental observations.

According to [5], the dielectric relaxation frequencies obey the Arrhenius relation

$$\omega = \omega_0 \exp(-U/kT). \quad (1)$$

As suggested by experimental data on dielectric relaxation [5], the activation energy U for $x = 0.03, 0.07,$ and 0.15 is $0.21, 0.24,$ and 0.3 eV and the values obtained for the frequency ω_0 are (in units of 10^{-11} s^{-1}) $1.1, 2.5,$ and 5 , respectively. If the internal friction peaks are connected with the same defects, then these data can be used to calculate the temperatures at which internal friction peaks should appear at a frequency of 25 Hz. For the concentrations $x = 0.03, 0.07,$ and 0.15 , these temperatures are found to be $120, 130,$ and 160 K, which agrees quite satisfactorily with the experimental results of $130, 135,$ and 165 K, respectively (Fig. 2b).

The second point consists in that high-temperature annealing of samples with subsequent quenching carried out in the presence of defects associated with oxygen vacancies should bring about an enhancement of internal friction losses. Indeed, as follows from Fig. 3, annealing at 1300°C followed by quenching to room temperature resulted in increased losses.

The mechanism of internal friction losses is similar to that of dielectric losses.

When considering the dielectric losses, the $\{\text{Mg}^{2+}-V_{\text{O}}\}$ defect should be treated as an electric dipole that can be reoriented by an alternating electric field [5]. In the case of internal friction losses, the same defect acts as an elastic dipole, whose symmetry breaks down under elastic deformation [9]. Assuming the relaxation mechanism of losses, we have

$$G = G_\infty - \delta G / (1 + \omega^2 \tau^2), \quad (2)$$

$$Q^{-1} = (\delta G / G) \omega \tau / (1 + \omega^2 \tau^2).$$

Here, $\delta G = G_\infty - G_0$; for $\omega \tau \gg 1$, $G = G_\infty$, while for $\omega \tau \ll 1$, $G = G_0$. Also, the quantity G_∞ is the shear modulus to which the relaxing defects cannot contribute because the time is too short and G_0 is the shear modulus containing the total contribution from the defects.

For the relaxation time τ in Eq. (2), the Arrhenius relation holds; therefore, as the temperature is lowered,

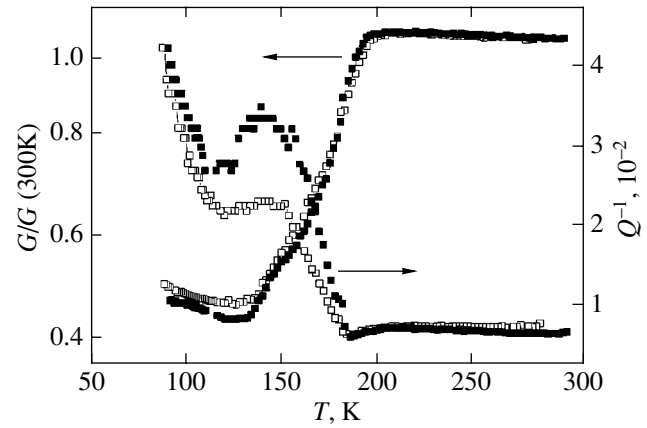


Fig. 3. Same as in Fig. 2 but for $x = 0.07$ in the starting sample (open circles) and a sample quenched to room temperature after annealing at 1300°C (filled circles).

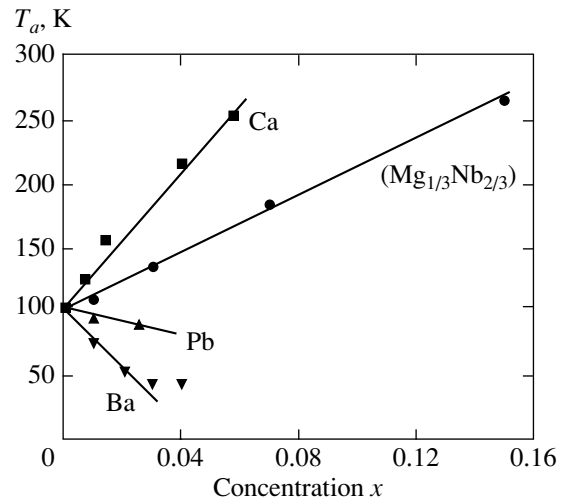


Fig. 4. Temperature T_d of the improper ferroelastic phase transition plotted vs. concentration x of $(1-x)\text{SrTiO}_3 + x\text{SrMg}_{1/3}\text{Nb}_{2/3}\text{O}_3$ solid solutions. Also shown for comparison are data for $\text{Sr}_{1-x}\text{A}_x\text{TiO}_3$ solid solutions with $A = \text{Ca}$ [2], Pb [3], and Ba [4].

the shear modulus should increase from G_0 at high temperatures to G_∞ in the low-temperature limit.

Let us estimate the value of $\delta G = G_\infty - G_0$ from the experimental internal friction losses. As follows from Eq. (2), for $\omega \tau = 1$, we have $Q^{-1} = Q_{\text{max}}^{-1} = \delta G / 2G$. The experimental value of Q_{max}^{-1} (the amplitude above the background) is on the order of 10^{-2} . The change in the shear modulus should be of the same order of magnitude, i.e., $\delta G / G \approx 10^{-2}$. Such a change cannot be reliably detected in our experiments against the background of the giant change in the shear modulus at the phase transition.

Temperature T_a of the $O_h^1-D_{4h}^{18}$ phase transition in SrTiO₃-based solid solutions SrTi_{1-x}B_xO₃ and Sr_{1-x}A_xTiO₃

Substituting ion	dT_a/dx , 10 ² K	$(\partial T_a/\partial V)_x(\partial V/\partial x)$, 10 ² K	$(\partial T_a/\partial x)_V$, 10 ² K
B: (Mg _{1/3} Nb _{2/3})	11	-2.38	13.4
A: Ca	26	1	25
A: Pb	-6	-0.4	-5.6
A: Ba	-25	-2.2	-23

Now, we consider the dependence of the phase transition temperature T_a on the solid-solution concentration x . Let us determine the temperature T_a from the $G(T)$ graphs (Figs. 2, 3) as the temperature at which $G(T)$ is 0.8 of the value of $G(T)$ at the same temperature but does not contain the contribution from the phase transition. The values of T_a obtained in this way are plotted as a function of x in Fig. 4. Also shown for comparison are the data for Sr_{1-x}A_xTiO₃ solid solutions with $A = \text{Ca}$ [2], Pb [3], and Ba [4] (more complete data for the case of Pb and Ba can be found in [10]).

As follows from Fig. 4 and the data on the lattice parameter of the solid solutions, the changes in $T_a(x)$ and $a(x)$ are correlated, as already mentioned, in the cases of Ca , Pb , and Ba . As the lattice parameter of the solid solution decreases, its phase transition temperature T_a increases (Ca), and as the lattice parameter increases, the temperature T_a decreases (Pb , Ba). The reverse occurs with the SrTi_{1-x}(Mg_{1/3}Nb_{2/3})_xO₃ solid solution; indeed, an increase in the lattice constant of the solid solution is accompanied by an increase in the transition temperature T_a (Fig. 1).

A change in the transition temperature of a solid solution can be written as

$$dT_a/dx = (\partial T_a/\partial x)_V + (\partial T_a/\partial V)_x(\partial V/\partial x). \quad (3)$$

The term $(\partial T_a/\partial x)_V$ in this expression is the contribution from the second component of the solid solution to the variation of the transition temperature at a constant volume (the impurity contribution), and the second term on the right-hand side of Eq. (3) describes the dependence of the transition temperature on volume (the volume contribution).

The volume contribution can be recast in the form

$$(\partial T_a/\partial V)_x = -B(\partial T_a/\partial p)_x(1/V)(\partial V/\partial x). \quad (4)$$

Here, B is the bulk modulus and $(\partial T_a/\partial p)_x$ is the change in transition temperature under hydrostatic pressure.

For SrTiO₃, we have $B = 1.8 \times 10^{11}$ Pa and $\partial T_a/\partial p = 1.7 \times 10^{-8}$ K/Pa [11]. As follows from Fig. 1, $(1/a)da/dx = +2.6 \times 10^{-2}$ or $(1/V)(\partial V/\partial x) = +7.8 \times 10^{-2}$. From Eq. (4), the volume contribution is found to be $(\partial T_a/\partial V)_x(\partial V/\partial x) = -2.38 \times 10^2$ K. Next, we substitute

the experimental value $dT_a/dx = 11 \times 10^2$ K into Eq. (3) and obtain $(\partial T_a/\partial x)_V = +13.4 \times 10^2$ K for the impurity contribution.

The values of the volume and impurity contributions to the $T_a(x)$ dependence are given in the table. Also presented for comparison are data available on other SrTiO₃-based solid solutions [1]. As seen from the table, while the signs of the volume and impurity contributions to the change in T_a coincide for the solid solutions with substitution in the A position, the impurity contribution is an order of magnitude larger than the volume contribution. In the case of B substitution, the contributions are opposite in sign but the impurity contribution is about six times larger in magnitude than the volume contribution.

ACKNOWLEDGMENTS

The authors express their gratitude to N.V. Zaitseva for performing the x-ray diffraction measurements and V.V. Krasovskaya, B.S. Vcherashniĭ, and V.A. Yankovskaya for preparing the samples.

This study was supported by the program of the President of the Russian Federation (project no. NSh-2168.2003.2), the program "Physics of Solid-State Nanostructures," and the program of the Department of Physical Sciences, Russian Academy of Sciences.

REFERENCES

1. V. V. Lemanov, *Ferroelectrics* **226**, 133 (1999).
2. U. Bianchi, PhD Thesis (Gerhard-Mercator-Univ., Duisburg, 1996).
3. K. S. Aleksandrov, A. I. Krupny, V. J. Fritzberg, and A. N. Rubulis, *Phys. Status Solidi A* **15**, K177 (1973).
4. V. V. Lemanov, E. P. Smirnova, P. P. Syrnikov, and E. A. Tarakanov, *Phys. Rev. B* **54**, 3151 (1996).
5. V. V. Lemanov, A. V. Sotnikov, E. P. Smirnova, and M. Weihnacht, *Fiz. Tverd. Tela (St. Petersburg)* **44**, 1948 (2002) [*Phys. Solid State* **44**, 2039 (2002)].
6. S. A. Gridnev, V. I. Kudryash, and L. A. Shuvalov, *Izv. Akad. Nauk SSSR, Ser. Fiz.* **43** (8), 1718 (1979).
7. F. S. Galasso, *Structure, Properties, and Preparation of Perovskite-Type Compounds* (Pergamon, Oxford, 1969).
8. V. V. Lemanov, S. A. Gridnev, and E. V. Ukhin, *Fiz. Tverd. Tela (St. Petersburg)* **44**, 1106 (2002) [*Phys. Solid State* **44**, 1156 (2002)].
9. A. S. Nowick and B. S. Berry, *Anelastic Relaxation in Crystalline Solids* (Academic, New York, 1972; Atomizdat, Moscow, 1975).
10. V. V. Lemanov, E. P. Smirnova, A. V. Sotnikov, and M. Weihnacht (in press).
11. G. Sorge, G. Schmidt, E. Hegenbarth, and C. H. Frenzel, *Phys. Status Solidi* **37**, K17 (1970).

Translated by G. Skrebtsov

**LOW-DIMENSIONAL SYSTEMS
AND SURFACE PHYSICS**

Formation of an Icosahedral Structure during Crystallization of Nickel Nanoclusters

Yu. Ya. Gafner*, S. L. Gafner*, and P. Entel**

* Khakas State University, Abakan, 655017 Russia

e-mail: ygafner@khsu.ru

** Universität Duisburg-Essen, Duisburg, 47048 Germany

Received September 8, 2003

Abstract—The crystallization of nickel nanoclusters is investigated using a molecular dynamics simulation with tight-binding potentials. The formation of a cluster structure depends on the cooling conditions. Slow cooling results in the formation of a face-centered cubic structure, whereas fast cooling, according to the data obtained in 40% of the simulation experiments, leads to the formation of an icosahedral structure. The molecular dynamics simulation experiments demonstrate the possibility of controlling the formation of a structure of nickel nanoclusters during crystallization. © 2004 MAIK “Nauka/Interperiodica”.

1. INTRODUCTION

Investigation of the properties of small-sized metallic particles containing from several hundreds to several thousands of atoms is of great research interest due to their possible use as catalysts or surface nanostructures [1–4]. The properties of such particles are intermediate between those exhibited by molecules and crystalline solids. This makes them especially attractive for use in various fields of engineering. In this respect, the understanding of the mechanisms of formation of nanoclusters from a liquid or gas phase is particularly important for the controlled growth of low-dimensional structures with specified parameters. Elucidation of the internal structure of free clusters can play a key role in explaining their physical and chemical features.

The structure of metallic nanoclusters and, in particular, the size dependence of their properties have been intensively studied using experimental and theoretical methods over the course of more than 30 years. Computer simulations have demonstrated that, compared to conventional bulk materials, nanoclusters are characterized by several structural modifications. For example, nanoclusters of metals with a face-centered cubic lattice can exist in face-centered cubic, hexagonal closely packed, icosahedral, and decahedral modifications [5–11]. Some of these modifications are presented in Fig. 1. Metallic clusters with different symmetries were experimentally observed by Martin [7] with the use of an electron microscope. It should be noted that, in bulk face-centered cubic materials, the formation of other structures is suppressed kinetically, whereas nanoclusters of these materials can be obtained in different structural modifications with a great variety of physical and chemical properties.

Thermodynamically equilibrium modifications of metallic clusters have been thoroughly studied in the

framework of different theoretical models. The results of theoretical calculations performed by Iijima and Ichihashi [12] and K. Mannien and M. Mannien [13] indicate that, for some metals with a face-centered cubic lattice (such as gold and nickel), the icosahedral structure is metastable even in the case of small-sized clusters (containing less than 100 atoms), which is inconsistent with experimental observations. Furthermore, an increase in the cluster size is accompanied by a decrease in the stability of the icosahedral structure [12]. However, direct observations with the use of an electron microscope [7–10] have revealed that clusters containing even several thousands of atoms can exhibit icosahedral or decahedral morphology. These experiments have demonstrated that the formation of an icosahedral structure of a cluster is most likely governed by the kinetic rather than thermodynamic factors [14].

2. SIMULATION TECHNIQUE

In order to investigate how the kinetic factors affect the formation of a structure of nickel nanoclusters, we carried out a molecular dynamics simulation of heating of nickel nanoparticles with subsequent cooling to the formation of a crystal phase. The computer simulation was performed with the use of the tight-binding potentials proposed by Cleri and Rosato [15]. In the simulation experiment, a face-centered cubic nickel cluster consisting of 555 atoms was used as an initial structure. With the aim of completely destroying the long-range order in the nickel cluster, it was smoothly heated to a temperature of 1800 K, which is considerably higher than the melting temperature of nickel clusters ($T_{\text{melt}} = 1145$ K). During the simulation experiment, the temperature was determined from the mean kinetic energy of the atoms. The cluster was held at $T = 1800$ K for a

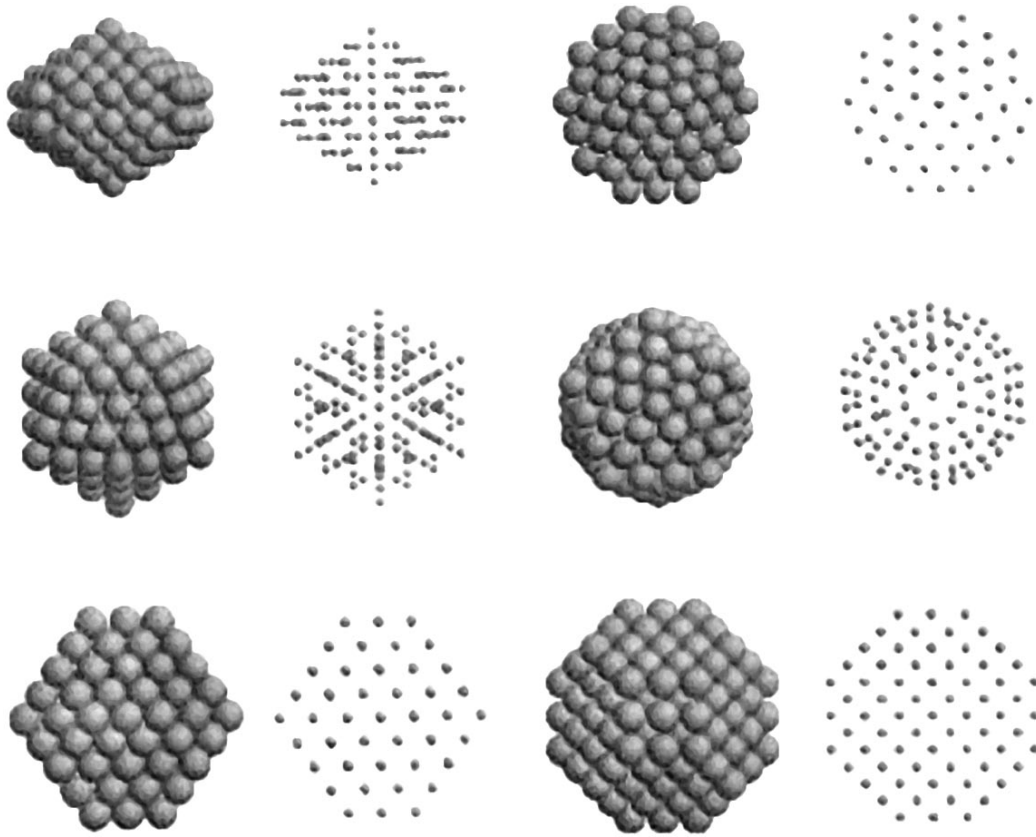


Fig. 1. Decahedral (upper row), icosahedral (middle row), and face-centered cubic (lower row) structures of the nanoclusters [1]. Each structure is drawn in two projections: the lateral view (first and second columns) and the top view (third and fourth columns).

long time, more precisely, for 200 ps ($1.0 \times 10^5 \Delta t$ where $\Delta t = 2$ fs is the time step in the molecular dynamics simulation experiment). Then, the cluster was cooled to a temperature of 300 K. The cooling and heating curves are depicted in Fig. 2, which shows the temperature dependence of the potential energy of the nickel nano-

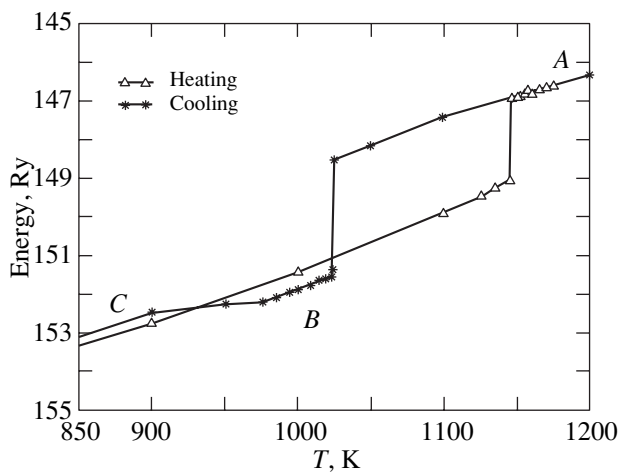


Fig. 2. Dependence of the potential energy E_p of the nickel nanocluster ($N = 555$) on the absolute temperature T .

cluster. The melting and crystallization points of the cluster were determined from the jumps in the potential energy as a function of temperature. The temperature was stabilized by two methods: (i) with the use of a Nose thermostat and (ii) according to the Anderson method. When simulating a constant temperature, the best results were obtained using the Nose thermostat. In this case, the total energy is represented as the sum of the kinetic and potential energies of the particles and the kinetic and potential energies of the thermal reservoir s :

$$H = \frac{1}{2} \sum_{i=1}^N m_i \dot{\mathbf{r}}_i^2 + \Phi(\mathbf{r}_1, \mathbf{r}_2, \dots, \mathbf{r}_N) + \left(\frac{d \ln s}{dt} \right)^2 \frac{Q}{2} + (3N + 1) k_B T_0 \ln s, \quad (1)$$

where Q is an adjustable parameter. The smooth variation in the temperature at a specified rate was simulated using the Anderson method:

$$H = \frac{1}{2} \sum_{i=1}^N m_i \dot{\mathbf{r}}_i^2 + \Phi(\mathbf{r}_1, \mathbf{r}_2, \dots, \mathbf{r}_N) + \frac{W}{2} \dot{V}^2 + P_0 V, \quad (2)$$

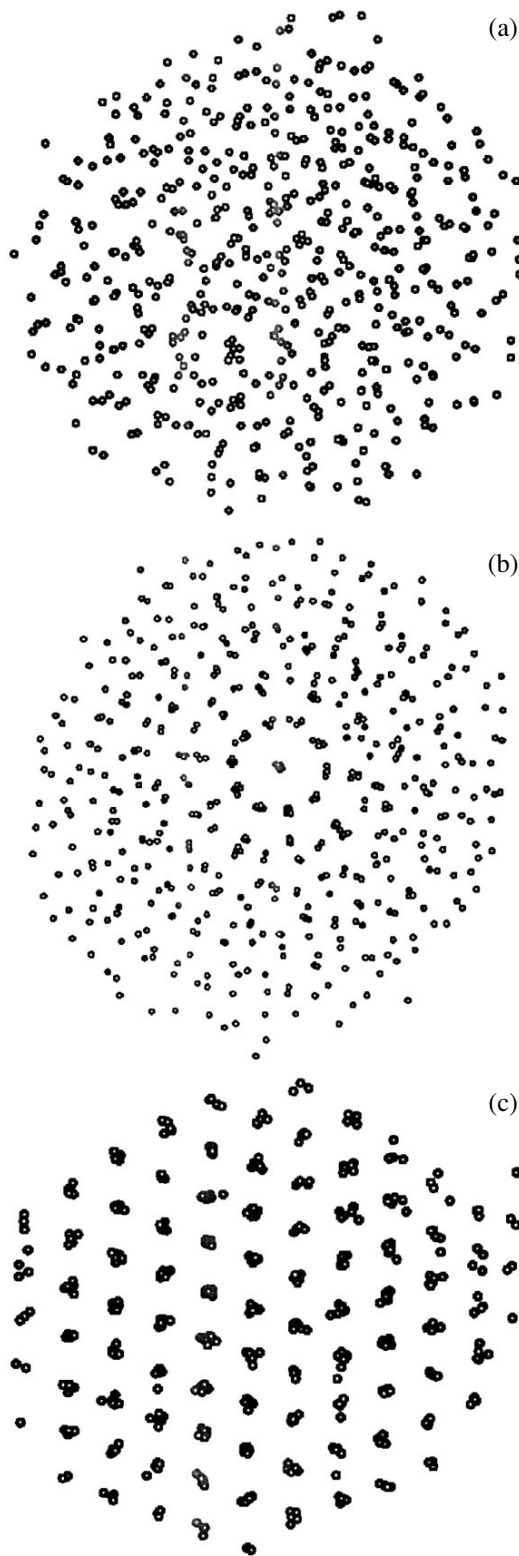


Fig. 3. Nickel cluster configurations corresponding to portions A, B, and C in the crystallization curve depicted in Fig. 2: (a) the nanocluster in a molten state, $T = 1200$ K; (b) the nanocluster immediately after crystallization, $T = 995$ K; and (c) the nanocluster after complete structural transformation, $T = 800$ K.

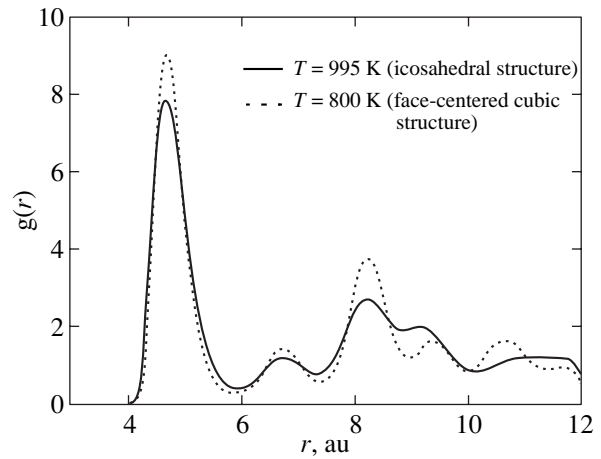


Fig. 4. Radial distribution function $g(r)$ of the nickel nanocluster ($N = 555$) for portions B and C in the crystallization curve depicted in Fig. 2.

where W is an adjustable parameter. This approach makes it possible to determine more exactly the melting and crystallization temperatures of simulated particles as compared to the method used by Qi *et al.* [16], according to which it was necessary to perform additional calculations (specifically of the maximum of the heat capacity) when determining these temperatures.

3. RESULTS AND DISCUSSION

It can be seen from Fig. 2 that, during cooling below the melting temperature, the simulated system tends to transform into an icosahedral structure (portion B in the cooling curve). However, the nickel nanocluster in this temperature range is in a very unstable state and undergoes transformation into a face-centered cubic structure with a further smooth decrease in the temperature. In order to analyze the crystallization of the nickel nanocluster, we consider the cluster configurations (Fig. 3), which correspond to the portions A, B, and C in the crystallization curve depicted in Fig. 2 (at temperatures $T = 1200$, 995 , and 800 K, respectively), and the radial distribution function (Fig. 4), which is calculated for the portions B and C in this curve. To avoid errors in determining the cluster structure due to side effects associated with thermal noise, the nanocluster was kept at the aforementioned temperatures for approximately 400 ps with the aim of attaining an equilibrium configuration.

At a temperature of 1200 K (which is higher than the crystallization temperature $T_{\text{cryst}} = 1025$ K), the nanocluster exists in a molten state and its particles strongly fluctuate, even though the cluster shape, as a whole, remains nearly spherical (Fig. 3a). An abrupt decrease in the potential energy (Fig. 2) indicates that the cluster at $T = 995$ K occurs already in a crystalline state (Figs. 3b, 4). In this case, the nanocluster has a facet structure with a pronounced fivefold symmetry, which

corresponds to an icosahedral configuration. With a further smooth decrease in the temperature, the nickel nanocluster undergoes a structural transformation with the formation of a face-centered cubic structure involving stacking faults (Fig. 3c). The formation of an icosahedral configuration upon fast cooling was observed in 40% of the simulation experiments. In other cases, the final face-centered cubic configuration of the nickel nanocluster is formed without a metastable icosahedral structure. In our simulation experiments performed with nickel, we did not reveal the formation of an icosahedral structure first on the cluster surface and then deep in the cluster core, as was observed for gold in [14].

The result obtained is in agreement with the classical theory of nucleation [17–19], according to which the final face-centered cubic structure of a cluster formed in the course of crystallization is energetically more stable than the icosahedral structure. However, numerous molecular dynamics simulations have demonstrated that, at $T = 0$ K, it is this icosahedral configuration that is energetically more favorable, at least for clusters containing from two to three thousands of atoms [13]. It should be noted that the metastable icosahedral structure (portion *B* in the cooling curve in Fig. 2) can be stabilized by instantaneous cooling to lower temperatures, for example, to temperatures in the range 600–700 K.

4. CONCLUSIONS

Thus, the structural properties of nickel nanoparticles were investigated using a molecular dynamics simulation of their melting and crystallization in terms of tight-binding potentials. The simulation experiments demonstrated the possibility of controlling the formation of a structure of nickel nanoclusters. The results obtained in the computer simulation allowed us to conclude that, after the onset of crystallization, the formation of a cluster structure strongly depends on the cooling conditions. Slow cooling leads to the formation of only a face-centered cubic structure, whereas fast cooling results in the formation of a metastable icosahedral structure, as was observed in 40% of the simulation experiments.

ACKNOWLEDGMENTS

We would like to thank Dr. R. Meyer (Universität Duisburg-Essen, Germany) for valuable assistance in performing this study.

This work was supported by the German Physical Society in the framework of SFB 445 “Nano-Partikel aus der Gasphase: Entstehung, Struktur, Eigenschaften.”

REFERENCES

1. F. Baletto, C. Mottet, and R. Ferrando, *Phys. Rev. B* **63**, 155408 (2001).
2. *Cluster of Atoms and Molecules*, Ed. by H. Haberland (Springer, Berlin, 1994).
3. P. Jensen, *Rev. Mod. Phys.* **71**, 1695 (1999).
4. P. Moriarty, *Rep. Prog. Phys.* **64**, 297 (2001).
5. A. Pinto, A. R. Pennesi, G. Faraci, G. D’Agostino, S. Mobilio, and F. Boscherini, *Phys. Rev. B* **51**, 5315 (1995).
6. M. Jose-Yacaman, R. Herrera, A. G. Gomez, S. Tehuacanero, and P. Schabes-Retchkiman, *Surf. Sci.* **237**, 248 (1990).
7. T. P. Martin, *Phys. Rep.* **273**, 199 (1996).
8. J. A. Ascencio, M. Perez, and M. Jose-Yacaman, *Surf. Sci.* **447**, 73 (2000).
9. J. M. Soler, M. R. Beltran, K. Michaelian, I. L. Garzon, P. Ordejon, D. Sanchez-Portal, and E. Artacho, *Phys. Rev. B* **61**, 5771 (2000).
10. C. L. Cleveland, U. Landman, T. G. Schaaf, M. N. Shafiqullin, P. W. Stephens, and R. L. Whetten, *Phys. Rev. Lett.* **79**, 1873 (1997).
11. F. Baletto, R. Ferrando, A. Fortunelli, F. Montalenti, and C. Mottet, *J. Chem. Phys.* **116**, 3865 (2002).
12. S. Iijima and T. Ichihashi, *Phys. Rev. Lett.* **56**, 616 (1986).
13. K. Mannien and M. Mannien, *Eur. Phys. J. D* **20**, 243 (2002).
14. H. S. Nam, Nong M. Hwang, B. D. Yu, and J. K. Yoon, *Phys. Rev. Lett.* **89**, 275502 (2002).
15. F. Cleri and V. Rosato, *Phys. Rev. B* **48**, 22 (1993).
16. Y. Qi, T. Cagin, W. L. Johnson, and W. A. Goddard, *J. Chem. Phys.* **115**, 385 (2001).
17. B. Mutaftschiev, in *Handbook of Crystal Growth*, Ed. by D. T. J. Hurle (Elsevier, Amsterdam, 1993).
18. H. Reiss, P. Mirabel, and R. L. Whetten, *J. Phys. Chem.* **92**, 7241 (1988).
19. L. S. Bartell, *Annu. Rev. Phys. Chem.* **49**, 43 (1998).

Translated by I. Volkov

**LOW-DIMENSIONAL SYSTEMS
AND SURFACE PHYSICS**

Spectroscopy of the Photonic Stop Band in Synthetic Opals

A. V. Baryshev, A. A. Kaplyanskiĭ, V. A. Kosobukin, M. F. Limonov, and A. P. Skvortsov

Ioffe Physicotechnical Institute, Russian Academy of Sciences, Politekhnikeskaya ul. 26, St. Petersburg, 194021 Russia

e-mail: m.limonov@mail.ioffe.ru

Received December 1, 2003

Abstract—The photonic band gap of opals has been studied experimentally from their optical transmission spectra as a function of the incident beam orientation in the opal crystal lattice. The measurements were carried out for all high-symmetry points on the surface of the Brillouin zone of an fcc lattice. The experimental dependence of the energy position of the photonic band gap on the light wave vector direction is well described by the set of theoretical relations developed for the stop bands originating from the Bragg diffraction of light on {111}-type planes of the twinned fcc lattice of synthetic opals. © 2004 MAIK “Nauka/Interperiodica”.

1. INTRODUCTION

Photonic crystals are weakly absorbing materials with three-dimensional periodic modulation of the dielectric permittivity, in which Bragg diffraction of electromagnetic waves gives rise to the formation of bands in the frequency spectrum that are forbidden for the propagation of electromagnetic waves. Depending on the actual crystal symmetry and the amplitude of the permittivity modulation, the formation of a three-dimensional (complete) photonic stop band [1, 2] or of one-dimensional spectral stop bands in certain directions of the light wave vector in the photonic crystal [3] is possible. Theoretically, a complete photonic band gap should suppress spontaneous radiation from a sample and give rise to other optical effects of considerable significance in basic science and applications [1, 3–5].

Whether a complete photonic band gap is present or absent in a given crystal structure can be determined through study of the photonic band gap by scanning the light wave vector over the whole Brillouin zone surface, because the tips of the wave vectors of the incident and diffracted light lie on the surface of the Brillouin zone under the conditions of Bragg diffraction. Of particular interest is the investigation of the photonic band gap in the visible region of the electromagnetic spectrum. As far as we know from the literature, there is no clear cut evidence of the observation of a complete photonic band gap in this spectral region. One-dimensional stop bands, however, have been observed in the optical range in a number of materials, such as synthetic opals [6] and related inverted opals [7], colloidal crystals [8], and periodic structures made up of spherical TiO₂ microparticles [9]. Most publications [6, 10–16] deal with investigation of the photonic band gap in opals (three-dimensional structures made up of tightly packed spherical α -SiO₂ particles a few hundred nanometers in diameter). Experiments with opals have been reduced primarily to a study of the photonic band gap in the vicinity of the high-symmetry point L on the

surface of the Brillouin zone of an fcc lattice. The dependence of the opal photonic band gap on the wave vector over the entire Brillouin zone has thus far remained an open question.

The major goal of the present paper is to investigate the variation in the spectral position (i.e., dispersion) of the photonic band gap in opals as the wave vector of the incident light wave sweeps the Brillouin zone surface. Optical studies of light diffraction from high-quality synthetic opals obtained by careful preliminary selection and characterization of samples were reported in [17–19]. The results obtained indicate, in particular, the possibility of measuring the photonic band gap dispersion. In this study, measurements of optical transmission spectra as a function of light vector direction in the opal lattice were performed on preliminarily selected samples of synthetic opals of a high degree of perfection. The experimental data on the position of the bands (stop bands) in the transmission spectra were compared in considerable detail with the relations derived from the theory of Bragg diffraction of light waves from different planes of the opal lattice. It was established that the measured dependences of the energy position of a photonic band gap on the wave vector position agree well with the positions of the stop bands determined by Bragg diffraction on {111}-type planes of the twinned fcc opal lattice.

In Section 2, we discuss the real crystal structure of synthetic opals and the specific features of their Brillouin zone. In Section 3, these features are used to define three planes of light wave vector scanning, which cover all high-symmetry points on the surface of the Brillouin zone. In Section 4, the experimental technique employed to characterize the samples and to measure optical transmission spectra is described. The experimental results obtained in these measurements are presented in Section 5 and discussed in Section 6 in terms of the theory of Bragg diffraction of light waves. The main conclusions are summed up in Section 7.

2. THE STRUCTURE OF SYNTHETIC OPALS

Opals are essentially self-assembled structures made up of monodisperse $a\text{-SiO}_2$ particles of spherical shape a few hundred nanometers in size. Directed growth of a sample arranges the $a\text{-SiO}_2$ spheres in closely packed layers stacked perpendicular to the sample growth axis. Alternation of such hexagonal closely packed layers along the growth axis in different sequences of positions A , B , and C may bring about the formation of either an fcc lattice (ordered $\dots ABCABC\dots$ layer arrangement), a hexagonal close-packed structure (ordered $\dots ABABAB\dots$), or, again, a structure with a disordered layer sequence (for example, $\dots ABACBAC\dots$). All these structures can be characterized by a stacking correlation coefficient p , which is equal to the probability that three layers will follow one another to occupy three different positions out of the set A , B , and C . If the first layer of spheres occupies position A and the second, position B , then the third layer may be found either in position C with a probability p or in position A with a probability of $1 - p$. For $p = 1$, the stacking is that of an fcc lattice; for $p = 0$, it is a hexagonal close-packed lattice; and for $0 < p < 1$, the layer stacking is characteristic of a structure disordered along the $[111]$ growth axis [20].

An analysis of experimental data on light diffraction performed on samples of synthetic opals in [17–19] yielded $p \approx 0.8$ for the stacking correlation coefficient. This comparatively large value of the coefficient p relates to the most uniform regions of the samples. This value means that the samples contain fairly extended domains made up of sequences of hexagonal layers regularly stacked perpendicular to the growth axis to make up an fcc lattice. Therefore, in what follows, we use the universally accepted notation of the planes and axes for an ideal (reference) fcc lattice. We identify the growth plane parallel to which these layers are stacked as the (111) plane of the fcc lattice. Two types of fcc stacking are possible for the structure under study, namely, $ABCABC\dots$ and $CBACBA\dots$, which are denoted subsequently as fcc-I and fcc-II. In synthetic opals, these two types of fcc stacking alternate randomly. The twinned opal structure forming in this way has a unique feature in that the system of closely packed (111) growth planes with an ordered arrangement of $a\text{-SiO}_2$ spheres over sufficiently large distances in these planes ($\sim 10^2\text{--}10^3 \mu\text{m}$) differs radically from the three other systems of fcc planes, more specifically, of the $(\bar{1}11)$, $(1\bar{1}1)$, and $(11\bar{1})$ planes, in which the spheres are arranged randomly. Accordingly, the growth axis $[111]$ in the structure of a real opal is likewise specific with respect to the three other axes, $[\bar{1}11]$, $[1\bar{1}1]$, and $[11\bar{1}]$, which would be equivalent to it in an ideal fcc lattice.

Both of the ideal lattices, fcc-I and fcc-II, are characterized by the Brillouin zone. One of these zones is sent into the other either under mirror reflection in a

plane parallel to the (111) growth plane or through rotation by 60° about the $[111]$ vertical growth axis (the $\Gamma \rightarrow L$ direction in the reciprocal lattice). We call the set of two Brillouin zones belonging to the fcc-I and fcc-II lattices the Brillouin zone of the twinned fcc lattice. The validity of such a consideration of the Brillouin zone of the twinned fcc lattice rests in our case on the structure of the samples studied and the actual experimental conditions. The fact is that the characteristic regularity scale of the fcc-I and fcc-II structures along the growth axis in the opal structure with a stacking correlation coefficient $p \approx 0.8$ is about ten layers ($\sim 3 \mu\text{m}$), which is two orders of magnitude less than the light beam cross section. As a consequence, the properties of the fcc-I and fcc-II structures, as well as the specific features of their Brillouin zones, become manifest in an additive manner in light transmission and Bragg diffraction experiments.

3. FORMULATION OF THE PROBLEM

We report here on a study of the transmission spectra of opals obtained under direct propagation of white light. The characteristic transmission dips in these spectra are closely related to the photonic band gap of the opals, which forms in Bragg diffraction from different plane systems of the fcc lattice. The Bragg diffraction condition for a light wave can be expressed through the Laue equation:

$$\mathbf{K}' = \mathbf{K} + \mathbf{b}_{(hkl)}. \quad (1)$$

Here, $\mathbf{K}(\mathbf{K}')$ is the wave vector of the incident (diffracted) electromagnetic wave and $\mathbf{b}_{(hkl)}$ is a reciprocal lattice vector of the crystal, which is perpendicular to the plane (responsible for diffraction) with the Miller indices (hkl) . For a given $\mathbf{b}_{(hkl)}$, the end points of the vectors \mathbf{K} and \mathbf{K}' satisfying condition (1) with $|\mathbf{K}'| = |\mathbf{K}| = 2\pi/\lambda$ lie on the surface of the Brillouin zone. Thus, vector triangle (1) defines the relevant scheme of scanning of the Brillouin zone surface; namely, by properly changing the incident wave vector \mathbf{K} (i.e., the light wavelength λ and the angle of incidence Θ , which is equal to the angle between the vectors \mathbf{K}' and $\mathbf{b}_{(hkl)}$), one can, according to Eq. (1), scan various points on the surface of the Brillouin zone.

The Brillouin zone of the twinned fcc lattice of synthetic opals has hexagonal symmetry; namely, rotation through 60° about the growth axis brings it into coincidence with itself (the C_6 symmetry axis is parallel to the $[111]$ sample growth direction). With this in mind, the main information on dispersion (dependence on the wave vector) of the photonic band gap position can be obtained by selecting three paths for scanning the Brillouin zone surface that include all high-symmetry points of the surface. These paths lie in sections I, II, and III of the Brillouin zone and are presented in Figs. 1a, 1c, and 1e, respectively.

Consider the specific high-symmetry points on the surface of the Brillouin zone through which the end point of the scanning wave vector \mathbf{K} will pass. Path I in the reciprocal lattice can be represented schematically as (Figs. 1a, 1b)

$$L \rightarrow U \rightarrow X \rightarrow U \rightarrow P \quad (2a)$$

for fcc-I and

$$L \rightarrow K \rightarrow L' \rightarrow P \quad (2b)$$

for fcc-II. Note that, in a twinned structure, in addition to the $\Gamma \rightarrow L$ direction along the [111] axis, the scanning path (2b) is complemented by an inequivalent direction $\Gamma \rightarrow L'$, which makes an angle of 70.5° with the [111] axis. In Eqs. (2a) and (2b), we introduced a symbol P to denote the point where vector $\mathbf{b}_{[\bar{2}11]}$ crosses the surface of the Brillouin zone (point P is not a standard high-symmetry point in the Brillouin zone of the fcc lattice).

Path II is drawn through the points

$$L \rightarrow W \rightarrow M \rightarrow K \quad (3)$$

for both the Brillouin zones of fcc-I and fcc-II (Figs. 1c, 1d). Equation (3) contains another nonstandard point M , whose significance will become clear in the discussion of the experimental data.

Path III lies in section III of the reciprocal lattice [the (111) growth plane] and is

$$P \rightarrow K \quad (4)$$

for the Brillouin zones of both fcc-I and fcc-II (Figs. 1e, 1f).

Sections I ($L \rightarrow P$) and II ($L \rightarrow K$) of the Brillouin zone pass through the [111] growth axis and make an angle of 30° with each other, while section III ($P \rightarrow K$) is perpendicular to the [111] growth axis and closes the first two sections. As a result, part of the Brillouin zone surface of the twinned fcc structure is cut out inside an octant that includes all high-symmetry points of the reciprocal lattice (Fig. 1). On completing these three paths, one obtains full information on the dispersion of the photonic band gap position.

4. EXPERIMENTAL TECHNIQUE

For the measurements, we used samples of synthetic opals that were properly oriented and characterized in considerable detail in our earlier studies [17–19, 21]. It was established in [21] that the sample structure varied markedly along the growth axis and that the most ordered regions corresponded to later growth stages. Samples (not more than 0.5 mm thick) for studying the photonic band gap were cut from these ordered regions along different opal crystallographic axes. Below, we present the results obtained in a study of an opal sample with a diameter of spherical $a\text{-SiO}_2$ particles of 270 nm.

Images of (111) growth layers obtained by atomic force microscopy [21] reveal a high degree of $a\text{-SiO}_2$ sphere packing order in these layers, with long-range

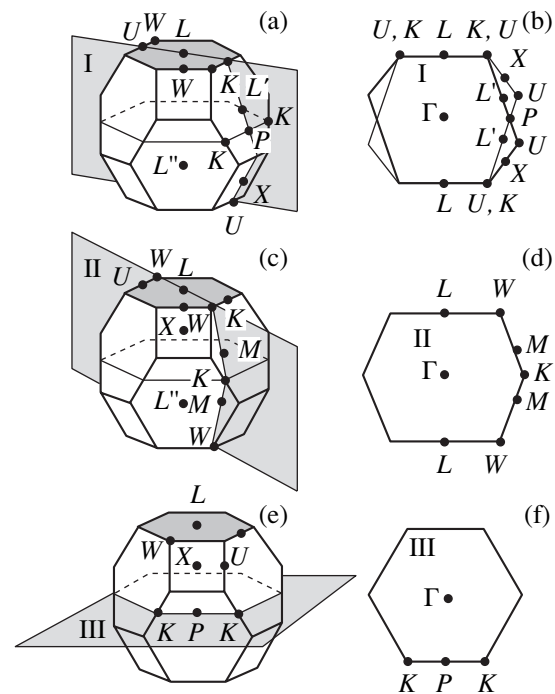


Fig. 1. (a, c, e) Brillouin zone of a twinned fcc lattice with identification of the high-symmetry points and three scanning planes and (b, d, f) cuts of the Brillouin zones of the fcc-I and fcc-II lattices by planes I, II, and III.

order extending over hundreds of microns in each layer. In those experiments, the crystallographic axes were linked to the geometric shape of each sample.

Optical spectra were obtained in transmission geometry on a DF-170 JOUAN double-beam spectrophotometer (wavelength range 400–700 nm) and a DFS-12 spectrometer (in the latter case, an incandescent lamp served as a light source and the beam was collimated with a diaphragm and a lens). The sample could be rotated about its vertical axis to study light transmission spectra with the opal lattice oriented differently relative to the incident beam. The total light beam cross-sectional area on the sample surface was $0.5\text{--}1\text{ mm}^2$. In both experimental setups, the opal sample was mounted at the center of a spherical vessel 5-cm in diameter with an immersion liquid, whose refractive index was chosen to be close to its average value for the opal, thus substantially reducing incoherent (diffuse) scattering from the sample surface. As a result, practically no light was either reflected or refracted by the sample surface, which made the part played by the shape of the sample and its surface relief insignificant. The immersion liquid used in this study was isopropyl alcohol with a refractive index $n \approx 1.37$. The effective refractive index of the opal–isopropyl-alcohol structure is $n_{\text{eff}} \approx 1.36$, which corresponds to a photonic crystal with a weak permittivity contrast.

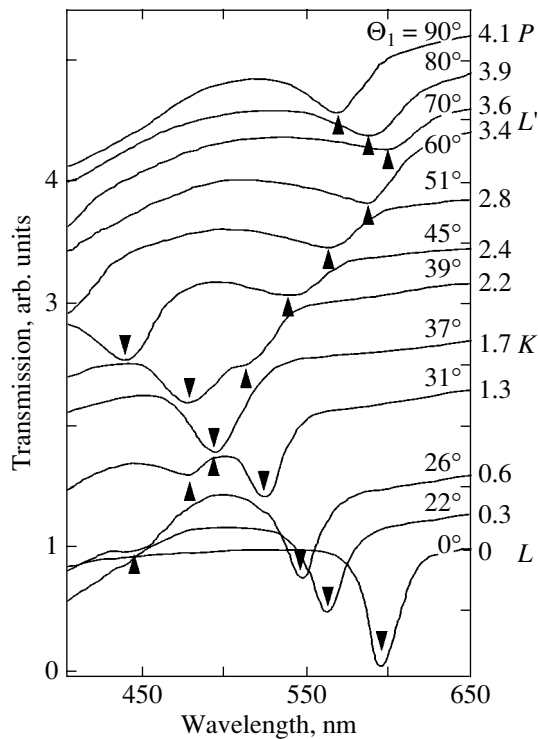


Fig. 2. Transmission spectra of opal samples measured at different angles of incidence Θ_I by scanning the Brillouin zone along path I ($L \rightarrow P$ in plane I). The spectra are translated vertically upwards by the amount specified for each spectrum.

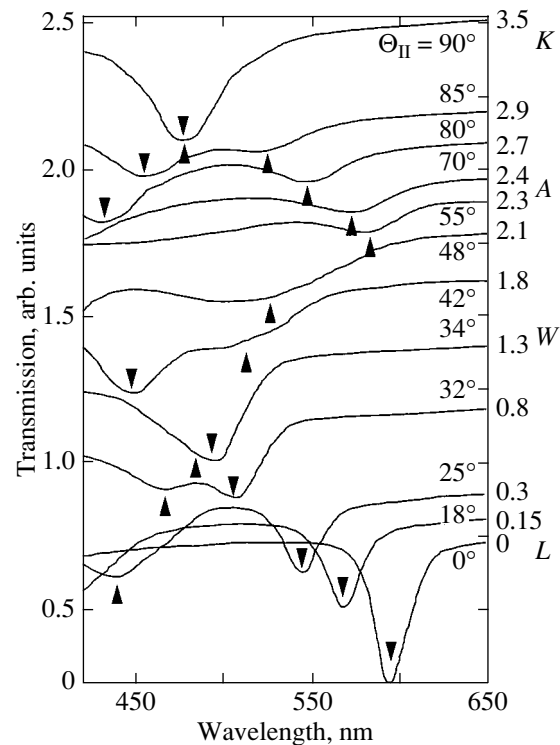


Fig. 3. Transmission spectra of opal samples measured at different angles of incidence Θ_{II} by scanning the Brillouin zone along path II ($L \rightarrow K$ in plane II). The spectra are translated vertically upwards by the amount specified for each spectrum.

5. EXPERIMENTAL RESULTS

The main goal of this experimental work was to investigate the transmission spectra of an oriented opal sample illuminated by white light for different angles of incidence of light Θ on the sample surface. Measurements were conducted with different sample orientations, thus permitting one to scan the surface of the Brillouin zone of the twinned opal fcc lattice along three paths, (2)–(4). The spectral response of the transmission coefficient $T_{\mathbf{K}}(\lambda) = I_{\mathbf{K}}(\lambda)/I_0(\lambda)$ was determined as the ratio of the intensity $I_{\mathbf{K}}(\lambda)$ of a beam with wave vector \mathbf{K} passing through the sample to the intensity $I_0(\lambda)$ of the reference beam. The results of the measurements are displayed in Figs. 2–4 in arbitrary units, because the effective length of the light path through the sample shaped as a rectangular platelet and, as a consequence, the intensity $I_{\mathbf{K}}(\lambda)$ varied substantially with the angle of incidence. In addition, the spectral intensity was normalized to a value of order unity at a wavelength of 650 nm.

The transmission spectra were studied in considerable detail as a function of the angle of incidence of light Θ_I in scanning plane I (Fig. 2), Θ_{II} in plane II (Fig. 3), and Θ_{III} in plane III (Fig. 4). The scanning angles in our experiments were varied in the ranges $0^\circ \leq \Theta_I \leq 90^\circ$, $0^\circ \leq \Theta_{II} \leq 90^\circ$, and $0^\circ \leq \Theta_{III} \leq 30^\circ$. The

transmission spectra reveal characteristic bands (dips) whose position, width, and depth depended substantially on the angles Θ_i defining the directions of light wave propagation in the opal lattice when scanning along the i th path. In addition, some spectra show noticeable transmission, which depends on the wavelength of light but has no structure in the spectral range studied.

Figure 2 presents transmission spectra measured with white light striking the sample at different angles Θ_i , which corresponds to changing the direction of the wave vector \mathbf{K} in plane I from the $\Gamma \rightarrow L$ to the $\Gamma \rightarrow P$ direction. We measured a series of transmission spectra with an average step of 2° in angle Θ_i . Figure 2 shows the most typical of them. The spectrum relating to normal incidence of light ($\Theta_I = 0$) on the (111) growth plane of opal (direction $\Gamma \rightarrow L$) exhibits the deepest and narrowest band at a wavelength of 595 nm (2.04 eV). We see that the band in the transmission spectra measured for oblique beam incidence on the (111) growth plane shifts to shorter wavelengths, its width increases, and the depth of the spectral dip decreases. As the scanning angle is further increased ($\Theta_I \geq 20^\circ$), a second band enters the operating range of the spectrophotometer ($\lambda > 400$ nm) on the short-wavelength side and shifts to longer wavelengths with

increasing Θ_I . As the angle increases, these bands approach each other to finally overlap at $\Theta_I \approx 35^\circ$ and a wavelength of ≈ 485 nm (2.56 eV). The angle $\Theta_I \approx 35^\circ$ in scanning plane I corresponds to the high-symmetry direction $\Gamma \rightarrow U$ in the Brillouin zone of fcc-I and to the $\Gamma \rightarrow K$ direction in the Brillouin zone of fcc-II (Fig. 1b). Note that the crossing of the spectral bands is not accompanied by noticeable interference. As the angle is further increased ($\Theta_I > 35^\circ$), the two bands diverge. The band originating from the 595-nm band (at $\Theta_I = 0$) continues to shift to shorter wavelengths and leaves the spectral region covered ($\lambda < 400$ nm) at $\Theta_I = 50^\circ$. The second band also continues to shift to longer wavelengths, and at $\Theta_I \approx 70^\circ$ its position corresponds to the maximum wavelength, ≈ 595 nm. This value coincides exactly with the initial position of the first band at $\Theta_I = 0$ (the $\Gamma \rightarrow L$ direction in the fcc-I and fcc-II structures), and the scanning angle $\Theta_I = 70.5^\circ$ can be identified with the $\Gamma \rightarrow L$ direction in the fcc-II lattice (Fig. 1b). At still larger angles ($\Theta_I > 70.5^\circ$), this band shifts to shorter wavelengths λ , and at $\Theta_I = 90^\circ$ (the $\Gamma \rightarrow P$ direction) its position in the spectrum corresponds to $\lambda \approx 565$ nm (2.19 eV).

Figure 3 presents transmission spectra obtained at different angles Θ_{II} in scanning plane II, which corresponds to the wave vector \mathbf{K} turned from the original $\Gamma \rightarrow L$ direction to $\Gamma \rightarrow K$ (Figs. 1c, 1d). The spectrum with a band at $\lambda \approx 595$ nm taken under normal incidence of light on the (111) growth plane coincides with the corresponding spectrum displayed in Fig. 2. As the scanning angle Θ_{II} increases, this band shifts to shorter wavelengths until, at $\Theta_{II} \approx 38^\circ$, it crosses another band at wavelength $\lambda \approx 480$ nm (2.58 eV). This second band enters the operating range of the spectrophotometer ($\lambda > 400$ nm) starting from the angle $\Theta_{II} = 20^\circ$ and shifts thereafter to longer wavelengths. The angle $\Theta_{II} = 39.2^\circ$ in scanning plane II corresponds to the high-symmetry direction $\Gamma \rightarrow W$ in the Brillouin zone of both fcc lattices making up the twin structure (Figs. 1c, 1d). These two bands diverge for $\Theta_{II} > 39.2^\circ$. Just as in the case of scanning in plane I, the band originating from the band at 595 nm (at $\Theta_{II} = 0^\circ$) continues to move to shorter wavelengths and then leaves the measurement range ($\lambda < 400$ nm) for angles $\Theta_{II} > 50^\circ$. The other band continues to shift to longer wavelengths. However, in contrast to scanning I, where the maximum wavelength of ≈ 595 nm was reached at $\Theta_I = 70^\circ$ (the $\Gamma \rightarrow L$ direction), the maximum wavelength attained in scanning in plane II is ≈ 580 nm (2.14 eV) at $\Theta_{II} \approx 60^\circ$. As the angle is increased further ($\Theta_{II} > 60^\circ$) up to the end of scanning in plane II (the $\Gamma \rightarrow K$ direction), this band shifts in position to shorter wavelengths. This band is weak and can be resolved against the background of the second, stronger band only up to angles $\Theta_{II} \approx 85^\circ$, at which the wavelength becomes $\lambda \approx 520$ nm (2.38 eV).

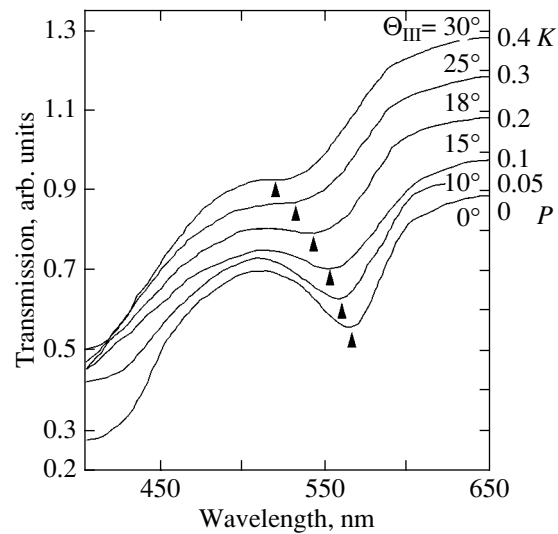


Fig. 4. Transmission spectra of opal samples measured at different angles of incidence Θ_{III} by scanning the Brillouin zone along path III ($P \rightarrow K$ in plane III). The spectra are translated vertically upwards by the amount specified for each spectrum.

When scanning the path from point P to point K in plane III (Figs. 1e, 1f), the incident light propagates in the (111) hexagonal layer plane perpendicular to the [111] growth axis. The initial, $\Gamma \rightarrow P$, and the final, $\Gamma \rightarrow K$, directions of wave vector \mathbf{K} in scanning III coincide with the final directions of vector \mathbf{K} reached in scanings I and II, respectively. As a result, the set of paths I, II, and III make up a closed contour on the surface of the Brillouin zone. Figure 4 presents transmission spectra corresponding to scanning III with the angle Θ_{III} changed by 30° through rotation of the crystal about the [111] growth axis. We see one band, which shifts monotonically with increasing Θ_{III} from $\lambda \approx 565$ nm (2.20 eV; $\Gamma \rightarrow P$ direction) to ≈ 525 nm (2.36 eV; $\Gamma \rightarrow K$). The second, short-wavelength band was not observed in this scanning in the transmission spectra near the K point ($\Theta_{III} \rightarrow 30^\circ$), which should be assigned to intense light scattering setting in for $\lambda < 500$ nm. A certain difference seen between the spectra obtained in scanings II and III near the K point (Figs. 3, 4) may be caused by deviation of the real from the theoretical scanning path (such a deviation appears more probable in scanning II, because scanning III occurs in the well-defined growth plane of the sample). Furthermore, the measurement error originates from the different thicknesses of the two samples used in these two scanings. The difference in thickness arises as a result of the difference in the shape of the samples determined by the actual conditions of sample fixation provided for rotation in different planes.

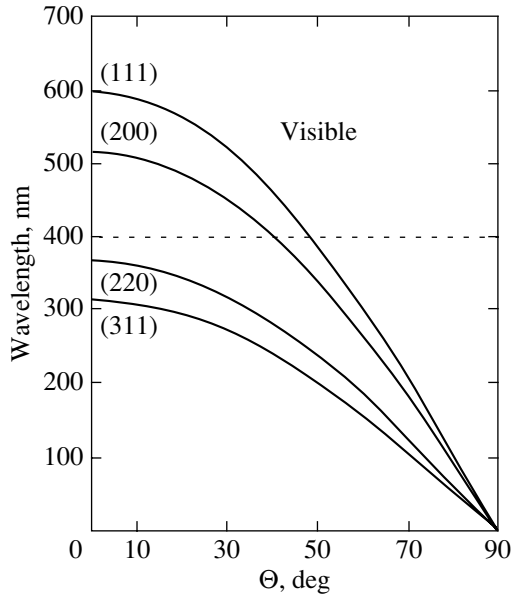


Fig. 5. Bragg wavelength plotted vs. angle of incidence for the case of diffraction from systems of different fcc lattice planes. The calculations are performed with the parameters $R = 135$ nm and $n_{\text{eff}} \approx 1.36$.

6. DISCUSSION OF THE RESULTS

In accordance with current concepts, the position of the minimum of the characteristic band in the transmission spectrum of a photonic crystal observed in our experiments corresponds to the Bragg wavelength. The behavior of the bands in the transmission spectra (Figs. 2–4) correlates well with the spectral and angular dependences of the intensity of Bragg diffraction from the opal structure studied by us earlier [17–19]. Theory offers the following general relation for the intensity of Bragg diffraction (elastic light scattering) with the wave vector transformation $\mathbf{K} \rightarrow \mathbf{K}'$:

$$I(\mathbf{K}' - \mathbf{K}) = A|\varepsilon(\mathbf{K}' - \mathbf{K})|^2 S(\mathbf{K}' - \mathbf{K}). \quad (5)$$

Here, $S(\mathbf{K}' - \mathbf{K})$ is the structural factor, $\varepsilon(\mathbf{K}' - \mathbf{K})$ are the Fourier components of the periodic dielectric function $\varepsilon(\mathbf{r}) = \varepsilon(\mathbf{r} + \mathbf{a})$, and \mathbf{a} is a direct-lattice translation vector. The structural factor has maxima in the scattering directions defined by the condition $\mathbf{K}' - \mathbf{K} = \mathbf{b}$ [see Eq. (1)]. The diffraction intensity is nonzero for the crystal planes for which $\varepsilon(\mathbf{b}) \neq 0$.

As is evident from condition (1), Bragg diffraction from a crystal plane follows the law of mirror reflection relative to vector \mathbf{b} , which acts as the normal to this plane. Since the optical absorption and background reflection in opals are small, the transmission and Bragg diffraction spectra are mutually complementary, which can be written as

$$T_{\mathbf{K}}(\lambda) = 1 - \sum_{\mathbf{b}} I_{\lambda}(\mathbf{K}' - \mathbf{K})|_{\mathbf{K}' = \mathbf{K} + \mathbf{b}}. \quad (6)$$

Here, $T_{\mathbf{K}}(\lambda)$ is the dependence of the transmission spectrum on wavelength λ for a given direction \mathbf{K} of the incident wave and $I_{\lambda}(\mathbf{K}' - \mathbf{K})|_{\mathbf{K}' = \mathbf{K} + \mathbf{b}}$ is the Bragg diffraction intensity from a crystal plane with vector \mathbf{b} at a given wavelength of light. The summation over the reciprocal lattice vectors \mathbf{b} in Eq. (6) means that all Bragg diffraction processes defined by Eq. (1) are taken into account.

In accordance with Eq. (1), the dependence of the Bragg wavelength on the angle of incidence of light Θ on the (hkl) plane in an ideal fcc lattice can be written as

$$\lambda_{(hkl)}(\Theta) = 2d_{(111)}n_{\text{eff}}\left(\frac{3}{h^2 + k^2 + l^2}\right)^{1/2} \cos \Theta. \quad (7)$$

The quantity $d_{(111)}n_{\text{eff}} \approx 300$ nm entering this expression was measured for our opal samples in [21]. Figure 5 plots Eq. (7) for light diffraction from the low-index planes $\{111\}$, $\{200\}$, $\{220\}$, and $\{311\}$ of the opal fcc lattice. For such samples, diffraction in the visible region (400–700 nm) is seen to be possible from the $\{111\}$ - and $\{200\}$ -type plane systems only; the diffraction conditions for other plane systems are satisfied in the near UV region. The $\lambda_{(hkl)}(\Theta)$ dependences for the low-index $\{210\}$ and $\{211\}$ planes are not shown in Fig. 5, because for these planes the structural factor in Eq. (5) is zero [22]. We will discuss subsequently only diffraction of visible light from $\{111\}$ - and $\{200\}$ -type planes of our samples.

As already mentioned, the photonic band gap forms as a result of Bragg diffraction of light waves from a periodically modulated dielectric structure [1–5]. In the case of Bragg diffraction of light from a plane system with Miller indices (hkl) , we obtain, by analogy with Eq. (7), the following dependence of the Bragg wavelength in vacuum on the angle of incidence of light θ on the sample:

$$\lambda_{(hkl)}(\theta) = 2d_{(111)}n_{\text{eff}}\left(\frac{3}{h^2 + k^2 + l^2}\right)^{1/2} \times \Phi_{(hkl)} \cos(\theta - \Psi_{(hkl)}). \quad (8)$$

Here, the angle $\Psi_{(hkl)}$ and the geometric factor $\Phi_{(hkl)}$ ($0 < \Phi_{(hkl)} \leq 1$) are determined by the mutual orientation of the vectors \mathbf{K} , $\mathbf{b}_{(hkl)}$, and $\mathbf{b}_{(111)}$; the angle θ is measured from the vector $\mathbf{b}_{(111)}$. It thus follows that the condition of Bragg diffraction (8) defines the position of the photonic stop bands for the spatial directions determined by the angle θ . One of the goals of our study was to verify this conclusion experimentally.

Figure 6 plots the Bragg diffraction wavelengths calculated for scannings I (Fig. 6a) and II (Fig. 6b) of the Brillouin zone of a twinned fcc structure. These quantities were derived from Eq. (8) for each plane of the $\{111\}$ and $\{200\}$ sets and are shown as functions of the angle θ . Although the calculations were made with the parameter $d_{(111)}n_{\text{eff}} \approx 300$ nm of a specific photonic structure, such plots can be derived for any fcc structure

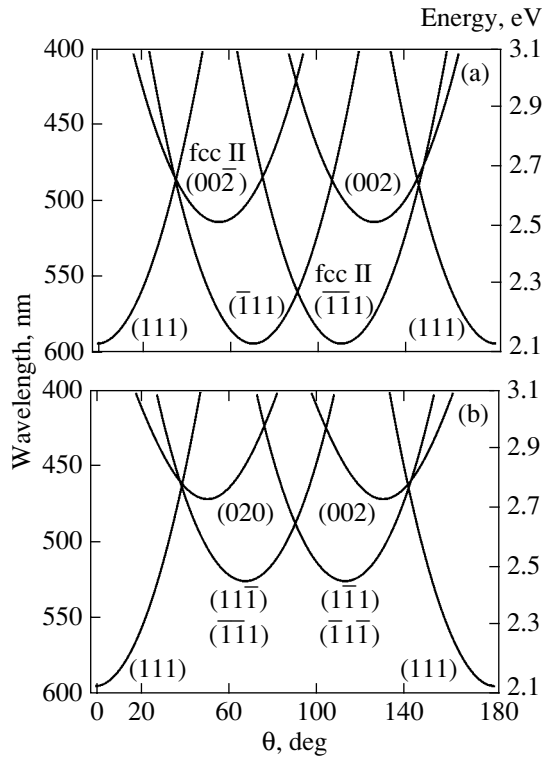


Fig. 6. Bragg wavelength vs. angle of incidence for the case of diffraction from systems of different fcc lattice planes calculated from Eq. (8) for scannings (a) I and (b) II of the Brillouin zone. The calculations are made with $R = 135$ nm and $n_{\text{eff}} \approx 1.36$ for the visible range ($\lambda > 400$ nm).

from Fig. 6 using linear scaling with the parameter dn_{eff} . The position of the stop bands is scaled with the parameter dn_{eff} in the same way.

The experimental energy positions of the band minima in the transmission spectra obtained by processing the spectra (Figs. 2–4) are presented in Fig. 7. For comparison, solid lines plot the $\lambda_{(hkl)}$ relations calculated from Eq. (8) corresponding to the three Brillouin zone scannings (I, II, III in Fig. 1). The scanning paths are shown on the bottom scale of Fig. 7 for the fcc-I and fcc-II structures. Using the data from Fig. 7, let us discuss the evolution of the photonic band gap of synthetic opals as the surface of the Brillouin zone is scanned. As seen from Fig. 7, the calculated energy positions of the stop bands corresponding to $\{111\}$ -type planes are, on the whole, in agreement with the experimental data. In particular, there is good agreement for the energy position of the photonic band gap (2.09 eV) at the two L points of the Brillouin zone. To these points in scanning I correspond the angles $\Theta_I = 0$ and 70.5° , which define the orientation of the (111) growth and $(\bar{1}\bar{1}\bar{1})$ non-growth diffraction planes, respectively. The energy minimum in the position of the photonic band gap corresponding to the L point identifies the low-energy edge of the opal photonic band gap.

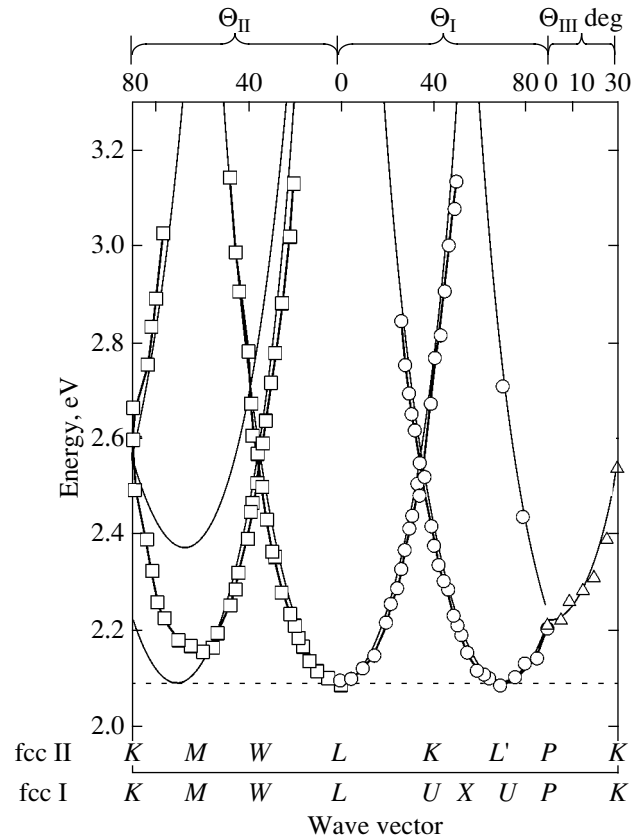


Fig. 7. Experimental energy position of the band minima in the transmission spectra displayed in Figs. 2–4 (circles correspond to scanning I; squares, to scanning II; triangles, to scanning III). Solid lines plot relations (8) calculated with the same parameters as those in Fig. 6.

The good agreement between the experimental data (Fig. 7) and Eq. (8) suggests that the main features of the photonic band gap in the visible region (1.5–3.0 eV) are accounted for by the Bragg diffraction of light from $\{111\}$ -type planes of the twinned fcc structure. The spectral position of the band minima in the transmission spectra obtained for different orientations is seen to be in accord with the Bragg wavelengths for reflection from $\{111\}$ -type planes. Diffraction of light from $\{200\}$ -type planes was not observed in our present experiments, which most probably should be attributed to the smallness of the Fourier components $\epsilon(\mathbf{b}_{(200)})$ (according to [23], $|\epsilon(\mathbf{b}_{(200)})|/|\epsilon(\mathbf{b}_{(111)})| \sim 10^{-1}$ for unfilled opal).

A certain disagreement between the experimental data and calculations is observed in scanning II, particularly, close to the M point (Fig. 7). The experimental dependence of the stop band energy on the angle Θ_{II} passes through a minimum at ≈ 2.15 eV (577 nm), which lies below a minimum at the calculated curve in energy [the theoretical value of the minimum energy at point M is ≈ 2.37 eV (522 nm)] but is still above the absolute minimum of ≈ 2.08 eV (596 nm) corresponding to the L

point (dashed line in Fig. 7). This disagreement can be explained if we look at the scheme of the Brillouin zone shown in Fig. 1. The M and L points of the Brillouin zone are seen to lie in very close planes parallel to the (111) growth plane. It may be conjectured that, in real samples of synthetic opals, different regions in the (111) growth layer are slightly misoriented with respect to the [111] growth axis (in the Θ_{III} angle). In this case, the regions on the surface of the Brillouin zone that lie close to the L point (and, hence, in which the photonic band gap energy is lower than at the M point) additionally contribute to the experimentally observed band in the transmission spectra.

The experimentally observed band in the transmission spectrum provides information not only on the energy position of the corresponding stop band but also on its width, which is larger the higher the contrast (modulation depth) of the permittivity. Indeed, the band gap width of an ideal photonic crystal can be estimated as [2]

$$\frac{\Delta\lambda_{\mathbf{b}}}{\lambda_0} = \frac{|\varepsilon(\mathbf{b})|}{\varepsilon_0}, \quad (9)$$

where λ_0 is the wavelength of light in the crystal, $\varepsilon(\mathbf{b})$ are the Fourier components of the permittivity, and $\varepsilon_0 = \varepsilon(0)$. Using the value $\varepsilon_0 = 1.35^2$ and the estimate $|\varepsilon(\mathbf{b}_{(111)})| \leq 0.1$, we find from Eq. (9) $\Delta\lambda_{\mathbf{b}}/\lambda_0 \leq 0.05$. This width correlates well with the stop band width calculated within the one-dimensional model of a photonic crystal described in [21].

Using the value of the intrinsic width of the photonic band gap $\Delta\lambda_{\mathbf{b}}$ as a reference, let us consider possible mechanisms of the additional broadening of the transmission bands. As is evident from Figs. 2 and 3, the transmission band corresponding to the photonic band gap near the L point for the (111) growth plane ($\Theta_1 = 0^\circ$) is substantially narrower than the band near point L' related to the nongrowth ($\bar{1}\bar{1}\bar{1}$) plane ($\Theta_1 = 70.5^\circ$) and than the band near the M point, which is also related to the ($\bar{1}\bar{1}\bar{1}$) nongrowth plane. The band width for the (111) growth plane is minimal, ≈ 20 nm, which corresponds to $\Delta\lambda_{\mathbf{b}}/\lambda_0 \approx 0.1$, a figure close to the theoretical estimate obtained from Eq. (9). The width of the other bands is 30–50 nm. This difference can be accounted for by relating the band width in a transmission spectrum to the extent to which the corresponding Bragg planes deviate from perfection. We may recall that the (111) growth plane is substantially more perfect than the {111}-type nongrowth planes, in which the tight hexagonal packing of a -SiO₂ spheres is distorted by random stacking of the (111) growth layers along the [111] growth axis. As pointed out in Section 2, the stacking correlation coefficient in the samples studied is $p \approx 0.8$; the formation of twins in which regions of the regular fcc structure consisted of about ten hexagonal layers was most probable. Structural imperfections of

the {111}-type nongrowth planes decrease the size of the regions with regular a -SiO₂ sphere arrangement in these planes and broaden the corresponding bands in the transmission spectra, as well as decrease the dip depth in these bands.

Note one more characteristic feature of the transmission spectra. The stop band appearing under normal incidence of light on the (111) opal growth plane is observed against the background transmission ($\approx 90\%$) depending only weakly on λ (Figs. 2, 3). The weak spectral dependence of the background transmission coefficient outside the stop band can be attributed to a decrease in the absorption coefficient of the plate with increasing wavelength [21]. Figures 2–4 show, however, that, as the angle of incidence deviates from normal, particularly at large angles Θ , the dependence of the background transmission coefficient on wavelength becomes appreciable and the background transmission falls off noticeably with decreasing λ . This behavior of the transmission spectra can be interpreted using the results from studies [17–19, 24] on light diffraction in opals. Indeed, the diffraction of white light from the opal (111) growth planes at small angles Θ satisfies the Bragg condition (1) and the spectral composition of the diffracted light is confined in a narrow wavelength interval. In this case, the background in the transmission spectra is constant because there is no diffraction within a broad spectral range, which is in accord with the energy balance equation (6). At large angles of incidence Θ , however, the diffraction patterns observed are more complex and result from spectral decomposition of white light undergoing diffraction from the (111) growth planes, which are stacked randomly along the growth axis. It is this broadening of the spectral composition of light removed from the transmission channel through diffraction that gives rise to the decrease in background transmission with increasing angle Θ , in accordance with Eq. (6).

7. CONCLUSIONS

An integrated program for measuring transmission spectra in this study and the Bragg diffraction of light in [17–19, 24] has yielded a broad picture of the photonic band gap in synthetic opals. In contrast to the available publications, in which the photonic band gap was studied only in the vicinity of the L point in the Brillouin zone [6, 8, 10–12], the dispersion of the photonic band gap was measured in this study over the whole surface of the Brillouin zone of the twinned opal fcc lattice. Our results provide direct evidence of the absence of a full photonic band gap in synthetic opals with a weak contrast in permittivity. For an opal with the parameter $d_{(111)}n_{\text{eff}} \approx 300$ nm, the dispersion of the photonic band gap in the visible region is fitted well by the set of dispersion relations for the stop bands corresponding to {111}-type planes of the twinned fcc structure. The observed nonuniform band broadening and the presence of a background in the transmission spec-

tra is accounted for by the existence of different types of structural disorder in real synthetic opals.

ACKNOWLEDGMENTS

The authors would like to thank M.I. Samoïlovich for providing samples for the measurements and to D.E. Usvyat, K.B. Samusev, and Yu.É. Kitaev for helpful discussions.

This study was supported by the Russian Foundation for Basic Research, project nos. 02-02-17689 and 02-02-17601.

REFERENCES

1. E. Yablonovitch, *Phys. Rev. Lett.* **58** (20), 2059 (1987).
2. S. John, *Phys. Rev. Lett.* **58** (23), 2486 (1987).
3. K. Busch and S. John, *Phys. Rev. E* **58** (3), 3896 (1998).
4. *Confined Electrons and Photons. New Physics and Applications*, Ed. by E. Burstein and C. Weisbuch (Plenum, New York, 1995); J. D. Joannopoulos, R. D. Meade, and J. D. Winn, *Photonic Crystals* (Princeton Univ. Press, Princeton, N.J., 1995).
5. E. Yablonovitch, *J. Phys.: Condens. Matter* **5**, 2443 (1993).
6. V. N. Astratov, V. N. Bogomolov, A. A. Kaplyanskii, A. V. Prokofiev, L. A. Samoïlovich, S. M. Samoïlovich, and Yu. A. Vlasov, *Nuovo Cimento D* **17** (11–12), 1349 (1995); Yu. A. Vlasov, V. N. Astratov, O. Z. Karimov, A. A. Kaplyanskii, V. N. Bogomolov, and A. V. Prokofiev, *Phys. Rev. B* **55** (20), R13357 (1997).
7. A. A. Zakhidov, R. H. Baughman, Z. Iqbal, C. Cui, I. Khairulin, S. O. Dantas, J. Marti, and V. G. Ralchenko, *Science* **282**, 897 (1998).
8. I. I. Tarhan and G. H. Watson, *Phys. Rev. Lett.* **76** (2), 315 (1996).
9. J. E. G. J. Wijnhoven and W. L. Vos, *Science* **281**, 802 (1998).
10. V. N. Bogomolov, S. V. Gaponenko, I. N. Germanenko, A. M. Kapitonov, E. P. Petrov, N. V. Gaponenko, A. V. Prokofiev, A. N. Ponyavina, N. I. Silvanovich, and S. M. Samoïlovich, *Phys. Rev. E* **55** (6), 7619 (1997).
11. S. G. Romanov, N. P. Johnson, A. V. Fokin, V. Y. Butko, and C. M. Sotomayor Torres, *Appl. Phys. Lett.* **70** (16), 2091 (1997).
12. H. Míguez, C. López, F. Meseguer, A. Blanco, L. Vazquez, R. Mayoral, M. Osana, V. Fornés, and A. Mifsud, *Appl. Phys. Lett.* **71** (1), 1148 (1997); H. Míguez, A. Blanco, F. Meseguer, C. López, H. M. Yates, M. E. Pemble, V. Fornés, and A. Mifsud, *Phys. Rev. B* **59** (3), 1563 (1999).
13. A. Reynolds, F. López-Tejeira, D. Cassagne, F. J. Garsía-Vidal, C. Jouanin, and J. Sánchez-Dehesa, *Phys. Rev. B* **60** (16), 11422 (1999).
14. V. G. Golubev, V. A. Kosobukin, D. A. Kurdyukov, A. V. Medvedev, and A. B. Pevtsov, *Fiz. Tekh. Poluprovodn. (St. Petersburg)* **35** (6), 710 (2001) [*Semiconductors* **35**, 680 (2001)]; V. G. Golubev, J. L. Hutchison, V. A. Kosobukin, D. A. Kurdyukov, A. V. Medvedev, A. B. Pevtsov, J. Sloan, and L. M. Sorokin, *J. Non-Cryst. Solids* **299–302**, 1062 (2002).
15. Yu. A. Vlasov, V. N. Astratov, A. V. Baryshev, A. A. Kaplyanskii, O. Z. Karimov, and M. F. Limonov, *Phys. Rev. E* **61** (5), 5784 (2000).
16. J. Huang, N. Eradat, M. E. Raikh, Z. V. Vardeny, A. A. Zakhidov, and R. H. Baughman, *Phys. Rev. Lett.* **86** (21), 4815 (2001).
17. A. V. Baryshev, A. A. Kaplyanskii, V. A. Kosobukin, M. F. Limonov, K. B. Samusev, and D. E. Usvyat, in *Proceedings of 10th International Symposium on Nanostructures: Physics and Technology* (St. Petersburg, 2002), p. 120.
18. A. V. Baryshev, A. A. Kaplyanskii, V. A. Kosobukin, M. F. Limonov, K. B. Samusev, and D. E. Usvyat, *Physica E (Amsterdam)* **17**, 426 (2003).
19. A. V. Baryshev, A. A. Kaplyanskii, V. A. Kosobukin, M. F. Limonov, K. B. Samusev, and D. E. Usvyat, *Fiz. Tverd. Tela (St. Petersburg)* **45** (3), 434 (2003) [*Phys. Solid State* **45**, 459 (2003)].
20. C. Kittel, *Introduction to Solid State Physics*, 6th ed. (Wiley, New York, 1986; Nauka, Moscow, 1978).
21. A. V. Baryshev, A. V. Ankudinov, A. A. Kaplyanskiĭ, V. A. Kosobukin, M. F. Limonov, K. B. Samusev, and D. E. Usvyat, *Fiz. Tverd. Tela (St. Petersburg)* **44** (9), 1573 (2002) [*Phys. Solid State* **44**, 1648 (2002)].
22. R. J. Carlson and S. A. Asher, *Appl. Spectrosc.* **38** (3), 297 (1984).
23. H. M. van Driel and W. L. Vos, *Phys. Rev. B* **62** (15), 9872 (2000).
24. A. V. Baryshev, A. A. Kaplyanskii, V. A. Kosobukin, K. B. Samusev, D. E. Usvyat, and M. F. Limonov, *Phys. Rev. B* **70** (2004) (in press).

Translated by G. Skrebtsov

LOW-DIMENSIONAL SYSTEMS
AND SURFACE PHYSICS

Intercalation of Silver Atoms under a Graphite Monolayer on Ni(111)

A. G. Starodubov, M. A. Medvetkii, A. M. Shikin, and V. K. Adamchuk

Fock Institute of Physics, St. Petersburg State University,
ul. Ul'yanovskaya 1, Petrodvorets, St. Petersburg, 198504 Russia

e-mail: arkstar@mail.ru

Received October 30, 2003

Abstract—The process of silver intercalation under a graphite monolayer (GM) grown on the (111) nickel single-crystal face, GM/Ni(111), is studied. The experiments were conducted in ultrahigh vacuum. The systems were formed *in situ* in a vacuum chamber under direct monitoring of each stage in the formation of the systems by angle-resolved UV photoelectron spectroscopy and LEED. The possibility of silver intercalation in the GM/Ni(111) system was studied in the course of deposition of various amounts of the metal on the given subject with subsequent heat treatment. It was established that the process occurs optimally under cyclic alternation of the operations of adsorbate (Ag) deposition on the GM/Ni(111) surface and subsequent annealing of the system. In the intermediate stages of GM/Ag/Ni(111) formation, the GM on Ni(111) was found to exist in two phases. Ag intercalation under a graphite monolayer on Ni(111) at room temperature was verified. © 2004 MAIK “Nauka/Interperiodica”.

1. INTRODUCTION

Graphite-based multilayer systems formed by intercalating various materials into the interlayer space are attracting considerable attention because of their unique properties and their application potential [1, 2]. Some elements, such as gold, silver, and copper, cannot, however, be intercalated into bulk graphite by standard technologies [1]. Fabrication of intercalated systems based on noble metals with the purpose of obtaining new types of objects and investigating them can only be accomplished through the use of a single graphite monolayer deposited on the surface of *d* metals or their carbides [2–18].

Thin films of noble metals (in particular, Au and Cu) of variable thickness, prepared by intercalation under a graphite monolayer, are bounded on one side by the graphite monolayer and on the other, by the substrate surface plane. This confers clearly pronounced two-dimensional properties to the given systems. In addition, as shown in [19], a graphite monolayer also acts as a passivator by protecting the metal from interaction with the active components of the atmosphere.

Our earlier publications [12–16] reported on a study of gold and copper intercalation under a graphite monolayer (GM). We showed the possibility of inserting atoms of noble metals under a GM on Ni(111) and investigated the electronic structure and phonon spectra of such intercalated systems using photoelectron spectroscopy, low-energy electron energy-loss spectroscopy (LEELS), and scanning tunneling microscopy.

It was shown by Tontegode and his group of researchers [4–7] that, while silver also belongs to the

group of noble metals, a system with silver atoms intercalated under a GM is unique in terms of its properties and the specific features of the intercalation process involved. Attempts at inserting silver directly under a GM formed on a patterned Ir foil failed [4–7], and this goal could only be attained by substituting silver atoms for the preintercalated alkali metal atoms. The limiting concentration of the Ag atoms penetrating under the GM in this case was one monolayer (ML), in comparison with the systems studied earlier, GM/Au/Ni(111) and GM/Cu/Ni(111), where the intercalant thickness reached 1–2 MLs.

The present communication reports on a comparative study of the possibility of intercalating various amounts of silver predeposited on the GM/Ni(111) surface (ranging from a monolayer coverage to tens of Ag monolayers). Direct evidence was obtained of the intercalation of the metal under a GM. Special experiments permitted us to compare the possibilities inherent in step-by-step intercalation at standard ($T = 375^\circ\text{C}$) and room temperature. The electronic structure of the intercalated systems thus formed was studied, and the mechanisms by which silver interacts with the GM/Ni(111) system were analyzed.

2. EXPERIMENTAL CONDITIONS

Experiments were carried out on an ADES-400 commercial angle-resolving photoelectron spectrometer (VG Scientific).¹ The equipment included a 150°

¹The authors express their gratitude to Prof. Kaindl, Free University of Berlin, for giving us the chance to use this instrument.

spherical-sector analyzer (angular resolution 2°), a gas-discharge UV helium lamp (UVS-10/35), an ion gun, and a gas admission system. The energy resolution of the analyzer was 50 meV. The UV lamp radiation was incident at an angle of 55° to the sample surface normal. The photon sources were the He-I and He-II resonance lines with energies of 21.2 and 40.8 eV, respectively. The sample orientation and the surface structure periodicity were determined by the LEED method. The diffraction patterns were imaged by a four-grid retarding-field energy analyzer. These patterns were used to adjust the principal azimuthal directions (ΓM , ΓK) of the surface Brillouin zone, after which angle-resolved photoelectron measurements were conducted within the polar angle range from -20° to 45° with respect to the sample surface normal (0° corresponds to emission along the normal). The sample temperature was monitored with a Ni-Ni/Cr thermocouple. The metal was deposited from a silver weight mounted on a W-Re spiral. The exact amount of deposited material (Θ) was measured with a quartz microbalance. The experiment was performed in ultrahigh vacuum. The base pressure in the chamber at the time of spectrum was recorded did not exceed 1×10^{-10} Torr.

The surface of the nickel single crystal was specially prepared by repeated ion etching alternated with annealing in an oxygen and a hydrogen atmosphere until the photoelectron spectra acquired the shape typical of a clean Ni(111) face [14, 15]. The diffraction pattern measured after this procedure demonstrated, as expected, hexagonal symmetry, thus indicating the good quality of the crystal structure.

Monolayer coverage of graphite on the nickel surface was produced by propylene cracking, a technology described in [12–16]. The sample was exposed to propylene C_3H_6 for 5 min at a gas pressure of 1×10^{-6} Torr and a substrate temperature of $500^\circ C$.

After the formation of the first monolayer, there is practically no further growth of graphite layers (as indicated in [3, 4]), which results from reduced reactivity of the surface. The substantial differences between the growth rates make it possible to monitor the thickness of the graphite coating with high accuracy. For instance, whereas the formation of 1 ML of graphite requires an exposure of a few hundred langmuirs, the exposure needed for deposition of the second layer is tens of thousands of langmuirs [20]. This observation permits us to choose conditions favoring the formation of only one monolayer of graphite on the Ni(111) surface.

The electronic and crystal structures of the system thus formed were identified by LEED and photoelectron spectroscopy. After the GM formation, the diffraction pattern did not change dramatically, with bright reflections at the hexagon corners still prevailing. In view of the slight difference (less than 2%) between the (0001)graphite and Ni(111) face lattice constants, this behavior may indicate the formation of a structure that

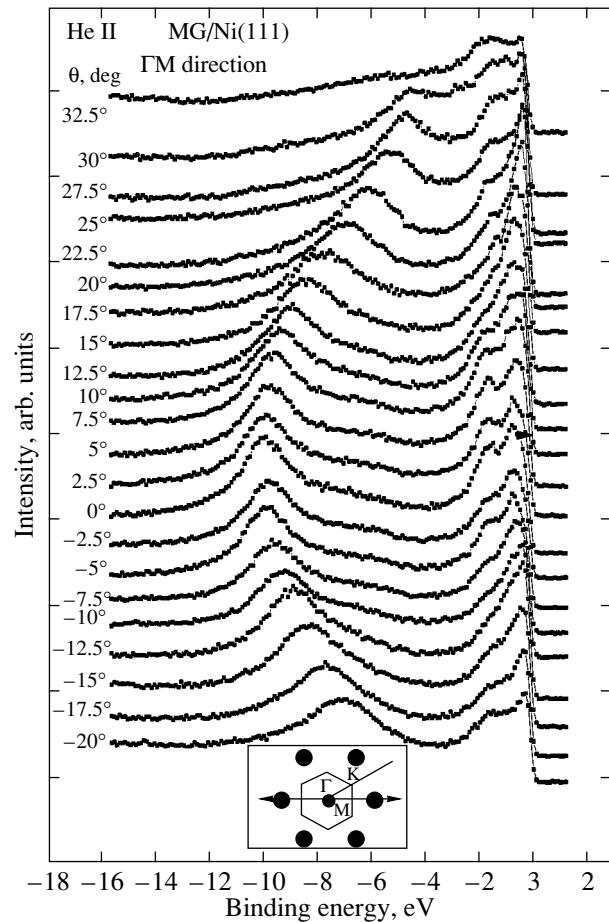


Fig. 1. Photoelectron spectra ($h\nu = 40.8$ eV) obtained for the GM/Ni(111) system under variation of the polar angle θ in the plane corresponding to the ΓM direction of the two-dimensional Brillouin zone of graphite. 0° corresponds to emission in the normal direction. Shown below is the graphite two-dimensional Brillouin zone specifying the directions in which the angular dependence was studied. Filled circles identify the LEED pattern reflections.

is coherent with that of the substrate. The presence of features corresponding to graphite in the photoelectron spectra, as will be shown later, and the general pattern of dispersion of these features suggest that the starting point of our studies was indeed a graphite monolayer on Ni(111), an object with well-defined properties.

3. EXPERIMENTAL RESULTS

Figure 1 presents a series of angle-resolved photoelectron spectra ($h\nu = 40.8$ eV) obtained for the GM/Ni(111) system. The spectra were measured with photoelectrons emerging in the ΓM direction of the two-dimensional Brillouin zone of graphite for various polar angles reckoned from the surface normal.

These experimental relations exhibit distinct peaks corresponding to electron excitation from the d states of Ni and π states of graphite lying in the binding-energy

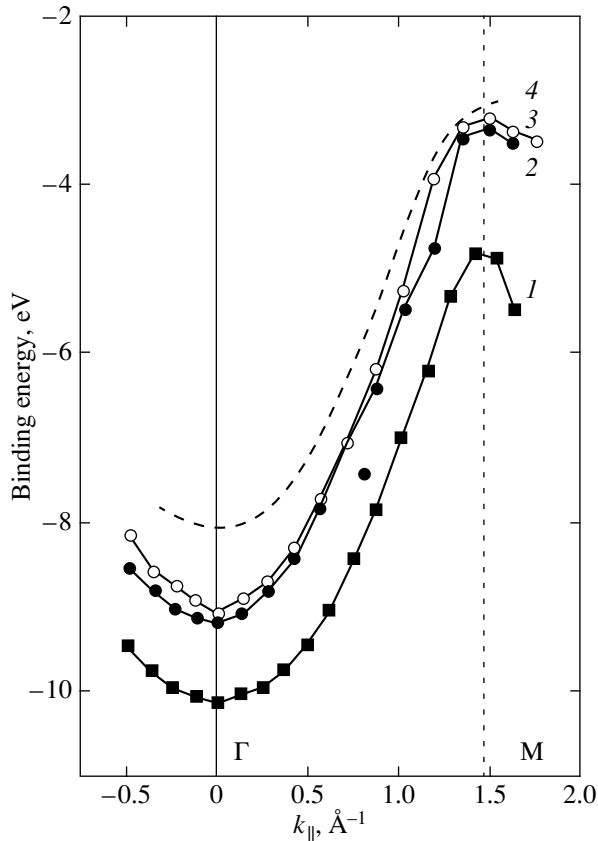


Fig. 2. Band dispersion in the ΓM direction of the two-dimensional Brillouin zone of graphite for the following systems: (1) GM/Ni(111); (2, 3) GM/Ag/Ni(111) for deposited silver concentrations of 3.0 and 4.7 MLs, respectively; and (4) bulk graphite (dashed line).

regions 0–2.5 and 4–10 eV, respectively. Some spectra also contain weak features in the binding-energy region 4–6 eV (normal emission), which can be assigned to the $\sigma_{2,3}$ graphite states. The decisive part in the interaction mechanism between the graphite substrate and the GM is played by the graphite π states [2], whose dispersion was studied by us before and after intercalation. Unfortunately, in the course of angular measurements, the sample position underwent a slight displacement relative to the axis of analyzer rotation due to the specific design of the manipulator. This led to accumulated error, and, as a result, the π -state branch was somewhat squeezed in the angle. Assuming this contraction to be due exclusively to the specific features of the experiment, we calibrated the setup against the published data on GM/Ni(111) [14, 15]. Based on this calibration, the graphs of Fig. 2 should be related to the dispersion of electronic states in the GM/Ni(111) valence band along the ΓM direction. The dashed line in Fig. 2 shows the experimental data obtained in [14] for a graphite single crystal. Comparison with the data for bulk graphite shows that the π -state branch of the GM/Ni(111) system is shifted toward higher binding energies (BEs) by

about 2.0 eV. Note the specific pattern of this shift; on reaching its maximum value at the Γ point, it falls off as the Brillouin zone edge is approached. This shift, as established in [2], is caused by hybridization of the π states of graphite with the d states of Ni.

Figure 3a displays photoelectron spectra (normal emission) (1) for the clean Ni(111) surface, (2) for the surface coated by a graphite monolayer, (3) for GM/Ni(111) with a silver layer with surface concentration $\Theta = 11$ MLs, and (4) for the same system as (3) but heated to a temperature of 375°C. The photoelectron spectrum 1 of the clean Ni(111) surface has peaks of the Ni d states with binding energies of 0.5 and 1.5 eV. The formation of a graphite monolayer on Ni(111) (curve 2) is accompanied by the appearance of a peak due to the graphite π states localized in the energy region of 10.2 eV and a weakening of the nickel d states in the photoelectron spectra. Deposition of 11 Ag monolayers on this system (curve 3) results in an almost complete disappearance of the graphite and nickel peaks (i.e., complete suppression of signals from the GM/Ni(111) system by silver) and the appearance of a structure characteristic of the silver d states in the binding energy range 4–8 eV. Annealing the system at $T = 375^\circ\text{C}$ restores the graphite π -state peak but in a position shifted toward lower binding energies to ~ 9.0 eV, as well as the peaks due to the Ni d states with a substantially weaker intensity (curve 4).

Figure 4 displays photoelectron spectra obtained for various angles from a GM/Ag/Ni(111) system with a layer of Ag about ~ 5 ML thick repeatedly added and annealed at 375°C (ΓM direction of the two-dimensional Brillouin zone). A common feature in the series of these spectra is the dispersion of the π states of graphite and a nearly dispersion-free behavior of the $4d$ states of the silver valence band. The features corresponding to the π states are identified by vertical arrows. They were used to construct curve 3 for the dispersion in Fig. 2. As follows from a comparison with the GM/Ni(111) system, the π -state branch of the GM/Ag/Ni(111) system is shifted by 1–1.5 eV to the region of energies characteristic of single crystal graphite.

4. DISCUSSION OF THE RESULTS

Now, we consider in more detail the mechanisms for interaction in the three-component GM/Ni(111) + Ag system under study and analyze the main changes occurring in the sample. A noticeable feature in the band structure of the system, which becomes manifest after silver deposition on the GM/Ni(111) and thermal annealing, consists in an appreciable shift of the graphite π states by ~ 1 –1.5 eV toward decreased binding energies (Fig. 3a). This shift was assigned in [15, 16] to penetration of the intercalant under the GM and suppression of its strong covalent bonding to the Ni(111) substrate. Similar changes observed in the spectra of the gold and copper systems, GM/Au/Ni(111) and

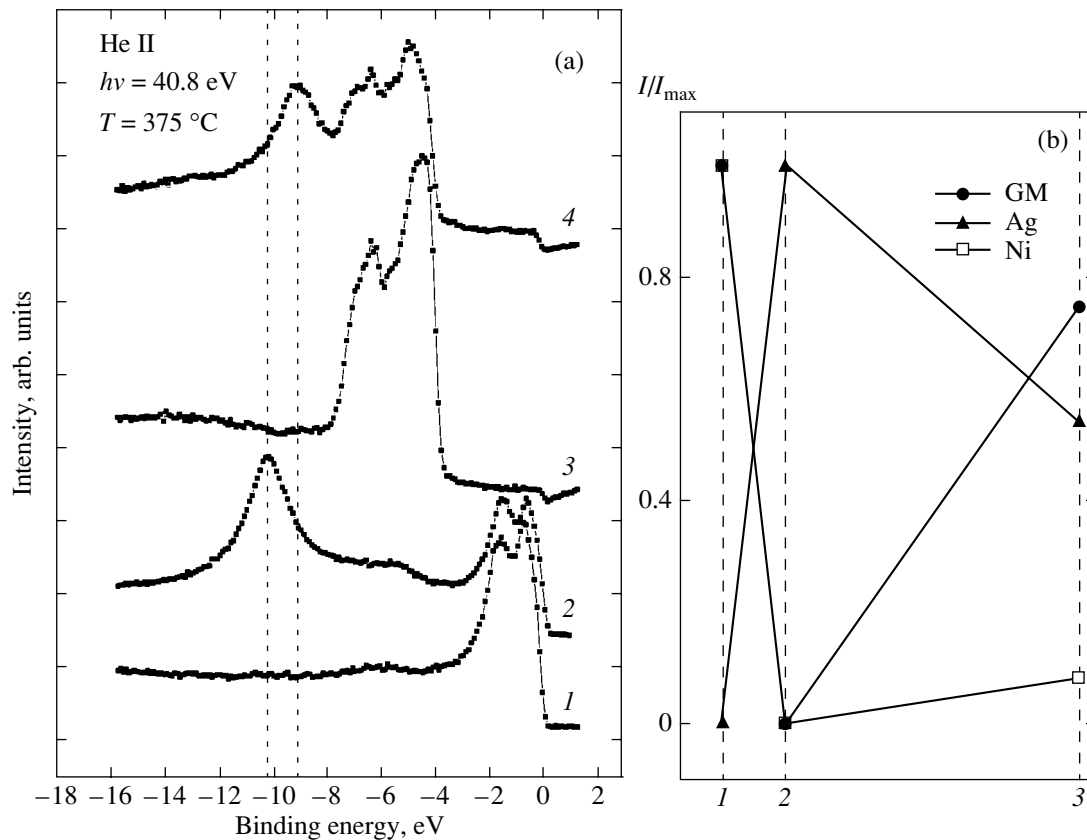


Fig. 3. (a) Photoelectron spectra ($h\nu = 40.8$ eV) measured for normal emission. (1) Clean Ni(111); (2) graphite monolayer on Ni(111); (3) 11 MLs of Ag deposited on the GM/Ni(111) surface; and (4) the preceding system heated to 375°C. (b) Normalized peak intensities of the graphite π states, Ag 4*d* states, and Ni 3*d* states. (1) Clean GM/Ni(111); (2) same as in (1) but with 11 MLs of Ag deposited on top of GM/Ni(111) at room temperature; and (3) same as in (2) but after annealing of the system up to 375°C. The normalization was made against the amplitude of the signal obtained in a given state.

GM/Cu/Ni(111), were considered to be related to penetration of the Au and Cu atoms under the graphite monolayer. In our case, thermal annealing occurred in the same temperature region (350–400°C) that is needed to ensure intercalation of Au and Cu under the GM on the Ni(111) surface [12–16]. The same values were used in LEELS studies of the interaction of silver with a GM [17, 18]. The similarity of the conditions and the observed shift of the graphite π states in binding energy provides compelling evidence for silver behaving in our case in much the same way, thus suggesting Ag intercalation under the GM. Let us estimate the spatial silver location from the intensities of the Ag, C, and Ni peaks in each stage of formation of the system (clean GM/Ni(111) substrate, silver deposition, heat treatment). Figure 3b shows the relative variation of the graphite, nickel, and silver peak intensities measured under normal emission and reflecting the transformation of the system in the course of Ag deposition and annealing of the system. In Fig. 3b, state 1 refers to the GM/Ni(111) system; state 2, to the system after Ag deposition on GM/Ni(111); and state 3, to the system after annealing. We see that, after the deposition of silver, the peak intensities of the graphite π states and Ni

d states drop practically to zero, with only the silver features prevailing. After the annealing (state 3), the graphite π -state peak grows in amplitude. The silver peak intensity decreases after the annealing by about one-half, and the nickel features remain barely visible on top of the broad plateau adjoining the Fermi level. This relative amplitude of the signals indicates that silver atoms are located above the metallic Ni substrate and that the atoms of carbon are on the surface of the system. This is direct evidence of Ag intercalation under the GM.

However, while the amplitude of the signal due to the graphite π states does increase after the anneal, it does not reach the level corresponding to GM/Ni(111) (state 3 in Fig. 3b). This is because the silver atom redistribution brought about by the increase in the sample temperature gives rise to several processes. In the initial stage, after deposition of a large amount (~11 MLs) of Ag on the GM/Ni surface, the adsorbate film completely suppresses the signals due to graphite and nickel (spectrum 3 in Fig. 3a). After the system was heated, part of the atoms penetrate under the GM, while others tend to escape from the working surface and migrate toward the sample periphery or coalesce into

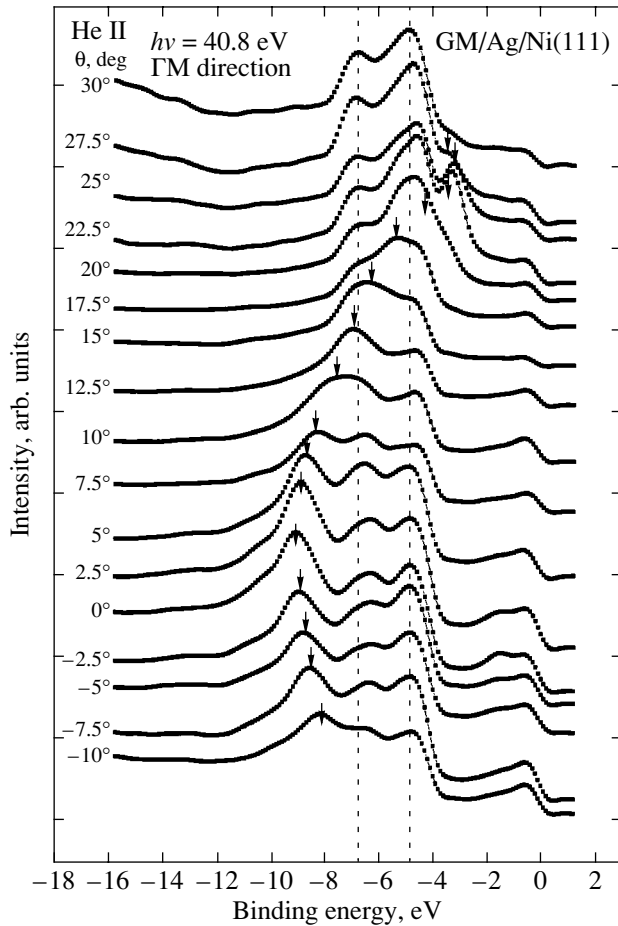


Fig. 4. Photoelectron spectra ($h\nu = 40.8$ eV) obtained for the GM/Ag/Ni(111) system with the polar angle θ varied in the plane corresponding to the ΓM direction of the graphite surface Brillouin zone. Arrows specify the positions of the graphite π -state peak, which served as a basis for constructing the dispersion relation in Fig. 2. Dashed lines identify the peak positions of the Ag $4d$ states.

larger formations (compared to atomic size). The coalescence and buildup of Ag should occur preferentially at the boundaries of the graphite islands, which may be considered to be defects in the GM structure. Such behavior of the silver atoms affects the signal intensity redistribution for all three elements, C, Ag, and Ni (state 3 in Fig. 3b). Raising the sample temperature to 375°C does not restore the amplitude of the graphite π -state peak completely. As a result, the peak diminishes, compared to that for the GM/Ni(111) system, by about 25%. It appears natural to assume that the reason for this lies in the silver left on the GM surface and captured by adsorption centers located along the boundaries of the graphite islands. Thus, the fraction of the GM free surface in this particular case is approximately 75% of the surface area. Therefore, the Ag signal originates actually from two silver states, more specifically, from the silver remaining on the graphite surface and from the silver that penetrated under the GM.

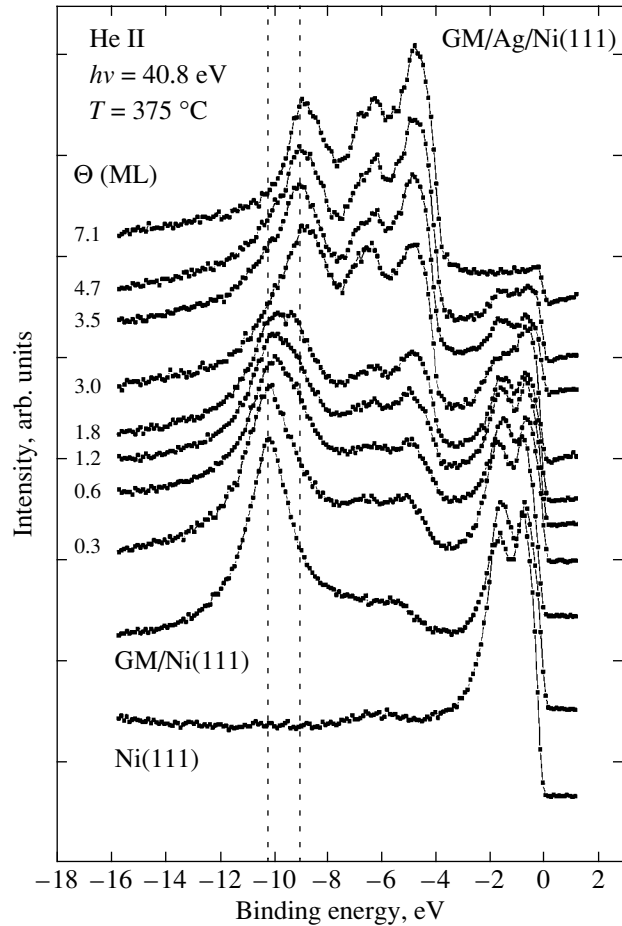


Fig. 5. Variation of photoelectron spectra ($h\nu = 40.8$ eV, normal emission) under intercalation of Ag with increasing total concentration Θ (annealing to $T = 375^\circ\text{C}$).

As known from experiments on Ag adsorption on graphite, the silver layer in the initial stages of growth has an island structure [21]. One could expect similar behavior on the GM/Ni(111) surface. Indeed, photoelectron spectra exhibit features near the Fermi level that correspond to the substrate signal even for pre-coating thicknesses of the order of 5–7 MLs. This suggests that the growth of a silver film on the surface of bulk graphite and on GM/Ni(111) follows an island pattern. STM studies of Cu deposition on a GM on Ni(111) and of Cu intercalation under a GM on Ni(111) [15] also attest to the island growth of the predeposited Cu layer, which is close in electronic properties to Ag.

The measured angular energy distributions of the outgoing electrons (Fig. 4) and the calculated valence-state dispersion (Fig. 2) show that the new system retains its quasi-two-dimensional graphite-like character. This suggests that the electronic and geometric characteristics of a GM on the surface remain unchanged.

The spectra displayed in Fig. 5 permit more comprehensive analysis of the intermediate stages in intercala-

tion. We see here photoelectron spectra that reveal the evolution of the GM/Ni(111) system as silver is being deposited stepwise on its surface to various total thicknesses (starting from 0.3 to 7.1 MLs), with each deposition step followed by annealing to 375°C. The bottom spectrum shows the original state of the system and is seen to derive from the Ni d states, as well as from the graphite π states localized near 10.2 eV. The spectra obtained with up to 1.8 ML of deposited silver reveal features typical of the silver d states against the background of decay of the graphite and nickel peaks related to the GM/Ni(111) system. Note a certain broadening of the graphite π -state peak and its simultaneous shift toward lower binding energies. After the total thickness has reached 3.5 MLs, the shift of the π states toward lower binding energies in the photoelectron spectra already becomes considerable, about 1.2 eV. Further deposition of silver and annealing of the system do not bring about significant changes in the energy of this feature; only a gradual weakening of the signal due to the substrate is observed. As a result, the double-humped peak characteristic of the Ni d states degenerates into a nearly flat step, on which one can nevertheless discern barely visible features with binding energies of 0.5 and 1.5 eV. The column of figures on the left of Fig. 5 identifies the thickness of the deposited layers. These figures are of arbitrary character and specify only the total amount of Ag applied to the GM surface during the experiment. As already mentioned, only a fraction of the intercalant penetrates under a GM and each heating of the system is accompanied by migration of silver atoms over the surface in addition to insertion, as a result of which part of them escape to an area inaccessible for analysis.

It appears natural to assume that, in the initial stages, where the silver concentration is not high enough to saturate the GM-substrate interlayer space (over the entire sample area), a certain intermediate state prevails. In this case, part of the Ag atoms have already penetrated under the GM, while part of the GM remains in the initial state; i.e., the surface can be divided into regions with and without intercalated silver atoms. In particular, it is this situation that the bottom spectra in Fig. 5, which correspond to a total thickness of the deposited film of up to 1.8 ML, should reflect. The π -state peak in this early stage is broadened, and the center of gravity of this feature shifts toward lower BEs. The shift is quite substantial in the case of thick coverages (the upper spectra in Fig. 5). Starting with concentrations above 3.0 MLs and going upwards, the position of the graphite π -state peak remains unchanged as the amount of the adsorbate is increased. Thus, there is an initial stage of the system, namely, a GM on Ni(111), and a final stage (a system with a saturated layer of intercalated silver), which are characterized by π -state binding energies of 10.2 and 9.0 eV, respectively. Assuming all the intermediate spectra to be the sums of two signals associated with the above states and assigned certain weights, one can

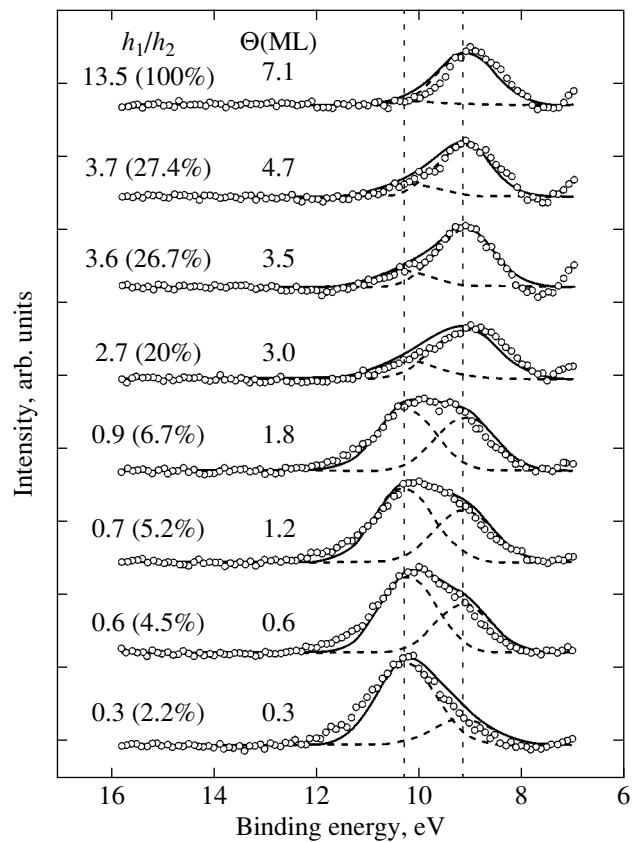


Fig. 6. Unfolding of the spectrum obtained in the region of the π states of graphite on Ni(111) after silver intercalation for different values of the total Ag surface concentration. h_1/h_2 is the intensity ratio of intercalated (h_1) and nonintercalated (h_2) states of the GM on Ni(111).

fit the experimental curve by the sum of two such components. To do this, the π -state peak was decomposed (after subtracting the background) into two constituent Gaussians, with their half-width serving as a fitting parameter. The result of this unfolding is shown in Fig. 6. The dashed lines display the contributions from each of the components, and the solid line describes their sum, which in most cases is seen to be in good agreement with the experiment. The decompositions made with other positions of the maxima (not 10.2 and 9.0) do not agree with the experiment, which provides a compelling argument for the validity of the above reasoning.

Assuming that the concentration of the silver that penetrated under the GM on Ni(111) for the final state is 1 ML and that the silver is uniformly distributed under the GM, the relative contribution from the second (low-energy) component of the π states to the total spectrum should correlate with the fraction of the GM bound to the Ni(111) substrate through the Ag atoms. This suggests that, to ensure efficient penetration of ~ 1 ML of Ag under the GM for the given method of formation of the system, one should preliminarily deposit

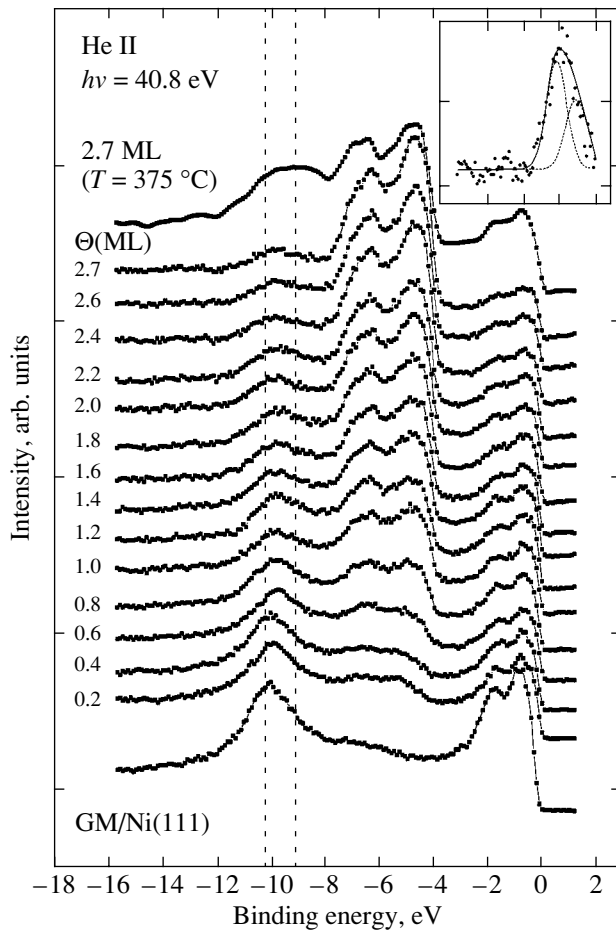


Fig. 7. Photoelectron spectra (normal emission) obtained under Ag deposition on GM/Ni(111) at room temperature. Top spectrum corresponds to the system with $\Theta = 2.7$ MLs heated to $T = 375^\circ\text{C}$. Dashed lines correspond to maxima of the two components of the graphite π -state peak. Inset shows decomposition of the graphite π -state peak into two components corresponding to the intercalated and nonintercalated states of the GM on Ni(111) for a silver concentration of 1.8 ML.

three to four MLs of silver on the GM/Ni(111) surface. The assumption that Ag is present under the GM in a monolayer concentration appears reasonable. Indeed, after the second component of the π states has saturated (with a preliminary coverage of 3–4 MLs), there is practically no change in the structure of the peak and in its intensity and energy with increasing Θ . At the same time, further decay of the Ni d state peak in intensity with the thickness of the predeposited Ag layer increasing to 11 MLs may indicate an increase of the intercalated silver layer in thickness.

Thus, the above experimental data and their analysis may be considered an additional argument for silver intercalation under a GM grown on Ni(111). Moreover, the reasoning presented here shows convincingly that the intercalation process is indeed accompanied by a complex behavior of the metal deposited on

GM/Ni(111), including intercalation of the material and its coalescence and migration. At the same time, it should be stressed that the GM itself in this system is a fairly stable formation and retains its geometric and electronic properties in the course of these processes.

In order to study the temperature dependence of the intercalation process, an attempt was undertaken to detect Ag intercalation at room temperature. This was done by successive deposition of small amounts of silver on GM/Ni(111) without intermediate heating (the total amount of the deposited material was $\Theta = 2.7$ MLs). The results obtained are displayed in Fig. 7. The bottom spectrum shows the state of the original GM/Ni(111) system, and the subsequent spectra show its evolution with increasing silver coverage. As in the case with intermediate heating of the system, this experiment also reveals a broadening of the peak accompanied by a shift toward lower binding energies. Although the increase in the half-width and the shift of the graphite π states are less obvious, the corresponding treatment of the data enables us to unfold the peak of graphite π states into two constituents with the same binding energies as derived earlier. This implies that the pattern of the relevant processes remained unchanged. The inset in Fig. 7 demonstrates this type of treatment. Deconvolution of the graphite π -state peak into components performed for a spectrum corresponding to a total coating thickness of 1.8 ML reveals a shifted peak of π states, which indicates the presence of silver under the GM. The data relating to the system obtained by depositing silver on the sample without heating suggest that, while the temperature factor plays an important part in intercalation, the intercalation process itself is not of activated character; in other words, insertion of silver atoms under the GM takes place already at room temperature. Annealing the system only intensifies the intercalation process (see the top spectrum in Fig. 7).

The totality of our data also shows that intercalation of one silver atom changes the electronic structure of only the nearest hexagon located above it in the graphite layer (or in its nearest neighbor environment), whereas the other carbon atoms remain strongly bonded to the Ni surface. This means that, in penetrating under the GM over the boundaries of graphite islands and propagating in the space between the GM and the Ni(111) surface, the Ag atoms do not affect the total area of the substrate surface. They most probably coalesce in dense formations near the boundaries of graphite domains to produce a separate intercalated graphite-coating phase and a phase of the graphite layer residing in its original state. This behavior is reflected in the spectra in the form of two components of the graphite π -state peak in the intermediate intercalation stages. Thus, decomposition of the graphite π -state peak and estimation of the relative magnitude of the shifted and unshifted components, as performed in Fig. 6, provide the fraction of the GM surface under which silver has penetrated.

To sum up, systems obtained both by simultaneous deposition of large amounts of silver and by alternation of the deposition–annealing cycles, as well as by intercalation at room temperature, revealed the presence of two phases of existence of a graphite layer in various stages of formation. These two phases correspond to the position of the graphite layer hexagons above the inserted silver atoms or, as before, bonded directly to the Ni(111) substrate.

It should be pointed out that heating a system obtained by step-by-step deposition of silver at room temperature to $T = 375^\circ\text{C}$ does not produce a spectrum of a clearly pronounced intercalant (Fig. 7). The peak due to the π states of graphite remains diffuse; i.e., at given concentrations $\Theta = 2.7$ MLs) of silver predeposited at room temperature, a substantial contribution under heating comes from the accumulation of silver atoms in islands on the GM surface, a factor hindering complete intercalation of the system. If the Ag coverage is increased to surface concentrations of the order of 7–10 MLs (i.e., with silver coating practically the entire surface), the spectrum obtained after annealing of the system becomes similar to the spectra presented in Figs. 3 and 4. Summing up, one can say that the contribution from the processes giving rise to silver coalescence in islands at low concentrations of deposited silver is quite high, a factor substantially hindering the intercalation process, which requires the presence of a certain amount of silver atoms near the boundaries of the graphite domains. At large coverages, the silver concentration (despite the competing coalescence process) becomes high enough for efficient intercalation.

5. CONCLUSIONS

The results of our studies can be summed up as follows:

(1) We have obtained direct evidence of the intercalation of silver under a graphite monolayer formed on the Ni(111) surface. Silver atoms penetrate into the interlayer space between the GM and Ni(111), thus blocking (substantially reducing) the strong covalent bonding between the GM and the substrate. As a result, the electronic structure of the valence band of the GM/Ag/Ni(111) system formed reveals a general shift of the graphite π -state peak toward lower binding energies by 1.0–1.5 eV, depending on the actual position in the Brillouin zone. The graphite-like character of the π -band dispersion is retained. The spatial position of the layers of the elements making up the system, namely, C, Ag, and Ni, was established. The system formed was described as a set of layers of graphite and silver and a nickel substrate surface, with metal being present at the same time at boundaries of graphite domains in the form of islands.

(2) We have shown that, in the initial stages of silver intercalation under a GM, the system surface area can be divided into two parts, with and without intercalated

silver atoms, with different electronic structure of the valence bands. It was established that the changes in the spectra in the region of the graphite π states can be considered a superposition of two components corresponding to the clean and saturated states of the system, with their characteristic binding energies. The experimental data obtained enable one to follow the evolution of the electronic structure of the system with variation of the silver concentration under the GM.

(3) It has been established that silver intercalation under a GM on Ni(111) follows the same scenarios under repeated deposition–annealing cycles and under silver deposition at room temperature. Increasing the temperature only intensifies the process of adsorbate penetration into the interlayer space.

(4) It has been shown that the graphite monolayer in this system is a sufficiently stable formation and retains its main geometric and electronic properties in the course of intercalation.

ACKNOWLEDGMENTS

This study was made at the Physical Electronics Laboratory, Fock Institute of Physics, St. Petersburg State University, and supported by the program “Fullerenes and Atomic Clusters” and the INTAS Foundation, project no. 2001-2136.

REFERENCES

1. M. S. Dresselhaus and G. Dresselhaus, *Adv. Phys.* **30**, 139 (1981).
2. A. Nagashima, N. Tejima, and C. Oshima, *Phys. Rev. B* **50**, 17487 (1994).
3. A. Nagashima, K. Nuka, K. Sato, H. Itoh, T. Ichinokawa, C. Oshima, and S. Otani, *Surf. Sci.* **287**, 609 (1993).
4. A. Ya. Tontegode, *Prog. Surf. Sci.* **38**, 201 (1991).
5. N. R. Gall, S. N. Mikhailov, E. V. Rut'kov, and A. Ya. Tontegode, *Surf. Sci.* **226**, 381 (1990).
6. N. R. Gall, E. V. Rut'kov, and A. Ya. Tontegode, *Int. J. Mod. Phys. B* **11**, 1865 (1997).
7. A. Ya. Tontegode and E. V. Rut'kov, *Usp. Fiz. Nauk* **163** (11), 57 (1993) [*Phys. Usp.* **36**, 1053 (1993)].
8. A. M. Shikin, V. K. Adamchuk, S. L. Molodtsov, C. Laubschat, and G. Kaindl, *Phys. Rev. B* **51**, 13586 (1995).
9. A. M. Shikin, S. L. Molodtsov, A. G. Vyatkin, V. K. Adamchuk, N. Franko, M. Martin, and M. C. Aensio, *Surf. Sci.* **429**, 287 (1999).
10. A. M. Shikin, V. K. Adamchuk, S. Siebentritt, K.-H. Rieder, S. L. Molodtsov, and C. Laubschat, *Phys. Rev. B* **61**, 7752 (2000).
11. S. Saito and A. Oshiyama, *Phys. Rev. B* **49**, 17413 (1994).
12. A. M. Shikin, D. Farias, and K.-H. Rieder, *Europhys. Lett.* **44**, 44 (1998).
13. A. M. Shikin, D. Farias, V. K. Adamchuk, and K.-H. Rieder, *Surf. Sci.* **424**, 155 (1999).

14. A. M. Shikin, G. V. Prudnikova, V. K. Adamchuk, F. Moresko, and K.-H. Rieder, *Phys. Rev. B* **62**, 13202 (2000).
15. Yu. S. Dedkov, A. M. Shikin, V. K. Adamchuk, S. L. Molodtsov, C. Laubschat, A. Bauer, and G. Kaindl, *Phys. Rev. B* **64**, 035405 (2001).
16. A. M. Shikin, Yu. S. Dedkov, V. K. Adamchuk, D. Farias, and K.-H. Rieder, *Surf. Sci.* **1**, 1 (2000).
17. D. Farias, A. M. Shikin, K.-H. Rieder, and Yu. S. Dedkov, *J. Phys.: Condens. Matter* **11**, 8453 (1999).
18. D. Farias, K.-H. Rieder, A. M. Shikin, V. K. Adamchuk, T. Tanaka, and C. Oshima, *Surf. Sci.* **454–456**, 437 (2000).
19. V. A. Mozhayskiy, A. Yu. Varykhalov, A. G. Starodubov, A. M. Shikin, S. I. Fedoseenko, and V. K. Adamchuk, *Phys. Low-Dimens. Semicond. Struct.*, No. 1/2, 105 (2003).
20. A. Nagashima, H. Itoh, T. Ichinokawa, C. Oshima, and S. Otani, *Phys. Rev. B* **50**, 4756 (1994).
21. F. Pattney and W. D. Schneider, *Phys. Rev. B* **50**, 17560 (1994).

Translated by G. Skrebtsov

POLYMERS
AND LIQUID CRYSTALS

Photogeneration of Electrons and Holes
in Amorphous Molecular Semiconductors

N. A. Davidenko*, N. G. Kuvshinskii*, S. L. Studzinskii*, N. G. Chuprin*, N. A. Derevyanko**,
A. A. Ishchenko**, and A. J. Al-Kahdymi***

* Shevchenko National University, Vladimirskaya ul. 64, Kiev, 01033 Ukraine

** Institute of Organic Chemistry, National Academy of Sciences of Ukraine, Murmanskaya ul. 5, Kiev, 02094 Ukraine

*** National Technical University of Ukraine, Kiev, 03056 Ukraine

Received March 27, 2003; in final form, August 26, 2003

Abstract—This paper reports on the results of investigations into the photoconducting properties of amorphous molecular semiconductors based on films of two types: (i) poly(styrene) films doped with epoxypropylcarbazole (EPC) and a cationic polymethine dye (PD1) and (ii) poly(styrene) films doped with tetranitrofluorenone (TNF) and an anionic polymethine dye (PD2). Films of the first type possess *p*-type conductivity, whereas films of the second type exhibit *n*-type conductivity. It is found that, for films with *n*-type conductivity, unlike films with *p*-type conductivity, the activation energy of photogeneration of mobile charge carriers decreases with a decrease in the optical wavelength in the absorption range of the dyes. The possible mechanisms of the influence of the photoexcitation energy on the initial distance between charge carriers in electron–hole pairs are analyzed. The inference is made that, when the excess thermal energy of excited dye molecules dissipates at a low rate, the distance between the photogenerated electrons and photogeneration centers increases as compared to the distance between the photogenerated holes and photogeneration centers due to the electron–nucleus interaction. © 2004 MAIK “Nauka/Interperiodica”.

1. INTRODUCTION

Since amorphous molecular semiconductors can change their optical and electrical characteristics under exposure to light in the visible and near-IR ranges, these materials are widely used as media for recording and displaying optical information, converting solar energy, and controlling light emission [1–3]. Amorphous molecular semiconductors are solid solutions in which molecules have no translational symmetry [4]. In the general case, these semiconductors can be considered true solutions that involve three types of compounds in a neutral film-forming binder. Molecules of two compounds in a solid solution form transfer bands of electrons and holes, whereas molecules of the third compound serve as centers of photogeneration and (or) recombination of charge carriers. The electron-transfer band is formed by the lowest unoccupied molecular orbitals (LUMOs) of molecules that possess acceptor properties and are separated by a mean distance $R_n = N_a^{-1/3}$ (where N_a is the concentration of acceptor molecules in an amorphous molecular semiconductor). The hole-transfer band is formed by the highest occupied molecular orbitals (HOMOs) of molecules that exhibit donor properties and are separated by a mean distance $R_p = N_d^{-1/3}$ (where N_d is the concentration of donor molecules in an amorphous molecular semiconductor). The electronic levels of the molecules forming the charge-transfer bands are not split and remain local. Note that,

in this case, the localization length α_n of the electron wave functions of acceptor molecules can differ from the localization length α_p of the hole wave functions of donor molecules.

The transport of charge carriers in the transfer band occurs through tunneling transitions between local levels of the molecules. The majority of the amorphous molecular semiconductors used in practice [5] (with only a few exceptions [4]) are characterized by the following empirical dependences of the electron mobility μ_n and the hole mobility μ_p in the corresponding transfer bands on the external electric field strength E and the temperature T :

$$\mu_n \sim R_n^2 \exp(-2R_n/\alpha_n) \times \exp(-(W_{0n} - \beta E^{1/2})(1/T - 1/T_0)/k_B), \quad (1)$$

$$\mu_p \sim R_p^2 \exp(-2R_p/\alpha_p) \times \exp(-(W_{0p} - \beta E^{1/2})(1/T - 1/T_0)/k_B). \quad (2)$$

Here, W_{0n} and W_{0p} are the activation energies of the electron and hole mobilities in a zero electric field ($E = 0$), respectively; β is the coefficient numerically coinciding with the theoretical value of the Pool–Frenkel constant; k is the Boltzmann constant; and T_0 is the temperature corresponding to the intersection point of the experimental dependences (extrapolated to the high-temperature range) of $\log(\mu_n)$ and $\log(\mu_p)$ on $1/T$ at

different electric-field strengths E . It is worth noting that the first factor in relationships (1) and (2) has a form similar to the expression for the probability of the tunneling transition of an electron between localized states. Furthermore, the second factor has a form similar to the expression for the probability that, during its motion in an external electric field, the charge carrier overcomes the potential barrier produced by an oppositely charged center. Consequently, the transport of charge carriers within the transfer bands can be treated as a process involving diffusion inside molecules and hoppings (tunneling) between these molecules.

When a photon with energy $h\nu$ is absorbed by a photogeneration center in an amorphous molecular semiconductor, an electron and a hole appear to be separated and can leave the photogeneration center. In this case, the electron and the hole pass into the corresponding charge-transfer band and form a Coulomb-bound electron-hole pair with an initial distance r_0 between charge carriers. The quantum yield Φ_0 of the formation of an electron-hole pair is determined by the intramolecular conversion and interconversion of the molecule of the photogeneration center, the ratio of the HOMO and LUMO energies of the photogeneration center to the energies of the corresponding molecular orbitals of the molecules forming the electron-transfer and hole-transfer bands, steric factors, the distance from the photogeneration center to the molecules of the transfer bands, and the spin conversion in the electron-hole center. The charge carriers in the electron-hole center either can be widely spaced, thus producing free non-equilibrium photoconduction centers, or can recombine at the photogeneration center. For the majority of amorphous molecular semiconductors, the quantum yield η of photogeneration of free charge carriers can be represented by the empirical relationship [5]

$$\eta \sim \Phi_0 R_n R_p \exp(-R_n/\alpha_n - R_p/\alpha_p) \times \exp(-(W_{\text{OPH}} - \beta E^{1/2})(1/T - 1/T_0)/k_B), \quad (3)$$

where W_{OPH} is the activation energy of photogeneration of free charge carriers in a zero electric field ($E = 0$) and T_0 is the temperature corresponding to the intersection point of the experimental dependences (extrapolated to the high-temperature range) of $\log(\eta)$ on $1/T$ at different electric-field strengths E . It should be noted that, according to the model of two-stage photogeneration of charge carriers through the formation of electron-hole pairs and their dissociation, the activation energy W_{OPH} can be identified with the energy of the Coulomb interaction between the electron and the hole in the electron-hole pair [1, 5]:

$$W_{\text{OPH}} = q^2/4\pi\epsilon_0\epsilon r_0, \quad (4)$$

where q is the elementary charge, ϵ_0 is the permittivity of free space, and ϵ is the permittivity.

The above scheme of photogeneration, transfer, and recombination of charge carriers in amorphous molecular semiconductors very roughly reflects the real situation, but it is sufficient for demonstrating the substantial differences between these processes and those occurring in crystalline and amorphous vitreous semiconductors. This scheme can serve as an illustration of the possible ways of preparing amorphous molecular semiconductors used both in media for recording optical information (electrography, holography) and in photoelectric converters. The basic requirement placed on these semiconductor materials consists in increasing the efficiency of photogeneration of electron-hole pairs with a maximum initial distance between charge carriers. However, the problem concerning the dependence of these parameters on the type of charge carrier (a hole or an electron) that is the first to leave the photogeneration center during the formation of an electron-hole pair has received little attention in the literature. At the same time, this problem could turn out to be important, because an electron escapes from an excited center of photogeneration upon intermolecular electronic transition from the LUMO of this center to the LUMO of an acceptor molecule, whereas a hole escapes upon intermolecular electronic transition from the HOMO of the donor molecule to the HOMO of the photogeneration center. These processes are not identical, especially as the electron occupying the LUMO of the photogeneration center rather than the HOMO of the donor molecule is involved in relaxation of the excited state of the center. In this respect, the purpose of the present work was to elucidate how the activation energy of photogeneration of free charge carriers and the initial distance between charge carriers in electron-hole pairs depend on the type of photogenerated carries (electrons or holes) and also to refine the model of photogeneration of electrons and holes.

2. SAMPLE PREPARATION AND EXPERIMENTAL TECHNIQUE

For this purpose, we prepared amorphous molecular semiconductors based on films of two types: (i) poly(styrene) (PS) films doped with a cationic polymethine dye (PD1) and epoxypropylcarbazole (EPC) as an electron donor and (ii) poly(styrene) films doped with an anionic polymethine dye (PD2) and tetranitrofluorenone (TNF) as an electron acceptor. The structural formulas of the dopant molecules are presented in Fig. 1.

Poly(styrene) films are transparent, do not exhibit intrinsic photoconductivity in the visible and near-IR ranges, can easily be prepared, and are convenient objects for investigating the intermolecular interactions upon their doping with organic compounds. Polymethine dyes serve as sensitizers of photoconductivity and electroluminescence in photoconducting polymers, because they can efficiently convert the luminous energy, are characterized by intense absorption and

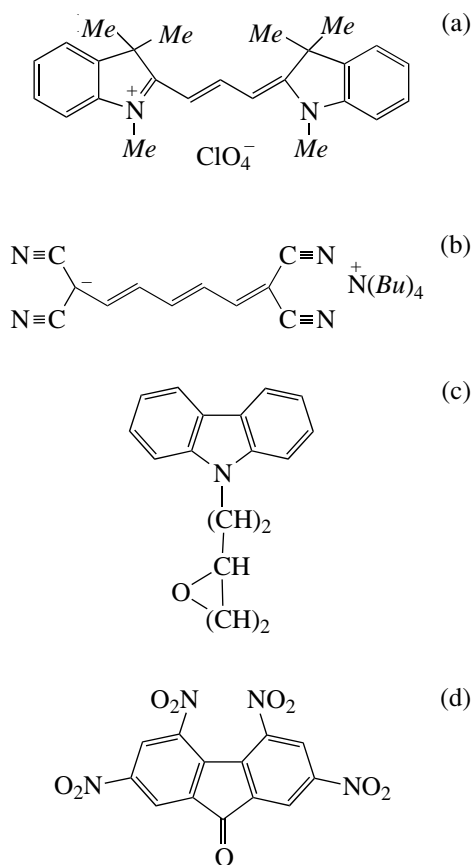


Fig. 1. Structural formulas of (a) cationic polymethine dye, (b) anionic polymethine dye, (c) epoxypropylcarbazole, and (d) tetranitrofluorenone molecules.

luminescence bands over a wide spectral range [6], and are suitable for simulating the dependences of the photoelectric properties of amorphous molecular semiconductors on the molecular structure. The choice of the polymethine dyes PD1 and PD2 as the objects of our investigation was made for the following reasons. In the visible range, the shapes and maxima of the electronic absorption spectra of these dyes in poly(styrene) films are similar to each other (Fig. 2) and are determined by only one electronic transition. On the other hand, in amorphous molecular semiconductors, the PD1 dye molecules play the role of photogeneration centers of holes, whereas the PD2 dye molecules serve as photogeneration centers of electrons. The last circumstance is associated both with the opposite electrical charges of the colored ionic organic structures PD1 and PD2 and with the substantial difference in their HOMOs and LUMOs [7]. Amorphous molecular semiconductors containing carbazole groups possess *p*-type conductivity, and films based on poly(*N*-vinylcarbazole) or poly(*N*-epoxypropylcarbazole) have found wide application in holographic and electrographic recording media [1, 4]. Therefore, polymer films doped with the EPC monomer are convenient model objects for use in

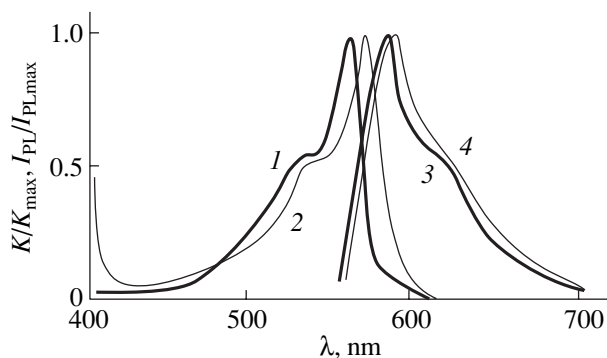


Fig. 2. (1, 2) Optical absorption spectra and (3, 4) photoluminescence spectra of the polymer films: (1, 3) PS + 30 mol % EPC + 1 mol % PD1 and (2, 4) PS + 20 mol % TNF + 1 mol % PD2.

studying the intermolecular transfer of holes. Fluorenone-based electron acceptors are used for providing *n*-type conductivity in amorphous molecular semiconductors, and, consequently, polymer films doped with TNF are appropriate for investigating the intermolecular transfer of electrons.

In order to determine the dependences of the activation energy of photogeneration and the initial distance between charge carriers in electron-hole pairs on the type of mobile carriers that are the first to leave the photogeneration centers upon the formation of electron-hole pairs, the activation energies of photogeneration of holes and electrons were investigated as functions of the electric field strength E and the wavelength of light used for photogenerating charge carriers. The activation energy of photogeneration of holes W_{PHp} was determined for the films PS + N_d mol % EPC + N_1 mol % PD1 with unipolar *p*-type conductivity, whereas the activation energy of photogeneration of electrons W_{PHe} was obtained for the films PS + N_d mol % TNF + N_2 mol % PD2 with unipolar *n*-type conductivity.

The optical absorption, photoluminescence, and photoconductivity spectra of the polymer films PS + N_d mol % EPC + N_1 mol % PD1 and PS + N_d mol % TNF + N_2 mol % PD2 were measured in the wavelength range $\lambda = 400$ – 1000 nm. The concentrations of donors N_d , acceptors N_a , and dyes N_1 or N_2 were varied from zero to 30, 20, and 1% with respect to the polymer weight, respectively. The samples to be studied were prepared by drying polymer solutions with dopants in dichloroethane, which were spread over the surfaces of glass substrates either with an SnO₂ transparent conducting layer or without this layer. The drying was performed in a desiccator at a temperature of 80°C for 4 h. The thickness of the polymer films prepared was measured with the use of an MII-4 interference microscope and was equal to 0.6–3 μm . The samples without conducting layers were used for recording the spectra of the absorption coefficient κ and the photoluminescence

intensity I_{PL} of polymers films on a KSVIP-23 spectrometric computer complex. In order to prepare samples with a sandwich structure, an aluminum film was thermally evaporated on the surface of polymer film samples with SnO_2 layers in a vacuum chamber. The sandwich samples thus prepared were used to measure the photocurrent density j_{PH} upon exposure to monochromatic light. For these purposes, the samples were exposed to monochromatic light from an incandescent lamp with a set of optical filters. The light intensity I was varied in the range $0.2\text{--}5\text{ W/m}^2$ with the use of neutral optical filters. The strength E of the electric field induced in the polymer films by applying the electrical voltage across the Al and SnO_2 contacts was measured in the range $(1\text{--}20) \times 10^7\text{ V/m}$. The kinetics of photoconduction during irradiation and after its termination was recorded on a storage oscilloscope. The dependences of the photocurrent density j_{PH} on the electric field strength E and the temperature T were measured using the samples placed in a thermostat with an optical window whose temperature could be changed from 293 to 343 K. The activation energies of photogeneration of holes W_{PHp} and electrons W_{PHe} were determined from the experimental temperature dependences of the photocurrent density j_{PH} .

3. EXPERIMENTAL RESULTS

The polymer films $\text{PS} + N_d\text{ mol \% EPC}$ do not exhibit optical absorption in the wavelength range $\lambda > 400\text{ nm}$. As can be seen from Fig. 2, the optical absorption spectra of the polymer films $\text{PS} + N_a\text{ mol \% TNF}$ are characterized by the red fundamental absorption edge of TNF (curve 2) [5]. The absorption coefficient κ increases in direct proportion with the acceptor concentration N_a . However, the shape of the absorption band with an increase in the acceptor concentration remains unchanged. This suggests that the EPC and TNF molecules have a weak tendency toward aggregation in the poly(styrene) films [6]. Therefore, these films can be treated as solid solutions. In the sandwich samples containing the polymer films $\text{PS} + N_d\text{ mol \% EPC}$ and $\text{PS} + N_a\text{ mol \% TNF}$, no photocurrent is observed in the studied ranges of electric field strengths E , temperatures T , and wavelengths λ .

The optical absorption spectra of the polymer films $\text{PS} + N_d\text{ mol \% EPC} + N_1\text{ mol \% PD1}$ and $\text{PS} + N_a\text{ mol \% TNF} + N_2\text{ mol \% PD2}$ exhibit new absorption bands (Fig. 2, curves 1, 2) due to the electronic absorption of PD1 and PD2, respectively. The normalized absorption and photoluminescence spectra of these dyes have a symmetric shape and only slightly change with a variation in the dopant concentration in poly(styrene). Analysis of the above spectra shows that the effects of dye aggregation and the formation of charge-transfer complexes between EPC and PD1 or TNF and PD2 are insignificant in the films under investigation.

Therefore, these films can also be considered solid solutions.

In the sandwich samples with the polymer films $\text{PS} + N_d\text{ mol \% EPC} + N_1\text{ mol \% PD1}$ and $\text{PS} + N_a\text{ mol \% TNF} + N_2\text{ mol \% PD2}$, the photoconductivity is observed in the absorption range of the dyes. After the onset of exposure of these samples to monochromatic light in an external electric field, the electric current in the amorphous molecular semiconductor increases and, within 40–60 s, reaches a quasi-stationary value j_{PH} , which only slightly changes in the course of further exposure. After termination of exposure, the electric current decreases. The kinetic curves characterizing the rise and relaxation of the photocurrent are symmetric. At constant values of E and I , the photocurrent density j_{PH} increases with an increase in the concentration N_d and (or) N_a . The dependences of the photocurrent density j_{PH} on the electric field strength E can be approximated by straight lines in the $E^{1/2}\text{--}\log j_{PH}$ coordinates and then can be analytically described by an expression similar to relationship (3). The activation energies of photocurrent W_{PHp} and W_{PHe} , which were calculated from the slopes of the dependences of $\log j_{PH}$ on $1/T$, decrease with an increase in the electric field strength E . The dependences $W_{PHp}(E)$ and $W_{PHe}(E)$ in the $E^{1/2}\text{--}W_{PHp}$ and $E^{1/2}\text{--}W_{PHe}$ coordinates exhibit a linear behavior, and their slopes are equal to $(4.8 \pm 0.3) \times 10^{-5}\text{ eV (V/m)}^{-1/2}$, which is close to the Pool–Frenkel constant [4, 8]. The portions of these dependences extrapolated to $E = 0$ intersect the axis of ordinates. This allows one to determine the activation energies of photogeneration of holes and electrons W_{0PHp} and W_{0PHe} in a zero electric field and to calculate the distances between charge carriers in electron–hole pairs before dissociation.

However, a decrease in the wavelength λ at constant electric field strengths E leads to an insignificant change in the activation energy of hole photogeneration W_{PHp} and a decrease in the activation energy of electron photogeneration W_{PHe} . It turned out that, as the wavelength λ decreased, the activation energy of hole photogeneration and the initial distance r_{0p} between charge carriers in electron–hole pairs only slightly changed for the polymer films $\text{PS} + N_d\text{ mol \% EPC} + N_1\text{ mol \% PD1}$, whereas the activation energy of electron photogeneration decreased and the initial distance r_{0e} between charge carriers in electron–hole pairs increased for the polymer films $\text{PS} + N_a\text{ mol \% TNF} + N_2\text{ mol \% PD2}$. For example, at optical wavelengths of 540, 445, and 420 nm, we obtained $W_{0PHp} = (0.97 \pm 0.05)\text{ eV}$ and $r_{0p} = 5.6 \pm 0.1\text{ \AA}$ for samples with the polymer films $\text{PS} + 30\text{ mol \% EPC} + 1\text{ mol \% PD1}$. For samples with the polymer films $\text{PS} + 20\text{ mol \% TNF} + 1\text{ mol \% PD2}$ upon exposure to light at the same wavelengths, we obtained the following parameters: $W_{0PHe1} = (1.05 \pm 0.05)\text{ eV}$ and $r_{0e1} = (5.4 \pm 0.1)\text{ \AA}$ at $\lambda = 540\text{ nm}$,

$W_{\text{OPHe}2} = (0.72 \pm 0.05)$ eV and $r_{0e2} = (7.8 \pm 0.1)$ Å at $\lambda = 445$ nm, and $W_{\text{OPHe}3} = (0.54 \pm 0.05)$ eV and $r_{0e3} = (10.5 \pm 0.1)$ Å at $\lambda = 420$ nm. Note that the distances between charge carriers in electron–hole pairs were calculated using the permittivity $\epsilon = 2.55$ for poly(styrene) under the assumption that this quantity is approximately equal for different electron–hole pairs. Indeed, since the samples under investigation can be treated as solid solutions, the nearest environments of donor, acceptor, and dye molecules predominantly contain monomer units of the poly(styrene) solid binder.

4. DISCUSSION

Thus, it is established that the experimental dependences of $\log j_{\text{PH}}$ on $E^{1/2}$ exhibit a linear behavior, the coefficient β in relationship (3) is close to the theoretical value of the Pool–Frenkel constant, and the dependences of j_{PH} on E can be described by relationship (3) for amorphous molecular semiconductor films with polymethine dyes PD1 and PD2. Therefore, the experimental results obtained for these films can be analyzed in the framework of the previously developed models of photogeneration and transfer of charge carriers in amorphous molecular semiconductor films [4, 8]. According to the model concepts, the photogeneration of charge carriers from photogeneration centers (in our case, the role of photogeneration centers is played by dye molecules) proceeds in two stages. At the first stage of the photogeneration, the absorption of a photon by a dye molecule leads to the formation of a bound electron–hole pair. At the second stage of the photogeneration, the electron–hole pair dissociates into free charge carriers under the action of heating and an external electric field.

The first and second stages of the photogeneration are completed at the instant of time when, after absorption of a photon by the photogeneration center, the charge carrier transferred from this center (dye molecule) to a molecule of the corresponding transfer band reaches thermal equilibrium with the environment. Prior to this instant of time, the following processes occur in sequence: (i) absorption of the photon and excitation of the dye molecule, (ii) intramolecular conversion in the excited dye molecule and the intermolecular electronic transition from the dye molecule to a molecule of the corresponding transfer band, and (iii) partial dissipation of the energy of the excited dye molecule and (or) the charge carrier escaping from it. It is owing to these processes that the charge carrier can appear to be either at a shorter distance or at a longer distance from the photogeneration center. In the experiments, this difference manifests itself in different activation energies of photogeneration in a zero electric field. In this respect, in order to explain the weak dependence of the activation energy for photogeneration of holes on the wavelength of light used for photogenerating charge carriers, on the one hand, and the

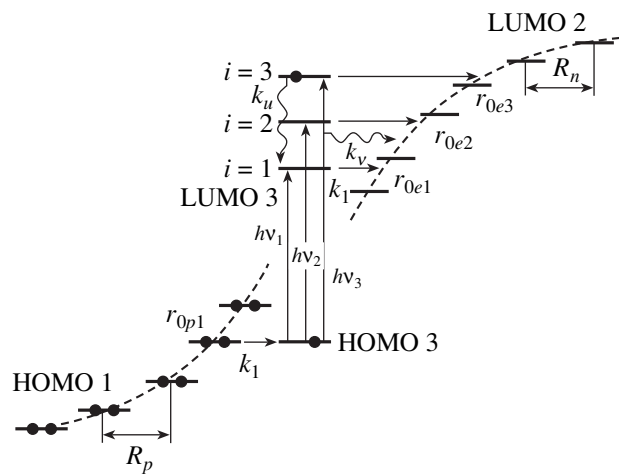


Fig. 3. Diagram of electronic transitions during photogeneration of holes and electrons. HOMO 1 is the highest occupied molecular orbital of donor molecules; LUMO 2 is the lowest unoccupied molecular orbital of acceptor molecules; and HOMO 3 and LUMO 3 are the highest occupied and lowest unoccupied molecular orbitals of dye molecules, respectively.

experimentally observed decrease in the activation energy for photogeneration of electrons with a decrease in the wavelength, on the other hand, we will analyze the possible mechanisms of formation of electron–hole pairs.

In the visible range, the PD1 and PD2 dyes used in the aforementioned experiments are characterized by only one electronic transition. In the temperature range covered, this transition for an individual dye molecule can be interpreted as the intramolecular transition of an electron from the lower vibrational level of the HOMO to the i th discrete vibrational level of the LUMO. The correlation between the processes of dissipation of the excitation energy and photogeneration of charge carriers can be illustrated by the diagram shown in Fig. 3. For this purpose, we introduced the following designations: $h\nu_i$ and P_i are the photon energy and the efficiency of photoexcitation of a dye molecule from the singlet ground state S_0 to the unrelaxed singlet excited state S_i , respectively; N_i is the concentration of dye molecules in the unrelaxed state S_i ; $h\nu_1$ is the photon energy corresponding to the 0–0 transition; $U = h\nu_i - h\nu_1$ is the difference between the photon energies of excitation and 0–0 transition; k_{ij} is the rate constant of the internal conversion of the excited dye molecule from the S_i state to the S_1 state; k_v is the rate constant of the dissipation of the energy U to the environment; k_{SU} and k_S are the rate constants of the nonradiative and radiative S_1 – S_0 transitions, respectively; n_i is the concentration of electron–hole pairs in which the charge carrier in a molecule of the corresponding transfer band is formed through the intermolecular electronic transition from the S_i state or has a potential energy identical to that of

the electron in this state and is located at the distance r_{0i} from the photogeneration center; k_i is the rate constant of the formation of an electron–hole pair from the S_i state; k_{-i} is the rate constant of the recombination of an electron–hole pair through the S_i state; and k_{Di} is the rate constant of the diffusion of charge carriers in the corresponding transfer band outward from the photogeneration center.

For the majority of organic dyes and related compounds, the relaxation of excited states to the ground state proceeds in the course of the S_1 – S_0 transition [6]. Therefore, it can be assumed that the energy U of the excited dye molecule dissipates either through the transfer of the energy of thermal vibrations from this dye molecule to adjacent molecules [9] or as a result of an increase in the kinetic energy of the charge carrier upon intermolecular electronic transition during the formation of an electron–hole pair [10]. The latter case was considered in [10] for explaining the dependences of the activation energy W_{OPHe} and the distance r_{0e} on the photon energy $h\nu_i$ for organic crystals. In [10], it was assumed that electrons are photogenerated from the highest excited states of molecules. In the course of the formation of an electron–hole pair, the electron moves away from the photogeneration center in the conduction band of the crystal and loses excess kinetic energy due to the electron–phonon interaction with the crystal lattice. An increase in the excitation energy is accompanied by an increase in the kinetic energy of the electron and in the distance r_{0e} . However, in our earlier works [11–13], we demonstrated that the intermolecular electronic transitions upon photogeneration or recombination of charge carriers in amorphous molecular semiconductors occur through electron tunneling between two molecules, namely, between the photogeneration center and the molecule of the corresponding transfer band. This implies that, when the charge carrier moves away from the photogeneration center, the energy of this carrier changes only as a result of the interaction with the electron–nucleus system of molecules involved in the corresponding transfer band. Moreover, it should be emphasized once again that amorphous molecular semiconductors differ from organic crystals in that their molecules in the transfer bands have no translational symmetry, do not form broad energy bands and, at low concentrations, are surrounded by the polymer binder.

The mechanism of photogeneration of charge carriers in amorphous molecular semiconductors can be refined using a system of kinetic equations describing the changes in the concentrations of excited dye molecules and electron–hole pairs with variations in the distance r_{0i} between the charge carriers:

$$\begin{aligned} \frac{dN_i}{dt} = & P_i + N_{i+1}k_U + n_i k_{-i} N \\ & - N_i(k_U + (k_{SU} + k_S)\delta_{i1} + k_i), \end{aligned} \quad (5)$$

$$\frac{dn_i}{dt} = N_i k_i + n_{i-1} k_{Di-1} - n_i(k_{-i} + k_{Di}), \quad (6)$$

where $\delta_{i1} = 1$ ($i = 1$) and 0 ($i > 1$).

The internal conversion and the S_1 – S_0 transitions are competing processes in the course of the formation of an electron–hole pair from excited states of the photogeneration center. Let us now analyze the system of equations (5) and (6) for different relationships between the rate constants of the corresponding processes.

(1) For $k_U \gg k_i$ and $(k_{SU} + k_S) \gg k_i$, electron–hole pairs cannot undergo photogeneration, because the relaxation of excited states and the S_1 – S_0 transition are the fastest processes.

(2) For $k_V \gg k_U > k_i > (k_{SU} + k_S)$, the electron transfer from the excited dye molecule to the acceptor molecule can occur only from the S_1 state irrespective of the photoexcitation energy. The excess energy U is completely dissipated by the time the electron–hole pair is formed. For holes and electrons, the concentration distributions of electron–hole pairs over distances between charge carriers in the pairs are described by a delta function and these distributions do not depend on the photon energy $h\nu_i$. Most likely, this is not the case for our experiments, because such a dependence on the photon energy $h\nu_i$ is observed for amorphous molecular semiconductors based on the polymer films PS + 20 mol % TNF + 1 mol % PD2.

(3) For $k_i \gg k_V > k_U > (k_{SU} + k_S)$, the excited center of photogeneration has no time to undergo an internal conversion within the time interval between the absorption of the photon with energy $h\nu_i$ and the formation of an electron–hole pair; in this case, the electron is involved in an intermolecular transition from the S_i excited state during the formation of an electron–hole pair. Upon photogeneration of a hole, the intermolecular transition occurs through the transfer of an electron from the HOMO of the donor molecule (in the hole transfer band) to the partially occupied HOMO of the dye molecule located at the distance r_{0p} from the donor molecule (Fig. 3). Since the photoexcitation energy $h\nu_i$ does not affect the HOMO energy of the donor and dye molecules, the distance r_{0p} does not depend on the energy $h\nu_i$. This inference is confirmed by our experimental data obtained for samples with the polymer films PS + 30 mol % EPC + 1 mol % PD1, for which an increase in the energy $h\nu$ does not lead to a change in the activation energy of photogeneration of charge carriers.

For the above relationship between the rate constants with allowance made for the tunneling mechanism of formation of electron–hole pairs, it can be expected that the electron escaping from the excited dye molecule should transfer to the acceptor molecule (in the electron transfer band) located at a distance r_{0ei} from the dye molecule. Consequently, an increase in the photon energy should result in an increase in the distance between the photogeneration center and the electron (Fig. 3). However, in the case of samples with

the polymer films PS + N_a mol % TNF + N_2 mol % PD2, the increase in the distance r_{0ei} with an increase in the photon energy $h\nu_i$ is not nearly so appreciable as could be expected. In particular, for samples with the polymer films PS + 20 mol % TNF + 1 mol % PD2 upon exposure to light at wavelengths of 540, 445, and 420 nm, the activation energies of photogeneration of electrons in a zero electric field and the distances r_{0ei} should be as follows: $W_{0PHe1} = 1.05$ eV and $r_{0e1} = 5.4$ Å at $\lambda = 540$ nm, $W_{0PHe2} = 0.56$ eV and $r_{0e2} = 10.1$ Å at $\lambda = 445$ nm, and $W_{0PHe3} = 0.4$ eV and $r_{0e3} = 14.2$ Å at $\lambda = 420$ nm. Here, the activation energy of photogeneration of electrons is determined as the difference between the activation energy of photogeneration upon the formation of an electron-hole pair from the S_1 state and the energy $h\nu_i - h\nu_1$. The photon energy $h\nu_i$ is calculated from the wavelength λ corresponding to the intersection point of the normalized dependences of the absorption coefficient and the photoluminescence intensity for the amorphous molecular semiconductor films (Fig. 2). The distances r_{0e2} and r_{0e3} thus calculated turned out to be substantially larger than those determined from the experimental temperature dependence of the photocurrent density j_{PH} .

(4) For $k_U > k_i > k_V > (k_{SU} + k_S)$, the excited center of photogeneration has time to undergo an internal conversion within the time interval between the absorption of the photon with energy $h\nu_i$ and the formation of an electron-hole pair. The formation of an electron-hole pair from the S_1 excited state occurs concurrently with the dissipation of the thermal energy U . In the course of intermolecular vibrational relaxation, the excited molecule of the photogeneration center nonradiatively transfers excess absorbed light energy to vibrational states of the surrounding polymer molecules. The higher the mobility of polymer chains and the higher the elasticity of the polymer, the more efficient the transfer of the excess vibrational energy (heat transfer) from the dye molecule to polymer molecules and donor and (or) acceptor molecules [14]. This can lead to a considerable increase in the distance between the charge carriers in the electron-hole pair, because the intermolecular electronic transition proceeds between the molecule of the photogeneration center and molecules of the transfer band, which, at thermal energies $U > 0$, are not at thermal equilibrium and have excess vibrational energy. The excess thermal energy depends on the dissipation mechanism and the distance from the photogeneration center and favors an increase in the distance between the mobile charge carrier in the electron-hole pair and the photogeneration center to a distance at which all the molecules are at thermal equilibrium. For identical energies U , mechanisms of dissipation of excess thermal energy, rate constants k_i and k_V , and numbers of molecules forming the nearest environment of an individual molecule, the distance r_{0ei} is larger than the distance r_{0pi} . This difference can be explained as

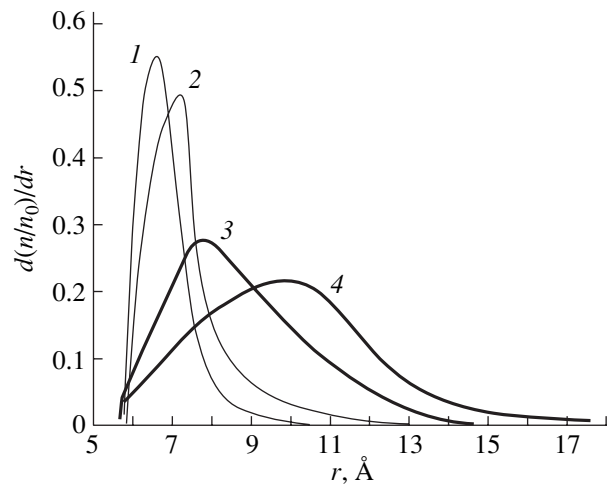


Fig. 4. Dependences of $d(n/n_0)/dr$ on r for amorphous molecular semiconductors based on the films (1, 2) PS + 30 mol % EPC + 1 mol % PD1 and (3, 4) PS + 20 mol % TNF + 1 mol % PD2 under exposure to light at wavelengths of (1, 3) 445 nm ($U = 0.49$ eV) and (2, 4) 420 nm ($U = 0.65$ eV).

follows. In the course of photogeneration of electrons, the intermolecular electronic transitions occur between “hot” and “cold” molecules. On the other hand, during the photogeneration of holes, the intermolecular transitions proceed through the transfer of an electron from the HOMO of the donor molecule (in the hole transfer band), which is located far from the photogeneration center and acquires a small excess of thermal energy from it. Therefore, the hole moves away from the photogeneration center through the intermolecular electronic transitions between cold and hot molecules.

It is important to note that the distribution of electron-hole pairs over distances r between charge carriers cannot be described by a delta function and depends on the thermal energy U . Figure 4 shows the numerically simulated distribution functions $n_i(r)$ at different energies U for amorphous molecular semiconductors based on the polymer films PS + 30 mol % EPC + 1 mol % PD1 (curves 1, 2) and PS + 20 mol % TNF + 1 mol % PD2 (curves 3, 4). These distribution functions were obtained by solving the system of equations (5) and (6) under the following conditions: $T = 293$ K, $k_{-i} \ll k_i$, $k_i \sim k_S = 5 \times 10^{10} \text{ s}^{-1}$ [6], the number of molecules forming the nearest environment of an individual molecule is equal to six, and $k_{Di} = v_D \exp[-q^2(1/r_i - 1/r_{i+1})/4\pi\epsilon_0\epsilon(k_B T + U/m)]$. Here, $\epsilon = 2.55$; v_D is the frequency factor, which accounts for the diffusion of charge carriers inside molecules and the tunneling of charge carriers between molecules (this factor was taken to be close to 10^{12} s^{-1} [12]); and m is the number of events of dissipation of the thermal energy U from molecules by the instant of time t with the rate constant $k_V = 5 \times 10^{10} \text{ s}^{-1}$ [9]. The thermal equilibrium condition was assumed to be $U/mk_B = 1$ K. It was found that, as

the energies $h\nu$ and U increase, the mean distance between the photogenerated electron and the photogeneration center increases to a greater extent than the corresponding distance in the case of photogeneration of holes. This is in agreement with the aforementioned experimental dependence of the photocurrent density j_{PH} on the temperature for the amorphous molecular semiconductors under investigation.

5. CONCLUSIONS

Thus, the performed analysis of the experimental results made it possible to interpret the dependences of the activation energy for photogeneration of charge carriers in amorphous molecular semiconductors on the optical wavelength and to propose practical recommendations for the choice of amorphous molecular semiconductor materials with a high quantum yield of photogeneration of charge carriers in the short-wavelength range of the optical absorption spectrum. It is our opinion that, in amorphous molecular semiconductors, the photogeneration of mobile charge carriers occurs through the electron–nucleus interaction and that the dissipation of excess thermal energy U can favor an increase in the mean distance between charge carriers in electron–hole pairs. This effect is more pronounced in amorphous molecular semiconductors with n -type conductivity and is less pronounced in amorphous molecular semiconductors with p -type conductivity. Therefore, in order to increase the quantum yield of photogeneration of charge carriers, it is necessary to choose molecules of photogeneration centers, electron donors, electron acceptors, and polymer binders in such a way as to ensure a relatively low rate of heat exchange between these molecules. One way of doing this is to increase the rigidity of molecules forming amorphous molecular semiconductors.

REFERENCES

1. P. M. Borsinberger and D. S. Weiss, *Photoreceptors for Xerography* (Marcel Dekker, New York, 1998).
2. V. Ya. Kabanov, *Khim. Vys. Énerg.* **34** (4), 243 (2000).
3. J. Rostalski and D. Meissner, *Sol. Energy Mater. Sol. Cells* **61**, 87 (2000).
4. D. Hertel, H. Bassler, U. Scherf, and H. Horhold, *J. Chem. Phys.* **110**, 9214 (1999).
5. N. G. Kuvshinskiĭ, N. A. Davidenko, and V. M. Komko, *Physics of Amorphous Molecular Semiconductors* (Lybid', Kiev, 1994).
6. A. A. Ishchenko, *Structure and Spectral–Luminescent Properties of Polymethine Dyes* (Naukova Dumka, Kiev, 1994).
7. N. A. Davidenko and A. A. Ishchenko, *Teor. Éksp. Khim.* **38** (2), 84 (2002).
8. M. Pope and C. E. Swenberg, *Electronic Processes in Organic Crystals* (Clarendon, Oxford, 1982).
9. V. A. Gaĭsenok and A. M. Sarzhevskii, *Anisotropy of Absorption and Luminescence of Polyatomic Molecules* (Minsk Univ., Minsk, 1986).
10. É. A. Silin'sh, M. V. Kurik, and V. Chapek, *Electronic Processes in Organic Molecular Crystals: Localization and Polarization Phenomena* (Zinatne, Riga, 1988).
11. N. A. Davidenko and N. G. Kuvshinsky, *Inf. Rec. Mats.* **21**, 185 (1993).
12. A. K. Kadashchuk, N. I. Ostapenko, N. A. Davidenko, N. G. Kuvshinskiĭ, and N. V. Lukashenko, *Fiz. Tverd. Tela* (St. Petersburg) **39** (7), 1183 (1997) [*Phys. Solid State* **39**, 1047 (1997)].
13. N. A. Davidenko, S. L. Studzinskiĭ, N. A. Derevyanko, A. A. Ishchenko, Yu. A. Skryshevskii, and A. J. Al-Kahdymi, *Fiz. Tekh. Poluprovodn.* (St. Petersburg) **36** (10), 1248 (2002) [*Semiconductors* **36**, 1169 (2002)].
14. V. I. Bezrodnyĭ and A. A. Ishchenko, *Kvantovaya Élektron.* (Moscow) **30**, 1043 (2000).

Translated by O. Borovik-Romanova

POLYMERS
AND LIQUID CRYSTALS

Paramagnetic Centers in Nonmetallic Amorphous
Polyphthalocyanines

Yu. A. Koksharov* and A. I. Sherle**

* Moscow State University, Vorob'evy gory, Moscow, 119992 Russia

e-mail: koksharo@epr.phys.msu.ru

** Semenov Institute of Chemical Physics, Russian Academy of Sciences, ul. Kosygina 4, Moscow, 117977 Russia

Received November 24, 2003

Abstract—Electron paramagnetic resonance (EPR) spectra of nonmetallic amorphous polyphthalocyanines are investigated in the temperature range 295–500 K. The EPR spectrum of nonmetallic amorphous polyphthalocyanine samples at room temperature prior to heating is a narrow singlet of approximately Lorentzian shape with a linewidth $\Delta H_{pp} \approx 1.7$ Oe, a splitting factor $g = 2.00$, and an intensity $I_{EPR} \approx 10^{17}$ spins/g. It is found that the intensity and linewidth of the EPR spectrum increase with increasing temperature. Beginning with a characteristic temperature T_1 , both parameters, ΔH_{pp} and I_{EPR} , become dependent on time (under isothermal conditions). Computer calculations of the spectra demonstrate that the EPR spectrum can be represented as a superposition of two lines with substantially differing parameters whose dependences on the temperature and microwave power also differ significantly. The possible reasons for the existence of electron paramagnetic resonance centers of two types with different degrees of delocalization of a charge carrier with a magnetic moment in nonmetallic amorphous polyphthalocyanines are discussed. © 2004 MAIK “Nauka/Interperiodica”.

1. INTRODUCTION

Polyphthalocyanines are semiconductor organic materials that exhibit a great variety of interesting and useful properties. These materials have found extensive application as dyes (for example, in modern laser disks), catalysts, and active elements in gas sensors and hold considerable promise for use in molecular electronics. It is known that phthalocyanine molecules are characterized by a high thermal stability. Owing to this remarkable property, it has become possible to prepare high-purity thin films through thermal evaporation of phthalocyanines. Although phthalocyanines of different modifications have been intensively investigated over the last 40–60 years, their properties are still not clearly understood. In particular, nonmetallic crystalline phthalocyanines, oligophthalocyanines, and polyphthalocyanines exhibit pronounced paramagnetic properties [1, 2] and strong electron paramagnetic resonance (EPR). It is believed that, for nonmetallic phthalocyanine compounds, the EPR signals are associated with the electron conjugated system [3]. However, even in the best understood case of crystalline phthalocyanines, the results of experimental studies on electron paramagnetic resonance are rather ambiguous [4]. Furthermore, there is virtually no reliable information on the EPR spectra of nonmetallic oligophthalocyanines and polyphthalocyanines.

In the present work, we investigated how the temperature and microwave power affect the parameters of

EPR spectra of nonmetallic amorphous polyphthalocyanines.

2. PREPARATION AND CHARACTERIZATION
OF SAMPLES

The compounds to be studied were synthesized according to the polycyclotetramerization reaction of pyromellitic acid tetranitrile in a molten monomer in the presence of 5 mol % urea at a temperature of 285°C for 5 h, followed by separation of the reaction product into two fractions soluble in organic solvents (acetone, dimethylformamide) and one insoluble fraction [5]. Polyphthalocyanine samples were prepared from the insoluble fraction in the form of a dark green powder. The grain size was approximately equal to 0.1 mm. Part of the polyphthalocyanine powder was evacuated under vacuum at a residual pressure of 10^{-3} Torr and room temperature for 4 h and was then stored in a sealed ampule.

The polyphthalocyanine compounds were identified using IR absorption and electronic absorption spectroscopy. The IR absorption spectra of samples prepared in the form of pellets with KBr in a ratio of 1.5 : 400 were measured on a Specord M-80 spectrophotometer. The electronic absorption spectra of the studied samples were recorded on a Specord UV–VIS spectrophotometer. In this case, the samples were placed in a quartz cell filled with concentrated sulfuric acid. The amount of free $-C\equiv N$ terminal groups was estimated from the inte-

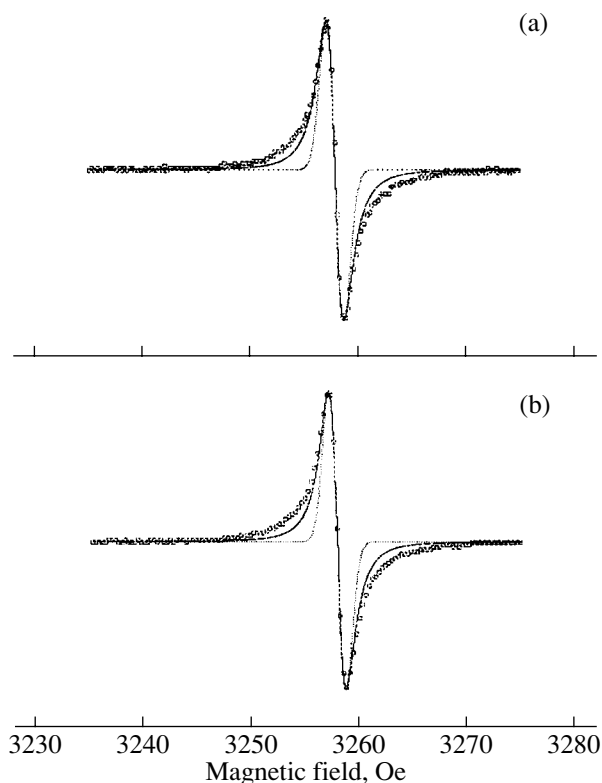


Fig. 1. EPR spectra of (a) unevacuated and (b) evacuated samples of nonmetallic amorphous polyphthalocyanine at a temperature of 295 K prior to heating. The microwave power is 1 mW. The solid and dotted lines represent Lorentzian and Gaussian line shapes, respectively.

grated intensity of the absorption band at 2230 nm^{-1} in the IR absorption spectrum ($A_{\text{C}\equiv\text{N}}$) according to the formula $A_{\text{C}\equiv\text{N}} = 2.4D\Delta V_{1/2}/L$, where D is the optical density, $\Delta V_{1/2}$ is the half-width of the absorption band, and L is the thickness of the pellet (expressed in centimeters). For the polyphthalocyanine samples under investigation, the percentage of free $\text{-C}\equiv\text{N}$ terminal groups was equal to 10%. The analysis of the x-ray diffraction patterns (DRON-3 x-ray diffractometer, $\text{CuK}\alpha$ radiation, Ni filter) showed that the polyphthalocyanine samples are amorphous.

The EPR spectra of polyphthalocyanine samples were recorded in the X band (at an operating frequency of $\sim 9.15 \text{ GHz}$) on a Varian E-4 spectrometer equipped with an E-257 nitrogen thermoelectric device and interfaced with a personal computer. The EPR measurements were performed in the temperature range 295–490 K. The temperature was measured with the use of a platinum resistor to an accuracy of $\pm 1 \text{ K}$. The linewidth ΔH_{pp} and the amplitude A of the EPR signals were determined using a peak-to-peak method. The EPR signals were digitized, entered on a personal computer with the use of an analog-to-digital converter, and stored in computer memory for further processing. The

computer codes used for processing the EPR spectra were developed by one of the authors (Yu. A. K.).

3. TEMPERATURE DEPENDENCES OF THE PARAMETERS OF THE EPR SPECTRA

The EPR spectrum of nonmetallic amorphous polyphthalocyanine samples at room temperature is a narrow singlet of approximately Lorentzian shape with a linewidth $\Delta H_{\text{pp}} \approx 1.7 \text{ Oe}$ and a splitting factor $g = 2.00$ (Fig. 1). The typical experiment for measuring the temperature dependence of the parameters of the EPR spectrum was performed as follows. A sample and a temperature-sensitive element were placed in an ampule at the center of a continuous-flow quartz cryostat mounted in the cavity of the spectrometer. The sample was slowly heated at a rate of one degree per minute. After the temperature was stabilized, the EPR spectra were recorded at 5- to 10-min intervals. In cases when no significant increases in the intensity and linewidth of the EPR signal were observed, the sample was heated to a higher temperature. When the parameters of the EPR signal became dependent on time, the temperature was stabilized and the EPR spectra were recorded at 5- to 10-min intervals. After the rate of change in the parameters of the EPR spectrum decreased significantly, the sample was again heated and the above procedure was repeated.

The temperature–time dependences of the linewidth and intensity of the EPR signal for unevacuated and evacuated samples of nonmetallic amorphous polyphthalocyanine are shown in Fig. 2. The intensity I_{EPR} of the EPR signal was determined as the product $A(\Delta H_{\text{pp}})^2$. For the studied samples at room temperature prior to heating, the intensity I_{EPR} corresponds to approximately 10^{17} spins/g. As the temperature increases above room temperature, the intensity of the EPR signal for samples of both types does not decrease. This indicates that the Curie law does not hold for these samples. It can be seen from Fig. 2a that, for the unevacuated polyphthalocyanine sample, the linewidth and intensity of the EPR signal become dependent on time beginning at temperature $T_{1nv} \approx 350 \text{ K}$ and increase under isothermal conditions. For the evacuated polyphthalocyanine sample, a similar effect manifests itself beginning at temperature $T_{1v} \approx 410 \text{ K}$ (Fig. 2). It is worth noting that, even at the highest temperature ($\sim 490 \text{ K}$) used in this experiment, the linewidth of the EPR signal does not exceed 2.4 Oe (Fig. 2). The relative increase in the intensity of the EPR signal with an increase in the temperature in the range from 295 to 490 K is more pronounced for the unevacuated sample (400%) than for the evacuated sample (300%). Upon cooling of the samples to room temperature, the linewidth of the EPR signal returns to its initial value ($\Delta H_{\text{pp}} \approx 1.7 \text{ Oe}$). However, the intensity of the EPR signal after heating the sample is substantially (two to six times) higher than the intensity of the EPR signal of the

sample prior to heating. The increase in the intensity of the EPR signal after heating is most pronounced for the evacuated sample at high microwave powers (see the next section).

4. DEPENDENCES OF THE PARAMETERS OF THE EPR SPECTRA ON THE MICROWAVE POWER

Figure 3 shows the dependences of the linewidth ΔH_{pp} , the amplitude A , and the intensity I_{EPR} of the EPR spectrum on the microwave power P for unevacuated and evacuated samples of nonmetallic amorphous polyphthalocyanine. The EPR spectra were measured at room temperature prior to and after the samples were heated according to the procedure described above (Fig. 2). The intensity of the EPR signal was calculated using double integration of the experimental spectrum. As can be seen from Fig. 3, the dependences $\Delta H_{pp}(P)$, $A(P)$, and $I_{EPR}(P)$ for the unevacuated and evacuated samples are similar to each other and practically do not change upon heating to 490 K. The effect of heating of the samples most clearly manifests itself in a decrease in the saturation of the EPR signal with an increase in the microwave power (see insets to Fig. 3). This is also indicated by the appearance of a maximum in the curves $A(P)$ for the unevacuated and evacuated samples after heating. As the microwave power increases from 0.5 to 200 mW, the linewidth of the EPR spectrum for both samples increases by approximately 35%, which suggests a homogeneous broadening of the EPR lines.

5. COMPUTER CALCULATION OF THE EPR SPECTRA

The shape of the EPR spectrum for the samples of nonmetallic amorphous polyphthalocyanines under investigation can be described by a Lorentzian function rather than by a Gaussian function; however, this spectrum cannot be adequately represented by only one Lorentzian line (see Fig. 1). As was noted by Tanaka *et al.* [6] and, even earlier, by Dulov and Slinkin [7], semiconductor polymers with an extended system of π conjugation are characterized by two types of EPR-active centers. In this respect, we decomposed the experimental EPR spectra into two Lorentzian lines with different parameters and examined the dependences of the parameters of each Lorentzian line on the temperature and microwave power. The spectra were decomposed according to the following procedure. The experimental values of the linewidth ΔH_{pp} and amplitude A were obtained from the measured EPR spectra and were then used to determine the parameters Γ , H_R , and Y_{max} of the Lorentzian line in the zeroth-order approximation [8]:

$$Y = Y_{max} \Gamma^2 / [\Gamma^2 + (H - H_R)^2].$$

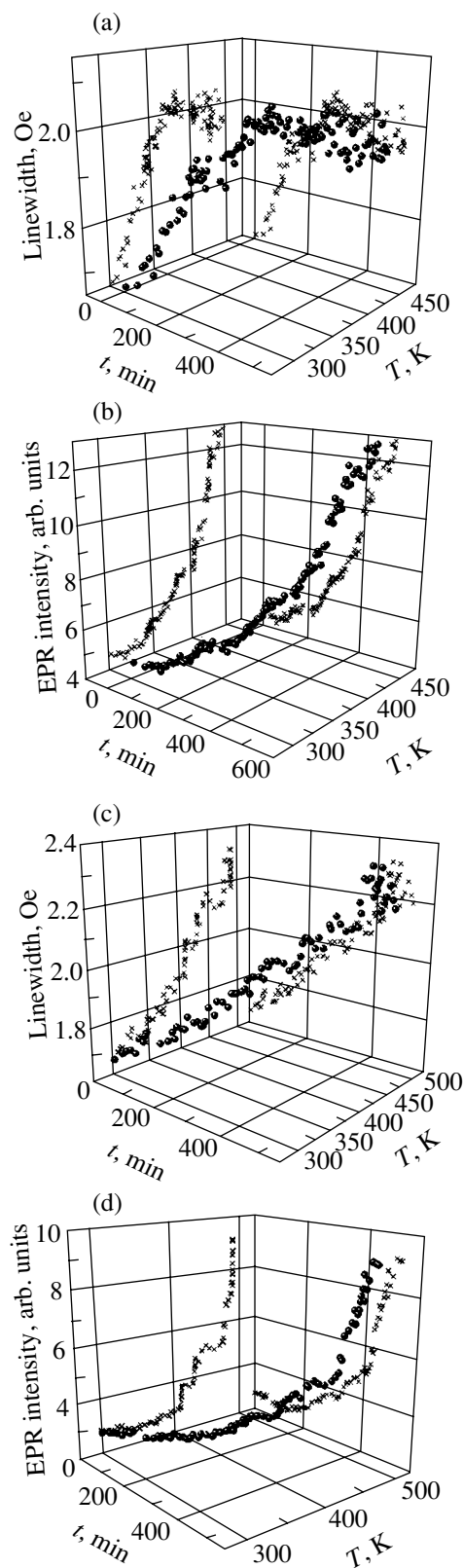


Fig. 2. Temperature–time dependences of (a, c) the linewidth and (b, d) the intensity of the EPR signal for (a, b) unevacuated and (c, d) evacuated samples of nonmetallic amorphous polyphthalocyanine. Crosses indicate projections onto the coordinate planes.

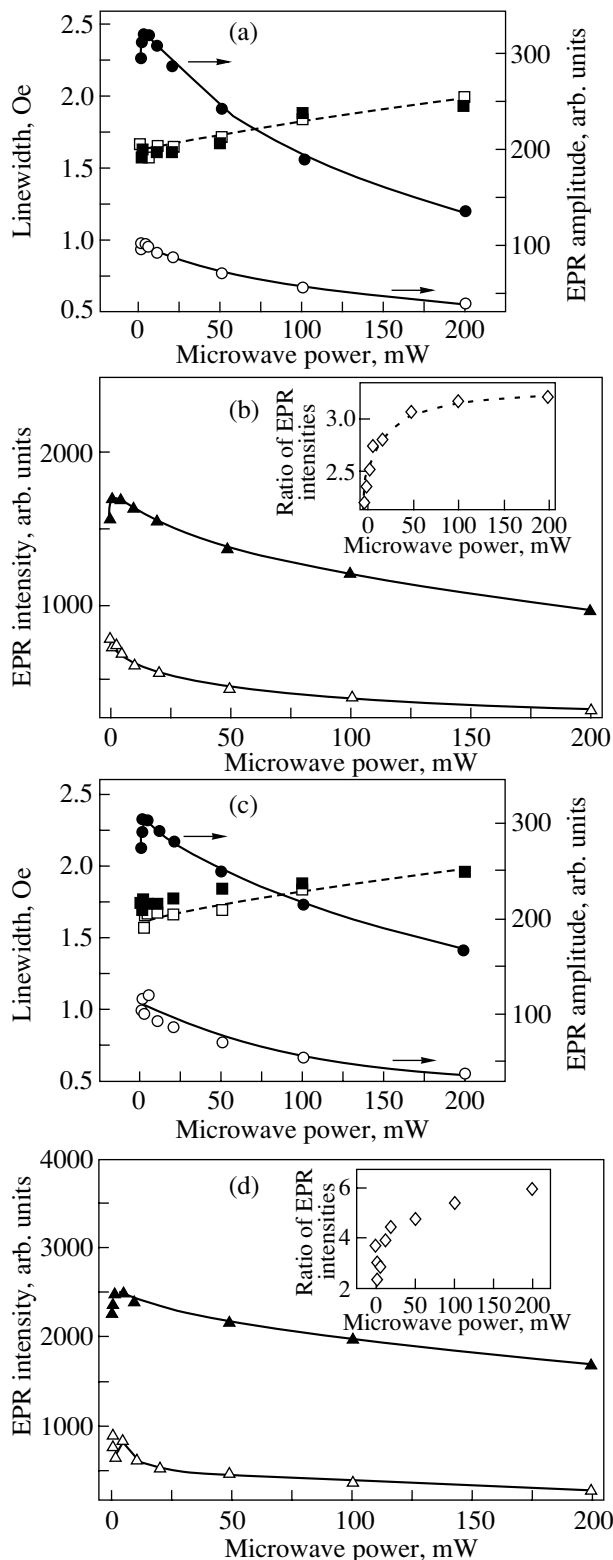


Fig. 3. Dependences of the linewidth (squares), the amplitude (circles), and the intensity (triangles) of the EPR signal on the microwave power for (a, b) unevacuated and (c, d) evacuated samples of nonmetallic amorphous polyphthalocyanine prior to heating (closed symbols) and after cooling from the maximum temperature to room temperature (open symbols). The insets show the dependences of the ratio of the EPR intensity after heating to the EPR intensity prior to heating of the samples on the microwave power.

The EPR lines with the parameters determined by this method are depicted in Fig. 1.

The final theoretical spectrum was obtained by minimizing the squared deviations of the theoretical and experimental lines according to a modified method of gradient minimization. In our calculations, we varied the parameters Γ , H_R , and Y_{\max} for the two Lorentzian lines (i.e., a total of six parameters were varied). The correctness of the minimization procedure was checked by specifying different initial conditions for calculating the parameters of the second Lorentzian line (for the first Lorentzian line, we used the parameters obtained in the zeroth-order approximation). When the results of the minimization under different initial conditions coincided accurate to within 1%, the convergence of the method used was accepted as satisfactory.

The results of the computer calculations demonstrated that the EPR spectra of nonmetallic amorphous polyphthalocyanines can be represented by two lines of Lorentzian shape, one of which is relatively narrow and the other line is rather broad. The parameters characterizing the width of the narrow and broad lines at room temperature are $\Delta H_{pp1} = 2\Gamma_1/\sqrt{3} \approx 1.6$ Oe and $\Delta H_{pp2} = 2\Gamma_2/\sqrt{3} \approx 4.9$ Oe, respectively. The intensity of the broad line (at low microwave powers) exceeds the intensity of the narrow line; however, the amplitude of the broad line is smaller than that of the narrow line. Consequently, the sum of these two Lorentzian lines is characterized by a linewidth close to ΔH_{pp1} . Note that the experimental spectrum has a linewidth $\Delta H_{pp} \approx 1.7$ Oe (Fig. 2). Figure 4 depicts the dependences of the amplitude, the parameter Γ , and the intensity of the EPR spectrum represented by two lines of Lorentzian shape on the microwave power for an unevacuated sample of nonmetallic amorphous polyphthalocyanine at room temperature. For the unevacuated sample at room temperature, the EPR signal represented by the broad Lorentzian line is saturated more rapidly than the EPR signal corresponding to the narrow Lorentzian line. At a microwave power $P = 200$ mW, the signal intensities become identical (see inset to Fig. 4b). After heating to 490 K, the relative contribution from the broad Lorentzian line to the intensity of the total EPR spectrum decreases significantly (Fig. 4). In particular, prior to heating, the intensity of the broad Lorentzian line exceeds the intensity of the narrow Lorentzian line by a factor of 5 (at $P = 0.5$ mW). However, after heating, the ratio of the intensity of the broad Lorentzian line to the intensity of the narrow Lorentzian line is equal to only 1.8.

An analysis of the temperature dependences of the parameters of the two Lorentzian lines for the unevacuated sample confirms the fact that the intensity of the broad Lorentzian line decreases upon heating. It can be seen from Fig. 5 that, beginning at approximately 380 K, the intensity of the narrow Lorentzian line drastically increases (by several factors), whereas the inten-

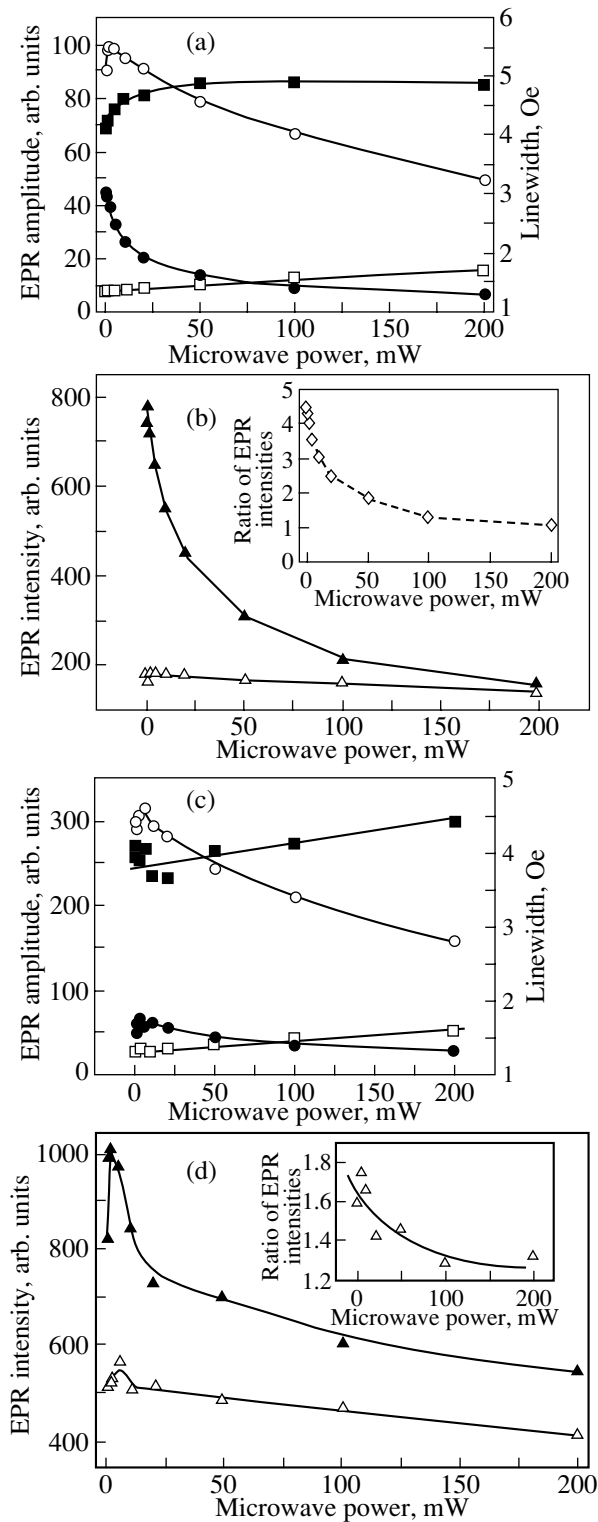


Fig. 4. Dependences of the amplitude (circles), the parameter Γ (squares), and the intensity (triangles) of the EPR spectrum represented by two lines of Lorentzian shape on the microwave power for an unevacuated sample of nonmetallic amorphous polyphthalocyanine at room temperature: (a, b) prior to heating and (c, d) after heating. The open and closed symbols indicate the narrow and broad Lorentzian lines, respectively. The insets show the ratio of the EPR intensity of the broad Lorentzian line to the EPR intensity of the narrow Lorentzian line as a function of the microwave power.

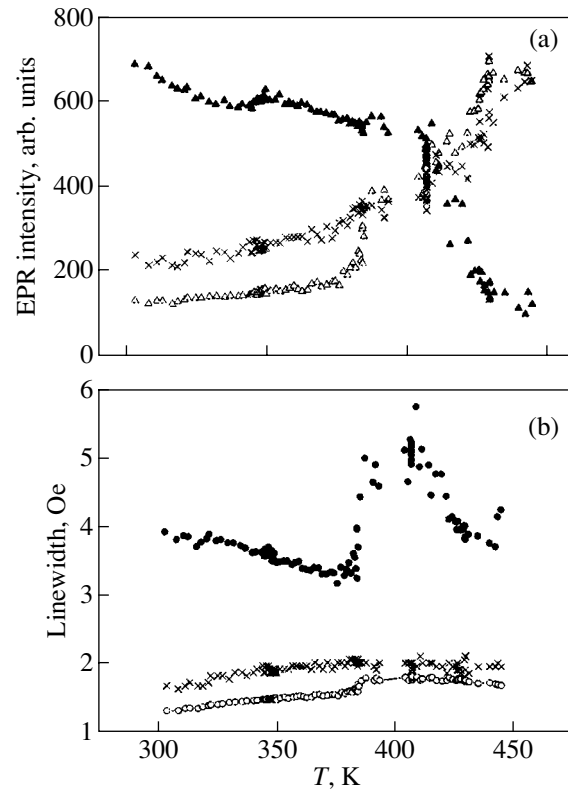
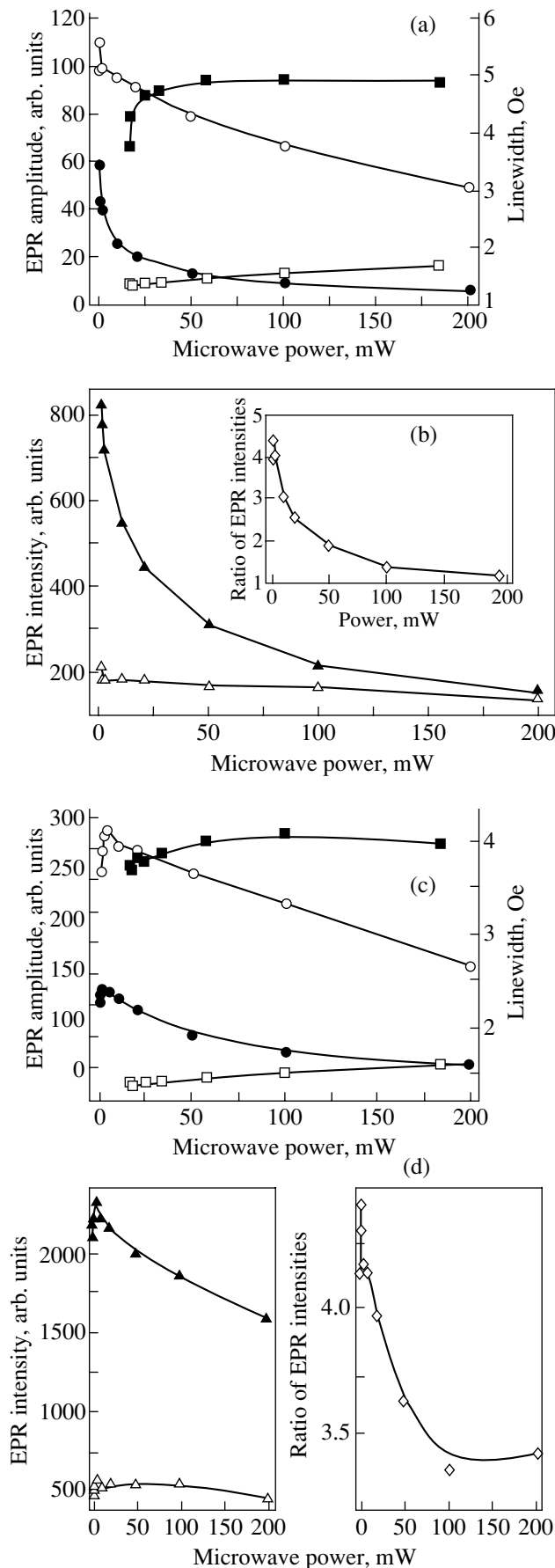


Fig. 5. Temperature dependences of (a) the intensity and (b) the parameter Γ of the EPR spectrum represented by two lines of Lorentzian shape for an unevacuated sample of nonmetallic amorphous polyphthalocyanine. The open and closed symbols indicate the narrow and broad Lorentzian lines, respectively. Crosses indicate experimental values of (a) the intensity I_{EPR} and (b) the linewidth ΔH_{pp} .

sity of the broad Lorentzian line considerably decreases. At temperatures above 450 K, the intensity of the broad Lorentzian line becomes one order of magnitude lower than the intensity of the narrow Lorentzian line (Fig. 5). It is worth noting that this significant decrease in the intensity of the broad Lorentzian line is not irreversible. Upon cooling of the unevacuated sample from 490 K to room temperature, the intensity of the broad Lorentzian line, as before, exceeds (in magnitude) the intensity of the narrow Lorentzian line; however, this excess is several times smaller than that observed prior to heating (Fig. 4). The linewidths of both components are also characterized by an increase at temperatures $T > 480$ K, which is especially pronounced for the broad component (Fig. 5).

Figure 6 shows the dependences of the amplitude, the parameter Γ , and the intensity of the EPR spectrum represented by two lines of Lorentzian shape on the microwave power for an evacuated sample of nonmetallic amorphous polyphthalocyanine at room temperature. Prior to heating, the dependences $\Gamma(P)$, $Y_{\text{max}}(P)$, and $I_{\text{EPR}}(P)$ for the evacuated and unevacuated samples are very similar (Figs. 4, 6) not only qualitatively but



also quantitatively. However, after heating, the intensity of the broad Lorentzian line for the evacuated sample decreases (with respect to the intensity of the narrow Lorentzian line) to a lesser extent as compared to that for the unevacuated sample (Figs. 4, 6). It can be seen from Fig. 6 that, for the evacuated sample after heating, the decrease observed in the saturation of the EPR signal represented by the broad Lorentzian line is more pronounced than that for the signal corresponding to the narrow Lorentzian line.

The temperature dependences of the parameter Γ and the intensity of the EPR spectrum represented by two lines of Lorentzian shape for the evacuated sample of nonmetallic amorphous polyphthalocyanine are depicted in Fig. 7. As can be seen, the parameter Γ for the broad Lorentzian line begins to increase appreciably (by several tens of percent) at temperatures $T > 430$ K (for the unevacuated sample, an analogous increase is observed at $T > 380$ K), whereas the intensities of both components significantly increase at $T > 410$ K (Fig. 7b), i.e., beginning from temperatures at which the intensity of the EPR signal becomes dependent on time (Fig. 2). At the highest temperatures (~ 490 K) used in our experiment, the intensities of the broad and narrow Lorentzian lines are equal to each other (Fig. 7). It should be noted that, for the unevacuated sample heated to these temperatures, the intensity of the broad Lorentzian line is substantially less than the intensity of the narrow Lorentzian line (Fig. 5).

6. RESULTS AND DISCUSSION

Since compounds based on phthalocyanine exhibit polymorphism, their investigation is severely complicated. In particular, nonmetallic crystalline phthalocyanine can exist in three modifications, namely, the α , β , and x modifications. The α modification of phthalocyanine is considered to be metastable and, under external actions (for example, upon heating), can transform into the stable β modification [9]. As was shown by Guillaud *et al.* [10] and Gould [11], apart from the α and β modifications, phthalocyanine can exist in the x form; moreover, the α modification itself has three more forms. According to Kubiak *et al.* [12], the x form is a modification of the β form. Taking into account that oligophthalocyanines and polyphthalocyanines are characterized by a great diversity of structures [13, 14], the

Fig. 6. Dependences of the amplitude (circles), the parameter Γ (squares), and the intensity (triangles) of the EPR spectrum represented by two lines of Lorentzian shape on the microwave power for an evacuated sample of nonmetallic amorphous polyphthalocyanine at room temperature: (a, b) prior to heating and (c, d) after heating. The open and closed symbols indicate the narrow and broad Lorentzian lines, respectively. The inset and rhombuses show the ratio of the EPR intensity of the broad Lorentzian line to the EPR intensity of the narrow Lorentzian line as a function of the microwave power.

fact that there exist two types of EPR-active centers in nonmetallic polyphthalocyanines is not surprising. On the other hand, no exhaustive explanation of the origin of unpaired electron spins in conjugated polymers has been offered to date. Boguslavskii and Vannikov [3] considered the following possible sources of EPR signals in polymers with conjugated bonds: (1) inorganic paramagnetic impurities, (2) organic radicals formed in the course of polymerization, (3) polymer molecules in a triplet state, (4) stabilized double radicals, (5) polar states induced by charge transfer (including charge-transfer complexes), and (6) quasi-free charge carriers. Detailed analysis allows us to assume that the most plausible hypotheses are associated with stable double radicals and charge-transfer complexes [3, 7].

The second hypothesis, as applied to polyphthalocyanines (especially to amorphous polyphthalocyanines), is considered the most credible owing to many factors favorable for charge transfer. These factors include an extended π -electron conjugated system, which ensures a high polarizability and readability of ionization of the molecules; polydispersity (the presence of molecules with different molecular weights), which is responsible for the difference both in electron affinity and in ionization potential between the molecules; and structural disorder, which provides a wide variety of local interactions between the molecules.

The Lorentzian line shape of the EPR signals for polyphthalocyanines indicates the occurrence of strong exchange interactions of EPR-active centers and the homogeneous mechanism of broadening of the EPR lines. This can also be judged from both the strong dependence of the EPR linewidth on the microwave power and the considerable decrease in the amplitude of the EPR signals even at low microwave powers [8]. The homogeneous broadening of the EPR lines suggests that there is a relatively small spread of parameters of the EPR spectrum (resonance fields and linewidths) for different centers. Possibly, it is owing to this circumstance that the experimental EPR spectra can be represented to a sufficient accuracy by only two lines (rather than by a greater number of lines).

The large difference between the widths of the two Lorentzian lines (into which we managed to decompose the experimental EPR spectra) can be associated with the different degrees of delocalization of the corresponding sources of the EPR signals. It is known that an increase in the degree of delocalization of a charge carrier with a magnetic moment, as a rule, leads to a decrease in the EPR linewidth [8]. An important point is that the effect of saturation of the EPR signal with an increase in the microwave power is more pronounced for the broad component of the EPR spectrum (Figs. 4, 6). This indicates a slower spin relaxation of the corresponding centers.

It can be assumed that the samples of polyphthalocyanines studied contain EPR-active centers of two types. Centers of the first type are characterized by a

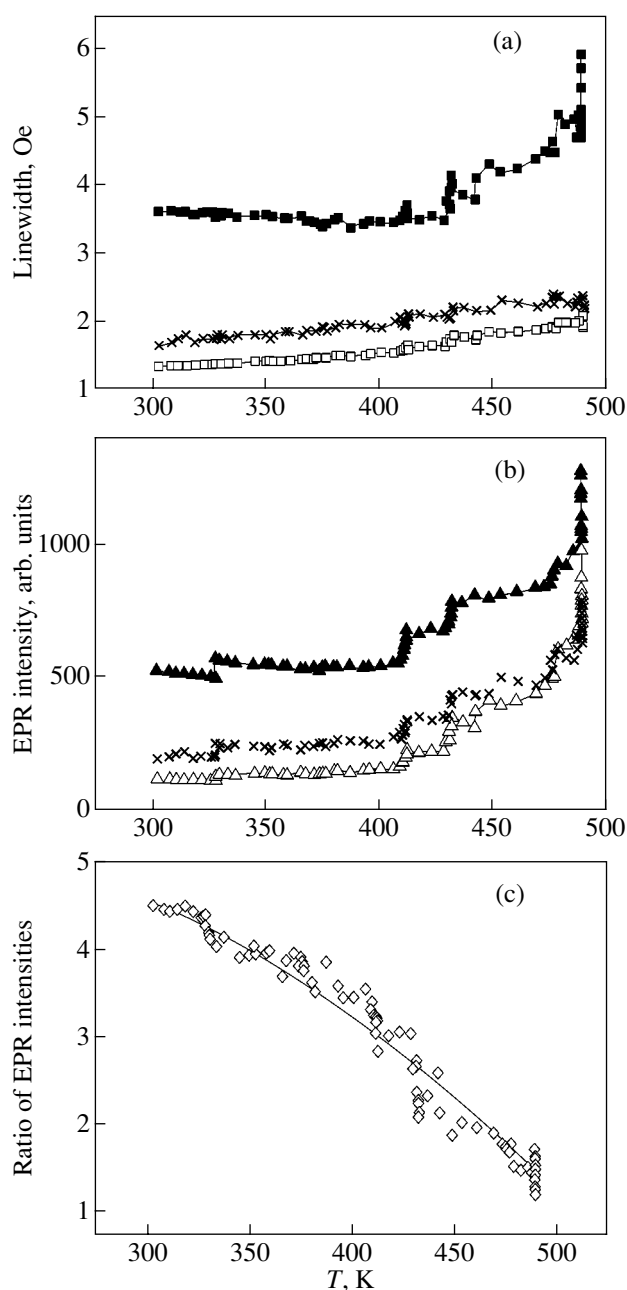


Fig. 7. Temperature dependences of (a) the parameter Γ , (b) the intensity of the EPR spectrum represented by two lines of Lorentzian shape, and (c) the ratio of the EPR intensity of the broad Lorentzian line to the EPR intensity of the narrow Lorentzian line for an evacuated sample of nonmetallic amorphous polyphthalocyanine. The open and closed symbols indicate the narrow and broad Lorentzian lines, respectively. Crosses indicate experimental values of (a) the linewidth ΔH_{pp} and (b) the intensity I_{EPR} .

high degree of delocalization, short times of relaxation, and a narrow EPR line. Centers of the second type are localized to a greater extent (most likely, they are not related to the π -electron conjugated system) and, as a consequence, cannot undergo fast spin relaxation. Moreover, centers of the second type are characterized

by a relatively broad EPR line. It is of interest to note that the experimental EPR spectra of crystalline phthalocyanines (in these measurements, we used commercial powder samples) have a linewidth of 4–5 Oe and exhibit a fast decrease in the intensity of the EPR signal with an increase in the microwave power, as was observed for the EPR signal represented by the broad Lorentzian line (Figs. 4, 6). It seems likely that the EPR signals for crystalline phthalocyanines and the EPR signals corresponding to the broad line for polyphthalocyanines are of similar origin.

According to our data, the number of strongly localized (“isolated”) EPR-active centers in nonmetallic polyphthalocyanines exceeds the number of delocalized centers. Upon smooth heating of the polyphthalocyanine samples to temperatures in the range 400–500 K, the number of isolated EPR-active centers decreases, whereas the number of delocalized centers increases. This can be associated with the increase in the size of the regions involved in the electron conjugated system in the polyphthalocyanine samples subjected to heat treatment. It is worth noting that, for preliminarily evacuated samples, the effect of temperature on the EPR characteristics of the polyphthalocyanine is less pronounced. It can be assumed that, during heating, absorbed molecules of gases (O₂, N₂, H₂O) and the remaining molecules of solvents (which are present in a relatively large amount in unevacuated samples), in one way or another, encourage an increase in the size of the regions involved in the electron conjugated system (for example, they can provide a higher lability of the structure).

7. CONCLUSIONS

Since the regions involved in the electron conjugated system play a key role in the formation of specific properties of conjugated polymers (including those responsible for electron transport, optical and magnetic properties, etc.), the results of analyzing the correlation between the parameters of the EPR spectra and the size of the electron conjugation regions are of fundamental and practical importance. In this respect, it is necessary

to perform further investigations, in particular, into the influence of the synthesis conditions (primarily, the temperature and duration of the synthesis) on the properties of nonmetallic amorphous polyphthalocyanines.

ACKNOWLEDGMENTS

This work was supported by the International Scientific and Engineering Center, project no. 1838.

REFERENCES

1. *Organic Semiconductors*, Ed. by V. A. Kargin (Nauka, Moscow, 1968).
2. J. M. Assour and S. E. Harrison, *J. Phys. Chem.* **68**, 872 (1964).
3. L. I. Boguslavskii and A. V. Vannikov, *Organic Semiconductors and Biopolymers* (Nauka, Moscow, 1968).
4. J. R. Harbour and R. O. Loutfy, *J. Phys. Chem. Solids* **43**, 513 (1982).
5. V. R. Épshtein and A. I. Sherle, *Vysokomol. Soedin., Ser. A* **32**, 1655 (1990).
6. K. Tanaka, H. Ago, Y. Matsuura, T. Kuga, T. Yamabe, S. Yata, Y. Hato, and N. Ando, *Synth. Met.* **89**, 133 (1997).
7. A. A. Dulov and A. A. Slinkin, *Organic Semiconductors* (Nauka, Moscow, 1970).
8. J. E. Wertz and J. R. Bolton, *Electronic Spin Resonance: Elementary Theory and Practical Applications* (McGraw-Hill, New York, 1972; Mir, Moscow, 1975).
9. J. Simon and J.-J. Andre, *Molecular Semiconductors* (Springer, Berlin, 1985; Mir, Moscow, 1988).
10. G. Guillaud, J. Simon, and J. P. Germain, *Coord. Chem. Rev.* **178–180**, 1433 (1998).
11. R. G. Gould, *Coord. Chem. Rev.* **156**, 237 (1996).
12. R. Kubiak, J. Janczak, and K. Ejsmont, *Chem. Phys. Lett.* **245**, 249 (1995).
13. D. Wohrle, *Macromol. Rapid Commun.* **22**, 68 (2001).
14. N. B. McKeown, *J. Mater. Chem.* **10**, 1979 (2000).

Translated by O. Borovik-Romanova

**FULLERENES
AND ATOMIC CLUSTERS**

Stoichiometric Synthesis of Fullerene Compounds with Lithium and Sodium and Analysis of Their IR and EPR Spectra

**S. N. Titova, G. A. Domrachev, S. Ya. Khorshev, A. M. Ob'edkov, L. V. Kalakutskaya,
S. Yu. Ketkov, V. K. Cherkasov, B. S. Kaverin, K. B. Zhogova, M. A. Lopatin,
V. L. Karnatsevich, and E. A. Gorina**

*Razuvaev Institute of Organometallic Chemistry, Russian Academy of Sciences, ul. Tropinina 49,
Nizhni Novgorod, 603950 Russia*

e-mail: amo@imoc.sinn.ru

Received November 12, 2003

Abstract—A modified method is proposed for preparing fullerene compounds with alkali metals in a solution. The compounds synthesized have the general formula $Me_nC_{60}(THF)_x$, where $Me = Li$ or Na ; $n = 1-4, 6, 8$, or 12 ; and $THF =$ tetrahydrofuran. The use of preliminarily synthesized additives $MeC_{10}H_8$ makes it possible to prepare fullerene compounds with an exact stoichiometric ratio between C_{60}^{n-} and Me^+ . The IR and EPR spectra of the compounds prepared are analyzed and compared with the spectra of their analogs available in the literature. The intramolecular modes $T_u(1)-T_u(4)$ for the C_{60}^{n-} anion are assigned. The splitting of the $T_u(1)$ mode into a doublet at room temperature for $Me_nC_{60}(THF)_x$ ($n = 1, 2, 4$) compounds indicates that the fullerene anion has a distorted structure. An increase in the intensity of the $T_u(2)$ mode, a noticeable shift of the $T_u(4)$ mode toward the long-wavelength range, and an anomalous increase in the intensity of the latter mode for the $Li_3C_{60}(THF)_x$ complex suggest that, in the fullerene anion, the coupling of vibrational modes occurs through the charge-phonon mechanism. The measured EPR spectra of lithium- and sodium-containing fullerene compounds are characteristic of C_{60}^- anions. The g factors for these compounds are almost identical and do not depend on temperature. The g factor for the C_{60}^{3-} anion depends on the nature of the metal and differs from the g factor for the C_{60}^- anion. © 2004 MAIK "Nauka/Interperiodica".

1. INTRODUCTION

The electron-acceptor ability of fullerenes is one of the most important properties of these compounds. Research into the formation of fullerene complexes with alkali metals, which is accompanied by electron-density transfer from metal atoms to fullerene molecules, has revealed very interesting electrical properties exhibited by the resultant complexes. In the last decade, these properties have been a subject of extensive theoretical and experimental investigation.

The electronic structure of C_{60}^{n-} anions has been thoroughly studied using electron paramagnetic resonance (EPR), ultraviolet (UV), and nuclear magnetic resonance (NMR) spectroscopy. The results obtained thus far for fullerene compounds [1] clearly demonstrate that the C_{60} fullerene much more readily reacts with oxygen than considered previously. The oxygen-containing impurities (especially, $C_{120}O$) revealed in initial fullerene samples substantially affect the EPR and ^{13}C NMR spectra of the compounds under investigation, which makes correct interpretation of their elec-

tronic structure difficult. Moreover, fullerene compounds with alkali metals are highly reactive and readily interact with both polar solvents [such as tetrahydrofuran (THF) and dimethyl sulfoxide] and halogen-containing solvents. This also hampers the study of these complexes in solutions with the use of the aforementioned techniques. In this respect, infrared (IR) spectroscopy is one of the most appropriate methods for elucidating the nature of fullerene compounds with alkali metals. Derivatives of lithium and sodium are chosen as the objects of our investigation, because the properties and structure of these compounds (especially of those with higher reduction states of the fullerene) are poorly understood as compared, for example, to potassium derivatives. For Li_nC_{60} compounds, this circumstance is most likely associated with the fact that the lithium fullerenes are rather difficult to prepare through gas-phase synthesis because of the very low pressure of lithium vapor (10^{-9} Torr at $200^\circ C$ as compared with 10^{-4} Torr for sodium at $300^\circ C$). It should also be noted that Li_nC_{60} and Na_nC_{60} compounds are promising for use as initial reactants in synthesizing new organic and organoelement fullerene complexes.

2. EXPERIMENTAL TECHNIQUE

All the compounds prepared in this work are highly sensitive to oxygen and moisture. For this reason, fullerene compounds with alkali metals of the general formula $Me_nC_{60}(THF)_x$ ($Me = Li, Na; n = 1-4, 6, 8, 12$) were synthesized and isolated in evacuated ampules and all-sealed devices. Solvents (toluene, tetrahydrofuran) were dried over sodium benzophenone ketyl and distilled into a reaction ampule immediately before use. The IR spectra were recorded on a UR-20 spectrometer. Samples were prepared as Nujol mulls in evacuated systems filled with dry argon. The EPR spectra were measured on a Bruker ER 200 D-SRC spectrometer equipped with an ER 4105DR double cavity (operating at a frequency of approximately 9.5 GHz) and an ER 4111 VT temperature controller. The g factors were determined using the DPPH compound as a standard.

3. SYNTHESIS OF $Li_1C_{60}(THF)_x$

Lithium naphthalenide was preliminarily synthesized from lithium (0.011 g, 1.57 mmol) and naphthalene (0.211 g, 1.65 mmol). A solution of lithium naphthalenide in tetrahydrofuran (5 ml) was added to a solution of the C_{60} fullerene (1.008 g, 1.40 mmol) in toluene (100 ml) with vigorous stirring for 30 min at a temperature of 5–10°C. The reaction rate was equal to the mixing rate of the reactants. After the $Li_1C_{60}(THF)_x$ compound precipitated out, the solution was decanted and the product was extracted three times with toluene, dried, and isolated. The yield of $Li_1C_{60}(THF)_x$ was 95% with respect to the lithium weight. The other $Me_nC_{60}(THF)_x$ compounds were synthesized in a similar manner with special attention paid to the stoichiometric ratio between C_{60} and $C_{10}H_8Me$. As a result, we prepared the $Me_nC_{60}(THF)_x$ compounds, where $Me = Li$ or Na and $n = 1-4, 6, 8, 12$. The compounds synthesized were characterized by IR spectroscopy. IR spectra, ν (cm^{-1}): 516, 528, 576, 890, 916, 1045, 1183, and 1395 for $Li_1C_{60}(THF)_x$; 516, 526, 576, 890, 916, 1045, 1183, and 1345 for $Li_2C_{60}(THF)_x$; 575, 785, 890, 916, 1045, 1183, and 1345 for $Li_3C_{60}(THF)_x$; 516, 527, 576, 785, 890, 916, 1045, 1185, and 1345 for $Li_4C_{60}(THF)_x$; 576, 785, 890, 916, 1045, 1185, and 1345 for $Li_6C_{60}(THF)_x$; 575, 785, 890, 916, 1045, 1171, and 1345 for $Li_8C_{60}(THF)_x$; 572, 780, 890, 970, 1045, 1171, and 1345 for $Li_{12}C_{60}(THF)_x$; 528, 579, 1060, 1180, and 1372 for $Na_1C_{60}(THF)_x$; 512, 528, 576, 890, 916, 1045, 1183, and 1355 for $Na_2C_{60}(THF)_x$; 512, 528, 574, 890, 916, 1045, 1183, and 1350 for $Na_3C_{60}(THF)_x$; 529, 576, 890, 960, 1045, 1182, and 1365 for $Na_4C_{60}(THF)_x$; 528, 576, 890, 960, 1045, 1183, and 1352 for $Na_6C_{60}(THF)_x$; 528, 573, 890, 960, 1045, 1183, and 1352 for $Na_8C_{60}(THF)_x$; and 528, 573, 890, 960, 1171, and 1355 for $Na_{12}C_{60}(THF)_x$.

The $Li_nC_{60}(THF)_x$ compounds synthesized are dark brown solids. The $Na_nC_{60}(THF)_x$ derivatives are black solids. These compounds readily interact with polar solvents (such as tetrahydrofuran, dimethyl sulfoxide, and organic halogen-containing compounds) and are insoluble in aliphatic and aromatic hydrocarbons. It was found that the $Na_2C_{60}(THF)_x$ derivative self-ignites in air.

4. EXPERIMENTAL RESULTS AND DISCUSSION

One of the main difficulties encountered in preparing fullerene compounds with alkali metals is associated with the necessity of ensuring an exact stoichiometric ratio between the fullerene anion and the metal cation. The gas-phase method that has been most universally employed for synthesizing Me_nC_{60} compounds also has this disadvantage and, furthermore, requires long times (up to two weeks) and high temperatures (up to 500°C). The rate of gas-phase synthesis is limited by two main processes, namely, mass transfer of metal atoms in the gas phase and diffusion of metal cations in the C_{60} solid phase. Reducing the C_{60} fullerene in the liquid phase makes it possible to avoid these processes.

We proposed a simple method for preparing $Me_nC_{60}(THF)_x$ stoichiometric compounds in a toluene solution with preliminary synthesis of naphthalenide complexes of alkali metals in a tetrahydrofuran solution. To put it differently, the mixing of homogeneous solutions of the initial components enables one to perform the reaction with the formation of the desired compounds on the molecular level with precise control over the stoichiometric ratio between C_{60}^{n-} and nMe^+ . Since the electron affinity of the C_{60} fullerene is 1 eV greater than that of aromatic polycyclic hydrocarbons [2], the reduction of C_{60} with naphthalenide complexes of lithium or sodium proceeds rather readily and at a high rate. Proper choice of the solvent for the synthesis is of utmost importance. Boyd *et al.* [3] showed that toluene is one of the most suitable solvents and that tetrahydrofuran taken in small amounts ($\approx 5\%$) promotes electron-transfer reactions. We used the proposed method for synthesizing the $Me_nC_{60}(THF)_x$ ($Me = Li, Na; n = 1-4, 6, 8, 12$) compounds. The yield was approximately equal to 95%. The compounds prepared were investigated using IR spectroscopy.

In this work, fullerene compounds containing eight and twelve metal atoms (in which the t_{1g} orbital of C_{60} is partially occupied by electrons) were synthesized and studied relying on the data obtained in [4, 5]. Zimmermann *et al.* [4] and Cristofolini *et al.* [5] carried out theoretical calculations, analyzed the mass spectra of a mixture of Li_nC_{60} compounds prepared by the gas-phase method, and proved that the $Li_{12}C_{60}$ fulleride is a stable compound with a maximum lithium content. This compound has a structure in which 12 lithium cations each are located above the pentagon of the

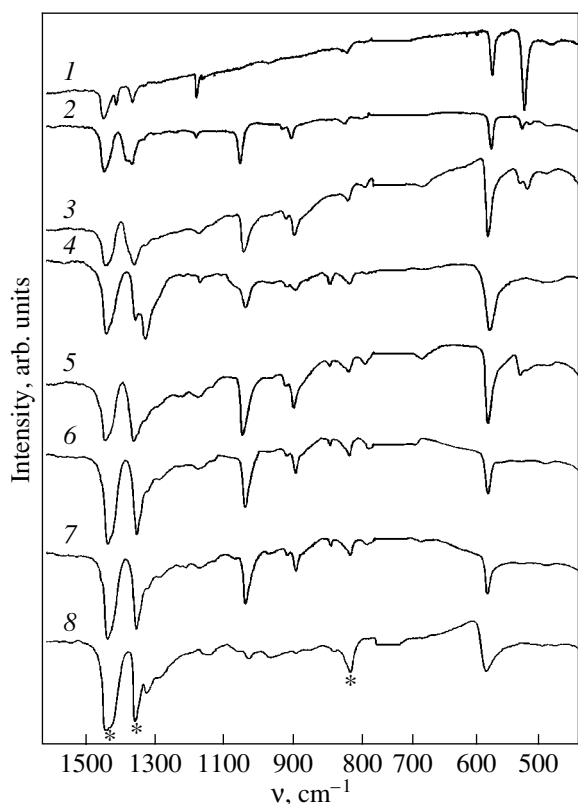


Fig. 1. IR spectra of (1) fullerene, (2) $\text{Li}_1\text{C}_{60}(\text{THF})_x$, (3) $\text{Li}_2\text{C}_{60}(\text{THF})_x$, (4) $\text{Li}_3\text{C}_{60}(\text{THF})_x$, (5) $\text{Li}_4\text{C}_{60}(\text{THF})_x$, (6) $\text{Li}_6\text{C}_{60}(\text{THF})_x$, (7) $\text{Li}_8\text{C}_{60}(\text{THF})_x$, and (8) $\text{Li}_{12}\text{C}_{60}(\text{THF})_x$ (* Nujol mull).

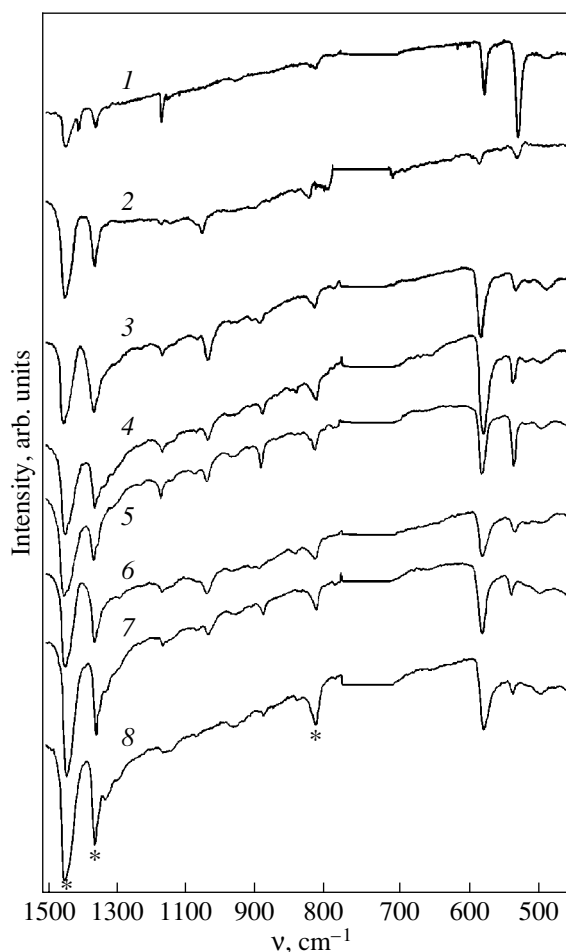


Fig. 2. IR spectra of (1) C_{60} , (2) $\text{Na}_1\text{C}_{60}(\text{THF})_x$, (3) $\text{Na}_2\text{C}_{60}(\text{THF})_x$, (4) $\text{Na}_3\text{C}_{60}(\text{THF})_x$, (5) $\text{Na}_4\text{C}_{60}(\text{THF})_x$, (6) $\text{Na}_6\text{C}_{60}(\text{THF})_x$, (7) $\text{Na}_8\text{C}_{60}(\text{THF})_x$, and (8) $\text{Na}_{12}\text{C}_{60}(\text{THF})_x$ (* Nujol mull).

fullerene fragment retaining icosahedral symmetry. According to [4, 5], lithium cations in the Li_8C_{60} compound are located at vertices of the cube and above the hexagons of the fullerene fragment. Chen *et al.* [6] used the gas-phase method in order to synthesize a series of fullerene compounds with alkaline-earth metals of the general formula Me_nC_{60} ($\text{Me} = \text{Ca}, \text{Ba}; n = 3, 4, 6$), in which the reduction state of the fullerene varies from 6 to 12. Moreover, those authors measured the Raman spectra of Ba_nC_{60} ($n = 3, 4, 6$) compounds. It was found that the Raman spectra of the Ba_3C_{60} and K_6C_{60} fullerides are very similar to each other. This suggests that the fullerene anions in these compounds have the same electronic structure. The hybridization of barium with C_{60} π orbitals was observed for higher reduction states of the C_{60} fullerene. In the immediate future, the Raman spectra of the compounds synthesized in the present work will be measured and compared with the Raman spectra of Ba_nC_{60} fullerides.

Figures 1 and 2 show the IR spectra of the $\text{Li}_x\text{C}_{60}(\text{THF})_x$ and $\text{Na}_x\text{C}_{60}(\text{THF})_x$ compounds. The vibrational modes $T_u(1)$ – $T_u(4)$ for these compounds are presented in Table 1. It is known that, owing to its high symmetry (I_h), the C_{60} fullerene exhibits only four IR-active modes, namely, $T_u(1)$, $T_u(2)$, $T_u(3)$, and $T_u(4)$ at

frequencies of 527, 576, 1183, and 1429 cm^{-1} , respectively [7]. A change in symmetry and the redistribution of the electron density upon the formation of fullerene compounds with alkali metals manifest themselves in the IR spectra. In the literature, these effects, as a rule, are interpreted in terms of the charge–phonon mechanism [8], according to which the filling of the C_{60} t_{1u} orbital with electrons is accompanied by coupling of the T_u vibrational modes with virtual electronic transitions from the t_{1u} orbital to the higher lying t_{1g} orbital. It was shown that, for intercalated Me_nC_{60} compounds, the charge effect is more pronounced for the $T_u(4)$ mode and is somewhat weaker for the $T_u(2)$ mode. The $T_u(3)$ mode remains virtually unchanged [9]. The $T_u(1)$ mode is associated with the radial motion of carbon atoms and is more sensitive to intramolecular processes, which, in some cases, can lead to a distortion of the fullerene structure, as was observed for a number of compounds in the experiments. For example, according to the x-ray diffraction data obtained by Penicaud *et al.*

Table 1. Frequencies ν (cm^{-1}) of the absorption bands assigned to the $T_u(1)$ – $T_u(4)$ vibrations in the IR spectra of the C_{60} fullerene and $\text{Me}_n\text{C}_{60}(\text{THF})_x$ ($\text{Me} = \text{Li}, \text{Na}; n = 1\text{--}4, 6, 8, 12$) compounds

Compound	$T_u(1)$	$T_u(2)$	$T_u(3)$	$T_u(4)$
C_{60}	527	576	1183	1429
$\text{Li}_1\text{C}_{60}(\text{THF})_x$	516, 528	576	1183	1395
$\text{Li}_2\text{C}_{60}(\text{THF})_x$	516, 526	576	1183	1345
$\text{Li}_3\text{C}_{60}(\text{THF})_x$	–	575	1183	1345
$\text{Li}_4\text{C}_{60}(\text{THF})_x$	516, 527	576	1185	1345
$\text{Li}_6\text{C}_{60}(\text{THF})_x$	–	576	1185	1345
$\text{Li}_8\text{C}_{60}(\text{THF})_x$	–	575	1171	1345
$\text{Li}_{12}\text{C}_{60}(\text{THF})_x$	–	572	1171	1345
$\text{Na}_1\text{C}_{60}(\text{THF})_x$	528	579	1180	1372
$\text{Na}_2\text{C}_{60}(\text{THF})_x$	512, 528	576	1183	1355
$\text{Na}_3\text{C}_{60}(\text{THF})_x$	512, 528	574	1183	1350
$\text{Na}_4\text{C}_{60}(\text{THF})_x$	529	576	1182	1365
$\text{Na}_6\text{C}_{60}(\text{THF})_x$	528	576	1182	1352
$\text{Na}_8\text{C}_{60}(\text{THF})_x$	528	573	1183	1352
$\text{Na}_{12}\text{C}_{60}(\text{THF})_x$	528	573	1171	1355

[10], the fullerene spheroid in the $[(\text{Ph}_4\text{P})_2\text{I}]^+\text{C}_{60}^-$ compound turns out to be prolate along one axis and has diameters of 7.064, 7.064, and 7.106 Å. By contrast, the fullerene spheroid in the $[\text{PPN}^+]_2\text{C}_{60}^{2-}$ compound has three different diameters: 7.040, 7.106, and 7.126 Å [11]. Dahlke and Rosseinsky [12] carried out a neutron powder diffraction study of the CsC_{60} fulleride and revealed that the distortion of symmetry is more pronounced for the C_{60}^{4-} anion and less pronounced for the C_{60}^{3-} , C_{60}^{5-} , and C_{60}^{6-} anions as compared to the spherical C_{60} fullerene.

The vibrational modes $T_u(1)$ – $T_u(4)$ in the IR spectra of $\text{Li}_n\text{C}_{60}(\text{THF})_x$ compounds (Fig. 1) exhibit a more complex behavior than in the IR spectra of the $\text{Na}_n\text{C}_{60}(\text{THF})_x$ derivatives (Fig. 2). A comparison of the IR spectra of the $\text{Li}_n\text{C}_{60}(\text{THF})_x$ derivatives with the IR spectrum of the pure C_{60} fullerene shows that, for these derivatives, unlike the pure fullerene, the band associated with the $T_u(1)$ vibrations is characterized by a lower intensity and the $T_u(1)$ mode is split into two components (for $n = 1, 2, 4$). The measured splitting $\Delta\nu = 8\text{--}12 \text{ cm}^{-1}$ (for $n = 1, 2, 4$) indicates that the fullerene anions have a slightly distorted structure. Furthermore, as can be seen from Fig. 1, the splittings of the $T_u(1)$ mode for the $\text{Li}_1\text{C}_{60}(\text{THF})_x$, $\text{Li}_2\text{C}_{60}(\text{THF})_x$, and $\text{Li}_4\text{C}_{60}(\text{THF})_x$ compounds differ in character. It was revealed that the IR spectra of the fullerene derivatives with $n = 3, 6, 8$, and 12 do not contain the band assigned to the $T_u(1)$ vibrations. It is worth noting that the band

associated with the $T_u(1)$ vibrations was also not observed in the IR spectra of the K_nC_{60} compounds ($n = 3, 4, 6$) prepared by doping of fullerene films [13]. The band attributed to the $T_u(2)$ mode at a frequency of 576 cm^{-1} is almost not shifted at all, but its intensity increases significantly. The absorption band of the $T_u(3)$ mode is broadened by $\approx 5 \text{ cm}^{-1}$ for the derivatives with $n = 4, 6$, and 12 and is shifted (by $\approx 13 \text{ cm}^{-1}$) toward the long-wavelength range for the compounds with $n = 8$ and 12. According to Kamaras *et al.* [14], this behavior is explained by the increase in the intermolecular distance in the fullerides. The band observed at a frequency of 1429 cm^{-1} , which corresponds to the $T_u(4)$ mode of the pure C_{60} fullerene, is shifted to 1395 cm^{-1} for the $\text{Li}_1\text{C}_{60}(\text{THF})_x$ compound and to 1345 cm^{-1} (i.e., by 84 cm^{-1}) for the other lithium derivatives of the fullerene. The substantial shift and the increase observed in the intensity of the absorption band of the $T_u(4)$ mode with an increase in the charge of the fullerene anion are consistent with the charge–phonon mechanism [8]. The anomalously high intensity of the absorption band associated with the $T_u(4)$ mode for the compound with $n = 3$ is in agreement with the data obtained by Pichler *et al.* [13]. In [13], the considerable increase in the intensity of the band assigned to the $T_u(4)$ vibrations in the metallic phase ($n = 3$) was explained in terms of the effects brought about by both free charge carriers in the conduction band and the low-energy transitions $t_{1u} \rightarrow t_{1u^*}$. It was found that, for doped samples of K_3C_{60} , K_4C_{60} , and K_6C_{60} , the absorption band attributed to the $T_u(4)$ mode is also appreciably shifted to 1363, 1352, and 1341 cm^{-1} , respectively [13]. A comparison of these data with our results gives grounds to assume that the charge of the fullerene anion in the $\text{Li}_3\text{C}_{60}(\text{THF})_x$ compound is close to -3 .

It can be seen from the IR spectra that all the fullerene compounds of lithium and sodium contain tetrahydrofuran solvate molecules. This is indicated by the absorption bands at frequencies of 890, 916, and 1045 cm^{-1} . Note that the number of tetrahydrofuran solvate molecules in the $\text{Li}_n\text{C}_{60}(\text{THF})_x$ compounds is larger than that in the $\text{Na}_n\text{C}_{60}(\text{THF})_x$ compounds, because the charge density of the lithium ion is higher than the charge density of the sodium ion (the ionic radii of Li^+ and Na^+ are equal to 0.63 and 0.97 Å, respectively [5]). A comparison of the absorption bands of the coordinated tetrahydrofuran with the absorption bands of pure tetrahydrofuran (915 and 1070 cm^{-1}) suggests that there is a rather strong interaction between the tetrahydrofuran molecules and the metal cations. Therefore, it seems reasonable that the donor ability of lithium atoms should increase substantially and that a considerable part of the charge should be transferred to the fullerene fragment. In [4], it was assumed that, unlike the other metal atoms, the lithium atoms can be involved in covalent bonding with carbon atoms of the

fullerene fragment, which, in turn, should lead to a decrease in the charge of the fullerene anion. However, the IR spectra indicate a significant charge transfer from lithium atoms to the fullerene fragment.

The absorption bands in the IR spectra of the sodium fullerene compounds are less pronounced than those in the IR spectra of the $\text{Li}_n\text{C}_{60}(\text{THF})_x$ compounds. However, the $T_u(1)$ – $T_u(4)$ vibrational modes for these derivatives exhibit a similar behavior. Unlike the IR spectrum of the pure C_{60} fullerene, the IR spectra of the derivatives are characterized by an inverse intensity ratio of the bands at frequencies of 527 and 576 cm^{-1} , which correspond to the $T_u(1)$ and $T_u(2)$ modes. The splitting of the band at 527 cm^{-1} is insignificant for the compound with $n = 2$ and is somewhat larger for the compound with $n = 3$. In contrast to the spectra of the $\text{Li}_n\text{C}_{60}(\text{THF})_x$ compounds, the band at 527 cm^{-1} does not disappear in the spectra of the $\text{Na}_n\text{C}_{60}(\text{THF})_x$ compounds with $n = 3, 6, 8,$ and 12 ; however, its relative intensity considerably decreases when changing over from $n = 4$ to $n = 12$. The band of the $T_u(3)$ mode is broadened by $\sim 5 \text{ cm}^{-1}$ for the compounds with $n = 6, 8,$ and 12 and is shifted by $\sim 13 \text{ cm}^{-1}$ for the compound with $n = 12$. The band associated with the $T_u(4)$ vibrational mode is shifted, as is the case in the spectra of the $\text{Li}_n\text{C}_{60}(\text{THF})_x$ compounds (Table 1), but the relative intensity of this band is substantially less than that for the fullerene compounds with lithium. The intensity of the band attributed to the $T_u(4)$ vibrations in the $\text{Na}_3\text{C}_{60}(\text{THF})_x$ compound is not as anomalously high as in the case of the $\text{Li}_3\text{C}_{60}(\text{THF})_x$ compound. In this respect, it should be noted that no phase with metallic conductivity is found for the intercalated Na_3C_{60} fulleride [15].

According to the data available in the literature [16], the absorption band observed at a frequency of 785 cm^{-1} in the IR spectra of the lithium and sodium fullerene derivatives (except for the derivatives with $n = 1$ and 2) can be assigned to dimeric fullerene anions.

In this work, solid samples of $\text{Me}_n\text{C}_{60}(\text{THF})_x$ ($\text{Me} = \text{Li, Na}; n = 1, 3$) were also studied by EPR spectroscopy. As was shown earlier by Allemand *et al.* [17], the most characteristic spectrum is observed for fullerene radical monoanions. The specific features of this spectrum are as follows: (i) the g factor differs significantly from the g factor of the free electron, and (ii) the linewidth drastically increases with increasing temperature. Such a temperature dependence is not observed for the EPR spectra of aromatic radical anions with structures similar to the structure of the C_{60}^- anion. It is assumed that these features of the C_{60}^- radical anion are associated with both the high symmetry of the fullerene fragment and the degenerate molecular orbital occupied by an unpaired electron.

Table 2. Values of the g factor and EPR linewidth ΔH for $\text{Me}_n\text{C}_{60}(\text{THF})_x$ ($\text{Me} = \text{Li, Na}; n = 1, 3$) compounds

Compound	T, K	g factor	$\Delta H, \text{mT}$	$\frac{\Delta H(285 \text{ K})}{\Delta H(125 \text{ K})}$
C_{60}	120	2.0027	0.2	
C_{60}	290	2.0027	0.2	
$\text{Li}_1\text{C}_{60}(\text{THF})_x$	120	1.9990	2.700	
$\text{Li}_1\text{C}_{60}(\text{THF})_x$	285	1.9987	5.400	2
$\text{Na}_1\text{C}_{60}(\text{THF})_x$	125	1.9992	1.560	
$\text{Na}_1\text{C}_{60}(\text{THF})_x$	285	1.9990	2.360	1.5
$\text{Li}_3\text{C}_{60}(\text{THF})_x$	115	2.0023	0.280	
$\text{Li}_3\text{C}_{60}(\text{THF})_x$	285	2.0023	0.470	1.7
$\text{Na}_3\text{C}_{60}(\text{THF})_x$	125	2.0011	0.130	
$\text{Na}_3\text{C}_{60}(\text{THF})_x$	285	2.0013	0.327	2.5

It can be seen from Table 2 that the EPR linewidth for the $\text{Li}_1\text{C}_{60}(\text{THF})_x$ compound is maximum at a temperature of 285 K and decreases by a factor of 2 at 120 K. The linewidth for the $\text{Na}_1\text{C}_{60}(\text{THF})_x$ compound is approximately 2.2 times narrower than that for the $\text{Li}_1\text{C}_{60}(\text{THF})_x$ compound (at 285 K). This linewidth decreases by a factor of 1.5 with a decrease in the temperature to 125 K.

The linewidth for the C_{60}^{3-} radical anion in the $\text{Me}_3\text{C}_{60}(\text{THF})_x$ compounds is approximately one order of magnitude smaller than that for the C_{60}^- radical anion in the $\text{Me}_1\text{C}_{60}(\text{THF})_x$ derivatives for each metal. As the temperature decreases from 285 to 120 K, the values of ΔH for the $\text{Li}_3\text{C}_{60}(\text{THF})_x$ and $\text{Na}_3\text{C}_{60}(\text{THF})_x$ compounds decrease by factors of 1.7 and 2.5, respectively. These results are in good agreement with the data obtained by Rosseinsky [18].

The g factor for the C_{60}^- radical anion does not depend on the nature of the metal or on the temperature. A similar inference was previously made by Solodovnikov [19]. The g factors for the C_{60}^- and C_{60}^{3-} radical anions differ from each other. In the EPR spectra of the $\text{Me}_3\text{C}_{60}(\text{THF})_x$ compounds, the g factor for the C_{60}^{3-} radical anion depends on the nature of the metal and is independent of the temperature.

According to Paul *et al.* [1], the EPR signal with $g = 2.0027$ in the spectra of the fullerene derivatives is associated with the presence of oxygen-containing impurities (C_{120}O) in the sample. Note that a narrow signal of oxygen-containing impurities was also observed in the spectra of the compounds under investigation.

Thus, we can make the inference that the IR spectra of the lithium- and sodium-containing fullerene compounds synthesized in this work exhibit bands associated with the $T_u(1)$ – $T_u(4)$ vibrational modes. These

modes are characterized by a different behavior with an increase in n , and their evolution is most pronounced in the spectra of the $\text{Li}_n\text{C}_{60}(\text{THF})_x$ compounds. In particular, the intensity ratio of the $T_u(1)$ and $T_u(2)$ vibrational modes for the fullerene compounds differs from that for the pure C_{60} fullerene. The $T_u(1)$ mode can be split in different ways and is absent in a number of the compounds synthesized. The absorption band of the $T_u(4)$ vibrations is considerably shifted toward the long-wavelength spectral range, and its intensity is anomalously high for the $\text{Li}_3\text{C}_{60}(\text{THF})_x$ compound. These results, together with the data of EPR spectroscopy, provide a basis for further in-depth investigation into the physical characteristics of the prepared compounds with the use of magnetic susceptibility measurements and x-ray diffraction analysis.

In conclusion, it should also be noted that we observed the disproportionation reaction for the $\text{Li}_1\text{C}_{60}(\text{THF})_x$ compound. Holding this compound in a toluene–tetrahydrofuran solution (20 : 1) for one day (or longer) at room temperature leads to disproportionation with the formation of the C_{60} fullerene and the $\text{Li}_2\text{C}_{60}(\text{THF})_x$ derivative, which were isolated and characterized by IR spectroscopy. No similar reactions were observed for the other compounds. Chen *et al.* [20] studied the $\text{K}_1\text{C}_{60}(\text{THF})_x$ compound but did not reveal disproportionation of the fullerene radical anion. However, Trulove *et al.* [21] observed disproportionation of C_{60}^- when recording the UV spectra of a C_{60} fullerene suspension in dimethyl sulfoxide with tetrabutylammonium hexaphosphate.

ACKNOWLEDGMENTS

This work was supported by the grant from the President of the Russian Federation (project no. NSh-1652.2003.3), the International Scientific and Technical Center (project no. 2511), the federal scientific and technical program “Controlled Synthesis of Fullerenes and Other Atomic Clusters,” the program of the Presidium of the Russian Academy of Sciences “Fundamental Problems in the Physics and Chemistry of Nanosystems and Nanomaterials,” the program of the Presidium of the Russian Academy of Sciences “Controlled Synthesis of Compounds with Specified Properties and the Design of Functional Materials Based on These Compounds,” and the program of the Division of Chemistry and Materials Sciences of the Russian Academy of Sciences “Theoretical and Experimental Investigation of the Nature of Chemical Bonding and Mechanisms of the Most Important Chemical Reactions and Processes.”

REFERENCES

1. P. Paul, K.-C. Kim, D. Sun, P. Boyd, and C. Reed, *J. Am. Chem. Soc.* **124** (16), 4394 (2002).
2. S. Yang, C. Pettiette, J. Conceicao, O. Cheshnovsky, and R. Smalley, *Chem. Phys. Lett.* **139**, 233 (1987).
3. P. Boyd, P. Bhyrappa, P. Paul, J. Stinchcombe, R. Bolskar, Y. Sun, and C. Reed, *J. Am. Chem. Soc.* **117** (10), 2907 (1995).
4. U. Zimmermann, N. Malinowski, A. Burkhardt, and T. P. Martin, *Carbon* **33** (7), 995 (1995).
5. L. Cristofolini, M. Ricco, and R. Renzi, *Phys. Rev. B* **59** (3), 8343 (1999).
6. X. H. Chen, S. Taga, and Y. Iwasa, *Phys. Rev. B* **60** (6), 4351 (1999).
7. J. P. Hate, T. J. Dennis, H. W. Kroto, R. Taylor, A. W. Allaf, S. Balm, and D. R. Walton, *J. Chem. Soc., Chem. Commun.* 412 (1991).
8. M. J. Rice and Hau-Yong Choi, *Phys. Rev. B* **45** (17), 10173 (1992).
9. L. R. Narasimhan, D. N. Stoneback, A. F. Hebard, R. C. Haddon, and C. K. N. Patel, *Phys. Rev. B* **46** (4), 2591 (1992).
10. A. Penicaud, A. Perez-Benitez, R. Gleason, V. E. Munoz, and P. R. Escudero, *J. Am. Chem. Soc.* **115** (22), 10392 (1993).
11. P. Paul, Z. Xie, R. Bau, P. D. W. Boyd, and C. A. Reed, *J. Am. Chem. Soc.* **116** (9), 4145 (1994).
12. P. Dahlke and M. Rosseinsky, *Chem. Mater.* **14** (3), 1285 (2002).
13. T. Pichler, R. Winkler, and H. Kuzmany, *Phys. Rev. B* **49** (22), 15879 (1994).
14. K. Kamaras, D. B. Tanner, L. Forro, M. C. Martin, L. Mihaly, H. Klos, and B. Gotshy, *J. Supercond.* **8**, 621 (1995).
15. S. P. Solodovnikov, *Izv. Akad. Nauk, Ser. Khim.* 2190 (1995).
16. Y. Iwasa, K. Tanone, T. Mitani, A. Izuoka, T. Sugawara, and T. Yagi, *J. Chem. Soc., Chem. Commun.* 1411 (1998).
17. P.-M. Allemand, G. Szdanov, A. Kock, K. Khemani, F. Wudl, Y. Rubin, M. Alvarez, S. Anz, and R. Whetten, *J. Am. Chem. Soc.* **113** (7), 2780 (1991).
18. M. Rosseinsky, *J. Mater. Chem.* **5**, 1497 (1995).
19. S. P. Solodovnikov, *Izv. Akad. Nauk, Ser. Khim.* 669 (1998).
20. J. Chen, Zu-Eu Huang, R.-F. Cai, Q.-F. Shao, S.-M. Chen, and H.-J. Ye, *J. Chem. Soc. Chem. Commun.* 2177 (1994).
21. P. C. Trulove, R. T. Carlin, G. R. Eaton, and S. S. Eaton, *J. Am. Chem. Soc.* **117** (23), 6265 (1995).

Translated by O. Borovik-Romanova

FULLERENES AND ATOMIC CLUSTERS

Thermally Stimulated Desorption of C₆₀ and C₇₀ Fullerenes from Rigid-Chain Polyimide Films

A. O. Pozdnyakov*, B. M. Ginzburg*, T. A. Maricheva**,
V. V. Kudryavtsev**, and O. F. Pozdnyakov***

* Institute for Problems in Mechanical Engineering, Russian Academy of Sciences,
Bol'shoi pr. 61, Vasil'evskii Ostrov, St. Petersburg, 199178 Russia
e-mail: ao.pozd@mail.ioffe.ru

** Institute of Macromolecular Compounds, Russian Academy of Sciences,
Bol'shoi pr. 31, St. Petersburg, 199004 Russia

*** Ioffe Physicotechnical Institute, Russian Academy of Sciences,
Politekhnicheskaya ul. 26, St. Petersburg, 194021 Russia

Received October 6, 2003; in final form, November 27, 2003

Abstract—Polyimide–fullerene composite thin coatings are investigated using thermal desorption mass spectrometry in the temperature range 20–800°C. It is found that, at temperatures below the temperature of decomposition of the polymer matrix, thermally stimulated desorption of fullerene molecules is limited by the diffusion of fullerene molecules in the matrix. The diffusion coefficients and activation energies of diffusion of C₆₀ and C₇₀ fullerene molecules are determined from the experimental data on thermally stimulated desorption in the framework of several approaches. It is revealed that the diffusion of C₇₀ molecules in the polyimide matrix is more hindered than the diffusion of C₆₀ molecules in the same matrix. © 2004 MAIK “Nauka/Interperiodica”.

1. INTRODUCTION

Although fullerene-containing polymer systems have been intensively studied in recent years [1–4], there is virtually no data on the transport properties of fullerene molecules in polymer matrices. Fink *et al.* [5] made an attempt to determine the diffusion coefficient of C₆₀ fullerene molecules in a polyimide matrix. In [5], the diffusion coefficient of C₆₀ fullerene molecules at room temperature was estimated using neutron depth profiling of polyimide samples in which tracks were preliminarily produced by high-energy ions.

Thermal desorption mass spectrometry is highly sensitive to molecular flow in a gaseous phase. This makes it possible to obtain detailed information on the fullerene state in a polymer–fullerene system at an extremely low fullerene content (less than 1 wt %). This information cannot be derived by other extensively employed methods of thermal analysis (for example, thermal gravimetric analysis), because the sensitivity of these methods is considerably less than that of thermal desorption mass spectrometry. In our previous works [6–8], fullerene-containing polymer systems were investigated using thermal desorption mass spectrometry. It was shown that the interaction of macromolecules with fullerene molecules and the structural state of fullerene molecules in a polymer matrix can manifest themselves in the thermal desorption spectra of fullerene molecules and the products of destruction of the polymer matrices. Owing to the high thermal stability of polyimide,

the processes of thermally stimulated desorption of fullerene molecules can be thoroughly studied at temperatures below the decomposition temperature of the polymer matrix. In the present work, we investigated the thermally stimulated desorption of C₆₀ and C₇₀ fullerene molecules upon heating of an insoluble rigid-chain polyimide doped with these fullerenes.

2. SAMPLE PREPARATION AND EXPERIMENTAL TECHNIQUE

Polyimide–fullerene mixtures were prepared using a polyimide prepolymer, polyamic acid (PAA), which was synthesized from 3,3',4,4'-oxydiphthalic anhydride (ODPA), *p*-phenylenediamine (PPD), and 2,5-bis(4-aminophenyl)pyrimidine (APP). The components of the ODPA–PPD–APP copolyimide were taken in the molar ratio 100 : 50 : 50. A solution of PAA and the fullerene in dimethylacetamide was prepared according to the procedure described in our earlier work [8]. The purity of C₆₀ and C₇₀ fullerenes was higher than 98%. The calculated weight of the fullerene in the initial PAA solution amounted to 2% of the weight of the PAA synthesized, which corresponded to a fullerene concentration of $2.3 \times 10^{19} \text{ cm}^{-3}$ in the coating. The precipitate was filtered off, and the PAA–fullerene solutions were poured onto a stainless steel substrate (heater) with the aim of forming a coating. The samples were dried in air for 1 h. Then, at the second stage of producing the polyimide coating, the PAA–fullerene system was subjected

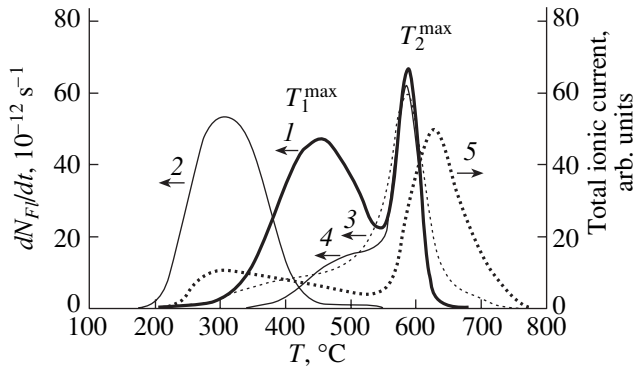


Fig. 1. Thermal desorption spectra of (1) C_{60} fullerene molecules from a polyimide- C_{60} composite coating $\sim 2 \mu\text{m}$ thick, (2) C_{60} fullerene molecules from a pure C_{60} thin layer (calculated thickness $\sim 10 \text{ nm}$) deposited on the surface of a pure polyimide, (3) C_{60} fullerene molecules from a polyimide- C_{60} composite coating prepared after reprecipitation of a PAA- C_{60} solution in toluene, and (4) C_{70} fullerene molecules from a polyimide- C_{70} composite coating $\sim 2 \mu\text{m}$ thick. (5) Typical temperature dependence of the total ionic current measured during heating of the coatings. Experimental conditions: pressure, 10^{-5} Pa ; heating rate, 7 K s^{-1} .

to thermal imidization. For this purpose, the PAA and PAA-fullerene films were heated in a vacuum chamber of the mass spectrometer to a temperature of $\sim 280^\circ\text{C}$, which resulted in the formation of polyimide-fullerene coatings. The calculated thickness of the coatings formed on the substrate was approximately equal to $2 \mu\text{m}$.

The processes of thermally stimulated desorption were investigated on an MX-1320 magnetic mass spectrometer (energy of ionizing electrons, 70 eV) equipped with a device for controlled heating of the samples. The samples were heated at a constant rate of 7 K s^{-1} . The pressure in the chamber of the mass spectrometer prior to the experiment was maintained at 10^{-5} Pa . The rates of formation of identified volatile products were calculated using the measured absolute sensitivity of the instrument to flow of fullerene vapors formed during heating of a thin fullerene film (with known weight) deposited on the surface of the preliminarily prepared polyimide coating (Fig. 1, curve 2). In our experiments on thermally stimulated desorption, we measured the intensity of the principal line of the mass spectrum of the corresponding fullerene (for the C_{60} and C_{70} fullerenes, $m/e = 720$ and 840 , respectively) simultaneously with the total ionic current, whose intensity is directly proportional to the rate of release of all volatile products from the analyzed sample and, hence, to the rate of mass losses for this sample.

3. RESULTS AND DISCUSSION

Analysis of the mass spectra recorded upon heating of the polyimide- C_{60} composite coating revealed that,

at temperatures in the range $\sim 200\text{--}500^\circ\text{C}$, the mass spectrum of the coating coincides with the mass spectrum of pure fullerene C_{60} (the energy of ionizing electrons is 70 eV [9]). The latter spectrum contains a principal line of singly charged C_{60}^+ ions ($m/e = 720$, where m is the ion mass and e is the ion charge) and a line of doubly charged C_{60}^{2+} ions ($m/e = 360$) with a lower intensity. At higher temperatures ($\sim 400\text{--}600^\circ\text{C}$), the mass spectrum involves a more complex set of lines with a ratio m/e in the range $\sim 300\text{--}800$, including the line assigned to C_{60}^+ ions with a ratio $m/e = 720$. The thermal desorption spectra were obtained by measuring the intensity of the line attributed to singly charged ions with a ratio $m/e = 720$.

The experimental data on thermally stimulated desorption are presented in Fig. 1. It can be seen from this figure that the temperature of desorption of C_{60} molecules from the composite film (Fig. 1, curve 1) is substantially higher (above 300°C) than that of desorption of C_{60} molecules from the surface of the polyimide substrate (Fig. 1, curve 2). The thermal desorption spectra exhibit maxima at temperatures of ~ 450 (T_1^{max}) and 590°C (T_2^{max}). As can be seen from the temperature dependence of the total ionic current (Fig. 1, curve 5), the desorption of the residual solvent and the imidization product (water) under the same experimental conditions occurs at lower temperatures ($T^{\text{max}} \sim 300^\circ\text{C}$).

The volume concentration of unbound fullerene molecules in the coating was calculated from the number of fullerene molecules desorbed at the low-temperature stage. According to thermal desorption mass spectrometry, the concentration of fullerene molecules in the unbound state is estimated at $\sim 1.5 \times 10^{19} \text{ cm}^{-3}$. This concentration is less than the calculated concentration of fullerene molecules in the initial solutions ($2.3 \times 10^{19} \text{ cm}^{-3}$). Therefore, it can be inferred that the fullerene molecules are contained in the precipitate formed upon treatment of the PAA-fullerene solutions. This is also confirmed by visual examination of the solutions in the visible spectral range. The solutions of PAA- C_{60} mixtures are violet in color, which is characteristic of fullerene C_{60} . In turn, the PAA solution is pale yellow in color. It is reasonable to assume that the change in color of the PAA- C_{60} solution is caused by the absorption of dissolved C_{60} fullerene molecules in the visible range. In order to verify that the PAA- C_{60} solution contains unbound C_{60} molecules, the solution was precipitated in toluene, which served as a precipitant for PAA and as a solvent for the C_{60} fullerene. This led to the formation of a precipitate. The toluene solution over the precipitate remained violet in color, which is characteristic of C_{60} solutions in toluene. It should be noted that, after redissolving in dimethylacetamide, the PAA- C_{60} precipitate formed in toluene changed to a

pale yellow color similar to the color of the PAA solution. These findings confirm the above inference that the initial PAA-C₆₀ solution contains C₆₀ fullerene molecules in the unbound state. The experimental data on thermally stimulated desorption from the PAA-C₆₀ coatings prepared from a solution of the PAA-C₆₀ precipitate formed in toluene indicate that, in this case, the desorption of fullerene molecules at a temperature T_1^{\max} (Fig. 1, curve 3) is considerably less intensive than the desorption of fullerene molecules from the coatings produced from the initial solutions (Fig. 1, curve 1).

Analysis of the thermal desorption spectra of the C₆₀ and C₇₀ fullerene-containing coatings (see curves 1 and 4 in Fig. 1, respectively) with the same calculated thickness also demonstrates that, for the C₆₀ and C₇₀ fullerenes, the temperatures T_1^{\max} differ significantly (the difference can be as large as ~50°C), whereas the temperatures T_2^{\max} are virtually identical. The low-temperature stage of the desorption is observed at temperatures that are too low to initiate thermal decomposition of the polyimide matrix (Fig. 1, curve 5) but are high enough for additional volatile products to be formed in the temperature range above ~570°C. This gives grounds to believe that the difference between the curves of thermal desorption of the C₆₀ and C₇₀ fullerene molecules at the low-temperature stage is associated with the properties and geometry of diffusing particles rather than with the processes of destruction and structure formation of the polyimide matrix. In particular, the latter processes lead to an increase in the thermal expansion coefficient of the ODP-PPD-APP copolyimide in the vicinity of the glass transition temperature (~320°C) [10]. Recall that C₇₀ fullerene molecules have the shape of an ellipsoid of revolution whose major and minor axes are equal to ~0.78 and ~0.7 nm, respectively, whereas C₆₀ fullerene molecules have the shape of a sphere ~0.7 nm in diameter. On this basis, the results obtained can be explained, for example, by the fact that the size of ellipsoidal C₇₀ fullerene molecules is greater than the size of spherical C₆₀ fullerene molecules.

The high-temperature stage of the desorption (T_2^{\max}) is observed at temperatures close to the temperature of the onset of thermal decomposition of polyimide macromolecules (Fig. 1, curve 5 for the temperature dependence of the total ionic current). However, the temperature T_2^{\max} corresponding to the high-temperature stage is somewhat lower than the temperature of the maximum in the curve for the total ionic current. In our opinion, the desorption of fullerene molecules at this stage is governed by complex processes of thermally stimulated destruction of the polyimide matrix. As was done in our earlier work [8], we assume that

strong chemical bonds between the polyimide macromolecules and the fullerene molecules begin to dissociate in the temperature range under consideration. The assumption regarding the formation of strong polyimide-fullerene bonds is in agreement with the results of the IR spectroscopic study performed in [10]. According to these data, the IR spectra of polyimide-C₆₀ films contain lines characteristic of nonmodified fullerene C₆₀ and additional lines that are absent in the spectrum of a pure polyimide. In [10], the additional lines revealed in the IR spectrum were attributed to the formation of polyimide-fullerene adducts. This assumption is indirectly confirmed by the higher kinematic viscosity of PAA-C₇₀ solutions as compared to the viscosity of PAA-C₆₀ solutions, because, as a rule, the viscosity of solutions increases with an increase in the density of an interpenetrating network of PAA macromolecules. Up to this point, the question as to the specific type of bonding involved remains open. Nonetheless, since the reactions of addition of fullerene molecules to amines are well understood [11], we can argue that fullerene molecules in the PAA-fullerene solution interact with terminal amine groups of the polyamic acid.

The diffusion coefficient of fullerene molecules in the polyimide matrix at the low-temperature stage of thermally stimulated desorption can be estimated from the relationship $\overline{\Delta x^2} \sim D\tau$, where D is the diffusion coefficient, $\overline{\Delta x^2}$ is the mean square of the diffusion displacement of a molecule, and τ is the diffusion time. However, in order to apply this relationship, it is necessary to know the value of $\overline{\Delta x^2}$ and the diffusion time τ . The diffusion time τ can be determined from experiments on thermally stimulated desorption in the course of isothermal annealing of specially prepared polyimide-fullerene composite films at a specified temperature and a specified time of exposure to this temperature. The experimental results demonstrate that the low-temperature stage of the thermally stimulated desorption in the polyimide-C₆₀ coatings annealed at a temperature of 310°C is completed in ~5 min. Let us now assume that the diffusion toward the ends of the sample is negligible. Under this assumption, all fullerene molecules can be considered to be completely desorbed from the coating only in the case when the last fullerene molecule traverses the distance from the coating-substrate interface to the polymer-vacuum interface, i.e., a distance equal to the thickness L of the coating. Note that the assumption regarding negligible diffusion toward the ends of the sample is quite reasonable, because the thickness of the coatings under investigation is substantially smaller than their length or width: the thickness-to-length (thickness-to-width) ratio is approximately equal to 10⁻⁴. From the experimental data ($D \sim L^2/\tau$) obtained at a temperature of 310°C, we determined the diffusion coefficient $D \sim 10^{-14}$ m²/s in the case of isothermal annealing of the polyimide-C₆₀

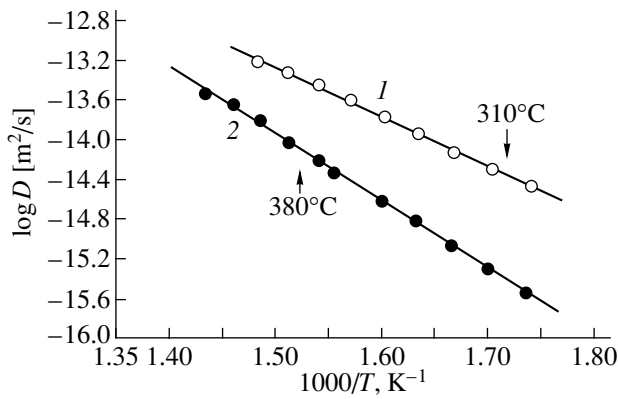


Fig. 2. Arrhenius curves plotted from the experimental curves of thermal desorption of (1) C_{60} and (2) C_{70} fullerene molecules. Arrows indicate the temperatures of isothermal experiments.

coating at 310°C. For the polyimide- C_{70} coating, the same diffusion coefficient of C_{70} fullerene molecules was obtained at a higher temperature (380°C).

It should be noted that the analysis of the diffusion process under consideration can be reduced to the problem of one-dimensional diffusion in a planar layer when the diffusant is desorbed from the outer surface of the layer. This model is a simplification of the real situation and involves a number of assumptions. These assumptions are as follows: (i) the diffusion mechanism remains unchanged during the experiment, and (ii) the diffusion coefficient is not anisotropic. Moreover, it is assumed that, at the initial instant of time, the fullerene concentration $c(x, 0)$ smoothly varies across the coating from a maximum at the coating-substrate interface to a minimum at the coating-vacuum interface. The temperature dependence of the diffusion coefficient can be represented by the relationship used in the free volume model of diffusion in bulk polymers: $D = D_0 \exp(-u/RT)$, where u is the activation energy of diffusion, T is the absolute temperature, and R is the gas constant. Then, at the low-temperature stage, the distribution of the fullerene concentration over the coating thickness in the course of linear heating can be parameterized (with respect to the coating thickness L , the heating rate β , and other possible parameters) using the solution to the equation of the second diffusion law [12]:

$$c(x, t) = \frac{2}{L} \sum_{k=0}^{\infty} \exp\left[-\frac{k^2 \pi^2}{L^2} \int_0^t D dt\right] \sin(k\pi x/L) \times \int_0^L c(x, 0) \sin(k\pi x/L) dx. \quad (1)$$

Here, x is the spatial coordinate along the direction perpendicular to the coating-vacuum interface, t is the time, and D is the diffusion coefficient, which is equal

to $D_0 \exp[-u/R(T_0 + \beta t)]$ under the conditions of our experiment.

In order to determine the initial approximations for u and D_0 (the thickness L was taken equal to the calculated thickness of the coating), we applied the approach proposed by Zholnin and Zaluzhnyi [12], according to which the diffusion coefficient D can be obtained using only the first term in expansion (1). Hence, the diffusion coefficient D can be written in the form

$$D = -(L/\pi)^2 (dN_{FI}/dt)/N_{FI}, \quad (2)$$

where dN_{FI}/dt is the desorption rate of fullerene molecules at a given temperature and N_{FI} is the number of fullerene molecules in the coating at this temperature, which is determined by integrating the corresponding portion of the experimental curve. The portions corresponding to the low-temperature stages in the experimental curves of thermal desorption of C_{60} and C_{70} fullerene molecules (Fig. 1) were recalculated according to expression (2). As a result, we obtained the dependences shown in Fig. 2. It can be seen that these dependences exhibit an Arrhenius behavior and are linear over a wide range of temperatures. The activation energies of diffusion of C_{60} and C_{70} fullerene molecules were determined using linear regressions of the temperature dependences of the diffusion coefficient and amounted to ~ 90 and ~ 130 kJ/mol, respectively. The diffusion coefficient D obtained by extrapolating the Arrhenius dependence to room temperature is approximately equal to 10^{-22} m²/s for C_{60} fullerene molecules in neat polyimide. This coefficient is substantially smaller than the diffusion coefficient $D \sim 10^{-17}$ m²/s determined in [5] from experimental data on the diffusion of C_{60} fullerene molecules in irradiated polyimide. This difference can be explained in terms of considerable loosening of the polyimide structure subjected to treatment with high-energy ions. The diffusion coefficients D calculated from relationship (2) are in good agreement with those obtained from the results of the aforementioned isothermal experiments (the temperatures of the isothermal experiments are indicated by arrows in Fig. 2). However, it should be kept in mind that, in the framework of our approach, the initial concentration distribution $c(x, 0)$ of fullerene molecules over the coating thickness remains unknown, because the sample was preliminarily heated to 280°C during imidization. This heat treatment can disturb the initial uniform distribution of fullerene molecules in the coating. Closer examination of the structure of the coatings with the aim of refining the activation energies of diffusion will be performed in further investigations.

The activation energy of diffusion of fullerene molecules in the polyimide matrix, which was determined within the above approaches, fits well the linear extrapolation (to the diameter of the C_{60} fullerene molecule) of the dependence of the activation energy for the penetration of gases and vapors through the KaptonTM

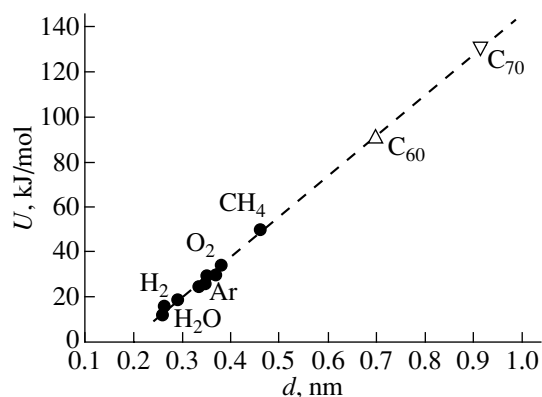


Fig. 3. Linear extrapolation (to the diameter of the C₆₀ molecule) of the dependence of the activation energy for the penetration of gases and vapors [13] through the Kapton™ polyimide sample on the molecular diameter of diffusing particles.

polyimide sample on the molecular diameter of diffusing particles (see the monograph by Ohya *et al.* [13]). Actually, for the C₆₀ fullerene, the molecular diameter is approximately equal to 0.7 nm; in this case, the activation energy is estimated at ~90 kJ/mol (Fig. 3). This result is in satisfactory agreement with the activation energy determined from the linear regression of the Arrhenius dependences for the ODP-PPD-APP copolyimide.

It should be noted that, on the molecular level, the nonspherical shape of C₇₀ fullerene molecules can lead to diffusion anisotropy (a decrease in the probability of hopping along one of the spatial coordinates). Consequently, the mean diffusion rate also decreases. This can be taken into account by introducing the effective diameter d of diffusing particles. It is seen from Fig. 3 that, for the C₇₀ molecule, unlike the C₆₀ molecule, the effective diameter d exceeds its maximum linear size (~0.78 nm) and is approximately equal to 0.92 nm.

4. CONCLUSIONS

Thus, the thermally stimulated desorption of fullerene molecules from polyimide–fullerene composite films was investigated. The diffusion coefficients of C₆₀ and C₇₀ fullerene molecules in a polymer matrix were determined and compared.

ACKNOWLEDGMENTS

This work was supported by the Division of Physical Sciences of the Russian Academy of Sciences in the framework of the “New Materials and Structures” program.

REFERENCES

1. G. P. Karpacheva, *Vysokomol. Soedin., Ser. C* **42** (11), 1974 (2000).
2. Yu. F. Biryulin, V. S. Vikhnin, and V. N. Zgonnik, *Fiz. Tverd. Tela (St. Petersburg)* **42** (1), 188 (2000) [*Phys. Solid State* **42**, 197 (2000)].
3. V. N. Zgonnik, L. V. Vinogradova, E. Yu. Melenevskaya, K. Yu. Amsharov, O. V. Ratnikova, Yu. F. Biryulin, A. V. Novoselova, and P. N. Lavrenko, *Fiz. Tverd. Tela (St. Petersburg)* **44** (4), 592 (2002) [*Phys. Solid State* **44**, 615 (2002)].
4. V. K. Koltover, T. A. Parnyuk, V. P. Bubnov, E. É. Laukhina, Ya. I. Éstrin, and É. B. Yagubskii, *Fiz. Tverd. Tela (St. Petersburg)* **44** (3), 506 (2002) [*Phys. Solid State* **44**, 529 (2002)].
5. D. Fink, R. Klett, C. Mathis, J. Vacik, V. Hnatowicz, and L. T. Chadderton, *Nucl. Instrum. Methods Phys. Res. B* **100**, 69 (1995).
6. A. O. Pozdnyakov, B. M. Ginzburg, O. F. Pozdnyakov, and B. P. Redkov, *Zh. Prikl. Khim. (Leningrad)* **73** (1), 134 (2000).
7. A. O. Pozdnyakov, O. F. Pozdnyakov, B. P. Redkov, V. N. Zgonnik, E. Yu. Melenevskaya, L. V. Vinogradova, and B. M. Ginzburg, *Pis'ma Zh. Tekh. Fiz.* **22** (18), 57 (1996) [*Tech. Phys. Lett.* **22**, 759 (1996)].
8. A. O. Pozdnyakov, B. M. Ginzburg, O. F. Pozdnyakov, B. P. Redkov, T. A. Maricheva, V. N. Artem'eva, and V. V. Kudryavtsev, *Pis'ma Zh. Tekh. Fiz.* **26** (17), 46 (2000) [*Tech. Phys. Lett.* **26**, 775 (2000)].
9. L. Dunsch, U. Kirbach, and K. Klostermann, *J. Mol. Struct.* **348**, 381 (1995).
10. A. O. Pozdnyakov, V. V. Kudryavtsev, and K. Friedrich, *Wear* **254**, 501 (2003).
11. A. Hirsch, *The Chemistry of Fullerenes* (Thieme, Stuttgart, 1994).
12. A. G. Zholnin and A. G. Zaluzhnyi, *Poverkhnost*, No. 10, 33 (1986).
13. H. Ohya, V. V. Kudryavtsev, and S. I. Semenova, *Polyimide Membranes—Applications, Fabrications, and Properties* (Kodansha, Tokyo, 1996).

Translated by O. Borovik-Romanova

**FULLERENES
AND ATOMIC CLUSTERS**

Conductance of a Single-Wall Carbon Nanotube in a One-Parameter Tight-Binding Model

S. S. Savinskiĭ and A. V. Belosludtsev

Udmurt State University, Krasnoarmeĭskaya ul. 71, Izhevsk, 426034 Russia

Received July 23, 2003; in final form, December 4, 2003

Abstract—The dependence of current–voltage characteristics of single-wall nanotubes on their radius and chirality is studied theoretically. It is shown that the conductance of a single-wall nanotube at low voltages can assume discrete values equal to zero for a dielectric tube and $4(e^2/h)$ for a conducting tube (e is the electron charge, h is the Planck constant). The current–voltage characteristic of a nanotube exhibits kinks related to the discreteness of the electron spectrum. The behavior of the conductance of the nanotube at zero temperature is analyzed in a quantizing longitudinal magnetic field that changes the type of tube conduction. In a magnetic field, the conductance of a dielectric tube at low voltages can assume a value of $2(e^2/h)$ in the region where the tube becomes conducting. In a weak magnetic field, a conducting tube becomes dielectric with an energy gap depending on the magnitude of the magnetic field. The conductance of a carbon nanotube is calculated as a function of the temperature and longitudinal magnetic field. © 2004 MAIK “Nauka/Interperiodica”.

1. INTRODUCTION

It is known that the conductance of a quantum wire can assume discrete values determined by the number of transverse modes occupied by electrons, which act as quantum channels for the current flow. Experimentally, these channels can be observed if the electron wavelength is comparable to the transverse size of the wire when the value of eV (e is the electron charge, V is the potential difference between the ends of the wire) is of the order of the distances between discrete electron energy levels (see, e.g., [1]). In a single-wall nanotube treated as a quantum wire, the discrete electron states with different values of the magnetic quantum number are analogous to transverse modes. Accordingly, the conductance of the nanotube can also assume discrete values. However, for this effect to be observed experimentally, the tube must be of sufficiently small radius, since the energy distance between quantum electron states is inversely proportional to the tube radius squared.

A geometrically ideal carbon tube can be represented as a cylindrical surface consisting of closely packed carbon “benzene rings” (without hydrogen atoms). Tubes with a length of up to one micron and a diameter that is hundreds of times smaller than the length were experimentally studied. It has been found that the geometrical orientation of carbon rings on the tube surface determines whether the tube is a dielectric or a conductor. This important property may make such tubes attractive candidates for applications in nanoelectronics. In this paper, we theoretically study the current–voltage characteristic of an arbitrary ideal single-wall carbon nanotube under the assumption that the system is in thermodynamic equilibrium. A simple geometrical model for calculating the carbon nanotube

conductance is suggested. In this model, we define a zone of nonequivalent electron quantum states, which is analogous to the Brillouin zone for crystalline solids. In calculating the current–voltage characteristic of the tube numerically, we use the ballistic approximation, in which the electron free path is assumed to be much greater than the tube size. Analogous calculations were performed for carbon nanotubes with the simplest “zig-zag” and “armchair” symmetries in theoretical study [2], where it was shown that, at zero temperature and low voltages, the conductance of the tube can assume discrete values that are multiples of e^2/h (h is the Planck constant).

Interest has been expressed in studying carbon nanotubes for several reasons: first, their high strength and the large values of their elastic moduli, which are actually equal to the elastic moduli of the graphite plane; second, the wide range of variation of the band gap in the π -electron spectrum (from zero to several electronvolts, depending on the tube radius and chirality); and, third, the high capillary and adsorption characteristics of the tube. Therefore, one might expect carbon nanotubes to find application in nanoelectronics and nanomechanical devices and as selective molecular adsorbates. Theoretical and experimental studies on the properties of carbon nanotubes are described in [3–6].

2. GEOMETRICAL STRUCTURE AND THE π -ELECTRON ENERGY SPECTRUM OF A CARBON TUBE

A carbon nanotube can be represented as a graphite sheet rolled into a cylindrical surface. Accordingly, we choose two perpendicular vectors \mathbf{C} and \mathbf{L} on the graphite sheet (Fig. 1). The vector \mathbf{C} connects two lat-

tice sites determined by basis vectors \mathbf{a}_1 and \mathbf{a}_2 , and the vector \mathbf{L} determines the length of the carbon nanotube. The vectors \mathbf{C} and \mathbf{L} define a rectangle on the graphite plane. The procedure of gluing this rectangle identifies points that lie on opposite sides of the rectangle and are separated by the vector \mathbf{C} . After gluing, the rectangle becomes a finite cylindrical surface and the basis vectors \mathbf{a}_1 and \mathbf{a}_2 become screw translations on the cylinder, which has radius $R = |\mathbf{C}|/2\pi$ (R is the nanotube radius).

We note that the basis vectors on the graphite sheet determine a unit cell with two carbon atoms and are equal in magnitude, $|\mathbf{a}_1| = |\mathbf{a}_2| = \sqrt{3}a_0$, where $a_0 = 1.42 \text{ \AA}$ is the distance between two nearest neighbor carbon atoms in graphite. After gluing a cylindrical surface with an infinite generatrix length, the basis vectors become operators of screw rotations, which are characterized by a translation along the cylindrical surface and the rotation angle; for example, for the vector \mathbf{a}_1 , these quantities are given by $\Delta\phi_1 = (\mathbf{a}_1\mathbf{C})/R$ and $\Delta z_1 = (\mathbf{a}_1\mathbf{L})/|\mathbf{L}|$. Analogous expressions can also be written for the other basis vector. Thus, the two operators of screw rotations on a carbon nanotube generate a symmetry group of the tube and there are two carbon atoms per unit cell of the tube.

The vector \mathbf{C} on the graphite layer is specified by two numbers (i_1, i_2) : $\mathbf{C} = i_1\mathbf{a}_1 + i_2\mathbf{a}_2$. These integers (i_1, i_2) are called chirality indices of the carbon nanotube, since they determine the angle at which the graphite layer is rolled (this angle is denoted by ϕ in Fig. 1). The radius and the chirality angle are easily expressed in terms of the chirality indices

$$R = \frac{\sqrt{3}a_0}{2\pi} \sqrt{i_1^2 - i_1i_2 + i_2^2}, \quad \tan\phi = \frac{\sqrt{3}i_2}{2i_1 - i_2},$$

and the parameters of the two operators of screw rotation take the form

$$\begin{aligned} \Delta\phi_1 &= \frac{\sqrt{3}a_0}{R} \cos\phi, \\ \Delta\phi_2 &= \frac{\sqrt{3}a_0}{R} \left(\cos\frac{\pi}{6} \sin\phi - \sin\frac{\pi}{6} \cos\phi \right), \\ \Delta z_1 &= -\sqrt{3}a_0 \sin\phi, \\ \Delta z_2 &= \sqrt{3}a_0 \left(\cos\frac{\pi}{6} \cos\phi + \sin\frac{\pi}{6} \sin\phi \right). \end{aligned}$$

The parameters of operators (1) are involved in the spectrum of π -electron quantum states of the carbon tube, which depends on two quantum numbers (m, k) , where $m = 0, \pm 1, \pm 2, \dots$ is the magnetic quantum number and $\hbar k$ is the electron quasimomentum along the nanotube axis. In the tight-binding approximation, the

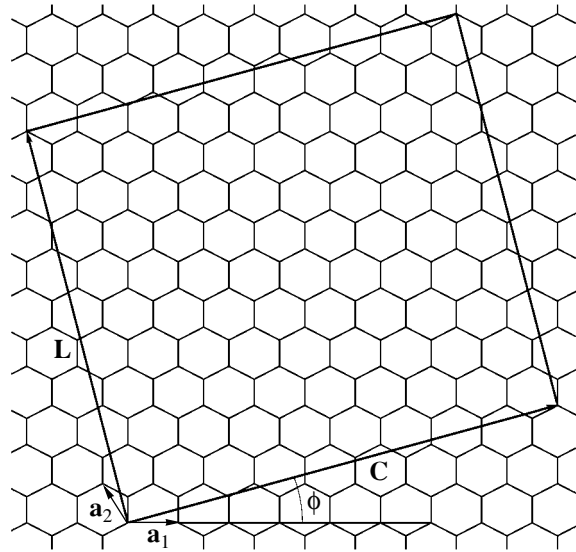


Fig. 1. Fragment of a graphite plane. \mathbf{a}_1 and \mathbf{a}_2 are basis vectors of the unit cell, \mathbf{C} is the vector generating the cylindrical nanotube, \mathbf{L} determines the tube length, and ϕ is the chirality angle.

energy of π electrons in a state with quantum numbers (m, k) (disregarding spin) is

$$\begin{aligned} E_{m,k}^{\pm} &= E^0 \pm |H_{m,k}|, \\ H_{m,k} &= \beta (1 + \exp(-im\Delta\phi_2 - ik\Delta z_2)) \\ &\quad \times (1 + \exp(-im\Delta\phi_1 - ik\Delta z_1)), \end{aligned} \quad (2)$$

where $(\Delta\phi_1, \Delta z_1)$ and $(\Delta\phi_2, \Delta z_2)$ are given by Eqs. (1); β is a parameter equal to a matrix element of the Hamiltonian, which can be expressed in terms of the wave functions of electrons of the nearest neighbor atoms (in what follows, we set $\beta = 2.2 \text{ eV}$); the \pm signs in Eq. (2) refer to two energy bands; and E^0 is the binding energy of a π electron in a free carbon atom, whose value does not affect the subsequent calculations (we set it equal to zero in what follows).

In the literature, other forms of expression (2) are also used [3] and the value of the parameter β is varied from 2 to 3 eV (see, e.g., [7, 8]). We note that a more correct expression for the electronic spectrum in the tight-binding approximation contains three different parameters (rather than one parameter β), which are equal to the matrix elements relating an atom to its three nearest neighbors. The values of these parameters depend on the tube radius and chirality [9]. Actually, formula (2) is valid for a nanotube of large radius.

Phenomenological parametric models are also used in the literature to calculate the electronic spectrum of π electrons on the cylindrical surface of a tube with inclusion of spin-orbit interaction [10]; however, these models do not take into account the dependence of the spectrum on the nanotube symmetry. Apparently, final choice of the most adequate model of the π -electron

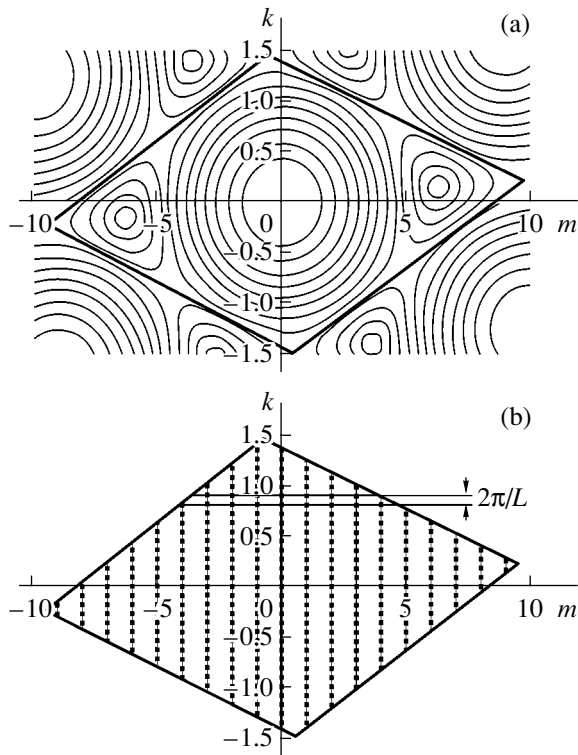


Fig. 2. Nonequivalent quantum states and constant-energy curves for π electrons of a carbon (10, 9) nanotube. (a) Constant-energy curves on the (m, k) plane, and (b) discrete quantum states of a finite-length carbon nanotube.

energy spectrum and of the numerical values of the spectral parameters can be made after accumulating quantitative experimental data on the electronic characteristics of single-wall nanotubes of arbitrary chirality.

Thus, using the one-parameter formula (2) for the π -electron energy spectrum of a single-wall carbon nanotube, the nanotube symmetry can be taken into account in the simplest way.

The electron energy given by Eq. (2) is a doubly periodic function of quantum numbers m and k , whose nonequivalent values satisfy the inequalities

$$\begin{aligned} |m\Delta\varphi_1 + k\Delta z_1| &\leq \pi, \\ |m\Delta\varphi_2 + k\Delta z_2| &\leq \pi. \end{aligned} \quad (3)$$

The set of quantum states (m, k) for which inequalities (3) are satisfied lies within a tetragon on the (m, k) plane. This tetragon is analogous to the Brillouin zone used to describe the electronic spectra of crystals. In Fig. 2a, constant-energy curves on the (m, k) plane are plotted for the (10, 9) nanotube and the corresponding band of nonequivalent states is shown. The energy reaches a maximum at the band center; at singular points (m_*, k_*) in the zone, the energy of each branch of spectrum (2) vanishes.

The choice of the zone is not unique; it follows from Fig. 2a that this zone can be chosen either as another

equivalent tetragon or as a hexagon whose vertices are located at the points where energy (2) is zero.

For a finite-size nanotube, the quantum number k assumes discrete values that are multiples of $2\pi/L$. As an example, Fig. 2b shows the zone for a finite (10, 9) tube; the allowed quantum states (m, k) within this zone are indicated by points.

At zero temperature, π electrons occupy all allowed states of the zone with energies corresponding to the lower branch of spectrum (2); therefore, the chemical potential is equal to the energy E^0 , which is taken to be zero.

Singular points (m_*, k_*) of the zone can be found using the following arguments. It follows from Eq. (2) that the electron energy is equal to the product of the parameter β and the modulus of a complex number that is the sum of three complex numbers (the first of them is unity, and the moduli of the second and third numbers are also equal to unity). This sum vanishes if the phases of the second and third complex numbers are $\pm 2\pi/3$; the corresponding conditions can be written as two systems of linear equations for m and k :

$$\begin{cases} m\Delta\varphi_1 + k\Delta z_1 = \pm \frac{2}{3}\pi \\ m\Delta\varphi_2 + k\Delta z_2 = \pm \frac{2}{3}\pi. \end{cases} \quad (4)$$

We note that the two systems of equations (4) differing in the sign (+ or -) in the right-hand side can be obtained using the substitution $m \rightarrow -m$ and $k \rightarrow -k$. The solutions to system (4) satisfying inequalities (3) are symmetric with respect to the origin and have the form

$$\begin{aligned} m_* &= \pm \frac{2\pi}{3} \frac{\Delta z_1 - \Delta z_2}{\Delta\varphi_2\Delta z_1 - \Delta\varphi_1\Delta z_2}, \\ k_* &= \pm \frac{2\pi}{3} \frac{-\Delta\varphi_1 + \Delta\varphi_2}{\Delta\varphi_2\Delta z_1 - \Delta\varphi_1\Delta z_2}. \end{aligned} \quad (5)$$

By substituting the coordinates of screw rotation operators (1) into Eqs. (5), we express m_* and k_* in terms of the nanotube chirality indices:

$$m_* = \pm \frac{i_1 + i_2}{3}, \quad k_* = \pm \frac{2\pi}{3} \frac{i_1 - i_2}{a_0 \sqrt{i_1^2 - i_1 i_2 + i_2^2}}. \quad (6)$$

From Eq. (2), we can also find the dependence of the energy gap of a nanotube on its radius and chirality indices. With this aim, we calculate the derivative of the electron energy with respect to the magnetic quantum number at the point (m_*, k_*) of the zone and estimate the shortest energy distance from the point m_* to the nearest curve (Fig. 3a) with an integer magnetic quantum number m using linear interpolation of the electron energy in the vicinity of this point. In this way, we

obtain the following formula for estimating the energy gap width:

$$\begin{aligned} \Delta &= 2 \left| \frac{\partial H_{m,k}}{\partial m} \right| |m_* - m| \\ &= 2\beta |\Delta\phi_1 + (\Delta\phi_1 + \Delta\phi_2) \exp(-im_*\Delta\phi_1 - ik\Delta z_1)| \\ &\quad \times |m_* - m|. \end{aligned} \quad (7)$$

According to Eq. (7), if m_* is an integer, the gap width Δ vanishes and the corresponding tube is a conductor. It follows from Eq. (6) that this is possible if the sum of the tube indices is a multiple of three; otherwise, the quantity $|m_* - m|$ in Eq. (7) is equal to $1/3$. Thus, knowing the chirality indices and using Eq. (6), we can determine whether a carbon nanotube is conducting or insulating. Using Eq. (7), we can approximately estimate the energy gap for a dielectric tube, which is proportional to the angular parameters of the screw rotation operators and, according to Eq. (1), is inversely proportional to the tube radius. In the literature, a rough formula for estimating the nanotube energy gap $\Delta \approx \beta \frac{a_0}{R}$ was discussed [2]; this formula follows from Eq. (7).

3. CONDUCTANCE OF AN IDEAL NANOTUBE

Let contacts be attached to the left and right ends of the tube, and let a voltage V be applied to the contacts. We assume that the electron mean free path is greater than the nanotube size. In this case, electrons pass from one end of the tube to the other without scattering. If the system is in thermodynamic equilibrium, then we can assume that the difference in the chemical potentials at the left and right ends of the tube is eV ; therefore, the electron fluxes from the left and right ends of the tube are different, giving rise to electric current. We note that the chemical potential of a carbon nanotube does not depend on temperature due to the symmetry of the branches of energy spectrum (2).

The electron flux passing through an arbitrary cross section from any end of the tube is given by

$$J = \frac{2e}{\hbar L} \sum_{m,k} \frac{\partial E_{m,k}}{\partial k} f_{m,k}, \quad (8)$$

where $f_{m,k} = \left(1 + e^{\frac{\mu - E_{m,k}}{k_B T}} \right)^{-1}$ is the Fermi–Dirac function, k_B is the Boltzmann constant, and μ is the chemical potential, which is set equal to zero for one end of the tube and to eV for the other end; the summation is performed over the two branches of electron spectrum (2) for all values of m and k lying within the zone of allowed states in which the electron velocities are directed one way (for example, for the flux from the left

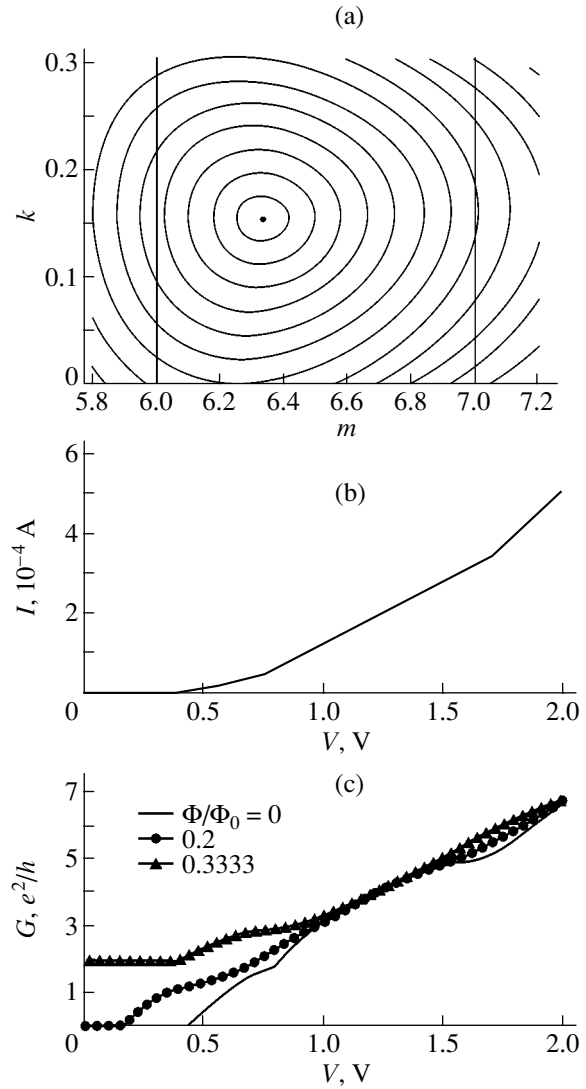


Fig. 3. Calculated current–voltage characteristic and conductance of a carbon (10, 9) nanotube. (a) Constant-energy curves near the (m_*, k_*) state with a step in energy of 0.1 eV, (b) the current–voltage characteristic, and (c) the conductance as a function of applied voltage at various values of the magnetic flux through a cross section of the tube.

end of the tube, we take into account the electrons whose velocities are directed to the right end); the factor of two before the sum accounts for the electron spin. Expression (8) allows a simple physical interpretation. Let us consider an arbitrary cross section of the tube and an arbitrary quantum electron state. An electron in the specified quantum state can pass across the specified cross section during a unit time if it is located in any cross section of the tube lying at a distance from the specified cross section that is numerically equal to the electron velocity; therefore, the probability of finding the electron at a given distance from the chosen cross section is equal to the ratio of the electron velocity to the total tube length. The Fermi–Dirac function in

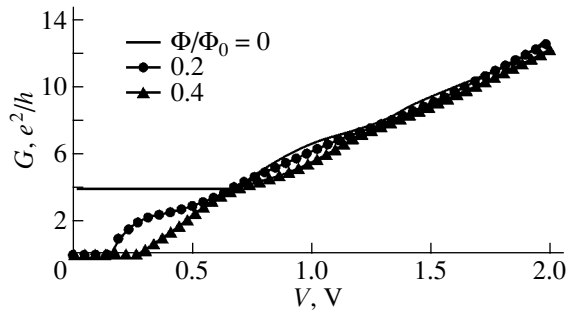


Fig. 4. Conductance of a carbon (20, 10) nanotube as a function of applied voltage at various values of the magnetic flux through a cross section of the tube.

Eq. (8) defines the occupation probability of the chosen quantum state. In the limit $L \rightarrow \infty$, the quantum number k assumes continuous values; hence, the summation over this quantum number can be replaced by integration over k ; for any fixed value of the discrete quantum number m , the integration limits are defined geometrically by the position of the line of allowed states on the (m, k) plane with respect to the zone boundaries (Fig. 2a). Consequently, formula (8) can be written as

$$J = \frac{2e}{h} \sum_{m,k} \frac{\partial E_{m,k}}{\partial k} \frac{2\pi}{L} f_{m,k} = \frac{2e}{h} \sum_m \int \frac{\partial E_{m,k}}{\partial k} f_{m,k} dk.$$

Expression (8) for the electron flux assumes the simplest form at zero temperature ($T = 0$). In this case, the Fermi–Dirac function can be represented as a step function of the form $f_{m,k} = \Theta(\mu - E_{m,k})$ and the electric current (which is equal to the difference in the electronic fluxes from the left and the right ends of the tube) is

$$I = J_L - J_R = \frac{2e}{h} \sum_m (eV - E_{\min}^m) \Theta(eV - E_{\min}^m), \quad (9)$$

where E_{\min}^m is the energy minimum of the positive branch of spectrum (2) for a given value of the magnetic quantum number m ; the sum in Eq. (9) is taken over the states with different values of the magnetic quantum number of the positive branch of spectrum (2) for which $E_{m,k} \leq eV$. For a conducting tube, one of the values of E_{\min}^m for $m = m_*$ vanishes, whereas for a dielectric tube $E_{\min}^m \geq \Delta/2$. Therefore, in a conducting tube, the current arises at arbitrarily low voltages between the ends of the tube, whereas in a dielectric tube the current appears only for voltages satisfying the inequality $eV \geq \Delta/2$. According to Eq. (9), the number of terms in the sum depends on the applied voltage and is greater than or equal to two for a conducting tube, whereas for a dielectric tube it is greater than or equal to zero.

In a dielectric tube, the number of terms in sum (9) is zero until the condition $eV \geq \Delta/2$ is satisfied. The

appearance of new terms in sum (9), related to the variation in the voltage V applied to the tube, changes the slope of the current–voltage characteristic of the nanotube (Fig. 3b).

An increase in the tube radius decreases the distance between the minimum energies E_{\min}^m for different values of m , thus resulting in an increase in the density of points at which the slope of the current–voltage characteristic changes. In the limit of large tube radii, the current–voltage characteristic of a nanotube has a parabolic form.

The above arguments on the summation rules in Eq. (9) are illustrated in Fig. 3a, where constant-energy curves in part of the region of nonequivalent values of the quantum numbers are plotted for a carbon (10, 9) nanotube. The energy step for constant-energy curves is taken to be 0.1 eV. The point in Fig. 3a corresponds to the values of (m_*, k_*) at which the electron energy vanishes, and the two straight lines determine the allowed quantum states for an infinitely long nanotube with $m = 6$ and 7. It follows from Fig. 3a that the curve corresponding to allowed states with $m = 6$ touches the 0.42-eV constant energy curve and that the line with $m = 7$ touches the 0.78-eV constant energy curve. Thus, at zero temperature, the electric current appears in the tube only at voltages $V \geq 0.42$ V; under these conditions, the channel with $m = 6$ opens first and then, at a voltage of $V = 0.78$ V, the second channel opens with $m = 7$. Accordingly, at temperature $T = 0$, kinks on the current–voltage characteristic of the (10, 9) nanotube are observed at voltages $V = 0.42$ and 0.78 V. Figure 3b shows the current–voltage characteristic numerically calculated from Eq. (9) for a carbon (10, 9) nanotube; kinks are visible at voltages $V = 0.42$ and 0.78 V.

From Eq. (9), we can easily obtain the conductance of a carbon nanotube at zero temperature:

$$G = \frac{I}{V} = \frac{2e^2}{h} \sum_m \left(1 - \frac{E_{\min}^m}{eV}\right) \Theta(eV - E_{\min}^m). \quad (10)$$

The summation rules in Eq. (10) are the same as those in Eq. (9). For a conducting nanotube, one of the values of E_{\min}^m for $m = m_*$ is zero and, at low voltages V , the sum in Eq. (10) has only two terms, each of which is equal to unity. Therefore, the conductance of a conducting tube is equal to $4(e^2/h)$ (Fig. 4), as was indicated in [2]. For a dielectric tube at low voltages, the number of terms in Eq. (10) is zero and the conductance of the tube is also zero; for voltages $eV \geq \Delta/2$, the tube becomes conducting and nonzero terms appear in the sum in Eq. (10).

If a magnetic field is applied parallel to the carbon nanotube axis, formula (2) for the energy spectrum remains unchanged, but the quantum number m in it has to be replaced by $m + \Phi/\Phi_0$, where $\Phi = \pi R^2 B$ is the magnetic flux through the cross section of the nano-

tube, $\Phi_0 = c\hbar/e$ is the magnetic flux quantum, c is the velocity of light in vacuum, and B is the magnetic induction. Accordingly, the value of m_* on the (m, k) plane at which energy (2) vanishes is displaced in a magnetic field. For a conducting tube, the displacement implies the emergence of a gap in the energy spectrum. The width of this gap can be estimated from Eq. (7), according to which the energy gap is proportional to the magnetic field.

In Fig. 3c, the conductance of the (10, 9) tube [calculated from Eq. (10)] is shown as a function of voltage at different values of the magnetic flux. At zero magnetic flux, the (10, 9) tube is dielectric with an energy gap of 2×0.42 eV; for a magnetic flux of $\frac{\Phi}{\Phi_0} = \frac{1}{3}$, the gap is closed and the tube becomes conducting. With a further increase in the magnetic field, a gap appears again and reaches a maximum value at $\frac{\Phi}{\Phi_0} = \frac{1}{2}$. A subsequent increase in the magnetic field results in a variation of the gap width, which is symmetric with respect to the magnetic flux $\frac{\Phi}{\Phi_0} = \frac{1}{2}$.

Figure 4 shows the voltage dependence of the conductance of a conducting carbon (20, 10) nanotube at zero temperature numerically calculated from formula (10) at different values of the magnetic flux through the cross section of the tube. If a magnetic field is switched on, the (20, 10) tube becomes dielectric (Fig. 4); the energy gap increases with magnetic flux Φ/Φ_0 and then, after reaching a maximum value at $\frac{\Phi}{\Phi_0} = \frac{1}{2}$, decreases with increasing magnetic flux and vanishes at $\Phi/\Phi_0 = 1$.

At nonzero temperatures, dielectric tubes become conducting if the condition $k_B T \sim \Delta$ is satisfied. Figure 5 shows the numerically calculated conductance of the carbon (210, 10) nanotube, which is a narrow-gap dielectric. The calculations were performed for low voltages and various temperatures and magnetic fields. The conductance was calculated using formula (8) for electrons going from the left-hand and right-hand ends of the tube. It follows from Fig. 5 that, at temperatures near 200 K, the conductance depends on the magnetic field only weakly and is a growing function of temperature.

All numerical calculations presented in Figs. 3–5 were performed for finite tubes of length $L = 10^5$ Å.

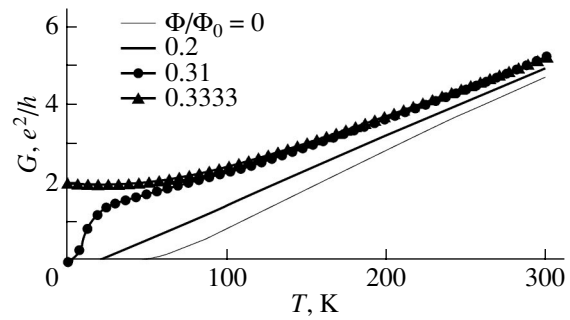


Fig. 5. Dependence of the conductance of a carbon (210, 10) nanotube on temperature and magnetic flux for vanishing voltage.

Our calculations of the temperature dependence of the conductance of single-wall carbon nanotubes are in qualitative agreement with the experimental data on the temperature dependence of the resistance of a bunch of multilayer nanotubes described in review [3].

REFERENCES

1. V. Ya. Demikhovskii and G. A. Vugalter, *Physics of Low-Dimensional Quantum Structures* (Logos, Moscow, 2000).
2. M. F. Lin and K. W.-K. Shung, *Phys. Rev. B* **51** (3), 7592 (1995).
3. A. V. Eletskiĭ, *Usp. Fiz. Nauk* **167** (9), 945 (1997) [*Phys. Usp.* **40**, 899 (1997)].
4. M. S. Dresselhaus, G. Dresselhaus, and P. C. Eklund, *Science of Fullerenes and Carbon Nanotubes* (Academic, New York, 1996).
5. A. V. Eletskiĭ, *Usp. Fiz. Nauk* **170** (2), 113 (2000) [*Phys. Usp.* **43**, 111 (2000)]; R. E. Smolli, *Usp. Fiz. Nauk* **168** (3), 323 (1998).
6. P. Avouris, *Acc. Chem. Res.* **35**, 1026 (2002).
7. A. V. Kotosonov and V. V. Atrazhev, *Pis'ma Zh. Éksp. Teor. Fiz.* **72** (2), 76 (2000) [*JETP Lett.* **72**, 53 (2000)].
8. A. A. Ovchinnikov and V. V. Atrazhev, *Fiz. Tverd. Tela (St. Petersburg)* **40** (10), 1950 (1998) [*Phys. Solid State* **40**, 1769 (1998)].
9. D. J. Klein, W. A. Seitz, and T. G. Schmalz, *J. Phys. Chem.* **97**, 1231 (1993).
10. L. I. Magarill, D. A. Romanov, and A. V. Chaplik, *Zh. Éksp. Teor. Fiz.* **113** (4), 1411 (1998) [*JETP* **86**, 771 (1998)].

Translated by I. Zvyagin